# UNIVERSITY OF CAPE TOWN

# FACULTY OF ENGINEERING AND THE BUILT ENVIRONMENT

# DEPARTMENT OF CIVIL ENGINEERING


**Biogenic Acid Corrosion of Sewer Concretes with Different Binders: In-situ and Model Studies, with Advancement of the Life Factor Prediction Method**

**By**

**Alice Titus Bakera**

Thesis Presented for the Degree of DOCTOR OF PHILOSOPHY in the Department of Civil Engineering

November 2022

Supervisor Emeritus Prof. Mark Alexander

Co-Supervisor Prof. Hans Beushausen

## Declaration

I, Alice Titus Bakera, hereby declare that the work on which this thesis is based is my original work (except where acknowledgements indicate otherwise) and that neither the whole work nor any part of it has been, is being, or is to be submitted for another degree in this or any other university. I authorise the University to reproduce for the purpose of research either the whole or any portion of the contents in any manner whatsoever.

Signature Signed by candidate Date 30 November 2022

## Abstract

Biogenic Acid Corrosion (BAC) is the biodeterioration of concrete caused by biological and chemical activities of bacteria that grow in an acidic environment. Such environments are typical in sewer systems, which collect wastewater from households, industries, and urban and stormwater runoff, and convey this to wastewater treatment plants. Since these sewer systems transport large volumes of sewage and are invariably buried under the ground, concrete pipes are customarily used. Concrete is widely known as a robust, flexible, and durable material in many aggressive environments, yet it can suffer from severe sewer corrosion.

Numerous techniques have been employed to eliminate or control the problem, including applying chemical or biological agents that decrease acid production, and surface treatment techniques that inhibit chemical attack and acid penetrability into the concrete. However, these techniques are expensive and variably effective, and some may lead to a loss of structural integrity and performance during the long service life of more than 50 years, due to a lack of long-term performance testing before they are introduced into the market.

The most reliable and affordable approach remains to modify concrete by incorporating readily available binders with high chemical and physicomechanical potential in resisting corrosion. Numerous studies have approached this technique using Portland Cement (PC) based systems with Supplementary Cementitious Materials (SCMs). However, other binder systems such as Calcium Aluminate Cement (CAC) and Calcium Sulpho-Aluminate cement (CSA) have been less studied, despite showing higher potential in suppressing biogenic corrosion.

Furthermore, most biogenic prediction models cannot effectively predict the performance of these binders in a sewer environment, especially when they are incorporated with different aggregates. For instance, the Life Factor Method (LFM), which is a common and often preferred method in sewer concrete design, is not formulated to enable the prediction of the corrosion rate of concrete comprising CAC, or specific PC-based systems with SCMs such as slag, fly ash, and silica fume.

The LFM model consists of two parts; the acid environment generation part, and the acid resistance part, also sometimes called the ‘material factor’, which defines the potential of concrete to resist corrosion due to acid. However, the current material factor in the model involves only an alkalinity factor (total calcium oxide content in concrete) as a significant resistance provider, while not considering other chemical compositions that significantly contribute to providing concrete with acid resistance.

A previous amendment of the model at the University of Cape Town (UCT) resulted in a 'material factor' approach that was highly empirical and complex, and therefore less practical and comprehensive in application. The model also could not handle modern binder systems in conjunction with aggregates, and the criteria for its refinement were somewhat self-contradictory.

Therefore, this study aimed to fundamentally re-think and improve the LFM model to cover a broader range of binder systems and aggregate types with their performance in different sewer conditions. Firstly, the deterioration mechanisms of concretes with different binder systems and different types of

aggregates were studied in different live sewer environments. Secondly, the mechanism of deterioration of the binder systems was further studied using a reactive transport modelling approach to understand the critical phases that govern the deterioration. Using the information from the first two goals, the LFM model was then improved and advanced to cover a wider range of binder systems, aggregate types, and sewer environments.

The study characterised the behaviour of three sewer sites in the Cape Town Metro (i.e., Langa Pump station (LPS) manhole, Northern Area Sewer manhole 19 (NAS M19) and manhole 54 (NAS M54)), monitoring techniques (i.e., visual observations, mass and thickness change, and concrete surface pH), The study also evaluated the influence of different concrete mixes using concrete microstructural analysis (Scanning Electron Microscopy (SEM), Quantitative Evaluation of Minerals (QEMSCAN), and X-Ray Diffraction (XRD) analysis), and reactive transport modelling (i.e., HYTEC modelling tool).

The concrete mixes were grouped into two batches: LH concrete and UCT concrete mixes. The LH concrete mixes consisted of four binder systems, i.e., a blend of 80% Sulphate Resisting Portland Cement and 20% Fly Ash (SRPC+FA), a similar blend with 11% iron-based additive (SRPC+FA+HC), a blend of 80% SRPC and 20% ground Limestone (SRPC+LS), and CSA. These mixes were cast with calcite and siliceous aggregates by Lafarge Holcim (LH) in Lyon, France and delivered to the UCT laboratory for sewer exposure. Before exposure, it was observed that the mixes exhibited significant compaction voids, but their condition was such to permit sewer exposure with the expectation of gathering useful information on these mixes. The UCT concrete mixes were prepared at UCT with local dolomite and siliceous aggregates, but using the same LH binders, i.e., SRPC+FA, SRPC+FA+HC, with some additional local binders, i.e. Portland cement blended with limestone (CEM II A-L), a blend of 50% CAC and 50% SRPC, CSA, and CAC. The LH concrete mixes were exposed to all three sites, while the UCT concrete mixes were exposed only to the LPS and NAS M19 after observing that NAS M54 was minimally aggressive. In terms of reactive transport modelling, only UCT concrete mixes were studied.

Regarding sewer characterisation, the LPS manhole has the most aggressive environment, followed by NAS M19 and NAS M54. The aggressivity of the LPS was due to its high $H_2S$ gas concentration and sewer hydraulic actions as it receives wastewater from a pump station. NAS M19 is located in the midsection of the sewer line and collects a mixture of domestic and industrial wastewater. It experiences occasional flooding, mainly during the winter season. NAS M54 is an upstream manhole with maximum gas concentrations below 10 ppm. Therefore, concrete mixes exposed at the LPS exhibited more severe corrosion than at NAS M19, while at NAS M54, only minor signs of corrosion were observed after two years. Also, it was observed that the aggressivity of the sewers varied with the seasons, with higher gas production during hot periods.

BAC monitoring and concrete microstructural analyses indicated that the Portland-based concretes (SRPC-based and CEM II A-L) experienced more severe deterioration compared to alumina-based concretes (CAC-based and CSA). CAC performed the best, followed by a blend of CAC+ SRPC concrete and then CSA, due to the formation of gibbsite and the high neutralisation potential provided by alumina-bearing phases over calcium oxide-bearing phases such as calcium silicate hydrates and portlandite. In terms of Portland-based concretes, it was observed that blending SRPC concrete with fly

ash improved the resistance potential over CEM II A-L, iron-based additives had little influence, and ground limestone in conjunction with calcite aggregates provided more acid-soluble material to neutralise the acid. In terms of aggregate performance, siliceous aggregates do not react with acid, and as a result, they eventually detach from the exposed surface. Dolomite and calcite aggregates dissolve in acid, and with magnesium carbonate, the rate of dolomite dissolution was slightly higher than calcite. The corrosion rate of the concrete depended on the relationship between the rate of deterioration of the cement matrix and the rate of deterioration of the aggregate matrix. Thus, concrete with similar cement and aggregate deterioration rates has a uniform corrosion front and a slower rate of corrosion, and vice versa.

The LFM model was modified with the information from the BAC monitoring and concrete microstructural analysis. The revised model has two key parameters: the sewer environment factor and the material resistance factor; the latter includes the acid neutralisation factor of the binder system and the aggregate reactivity factor. The sewer environmental factor evaluates the rate of acid generated on the exposed concrete surface while considering various factors associated with $H_2S$ gas adsorption and oxidation. The material resistance factor, on the other hand, evaluates the quantity of acid to be neutralised by a specific volume of exposed concrete while considering the influence of binder and aggregate. Ultimately, a ratio of sewer environmental and material resistance factors can assist in predicting and providing the corrosion rate of any concrete mix with any binder and aggregate types when subjected to a sewer environment. The corrosion rates predicted by this model correlated well with field-measured corrosion rates both in this study and in previous sewer studies at UCT. Therefore, this study provides engineers with a relatively simple tool for predicting the corrosion rate of sewer concrete, with recommendations for selecting the most durable sewer concrete mix designs.

## Acknowledgements

First, I want to praise and thank God, the Almighty, for providing me with countless blessings, wisdom, strength, and bravery to complete my PhD journey.

I sincerely thank my supervisor, Prof. Mark G. Alexander, for his patience, inspiration, guidance, and unwavering support of my research and academic endeavours. Without God sending him on my way, I am unsure where I would be.

I also to give thanks to my co-supervisor, Prof. Hans Beushausen, for putting his faith in me and pushing me beyond my comfort zone during my studies; and to Prof. Pilate Moyo, Head of Department and Co-Director of CoMSIRU, for his unwavering encouragement and guidance throughout my academic career.

I thank the Lafarge Holcim Innovation Center in Lyon, France for supporting and helping to fund this study. Special thanks to Dr Bruno Huet, for his assistance and training in modelling, and Samuel Meulenyzer, for his guidance, inspiration, and presence whenever required.

I owe a debt of appreciation to our French colleagues at the Laboratoire Matériaux et Durabilité des Constructions (LMDC)-INSA Toulouse; Dr Amr Aboulela, Prof Cédric Patapy, and Dr Matthieu Peyre-Lavigne) for collaborating with us. I specifically thank Professor Alexandra Bertron for her inspiration, guidance, and invaluable assistance.

I acknowledge support from the City of Cape Town, Water and Sanitation Department, specifically to Mr Anic Smit, for providing us with sewer sites; and to Mr Sakhiwo Nyatela, Mr Isaac Claassen, and Mr Demeon Eley, for their presence on-site whenever needed.

My sincere appreciation goes to Mr Alaster Goyns, of Pipeline Installation and Professional Engineering, for his invaluable assistance throughout this study; Prof Yunus Ballim of the University of the Witwatersrand, Johannesburg, for his inputs on advancing the LFM model; Miranda Waldron of the Electron Microscope Unit, Centre for Imaging and Analysis, UCT; and Andrea Molifie, Keshree Pillay, Rachel Cupido, Lorraine Nkemba, Sandeeran Govender and Russell Geland from the department of Chemical Engineering for assisting in conducting various analyses.

My sincere thanks go to the following organisations for their valuable support in one way or another: The Cement & Concrete South Africa); Sika South Africa (Pty) Ltd; Pretoria Portland Cement (PPC) Ltd; AfriSam South Africa (Pty) Ltd; The University of Dar es Salaam (Tanzania); and Imerys South Africa, specifically Tendayi Kaitano.

In addition, I thank everyone who works in the UCT Civil Engineering laboratories, namely, Nooredien Hassen, Chris Ceasar, Elvino Witbooi, Leonard Adams, Charles May, and the late Tahir Mohamed — for keeping me safe and providing valuable support both in and out of the laboratory. My fellow CoMSIRU students, naming a few, Ichebadu Amadi, Emmanuel Leo, Saarthak Surana, Areej Gamieldien, and Sean Alfred, for sharing moments and knowledge; and Civil Engineering administration staff; Gill Verster, Rowén Geswindt, and Zodwa Mcoteli, for their emotional and moral support.

Lastly, special thanks go to my family; my beloved father, Mr Titus Bakera; my lovely mother, Mrs Elda Rwechungura; my young sisters, Hope Titus and Livia Titus; and my friends, Narcia Bokenge, Suzanne Ghati Nyehita, Neema Kahabi, Hassan Mkala, Ansfrid Lekundayo and fJoseph Telemala for encouraging, motivating, and supporting me unceasingly throughout my life.

# Table of contents

# List of figures

# List of Tables

## Abbreviations and Notations

| | |
|---|---|
| AAC | Alkali-Activated Cements |
| Alag | Aluminate aggregate |
| ANN | Artificial Neural Network model |
| ASOB | Acidophilic Sulphide Oxidising Bacteria |
| BAC | Biogenic Acid Corrosion |
| BOD | Biochemical Oxygen Demand |
| CAC | Calcium Aluminate Cement |
| CAL | Calcareous aggregates |
| CCF | Crown Corrosion Factor |
| CEM II AL | Portland limestone cement denoted CEM II/A-L 52.5N |
| COD | Chemical Oxygen Demand |
| CSA | Calcium Sulpho-Aluminate cement |
| CSH | Calcium Silicate Hydrate |
| DI | Durability Index |
| DO | Dissolved Oxygen |
| FA | Fly Ash |
| HC | Iron-based additive or Hardcem® |
| HDPE | High-Density PolyEthylene |
| LC3 | Limestone Calcined Clay Cement |
| LFM | Life Factor Method |
| LH | Lafarge Holcim |
| LPS | Langa Pump station manhole |
| LS | Limestone |
| MIC | Microbially Induced Corrosion |
| NAS M19 | Northern Area Sewer manhole 19 |
| NAS M54 | Northern Area Sewer manhole 54 |
| NSOB | Neutrophilic Sulphide Oxidising Bacteria |
| OPI | Oxygen Permeability Index |
| PC | Portland Cement |
| PCCP | Prestressed Concrete Cylinder Pipes |
| PPC | Pretoria Portland Cement |
| PSD | Particle Size Distribution |
| PVC | PolyVinyl Chloride |
| QEMSCAN | Quantitative Evaluation of Minerals by Scanning Electron Microscopy |
| RCP | Reinforced Concrete Pipes |
| RH | Relative Humidity |
| SCMs | Supplementary Cementitious Materials |
| SIL | Siliceous aggregate |
| SOB | Sulphide Oxidising Bacteria |
| SRB | Sulphate Reducing Bacteria |
| SRPC | Sulphate Resisting Portland Cement |
| TCF | Turbulence Corrosion Factor |
| UCT | University of Cape Town |
| VES | Virginia Experimental Sewer |
| WSI | Water Sorptivity Index |

# CHAPTER 1. INTRODUCTION

## 1.1. Background

Rapid urbanisation and industrialisation require modern sanitation infrastructure that can handle enormous amounts of wastewater while ensuring a long service life, preferably more than 50 years. A sewer system is an essential element of modern sanitation infrastructure, which collects and conveys industrial and domestic wastewater and runoff from urban sources to wastewater treatment plants, where it is treated before being discharged into natural water bodies. It improves human health and living conditions by protecting them against water-borne diseases, unsanitary environments, and noxious odours. Also, it protects the environment from water, soil, and air pollution and toxins (Pikaar et al., 2014).

Underground piping systems, a significant part of the sewer system, collect wastewater from various sources and connect other sewer components, such as manholes, pumping stations, storm overflows, and screening chambers. These piping systems can be manufactured from plastic, vitreous clay, concrete, steel, or cast iron, among other materials. These materials are selected based on installation conditions, soil corrosivity, temperature, safety requirements, and cost.

Steel pipes are expensive and require regular maintenance owing to periodic restoration of anti-corrosive and waterproof coatings, to slow corrosion and prevent underground water contamination. Plastic pipe usage, such as PolyVinyl Chloride (PVC), High-Density PolyEthylene (HDPE), and Acrylonitrile-Butadiene-Styrene (ABS), is another example. However, they are often costly and susceptible to penetration and deterioration due to petroleum hydrocarbons in soil and ultraviolet rays. They also require specific bedding systems for flexibility and occasionally fail due to inadequate or improper support from the surrounding soil. Thus, concrete often emerges as the material of choice due to its intrinsic strength, adaptability, low cost, flexibility, and durability for most applications (EPA, 2000; Petit-Boix *et al.*, 2014; EPA, 2013).

Prestressed Concrete Cylinder Pipes (PCCP) and Reinforced Concrete Pipes (RCP) are the most common types of concrete pipe used in sewer systems. Under certain sewer conditions, both pipe systems are susceptible to severe deterioration, resulting in structural and functional failure within their service life. The deterioration is not only exhibited in the sewer pipe but also in the manholes and wastewater treatment plants (Pistor & Taylor, 1935). According to Kaempfer and Berndt (1999), 40% of the deterioration is attributed to Biogenic Acid Corrosion (BAC), while 60% is ascribed to inadequate structural design, construction, installation, and inadequate control and maintenance. If engineering experts are well-informed, 60% of the failure can be eliminated. However, the challenge remains to eradicate the 40%.

Biogenic acid Corrosion (BAC)- also known as Microbially Induced Corrosion (MIC) – is the biological activity of Sulphide Oxidising Bacteria (SOB) on the unsubmerged concrete surfaces, which produces acid that corrodes the concrete microstructure and the underlying steel reinforcement. A sewer pipe contains biodegradable organic matter with sulphates ($SO_4^{2-}$) compounds in a slime layer between the

submerged sewer concrete surface and wastewater, the so-called 'biofilm'. In favourable conditions of temperature and relative humidity (RH), and with insufficient dissolved oxygen, anaerobic reactions occur in the presence of Sulphate Reducing Bacteria (SRB) to reduce oxygen from the sulphate compounds. Consequently, Hydrogen sulphide ($H_2S$) and carbon dioxide ($CO_2$), the most corrosive gases, are produced (Wells, Melchers & Bond, 2009; Kiliswa, 2016).

Turbulent flow conditions and high velocities of some sewers facilitate the release of these gases to the sewer headspace (atmospheric sewer space above the wastewater). $CO_2$ reacts with the moisture absorbed by the unsubmerged concrete surfaces to form carbonic acid ($H_2CO_3$) (abiotic process), and $H_2S$ is oxidised to sulphuric acid ($H_2SO_4$) by SOB (abiotic and biotic processes). Consequently, the acids lower the concrete pH, facilitating further SOB proliferation and more sulphuric acid production. $H_2SO_4$ reacts with calcium silicate, calcium aluminate, and carbonate compounds of concrete to form gypsum and ettringite. Both gypsum and ettringite are expansive products leading to internal cracking and spalling of concrete, which provide sites for further acid penetration. Thus, concrete slowly loses its structural integrity and exposes the underlying steel reinforcement to corrosion (Parande *et al.*, 2006; Wells, Melchers and Bond, 2009; Grandclerc *et al.*, 2018).

BAC has both economic and environmental consequences on sewer infrastructure. Cracks, erosion, structural spalling, and corrosion of reinforcing steel can lead to wastewater leakage over time, eventually resulting in air, water, soil, and aesthetic pollution. About 500 million $m^3$/year of contaminated waters with sulphate, chloride and nitrogen compounds are associated with sewer leakage, posing a threat to the environment and human health (Kaempfer & Berndt, 1999). In addition, sewer deterioration results in a substantial increment in the direct and indirect costs attributed to sewer system repair and rehabilitation, which lead to a productivity loss of other functioning entities and lost wages due to social service interruptions (Bertron, 2014; Bertron et al., 2017; Elmasry, Hawari & Zayed, 2017).

Various repair and rehabilitation techniques have been employed to combat corrosion. For instance, lining techniques, which mainly use thermoplastic-based liners, are widely applied to avoid the disruptions associated with excavation and replacement of sewer pipes and increase the longevity of sewers. However, they are deemed expensive and less effective in certain situations, such as concrete surface profiles and infiltration between the liner and host pipe (EPA, 1999; Kung'u, 1999). Also, they might cause massive aggressive gas accumulations in sewers leading to corrosion of unprotected elements, such as manholes, and air pollution in case of any opening.

Other preventive measures such as the application of chemical or biological technologies (that decrease $H_2S$ production and emission) and protective coatings and acid-resistant cement (that prevent the chemical attack of concrete) have been investigated (De Muynck, De Belie & Verstraete, 2009; Haile et al., 2010; Berndt, 2011; Noeiaghaei et al., 2017). However, most protective materials such as epoxy coatings and antimicrobial polymer fibres or metal-zeolites are claimed to perform well in the laboratory but with little or no evidence of their field performance, while cementitious coatings, in general, may perform poorly (De Muynck, De Belie & Verstraete, 2009; Berndt, 2011). Available field performance indicates that epoxy coatings are notorious for delaminating and peeling from the concrete substrate, while antimicrobial agents tend to dissolve in wastewater (Noeiaghaei et al., 2017).

Therefore, these associated problems can be overcome by developing or improving cement-based liners or producing corrosion-resistant concrete pipes manufactured using available high-performance binder systems such as Alkali-Activated Cements (AAC), Calcium Aluminate Cement (CAC), Limestone Calcined Clay Cement ($LC^3$), Calcium Sulpho-Aluminate cement (CSA), and belite-y'elimite cement.These binders are expected to have better performance because their chemistry and microstructure should impart greater acid resistance. However, implementing these binder systems requires understanding of their deterioration mechanisms and potential to resist and possibly suppress BAC. Experimental study and thermodynamic modelling allow deterioration of these binder systems and resisting mechanisms to be determined and evaluated.

For engineering applications, prediction models, such as the 'Life Factor Method (LFM)', can be employed to predict the long-term performance of these binder systems used in concrete pipes. However, the LFM model needs further improvement and advancement to cover a broader range of binder and aggregate types with their field performance. The improvement should involve introducing factors that combine the influence of binders and aggregates in the concrete and sewer environmental factors. It also stands to reason that concrete quality, i.e., physical and mechanical parameters, including penetrability, is critical. Therefore, this study aimed to improve the BAC prediction model of concrete sewer pipes based on the LFM model, covering a broad range of binder systems, aggregate types and different sewer environments.

### 1.2. Motivation for the study

The first motivation of this study was the recommendations from previous work done at the University of Cape Town (UCT), specifically by Kiliswa (2016), that involved studying the composition and microstructure of Portland Cement (PC) and CAC-based concrete systems subjected to BAC in live sewer environments. Among the recommendations for further study were as follows.

i. Characterise and understand the influence of binder components, specifically calcium oxide (CaO), aluminium oxide ($Al_2O_3$), and ferric oxide ($Fe_2O_3$), on BAC. Kiliswa integrated $Al_2O_3$ and $Fe_2O_3$ into his 'Improved LFM' in conjunction with the alkalinity factor (i.e., calcium carbonate, ($CaCO_3$)), which is employed in the LFM model as the rate-controlling parameter for corrosion rate prediction of PC-based concretes. He surmised that these oxides have a neutralizing impact on acid and a bacteriostatic effect on the SOB. Hence, they are critical to developing the most accurate prediction model. However, this theory emphasized the necessity for more research to clarify and propose or establish their threshold values.
ii. Characterise the impact of sewer environmental factors, namely, $H_2S$ concentration, temperature and RH, on BAC, and establish sewer aggressivity factors for various sewer environments. In his 'Improved LFM', Kiliswa introduced a sewer aggressivity factor, which significantly influenced the corrosion rate prediction of PC- and CAC-based concrete. However, the proposed factor was 'biased' since it was derived solely from a single aggressive environment and overlapped with an existing environmental factor in the original LFM. Thus, there was the need and opportunity to improve the LFM further.

The second motivation was that limited studies focus on improving the prediction models that cover a range of binder systems. In the literature, PC and CAC-based systems are typically studied in the sewer environment (Grandclerc et al., 2018; Kiliswa, 2016; Peyre Lavigne et al., 2015), while existing models such as the SATIR (Säure, Angriff, Transport, Instationär, Reaktion) model (Beddoe & Dorner, 2005), Artificial Neural Networks (ANN) and Evolutionary Polynomial Regression (EPR) models (Alani & Faramarzi, 2014) are mainly calibrated with concrete laboratory performances. The question remains about predicting the performance of other binders such as blast-furnace slag cement, binary/ternary mixtures of plain PC with alumino-siliceous SCMs, super-sulphated cement, CSA, $LC^3$, and AAC.

Moreover, most prediction models give explicit relationships for concrete laboratory performance, not in-situ performance. Monteny *et al.* (2000) argued that numerous parameters are involved in the corrosion process, and the great diversity in the appraised sites and concrete mixes complicates comparing their performances. Therefore, a rational understanding of combining all these factors must be evaluated and considered for a better prediction model. Additionally, the aggregate component is sometimes neglected or not adequately considered.

Finally, the study was inspired by the enormous expenditure on buried sewer infrastructure in developing countries, which is associated with the lack of effective anti-corrosive binders coupled with models that can effectively predict the corrosion rate of concrete. The use of anti-corrosive binders, or at least binders with significantly enhanced acid resistance in BAC situations, would help avoid the high costs of imported commercial products for developing countries. No doubt, the need to develop such models would benefit the industry by providing cost-effective solutions and evaluating and improving concrete mix designs for sewer pipes.

Therefore, the arguments above indicate further advancement of the LFM model to cover a broader range of binder systems and aggregate types of concrete mixes subjected to various sewer aggressivity. The study was achieved by subjecting various concretes made with a broad range of binders to different aggressivity levels in live sewers. The mechanisms of deterioration of different binder systems, i.e., PC, SRPC, CSA and CAC, in biogenic sewer environments were studied. Furthermore, a thorough comprehension of the correlation between the prediction model and the actual performance of such binders was in mind.

### 1.3. Aim and objectives of the research

The overall aim of this research is to advance the BAC prediction of concrete sewer pipes based on the Life Factor Method (LFM), to cover a broad range of binder systems and aggregate types, for concrete mixes subjected to different sewer aggressivity levels.

This aim was achieved through the following specific objectives.

i. Study the influence of different binder systems, mainly CAC, CSA, PC, and SRPC with fly ash and iron-based additives, i.e., Hardcem (HC), in affecting biogenic acid corrosion of sewer concrete,
ii. Understand the mechanism of biogenic acid corrosion in concrete sewers when different binder systems and aggregates are used,

iii. Study biogenic corrosion of such concretes at different sewer aggressivity levels encountered in live sewer environments, and
iv. Use the insight and information from the above to advance and extend the Life Factor Method (LFM) for predicting concrete corrosion rates

The first three objectives were achieved through thermodynamic modelling and field experimental investigation of concrete specimens subjected to three live sewer environments for two years. The second objective provides information on combining aggregates and binders in sewer concrete mixes. This objective was achieved by studying two groups of binder systems, i.e., Portland-based and aluminate-based, and three aggregate types, i.e., dolomite, calcite and siliceous aggregates. The third objective gave information on the influence of different sewer conditions, such as temperature, RH, $H_2S$ gas concentration, and sewer hydraulic actions, on BAC. This objective was achieved by subjecting the concretes to three sewer environments coupled with information extracted from the literature. With this knowledge, the LFM model was successfully refined by evaluating, interpreting, and considering input parameters encompassing a broader spectrum of binder systems, aggregate types, and sewer environmental factors. As a result, a convenient, reliable, and simple LFM model for industrial applications was provided.

### 1.4. Research questions

The following were the critical questions of this study;

i. Can the literature shed further light on the role of the various binder and aggregate constituents and compositions on BAC?
ii. What is the contribution of sewer headspace conditions on BAC? Moreover, how do the different binders respond in different severities of the sewer environment?
iii. What performance correlations exist for the various binder systems when subjected to the live sewer environment?
iv. What is the influence of aggregates on the BAC of sewer concrete? How do different binder systems respond to different aggregate types in concrete under BAC?
v. How can all the factors contributing to BAC be combined, evaluated, and considered to provide a rational understanding of a better prediction model?
vi. Does the LFM model predict the performance of binder systems other than OPC and CAC? If not, what factors can be refined to increase its aptitude?

### 1.5. Research significance and scope

This study offers a user-friendly and relatively simple LFM model for sewer concrete design. The model can predict the corrosion rate of concrete mixes with various binder systems and aggregate types when subjected to various sewer environments. It also determines and suggests vital binder systems that suppress BAC. In addition, it provides suggestions on suitable binder-aggregate combinations that can improve the resistance potential of concrete under BAC. However, it is important for a designer to have sufficient knowledge on sewer environmental conditions, flow conditions, all of which are highly variable, as well as concrete chemistry.

Besides, this study brings awareness to engineers in predicting the corrosion rate of concrete based on various possible binders and aggregates, thereby avoiding unnecessary costs, financially and technically. Moreover, it assists the cement industry in developing binders that can withstand sewer environments, thereby increasing their market and the service life of the sewer structures constructed using the developed binder systems.

As an outcome of the knowledge derived from this research, governments, especially in the developing world, are provided with information that can assist in the proper investment of funds for the rehabilitation, repair and provision of functional and durable sanitation infrastructure. In doing so, governments improve human health and living standards and preserve the environment from the adverse effects of inadequate sanitation infrastructure.

Regarding the research scope, the study was conducted in three sewer sites in the City of Cape Town, South Africa. The concretes were designed based on selected binder systems provided by Lafarge Holcim (LH) in Lyon, France, and some additional binders from UCT, including a blend of Sulphate Resisting Portland Cement (SRPC) and Fly Ash (FA), a similar blend with Iron based additive, i.e. HardCem (HC), Portland Cement (CEM II AL[1]), CAC, CSA, and a blend of CAC and SRPC. The modelling aspect of this study employed two thermodynamic modelling tools, i.e., PhreeQc and HYTEC, and an empirical modelling approach, i.e., mathematic and chemistry principles, was adopted in refining and improving the LFM model.

### 1.6. Research collaboration

This study formed a three-way collaboration by three organisations: the Concrete Materials and Structural Integrity Research Unit (CoMSIRU) from the University of Cape Town (UCT), South Africa, the Laboratory of Materials and Durability of Constructions (LMDC) from the Institut National des Sciences Appliquées (INSA) of Toulouse, France, and LafargeHolcim (LH) in France. LH helped to fund the study and provided certain materials, while UCT and LMDC engaged in the field and laboratory investigations. UCT was involved in the field investigation due to its experience in live sewer activities for about 20 years. LMDC concentrated on laboratory activities because of their skills in developing highly specialised equipment for analysing the BAC corrosion rate of cementitious materials. In carrying out the study, analytical skills and results were exchanged among the organisations through interlaboratory visits, presentations and paper writing.

### 1.7. Thesis Outline

A schematic research design flow in Figure 1.1 illustrates the stages and components considered in structuring and provides a guideline for achieving the research's milestones. The design flow consists of five pillars, i.e., i) research introduction, ii) literature review, iii) experimental investigation, which includes sewer site environmental study, material selection and characterisation, and material

[1] CEM II AL is used in this study to denote CEM II A-L 52.5 N, Portland cement with allowable variations as follows: 6 – 20% limestone, 80 – 94% clinker, and 0 – 5% additives

performance in the field and through reactive transport modelling, iv) constructing and refining the LFM model, and finally, v) research conclusions and recommendations.

Based on the five pillars, eight chapters were obtained for this study. Chapter 1 is the introduction chapter which lays out the motivation of this study, research objectives and questions, and the significance of this research.

Chapter 2 is the literature review chapter which discusses the general background, mechanisms, and factors influencing BAC on sewer concrete. Various binder systems' performance and their chemical composition roles are also evaluated. Various mechanisms and prediction models of BAC are reviewed. The chapter is finalised by outlining the knowledge gaps on BAC on sewer concrete.

Chapter 3 is the experimental setup and investigation chapter. It delineates the material selected for this study, the concrete mix design and casting, the laboratory control tests, specimen preparation for sewer exposure, the BAC monitoring techniques, and microstructural analysis.

Chapter 4 is about sewer environment conditions. It describes sewer site selection criteria, background, and environmental conditions. The analysis and discussion of sewer environment properties and the relationship between the selected sites and the most corroded regions of a sewer pipe section are provided.

Chapter 5 is the experimental investigation: analysis and discussion of results chapter. The chapter discusses two batches of concrete mixes; LH concrete mixes, made of calcite aggregates and cast at the LH facility, and UCT concrete, made of dolomite aggregates and cast at the UCT civil engineering laboratory. The laboratory control test results, BAC monitoring analysis, i.e., visual observations, concrete surface pH measurements, mass and thickness change, and BAC microstructural analysis of concrete specimens from each batch subjected to three sewer sites for two years, are discussed and main insights and standpoints are summarised.

Chapter 6 covers the reactive transport modelling of sewer concrete binders. It provides a brief background on the HYTEC model, the aims of conducting thermodynamic modelling, the methodology implemented, and the results, analysis and discussion of the UCT binder systems. The chapter also compares the thermodynamic modelling results with the experimental investigation results.

Chapter 7 is the LFM improvement chapter. With the knowledge acquired from the previous chapters, this chapter elucidates techniques and principles attained and applied in accommodating binder, aggregate component, and sewer aggressivity parameters in the LFM model. The application of the model in predicting the corrosion rate of various concrete mixes and their corrosion with their rate measured in situ.

Finally, Chapter 8, covering conclusions and recommendations, provides insights, information and lessons accumulated from this study. The general conclusions are also drawn based on this study's objectives and research questions. The chapter closes with recommendations for further study.

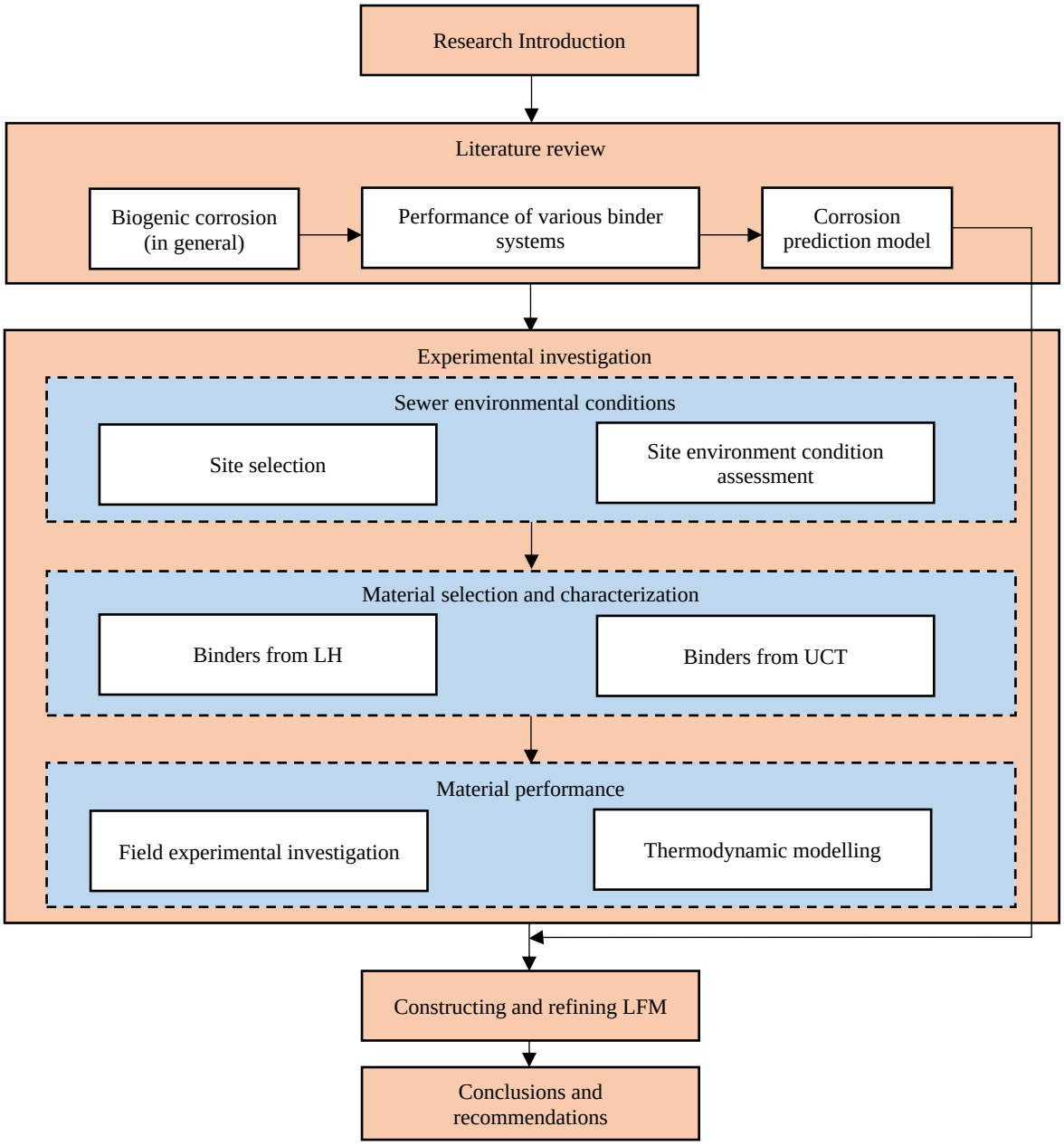


*Figure 1.1: Schematic design of the experimental investigation of this study*

# CHAPTER 2. LITERATURE REVIEW

## 2.1. Biogenic Acid Corrosion (BAC) overview

Biogenic Acid Corrosion (BAC) in concrete was first reported on the outfall sewer serving Los Angeles in 1899, where the concrete lining of the sewer and lime mortar used in the brickwork were intensively corroding and crumbling. The problem was attributed to the $H_2S$ gas generation that accumulates above the wastewater and dissolves into the moist sewer walls to form $H_2SO_4$. However, the interaction and connection between acid production and $H_2S$ presence in the sewer system were not well understood since it was believed that the process solely involved chemical reactions. In 1945, a bacteriologist named Parker encountered a similar problem in Australia and ascribed the problem to microorganisms that played a significant role in $H_2S$ gas and $H_2SO_4$ acid production (Dyer, 2017).

BAC occurs on the unsubmerged surfaces of sewer pipes. It is associated with $H_2SO_4$ attack due to microbial activities in the sewer system, not $H_2SO_4$ acid introduced from industrial wastewater. The microbial activities are responsible for chemical, physical and mineralogical damage to concrete structures. These activities occur both within the wastewater and on the unsubmerged sewer wall. The deterioration takes place after a series of processes which include;

i) sulphide specie generation in the wastewater,
ii) $H_2S$ gas emission from the aqueous to the gas phase,
iii) $H_2S$ gas adsorption and oxidation on the unsubmerged surfaces of sewer pipe, and finally,
iv) the formation of aggressive $H_2SO_4$ acid, which reacts with the concrete sewer wall and causes deterioration.

The following sections provide a general overview of the mechanism of BAC.

## 2.2. Biogenic Acid Corrosion (BAC) process

The wall of a concrete sewer pipe consists of the submerged and unsubmerged parts. The submerged wall is covered with flowing wastewater with sediments, above which there is sewer headspace in contact with aggressive gases. The headspace is confined by the unsubmerged wall with a condensate film, which creates suitable conditions for gas dissociation and microorganism growth (Figure 2.1). The characteristic of each component of the sewer pipe contributes to explaining the four stages that lead to BAC. These stages are delineated as follows:

### 2.2.1. Stage 1: Sewer installation

Concrete is initially immune to biological attack because of its high alkalinity. Its pH is about 12-13 due to cement hydration products, such as calcium hydroxide/portlandite] (CH), for concrete pipes made of plain PC. This condition is hostile to bacterial growth and proliferation. However, initial carbonation can lower this pH if the pipes are exposed to an uncontrolled environment before installation. After the installation of sewer concrete pipes, bed and sidewall erosion due to the flow of wastewater generates roughness and distorts the surface texture of the concrete wall, while the saturation and condensation of the wall cause alkali leaching on the concrete surfaces, which in turn, drops the alkalinity further (Wei et al., 2013).

Under favourable conditions provided by the wastewater, a slime layer known as 'biofilm' is formed as the intermediate layer between the submerged wall and wastewater. This film comprises a community of microorganisms living and attached to the concrete surface with more than 1-2 mm thickness and characterised by aerobic conditions at the liquid-biofilm interface, while anaerobic in the inner layer (Hvitved-Jacobsen, Vollertsen and Nielsen, 2013:200). However, the aerobic layer exists depending on the amount of Dissolved Oxygen (DO). Such microorganisms include pathogenic bacteria and SRB (e.g. *Desulfovibrio* and *Desulfomaculum*) (Jensen, Biggs and Karunakaran, 2016).

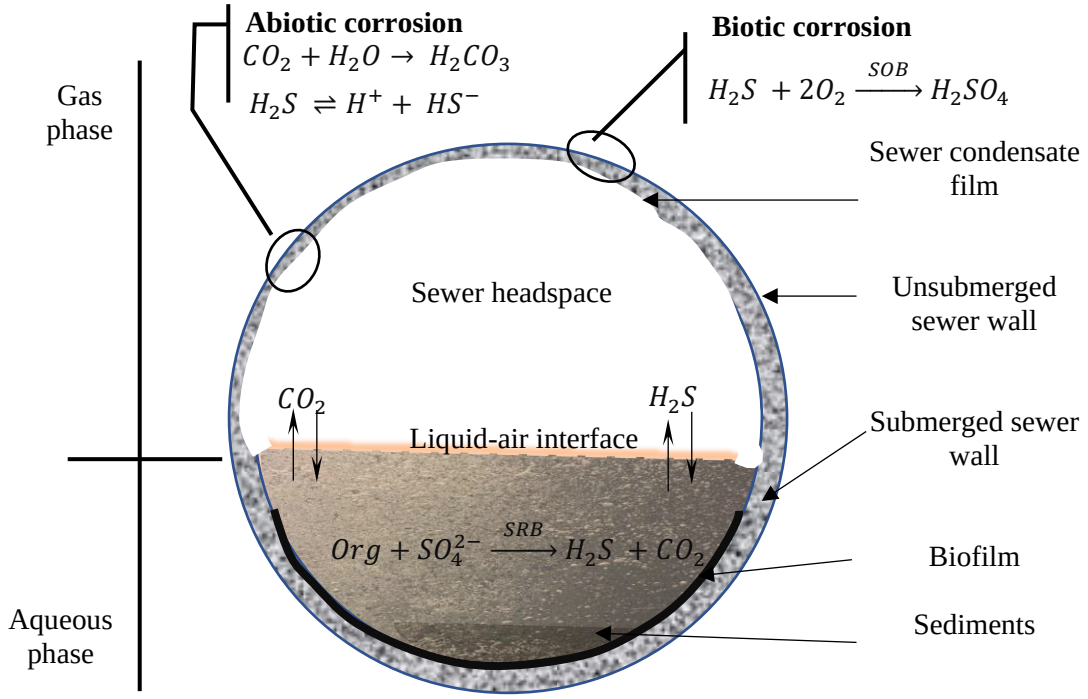


*Figure 2.1: Schematic of the corrosion process within a sewer, derived from Wells, Melchers and Bond (2009)*

### 2.2.2. Stage 2: Neutralisation of sewer concrete

SRBs are anaerobic bacteria that grow in the presence of organic matter and the absence of oxygen and nitrate environments with slow flow rates and relatively high temperatures. The anaerobic condition is due to the wastewater that hinders oxygen transportation and penetration and the sediments above the biofilm that provide the organic compounds. The presence of nitrate inhibits sulphate reduction as nitrate is a preferred electron acceptor to sulphate, thereby providing competition between SRBs and nitrate-reducing bacteria. SRBs reduce sulphates and oxidise biodegradable organic carbon in the wastewater to produce $H_2S$ and $CO_2$ gas, see Eq. 2.1. This environment is typically observed in the anaerobic parts of a sewer, commonly known as a septic sewer (Grengg et al., 2018; Zhang et al., 2008).

$$Organic\ matter\ (i.e.C) + SO_4^{2-} \xrightarrow{SRB} H_2S + CO_2 \quad (2.1)$$

At a high concentration of these gases and under sewer hydraulic action, mainly in gravity sewers, the gases escape from the aqueous phase to the sewer headspace by volatilisation (Okabe et al., 2007). Since $H_2S$ is denser than air, it accumulates partially above the waterline, while $CO_2$ is released into the atmosphere. The surface of the unsubmerged concrete wall usually has a thin layer of condensed water

with a relatively high pH due to concrete alkalinity. This layer is the so-called 'condensate film'. It dissolves relatively large quantities of $CO_2$ and $H_2S$. Under a sufficient supply of oxygen and moisture, these gases undergo abiotic chemical reactions; Carbonation and $H_2S$ oxidation. Carbonation involves converting $CO_2$ to carbonate ($CO_3^{2-}$) and bicarbonate ($HCO_2^-$) ions. $H_2S$ oxidation, at this stage, occurs merely chemically and leads to the formation of intermediate sulphide species such as elemental sulphur ($S^o$), thiosulphate ($S_2O_3^2$) and sulphite ($SO_3^{2-}$) (Figure 2.2). These reactions create acidic conditions that lower concrete pH to 9, thus providing a host condition for SOB propagation (Wells, Melchers and Bond, 2009; Jiang et al., 2014).

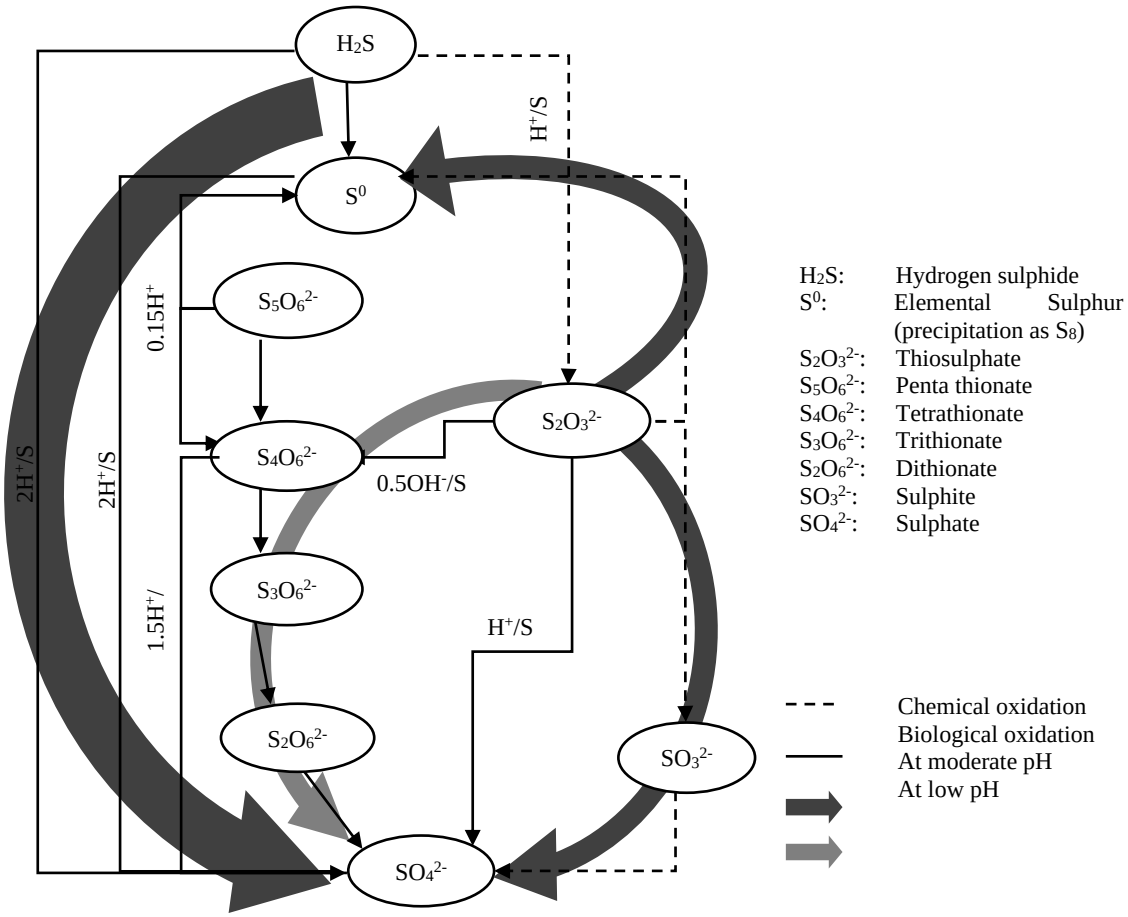


*Figure 2.2: Reduced Sulphur oxidation by abiotic (chemical) and biotic (biological) oxidation with associated acid production for one oxidized atom of sulphur, adapted from (Peyre Lavigne et al., 2015)*

However, Joseph et al. (2012) argued that the neutralisation of a concrete sewer pipe is primarily caused by $H_2S$ oxidation rather than carbonation. This is due to their observations on concrete coupons extracted from a sewer pipe with a surface pH of 10.6, then exposed in the corrosion chamber with 0 ppm of $H_2S$ for 12 months. The results showed an insignificant decrease in concrete pH and a minor $CaCO_3$ content formation, indicating no carbonation. However, the fact that the coupons showed lower pH than virgin concrete indicates that carbonation had already occurred before the exposure.

In summary, the initial pH reduction or neutralisation of the concrete surface is driven by two chemical reactions

- Carbonation: lowers the pH from 12 to 9, and the carbonate-bicarbonate-carbon dioxide equilibrium
- $H_2S$ oxidation lowers the pH to about 7.5 without microorganism involvement, that is, $H_2S$ oxidation to intermediate sulphide species.

### 2.2.3. Stage 3: Bacterial colonisation

Carbonation and $H_2S$ oxidation on the condensate film produce nutrients (from organic carbon) and provide energy sources (from the intermediate sulphide species) for further proliferation of aggressive microorganisms. Microorganisms such as Neutrophilic Sulphide Oxidising Bacteria (NSOB), Acidophilic Sulphide Oxidising Bacteria (ASOB), fungi and heterophilic microorganisms other than SOB feed on and convert the intermediate sulphide species ($S^o$ and $S_2O_3^{2-}$) to polythionate (Figure 2.2: Biological reactions), which subsequently convert to sulphuric acid (Joseph et al., 2012). At a pH of about 9, a succession of NSOB begins in the order; *Thiothrix*, *Thiobacillus plumbophilus*, *Thiomonas*, and *Halothiobacillus neapolitanus* species, depending on the available intermediate sulphide species on the concrete surface, concrete pH, temperature, and trophic property see Table 2.1 (Okabe et al., 2007).

NSOB generally reduce concrete pH to 4, which facilitates the population of ASOB. These bacteria become active in extreme conditions of pH from 4 to 0.5. At this pH range, ASOB, namely, *Mycobacterium*, *Acidiphilum acidophilum*, and *Acidithiobacilli* species, proliferate and colonise the surface (Table 2.1). *Acidithiobacilli* species occur in diverse strains depending on the pH range for optimal metabolic activities on the surface layer of corroded concrete. These strains include *Acidithiobacilli ferrooxidans*, *Acidithiobacilli thiooxidans*, and *Acidithiobacilli caldus* (Li et al., 2017). However, in sewer concrete corrosion, *Acidithiobacilli thiooxidans* are the most common and prominent species and are often found on the surface layer of corroded concrete (Okabe et al., 2007; Li et al., 2017; Noeiaghaei et al., 2017). Notwithstanding this, the role of *Acidithiobacilli ferrooxidans* in this layer remains debatable since Grengg et al. (2017) argue that f*errooxidans*, to some extent, are the key player in BAC.

By contrast, Li et al. (2017) found that fungi, such as *Fusarium* species, contributed to BAC since they existed in a symbiotic relationship with ASOB. Valix et al. (2012) also observed fungal activity on concrete samples extracted from a gravity sewer. They associated fungal activity with organic acids as their main metabolic products. Thus, the central role of fungi in sewer corrosion was in preparing the pipe surface for *thiobacilli* strain colonisation. This observation was also stressed by Gu et al. (1998), who found similar fungi (*Fusarium* species) playing a similar role. However, Okabe et al. (2007) found no evidence of such fungi during the entire period of sample monitoring. Therefore, they raised a need for further examination since the mechanism of the fungi is rarely studied in BAC.

Okabe et al. (2007) also observed heterotrophic bacteria other than SOB that shared similar functional characteristics of utilising various carbon sources, producing acids, and proliferating at a low pH and high salt concentrations. They postulated that these bacteria possibly had a synergistic relationship with ASOB, thereby decomposing inhibitory organic compounds excreted. Grengg et al. (2018) suggested that these bacteria play an essential role in a microbial cycle by consuming organic matter produced by

autotrophic bacteria, stimulating autotrophic metabolic activities and, finally, acid production. Similarly, further study is needed to prove their existence and the significance of their role.

*Table 2.1: SOB Succession at different concrete pH, temperature and trophic properties with their oxidising Sulphur species* (Islander et al., 1991; Roberts et al., 2002; Okabe et al., 2007; Grengg et al., 2017)

| SOB species | | Growth pH | Temperature (°C) | Trophic property[1] | Oxidising sulphur species |
|---|---|---|---|---|---|
| NSOB | *Thiothrix* | 7.0 | 10-30 | Mixotrophic[2] | $S_2O_3^{2-}$, $H_2S$ |
| | *Thiobacillus plumbophilus* | 4.0-6.5 | 9-41 | Autotrophic[3] | $H_2S$ |
| | *Thiomonas intermedia* | 5.0-7.5 | 15-37 | Mixotrophic | $S_2O_3^{2-}$, $S^0$ |
| | *Halothiobacillus neapolitanus* | 4.5-8.5 | 8-39 | - | $S_2O_3^{2-}$, $S^0$, $H_2S$ |
| | *Thiobacillus thioparus* | 4.5-10 | 15-42 | Autotrophic | $S_2O_3^{2-}$, $H_2S$, |
| | *Thiobacillus novellus* | 5.0-9.2 | 10-37 | Mixotrophic | $S_2O_3^{2-}$, |
| ASOB | *Thiobacillus intermedius* | 1.7-9.0 | 15-37 | Mixotrophic | $S_2O_3^{2-}$, |
| | *Mycobacterium* | - | - | Heterotrophic[4] | $S^0$ |
| | *Acidithiobacilli caldus* | - | - | Autotrophic | - |
| | *Acidithiobacilli thiooxidans* | 0.5-5.5 | 10-37 | Autotrophic | $S_2O_3^{2-}$, $S^0$ |
| | *Acidiphilum acidophilum* | 1.0-6.0 | 10-35 | Heterotrophic | $S_2O_3^{2-}$, $S^0$ |

[1] Trophic property: feeding levels of microorganisms*
[2] Mixotrophic: Relating to a combination of heterotrophic and autotrophic sustenance*
[3] Autotrophic: Relating to microorganisms that manufacture their food from inorganic substances, such as carbon dioxide, sulphate and nitrogen, using energy from light (photosynthesis) or inorganic chemical reactions (chemosynthesis)*
[4] Heterotrophic: Relating to microorganisms that cannot manufacture their food and instead obtain their food and energy by taking in organic substances*
*Extracted from ecology dictionaries

### 2.2.4. Stage 4: Concrete corrosion

As the result of concrete surface pH reduction and bacterial colonisation, sulphuric acid (see the biotic reactions in Section 2.3.3 attacks the concrete matrix. In the case of PC concrete, the acid reacts first with Portlandite (Eq. 2.2), followed by Calcium Silicate Hydrates (CSH) (Eq. 2.3), carbonate compounds either from aggregates or carbonation (Eq. 2.4) and other hydration products to form a soft white 'cottage cheese-like layer of corrosion products in the form of gypsum ($C\bar{S}$).

$$H_2SO_4 + CH \rightarrow C\bar{S} + 2H \quad (2.2)$$

$$H_2SO_4 + CSH \rightarrow C\bar{S} + S + 2H \quad (2.3)$$

$$H_2SO_4 + CaCO_3 \rightarrow C\bar{S} + H_2CO_3 \quad (2.4)$$

Gypsum usually is formed on the corroded layer when the pH is less than 3 (Grengg, Mittermayr, Ukrainczyk, Koraimann, et al., 2018). With time, gypsum thickness gradually increases due to its volume expansion of up to 124% compared to intact concrete. Calcium aluminates within the concrete matrix react with gypsum to form a more destructive and expansive mineral, 'Ettringite' - see Eq. 2.5. Wells, Melchers and Bond (2009); Jiang et al. (2014) observed that ettringite accumulates near the corrosion front (i.e., transition zone) where higher pH than 10.7 since ettringite is stable only at a pH

higher than that (see Figure 2.3) (Beddoe and Dorner, 2005; Germishuizen et al., 2018). Figure 2.3 also shows the pH stability of other cementitious matrixes (PC hydrates are thermodynamically unstable at pH values below 10 ).

$$3C\bar{S}.H_2 + C_3AH_{12} + H_{14} \rightarrow C_6A\bar{S}_3H_{32} \quad (2.5)$$

Ettringite has a significantly higher volume expansion than gypsum, ranging from 227% to 700% of concrete (Wells, Melchers and Bond, 2009). Therefore, gypsum and ettringite formation increase the expansion stresses that weaken the concrete microstructure and lead to internal cracking and spalling of concrete (House and Weiss, 2014). In turn, the cracks offer an excellent medium for bacterial growth and a larger surface area for chemical reactions, facilitating easier penetration of moisture and acid (Zhang et al., 2008).

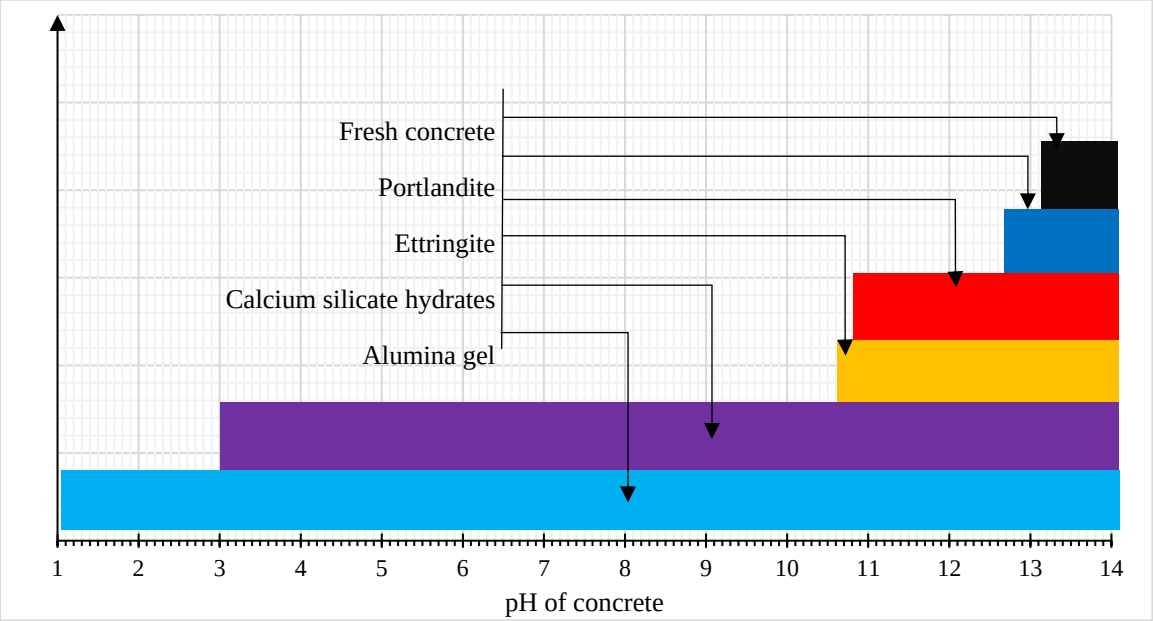


*Figure 2.3: Cementitious matrix phase stability pH*

According to Gutiérrez-Padilla et al. (2010) and Li et al. (2017), excess acid secretion in the corrosion layer causes ettringite decomposition to form gypsum. In some instances, ettringite is not detected in the corroded layer. Continuous acid production allows ionic diffusion through the corroded layer and internal cracking before reacting with sound concrete and underlying reinforcement. The general process weakens the sewer concrete structural integrity, thus decreasing the concrete load-bearing capacity, which may eventually result in overall sewer collapse.

Scrivener has reported the BAC severe at the 'crown region of sewer pipes, while Wells, Melchers and Bond (2009) and Goyns and Alexander (2018) noticed the severity immediately above the flowline known as the 'tidal region'. At the crown, the temperature differences between the concrete pipe walls and wastewater, especially during summer, facilitate the air movement in the headspace, which consequently influences the $H_2S$ gas transfer to the sewer crown for attack (EPA, 1974). Later, sewer hydraulic actions such as water flushing and occasional flooding enhance corrosion product removal,

leading to continuous exposure and corrosion of sound concrete (Li et al., 2017). The tidal region, on the contrary, is frequently wetted by wastewater, resulting in more frequent replenishment of nutrients, microbial inoculum, and moisture. It is also a region where aggressive acidic species settle ($H_2S$ is denser than air), and corrosion products and acid produced at the crown region drift. Hence, alkaline concrete at this site is attacked more readily than in other remote regions.

Figure 2.4 summarises all four stages involved in BAC. These stages are affected by the change in concrete pH with time which influences the microorganism colonisation and, finally, the production of acid, thus attacking the concrete, then leading to concrete corrosion.

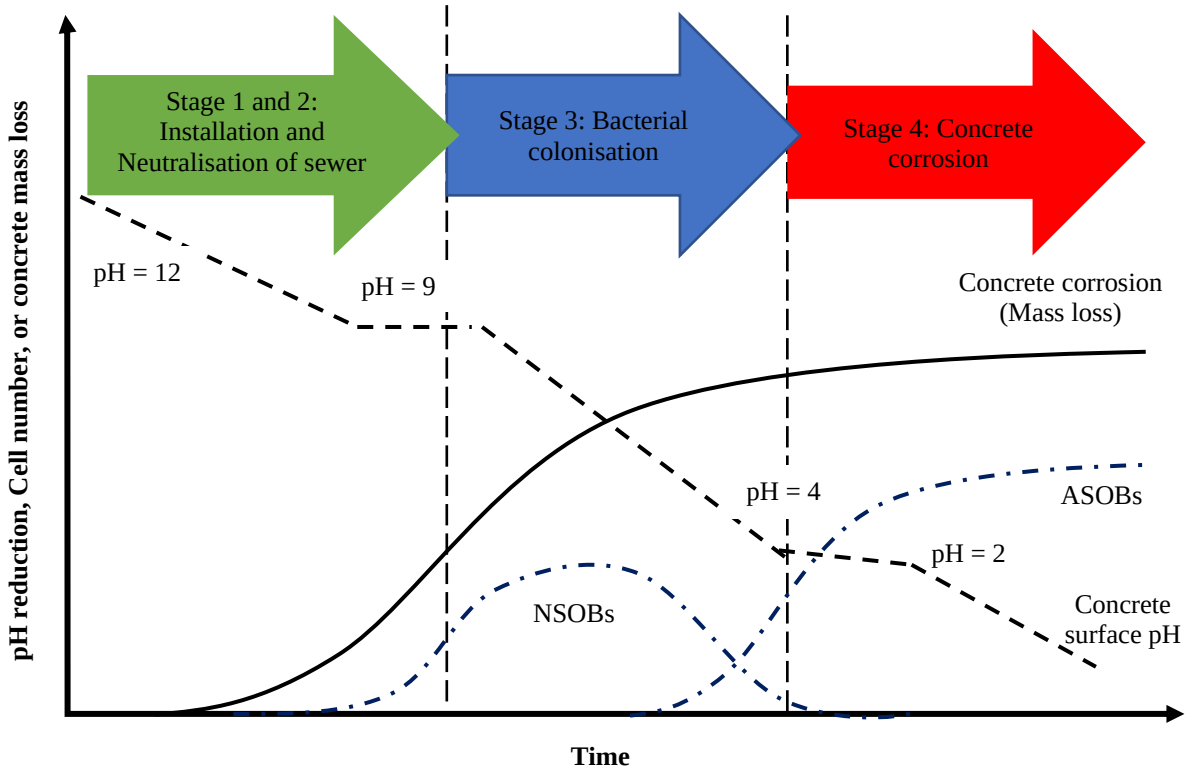


*Figure 2.4: The succession of different sulphide-oxidizing bacteria with the changes in surface pH due to the development of concrete corrosion in sewers, derived from (Islander et al., 1991).*

## 2.3. Factors influencing BAC

BAC is a complex phenomenon that involves multi-dimensional phase interactions; the aqueous, gaseous, biological, and mineralogical phases. The aqueous phase includes flowing wastewater and sediments. The gaseous phase consists of all gases dissociated above the flowline and dispersed in the sewer headspace. The biological phase consists of all microorganisms proliferated in the biofilm within the wastewater and condensate film on the unsubmerged wall. The mineralogical phase is the cementitious materials used for sewer pipe construction.

The general BAC process involves more than one biochemical cycle (sulphur, oxygen and nitrogen); however, the sulphur cycle depicted in Figure 2.5 is the most significant and responsible for concrete sewer corrosion. The sulphur cycle is the interaction of different actions and reactions attributed to various environmental, biological, chemical and physical factors that bring about the final degradation

of concrete. These factors are divided into four sets. The factors result in i) sulphide species generation in the wastewater, ii) $H_2S$ release or emission ($H_2S$) from the aqueous to the gaseous phase, iii) $H_2S$ adsorption and oxidation in the condensate film, and iv) concrete corrosion in the mineralogical phase.

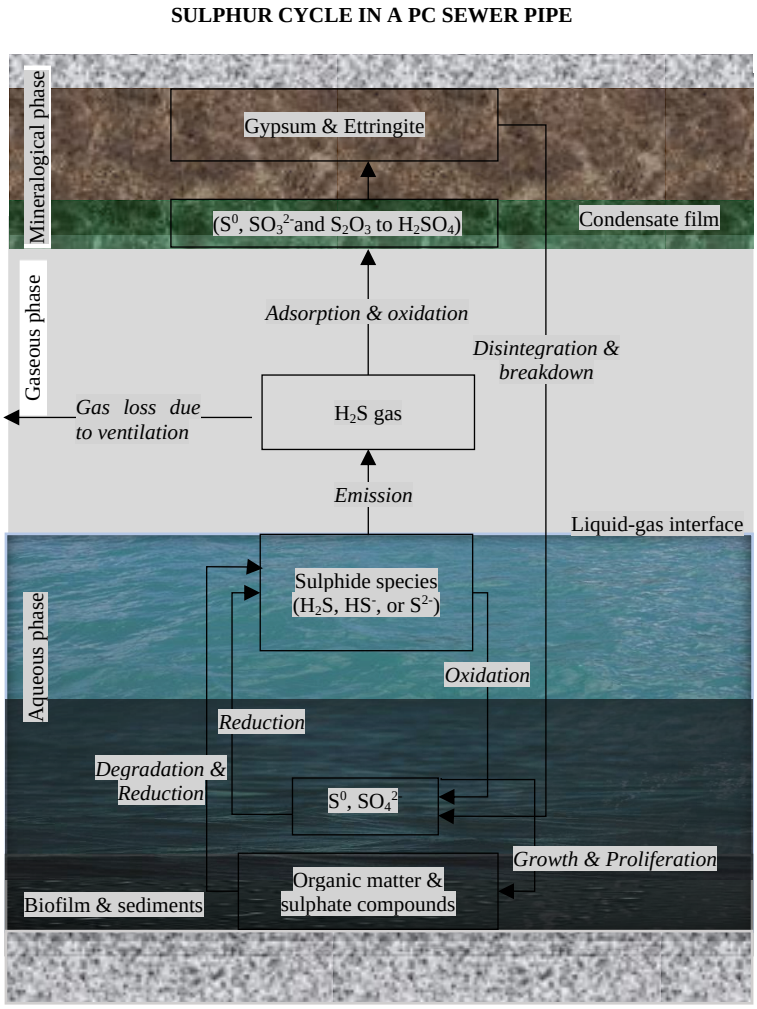


**Factors influencing BAC at each stage**

Concrete corrosion
- Material chemical properties
- Material integrity
- Sewer hydraulics

$H_2S$ adsorption and oxidation
- Concrete surface pH
- Relative Humidity
- Temperature
- Concentration of gases $CO_2$, $O_2$, & $H_2S$

$H_2S$ emission
- Sewer hydraulics
- Sewage pH
- Dissolved sulphide
- Sewer headspace temperature
- Metal concertation

Sulphide formation/build up
- Organic matter and nutrients
- Sulphate concentration
- Temperature
- Dissolved oxygen
- Retention time
- Sewer hydraulics

*Figure 2.5: Schematic sulphur cycle and factors influencing BAC in the sewer pipe at different phases (derived from Zhang et al., (2008))*

### 2.3.1. Sulphide species formation – Factors

Sulphates in sewage are primarily converted into three species; sulphide ($S^{2-}$), hydrosulphide ($HS^-$) and molecular hydrogen sulphide ($H_2S_{(aq)}$), depending on the sewage pH (Eq. 2.6 to 2.8) and Figure 2.6. However, $S^{2-}$ species is mostly less considered because of its insignificant presence even at a very high pH (Zhang et al., 2008; Oviedo, Johnson and Shipley, 2012). (Note: pK is a negative logarithm of the dissociation constant.)

$$Organic\ matter\ +\ SO_4^{2-} \xrightarrow{SRB} S^{2-} \qquad (2.6)$$

$$H_2S \leftrightarrow HS^- + H^+ \qquad pK = 7.05 \qquad \text{(Chapter 2.1)}$$

$$HS^- \leftrightarrow S^{2-} + H^+ \qquad pK = 17.89 \qquad \text{(Chapter 2.2)}$$

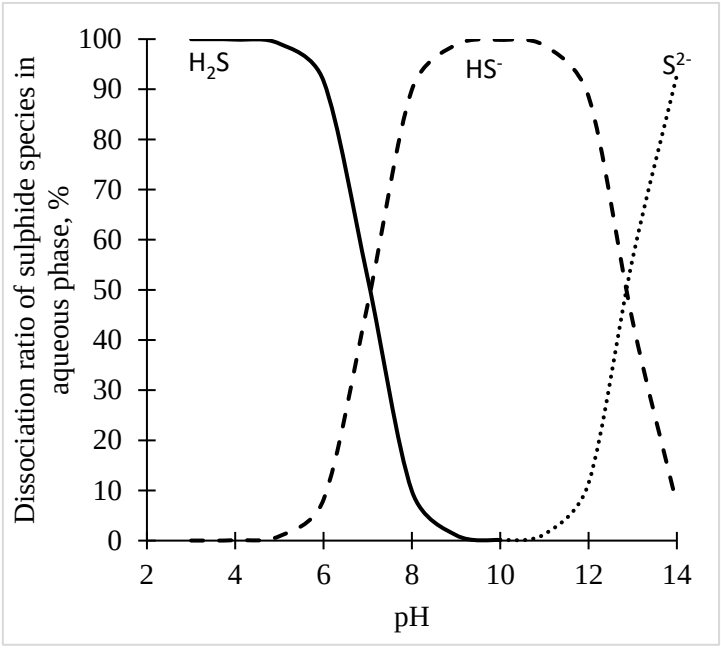


*Figure 2.6: Effect of pH on $H_2S$ generation*

The generation or conversion of these species depends significantly on the factors influencing SRB growth and proliferation in wastewater. These factors include:

*2.3.1.1.1. Biodegradable organic matter and nutrient concentration*

Wastewater comprises organic substances (such as formate, ethanol, glucose and lactate) and nutrients gathered from different sources of wastewater, which provide energy and food (such as proteins and amino acids) for SRB proliferation. These compounds diffuse into the biofilm in the sulphide production zone to feed SRB, as illustrated in Figure 2.7. A high concentration of these compounds significantly contributes to SRB growth and diversity. In the sulphide build-up estimation, the concentration of these compounds is considered proportional to the $BOD_5$ (5-day Biochemical Oxygen Demand) or COD (Chemical Oxygen Demand) if excess sulphate is available. $BOD_5$ is a measure of the amount of oxygen that is required for the bacteria to degrade the organic components present in wastewater. COD measures the oxygen needed to oxidise organic and inorganic matter in wastewater. $BOD_5$ is mainly used in municipal wastewater treatment plants and COD in industrial wastewater treatment plants. On the other hand, COD can be used to estimate the $BOD_5$ since the ratio of $COD/BOD_5$ is about 2.1.

*2.3.1.1.2. Sulphate compounds concentration*

Wastewater also comprises sulphate ($SO_4^{2-}$) compounds which are a source of oxygen for SRB at the sulphate production zone (see Figure 2.7) due to a limited amount of DO. The sulphate reduction increases with increasing sulphate concentration (Hvitved-Jacobsen, Vollertsen and Nielsen, 2013:223). SRB also utilises sulphate and organic compounds at a ratio of 2:1 depending on the nature of organics, indicating that sulphate compounds are two times more important for the growth of SRB than organic compounds (EPA, 1985).

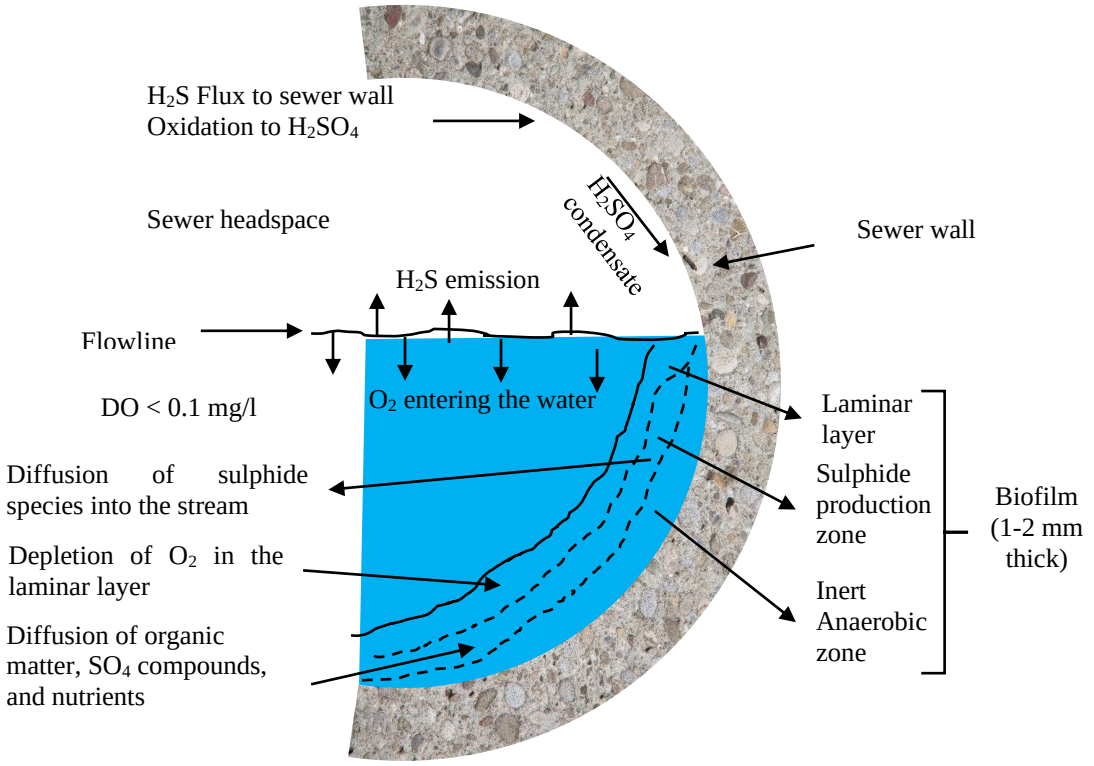


*Figure 2.7: Processes occurring in a sewer under sulphide species generation conditions adapted from EPA (1985)*

*2.3.1.1.3. Sewage temperature*

Temperature affects kinetic reactions of sulphate reduction and organic decomposition through thermodynamic activities. SRB is active at relatively high temperatures above 15-20ºC, although SRB can also survive at lower and higher temperatures (Jensen, 2009; Hvitved-Jacobsen, Vollertsen and Nielsen, 2013:223). Park et al. (2014) also stated that DO consumption increases with wastewater temperature, leading to anaerobic sewer conditions for SRB growth.

*2.3.1.1.4. Dissolved Oxygen (DO)*

A high DO content (>1 mg $O_2$ /l) in the biofilm prevents the dissolution of sulphide species into the wastewater. It influences the sulphur cycle by oxidising sulphide species to elemental sulphur ($S^0$) and sulphate ($SO_4^{2-}$). If it reaches the biofilm, sulphide species generation is significantly reduced. See Figure 2.5: the oxidation process in the aqueous phase is influenced by DO below the flowline (Hvitved-Jacobsen, Vollertsen and Nielsen, 2013:200-223).

*2.3.1.1.5. Retention time and topographical terrain*

A long retention time of the wastewater provides enough time for SRB microbial activities by allowing microbial population and organic matter sedimentation. Retention time depends on inflow magnitude and the topographical terrain. A flat terrain causes difficulties in achieving constant, rapid and continuous flow, thereby providing more time for bacteria to produce harmful species and vice versa (Wei et al., 2013).

*2.3.1.1.6. Sewer hydraulics*

Sewer hydraulics include the velocity and turbulence of wastewater flow. A moderate flow limits the turbulence, thereby suppressing the re-aeration of the wastewater and facilitating the production of thicker biofilms and depositions of sediments. An opposite effect is the increased thickness of the diffusive boundary layer above the biofilm, which can limit the supply of organic matter and nutrients to the biofilm, restricting sulphide production (Jensen, 2009). On the other hand, a flow velocity lower than the required self-cleaning velocity increases the retention time. As the depth of the wastewater increases, its flow velocity near the biofilm decreases due to the shear effect, thereby providing enough retention time for sulphide production, see Figure 2.8

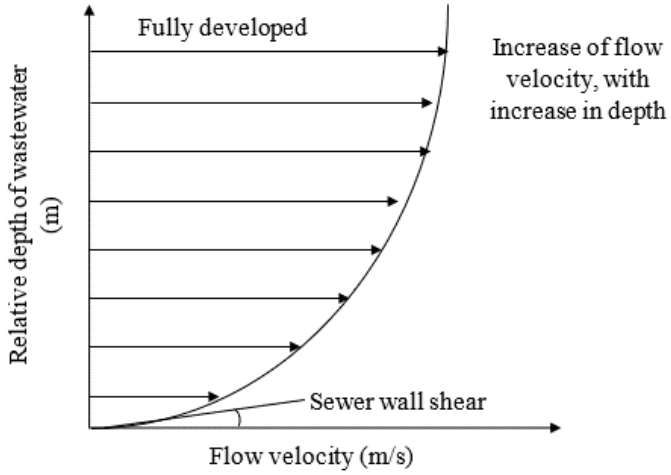


*Figure 2.8: Effect of wastewater depth on the flow velocity*

In summary, the concentration of biodegradable organic matter and nutrients, sulphate compounds, sewage temperature, DO, retention time, and sewer hydraulics govern microbial activity, thus increasing sulphide species generation in wastewater. At a high concentration of sulphide species, $H_2S_{(aq)}$ is released into the gaseous phase as a gas. $H_2S$ is the only species that can be released in the sewer headspace because, at a wastewater pH below 8, its concentration is often higher than other species (Park et al., 2014). The following subsection describes the factors associated with $H_2S$ emission in the gaseous phase.

### 2.3.2. $H_2S$ emission – Factors

$H_2S$ emission is a physiochemical process involving both the aqueous and gaseous phases. This process is based on the two-film theory, i.e., the mass transfer theory by Lewis and Whitman (1924) (Jung et al., 2015). The $H_2S$ emission rate is governed by steady-state molecular diffusion from the aqueous to gaseous film, separated by a liquid-gas interface. The mass transfer rate across the liquid-gas interface is driven by the difference in $H_2S$ concentrations between the phases. The emission is mainly dependent on the following factors;

*2.3.2.1.1. Sewer hydraulics*

Relatively high flow velocities and flow rates impact the flow turbulence and influence the equilibrium exchange of gases at the liquid-gas interface. This flow pattern can result from poor sewer hydraulic

design, which is also usually experienced at the discharge end of a forced main (Park et al., 2014). Matias, Matos and Ferreira (2014) indicated that increasing the flow rate and free-fall drop height reduced the time of accumulating the maximum $H_2S$ concentration in the gaseous phase. Besides, the various hydraulic actions, such as disintegrating and splashing wastewater droplets at water drops, influence the oxygenation of wastewater, which in turn, leads to the oxidation of sulphide species in the sewage (Jung et al., 2017). With oxygenation, the concentration of sulphide species is reduced, thus affecting $H_2S$ emission.

*2.3.2.1.2. Sewage pH and aqueous $H_2S$ concentration*

The equilibrium exchange of $H_2S$ is significantly influenced by sewage pH; with decreasing wastewater pH, $H_2S$ concentration in the sewer headspace increases (Jensen, 2009). Figure 2.6 exhibited that low pH values favour the rise in $H_2S_{(aq)}$ concentration in preference to $S^{2-}$ and $HS^-$ in the aqueous phase. With increasing $H_2S_{(aq)}$ concentration, the sulphide species equilibrium is disturbed, thereby leading to its release as a gas into the gaseous phase. Nevertheless, SRB responsible for sulphide production proliferate in the sewage with pH below 8; above this, their activities are reduced (Hvitved-Jacobsen, Vollertsen and Nielsen, 2013:223).

*2.3.2.1.3. Sewer headspace temperature*

Temperature influences the emission of $H_2S$ by increasing the diffusibility of the liquid-air interface. With increasing sewer headspace temperature, the liquid-gas transfer rates of $H_2S$ increase, hence higher emission of $H_2S$ into the sewer headspace (Yongsiri, Vollertsen & Hvitved-Jacobsen, 2004).

*2.3.2.1.4. Metal concentration*

Several metals such as iron, zinc, copper, lead and cadmium, typically found in municipal wastewater, form insoluble metallic sulphides upon reacting with dissolved sulphide. This reaction contributes to reducing the sulphide concentration in the sewage, thus, stabilising the equilibrium exchange of $H_2S$. As a result, in the wastewater treatment plant, such metals are added to mitigate $H_2S$ release. The typical range of concentrations of insoluble metallic sulphides in domestic wastewater is 0.2 to 0.3 mg/I. However, this concentration might be increased by wastewater discharge from industries which contain metal-bearing wastes (EPA, 1985). A provides more information regarding the effect of metal concentration in wastewater.

After emission, $H_2S$ can either be ventilated out of the system or adsorbed and subsequently oxidised to $H_2SO_4$ on the unsubmerged wall, see Figure 2.5. When ventilated to the atmosphere, it has a detrimental effect on living organisms and humans, while its transformation to $H_2SO_4$ is aggressive to the concrete structure. The following section thus explains the mechanism of sulphuric acid formation and attack on the concrete.

### 2.3.3. $H_2S$ adsorption and oxidation – Factors

Adsorption and oxidation of $H_2S$ result in the formation of sulphuric acid, which attacks concrete (mineralogical phases) and causes severe corrosion. The condensate film adsorbs $H_2S$ gas, which is subsequently oxidised to intermediate sulphide species (energy source), and then to $H_2SO_4$. $H_2SO_4$ provides a conducive environment for SOB flourishment as the concrete alkalinity decreases. Eq. 2.9

to 2.20 show both chemical and biological oxidation reactions of sulphide to intermediate species, then sulphuric acid, as depicted in Figure 2.2 (Hvitved-Jacobsen, Vollertsen and Nielsen, 2013:195-196; Barton, Fardeau and Fauque, 2014; Li et al., 2017).

- Chemical oxidation reactions of sulphide to intermediate sulphide species

$$H_2S \leftrightarrow HS^- + H^+ \quad (2.9)$$

$$2HS^- + O_2 \rightarrow 2S^0 + 2OH^- \quad (2.10)$$

$$2HS^- + 2O_2 \rightarrow S_2O_3{}^{2-} + H_2O \quad (2.11)$$

$$2HS^- + 3O_2 \rightarrow 2SO_3{}^{2-} + 2H^+ \quad (2.12)$$

$$SO_3{}^{2-} + S^0 \leftrightarrow S_2O_3{}^{2-} \quad (2.13)$$

$$4SO_3{}^{2-} + H^+ \rightarrow 3SO_4{}^{2-} + HS^- \quad (2.14)$$

- Biological Oxidation reactions of intermediate sulphide species to sulphuric acid

$$H_2S + 2O_2 \xrightarrow{SOB} SO_4{}^{2-} + 2H^+ \quad (2.15)$$

$$2S^0 + 3O_2 + 2H_2O \xrightarrow{SOB} 2SO_4{}^{2-} + 4H^+ \quad (2.16)$$

$$2S_2O_3{}^{2-} + 1/2O_2 + 2H^+ \xrightarrow{SOB} S_4O_6{}^{2-} + H_2O \quad (2.17)$$

$$S_xO_6{}^{2-} + S_2O_3{}^{2-} \xleftrightarrow{SOB} S_{x+1}O_6{}^{2-} + SO_3{}^{2-}; x = 3\ to\ 4 \quad (2.18)$$

$$S_xO_6{}^{2-} + H_2O \xrightarrow{SOB} S_{x-1}O_3{}^{2-} + SO_4{}^{2-} + 2H^+; x = 3\ to\ 5 \quad (2.19)$$

$$SO_4{}^{2-} + 2H^+ \rightarrow H_2SO_4 \quad (2.20)$$

$H_2SO_4$ subsequently attacks the vulnerable sewer cement matrix by changing its stability. The occurrence of these reactions also depends on various factors listed as follows;

*2.3.3.1.1. Sewer headspace conditions*

Sewer headspace, also known as 'sewer atmosphere', is characterised by a specific elevated temperature, RH, and airflow due to the influence of climate (winter and summer) or wastewater sources.

Temperature alters the microbial growth and sulphide oxidation reactions on the sewer wall by influencing $H_2S$ adsorption, which in turn, reduces $H_2S$ concentration in the sewer headspace (Jiang, Keller and Bond, (2014); Wu, Hu and Liu, (2018).

RH and airflow allow gaseous molecule circulation and adsorption by the condensate film. Li et al. (2017) reported that sulphuric acid on the sewer wall is formed when the RH ranges between 60% and 100%, while Grandclerc et al. (2017) observed an increased $H_2S$ adsorption rate with increasing RH. This RH variation is readily influenced by the temperature differences between the wastewater and sewer gaseous phase, the sewer wall temperature, and the external environment (Joseph et al., 2012). Therefore, climate and geography influence $H_2S$ corrosion (Saucier and Kaitano, 2018)

According to Nielsen, Hvitved-Jacobsen and Vollertsen (2012), increased airflow not only provides better mixing of the sewer atmosphere gases and ventilation but also reduces the thickness of the diffusive boundary layer at the liquid-gas interface, which in turn, results in a faster mass transfer of $H_2S$, and thus growth and acclimatisation of SOB. However, in cases where ventilation is not provided, the gas movement is decelerated, which slows $H_2S$ gas transfer.

*2.3.3.1.2. $H_2S$ gas concentration in the sewer headspace*

$H_2S$ concentration in the gaseous phase determines its adsorption, oxidation, and corrosion rate. According to Park et al. (2014) and Zhang et al. (2008), $H_2S$ concentrations within the range of 0.1 to 0.5 mg S/l trigger minor corrosion problems, while severe corrosion occurs at concentrations above 2.0 mg S/l. Above this concentration, the condensate film covered by SOB becomes fully penetrable by $H_2S$ gas, thereby influencing acid formation (Nielsen, Hvitved-Jacobsen and Vollertsen, 2012). $H_2S$ fluctuation is also postulated to affect biological sulphide oxidation (Jiang, Keller and Bond, 2014).

Joseph et al. (2012) observed concrete surface pH decreasing linearly with increasing H2S concentration in a laboratory study. However, Jiang et al. (2015) found that $H_2S$ concentration is merely an essential factor in initiating concrete corrosion at a concentration below 10 mg S/l. Above this concentration, the oxidation rate is the controlling factor; on the contrary, in long-term corrosion, higher $H_2S$ concentrations still affect the corrosion rates. Nevertheless, Sun et al. (2015) observed that a longer-term exposure of concrete to high $H_2S$ levels might result in a more significant accumulation of elemental sulphur in the corrosion layer, thus causing a more significant decrease in the sulphide adsorption rate after the exposure. Consequently, the activity of the SOB may be inhibited.

*2.3.3.1.3. $O_2$ gas concentration in the sewer headspace*

Oxygen gas in the corrosion layer is critical for SOB activity since it is used for oxidation reactions. However, Li et al. (2017) reported that its concentration decreases with concrete corrosion depth in the concrete microstructure, thus reducing the SOB population. Grengg et al. (2017) opposed this view since they observed no SOB population decrease with corrosion depth and thus suggested that oxygen-rich corrosion layers should not define SOB proliferation. This also indicates a need for further study to understand and demarcate the importance of oxygen on the SOB growth on the corroded layer.

### 2.3.4. Concrete corrosion – Factors

Once $H_2S$ adsorption and oxidation occur and $H_2SO_4$ acid is produced, the final process is the reaction between the concrete matrix and acid, i.e., BAC. This attack is commonly confused with the chemical sulphuric acid attack. These attacks might be similar in terms of the final effects but differ in their mechanisms and the ratio of their main corrosive products (gypsum and ettringite). BAC, as explained

previously, involves microorganisms which produce and convert $H_2S$ to intermediate acids such as thiosulphuric acid ($H_2S_2O_3$) and polythionic acid ($H_2S_xO_3$; x can be 3, 4, or 5), and later to sulphuric acid ($H_2SO_4$). These acids reduce the concrete surface pH, creating a more conducive environment for microorganism proliferation.

In contrast, chemical sulphuric acid attacks concrete chemically and mainly occurs at a specific acid pH or concentration. Furthermore, the corroded layer formed after a chemical sulphuric acid attack constitutes an extra barrier for further attack, while BAC creates excellent conditions for bacterial growth (Monteny et al., 2000; Gu, Bennett and Visintin, 2019). The following factors influence concrete corrosion;

*2.3.4.1.1. Sewer hydraulic actions*

Sewer hydraulic actions renew the sulphur cycle on the concrete surface by removing the corroded layer and microbial community, exposing sound concrete to further corrosion (Wells, Melchers and Bond, 2009), and significantly reducing the $H_2S$ oxidation rate for a short period (Nielsen et al., 2008; Wells and Melchers, 2014). Such hydraulic actions include frequent wastewater flushing in the tidal regions, occasional flooding, condensation of spray, the impacts of aerosols (colloidal suspension of particles dispersed in air or gas) on the crown region, and overflooding or overflow of sewer pipes during heavy rains (Li et al., 2017; Matias et al., 2017).

*2.3.4.1.2. Cementitious material heterogeneity*

The cementitious material heterogeneity includes the cementitious material's structural, durability, and mineralogical properties. These properties significantly contribute to the $H_2S$ adsorption and oxidation and the final corrosion process (Alexander, Bertron and de Belie, 2013).

Structural and durability factors, such as strength and penetrability, are associated with material porosity. BAC generally increases porosity in the concrete matrix due to decalcification which leads to strength reduction, mass and dimension loss, and crack growth which contributes to concrete penetrability (Islander et al., 1991; Beddoe & Dorner, 2005; Alexander, Bertron & Belie, 2013; House & Weiss, 2014). However, House and Weiss (2014) suggested that the material porosity might have a secondary effect on the corrosion rate, while Grandclerc et al. (2017) observed that the penetration of sulphur species depends on the type of mortars but does not correlate with the initial porosity of the mortars.

The mineralogical properties entail the aggregate types, binder type and quantity, and concrete microstructure. Studies (De Belie et al., 2004; Chang et al., 2005; Kiliswa and Alexander, 2014) show that aggregate types substantially influence the BAC. In sewer concrete, three types of aggregate are typically used; siliceous aggregates, calcareous aggregates, and aluminate-containing aggregates. Siliceous aggregates, which are acid insolubility, hasten the concrete paste corrosion. Calcareous aggregates, including dolomite and limestone, are soluble in acids; thus, they decelerate the attack by allowing uniform corrosion. Despite being soluble in acid, Aluminate-containing aggregates play a similar role as CAC in resisting BAC, see Section 2.4.2.

In the case of binder type, Kiliswa (2016) observed that CAC-based concrete outperformed PC-based concrete while incorporating Supplementary Cementitious Materials (SCM) in both PC and CAC-based concrete decelerated the attack. Herisson, Guinot and Saucier (2018) also observed that CAC concrete outperformed AAC and PC concrete. Hitherto, there are limited studies on the performance of other binders, such as LC[3], magnesium-based binders, and CSA. Kiliswa (2016) also observed that lower binder contents in PC, and higher binder contents in CAC concrete, led to less corrosion. Generally, these observations show that the performance of binders under BAC is more influenced by their chemical composition.

### 2.4. Binder chemical compositions

Binder chemical compositions of concrete refer to the mineralogical phases of binders that facilitate concrete structural and durability performance. These compositions undergo various hydration reactions to produce cementitious matrixes that contribute to the neutralisation[2] and bacteriostatic[3] effect of biogenic acid (Kiliswa, 2016). Because of this importance, reviewing and understanding their contributory mechanisms is crucial.

Binder systems consist mainly of the following chemical components; calcium oxide (C: CaO), alumina (A: $Al_2O_3$), silica (S: $SiO_2$), iron oxide (F: $Fe_2O_3$), magnesium oxide (M: MgO) and other minor oxides of sulphur (S), potassium (K) and sodium (Na). In South African sewer pipe construction, the commonly used binders are PC, possibly with supplementary cementitious materials as the host pipe and CAC as the sewer pipe linings in very aggressive conditions. However, other new binder systems are deemed competent in sewer construction. This section discusses the contribution of the chemical compositions of the three binder systems; PC, CAC and CSA under BAC.

#### 2.4.1. Portland cement (PC)

Portland cement is made by burning clay (aluminosilicate) and limestone in a kiln at a temperature of about 1450°C to form clinker. The clinker consists of four compounds; tricalcium silicate ($C_3S$), dicalcium silicate ($C_2S$), tricalcium aluminate ($C_3A$) and tetra calcium alumino-ferrite ($C_4AF$), which is mixed with a certain percentage of gypsum ($C\bar{S}$) to form cement. Under hydration, these clinker components hydrate to form CSH and CH, while $C_3A$ react with gypsum to form calcium sulphoaluminate hydrates (Ettringite) ($CA\bar{S}H$) at the very early stages. In the long term, ettringite transforms into harmlessly monosulphate.

Under BAC, the acid starts by reacting with CH, followed by CSH to form gypsum, and leaves silica-rich concrete (Grengg et al., 2017). The attack proceeds further by the reaction between the corrosion product 'gypsum' and calcium aluminate hydrates, and the available calcium sulphoaluminate hydrates and unhydrated tricalcium aluminate to form secondary 'ettringite' in the matrix, see Eq. 2.21 to 2.23.

[2] Neutralisation effect is the ability of cementitious materials (in a certain quantity) to neutralise a given quantity of acid.

[3] Bacteriostatic effect can be defined as the ability of the material to limit the growth of bacteria by interfering with abacterial protein production, DNA replication, or other aspects of bacterial cellular metabolism.

The acid attack generally causes decalcification resulting in concrete with less soluble hydrates in the form of amorphous hydrated oxides such as $SiO_2$, $Al_2O_3$, $Fe_2O_3$, MgO and some minor CaO (House and Weiss, 2014).

$$3C\bar{S}.H_2 + C_3AH_{12} + H_{14} \rightarrow C_6A\bar{S}_3H_{32} \quad (2.21)$$

$$2C\bar{S}.H_2 + C_4A\bar{S}H_{12} + H_{18} \rightarrow C_6A\bar{S}_3H_{32} \quad (2.22)$$

$$3C\bar{S}.H_2 + C_3A + H_{26} \rightarrow C_6A\bar{S}_3H_{32} \quad (2.23)$$

Despite CH being vulnerable to BAC, it plays a vital role in providing a neutralisation effect for the attacking acid, thereby reducing the destruction of the polymeric nature of the other calcium hydrate species by decalcification (Kiliswa, 2016).

The role of other less soluble oxides remaining after decalcification is not well discussed in the literature. For instance, the $SiO_2$ phase present as quartz in concrete is strongly resistant to acid attack, but this does not mean it contributes significantly to the binder's acid resistance per se, essentially having no neutralisation effect. The contribution of other oxides, such as $Al_2O_3$ and $Fe_2O_3$ to BAC is still under debate and is discussed below;

*2.4.1.1.1. Role of Aluminate phase in PC concrete*

High $Al_2O_3$ content in PC concrete is believed to increase the deterioration rate due to its potential to react with corrosion-end product 'gypsum' to form ettringite, see Eq. 2.21 to 2.23 (Alexander, Bentur, and Mindess, 2017; Noeiaghaei et al., 2017). For this reason, several standards specify limits on tricalcium aluminate content for concretes used in sulphate environments, as it is central for reducing ettringite formation (Grengg, Mittermayr, Ukrainczyk, Koraimann, et al., 2018). However, Kiliswa (2016) showed that PC concrete with alumina content (quantity unspecified), such as mixtures with alumina-containing aggregate or blends of PC and aluminate-rich SCMs, e.g. fly ash, experience corrosion rate reduction. Because of this, he believed that the aluminate phase must positively influence resisting BAC for two reasons; i) neutralisation capacity and ii) bacteriostatic effect.

When alumina-rich SCMs, such as fly ash and slag, are incorporated in PC concrete, alumino-ferrite phases and CSH with low Ca/Si ratios are formed (Dyer, 2017:17). It is possible that, under BAC, alumino-ferrite phases decompose to form amorphous gibbsite ($AH_3$): alumina gel) and ferrihydrite ($Fe_2O_3.0.5H_2O$), which usually persist at a low pH, see Figure 2.3 (Dyer, 2017:70). These phases are also conjectured to contribute to the bacteriostatic effect which is deliberated in CAC-based concrete (Section 2.4.2).

*2.4.1.1.2. Role of Iron phase in PC concrete*

The role of $Fe_2O_3$ in PC concrete under BAC is also ambiguous. During hydration, the reactivity of ferrites changes consecutively: $C_2F \rightarrow C_6AF_2 \rightarrow C_4AF \rightarrow C_6A_2F$ to calcium aluminate and ferrite hydrates (Eq. 2.24 to 2.25). These hydrates have a higher A/F ratio than in the anhydrous phase, thereby allowing the formation of some iron hydroxide ($FH_3$) gel (Kurdowski, 2017:190). However, direct hydration of $C_2F$ produces $C_4FH_{13}$, $C_4FH_{19}$ and $FH_3$ gel. At a temperature above 38$^o$C, the hexagonal hydrates transform to $C_3FH_6$, rapidly decomposing to CH and $FH_3$. This reaction occurs much slower

than that of calcium aluminate. Thus it is sometimes overlooked, which brings about limited experimental evidence showing the formation of this gel in cement pastes (Kiliswa, 2016). Likewise, in most PC concrete, these phases are not discussed. Therefore, further study is required.

$$C_6A_2F + 3(OH)^- \rightarrow C_4AH_{19} + C_2AH_8 + FH_3 \quad (2.24)$$

$$2C_6A_2F + 6(OH)^- \rightarrow 3C_4(A_{2/3}F_{1/3})H_{19} + FH_3 \quad (2.25)$$

Under BAC, the iron hydroxide gel ($FH_3$) is hypothesised to react with sulphuric acid to form iron hydrosulphates (Eq. 2.26) (Grengg et al., 2017; Grengg, Mittermayr, Ukrainczyk, Koraimann, et al., 2018). Grengg et al. (2018) also observed that these hydrosulphates are mostly found within the deterioration layers as a red/brown corroded product which sometimes is mistakenly interpreted as evidence of steel reinforcement corrosion, even at a relatively low pH.

$$H_2SO_4 + FH_3 \rightarrow Fe(SO_4)(OH) \cdot 2H_2O \quad (2.26)$$

The influence of iron hydroxide gel under BAC is also explained differently in the literature. Kiliswa (2016) suggested that the iron phase provides either a bacteriostatic effect to acid-generating SOB, a neutralisation capacity to the attacking acid, or both. However, in his study, its mechanism of influence was not studied. Nonetheless, this suggestion is not supported by Jiang et al. (2014), who observed that the iron phase is a primary cause of internal microcracking/damage in the intact concrete. Microcracking facilitates the diffusion of aggressive acid into the concrete for a further BAC.

Jiang et al. (2014) also observed that the corrosion products, i.e. gypsum and ettringite, were not the preliminary cause of internal microcracking/ damage in the intact concrete, as Grengg et al. (2018) claimed. Jiang et al. argued that these products were only formed at the corroding surface, as Okabe et al. (2007) speculated. The corrosion front was even and parallel along the whole surface of exposed concrete, implying no sign of sulphuric acid penetration. Therefore, they claimed that the microcracking could be more likely ascribed to the cycle of iron dissolution and precipitation in the iron-rich zone observed in the concrete with a high pH beyond the corrosion front.

Grengg et al. (2017) viewed the iron phase influence in concrete differently. They also observed a massive iron accumulation in the intact concrete. In contrast, they claimed that iron accumulation might favour the growth and proliferation of *A. ferrooxidans*, thereby accelerating the corrosion. This scenario might happen near intact concrete where oxygen is limited, thus, inhibiting the growth of aerobic *A. thiooxidans*.

Therefore, the crucial aspects that lack understanding are the extent of iron precipitates formed to cause damage or influence the growth of A. *ferrooxidans*; and the ability of the concrete pores to accommodate the iron precipitates, acting as repositories to slow down the corrosion process. These aspects suggest that minimum iron content in cement may increase concrete resistance to BAC and vice versa, although its thresholds are unknown. Thus, the contribution of iron phases in BAC needs further study.

Generally, when PC only is adopted for sewer concrete, it performs poorly and can lead to earlier deterioration than the design period. Incorporating supplementary cementitious materials with high alumina or iron content is still an open question since the literature is unclear about their roles.

### 2.4.2. Calcium Aluminate Cement (CAC)

Calcium Aluminate Cement (CAC) is produced by sintering or melting limestone with bauxite or aluminium hydroxide mixtures, depending on the acceptable impurity level (i.e. $Fe_2O_3$ and $SiO_2$) in the product (Kurdowski, 2017:604). It consists mainly of two oxides, $Al_2O_3$ and CaO, which form three crystalline phases: calcium aluminate (CA), calcium di-aluminate ($CA_2$), and mayenite ($C_{12}A_7$). CA is the main phase with about 40% to 70% by weight of CAC composition, $CA_2$ is 25%, and $C_{12}A_7$ is less than 10%. CA is responsible for strength development, while $CA_2$ and $C_{12}A_7$ are responsible for controlling the setting time. CAC is commercially divided into four types depending on raw materials and production techniques (see Table 2.2).

*Table 2.2: Types and chemical composition of CAC (Kurdowski, 2017:604; Scrivener, Cabiron & Letourneux, 1999; Pereira et al., 2017)*

| CAC grade | Colour | Chemical composition, % | | | | Raw alumina material | Production technology | Production temperature, °C |
|---|---|---|---|---|---|---|---|---|
| | | $Al_2O_3$ | $Fe_2O_3$ | $SiO_2$ | CaO | | | |
| **Standard low alumina** | Grey or buff to black | 37-40 | 11-17 | 3-8 | 36-40 | Red bauxite | Melting | 1350 |
| **Low alumina, low iron** | Light buff or grey to white | 48-51 | 1-1.5 | 5-8 | 39-40 | Red bauxite | Melting | 1350 |
| **Medium alumina** | White | 51-60 | 1-2.5 | 3-6 | 30-40 | White bauxite | Sintering and melting | 1410-1450 |
| **High alumina** | White | 78-80 | 0-0.5 | 0-0.5 | 17-27 | Red bauxite | Sintering | 1760 |

The hydration of CAC leads to the formation of two calcium aluminate hydrates ($CAH_{10}$ and $C_2AH_8$) and gibbsite or alumina gel ($AH_3$); see Eq. 2.27 and 2.30. $CAH_{10}$ is formed at lower temperatures below 20°C, while $C_2AH_8$ is formed at increasing temperatures. Above 30°C, both hydrates transform into a stable phase, $C_3AH_6$ (Kurdowski, 2017:607); see Figure 2.9. The dissolution of these hydrates leads not only to the formation of additional gibbsite (Eq. 2.28 to 2.30) but also to a loss of the hydrate matrix volume leading to porosity increase and strength reduction (Dyer, 2017:18).

$$CA + 10H \rightarrow CAH_{10} \quad (2.27)$$

$$2CA + 11H \rightarrow C_2AH_8 + AH_3 \quad (2.28)$$

$$2CAH_{10} \rightarrow C_2AH_8 + AH_3 + 9H \quad (2.29)$$

$$3C_2AH_8 \rightarrow 2C_3AH_6 + AH_3 + 9H \quad (2.30)$$

Under BAC, CAC is widely known as a high acid-resistant binder due to; i) its long chain of dissolution (Figure 2.9); ii) neutralisation by its hydrates ( see Eq. 2.31 to 2.33 and Figure 2.9 whereby 6 moles of CAC neutralise about 24 moles of acid); iii) gibbsite stability at a lower pH of between 3 and 4, and iv) at a pH below 3, gibbsite reacts with $H_2SO_4$ to form aluminium sulphate $Al_2(SO_4)_3$ (Eq. 2.34), of which

ions such as $Al^{3+}$ are deemed to provide a bacteriostatic effect in the microbial ecosystem by binding with the DNA of SOB and halting the duplication of its cells. However, the $Al^{3+}$ bacteriostatic effect is not universally supported by the literature. Buvignier (2018) showed that the bacteriostatic effect of $Al^{3+}$ is only temporary since the microorganisms acclimate with time. Undoubtedly, the role of aluminium ions is still debated, particularly around quantifying its impact.

$$CAH_{10} + H_2SO_4 \rightarrow C\bar{S} + AH_3 + 9H \quad (2.31)$$

$$C_2AH_8 + 2H_2SO_4 \rightarrow 2C\bar{S} + AH_3 + 9H \quad (2.32)$$

$$C_3AH_6 + 3H_2SO_4 \rightarrow 3C\bar{S} + AH_3 + 9H \quad (2.33)$$

$$2AH_3 + 3H_2SO_4 \rightarrow Al_2(SO_4)_3 + 12\,H \quad (2.34)$$

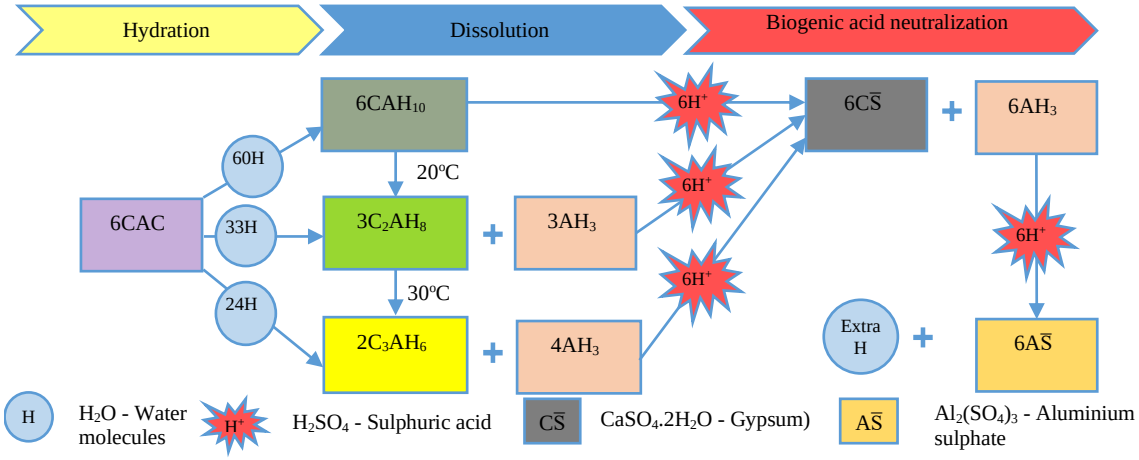


*Figure 2.9: CAC hydration and deterioration behaviour under BAC derived from Scrivener, Cabiron & Letourneux (1999)*

The contribution of $SiO_2$ in CAC concrete is only discussed when blended with SCMs with this oxide, such as fly ash and slag, to form hydrates, such as $C_2ASH_8$ (stratlingite) and $C_3SH_6$ (Kiliswa, 2016). However, under BAC, its influences are not well discussed, and this might be due to the same reason explained in Section 2.4.1.

In the case of $Fe_2O_3$, the literature provides little or no information about the iron hydroxide gel in CAC concrete. However, Kiliswa (2016) observed that $Fe_2O_3$ plays an active role during BAC mechanisms due to lower corrosion rates exhibited by CAC-based mixtures (CAC contains up to 18% $Fe_2O_3$). Bearing that in mind, understanding the contribution of $Fe_2O_3$ to BAC was not a significant focus of his study. For this reason, further study is required to understand its mechanism and contribution to suppressing BAC in the CAC concrete.

Besides the neutralisation and bacteriostatic effects provided by CAC concrete under BAC, CAC concrete also tends to resist deterioration physically or mechanically. It is believed that the nature of its deterioration zone consists of end products (i.e. gibbsite and stratlingite) that offer some mechanical or physical integrity to the deteriorated layer, thereby providing a barrier for further attack (Khan et al., 2019; Kiliswa, Scrivener & Alexander, 2019).

Apart from recent attention towards understanding the resisting mechanism of CAC, it has also been used for decades in sewer construction. The first documented sewer systems constructed with CAC were built in the 1950s in Australia and Malaysia. After 40 years, the inspection conducted at the Australian sewers (Mildura, Victoria, and Bundaberg, Queensland) exhibited good condition. In Malaysia, the Kuala Lumpur sewer system, made of PC concrete but internally lined by a CAC mortar of 13 mm, is also standing. At that time, the CAC liner was considered a sacrificial layer to replace after specific service life. In the 1960s, in Durban, South Africa, many kilometres of sewer pipes were constructed using CAC concrete with alumina-containing aggregates. Finally, in the 1980s, Egypt adopted CAC as a sacrificial layer. (Hewlett, 2004:Chapter 13).

### 2.4.3. Calcium SulphoAluminate (CSA) cement

Calcium SulphoAluminate (CSA) cement is a variant of CAC and was first synthesised by Ragozina in 1957 and developed by Alexander Klein in the 1960s. It is produced by burning a blend of limestone, bauxite, and anhydrite or gypsum at a temperature between 1250°C and 1300°C then blended with 15% to 25% of additional gypsum. At 800°C to 900°C, $C_2S$ and $C_2AS$ are formed. Above 1000°C, $C_2AS$ combines with gypsum ($C\bar{S}$) to form calcium sulphoaluminate (Ye'elimite: $C_4A_3\bar{S}$) and calcium sulpho-silicate (Ternesite: $C_5S_2\bar{S}$). At 1180°C, $C_5S_2\bar{S}$ converts to $C_2S$ and $C\bar{S}$. At the end of production, CSA consists of only three main phases; mainly Ye'elimite ($C_4A_3\bar{S}$), and minor Belite ($C_2S$) and gypsum ($C\bar{S}$) (Odler, 2003).

CSA is a low-carbon cement because less limestone is used during production, which lowers the carbon footprint. Also, it is an energy-saving cement since its calcination temperature is between 100°C and 150°C lower than PC, and it requires less grinding because its clinker is porous. Despite its merits, CSA has a short setting time due to the rapid and significant ettringite formation, which makes it challenging to apply in most concrete applications. It is also an expansive material with a lower pH than OPC. The pH values of the CSA pore solution are highly variable, ranging from 8.5 to 13 (Alonso et al., 2010). Because of this, CSA was initially used in special applications that required rapid setting, shrinkage compensation, and high early-age strength (Coppola et al., 2018).

Hydration of Ye'elimite depends significantly on the presence of gypsum and lime in the system; i) in pure water, it yields monosulphate and alumina gel (Eq. 2.35), ii) in the presence of gypsum, it yields ettringite, monosulphate, and gibbsite; however, monosulphate is mainly formed when gypsum is depleted (Eq. 2.36 and 2.37), iii) in the presence of CH only, it yields a hydrogarnet phase and AFm phase (Eq. 2.38), while iv) in the presence of both CH and gypsum, it yields ettringite solely with high expansion (Eq. 2.39) (Odler, 2003; Habert, 2014). Hydration of Belite takes place at a later stage due to its low reactivity. It reacts with amorphous $AH_3$ to form stratlingite ($C_2ASH_8$) rather than CSH (Eq. 2.40). Usually, Ye'elimite and gypsum hydrations occur in the first seven days, while belite remains unhydrated even after 90 days (Coppola et al., 2018).

$$C_4A_3\bar{S} + 18H \rightarrow C_4A\bar{S}H_{12} + 2AH_3 \quad (2.35)$$

$$2C_4A_3\bar{S} + 2C\bar{S}H_2 + 52H \rightarrow C_6A\bar{S}_3H_{12} + C_6A\bar{S}_3H_{32} + 4AH_3 \quad (2.36)$$

$$C_4A_3\bar{S} + 2C\bar{S}H_2 + 36H \rightarrow C_6A\bar{S}_3H_{32} + 2AH_3 \quad (2.37)$$

$$C_4A_3\bar{S} + 7CH + H \rightarrow C_3AH_6 + 2C_3A.C\bar{S}.CH.H \quad (2.38)$$

$$C_4A_3\bar{S} + 8C\bar{S}H_2 + 6CH + 74H \rightarrow 3C_6A\bar{S}_3H_{32} \quad (2.39)$$

$$C_2S + AH_3 + 5H \rightarrow C_2ASH_8 \quad (2.40)$$

CSA concrete has been used for 40 years in China to produce self-stressing concrete pipes. However, there is no documentation about its performance in sewer environments (Péra and Ambroise, 2004). The only related study is by Yang et al. (2018), who studied the performance of new artificial reef concrete made of CSA, sea sand and seawater compared to PC concrete with river sand and potable water in biogenic sulphuric acid for a marine environment. After subjecting concrete specimens to a biogenic sulphuric acid simulator with *Acidithiobacillus ferrooxidans* bacteria for 4 months, it was observed that CSA outperformed OPC in terms of mass and compressive strength losses. Besides, the following facts are of interest in studying its performance in sewer environments;

i) The amount of CH and CSH produced during its hydration is very low due to the absence of $C_3S$ and small quantities of $C_2S$ present (Aïtcin, 2008; Kleib et al., 2018). Thus, the absence of CH and CSH might reduce its susceptibility to BAC
ii) Its dominant hydration by-product is ettringite, which is stable at pHs above 10.7(Aïtcin, 2008). It is also an expansive phase, which might result in internal cracking and loss of strength in the long term. Therefore, Ye'elimit content in CSA is limited to 30% to 40% to avoid expansion effects (Coppola et al., 2018)
iii) Among other hydration products is alumina gel which, in CAC systems, contributes to the resistance to BAC as it is stable at a pH of 4. Therefore, it is hypothesised that this matrix might increase its potential to resist BAC.
iv) The pH of its interstitial solution is much lower than that of PC (Kleib et al., 2018). This might have a negative impact since the lower the pH, the higher the bacterial colonisation. (The reported pore solution pH values of CSA mortars are highly variable, ranging from 8.5 to 13(Kalogridis et al., 2000; Alonso et al., 2010))

### 2.4.4. Summary

The mechanisms and contribution of chemical compositions of four binder systems, i.e. PC, CAC, and CSA, were discussed. A summary of the anhydrous binder phases, hydration products, and corrosion by-products is given in Table 2.3. It was found that, in the sewer environment, PC is the worst performer, while CAC is the best performer. Therefore, CAC and PC can be used as performance benchmarks for ranking the performance of other binder systems.

PC poor performance is associated with CH and CSH matrices that are alkaline and prone to acidic attack. CAC performance is contributed by its long chain of dissolution, which provides high neutralisation capacity, and the alumina content, which produces soluble alumina gel. This gel is stable at a pH of 3-4, and when dissociating under BAC, it produces aluminium ions which offer a bacteriostatic effect. This effect is unlike heavy metals (8.1.1.9.A), which destroy the microorganisms

but deactivate their microbial activities. However, there are still disparities in various views, thus requiring better understanding. The contribution of the iron phase as part of binder chemical composition was also discussed; its influence still requires further examination as the literature contradicts it.

*Table 2.3: Chemical composition, hydration products, and precipitates of different binder types formed under sulphuric acid attack*

| **Binder type** | | **Portland cement** | **Calcium Aluminate Cement,** | **Calcium SulphoAluminate cement** |
|---|---|---|---|---|
| | | PC | CAC | CSA |
| **Anhydrous phases** | | $C_3S$<br>$C_2S$<br>$C_3A$ $C_4AF$<br>$C\bar{S}$ | CA<br>$CA_2$<br>$C_{12}A_7$ | $C_4A_3\bar{S}$,<br>$C_2S$<br>$C\bar{S}$ |
| **Hydration products** | **Main** | CSH<br>CH | $CAH_{10}$<br>$C_2AH_8$<br>$C_3AH_6$<br>$AH_3$ | $C_6A\bar{S}_3H_{32}$ |
| | **Minor** | $C_3AH_{12}$ $C_6A_2FH_6$ $C_6A\bar{S}_3H_{32}$<br>$FH_3$ | - | $C_6A\bar{S}_3H_{12}$<br>$C_2ASH_8$<br>$C_3AH_6$<br>$AH_3$ |
| **$H_2SO_4$ corrosion products** | | $C\bar{S}$ $C_6A\bar{S}_3H_{32}$ | $C\bar{S}$<br>$A\bar{S}$ | ?? |
| C: CaO<br>S: $SiO_2$ | | F: $Fe_2O_3$<br>A: $Al_2O_3$ | $\bar{S}$: $SO_3$<br>H: $H_2O$ | N: $Na_2O$<br>$\bar{C}$: $CO_2$ |

The influence of CSA is not well documented in the literature despite being used in Asia (China) for concrete pipe construction. It is, therefore, interesting to study the influence of its hydration products, mainly ettringite (aluminate containing hydrates) and gibbsite, which in the CAC system contribute to resisting the attack. Therefore, more research is needed in this area.

Besides modification of the concrete microstructure by altering the binder chemical composition, there are other approaches to mitigating BAC in concrete, see Appendix A.

## 2.5. Biogenic acid corrosion (BAC) modelling

When designing a sewer system, several physical, chemical, and biological processes and financial and functional requirements must be well-thought-out to ensure proper system serviceability. The best way to consider these processes and requirements is by predicting the service life and designing the sewer corresponding to that service life. It can be achieved by having adequate and reliable prediction models considering all BAC contributory factors. These service life prediction models assist engineers and researchers in not only predicting the service life of a concrete structure, which remains in its intended function without approaching serviceability and durability limit states but also in understanding the BAC mechanism (Alexander & Beushausen, 2019).

The desired service life of a sewer is often set at about 100 years, which is enough time for a sewer to serve about three generations with anticipated maintenance but without major repairs being necessary. However, achieving this lifetime is challenging due to the changes in sewer environments, which are

becoming more aggressive with time, ongoing changes in construction materials and techniques, and dynamic improvements in knowledge about the mechanism of attack in sewers (Alexander & Beushausen, 2019). Because of these disputes, most existing prediction models are inadequate and some obsolete. Prediction models herein are either a single mathematical expression or many expressions combined in a program to simulate or relate the behaviours of various factors contributing to BAC. When designing a new sewer system, such expressions are used to determine a durable and cost-effective material that can accommodate the anticipated corrosive condition.

Most existing models were developed to accommodate sewer conditions of earlier times when populations were lower, the nature of wastewater was less contaminated, and the culture of the served community and climate conditions were different. Authorities set regulations controlling the quantity and quality of wastewater released from industries, but domestic wastewater also consists of components that facilitate the growth of bacteria (Hvitved-Jacobsen et al., 1988). Environmental changes also pose challenges for sewers, for example, in countries affected by drought. With limited water usage, the wastewater flow declines with increasing retention time and concentration of biodegradable matter and nutrients for bacterial growth, eventually leading to high $H_2S$ production (Chappelle et al., 2019).

Ongoing changes in construction materials due to technological developments also affect the development of service life prediction tools. Several modern materials, such as newer and different cement, modern chemical admixtures, and antimicrobial additives, are being introduced into the industry with unknown performance levels in many cases. With sewer deterioration rates being relatively slow, the industry is often unwilling to invest time and money in studying and understanding newer materials or establishing prediction models that can accommodate these materials. Despite the advancement and availability of computer-based modelling and simulation platforms, researchers have fewer incentives to utilize them readily. Even when these platforms are applied, there is limited information or field data to assist calibration.

Therefore, the subsequent sections aim to review various prediction models and understand their applications and limitations. This knowledge, then, can assist in modifying or refining the commonly used prediction model in sewer concrete, the ‘LFM’ model. The knowledge acquired from the previous sections is crucial in reviewing the competence and significance of the existing models.

### 2.6. BAC service life prediction approach

The service life of a sewer system can be predicted using two approaches (Wells & Melchers, 2014b);

- The traditional approach assesses the conditions of an existing sewer concrete by visual inspection. With the aid of an extrapolation approach and successive visual inspections, the future remaining service life can be predicted. Thus, the existing system can be designed based on predicted service life.
- The second approach uses inventory data such as sewer environmental conditions, sewer construction materials, and structural and durability properties of existing sewers to predict the service life of a new sewer. This technique, however, requires models to correlate and interpret

the inventory data into practical meaning. These models are generally empirical prediction models formulated after long-term field and laboratory observations.

Developing any empirical prediction model for sewer concrete requires understanding the factors explicated in Section 2.3, simulating the influence of each factor, and applying scientific and mathematic knowledge to explain interrelation and interdependence. As discussed in Section 2.2, BAC is categorised into four stages: sulphide build-up, $H_2S$ emission, $H_2S$ adsorption and oxidation, and concrete deterioration/corrosion. At each stage, various models have been developed to simulate each stage leading to the final process. Therefore, it is essential to review the whole range of models developed in each stage to understand their contribution to predicting concrete sewer service life, with the main emphasis of this study strictly on the last stage –concrete corrosion.

## 2.7. Sulphide build-up prediction

The models for predicting sulphide formation are the basis for understanding and predicting corrosion rates of concrete sewers. At this stage, sulphide concentration in the wastewater can be estimated and assist in predicting the quantity of sulphide released in the gas phase. This information provides the basis for the extent of sulphide released, adsorbed by an unsubmerged concrete wall, and subsequently oxidised to sulphuric acid.

Pomeroy (1976) categorised sulphide build-up prediction in concrete sewer pipes based on the flow states of wastewater, i.e. full or partially full flow. This is because each state has different factors that alter the growth of SRB and sulphide build-up.

### 2.7.1. Prediction equations for full-flow pipes

Sulphide is mainly produced in the anaerobic condition, which is strictly not attained in fast-flowing, turbulent flow, and partially full sewers. This condition is mainly achieved in full-flowing gravity sewers, pressure mains and stagnant zones, where organic nutrients are abundant, DO is depleted, and the amount of sulphide produced in the submerged biofilm and the wastewater is substantial.

Therefore, sulphide build-up is considered a total sulphide produced in the biofilm and that produced in the wastewater. With these assumptions, Pomeroy (1959) and Boon and Lister (1975) (Elmaleh et al., 1998) formulated Eq. 2.41 and 2.42, respectively. These equations are similar but differ in COD and BOD, whose ratio is about 2:1. Also, Eq. 2.41 estimates the maximum rate of sulphide build-up, while Eq. 2.42 predicts the average rate.

Flow velocity and sulphate concentration in the wastewater were not considered when formulating these equations. It was assumed that wastewater flow velocity and sulphate concentration are sufficient to avoid significant nutrient depletion (Pomeroy & Parkhurst, 1977).

$$\frac{d[S]}{dt} = 10^{-3}[BOD](1.07)^{(T-20)}(1 + 0.37d)r^{-1} \quad (2.41)$$

$$\frac{d[S]}{dt} = 0.28X10^{-3}[COD](1.07)^{(T-20)}(1 + 0.37\mathrm{d})r^{-1} \quad (2.42)$$

Where;

[S] Dissolved sulphide concentration in the sewage (mg/l)

$d$ Sewer hydraulic diameter (m)

| | | | |
|---|---|---|---|
| $T$ | Temperature | $[S0_4]$ | Sulphate concentration (g S/m$^3$) |
| $[BOD]$ | Biochemical oxygen demand (mg/L) | $v$ | Sewer flow velocity, m/s |
| $[COD]$ | Chemical Oxygen Demand (mg/L) | $t$ | Time (s) |
| $r$ | Sewer hydraulic radius (m) | $s$ | Sewer's gravity (m/m) |

However, flow velocity and sulphate concentration were considered in formulating Eq. 2.43 (Elmaleh et al., 1998). It was assumed that the supply of nutrients into the biofilm for sulphide production is limited when the flow velocity is very slow or approximate to zero. A moderate velocity appears to maintain the nutrient supply, while a higher velocity than the moderate does not affect the build-up rate. This assumption was opposed by Pomeroy (1959), who observed that, in pipes flowing full, the influence of velocity is minor if it is below 1.2 m/s, while the velocities necessary to prevent build-up in the flowing sewage depend on the effective BOD, see Eq. 2.44. Similarly, sulphate concentration is a limiting factor only if its amount is less than a value between 10 % and 25 % of the BOD or between 4 % and 10 % of the COD (Pomeroy, 1976).

$$\frac{d[S]}{dt} = 5X10^{-3} v[BOD]^{0.8}[S0_4]^{0.4}(1.14)^{(T-20)}d^{-1} \tag{2.43}$$

$$v = 0.137x\left([BOD](1.07)^{(T-20)}\right)^{0.496} \tag{2.44}$$

Hvitved-Jacobsen et al. (1988) developed an empirical Eq. for sulphide flux prediction from a biofilm in pressure mains, see Eq. 2.45. They observed that the rate of sulphide build-up depended on the nature/quality of wastewater, i.e. different organic compounds and sulphate reducing potential. Therefore, they introduced the parameter '$a$' in the equation to distinguish the water quality. The values of '$a$' were;

- 0.0015 for typical domestic sewage,
- 0.003 for both domestic and industrial sewage, and
- 0.006 for industrial sewage.

The first two values were restricted to a COD value less than 500 and 1000 g $O_2$/m$^{3,}$ respectively, and 50 g $O_2$/m$^3$ was deducted from COD to account for inactive soluble COD.

$$\frac{d[S]}{dt} = a\sqrt{[COD]-50}\,(1.07)^{(T-20)}r^{-1} \tag{2.45}$$

A similar model was evaluated and modified based on results obtained from two intercepting pressure mains in the Northern part of Jutland, Denmark (Nielsen, Raunkjær & Hvitved-Jacobsen, 1998), see Eq. (2.46). They observed that the sulphide build-up rate highly depends on the wastewater quality and temperature. Therefore, they established new values for the parameter '$a$';

- 0.001–0.002 for typical domestic wastewater without industrial sewage,
- 0.003–0.006 for wastewater from mixed domestic and industrial sources, and
- 0.007–0.010 wastewater with biodegradable organic matter from mainly food industries.

The temperature dependency value '1.07' was replaced by '1.03' because high sulphide production rates were observed at low temperatures.

$$\frac{d[S]}{dt} = a\sqrt{[COD] - 50}\,(1.03)^{(T-20)} r^{-1} \tag{2.46}$$

Elmaleh et al. (1998) observed that Eq. 2.46 predicted sulphide generation in full sewer pipes conveying wastewater with organic matter content of about 500-1000 mg/l of total COD. Therefore, they derived a further equation for sewer pipes conveying wastewater with organic content of less than 500 mg/l. They observed that sulphide generation is proportional to roughly the square of the COD, see Eq. 2.47.

$$\frac{d[S]}{dt} = 0.052x\ 10^{-3}[COD]^{1.9} \tag{2.47}$$

Boon (1995) derived an Eq. that predicts the average sulphide production, Eq. 2.48. Even though the equation did not necessarily reflect the worst conditions in a typical sewer, it provided a good correlation between predicted and observed sulphide concentrations found by Severn Trent Water.

$$\frac{d[S]}{dt} = 6.08\ x\ 10^{-3}[COD](1 + 0.004d)\ (1.07)^{(T-20)} r^{-1} \tag{2.48}$$

In conclusion, the critical parameters for determining sulphide generation in a full-flow sewer pipe are organic matter content, quality of wastewater, and temperature. However, there is a significant variation in COD's proportionality constants and exponent values. Some indicate that the proportionality constant stands for the quality of the wastewater. Others provide an empirical value mainly obtained from laboratory and site data. Therefore, the exponent value of COD depends on the laboratory or site data and varies from 0.5 to 2.

### 2.7.2. Prediction equations for partially full-flow pipes

Depending on the flow capacity and gradient of a sewer pipe, wastewater in the pipe can flow partially full, which is the standard mode of operation. In this case, the sewer pipe has a gas phase-filled part with oxygen gas that can dissolve in the water phase and $H_2S$ and $CO_2$ emitted from the water phase. The dissolved oxygen prevents sulphide build-up in the wastewater, and if it penetrates further to the biofilm, it can chemically and biologically oxidise part of sulphides to sulphate, thereby facilitating the sulphur cycle. With this knowledge, Pomeroy and Parkhurst (1977) designed an empirical Eq. (Eq. 2.49) for predicting the sulphide build-up in the water phase when the wastewater in the sewer pipe flows partially full.

$$\frac{d[S]}{dt} = M'[BOD](1.07)^{(T-20)} r^{-1} - N[S](sv)^{0.375} d^{-1} \tag{2.49}$$

The equation consists of two parts;

- The positive part indicates sulphide generated in the biofilm only, as Eq. (2.41) in the full pipe, and

- The negative part indicates sulphide losses due to the combined effects of chemical and biological sulphide oxidation, sulphide emission in the gaseous phase, and, indirectly, the effect of natural ventilation of sulphide in the gas phase.

The negative part of the equation was formulated after several experiments in the Los Angeles County Sanitation District sewer system by Pomeroy & Parkhurst (1977). They observed that the rate of sulphide loss due to sulphide oxidation and emission is proportional to both the rate of absorption of oxygen and sulphide concentration in the wastewater. Oxygen absorption rate depends on the flow gradient and velocity, while sulphide concentration, particularly $H_2S$, in the wastewater depends on the pH of the wastewater.

The coefficients M' and N depend on the effect of DO on the sulphide build-up; thus, there are two sets of these coefficients which vary with sewer pipe diameter up to 1 m;

- M' = 0.32 x $10^{-3}$ and N = 0.96, for sewers showing actual traits of sulphite build-up. The DO concentration in the wastewater stream herein is low, while sulphide built-up is in progress.
- M' = 0.32 x $10^{-3}$ and N = 0.64., for normal sewers rarely showing traits of sulphide build-up. In this case, the sulphide build-up is generally lower than predicted.

When the sewer diameter ranges between 1 and 2 m, and the flow depth is higher than half of the pipe diameter, the M' value is 0.5 x $10^{-3}$.

Sometimes, the rate of sulphate loss in the wastewater approaches the rate of sulphide generation in the biofilm. In this state, the sulphide concentration eventually reaches a limiting level, denoted as $[S]_{lim}$, and then the rate of sulphide build-up in the system equals zero. Thus, Eq. 2.49 is expressed as Eq. 2.50, and the sulphide limiting level is evaluated from Eq. 2.51.

$$M'[BOD](1.07)^{(T-20)}r^{-1} = N[S]_{lim}(sv)^{0.375}d^{-1} \tag{2.50}$$

$$[S]_{lim} = \frac{M'[BOD](1.07)^{(T-20)}d}{N(sv)^{0.375}r} \tag{2.51}$$

## 2.8. $H_2S$ emission prediction

The equilibrium between the water and gas phase is disturbed at a high sulphide species concentration in the wastewater. Depending on the factors expressed in Section 2.3.2, $H_2S$ gas is released into the gas phase. Various modelling equations have been developed to simulate the process. Lahav, Sagiv & Friedler (2006) sort these equations mainly into two categories;

- Empirical models which link sulphide emission with hydraulic sewer parameters describing flow conditions, i.e. mean flow velocity, sewer gradient and turbulence, and
- Empirical models based on gas transfer measurements by assessing a relationship between $H_2S$ and $O_2$ gas transfer and replacing the gas transfer coefficient of sulphide with that of oxygen

The first approach modifies Pomeroy and Parkhurst's model (Eq. 2.49). The negative part herein describes the rate of sulphide losses due to sulphide emission only, and the $H_2S_{(aq)}$ concentration,

$[H_2S]_{(aq)}$ as a substitute for the total sulfide concentration, $[S]$ (EPA, 1985), see Eq. 2.52. The $H_2S$ release is primarily controlled by the hydrodynamic condition of the wastewater flow.

$$\frac{d[S]}{dt} = -0.69[H_2S]_{aq}(sv)^{0.375}d^{-1} \quad (2.52)$$

Where:

| | |
|---|---|
| $[H_2S]_{aq}$ | Concentration of $H_2S_{(aq)}$ which is equal to $\left(\frac{[S]}{1+\left(\frac{K_{S1}}{10^{-pH}}\right)+\left(\frac{K_{S1}.K_{S2}}{10^{-2pH}}\right)}\right)$ $\frac{1}{1+\left(\frac{K_{S1}}{10^{-pH}}\right)+\left(\frac{K_{S1}.K_{S2}}{10^{-2pH}}\right)}$ is the ratio between dissolved $H_2S$ in the aqueous phase and total sulphide concentration |
| $K_{s1,2}$ | Thermodynamic equilibrium constants for the sulfide weak-acid system adjusted for Debye–Huckel effects |

The second approach is a modified sewer re-aeration equation developed by Yongsiri, Vollertsen & Hvitved-Jacobsen (2004) (Eq. 2.53). The equation associates the $H_2S$ emission rate with the overall mass transfer coefficient for $H_2S$ ($K_L a_{H_2S}$), temperature, ionic strength and pH values, and links with the overall mass transfer coefficient of oxygen ($K_L a_{O_2}$) given in Eq. 2.54 (Yongsiri et al., 2004). The gas release here is primarily controlled by $H_2S$ concentration gradients within the water film at the air-water interface.

$$K_L a_{H_2S} = (1.736 - 0.196\ x\ pH)K_L a_{O_2} \quad at\ 4.5 < pH < 8.0 \quad (2.53)$$

$$K_L a_{O_2} = 0.86(1 + 0.2Fr^2)(sv)^{0.375}d^{-1}\theta^{(T-20)} \quad (2.54)$$

Where;

| | |
|---|---|
| $Fr$ | Froude number is given as $v/\sqrt{gd}$ , where g is the acceleration due to gravity and d is the density of water |
| T | Temperature, K |
| $\theta$ | Temperature coefficient for reaeration, 1.024 |

When combining Eq. 2.53 and 2.54, the $H_2S$ emission rate based on adopting sewer reaeration models is given in Eq. 2.55.

$$\frac{d[S]}{dt} = 0.86(1 + 0.2Fr^2)(sv)^{0.375}d^{-1}\theta^{(T-20)}(1.736 - 0.196pH) \quad (2.55)$$

However, Lahav, Sagiv and Friedler (2006) claimed that the two approaches are unreliable for the following reasons. Firstly, Eq. (2.52) was primarily developed assuming that sulphide losses in the wastewater due to sulphide emission is minimal. Secondly, the gas transfer coefficients used in Eq. (2.55) were derived from thoroughly stirred vessels which did not simulate a typical gravity sewer flow. With these, the emission rates may be overestimated compared to those observed in a typical sewer. Therefore, Lahav et al. (2004) and Lahav, Sagiv and Friedler (2006) developed a new equation which considers the following assumptions:

- In the fast-flowing and very turbulent flow pattern mainly experienced in a gravity sewer, sulphide emission is the only process affecting the concentration of sulphide in the wastewater, and
- The rate of sulphide emission between the water and gas phases is equal to the product of the reaction's driving force and a mass transfer rate constant.

The driving force is essentially a difference between the concentration of $H_2S$ in the water phase and its saturation which depends on Henry's law constant, $K_H$ (Carrera et al., 2016). The mass transfer coefficient of $H_2S$ is related to the sewer environment mixing conditionn, which depends on hydraulic sewer characteristics such as head-loss and geometrical properties of a sewer. Thus, parameter G, a mean velocity gradient, was introduced as a measure of turbulence intensity and a link with the mass-transfer rate constant, see Eq. 2.56.

$$\frac{d[S]}{dt} = 8.0\ X10^{-3}\ G\ ([H_2S]_{aq} - K_H P_{H_2S})\ d^{-1} \quad (2.56)$$

Where:

| | |
|---|---|
| $G$ | Mean velocity gradient, given as $\sqrt{\gamma s \frac{v}{\mu}}$ , where γ is the unit weight of liquid, N/m$^3$ and μ is the dynamic viscosity. Ns/m$^2$ |
| $K_H$ | Henry's law constant |
| $P_{H_2S}$ | Partial pressure of Hydrogen sulphide gas concentration (ppm) |

In contrast, the developers of Eq. 2.56, namely Lahav's model, combined and applied the basic principles used in developing Eq. 2.52 and 2.55 and then compensated for their weaknesses. With this, the model can predict $H_2S$ emission better than the earlier models. Abdikheibari et al. (2016) demonstrate that the results predicted by this model correlated well with experimental results. On the other hand, Vollertsen et al. (2008) concluded that the $H_2S$ emission rate controls the corrosion rate, and high corrosion rates can occur even at a low $H_2S$ concentration in the gas phase.

## 2.9. $H_2S$ adsorption and oxidation prediction

Once $H_2S$ gas is present in the sewer headspace, it is then adsorbed and subsequently oxidised, chemically and biologically, to sulphuric acid on the surface of the sewer concrete wall. The rate of $H_2S$ adsorption and subsequent oxidation depends significantly on the properties of the pipe material. However, due to various pipe materials, it is not easy to estimate the extent to which $H_2S$ is adsorbed and subsequently oxidised. For instance, when concrete is used as pipe material, the fact that it is a heterogeneous material with different constituents in terms of its physical and chemical properties complicates understanding its response under $H_2S$ exposure.

EPA (1974) suggests that the amount of adsorbed and oxidised $H_2S$ on the concrete surface is equal to the bulk water $H_2S$ release, implying that all $H_2S$ emitted is immediately absorbed by concrete surfaces, resulting in zero $H_2S$ in the gas phase (Vollertsen et al., 2011). However, this assumption is invalid since $H_2S$ transfer into the concrete wall is not a rapid process. Despite the challenges, two studies have

attempted to model the rate of $H_2S$ adsorption and oxidation. The following subsections explain these models and their limitations.

### 2.9.1. Vollertsen et al., (2008): $H_2S$ oxidation and adsorption prediction model

According to Vollertsen et al. (2008), the $H_2S$ oxidation rate on the concrete surface equals the $H_2S$ adsorption rate, assuming that all $H_2S$ adsorbed must ultimately be oxidised. Thus, the $H_2S$ oxidation rate was determined as a slope of the measured $H_2S$ concentration in the gas phase over time and expressed as an exponential function of the $H_2S$ concentration, see Eq. (2.57).

$$\frac{d\left(P_{H_2S}\right)}{dt} = k_p P_{H_2S}^n \tag{2.57}$$

Where:

| | |
|---|---|
| $n$ | Reaction orders (0.45 to 0.75) |
| $k_p$ | Process rate constant (ppm$^{(1-n)}$/s) |

By applying the ideal gas law to Eq. 2.57, the volume oxidation rate is converted into a flux, $F_{H_2S}$ i.e. a surface-specific $H_2S$ oxidation rate, see Eq. 2.58.

$$F_{H_2S} = \frac{d\left(P_{H_2S}\right)}{dt} 0.1013 \frac{32}{RT} \frac{V_g}{A_c} = \left(0.1013 \frac{32}{RT} \frac{V_g}{A_c} k_p\right) P_{H_2S}^n \tag{2.58}$$

Considering that $0.1013 \frac{32}{RT} \frac{V_g}{A_c} k_p = k_F$ , which is defined as the $H_2S$ adsorption and oxidation rate, and 0.1013 is the atmospheric pressure. Then Eq. 2.58 can be expressed as Eq. 2.59.

$$F_{H_2S} = k_F P_{H_2S}^n \tag{2.59}$$

Where:

| | |
|---|---|
| $k_F$ | Surface specific process rate constant (0.005 mgS/m$^2$s) (ppm $H_2S$) $^{-n}$ |
| $V_g$ | Total gas volume (m$^3$) |
| $A_c$ | Concrete surface area subjected to sewer gas (m$^2$) |
| $R$ | Universal gas constant, (J/Kmol) |
| $F_{H_2S}$ | Surface-specific hydrogen sulphide oxidation rate, (gS/ m$^2$ s) |

It was observed that the $H_2S$ oxidation rate increases with increasing $H_2S$ concentration without showing any saturation tendency, even at a high $H_2S$ concentration. The rate Eq., therefore, follows a simple n$^{th}$ kinetic order with 'n' values ranging from 0.45 to 0.75 and an average rate constant ($k_p$) of 0.005 mg S m$^{-2}$ s$^{-1}$ (ppm $H_2S$)$^{-n}$. (Refer to Yuan (2014) for more information).

Nielsen, Hvitved-Jacobsen & Vollertsen (2012) modified Eq. 2.59 to simulate the effect of airflow velocity on the $H_2S$ adsorption and oxidation rate constant. It was found that the Reynold number (Re) could be used to show the relationship, see Eq. 2.60, where m = 0.65 and n =0.8. This equation is applied when the $H_2S$ release in the sewer system is due to turbulent conditions. In this case, the air-water equilibrium controls the concentration of $H_2S$ in the gas and water phase.

$$F_{H_2S} = k_F Re^m P_{H_2S}^n \tag{2.60}$$

Additionally, Sun et al. (2014) related the $H_2S$ adsorption rate to the $H_2S$ concentration as an exponential function (Eq. 2.61), Monod function (a mathematical model for the growth of microorganisms) (Eq. (2.62), and power function (Eq. 2.59). Table 2.4 shows the coefficients and the R-squared values. According to their findings, the exponential function had the highest prediction accuracy. The Monod function indicated a maximum (saturation) adsorption rate, $\mu_{max}$ which was considerably higher than that observed in the $H_2S$ adsorption test. With this, the Monod function cannot be used to define the relationship between the $H_2S$ adsorption rate and the $H_2S$ concentration, but it can well characterise the corrosion rate at various $H_2S$ concentrations. The power function, however, provided an excellent fit for the $H_2S$ adsorption rate. Its coefficient values related well to those Vollertsen et al. (2008) observed.

$$F_{H_2S} = \mu_{max}(1 - e^{-KP_{H_2S}}) \tag{2.61}$$

$$F_{H_2S} = \frac{\mu_{max} P_{H_2S}}{K_s + P_{H_2S}} \tag{2.62}$$

*Table 2.4:Kinetic parameters determined for various models according to (Sun et al., 2014)*

| **Coefficients** | $\mu_{max}$ | **K** | $K_s$ | $k_F$ | **n** | **$R^2$** |
|---|---|---|---|---|---|---|
| Unit | ($mg/m^2/h$) | (ppm) | ($ppm^1$) | ($mgS/m^2/h/ppm^{-n}$) | (-) | (-) |
| Exponential function | 497 | 0.0135 | - | - | - | 0.9960 |
| Monod function | 760 | - | 108 | - | - | 0.9948 |
| Power function | - | - | | 14 | 0.70 | 0.988 |

Where:

| | |
|---|---|
| $K$ | Empirical coefficient ($ppm^{-1}$) |
| $K_s$ | Half velocity constant (ppm) |
| $\mu_{max}$ | Maximum adsorption rate (mg $S/m^2/h$) |

Nevertheless, Eq. (2.59) to (2.62) are only valid for evaluating the $H_2S$ oxidation rate if the $H_2S$ adsorption rate is considered equal to the oxidation rate. However, the equations do not consider other significant oxidation influencing factors such as SOB growth, exposed surface absorption properties, and RH. Besides, (Grandclerc et al., 2017) observed that cementitious materials, such as CAC, which perform well in aggressive sewer environments, have high $H_2S$ adsorption rates. This observation indicates that not all adsorbed $H_2S$ is oxidised to sulphuric acid, and some might be trapped in the material microstructure without being oxidised.

### 2.9.2. Jensen et al. (2009): $H_2S$ oxidation prediction model

According to Jensen et al. (2009), under an adequate supply of $H_2S$ gas, $H_2S$ is immediately oxidised to elemental sulphur and sulphuric acid. In a continuous uptake of $H_2S$, a fraction of elemental sulphur is oxidised to sulphuric acid at the same rate as $H_2S$, while bacteria store the other fraction in the bacterial globules. When $H_2S$ depletes, the stored fraction is oxidised slowly into sulphuric acid by the SOB. The rate of $H_2S$ oxidation on the concrete corrosion layer can, therefore, be described as the combination of the following processes.

- Loss of $H_2S$ by adsorption and diffusion in the corrosion products expressed as a first-order kinetic, Eq. 2.63;

- Abiotic oxidation; is expressed as a power function for both $H_2S$ and $O_2$ concentration in the corrosion products. In this case, the corrosion products, expressed as the concentration of total solids, are assumed to catalyse the oxidation reaction. This relation is similar to that of the abiotic oxidation of sulphide in the wastewater (Nielsen, Vollertsen & Hvitved-Jacobsen, 2003), Eq. 2.64; and
- Biotic oxidation: is a saturation-type kinetic applied to simulate the bacterial growth process in suspended culture. A similar kinetic is applied in the wastewater by Hvitved-Jacobsen, Vollertsen & Nielsen (2013), Eq. 2.65. The principle behind this equation is the Monod type function, a mathematical model for the growth of microorganisms.

$$\frac{dS_{H_2S}}{dt} = -\mu_{loss} S_{H_2S} \tag{2.63}$$

$$\frac{dS_{H_2S}}{dt} = -v_{abio} {S_{H_2S}}^{a} {S_{O_2}}^{b} X_{TS} \tag{2.64}$$

$$\frac{dS_{H_2S}}{dt} = -w_{bio} \frac{S_{H_2S}}{K_{H_2S} + S_{H_2S}} \frac{S_{O_2}}{K_{O_2,H_2S} + S_{O_2}} X_{TS} \tag{2.65}$$

Where:

| | |
|---|---|
| $S_{H_2S}$ | $H_2S$ concentration, g $H_2S/m^3$ |
| $\mu_{loss}$ | Rate constant for auto-oxidation and losses, 7.7 x $10^{-3}$/h |
| $v_{abio}$ | Rate constant of abiotic hydrogen sulphide oxidation, 2.1 x $10^{-7}$ (g $H_2S$-S)$^{-0.17}$($m^3$)$^{1.17}$ / (g TS)/h |
| $S_{O_2}$ | Dissolved oxygen concentration, g $O_2/m^3$ |
| $X_{TS}$ | Total solid concentration, g $TS/m^3$ |
| $K_{O_2,H_2S}$ | Half saturation constant for oxygen in the oxidation of $H_2S$, 0.1 g $O_2/m^3$ |
| $K_{H_2S}$ | Half saturation constant for $H_2S$, 1.35 x $10^{-3}$ g $H_2S$-$S/m^3$ |
| $w_{bio}$ | Rate constant for the biotic oxidation of $H_2S$, 3.94 X $10^{-5}$ g $H_2S$-S /g TS/h |
| $a$ | Reaction order of $H_2S$ in the abiotic oxidation medium value is 1.17 |
| $b$ | Reaction order for oxygen in the abiotic oxidation of $H_2S$, the value of 0 |

However, in Eq. 2.64 and 2.65, the oxygen concentration was found as a non-limiting factor because the amount of dissolved oxygen within the corroded layer is abundant; thus, the biotic kinetic and the half-saturation constant for oxygen, under biotic oxidation, could not be determined. It was, therefore, concluded that biotic oxidation was the dominant process since the abiotic oxidation and losses by the adsorption and diffusion were only 1.5% and 1.1% of the biotic oxidation, respectively, see Figure 2.10

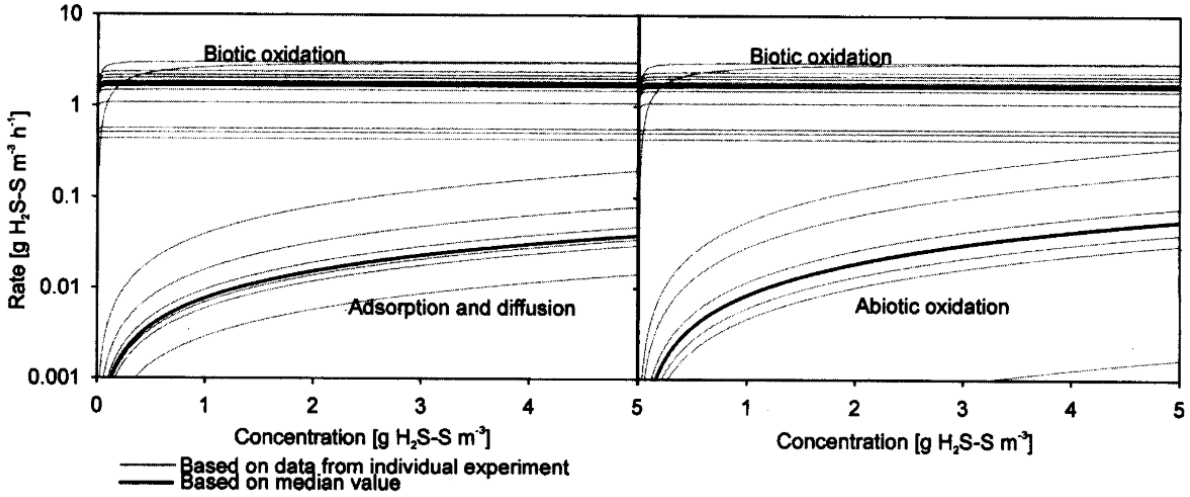


*Figure 2.10:Comparison of the simulated rate of biotic oxidation with the losses by adsorption and diffusion and abiotic oxidation (Jensen et al., 2009)*

Even though all oxidising influencing factors were considered in developing this model, it was yet developed based on a readily corroding sewer pipe. The model does not state if it can be applied on 'fresh' intact concrete. The model also does not consider the influence of sewer concrete chemical composition. Grandclerc et al. (2017) observed that the composition of ferrous compounds and hydroxyl ions in the moist layer of exposed concrete surface catalyses the $H_2S$ adsorption kinetic, while sulphate ions prevent the kinetic. The influence of ferrous compounds is associated with the redox reaction (Eq. 2.66), which rapidly converts $H_2S$ into elemental sulphur. The hydroxyl ions from the dissolution of portlandite or alumina gel tend to influence the dissociation of $H_2S$ gas, thereby accelerating the adsorption. However, the theory proposed to explain the prevention of the $H_2S$ adsorption process by sulphate ions was unclear, indicating a need for further study.

$$H_2S + 2Fe^{3+} \rightarrow S^o + 2Fe^{2+} + 2H^+ \quad (2.66)$$

### 2.9.3. Subsection summary

In summary, Figure 2.11 illustrates the factors required for modelling $H_2S$ adsorption and oxidation rate on the concrete sewer pipe. The figure shows that adsorption and oxidation are two different processes but interdependent. The adsorption process is mainly physical, involving physical factors including the concrete surface area, $H_2S$ concentration, sewer temperature, RH and sewer atmospheric pressure. The oxidation process, by contrast, takes place both chemically and biologically. It depends significantly on chemical and biological parameters. Therefore, adsorption and oxidation processes must be studied and understood separately to understand and simulate the processes involved in converting the $H_2S$ gas in the sewer headspace to sulphuric acid on the exposed sewer wall.

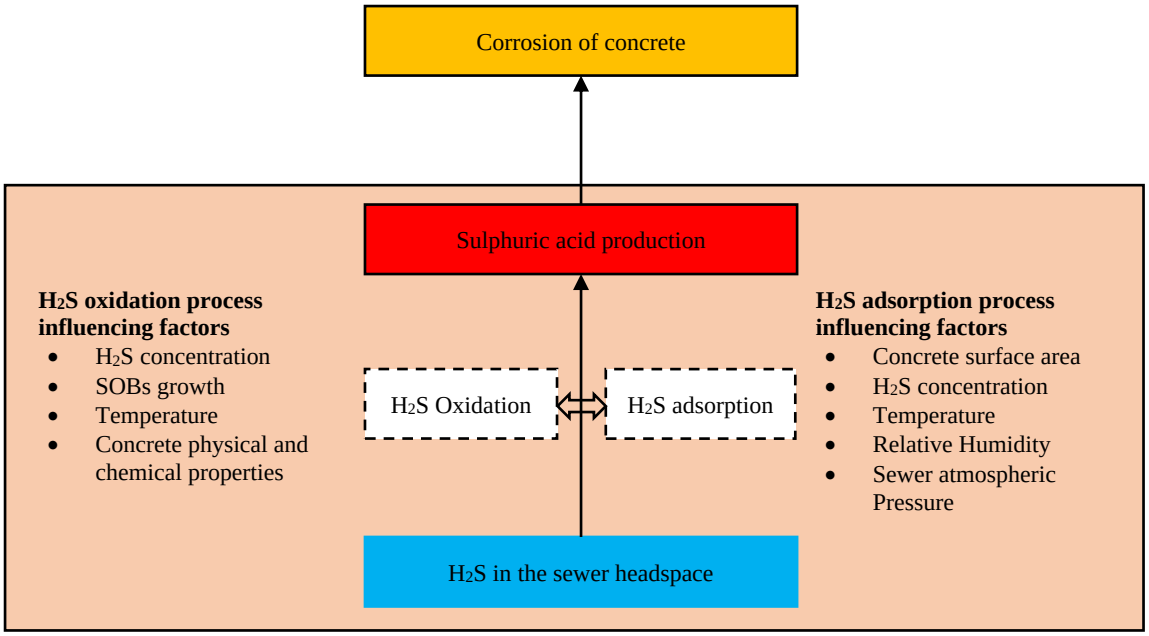


*Figure 2.11: Schematic diagram illustrating the processes and factors responsible for converting $H_2S$ gas in the sewer headspace to $H_2SO_4$ on exposed concrete surfaces before the corrosion process. The double-sided arrow indicates the interdependent relationship between $H_2S$ adsorption and subsequent oxidation of the $H_2S$ to $H_2SO_4$.*

## 2.10. Concrete corrosion prediction

The degree of concrete deterioration under BAC is determined by evaluating or measuring its corrosion rate. Concrete corrosion rate represents the volumetric loss of concrete by a unit of surface area when referring to a specific period. It is an essential parameter for estimating the service life of sewer concrete, given a cover depth enough to sacrifice over a specified period to protect the underlining steel reinforcement. The parameter is also used as a comparative and performance indicator of concrete with different mix designs and cementitious materials. The sewer aggressivity can also be evaluated by comparing the corrosion rate of similar materials subjected to different sites.

Numerous models predict the corrosion rate of concrete under BAC. These models can be divided into two approaches; the empirical modelling approach and the thermodynamic modelling approach (Beddoe, 2016).

The empirical modelling approach includes all models based on experimental observations of the behaviour and importance of various influencing factors to the final corrosion (Ikumi & Segura, 2019). This approach provides a practical and efficient tool for the sewer designer. The models developed under such conditions include the Life Factor Method (LFM) (EPA, 1992), Improved LFM (Kiliswa, 2016), Bilinear model (Wells & Melchers, 2015), WATS model (Jensen et al., 2009), and SATIR model (Beddoe & Dorner, 2005; Beddoe, 2016). Bakera, Alexander and Beushausen (2021) provide more details about this model.

On the other hand, the thermodynamic modelling approach involves applying the combined knowledge of thermodynamics principles and mathematical representations of the biochemical, chemical and transport processes involved in concrete deterioration. The approach aims to understand the durability

aspect of various cementitious materials when subjected to aggressive sewer environments. With the application of this approach, the existing or newly developed design tools can be improved accordingly, and this application is now possible due to the significant advancement in computational tools and valuable thermodynamic data (Le-Bescop et al., 2013).

The following subsection reviews a commonly used empirical prediction model, i.e., the Life Factor Method (LFM), for sewer concrete design. The subsections also highlight LFM limitations and how other empirical and thermodynamic modelling approaches can be applied to modify its effectiveness.

### 2.10.1. Life Factor Method (LFM)

The LFM (Eq. 2.67 to 2.69) is a widely used deterministic model in designing concrete subjected to BAC. It was derived from the three sets of factors influencing BAC: sulphide generation within the wastewater, $H_2S$ release from the sewer, and concrete corrosion rate.

$$C_{avg} = 11.4k\frac{\phi_{sw}}{A} \tag{2.67}$$

$$\phi_{sw} = 0.69(sv)^{0.375}[H_2S]_{aq}\frac{W}{P} \tag{2.68}$$

$$A = \frac{c(CaO_{cement}) + a(CaO_{agg})}{d} x \frac{100}{56} \tag{2.69}$$

Where;

| | | | |
|---|---|---|---|
| $C_{avg}$ | Average (annual) corrosion rate (mm/year) | $P$ | Perimeter of the pipe wall above the sewage surface (m) |
| $k$ | Efficiency factor | $W$ | Sewage surface width (m) |
| $\phi_{sw}$ | Average $H_2S$ flux to the pipe wall (g/m$^2$/h), | a and c | Aggregate and cement content in concrete (kg aggregate or cement/m$^3$ concrete) |
| $A$ | Alkalinity of the concrete material (g $CaCO_3$ per g concrete material) | d | Density of concrete (kg/m$^3$) |
| $S$ | Hydraulic gradient (m/m) | $CaO$ | Calcium oxide phase in cement and aggregate |
| $V$ | Hydraulic velocity (m/s) | 100/56 | Molar mass ratio of $CaCO_3$ and CaO |
| $J$ | Proportion of dissolved sulphides in sewage present as $H_2S$ (%) | | |

LFM model was first used to design PC-based concrete pipes for the Central Trunk Sewer by the city of Sacramento, California, the U.S.A., in 1976 and later expanded to other countries such as South Africa. During its application, it was observed that the predicted corrosion depths were smaller than the actual depths measured in most sewer sections, and the most corroded areas coincided with regions with daily sewage flow levels, at the crown, and high turbulence flow.

The nonconformity was attributed to certain assumptions made during the introduction of parameters, such as the efficiency factor 'k' and $H_2S$ flux. '$\phi_{sw}$', and the exclusion of parameters, such as turbulence

and the critical corroded area, during the model development. Based on these observations, in 1992, two factors, which are the crown corrosion factor (CCF), ranging from 1.5 to 2.0, and turbulence corrosion factor (TCF), ranging from (i) 1.0 to 2.5 for areas with typical turbulent flow conditions, and (ii) 5.0 to 10.0 for very turbulent junctions, were introduced in Eq. 2.67 to form Eq. 2.70.

$$C_{max} = \left(11.4\text{k}\frac{\Phi_{sw}}{A}\right).CCF.TCF \tag{2.70}$$

However, Eq. 2.70 fails to consider recent findings on the general knowledge of BAC and associated contributory factors. Recently, it has been discovered that BAC initiation time and corrosion rate depend on sewer environmental factors, such as $H_2S$ concentration, RH and temperature. It was also learnt that corrosion development or resistance potential is attributed to concrete alkalinity and other concrete chemical compositions, such as aluminium and iron oxides from binder and aggregates.

### 2.10.2. Improved LFM - 2016

In studying the LFM model regarding corrosion rates in the Virginia Experimental Sewer (VES) in South Africa, Kiliswa (2016) observed that Eq. 2.67 could well predict the total sulphides in the sewer and the corrosion rate of plain PC-based concrete. He also suggested that Eq. 2.70 can only be used to calibrate the model if the alkalinity factor is first investigated and adequately incorporated into the model. He arrived at this conclusion after observing that the model could not predict the corrosion of concrete consisting of blends of PC and other SCMs and CAC-based systems.

Therefore, Kiliswa refined the model by replacing the alkalinity factor, A, with an 'effective resistance capacity' ($RC_{eff,}$) and introducing another factor, 'sewer headspace aggressivity factor' q. He called this model the 'Improved LFM.' – Eq. 2.71 and 2.72. The 'effective resistance capacity' was introduced on the basis that incorporating the alkalinity factor (Eq. 2.69) only as the rate-controlling parameter of the corrosion rate of concrete under BAC was inaccurate. Other binder chemical compositions, such as $Al_2O_3$, and $Fe_2O_3$, contributed significantly to neutralising the attacking acid and providing the bacteriostatic effects but were omitted. The sewer headspace aggressivity factor was also introduced due to the influence of sewer headspace temperature and RH of a particular sewer. However, this factor was never characterised or conclusively quantified in his study.

$$C_{avg,t} = 11.4\text{k}\frac{\Phi_{sw}}{\left(RC_{eff}\right)^{1.49}}q \tag{2.71}$$

$$RC_{eff} = \left(\text{CaCO}_{3_{eqv.agg}}\right) + \left(CH_{eqv.CAC}\right) + \left(\frac{CH^{-1}_{eqv.PC}}{100}\right) + \left(AH_{3_{eqv}}\right) + \left(FeO(OH)_{eqv}\right) + \left(\frac{Al}{Ca}\right) + \left(\frac{Fe}{Ca}\right) \tag{2.72}$$

Where,

| | |
|---|---|
| $q$ | Sewer headspace aggressivity factor |
| $RC_{eff}$ | Effective resistance capacity, where Eqv. = Equivalent and agg. = Aggregate |
| | *$AH_3$* = Aluminium hydroxide gel; *CaO* = Calcium oxide phase in cement and aggregate; *CH* = Calcium hydroxide; *$CaCO_3$* = Calcium carbonate; *FeO(OH)* = Iron oxyhydroxide; and *Al*, *Ca*, and *Fe* = Aluminium, Calcium, and Iron |

### 2.10.3. LFM challenges

Despite Kiliswa's improvement, the LFM model is still limited. In the literature, binder constituents, such as CaO, $Al_2O_3$, and $Fe_2O_3$, influence the corrosion rate to counter how they are quantified in the Improved LFM model. According to Jiang et al. ( 2014 and 2016), the presence of iron phases in concrete under attack leads to the formation of iron oxide precipitates which cause internal cracking in the intact zone of the concrete. The cracking then contributes to transporting aggressive components into the intact zone, thereby accelerating the attack. On the other hand, the aluminium phase has been considered to contribute to the bacteriostatic effect. However, Buvignier (2018) found that, in the presence of aluminium ions in concrete, the microorganisms acclimate with time and consequently continue to proliferate. A lack of clarity in these crucial aspects indicates that a clear understanding of their roles must be established before further modifications and improvements to the LFM.

Further, the 'sewer aggressivity factor' introduced in the improved LFM conflicts with the 'efficiency factor'. Both factors are empirically evaluated and function of sewer headspace conditions, especially temperature and RH. Kiliswa (2016) states that the sewer aggressivity factor accounts for sewer headspace temperature and RH influence. However, a range of values has not been evaluated but can conceivably differ from one sewer to another. According to EPA (1974), the efficiency factor has never been measured, and its value depends on engineering judgement. Its value approaches unity when the rate of acid formation is slow and maybe as low as 0.3 to 0.4 when the rate of acid formation is rapid and if much condensate is formed (e.g. warm wastewater and cold pipe wall). Thus, these factors need re-consideration and reconciliation.

Using field data from the VES (Kiliswa, 2016), the improved LFM model could adequately predict the corrosion rate of PC and CAC-based concrete. However, its competence is unclear when predicting the corrosion rates of concretes made with other modern binder systems such as CSA. Regardless of the challenges, the LFM is still a practical and useful model that engineers can easily apply. Therefore, modifying this model to increase its broader usage can significantly contribute to sewer design and applications.

### 2.10.4. Other BAC prediction models

#### 2.10.4.1. WATS Model - 2013

Wastewater Aerobic-Anaerobic Transformations in Sewers (WATS) model is a conceptual and numerical model mainly applicable for simulating sewer processes and predicting $H_2S$ gas-associated problems in gravity sewers and force (pumped) mains. The main objective of the WATs model is to manage and control sewer processes that lead to concrete corrosion, human health impacts, and odour nuisance caused by hydrogen sulphide and volatile organic compounds (Hvitved-Jacobsen, Vollertsen & Nielsen, 2013; Nielsen et al., 2014). Notably, this model does not directly aim at sewer corrosion.

The model consists of various components and their corresponding transformation processes expressed by the rate equations and stoichiometric constants. A combination of the rate equations and stoichiometric constants results in several coupled differential equations, which can only be solved numerically (Nielsen et al., 2014). The transformation processes, i.e., aerobic, anoxic, or anaerobic transformations, can be divided into five conceptual process elements, i.e., sulphur cycle, aerobic,

heterotrophic transformations of organic matter, aerobic transformations of organic carbon and sulphur, anoxic, heterotrophic transformations of organic matter, and aerobic and anaerobic transformations or organic carbon and sulphur. Therefore, the sulphur and carbon cycles are central elements and the backbone of the WATS process concept.

Only sewer process elements for the sulphur cycle formulation are included in BAC. The sulphur cycle concerns both anaerobic and aerobic processes and includes all phases leading to concrete corrosion; the biofilm, the water phase, the sewer headspace, and the surfaces exposed to the sewer headspace. The matrices presented in Table 2.5 are considered as the differential of the first row is equal to the sum of the processes listed in the respective column. For instance, the rate of surface concrete corrosion is given in Eq. 2.73. A complete WATS model contains fifteen coupled differential equations solved by the Euler approach. For more details regarding the model, see (Hvitved-Jacobsen, Vollertsen & Nielsen, 2013).

*Table 2.5: WATS Sewer Process Model for Formulation of Sulphur Cycle as a Process Matrix (Hvitved-Jacobsen, Vollertsen & Nielsen, 2013)*

| **Process rate** | $\frac{d}{dt}(S_{SO_4})$ | $\frac{d}{dt}(S_O)$ | $\frac{d}{dt}(S_{(-II)})$ | $\frac{d}{dt}(P_{H_2S})$ | $\frac{d}{dt}(S_{H_2SO_4})$ | $\frac{d}{dt}(d_{corr})$ |
|---|---|---|---|---|---|---|
| $H_2S$ formation in biofilm, r1 | -1 | | 1 | | | |
| Chemical oxidation of sulphide in bulk water, r2 | 1 | $-\frac{1}{R_{Cwc}}$ | -1 | | | |
| Biological oxidation of sulphide in bulk water. r3 | 1 | $-\frac{1}{R_{Cwb}}$ | -1 | | | |
| Oxidation of sulphide in biofilm, r4 | 1 | $-\frac{1}{R_{Cfb}}$ | -1 | | | |
| H2S emission, r5 | | | -1 | $\frac{RT}{32}\frac{V_w}{V_g}$ | | |
| $H_2S$ oxidation at the concrete surface, r6 | | | | -1 | $\frac{RT}{32}$ | $\frac{100k}{\sigma_{conc}ART}\frac{V_g}{A_c}$ |

$S_{(-II)}$ = Sum of $H_2S$, $HS^-$, and $S^{2-}$ concentrations in the water phase (g S/m$^3$)
$S_{SO_4}$ = Sulphate concentration (g S/m$^3$)
$P_{H_2S}$ = $H_2S$ partial pressure in the gas phase (ppm)
$S_{H_2SO_4}$ = Sulphuric acid concentration in the water film of moist sewer surface (g S/m$^3$)
$S_O$ = dissolved oxygen concentration (g $O_2$/m$^3$)
$d_{corr}$ = Surface corrosion depth (m)
r# = process rate (/day)
$R_{Cwc}$ = Stoichiometric constant of chemical oxidation of sulphide in bulk water (g S/g $O_2$)
$R_{Cwb}$ = Stoichiometric constant of biological oxidation of sulphide in bulk water (g S/g $O_2$)
$R_{Cfb}$ = Stoichiometric constant of biological oxidation of sulphide in biofilm (g S/g $O_2$)
$R$ = Universal gas constant (=8.314 J/mol/K)
$T$ = Temperature (K)
$V_w$ = Gas volume (m$^3$)
$V_g$ = Water volume (m$^3$)
$k$ = Fraction of the produced sulfuric acid results in corrosion of about 0.5
$A_c$ = Concrete surface area,
$\sigma_{conc}$ = Specific mass of the concrete material (g/m$^3$)
A = Concrete alkalinity (the molar weight of $CaCO_3$ is 100 g/mol)

$$\frac{d}{dt}(d_{corr}) = \frac{100k}{\sigma_{conc}ART} x \frac{V_g}{A_c} x\, r6 \tag{2.73}$$

The WATS model clearly shows the relationship between sewer deterioration physical, chemical, and biological processes, although it neglects sulphide production in the biofilms. Each process in the model is described by an equation and depends on the user's choice among a large panel of empirical equations (Carrera et al., 2016). Compared with the LFM, the WATS model incorporates more variables, making it more complicated for engineering applications. Besides concrete alkalinity, other chemical compositions of concrete responsible for neutralising the attacking acid are not considered.

#### 2.10.4.2. Bi-linear model - 2015

Wells and Melchers (2015) developed a bi-linear model for predicting sewer pipe corrosion (Eq. 2.74). The model relates the corrosion rates to the sewer environmental conditions, i.e. sewer headspace temperature, RH, and $H_2S$ concentration. The influence of sewer headspace temperature is expressed as a function of the activation energy using the Arrhenius relationship. The corrosion rate of concrete is directly related to the square root of $H_2S$ concentration in the sewer headspace. The influence of RH was evaluated based on a relationship between the sewer RH and the concrete moisture content, which is a function of the concrete pore size distribution, the geometry and tortuosity of the individual pores, and the temperature of the concrete wall relative to that of the sewer headspace. Finally, the corrosion rate is directly proportional to the moisture content in the concrete pores. Eq. (2.74), therefore, predicts the corrosion rate of concrete corresponding to a specific sewer environment. While the bi-linear model considers factors most prediction models fail to incorporate, it still ignores the material aspect.

$$C_{avg} = A_S \, x \, {P_{H_2S}}^{0.5} x \left(\frac{0.1602H - 0.1355}{1 - 0.977\mathrm{R}H}\right) x \, e^{Ea/RT} \tag{2.74}$$

Where:

| | |
|---|---|
| $A_S$ | Scaling constant |
| $RH$ | Relative humidity |
| $Ea$ | Activation energy (kJ/mol) |

#### 2.10.4.3. SATIR Model – 2005 and 2016

The 'Säure, Angriff, Transport, Instationär, Reaktion' (SATIR) model (Beddoe & Dorner, 2005; Beddoe, 2016) is a numerical model for simulating the degradation of concrete exposed to static or flowing acidic media. The simulation describes the degradation process by diffusion of acid species through the initial porosity of the concrete at the exposed surface and the subsequent corroded layer produced by the dissolution of the cement matrix and, if needed, the dissolution of the aggregates, as shown in Figure 2.11.

Dissolving the cement matrix and aggregate particles produces hydroxyl and other dissolved ions associated with calcium, aluminium, iron and sulphur. The hydroxyl ions neutralise protons of the attacking acid, while other ions diffuse toward the concrete surface, leaving a porous corroded layer. The growth of the corroded layer depends on the acid diffusion rate through the corroded layer, subsequent reaction with the intact front and the precipitation of calcium salt. The degree of corrosion is defined by the thickness and porosity of the corroded layer and, if abrasion effects occur, the thickness of the removed material (Beddoe & Dorner, 2005; Beddoe, 2016).

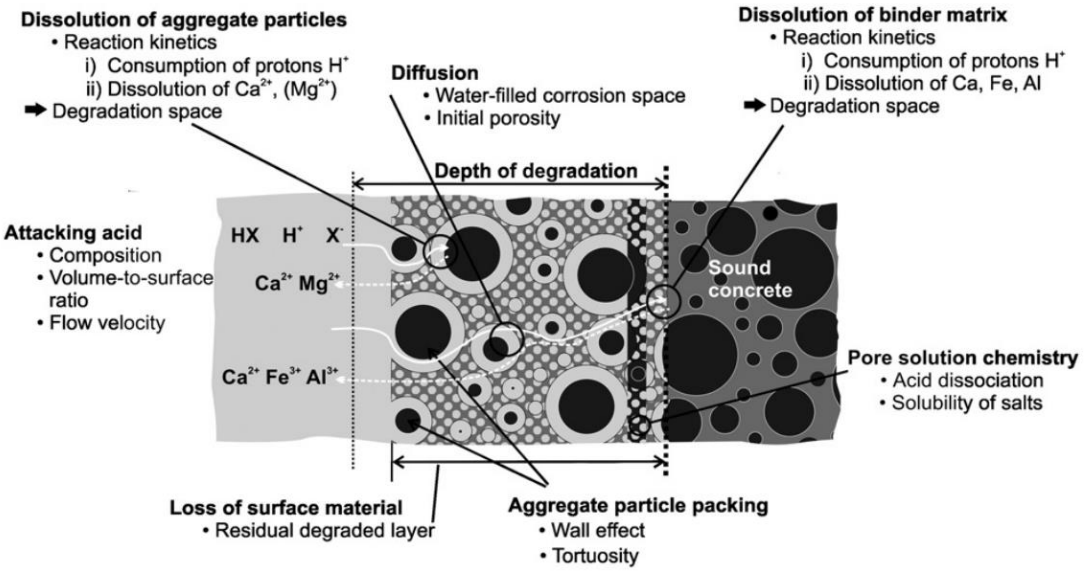


*Figure 2.12: Processes and conditions considered by the SATIR Model (Beddoe, 2016).*

For simplicity, the SATIR model considers only one transport process, i.e., diffusion. It entails mathematical equations that explain the aggressivity of the attacking acid and its state, i.e. static or flowing, the dissolution of the paste matrix, the diffusion of species through concrete pore solution at a certain depth, the aggregate solubility and distribution in near-surface concrete, the loss of concrete surface and the precipitation of gypsum. These equations are found in (Beddoe & Dorner, 2005; Beddoe, 2016).

The model clearly shows the chemical and transport interaction between the attacking acid and the exposed concrete. It covers the simulation of all chemically attacking acids (strong to weak acids) on PC concrete. In the case of the BAC, the model is applicable only after the onset of sulphuric acid production since it ignores the influence of sewer headspace conditions and the biological factors related to the production of the acid. It principally focuses on the material properties and their role in the final corrosion process. However, the model regards the concrete neutralisation capacity only as the total calcium, calculated from the binder's calcium content and the concrete's binder content, and not as an alkalinity factor as in the LFM and WATS models.

### 2.10.5. Application of other corrosion prediction models in improving the LFM

Based on the reviewed models, it was observed that most fail to effectively and efficiently incorporate concrete-associated factors such as aggregate and binder components, the so-called material aspect, in predicting concrete corrosion. However, some applicable principles that might be valuable in improving the LFM model were highlighted. The WATS model provides the principles for incorporating microbial growth rate, the bi-linear model for incorporating the sewer headspace conditions, and the SATIR model for understanding the chemical and transport interactions between concrete components and the attacking acids(Bakera, Alexander & Beushausen, 2021).

Primarily, the corrosion rate is evaluated by balancing the factors involved in the acid attack and the acid resistance (Figure 2.13). The acid attack involves factors associated with producing sulphuric acid

on the concrete surface, including the sewer environmental conditions and biological factors. Acid resistance is mainly governed by the material aspect, which neutralizes the attacking acid and possibly restricts microbial activities. The material aspect entails transport processes such as diffusion and capillary action of acid species into the concrete and dissolved ions into the corroded layer, and chemical reactions such as dissolution and precipitation of the concrete components and ionic exchange within the pore solution. The interaction between the chemical reactions and transport processes is complex and involves a wide range of parameters that might be complicated to assess individually.

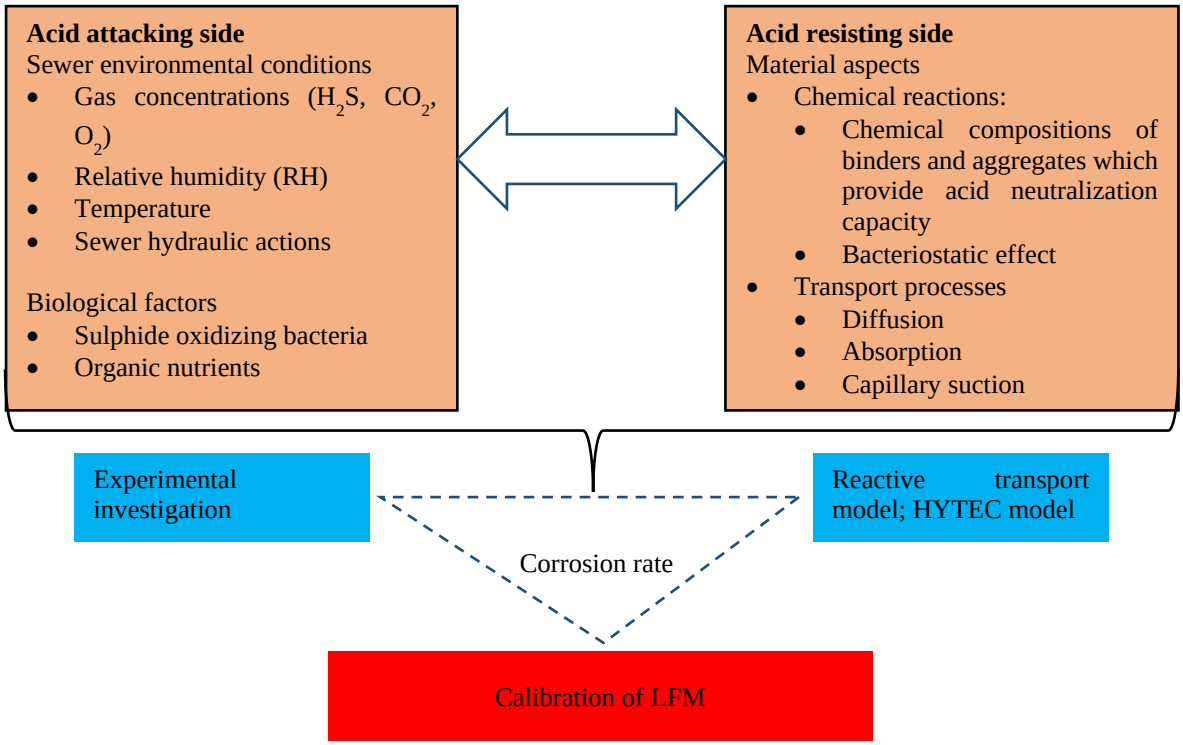


*Figure 2.13: Schematic diagram indicating essential factors for predicting the corrosion rate of concrete under BAC; the sewer environmental factors and material aspects.*

However, it is essential to define, understand, and quantify the influence of each parameter (chemical reaction and transport processes) to identify the key parameters that can be coupled in the LFM model as the material aspects. In this regard, a reactive transport model and field experimental investigation results are the best possible approaches to identify and quantify these parameters.

A reactive transport model is a thermodynamic modelling approach where thermodynamic equilibria of the chemical reactions in the mineral phases and pore solution are coupled with transport processes by diffusion and capillary action to evaluate the influence of various mineral species involved in concrete corrosion. While there are various reactive transport models in the literature, in this study, HYTEC is employed (Schmidt-Döhl & Rostásy, 1999a,b).

However, due to the challenges related to understanding the evolution and contribution of cementitious materials in the sewer environment, the thermodynamic modelling approach coupled with transport modelling, termed reactive transport modelling, is discussed in the subsequent section. The aim is to comprehend how to incorporate the influence of BAC's chemical reactions and transport processes in the LFM refinement.

## 2.11. Reactive transport modelling

Reactive transport models are mathematical formulations and numerical modelling approaches, mainly applied in hydrochemistry and geochemistry to simulate chemical processes coupled with fluid flow and ionic or molecular transport in subsurface environments. These models have been employed in the literature to address several issues, such as groundwater contamination, hydrothermal venting, carbon sequestration, and mining and mineralization activities (Steefel et al., 2015).

Recently, this approach has been of interest for simulating chemical reactions and transport processes in concrete and cement-based materials. Such models have been used to predict concrete long-term behaviour and durability performance when subjected to different aggressive environments (Lee, Windt & Lagneau, 2008).

Numerous reactive transport models, such as PHREEQC, HPx, PHT3D, Open-GeoSys (OGS), HYTEC, ORCHESTRA, TOUGHREACT, eSTOMP, HYDRO GEOCHEM, CrunchFlow, MIN3P, and PFLOTRAN, exist for these applications. (Steefel et al., 2015). These models consist of a set of chemical and transport governing equations that assist in simulating various phenomena involving porous media. However, in this study, HYTEC is more interesting because it is a versatile model whose application has been widely extended to studying cement and concrete degradation. A brief background on the chemical and transport processes involved in reactive transport models is discussed in Appendix B.

### 2.11.1. HYTEC Model – a brief background

HYTEC is a versatile reactive transport model developed at Mines-Paris Tech, based on a sequential iterative algorithm whose formulations and equations are displayed in van der Lee et al. (2003). This model was primarily developed for groundwater pollution studies, safety assessment of nuclear waste disposals, and geochemical studies. It integrates various features useful in 1-, 2- or 3-dimension modelling. It can model various flow regimes in porous media under saturated or non-saturated states. The transport mechanisms covered by HYTEC are advection, molecular diffusion and dispersion, and gas-phase advection and diffusion.

Various chemical processes are included in the model. These are surface complexation, ion exchange, aqueous-gas exchange, kinetic and equilibrium mineral and colloids precipitation-dissolution, equilibrium isotope fractionation, aqueous kinetics, radioactive decay chains and microbial-mediated heterogeneous and homogeneous reactions. These chemical processes can be modelled using a full chemical equilibrium, full chemical kinetics, or a mixed equilibrium–kinetic approach, as discussed in B. Thermodynamic data are procured from international databases (Steefel et al., 2015) coupled with the geochemical component from Chess|THERMODDEM (2014) database (der Lee, 1998).

The coupling of transport and chemical reactions is based on a set of mass balance equations numerically solved through the operator splitting approach using a sequential iterative algorithm and computed by the parallelisation computation approach, as detailed in B. Apart from the reaction-induced porosity-permeability, the model also accounts for the reaction consumption of phases. The alteration of porosity and permeability of the porous media due to chemical reactions potentially modifies the transport properties in the model. Thus, the effective diffusion coefficient in the transport

Eq. is corrected for porosity change based on a modified version of Archie's semi-empirical law (Eq. 2.75) (van der Lee et al., 2002).

$$D(\omega) = D_o \left(\frac{\omega - \omega_c}{\omega_o - \omega_c}\right)^m \tag{2.75}$$

Where

| | |
|---|---|
| $D_o$ | Initial effective diffusion coefficient |
| $D(\omega)$ | Modified effective diffusion coefficient |
| $m$ | Empirical coefficient |
| $\omega_o$ | the initial porosity |
| $\omega$ | Modified new porosity |
| $\omega_c$ | Critical porosity where diffusion stops |

The rate of change of total concentration of species j in the saturated medium is given by Eq. 2.76, where the total concentration of species ($c_j$) is a sum of the concentration of mobile species ($\tilde{c}_j$) and immobile species ($\bar{c}_j$), i.e., $c_j = \tilde{c}_j + \bar{c}_j$. The porosity ($\omega$) is included in the equations to denote the alteration of porosity due to chemical reactions. The transport operator ($\mathcal{L}$) is given in Eq. 2.77, where $D_j$ Includes diffusion and dispersion, which can be species-specific, $v$ is the filter (or Darcy) flow velocity, and $\nabla(\quad)$ refers to $\frac{\partial(\quad)}{\partial x}$.

$$\frac{\partial(\omega c_j)}{\partial t} = \mathcal{L}(\tilde{c}_j) \tag{2.76}$$

$$\mathcal{L}(\tilde{c}_j) = \nabla(\omega D_j \nabla \tilde{c}_j - v\tilde{c}_j) \tag{2.77}$$

Apart from the transport operator accounting for advection, diffusion, and dispersion, HYTEC consists of a reaction operator ($\mathfrak{R}$), which provides the relationship between the $c_j$ and $\tilde{c}_j$, see Eq. 2.78.

$$\tilde{c}_j = \mathfrak{R}(c_j) \tag{2.78}$$

The reaction operator is a function of chemical reactions, particularly those involved in immobilising part of the species, such as surface complexation, ion exchange, precipitation, dissolution of mineral phases, and colloidal retention. Figure 2.14 provides a schematic chart of the computational flow within a single time step of the HYTEC model.

The flow velocity ($v$) is evaluated from the permeability coefficient ($k$) and Darcy's law (Eq. 2.79). However, for an unsaturated medium, flow velocity is described by Richard's equation instead of Darcy's law (Lee, Windt & Lagneau, 2008)

$$v = -\frac{k}{\mu}\nabla(p - \rho g z) \tag{2.79}$$

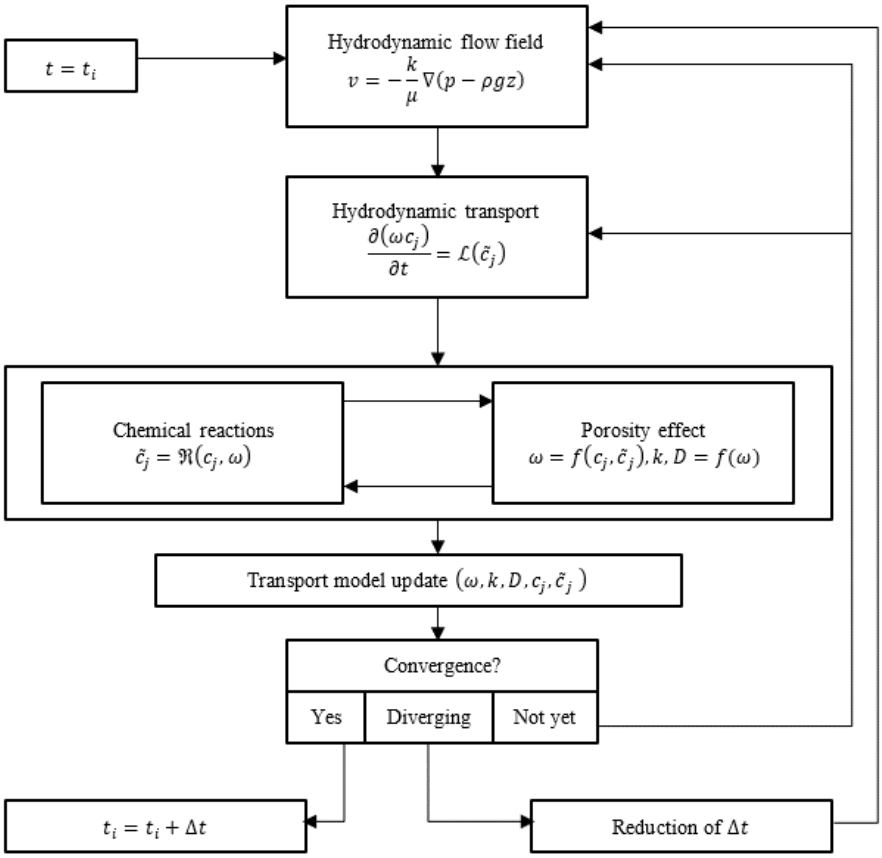


*Figure 2.14: Schematic computational flow chart of the HYTEC model within a one-time step (van der Lee et al., 2003)*

Where;

| | |
|---|---|
| j | Ionic species |
| $c_j$ | Total concentration of species |
| $\tilde{c}_j$ | Concentration of mobile species |
| $\bar{c}_j$ | Concentration of immobile species |
| $\mathcal{L}$ | Transport operator |
| $D_j$ | Diffusion and dispersion |
| $v$ | Filter (or Darcy) flow velocity |
| $\Re$ | Reaction operator |
| $k$ | Permeability coefficient |
| $z$ | Depth |
| $\rho$ | Fluid density |
| $g$ | Acceleration due to gravity |
| $p$ | Fluid pressure gradient |
| $\mu$ | Dynamic viscosity |
| $t$ | Time |

### 2.11.2. Various applications of Reactive transport models

Several studies have attempted to apply the reactive transport model to simulate BAC. Such studies include Boehm et al. (1998), who modelled the corrosion rate of concrete using a moving boundary

reaction-diffusion model. The model entails the biological generation of sulphuric acid, the diffusion of ions in the corrosion layer, and the dissolution of calcium carbonate as a main acid-neutralizing component of the concrete. However, the model was inadequate, which led Jahani et al. (2001) to refine it by improving the acid-neutralizing concrete component and redefining the initial and boundary conditions.

Chalupecký et al. (2012) applied a multiscale reaction-diffusion model to determine the corrosion of sewer concrete pipes. The model involved two critical features: continuous transfer of $H_2S$ from water to air phase and vice versa; and fast production of gypsum at the solid-gas interface. However, the model failed to accurately define the thermodynamic chemical reaction between the acid and cement hydrates.

Yuan (2014) developed a reactive transport model to simulate the degradation of Portland cement mortar exposed to sulphuric acid using a modelling platform based on Finite Volume. The following were taken into account when developing the model; dissolution and precipitation reactions of portlandite and gypsum; continuous variation (decrease) of the Ca/Si ratio during the dissolution reaction of C-S-H; diffusion of different species and thermodynamic equilibrium; changes of porosity and damage of materials induced by the production of gypsum; the coupling of $H_2SO_4$ production, transport equations and chemical reactions; and effect of pore-clogging resulting from carbonation on the biodeterioration rate during the initial period (Yuan et al., 2013, 2015).

With the principles developed by Yuan (2014), Grandclerc et al. (2018) simulated the behaviour of cementitious materials based on different types of cement in contact with sulphuric acid. Such cement includes plain Portland cement (CEM I), blended Portland cement (CEM III, CEM IV, and CEM V), and calcium aluminate cement (CAC). With the aid of the HYTEC model, the authors account for the dissolution of cement hydrates and the precipitation of deterioration products using chemical equilibrium associated with thermodynamic constants and the transport of different species during the sulphuric acid attack. However, the model does not include biological acid production, and the materials used were cement-paste based rather than concrete.

Larreur-Cayol et al. (2011) combined HYTEC modelling with experiments to investigate the performance of Portland cement paste exposed to three aggressive solutions made of acetic and oxalic acid. The aim was to characterise the degradation mechanisms by discriminating between acidic attack and complexation effects, determining the cement phase evolution, and assessing leaching sensitivity against calcium salts' solubility and molar volume. Finally, it was observed that the experimental observation using microstructural analysis, such as XRD and electron microprobe, and the HYTEC modelling led to similar results in terms of degradation rate and depth.

The above studies indicate that modelling BAC on concrete is possible. Thus, reactive transport models are essential for understanding the chemical and transport processes and mechanisms involved during concrete biodegradation. With this, various binder systems subjected to different aggressivity levels encountered in the sewer environment can be simulated and easily studied in a short period. In this study, therefore, only HYTEC model is adopted.

### 2.11.3. Application proposal of HYTEC model in this study

The HYTEC model application in this study is vital for understanding BAC's long-term mechanisms. The model can predict the BAC transport mechanism to the cementitious materials, the chemical reactions between the acid and cementitious material, and the phase evolutions and assemblages of cementitious materials during deterioration. The phase assemblages and evolutions can then be presented as a profile showing different deterioration zones with depth into the concrete.

With this, the most deterioration-influential phases and elements and the rates can be evaluated and determined to track the deterioration progress. The deterioration rate for cementitious materials and sewer aggressivity level from the HYTEC model can be compared against the actual deterioration phases and rates measured in a 'live' sewer using the BAC monitoring and microstructural analysis techniques. This way, the LFM model can be calibrated for a particular cementitious material, giving a more fundamental understanding of the deterioration phenomena.

## 2.12. Literature review – closure

This chapter highlighted current knowledge on concrete deterioration due to the BAC in a sewer. It has explained the mechanisms and factors involved in the steps leading to the final stage of concrete corrosion. The BAC mechanism was described in four progressive steps: sewer installation stage, concrete neutralisation, bacterial colonisation, and concrete corrosion. The factors associated with BAC were categorised into sulphide species generation, $H_2S$ emission, $H_2S$ adsorption and oxidation, and concrete corrosion. The chapter also reviewed the influence of modifying concrete microstructure with three binder systems to resist BAC. These binder systems include PC, CAC, and CAS cement. For each binder system, the roles of the chemical composition, such as Ca, Al and Fe phases, in influencing the attack were reviewed. The limitations of each binder were highlighted. It was observed that there are limited studies on the performance of concrete with CSA binders, thus drawing interest for further studies.

Besides, the chapter concentrates on the modelling aspect of BAC in the sewer system. The aim was to identify, understand, and predict the chemical, biological and physical processes involved in BAC to design a sewer concrete that can withstand the overall process over its service life. Therefore, various service life prediction equations and models according to the BAC mechanism were discussed. The final target was to understand the development of these approaches, their applications, and their limitations and, finally, extract the knowledge to employ in modifying the LFM, which is the basis of this study. With that in mind, a brief overview of service life prediction approaches and their importance was discussed.

A series of equations that describe sulphide species generation in wastewater depending on the flow state in a sewer pipe was reviewed. The available $H_2S$ emission adsorption and oxidation equations were highlighted. Finally, the core aspect of this literature review was discussed in-depth. The evolution, development, and challenges of the LFM were discussed. Existing corrosion rate prediction models' contributions to improving the LFM were examined. The importance of possibly applying reactive transport models to incorporate chemical and transport processes in the LFM was also

proposed. HYTEC model was then selected for that purpose, and a brief proposal on its application in the LFM model was provided.

In conclusion, this chapter highlighted the following knowledge gaps on BAC in sewer concrete that demand further investigation, in general.

i. Insufficient information on detailed preconditioning factors and mechanisms impact the proliferation of microorganisms on the submerged wall of concrete sewer pipes and how they are involved in forming biofilms in the aqueous phase.

ii. Information on the diversity, composition, and interaction of responsible SRB and other microorganisms on sulphide species formation is missing. The existence of fungi and heterotrophic bacteria other than SOB and their roles in biogenic acid formation also requires verification.

iii. Factors that favour iron accumulation in the transition zone and its influence on the corrosion rate and the growth of *A. ferrooxidans* require further exploration. Besides, the role and favourable conditions for *A. ferrooxidans* and their interaction with *A. thiooxidans* in creating conditions for altering concrete microstructure are not indicated.

iv. The effect of BAC on concrete steel reinforcement. Most studies in BAC are delegated to concrete matrix deterioration and less to the underlying steel bar inside the concrete. Various studies have indeed proposed to improve and increase the depth of the sacrificial layer of concrete or concrete cover that is anticipated to protect the reinforcement before the corrosion front reaches them. Yet there are few strategies to combat the attack if it reaches the reinforcement. Therefore, researchers should shift their interest in this area as more beneficial solutions might be recommended for the performance of sewers.

v. Despite various prediction equations and models discussed based on the BAC stages preceding concrete biodeterioration of the sewers, there is no clear interconnection among the approaches. Thus, it complicates the adoption of the basic principles used in these approaches to develop a model that is efficient and effective in predicting the corrosion rate of concrete.

vi. Most existing BAC prediction models were developed based on the performance of cement paste or mortar, which does not directly correlate with the performance of concrete in sewers. Due to this, the essential aggregate aspect, since aggregate comprises about 70% to 80% of the concrete composition, is neglected. With this, such models cannot be directly applied in designing sewer concrete for field use. Therefore, it is strongly suggested that concrete, as a fundamental component, should be considered in developing such models.

vii. The cements or binders most studied in the sewer environment are PC and CAC, with little focus on other modern binders such as CSA and AAC. This dynamic of sewer cementitious materials poses challenges in developing a reliable and more generally applicable model. Despite the challenges, there is a significant need to explore these materials and identify viable means of considering them in modelling, as the construction industry seems to develop an interest in them.

viii. Another vital aspect which is challenging is exploring the means of applying or utilizing sewer environmental conditions (i.e. temperature, RH and $H_2S$ concentration) in developing such models. Because these parameters are easily measured in a sewer and significantly define the aggressivity of a sewer.

ix. Finally, more focus should be directed towards applying the knowledge of thermodynamic modelling in comprehending the chemistry and response of various cementitious materials in sewers and possibly incorporating such knowledge in modelling. This direction proves beneficial in developing a reliable prediction model that engineers can easily apply during sewer concrete design when various modern binders are of their choice.

Despite many highlighted knowledge gaps, this study focuses mainly on filling the last five gaps, that is, understanding the performance of PC, CAC and CSA-based concrete in three different sewer environments; comprehending their chemical and transport processes that influence BAC mechanism through thermodynamic modelling, and lastly, refining the LFM model to incorporate various sewer environment conditions, aggregate components, and binder systems The other knowledge gaps are incorporated in the recommendations (Section 8.7) for further work.

# CHAPTER 3. EXPERIMENTAL SET-UP AND INVESTIGATION

## 3.1. Introduction

This chapter discusses the methodology used for the experimental investigation. It discusses methods for preparing, exposing, and analysing the performance of two batches of concrete mixes. The first batch encompassed concrete manufactured and delivered by LH and exposed to the three sewer sites (LPS, NAS M19, and NAS M54) discussed later in Chapter 4. The second batch entailed concrete manufactured at UCT using binders provided by LH and additional binders sourced locally and exposed to two sewer sites (LPS and NAS M19). The locally sourced binders were based on South African experience from previous studies (Alexander & Fourie, 2011; Kiliswa, 2016). Generally, the experimental setup and investigation chapter entails the following sections.

## 3.2. Material characterisation

One of the objectives of this study is to assess and comprehend the performance of concrete with various binder systems under different levels of sewer aggressivity. Thus, 'real' concrete was incorporated in the study since it is ultimately used in constructing concrete sewers. The traditional concrete ingredients, i.e., binder and fine and coarse aggregates, with a maximum aggregate size of 13 mm were used. The following criteria were considered in selecting and characterising the concrete constituents;

i. Historical performance of various binder systems in sewers with their chemical compositions and how they contribute to neutralising acid attack;
ii. Suitable concrete mix designs which comply with concrete for sewer pipe construction. Attention, herein, is directed towards types and content of aggregates, water/binder (w/b) ratio, and compaction or casting method; and
iii. The output concrete was to comply with actual sewer concrete mechanical and durability properties such as compressive strength, saturated density at 28 days, and Durability Indexes (DI) before exposure.

The following subsections describe the constituents used for concrete preparation. Properties such as relative density were identified using ASTM C188 (2017), specific surface area using BET analysis, Particle Size Distribution (PSD) using Mastersizer 2000 Ver. 5.60 equipment, and chemical composition using XRF analysis (SANS 50196-2, 2014). Table 3.1 provides physical properties, Table 3.2 provides chemical compositions, and Figure 3.1 provides particle size distributions.

### 3.2.1. Binders

The following binders were used to produce specific binder systems for this study.

#### 3.2.1.1. CEM II A-L 52.5 N (CEM II AL)

CEM II/A-L 52.5N is a Portland limestone cement manufactured and supplied by Pretoria Portland Cement (PPC) Company Limited in the Western Cape province of South Africa. It comprises the addition of 6 - 20% limestone extender, typically about 9%. According to SANS 50197-1 (2013), this cement is categorised under the 52.5 N strength class for conventional cement. This study used this type of cement to produce concrete considered highly vulnerable to sewer exposure. It was also selected

because it has been used in previous UCT sewer studies. Thus, comparing its performance with the available UCT sewer concrete performance database was necessary.

*Table 3.1: Physical properties of various binders, supplementary cementitious materials and fine and coarse aggregates.*

| Physical properties | Particle Relative density | D (0.1) (µm) | D (0.5) (µm) | D (0.9) (µm) | BET Surface area (m2/g) |
|---|---|---|---|---|---|
| **SRPC** | 3.14 | 2.0 | 7.4 | 16.5 | 0.89 |
| **CEM II** | 3.16 | 2.1 | 8.4 | 20.7 | 0.91 |
| **CSA** | 2.75 | 1.0 | 5.6 | 28.8 | 1.51 |
| **CAC** | 3.04 | 0.7 | 5.5 | 20.1 | 1.17 |
| **HC** | 3.50 | 1.9 | 8.2 | 23.5 | 0.91 |
| **LS** | 2.50 | 0.9 | 6.1 | 14.1 | 0.75 |
| **FA** | 2.20 | 1.2 | 9.9 | 70.3 | 2.96 |

*Table 3.2: Chemical composition of various binders, supplementary cementitious materials and fine and coarse aggregates.*

| Binders | Oxide formula and composition,wt. % | | | | | | | | | |
|---|---|---|---|---|---|---|---|---|---|---|
| | CaO | $SiO_2$ | $Al_2O_3$ | $Fe_2O_3$ | MgO | $SO_3$ | $TiO_2$ | Others | LOI | Total |
| **SRPC** | 67.95 | 21.45 | 3.14 | 2.17 | 0.95 | 1.85 | 0.14 | 0.68 | 1.63 | 99.98 |
| **CEM II AL** | 64.06 | 19.14 | 3.77 | 2.85 | 0.92 | 1.81 | 0.18 | 1.34 | 5.39 | 99.46 |
| **CSA** | 41.75 | 4.70 | 30.37 | 1.53 | 0.62 | 15.71 | 1.26 | 0.35 | 2.73 | 99.04 |
| **CAC** | 37.79 | 5.39 | 49.60 | 1.92 | 0.44 | 0.07 | 2.11 | 0.68 | 1.09 | 99.10 |
| **HC** | 17.05 | 33.61 | 5.10 | 40.69 | 0.93 | 2.12 | 0.32 | 2.55 | -4.12 | 99.40 |
| **LS** | 45.24 | 11.02 | 2.53 | 1.55 | 1.06 | 0.00 | 0.05 | 1.09 | 36.96 | 99.50 |
| **FA** | 4.32 | 53.72 | 32.94 | 3.23 | 1.07 | 0 | 1.71 | 6.99 | 1.03 | 99.10 |
| **PS** | 0.11 | 95.60 | 1.61 | 0.80 | 0.00 | 0.00 | 0.28 | 0.34 | 0.67 | 99.42 |
| **DCS** | 33.26 | 4.90 | 0.34 | 0.90 | 22.26 | 0.02 | 0.01 | 1.13 | 36.21 | 99.02 |

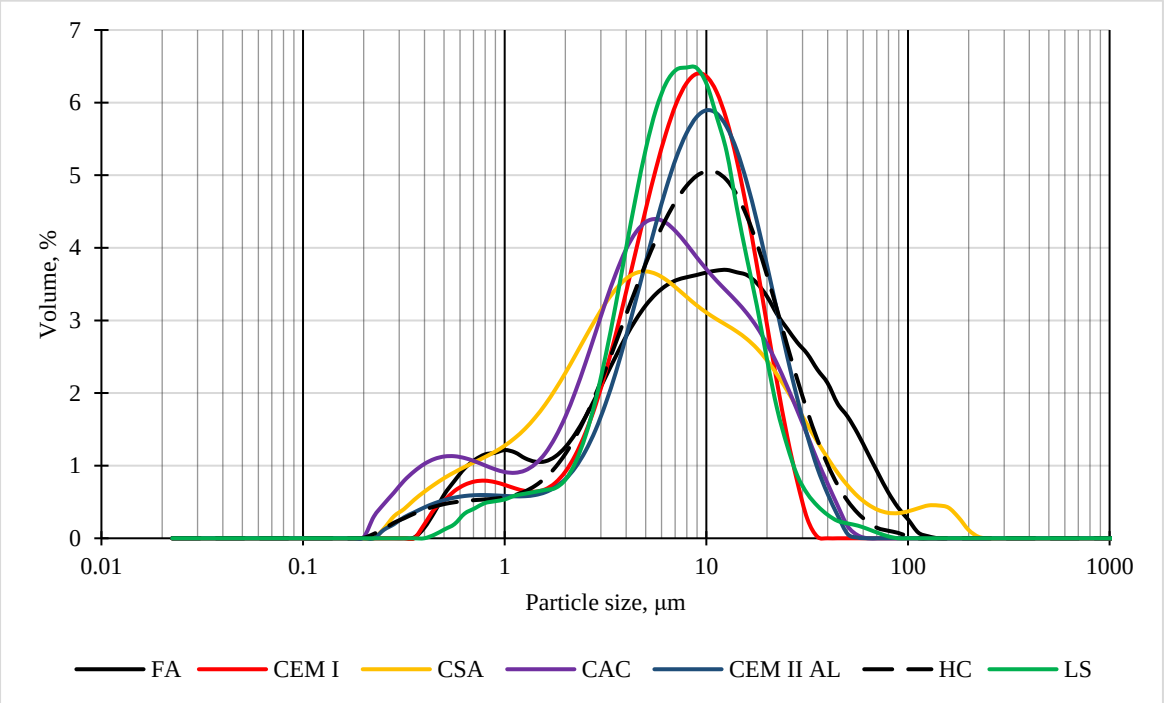


*Figure 3.1: Particle size distribution of various binder and supplementary cementitious materials.*

#### 3.2.1.2. CEM 1 52.5 N – SR3 (SRPC)

This study combined CEM I 52.5 N – SR3 with fly ash to form specific binder systems. LH supplied this cement. According to SANS 50197-1 (2013), it is classified as a Sulphate Resisting Portland Cement (SRPC) with $C_3A$ content of the clinker less than 3 % (SR3). It is also a range of cement with purported high resistance to aggressive environments, mainly sulphate attacks.

#### 3.2.1.3. Calcium Aluminate Cement (CAC)

Calcium Aluminate Cement (CAC) used in this study was SECAR® 51, produced and supplied by Imerys South Africa, as recommended by LH. It generally possesses excellent refractory properties and high early strength properties on its own. Combined with other reactive minerals such as calcium sulphate and Portland cement, it produces high strengths and shrinkage compensation through ettringite formation. Thus, it is mainly recommended for applications requiring rapid hardening properties, resistance to abrasion and mechanical shock, resistance to chemical attack and exposure to intermediate temperatures. More information regarding its application in sewers is discussed in Section 2.4.2.

#### 3.2.1.4. Calcium Sulpho-Aluminate (CSA) cement

Calcium Sulpho-Aluminate (CSA) cement used in this study was Calumex® Quick, which LH supplied. CSA provides improved resistance to sulphate attacks and other aggressive substances. It also has many possible applications where a rapid set and high early strength are required. More information is provided in Section 2.4.3

### 3.2.2. Supplementary Cementitious Materials (SCMs) and additives

The following SCMs were blended with the previously discussed binders to produce specific binder systems for this study.

#### 3.2.2.1. Fly Ash (FA)

Fly Ash (FA) is a by-product of burning pulverised coal in electric power plants. It is known as a pozzolanic material with high alumina and silica content. It partially substitutes hydraulic cement in concrete to improve concrete's structural and durability performance. In this study, FA replaced 20% of SRPC to produce a binder system which, according to Kiliswa (2016), may perform better than plain PC concrete.

#### 3.2.2.2. Limestone (LS)

LH used limestone to prepare cement with similar properties as CEM II A-L 52.5 N (On-site blend), which was achieved by blending 80% SRPC and 20% limestone in the laboratory. However, this blend is not a complete representation of CEM II A-L 52.5 N, as their concrete performance tends to differ.

#### 3.2.2.3. Iron-based additive or Hard-Cem (HC)

Iron-based additive or Hard-Cem (HC) is a hardening additive used in concrete to increase abrasion and erosion resistance. It mainly consists of metal iron oxide, which does not participate in the hydration process. Also, it has a negative Loss On Ignition (LOI) value, indicating the loss of combined water and

not gas during ignition. It also improves the durability of both air-entrained and non-air-entrained concretes. This study used this additive to enhance porosity reduction in the concrete with a binder system of 20% FA and 80% SRPC.

### 3.2.3. Water and Superplasticiser (SP)

Potable tap water was used for casting and curing. On the other hand, distilled water was used where standards were specified, for example, in the concrete surface pH measurements. BASF Master Glenium 7700, as recommended by LH, was used as a superplasticiser. It is a high-range water-reducing admixture with a relative density of 1.064. A dosage between 0.3 and 0.5% of the product by cement volume is commonly used. This study used the optimum dosage to achieve easy compaction by vibration for both LH and UCT concrete mix designs.

### 3.2.4. Philosophy of Binder selection

Binder systems for this study were designed based on the binders, and SCMs discussed in Section 3.2, aiming at producing sewer concretes with performance ranking between Portland-based and Aluminate based concretes. The CEM II AL concrete represents poorly performing concrete, while the CAC concrete presented the best-performing concrete in sewers. The binder system with a 0.5/0.5 ratio of CAC/ SRPC was established to understand whether its performance may assist in reducing sewer pipe manufacturing costs by minimising the amount of CAC while maintaining its best performance.

In the literature review chapter, Section 2.4.1, it was learnt that PC concrete with alumina content either from alumina-containing aggregates or blends with alumina-rich SCMs, e.g. fly ash, experiences corrosion rate reduction. Thus, the binder system with fly ash was derived, i.e., SRPC + FA. The literature also indicated the uncertainty on the role of iron phases in concrete. Therefore, it was advised to incorporate another binder system rich in iron to comprehend the function of the iron phases in the concrete under BAC. The selection of iron-based additive was based on an industrial project conducted in 2016 at the UCT civil engineering laboratory, where it was observed that a concrete mix with HC performed better in live sewer environments than those with plain PC. Thus, HC, an iron-based additive, was incorporated into the SRPC+FA binder system to enhance the formation of iron phases in the concrete.

The selection of the CSA binder system is well elaborated in the literature review, Section 2.4.3, which includes its long-term application in China on sewer pipe production without any substantial failure reported. Secondly, its hydration products include ettringite and alumina gel (gibbsite). Ettringite is chemically unstable at a pH below 10.7; it decomposes to form more gibbsite in an acidic environment. Gibbsite, however, contributes to the biogenic acid resistance, as demonstrated in the CAC binder systems. Also, compared with PC, it produces concrete with lesser CH and CSH phases, thus reducing its susceptibility to acid attacks, including BAC.

### 3.2.5. Aggregates

Klipheuwel Pit Sand (PS) (Figure 3.2– c) was sourced from the sand deposits of the Malmesbury-Klipheuwel region in Cape Town. These deposits consist of hillwash and colluvial sands, commonly known as siliceous pit sands. The sand is characterised by rounded particle shape, continuous grading,

and high fines content of up to 20% of 0.150 mm and 15% of 0.075 mm (Walker, 2013). These properties contribute to its superior quality with low water requirements; as a result, it provides an excellent source of fine aggregate.

Dolomite aggregates are calcareous aggregates from geological environments similar to limestone either by biological or chemical precipitation or by the deposition and compaction of coral, plant and animal remnants on the ocean and sea floors. Dolomite aggregate generally consists of 20 - 46% dolomite minerals ($MgCO_3$), 54 - 80% calcite ($CaCO_3$), and small amounts of other minerals or impurities, such as quartz. In South Africa, economically viable dolomite deposits are found in two locations; the Piketberg and Vredendal-Swellendam districts in the Western Cape province and the Lyttleton-Meyerton-Olifantsfontein areas in Gauteng Province (Angello, 2005).

This study sourced dolomite aggregates from the Olifantsfontein quarry, a 'high-quality dolomite aggregate source. The coarse dolomite aggregates with a maximum particle size of 13 mm (Figure 3.2– a) and dolomite crusher sand (Figure 3.2– b) were prepared from this source and supplied by Rocla Roodepoort. Their physical properties, namely compacted bulk density, particle relative density, and particle size distribution, were determined according to SANS 5844 (2006), SANS 5845 (2006) and SANS 201 (2008), respectively. Their results, including their chemical composition, are in Table 3.2 and Table 3.3.

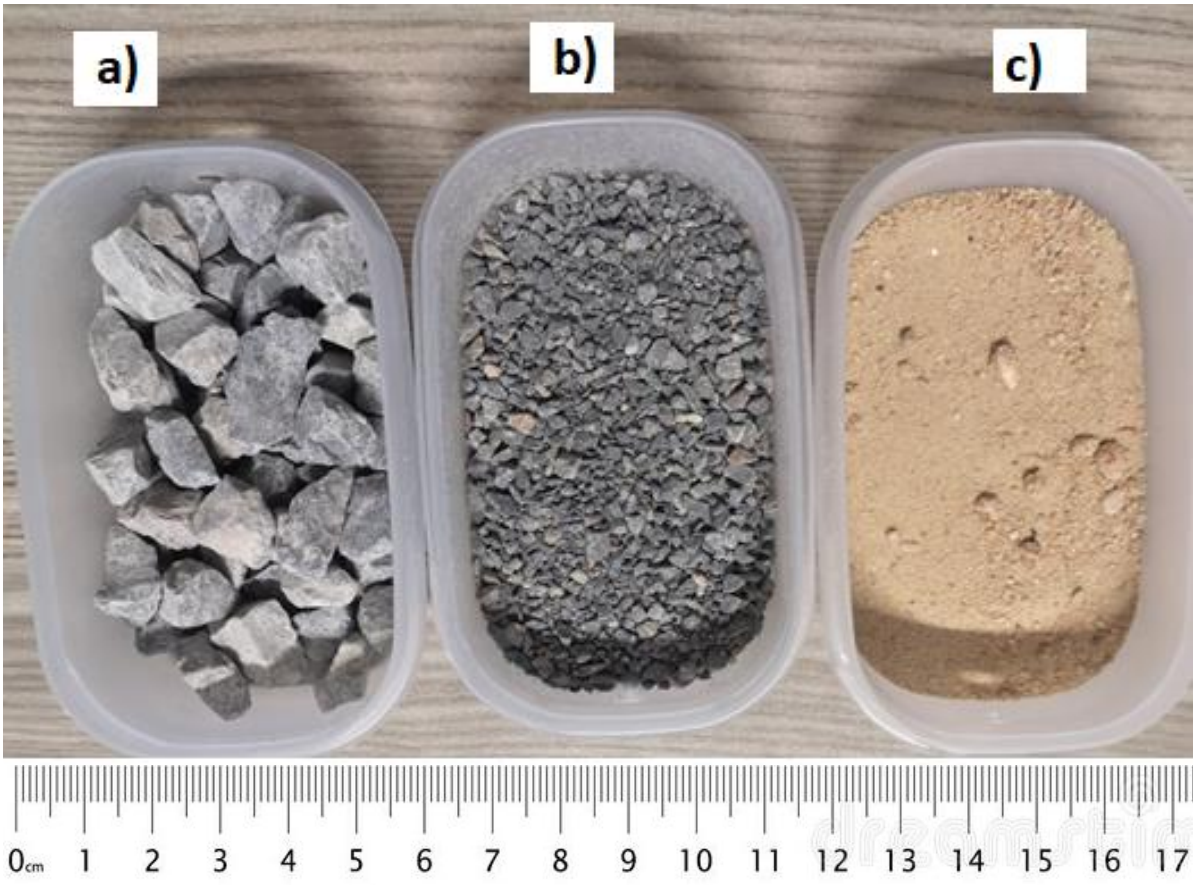


*Figure 3.2: Fine and coarse aggregates used for concrete preparation; a) Olifantsfontein Dolomite coarse aggregate (ODA), b) Olifantsfontein Dolomite crusher sand (CS), and c) Klipheuwel Pit Sand (PS).*

*Table 3.3: Physical properties of fine aggregates*

| Aggregates type | Fine aggregate | | Coarse Aggregates |
|---|---|---|---|
| | PS | CS | ODA |
| Relative density | 2.65 | 2.87 | 2.87 |
| Fineness modulus | 1.84 | 3.76 | - |
| Compacted bulk density (kg./m$^3$) | - | - | 1585 |
| ACV (%) | - | - | 12.0 |
| 10% FACT (kN) | - | - | 349 |
| Water absorption (%) | - | - | 0.6 |
| Acid insolubility | 93.90 | 6.28 | 4.18 |

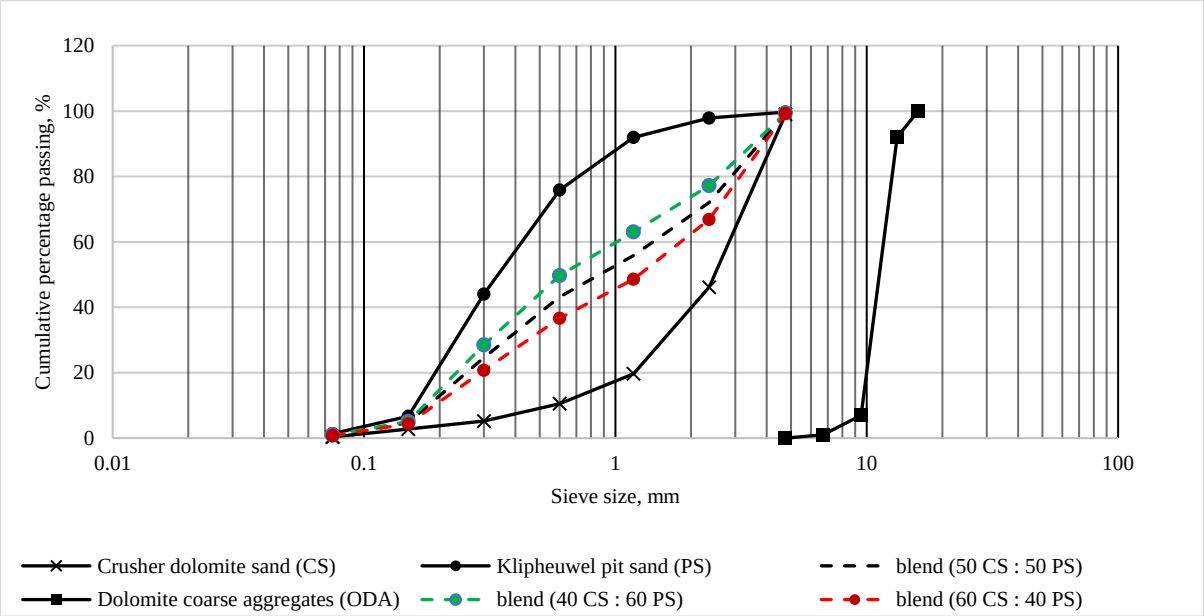


*Figure 3.3: Particle size distribution and blending for fine and coarse aggregates.*

## 3.3. Concrete mix design

Two types of concrete mix designs were used in this study. The first design, the so-called 'LH concrete' presented in Table 3.4, was prepared and cast by LH, and concrete cubes of 150 mm were delivered to the UCT civil engineering laboratory and prepared for field exposure according to Section 3.6.

After unwrapping the LH concrete cubes, it was observed that; i) the surfaces of the cubes were not smooth, which indicated poor compaction; ii) the cubes were expected to be compacted in layers, although no layering was observed on the surface of the cubes; iii) a high number of compaction voids was observed on the surface; iv) some cubes were cracked.

During coring, fine cohesive particles were observed, which indicated the use of fine particles of sand. The core cross-section's surface had larger compaction voids than usual, suggesting that the concrete was poorly compacted. Due to these observations, it was concluded that the LH concrete did not comply with the quality of concrete recommended for sewer concrete construction. Despite these shortcomings, it was decided to continue with field exposure and testing of the LH concrete to understand the performance of poorly compacted concrete in a sewer environment.

However, with such concerns, the mixes were redesigned and produced in the UCT laboratory. The second concrete mix design, the so-called 'UCT concrete', was carried out at UCT using the cementitious materials provided by LH and certain additional binders from South Africa, see Table 3.5.

*Table 3.4: LH concrete mix design – kg/m$^3$*

| **Mix label** | **SRPC+FA** | **SRPC+FA+HC** | **SRPC+LS** | **CSA** |
|---|---|---|---|---|
| **Binder systems** | **80% SRPC + 20% FA** | **80% SRPC + 20% FA + 11% HC** | **80% SRPC+ LS 20% In-lab blend** | **100% CSA** |
| **w/b** | | **0.4** | | |
| Constituents | | kg/m$^3$ | | |
| Binder | 280 | 280 | 350 | 350 |
| FA | 70 | 70 | 0 | 0 |
| HC, an addition of 11.4% of binder | 0 | 40 | 0 | 0 |
| Water | 133 | 133 | 133 | 133 |
| Siliceous fine aggregates | 483 | 483 | 483 | 483 |
| Calcite fine aggregates | 516 | 516 | 516 | 516 |
| Calcite coarse aggregates | 900 | 900 | 900 | 900 |
| Superplasticiser | 0.64 | 0.64 | 1.08 | 1.08 |
| % Total binder | 16 | 16 | 15 | 16 |
| Total | 2383 | 2422 | 2383 | 2383 |

*Table 3.5: UCT concrete mix design containing binders from LH** and UCT* and 0.34 w/b*

| **Mix** | 1* | 2** | 3** | 4** | 5* | 6* |
|---|---|---|---|---|---|---|
| **Type** | **CEM II AL** | **SRPC+FA** | **SRPC+FA +HC** | **CSA** | **CAC+SR PC** | **CAC** |
| Variables | 100% CEM II AL | 80% SRPC + 20% FA | 80% SRPC + 20% FA + 11%HC | 100% CSA | 50% CAC+50% SRPC | 100% CAC |
| **Constituents** | | | **kg/m$^3$** | | | |
| Cement | 412 | 329 | 329 | 412 | 206 | 412 |
| Fly Ash (FA) | 0 | 82 | 82 | 0 | 206 | 0 |
| HardCem,11.4% of binder | 0 | 0 | 47 | 0 | 0 | 0 |
| Potable water | 140 | 140 | 140 | 140 | 140 | 140 |
| Olifantsfontein dolomite coarse, 13 mm | 1050 | 1050 | 1050 | 1050 | 1050 | 1050 |
| Olifantsfontein dolomite crusher sand | 501 | 485 | 482 | 475 | 501 | 494 |
| Pit sand (filler) | 501 | 485 | 482 | 475 | 501 | 494 |
| **Total** | **2604** | **2571** | **2613** | **2550** | **2604** | **2590** |
| Total binder, % | 16% | 16% | 16% | 16% | 16% | 16% |

The UCT concrete mixes were designed according to the C&CI method (Fulton 2009:219). The critical aspects considered during design were limiting the w/b ratio to 0.34 and 16% of the total binder by the total mass of the dry concrete mix (these being standard industry practices). Based on Kiliswa's

findings, these values were important to consider. He found that a low w/b ratio ranging from 0.34 – 0.36 reduces the amount of porosity in the hardened concrete and is suitable for compaction and moulding when fresh concrete is used for sewer pipe fabrication using heavy mechanical compression in a factory. On the other hand, limiting binder content was associated with the performance of PC-based concrete, with lower binder content outperforming that with higher binder content. For these reasons, all mixes designed had similar binder content, intending to reduce the number of performance-influencing variables.

The constituents' contents were kept constant for all mixes, except the binder systems, which varied according to the binders and SCMs selected for use. Six concrete mixtures with different binder systems, as shown in Table 3.5, were designed and cast for the study. Superplasticiser enhanced concrete compaction with a w/b ratio of 0.34, giving a very stiff and dry fresh concrete without it.

### 3.4. UCT concrete mixing, casting, and curing method

All concrete mixes were prepared per SANS 5861-1 and SANS 5861-2. Initially, a static compaction technique developed at UCT was proposed and applied for specimen preparation (Alexander & Fourie, 2011; Kiliswa, 2016). However, this technique did not provide acceptable concrete quality since the concrete specimens performed poorly under DI testing. After vertical and horizontal cross-section cuts, coarse aggregates were found severely crushed. Thus, the technique was abandoned, and a typical vibration compaction technique was applied using a standard lab vibrating table.

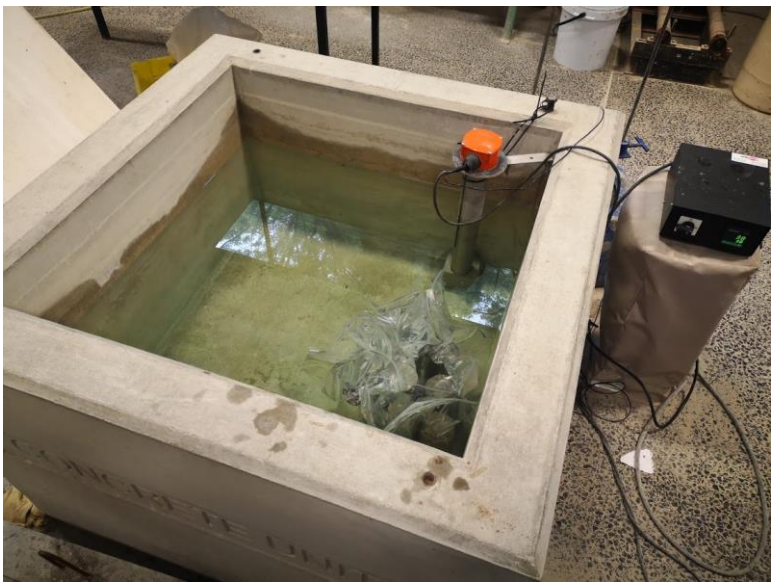

*Figure 3.4: Heat-curing technique: wrapping concrete specimens in air- and water-tight plastic bags and immersed in hot water curing bath maintained at 40±2 °C for 24 hrs.*

Three layers of concrete were filled in the mould, and each layer was uniformly tamped 23 times over the cross-section of the mould to ensure full compaction using the hemispherical end of the tamping rod. Concrete specimens for DI tests and field exposure were cast in cylindrical moulds of 100 mm diameter by 300 mm height, while for saturated density and compressive strength tests, 100 mm cubes were used. A total of five concrete cylinders and three concrete cubes were cast per mix.

After compaction, the specimens were left to set and harden for 24 hrs. Immediately after, they were demoulded and heat-cured for another 48 hrs. The heat-curing technique involved specimens wrapped in air- and water-tight plastic bags and immersed in hot water in a curing tank maintained at 40±2°C for 48 hrs, see Figure 3.4. Subsequently, the specimens were air-cured in a room maintained at a temperature of 20±3°C and RH of 50% to achieve similar maturity characteristics as sewer concrete pipes.

### 3.5. Laboratory quality control tests

Laboratory quality control tests were conducted before exposing the specimens to the sewer sites. These tests include compressive strength, saturated density measurements and DI. The compressive strength test and saturation density of the specimens were conducted on three concrete cubes of 100 mm after 28 days of curing (3 days of heat-curing and 25 days in normal curing). Afterwards, the cubes were taken from the curing tank, surface-dried using a paper towel, and their mass and dimensions were taken, followed by the compressive strength test (SANS 5863, 2006).

This study conducted two DI tests; the Oxygen Permeability Index (OPI) test and Water Sorptivity Index (WSI) test. Specimens for these tests were prepared per SANS 3001-CO3-1 (2015). The OPI and WSI tests were performed per SANS 3001-CO3-2 (2015) and the UCT DI manual (Alexander, Ballim & Mackechnie, 2018).

### 3.6. Specimen preparation for exposure

The concrete cylinders cast for site exposure were first cored, epoxy-coated, and then cut to obtain sample discs of 70 mm diameter and 50 mm thickness (Figure 3.5). About 20 discs were obtained from each mix to distribute into three exposure sites.

The cored specimens were epoxy coated on the cylindrical surfaces to allow exposure on the two opposite flat faces on the cut sections. The epoxy coating was applied in three layers on the sandpapered, cleaned, and dried surface. For the LH concrete specimens, Sikadur 32 N was used, which later was observed to not perform well in the sewer environment. The coating was peeling off, and sometimes, blisters were formed. Due to this, for the UCT concrete specimens, Sikagard 63 N was applied instead.

Once the disc specimens were ready for exposure, they were labelled as per mix type and exposure site. Initial masses, dimensions, and surface pH were measured, followed by immersion in tap water for 3 days to achieve full saturation. Afterwards, their masses were recorded and subsequently fixed in a plastic basket, see Figure 3.6. Three baskets were prepared, each per site.

Before positioning the baskets in their designated site, the specimens were inoculated in the sump pit at Langa pump station for 24 hrs. The inoculation allowed initial contact with microorganisms to establish a successful legume-bacterial symbiosis. Figure 3.7 shows baskets with specimens distributed to their designated site for exposure. Information regarding these sites is detailed in Chapter 4.

After setting for exposure, the BAC monitoring analysis commenced. The monitoring was conducted roughly monthly to quarterly for about 2 years. After each monitoring period, the specimens were retrieved from the sites to the laboratory for BAC monitoring analysis (Section 3.7) and BAC microstructural analysis (Section 3.8) at the end of the exposure cycle.

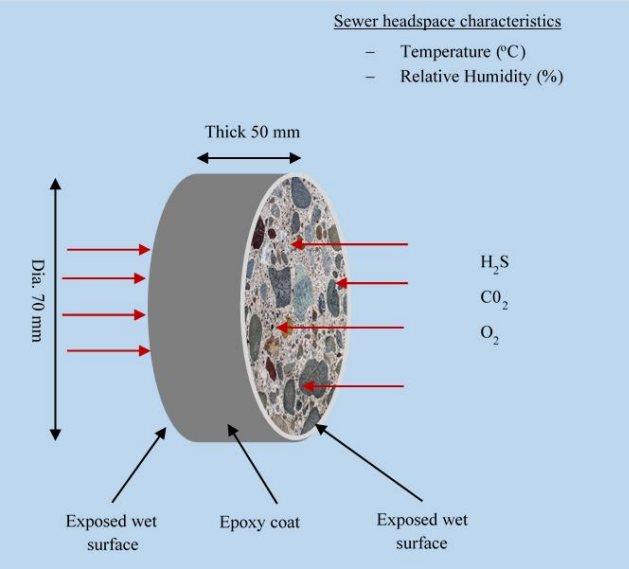


*Figure 3.5: Concrete specimen setup for site exposure*

*Figure 3.6: Concrete disc specimens fixed in the plastic basket for site exposure*


*Figure 3.7: Interior appearance of the manholes involved in the study and concrete exposure*

### 3.7. BAC monitoring analysis

BAC monitoring analysis includes visual observation, mass and dimension readings, and surface pH measurements. The visual observation involved assessing, recording, and photographing crazing, colour changes, and corrosion products on the specimens' exposed surface. A 6000 g mass balance and Vernier calliper were employed for mass and dimension measurements, respectively.

The concrete surface pH was determined by placing a point surface pH electrode (XSinstruments pH5FOOD) on a distilled water-damped concrete exposed surface and allowing the pH electrode to record a steady reading. Six independent pH measurements were carried out at different concrete matrices, i.e. aggregate and cement matrixes observed on the exposed surface, and the average value was calculated. According to Sun et al. (2014), this process was carried out to identify the BAC stage in each concrete mix.


*Figure 3.8: Surface pH measurement on an exposed concrete specimen*

### 3.8. BAC microstructural analysis

BAC microstructural analysis assesses the effect of BAC on concrete microstructure, and the techniques described in Table 3.6 were employed.

*Table 3.6: Microstructural analysis techniques used in this study and their objectives.*

| BAC microstructural analysis | Analysis objectives |
|---|---|
| SEM BSE images | – To study concrete morphology evolution before and after corrosion.<br>– To distinguish and identify the affected zone, corrosion front, and intact zone.<br>– To evaluate concrete corrosion depth. |
| QEMSCAN | – To determine and evaluate the change of concrete mineralogical phases from the corroded concrete surface deep into the intact concrete. |
| XRD | – To determine the mineralogical phases before and after the attack |

### 3.8.1. BAC microstructural analysis – Sample preparation

Samples for BAC microstructural analysis were extracted from a corroded concrete specimen, as shown in Figure 3.9. The SEM and QEMSCAN analysis sample was prepared following the standard sample preparation indicated in Scrivener, Snellings & Lothenbach (2016) and ASTM C1723 (2006). Without disturbing the corroded surface, the concrete specimen from the site was immersed in isopropanol for about seven days to remove free water as the analysis was performed under a high vacuum. Before cutting and sectioning the specimen along its depth to obtain a small sample of about 20 x 20 x 5 mm, the specimen was vacuum dried, followed by epoxy impregnation to support the microstructure and to avoid cracking during saw cutting. After impregnation, the specimen was cut and mounted in a mould with the studied surface, i.e., a 20 x 20 mm cross-section facing down. The sample in the mould was again epoxy impregnated, followed by surface polishing as recommended by Scrivener, Snellings and Lothenbach (2016). Before setting the polished sample for analysis, its polished surface was coated with a thin carbon coat to avoid surface charging because cement-based materials are non-conducting. When uncoated, electrons accumulate in the sample leading to charge build-up, which distorts the final image.

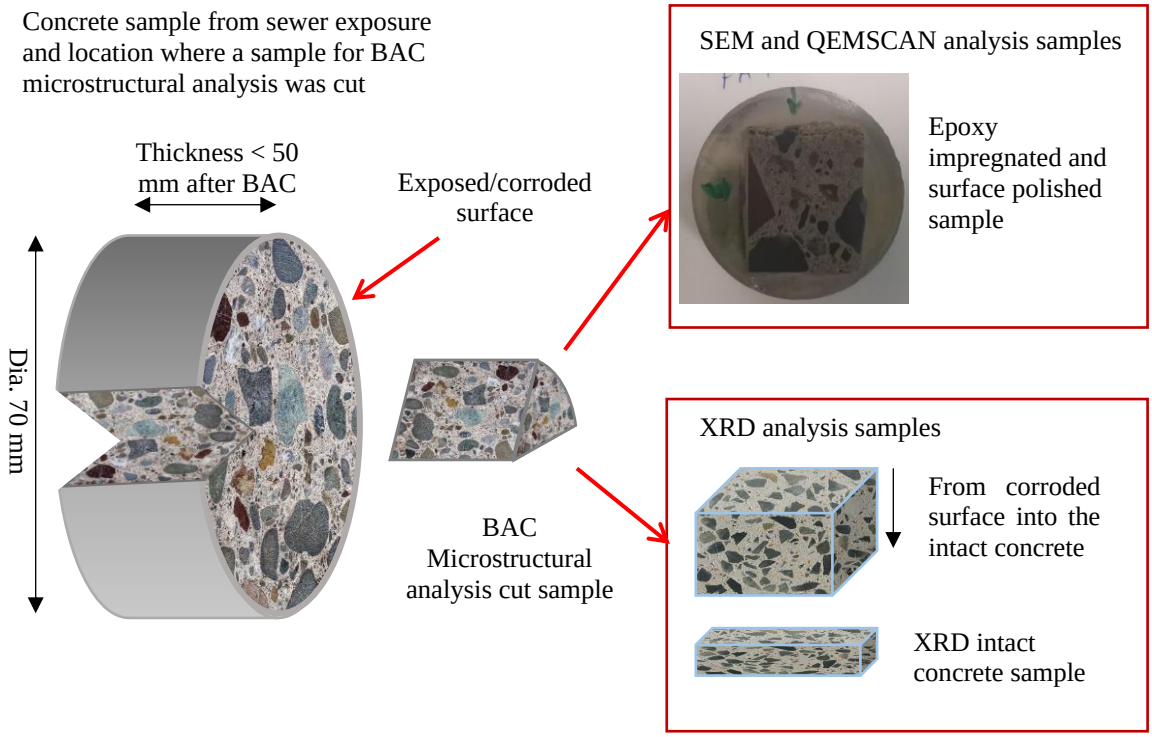


*Figure 3.9: A schematic drawing indicating sample preparation for BAC microstructural analysis of concrete specimens after sewer exposure*

XRD analysis samples were prepared as indicated in Figure 3.9. However, in this case, the sample was neither immersed in the isopropanol nor epoxy impregnate. The sample was cut from the corroded concrete specimens (direct from the site) to obtain a small cube (approximate 15 x 15 x 5 mm from the exposed surface) and a small disc from the intact concrete section.

### 3.8.2. Scanning Electron Microscopy (SEM)

SEM analysis is performed chiefly with Energy-Dispersive X-ray spectroscopy (EDS), where images are generated by raster-scanning in a vacuum chamber. A primary electron beam is focused on a sample. Depending on the electron detector mounted in the chamber, the sample can reflect three signals, i.e., secondary electrons (SE), backscattered electrons (BSE), and X-rays. These signals assist in imaging and X-ray microanalysis, thereby examining and determining sample properties such as surface morphology, elemental composition, and spatial distribution of components. Figure 3.10 illustrates an electron beam from the electron gun focused on the sample through electron optics and scanning coils in the SEM vacuum chamber.

This study conducted SEM analysis on the section-polished sample cut from the corroded specimen, as discussed in Section 3.8.1. The analysis was then conducted using FEI Nova NanoSEM 230 at the UCT Centre for Imaging and Analysis to obtain BSE images. BSE images were collected by a BSE detector in low vacuum mode with an accelerating voltage of 20 kV and beam intensity of 10. The working distance and magnification varied depending on the concrete type and information of interest. More settings are indicated in Chapter 5 on the SEM-BSE images collected.

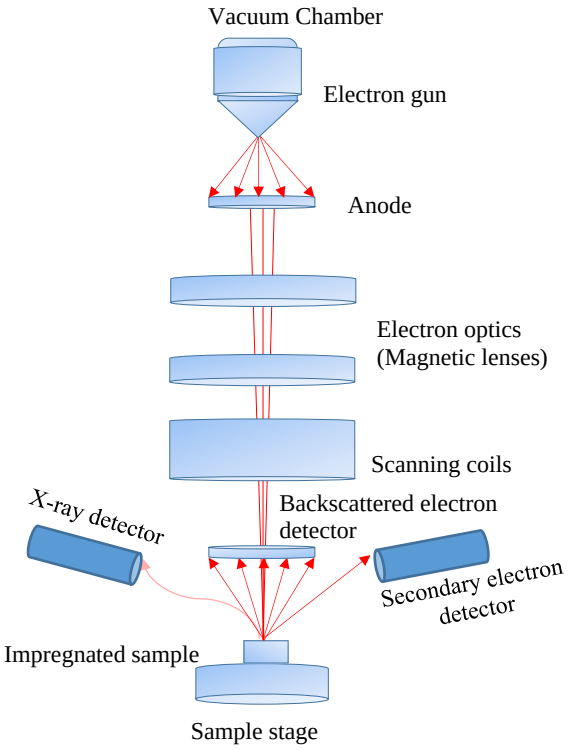


*Figure 3.10: Schematic drawing of a typical Scanning Electron Microscope (SEM) column with impregnated sample-beam interactions (SEM – Thomas Schmid (mygoodpage.org))*

### 3.8.3. QEMSCAN analysis

QEMSCAN (Quantitative Evaluation of Minerals by Scanning Electron Microscopy) is an analytical tool that provides rapid, reproducible and statistically reliable quantitative information on minerals of specific materials for various fields. It uses a field emission gun-scanning electron microscope

combined with high-resolution BSE, EDS, and a Spectral Analysis Engine (SAE) to analyse mineral phases in a sample.

During sample analysis, EDS spectra are attained using 1000 counts per pixel, measured at a point in the centre of the pixel. BSE brightness is calibrated by homogenous quartz, copper and gold standards, and with its support, areas of the sample that comprise mineral phases are identified. According to the BSE brightness and chemical compositions, the analysed mineral phases are classified as specific minerals and compared to a user-developed reference mineral library known as SIP (Species Identification Protocol) file (Bell et al., 2020).

In this study, the sample prepared for SEM analysis was used. The analysis was conducted using the QEMSCAN 650F machine, equipped with EDS, at an accelerating voltage of 25kV and a beam current of 10 nA. Mineral identification and distribution across the concrete microstructure were analysed using Species Identification Protocol (SIP) built in the iDiscover™ v.5.0 software. Other procedures were followed according to a protocol defined by Haberlah et al. (2012) and Bell et al. (2020).

### 3.8.4. XRD analysis

X-Ray Diffraction (XRD) analysis is one of the most prominent analytical techniques for qualitative and quantitatively analysing of crystalline phases in materials. It provides information such as the types and nature of crystalline phases, structural make-up of phases, degree of crystallinity, amount of amorphous content, and orientation of crystallites. In most cases, samples used for analysis are in finely ground powders or on the material surfaces, provided that the surface is relatively flat and not too rough.

XRD analysis involves exposing a sample with incident X-ray beams and measuring the diffraction of X-rays from the plane of atoms within the material. The diffracted X-rays produce XRD patterns with peaks of varying intensities at characteristic diffraction angles. Different crystal structures and their presence in the material are identified by analysing the diffracted intensity peaks, positions, angles, and powers. Figure 3.11 shows incident X-ray beams penetrating a stack of spacing ‘d’ planes at an incidence angle, θ. Each plane is pictured as reflecting a portion of the incident beam. The ‘reflected’ rays combine to form a diffracted beam if they differ in phase by a whole number of wavelengths. The Rietveld refinement technique is then applied to characterise the crystal structure and determine their chemical compositions (Scrivener, Snellings & Lothenbach, 2016).

In this study, the analysis was conducted at LMDC-INSA Toulouse, France, on flat surfaces of the intact concrete and corroded samples, as shown in Figure 3.8. The data were collected using a Brucker D8 diffractometer in the θ-θ configuration using a monochromator incident beam and CuKα radiation (λ=1.54Å) with a rotating sample holder. The mineralogical phases were identified using the EVA software. The corroded sample was analysed in layers from the exposed surface into depth, with the first layer being the corroded/exposed surface. After the analysis, the surface was ground using P800 sandpaper into concrete depth to obtain a second layer. The process continued until soft corroded deposits could no longer be ground readily.

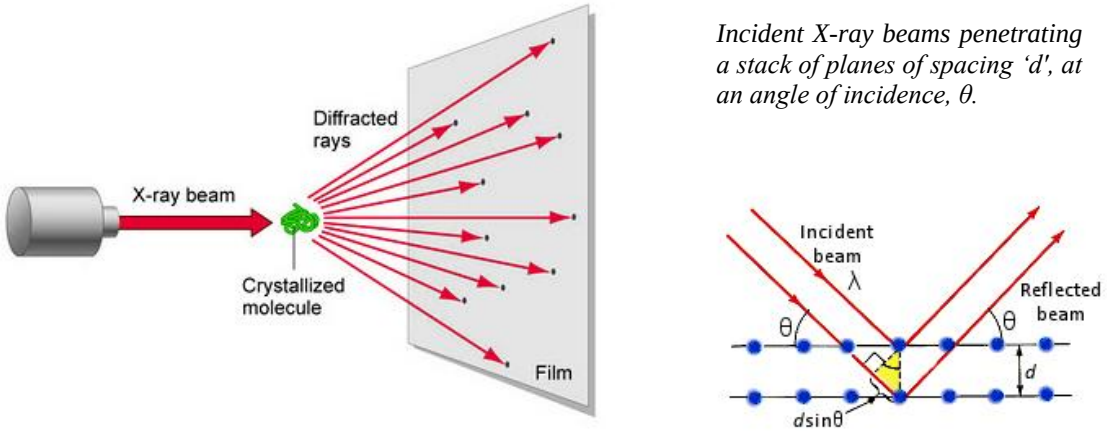


*Incident X-ray beams penetrating a stack of planes of spacing 'd', at an angle of incidence, θ.*

*Figure 3.11: Schematic for X-ray diffraction showing incident beams penetrating a crystallised molecule of a material to produce diffracted rays which are detected by a photographic film (Bijelic & Rompel, 2018)*

## 3.9. Chapter closure

This chapter explained the experimental set-up and field investigations adapted to achieve the purposes of this study. The chapter consists of eight main sections; i) the introduction, which informs the methodology adopted for this study; ii) material characterisation, which entails the general background of the materials utilised for this study and the philosophy of their selection; iii) concrete mix design, which describes the principles and methodology employed in designing two types of concrete batches; LH and UCT concrete; iv) UCT concrete mixing, casting and curing method, which illustrates criteria for mixing, casting, and curing concrete for sewer exposure; v) laboratory quality control tests, which explain the quality control test procedures for sewer concrete study, including compressive strength, saturated density and DI tests; vi) sample preparation for sewer exposure, which defined procedures for preparing specimens for exposure; vii) BAC monitoring analysis, which expresses a scheme for monitoring the deterioration of concrete; and finally, viii) BAC microstructure analysis entailing SEM, QEMSCAN, and XRD analysis.

# CHAPTER 4. SEWER ENVIRONMENTAL CONDITIONS

## 4.1. Introduction

Sewer environmental conditions define the state of the sewer sites where concrete specimens of this study were exposed for their performance examination. This section consists of three subsections: sewer site selection, sewer headspace condition assessment, and the relationship between selected sites and interior sections of a sewer pipe under BAC. Sewer site selection describes the criteria for determining sewer manholes for study and their historical background. Sewer headspace condition assessment covers the condition of the selected sites and provides the gas concentrations, ambient temperature, and RH. The last subsection relates the performance of the selected sites to the interior sections of a sewer pipe under BAC.

## 4.2. Sewer site selection

'Sewer sites' were the designated sewer localities in which concrete specimens for the study were exposed to explore their field performance over time. These localities can be within manholes, pipelines, or locations, such as wastewater pump stations or treatment facilities, where BAC is most pronounced or likely to occur. The selection of sites for the experiment is crucial when studying the field performance of concrete. It assists in identifying locations that are severely aggressive to cause significant corrosion on concrete over a relatively short period due to the constraints of the study period. Therefore, the City of Cape Town Water and Sanitation Department was consulted to identify suitable sites for this. These sites include;

i. The Northern Area Sewer (NAS), with two identified manholes of interest;
   - manhole 19 (NAS M19), located along Jan Smuts Drive (M17) near Epping Industrial. This site is a medium to high severity and
   - manhole 54 (NAS M54), situated in Thornton along the Elsieskraal river canal. This site is regarded as a low or less severe site, and

ii. The Langa pump station manhole (LPS), located behind the old Athlone Power Station, is a very aggressive site.

### 4.2.1. Northern Area Sewer (NAS)

The NAS has a total length of 8.7 km. It serves an area of approximately 4000 ha. It starts from the east of Jan van Riebeeck Drive (M12) and follows the course of the Elsieskraal River to Jan Smuts Drive (M17). It then turns south to follow the road to the Langa Pump Station, where wastewater is pumped to the Athlone Wastewater Treatment works.

Within this sewer line, two manholes were selected. The first manhole was a low-severity manhole, NAS M54 (Figure 4.1), located along Thornton Forest drive under the bridge near Thornton train station. The second manhole was a medium to high severity manhole, NAS M19 (Figure 4.3), located along Jan Smuts Drive, close to Epping Industrial area I and Langa cemetery.

The NAS M54 is the upstream manhole of the NAS line collecting wastewater from the NAS line along the Elsieskraal River canal and the sub-catchment area of Thornton, which includes wastewater from the Old Mutual Golf Course site, Conradie Hospital, and Viking Place, see Figure 4.2. The cumulative flow of this manhole is approximately 190 megalitre/day.


*Figure 4.1: NAS M54 location in Thornton Forest drive, along the Elsieskraal River canal under the bridge. Elsies River Canal is seen in the background in the photo.*

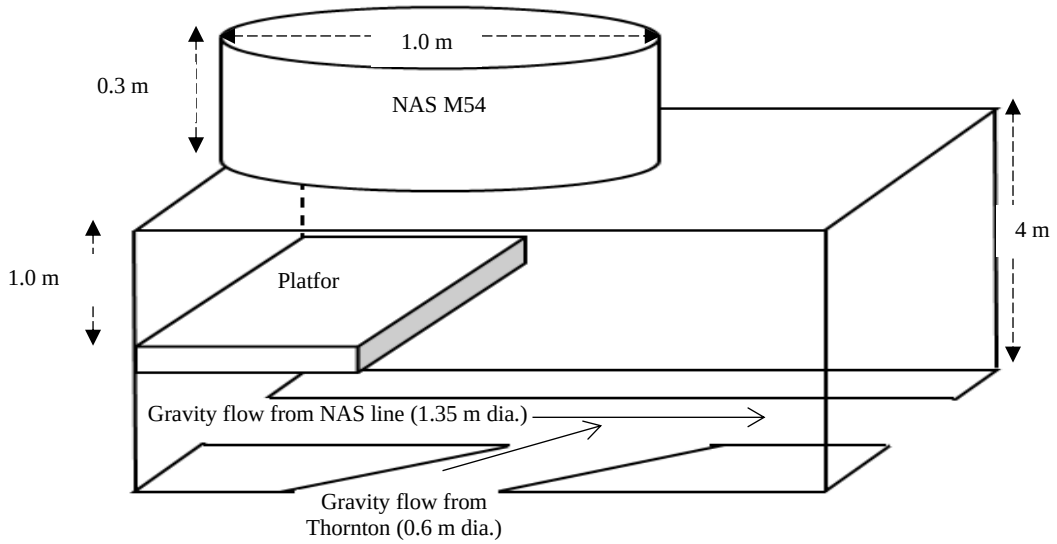


*Figure 4.2: Schematic of the NAS M54 showing its interior, wastewater collecting channels, and the concrete platform on which the baskets with concrete specimens were positioned for exposure*

*Figure 4.3: NAS M19 located along Jan Smuts Drive, near the Epping Industrial area 1 and Langa cemetery. (UCT and City of Cape Town personnel at the site).*

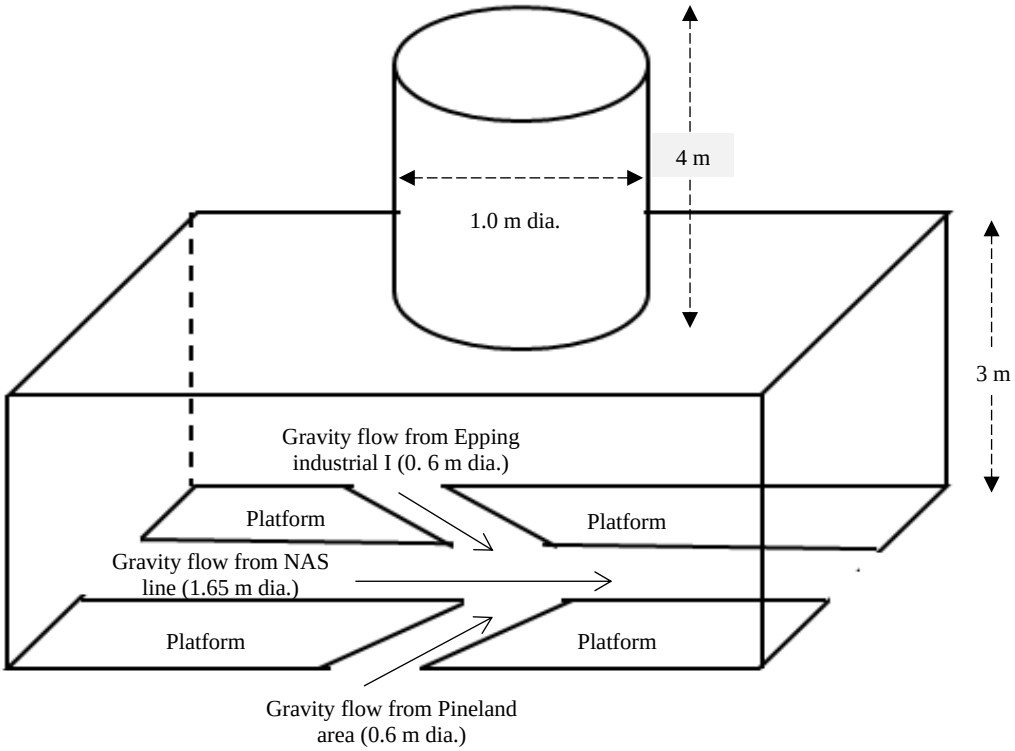


*Figure 4.4: Schematic of the NAS M19 showing its interior, wastewater collecting channels, and the concrete platform on which the basket with concrete specimens for this study was positioned*

The NAS M19 is the downstream manhole collecting wastewater from the NAS line and the sub-catchment area of the domestic area (Pineland) and the Epping Industrial area 1 (the largest and most centrally situated industrial area of Cape Town), see Figure 4.4. The cumulative flow of this manhole is approximately 260 megalitre/day. Therefore, NAS M54 mainly contains domestic wastewater, while NAS M19 includes a mixture of domestic and industrial wastewater.

### 4.2.2. Langa sewer pump station (LPS)

Langa Sewer Pump Station is located near the Old Athlone Power Station in Cape Town. The pump serves the catchment areas to deliver raw wastewater to the Athlone Wastewater Treatment plant across the N2 highway. The station consists of a minor pump station that receives only domestic wastewater, and the main pump station receives primarily domestic and industrial wastewater from NAS. The manhole used for this study is located between the two pump stations, as shown in Figure 4.5. It receives wastewater from the minor pump station and the domestic area (Kewtown) to the main pump station.

Initially, the manhole was 3 m deep and built of clay bricks with a fibre-concrete cover at the same level as the ground surface. However, during the 2020 COVID19 Pandemic national lockdown and some localised flooding, a lack of maintenance led to the manhole breakdown. It was then taken out of service for about four months to allow its reconstruction. It was rebuilt with bricks, but its top surface was raised to about 2 m above the ground surface. Figure 4.6 shows a view of the rebuilt manhole and its current interior state compared to its previous state.

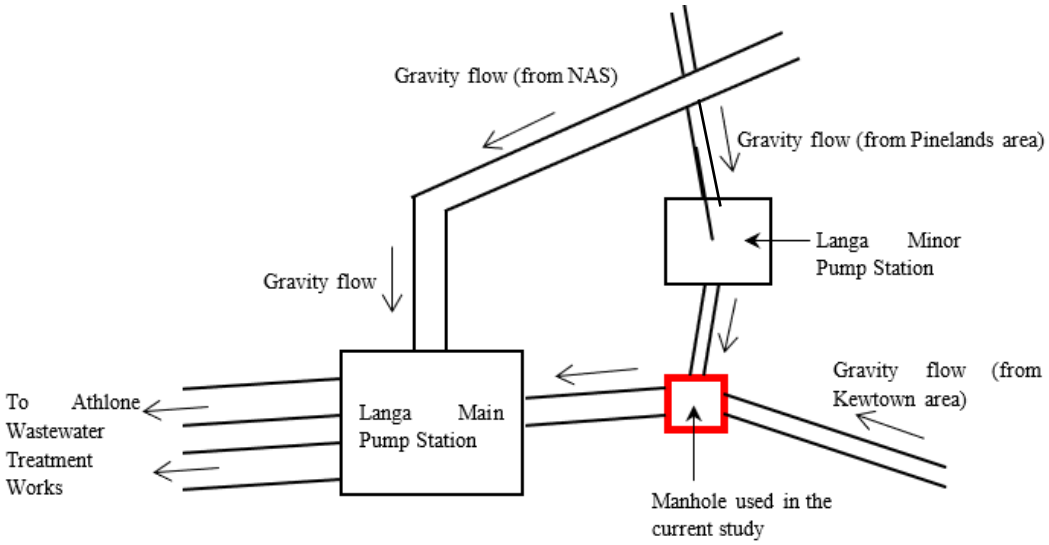


*Figure 4.5: Schematic of the sewer network at Langa Pump Station showing two feeders into the manhole used in the current study (20 m downstream of the Minor Pump Station)*

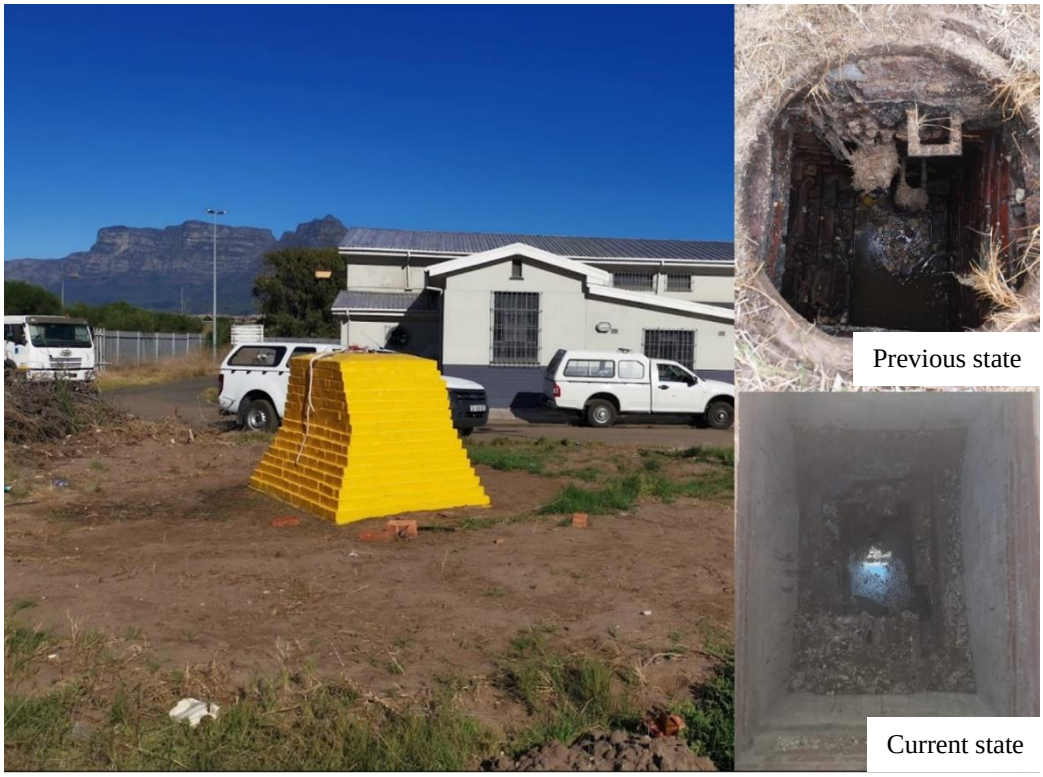


*Figure 4.6: LPS manhole located between the main and minor Langa sewage pump station buildings near the Old Athlone Power Station in Cape Town. The 'Previous state' shows the sewer condition before reconstruction, and the 'Current state' shows its condition after construction. The specimens were suspended in the sewer headspace, where wastewater regularly rises and falls.*

### 4.3. Sewer headspace condition assessment

Sewer headspace condition assessment evaluates the selected sites' sewer headspace gas concentrations ($H_2S$, CO and $CO_2$), ambient temperature, and RH. The assessed parameters are the most important in characterising a sewer's aggressivity since they provide a conducive environment for the proliferation of microbial organisms responsible for sulphuric acid production. These parameters were measured from March to November 2021 on a single selected day of the month for 12 hours each day. The primary aim of measuring these parameters was to identify their diurnal and seasonal fluctuations over the year, i.e., diurnally; morning, day, and evening hours, and seasonally; Summer (November to February), Autumn (March to April), Winter (May to August), and Spring (September to October).

The ambient temperature and RH were measured using a Hygrolog HL-20D data logger, while the gas concentrations were monitored with an Industria scientific MX6 Ibrid gas monitor. These devices were positioned where concrete specimens were exposed to ensure reading correspondence with the specimen exposure environments.

Therefore, Figure 4.7 to Figure 4.9 display the summary of $H_2S$, $CO_2$ and CO gas concentration measurements at the three sites from March to November 2021. The bar lines display the maximum and minimum concentrations, with the average concentrations at the centre of the line. The average concentration was determined by evaluating the area under the curves, shown in Appendix C, over the total duration of gas concentration measurements. Figure 4.10, on the other hand, shows the average temperature and RH measured in the sewer headspace of the three sites from March to November 2021.

### 4.3.1. $H_2S$ gas concentration

$H_2S$ gas concentration is crucial for initiating BAC on sewer concrete and determining its corrosion rates (Sun et al., 2014, 2015, 2019). However, this gas varies significantly due to diurnal, seasonal, and other periodic events occurring in sewers (Gutierrez, Sharma & Poch, 2009; Sun et al., 2019). According to Sun et al. (2019), such fluctuations affect gas diffusions into the corrosion layer due to the changing concentration gradient, which subsequently affects the sulfide oxidation processes.

Figure 4.7 shows the seasonal variations of $H_2S$ gas concentrations in three sites from March to November 2021. The bar lines show each month's maximum, average, and minimum concentrations per site. $H_2S$ concentrations at the LPS manhole show the highest concentration on maximum in March (365.5 ppm) and November (348.5 ppm) and the lowest in May (96.1 ppm) and June (78.2 ppm) of the year 2021. The remaining months had concentrations ranging between 200 ppm and 100 ppm. The average concentration of $H_2S$ gas was 59.5 ± 4.9 ppm in autumn, 51.5 ± 9.0 ppm in winter, 37.5 ± 1.2 ppm in spring, and 51.1 ± 2.0 ppm in summer. The wastewater in this manhole is periodically pumped from a minor pump station every 30 minutes; the gas concentration tends to rise and fall, creating a periodic curve (see Figure C.1). However, this behaviour is highly observed from August to November. The minor pump was under repair in the earlier months after experiencing a breakdown.

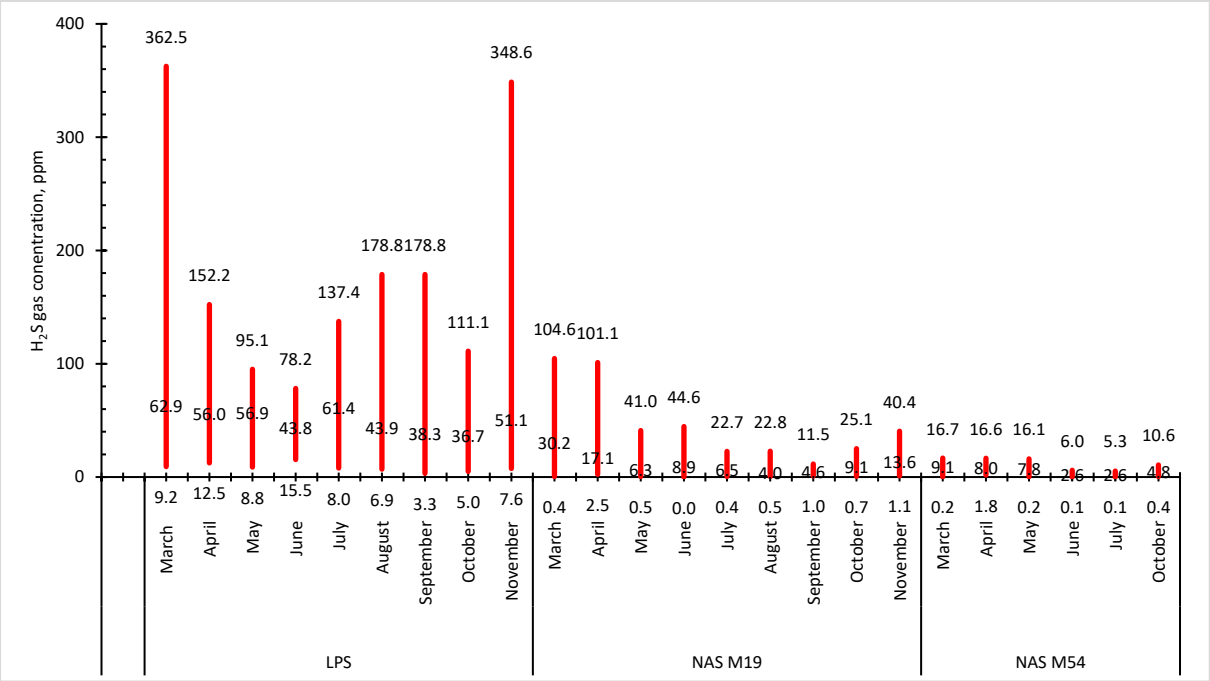


*Figure 4.7: Seasonal variation of $H_2S$ gas concentrations in three sewer sites from March to November 2021; the bars show the maximum, average, and minimum concentrations in order.*

In NAS M 19, the highest $H_2S$ concentrations, on maximum, were obtained in March (104.6 ppm) and April (101.1 ppm). In contrast, the lowest concentrations were obtained in September (11.5 ppm). Other months have $H_2S$ concentrations ranging from about 50 ppm to 20 ppm, i.e., May (41.0 ppm), June (44.6 ppm), July (22.7 ppm), August (22.8 ppm), October (25.1 ppm), and November (40.4 ppm). The maximum $H_2S$ concentrations in this manhole mainly depended on the peak hours of the population served by the NAS line. Therefore, diurnal discharge patterns of $H_2S$ gas concentration were observed,

with the highest peaks in the morning and evening hours; during the day, lower peaks (close to 0 ppm $H_2S$) were observed (see Figure C.1). On average, the $H_2S$ gas concentration was 23.6 ± 9.3 ppm in autumn, 6.4 ± 2.0 ppm in winter, 6.8 ± 3.2 ppm in spring and 13.6 ± 8.5 ppm in summer.

In the NAS M54, $H_2S$ concentrations for August and September were not captured. However, for the other months, the maximum $H_2S$ concentration obtained was 16.7 ppm in March, 16.6 ppm in April, 16.1 ppm in May, 6.0 ppm in June, 5.3 ppm in July, 10.6 ppm in October, and 13.5 ppm in November. The manhole has the lowest gas concentration compared to other manholes because it is situated on the upstream part of the NAS line, collecting only domestic wastewater from a small population. On average, the $H_2S$ gas concentration was 8.6 ± 0.8 ppm in autumn, 4.3 ± 3.0 ppm in winter, 4.8 ± 1.8 ppm in spring and 4.8 ± 2.0 ppm in summer.

Using average measurements, the LPS had the highest $H_2S$ gas concentration, followed by the NAS M19 and NAS M54 with the lowest. The maximum concentrations were mainly observed in November, March, and April, i.e., in summer and autumn, and the lowest was observed in May, June, July and August, i.e., in winter. This observation agreed with Kiliswa, Scrivener & Alexander (2019) that the $H_2S$ concentration is the lowest in winter and highest in summer. Concerning this rank, the performance of similar concrete subjected to these three sites is expected to show a similar performance rank. Therefore, concrete subjected to the LPS manhole is expected to have the highest corrosion rate and the lowest at the NAS M54.

In contrast, the diurnal curves of $H_2S$ concentration at the LPS were somewhat similar to those observed in Melbourne's Western Trunk Sewer in Australia (Sun et al., 2015). Also, Sun et al. indicated that occasional high $H_2S$ concentrations in the sewer headspace inhibit $H_2S$ adsorption by sewer concrete. Therefore, estimating the $H_2S$ adsorption based on the average $H_2S$ concentration may cause an overestimation or underestimation of the $H_2S$ adsorption and hence the corresponding corrosion rate if there are significant fluctuations in the $H_2S$ concentrations, which is commonly the case.

### 4.3.2. $CO_2$ gas concentration

In sewers, carbon dioxide ($CO_2$) gas is produced during the decomposition of organic matter. Under the influence of sewer hydraulics, it is emitted in the sewer headspace. A substantial accumulation of $CO_2$ in the sewer headspace initiates sewer corrosion by initially lowering the concrete surface pH. $CO_2$ gas combines with the moisture on the sewer condensate film to form carbonic acid, which reacts with the sewer concrete surface by lowering its pH from approximately 12 to 9 (Hudon, Mirza & Frigon, 2011). The reduction of concrete surface pH provides a conducive environment for SOB proliferation. Subsequently, SOB oxidises $H_2S$ gas to sulphuric acid responsible for BAC (Wei et al., 2013).

Figure 4.8 shows $CO_2$ gas concentrations for the three sites measured from March to November 2021. As previously explained, the bar lines show the maximum, average, and minimum concentrations of each month for each site. However, it is noted that 1.0% $CO_2$ gas concentration is equivalent to 10 000 ppm of $CO_2$ gas. The figure indicates that the sewer headspace of these manholes has much higher concentrations of $CO_2$ gas than $H_2S$ gas. Therefore, carbonation of the concrete specimen subjected to these sites is expected.

In the LPS, the highest $CO_2$ concentration, on maximum, was 5.0%, observed in March, April, October, and November. In May, the concentration was 2.7%, 3.8% in June, 0.7% in July, 1.7% in August, and 2.7% in September. On average, the concentration was 3.9 ± 0.9 % in Autumn, 1.6 ± 0.3 % in winter, 3.3 ± 0.9 % in spring, and about 5.0 % in summer. In the NAS M19, the maximum $CO_2$ concentrations were 1.2% in March, 1.8% in April, and 0.7% in May, while the remaining months had 5.0% $CO_2$ concentration. On average, the concentration was 0.9 ± 0.1 % in Autumn, 2.8 ± 0.5 % in winter, 4.8 ± 0.2 % in spring, and 4.3 ± 0.9 % in summer. In the NAS M 54, the maximum $CO_2$ concentration was 0.5% in March, 0.9% in April, 1.2% in May, 0.7% in June, 0.7% in July, 2.2% in October, and 3.8% in November. On average, the concentration was 0.4 ± 0.1 % in Autumn, 0.6 ± 0.1 % in winter, 1.2 ± 0.5 % in spring, and 1.8 ± 0.9 % in summer.

The figure also indicates that the NAS M54 has the lowest $CO_2$ gas concentration, while the LPS and the NAS M19 have the highest. Despite NAS M54 showing the lowest concentration, this $CO_2$ amount can significantly lower the concrete surface pH by carbonation. The difference between LPS and NAS M19 was observed in the first three months (March to May), where the LPS showed a wide range of gas concentrations from 0.0 to 5.0 %, while NAS M19 showed about 0.5 to 1.8 %. In the subsequent months, the concentrations for the LPS decreased, while in the NAS M19, the concentrations increased. In August and September, a very high concentration approximating a constant value of 5% was observed in the NAS M19 and in October and November for the LPS.

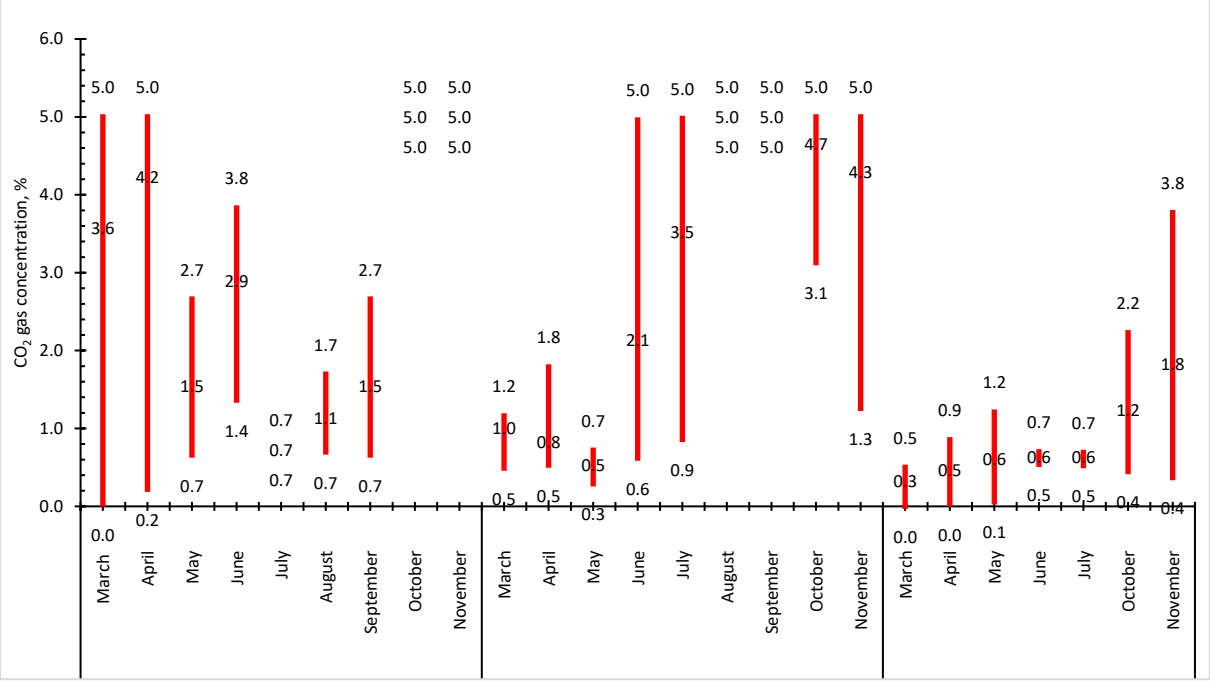


*Figure 4.8: Carbon dioxide ($CO_2$) gas, %, of three sewer sites measured from March to November 2021; the bars show the average, maximum and minimum concentrations.*

With such high $CO_2$ concentrations, the concrete subjected to these sites will likely experience significant carbonation on the exposed surface by continuously reacting with the cementitious matrix and lowering its pH. This, therefore, might affect the modelling results since the carbonation was not

considered. Moreover, there was an insignificant relationship between $CO_2$ and $H_2S$ concentrations, and no distinct diurnal or seasonal trend of $CO_2$ gas was observed.

### 4.3.3. CO gas concentration

Carbon monoxide gas is rarely reported as a significant contributor to BAC in sewer studies. However, it is widely known as a toxic gas. If inhaled in high concentrations for prolonged periods, it can cause fatality. The concern in this study is whether CO gas might affect the growth of microorganisms responsible for influencing BAC. Figure 4.9 shows CO gas concentration measured from March to November 2021 in three sites, with bars showing the maximum, average, and minimum concentrations of each month in each sewer.

LPS showed the highest concentration ranging from 0 ppm to about 1800 ppm throughout the year, while NAS M19 shows about 0 ppm to ≈ 400 ppm, with the highest readings, on maximum, in November and March and the lowest in July, while the NAS M54 shows the lowest CO gas concentration below 50 ppm.

It was also observed that the CO diurnal curves had similar trends as $H_2S$ diurnal curves; see Figure C.1 and Figure C.3 in Appendix C. The periods with high $H_2S$ peaks seemed to have high CO gas peaks. The rank of the sites from the highest to the lowest was also like that of the $H_2S$ gas concentration. The CO concentration at all sites was higher than the $H_2S$ gas concentration. This raises a discussion of whether CO gas plays any functional purpose in influencing the concentration of $H_2S$ gas in sewers.

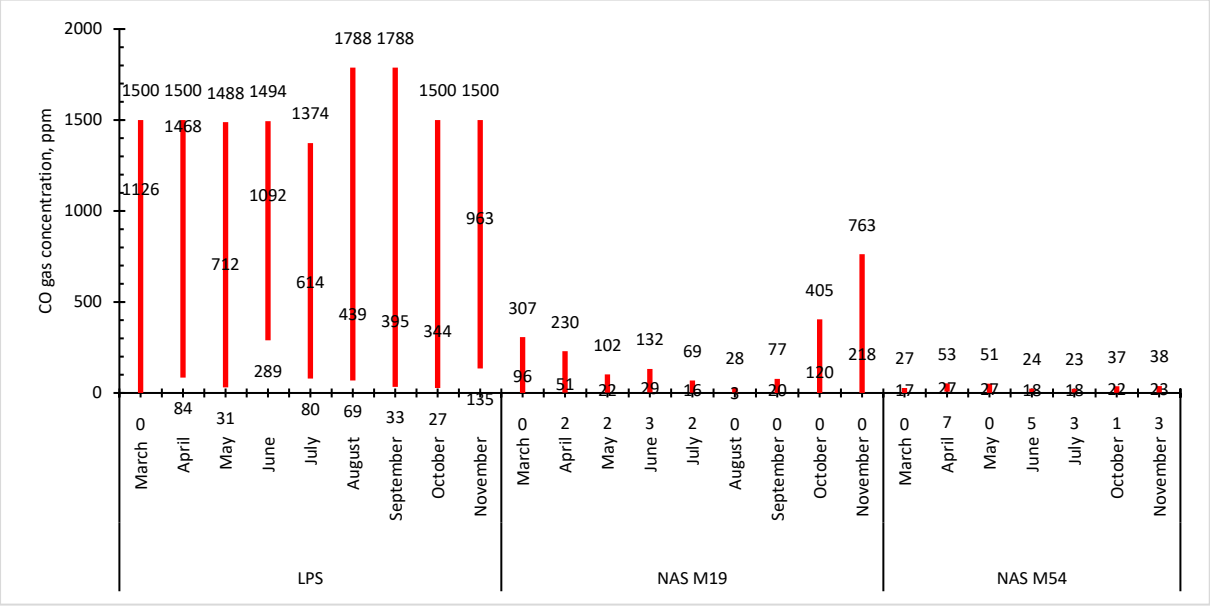


*Figure 4.9: Carbon monoxide gas in ppm of three sewer sites measured from March to November 2021; the bar shows the average, maximum and minimum concentration*

### 4.3.4. Temperature and RH of the sewer sites

Figure 4.10 shows the three sewer sites' average temperature and RH. The measurements were taken from March to November 2021. Also, measurements in August and September for the NAS M54 were not captured.

The average temperatures of the sites range between 15°C and 30°C, with a decrease from March to July, then an increase towards November, which complies with the annual seasons as winter occurs from May to August. Minor temperature variations among the sites were observed.

RH readings had the opposite trend to the temperature readings. RH increased from March to July and then decreased towards November, reflecting the year's seasons. The NAS M19 has the highest RH, followed by the LPS, and NAS M54 with the lowest. The average RH ranged between 70 % and 100 %, slightly higher than Li et al. (2017) observation, which reported that sulphuric acid on the sewer wall is formed when the RH in the sewer ranges between 60% and 100%.

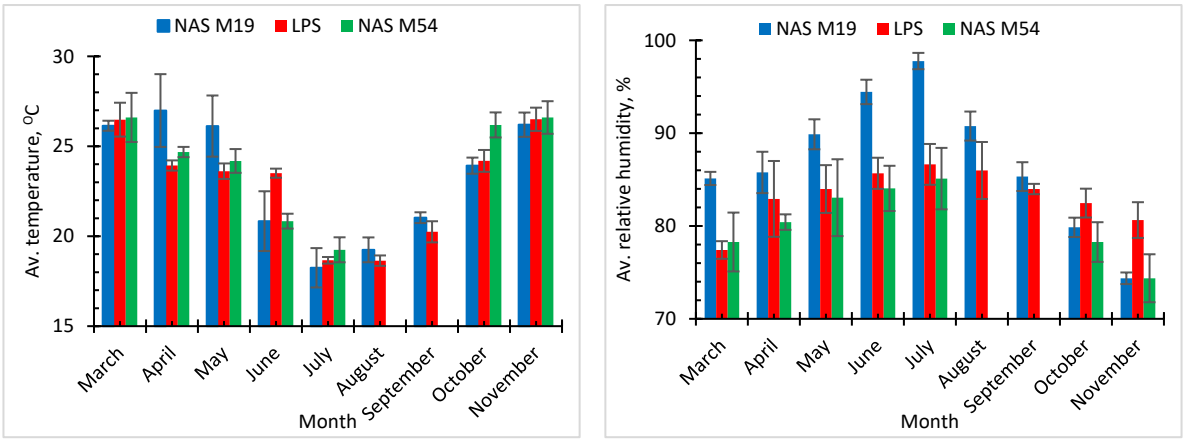


*Figure 4.10: Temperature and relative humidity measured from March to November 2021*

### 4.4. Relationship between selected site and sewer pipe section

Regarding the positioning of concrete specimens in the sewers, in the NAS M19 and M54, the baskets containing specimens were placed on the sewer concrete platforms shown in Figure 4.2 and Figure 4.4, respectively. The specimens on the NAS M19 platform were occasionally wetted by wastewater, while on the NAS M54 platform, only splash wastewater reached the platform. The degradation of concrete specimens on the platforms was mainly attributed to sulphuric acid build-up on the surface under the influence of RH, temperature, accumulation of the gases in the headspace and microbial activity, rather than by sewer hydraulic actions. The corroded concrete layer formed on the exposed surface was not washed away. Instead, this layer persisted in growing until its removal during regular BAC monitoring or if it was dislodged in situ by gravity. In the NAS M54, due to a low $H_2S$ gas concentration, the corroded layer formation took longer than for the NAS M19.

At the LPS, the specimens were hung in the sewer (manhole) headspace, about 5 m in depth (after re-construction). Due to the periodic wastewater pumping from the pump station, the specimens were subjected to continuous wetting and drying cycles. Consequently, the corroded concrete layer formed on the exposed surface was continuously eroded or washed away, leaving a newly exposed surface. Thus, the degradation of concrete subjected to the LPS was attributed to a combination of BAC and sewer hydraulic erosion.

With these observations in relation to a sewer pipe cross-section under BAC, the three sites can be related to three different zones of different aggressivity encountered in any sewer under BAC. The LPS

represents a mostly erosion zone, a tidal zone. The NAS M19 represents a partial erosion condition, mainly the area between the crown and tidal zones that occasionally experience erosion by the wastewater when the sewer is flooded. The NAS M54 represents a purely crown zone phenomenon, where the corrosion is attributed to gas concentration, temperature, and moisture content and less to sewer hydraulic actions, see Figure 4.11. Since the sewer environmental conditions of these sites differ significantly, this correlation describes only the aggressivity phenomena encountered in sewers.

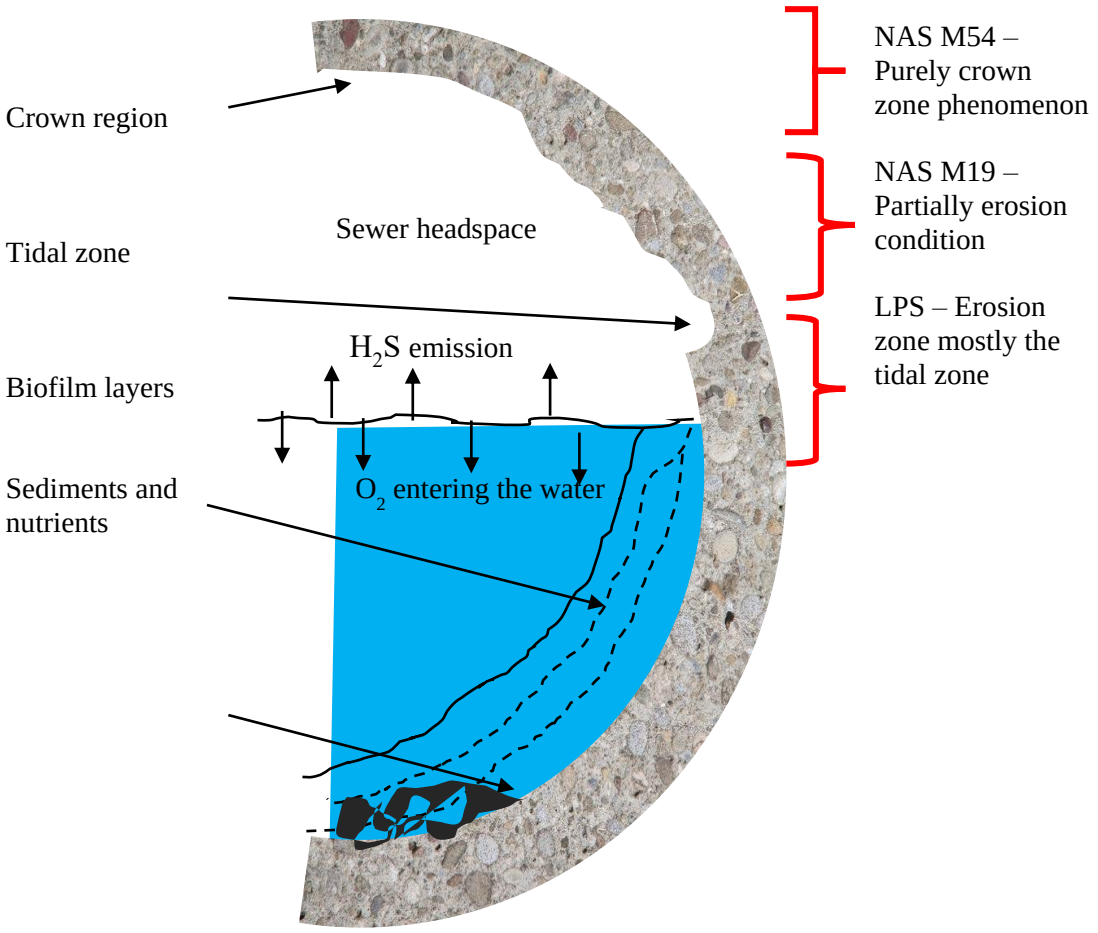


*Figure 4.11: Sewer pipe section related to the selected sites*

## 4.5. Chapter summary and conclusion

The chapter presented the sewer headspace conditions of three sites used in this study, i.e., the NAS M19, the NAS M54 and the LPS. The NAS M54 is the most upstream manhole of the Northern Area Sewer line that was studied, collecting only domestic wastewater, while the NAS M19 was a downstream manhole receiving a mixture of domestic and industrial wastewater. The LPS is the manhole between the minor and main pumps at the Langa pump station. It receives mainly domestic wastewater pumped periodically from the minor pump station and a continuous domestic wastewater flow. Thus, the study covers diverse sewer conditions that influence BAC.

Three sewer headspace conditions, i.e., gas concentrations ($H_2S$, CO and $CO_2$), ambient temperature, and RH, were measured and studied. The gas concentrations in the sewer headspace varied diurnally, seasonally, and sometimes due to periodic events occurring in sewers. At the LPS, the fluctuation of

the gas depends on the regular pumping of the wastewater from the pump station, which occasionally raises the gas concentration peak. At the NAS M19, the gas concentrations depended on the peak hours of sewer flow due to the population served by the sewer line, with the highest peaks observed in the morning and evening hours. In the NAS M54, the gas concentration is minimal, with peaks depending on the peak sewer flow.

At the LPS, the average $H_2S$ concentrations were 59.5 ± 4.9 ppm in autumn, 51.5 ± 9.0 ppm in winter, 37.5 ± 1.2 ppm in spring, and 51.1 ± 2.0 ppm in summer. The manhole showed the lowest average $H_2S$ concentration in spring and the highest in autumn. In the NAS M19, the average $H_2S$ gas concentration was 23.6 ± 9.3 ppm in autumn, 6.4 ± 2.0 ppm in winter, 6.8 ± 3.2 ppm in spring and 13.6 ± 8.5 ppm in summer. This manhole showed the lowest average $H_2S$ concentration in winter and the highest in autumn. In the NAS M54, the $H_2S$ gas concentration was 8.6 ± 0.8 ppm in autumn, 4.3 ± 3.0 ppm in winter, 4.8 ± 1.8 ppm in spring and 4.8 ± 2.0 ppm in summer. This manhole showed the lowest average $H_2S$ concentration in winter and the highest in autumn. Generally, all manholes indicated lower concentrations during the cold seasons and higher concentrations in the hot seasons.

In the case of $CO_2$ concentration, the LPS has an average concentration of 3.9 ± 0.9 % in autumn, 1.6 ± 0.3 % in winter, 3.3 ± 0.9 % in spring, and about 5.0 % in summer. The NAS M19 has the average concentration of 0.9 ± 0.1 % in Autumn, 2.8 ± 0.5 % in winter, 4.8 ± 0.2 % in spring, and 4.3 ± 0.9 % in summer. The NAS M 54 has an average concentration of 0.4 ± 0.1 % in Autumn, 0.6 ± 0.1 % in winter, 1.2 ± 0.5 % in spring, and 1.8 ± 0.9 % in summer. Generally, all sites showed the lowest average concentration in winter and the highest in summer. Despite seasonal fluctuations, the $CO_2$ gas in the sewer headspace remained high; thus, the carbonation of concrete surfaces is inevitable.

On the other hand, CO gas average concentration was the highest in the LPS throughout the year, followed by the NAS M19 and the NAS M54 showing the lowest. The CO diurnal curves seem to mimic the $H_2S$ diurnal curves. With this, a concern was raised on whether CO gas plays any functional purpose in influencing the concentration of $H_2S$ gas in sewers. Due to this, further study in this area is required.

In the case of sewer headspace temperature, the overall readings range between 15$^{o}$C and 30$^{o}$C, with the lowest values in winter and the highest in summer. The opposite trend was observed in the case of RH. The highest readings were detected in winter and the lowest in summer. Generally, RH readings ranged between 70% and 100%, which agrees with the literature to be a suitable condition for microbial activity, and hence, aggressive gas generation.

In conclusion, the LPS was related to a mostly erosion zone, i.e., a tidal zone in the sewer; the NAS M19 was associated with a partial erosion condition, mainly the area between the crown and tidal zones, and the NAS M54 to a purely crown zone, where the corrosion is attributed to sewer headspace conditions with the lowest gas concentration and less with the effect of sewer hydraulic actions. Most importantly, careful attention should be taken when selecting sewer environmental conditions parameters, especially $H_2S$ gas concentration, for sewer corrosion rate prediction. This is because corrosion rate prediction based on the average $H_2S$ concentration may overestimate or underestimate the corrosion rate since, in many cases, $H_2S$ concentrations in sewers fluctuate significantly.

# CHAPTER 5. EXPERIMENTAL INVESTIGATION: ANALYSIS AND DISCUSSION OF RESULTS

## 5.1. Introduction

This chapter discusses the experimental investigation results of sewer concrete prepared and analysed according to the experimental setup described in Chapter 3 and exposed to the sewer environments, elaborated in Chapter 4. The chapter is divided into four sections. The first section (Section 5.1); provides the chapter introduction, the second and third sections discuss the experimental investigation results of two concrete types: LH concrete (Section 5.2) and UCT concrete (Section 5.3), and the last section provides a chapter closure and remarks (Section 5.4). The sections on the LH mixes and the UCT mixes follow a similar pattern, resulting in some overlap between the sections.

It should be noted that the LH concrete mixes did not comply with the quality of concrete recommended for sewer concrete construction (see appendix D), which led to the preparation of the UCT concrete mixes. Nevertheless, it was decided to continue their field exposure to understand the performance of poorly compacted concrete in a sewer environment, since this would not alter the basic deterioration mechanisms.

LH concrete mixes were prepared with calcite aggregates and siliceous river sand, and UCT concrete mixes with high-quality dolomite aggregates and siliceous pit sand. LH concrete mixes were exposed to three sewer sites in the City of Cape Town, i.e., the LPS, NAS M19 and NAS M54, while UCT concrete mixes were only exposed to the LPS and NAS M19 after observing that NAS M54 is less aggressive.

Generally, this chapter aims to highlight; i) the importance of studying the performance of concrete in live sewer environments, ii) the influence of different sewer environments on concrete deterioration, iii) the behaviour of different concrete microstructures under BAC, and iv) the influence of aggregate types on the sewer concrete mixes.

## 5.2. LH concrete mixes: results and discussion

The primary purpose of the LH concrete mixes was to understand the influence of fly ash (FA), limestone (LS), and iron-based additives (HC) in improving the performance of Sulphate Resisting Portland Cement (SRPC) in sewers and to study the performance of Calcium Sulpho-Aluminate (CSA) cement as a novel binder system in the sewer. Calcite aggregates were used to study the combined influence of reactive aggregate and binder systems in sewer concrete. Generally, four concrete mixes, i.e., SRPC + FA, SRPC + FA + HC, SRPC + LS, and CSA, were prepared by LH and exposed to three sewer sites.

Therefore, this section discusses the following: laboratory control test results, i.e., compressive strength, saturated density and durability index results after 28 days of age, to indicate its quality for sewer exposure; the visual observation of concrete specimens exposed in three sewer sites for two years; LH concrete surface pH evolution with exposure time; LH concrete mass and thickness changes due to BAC; and concrete microstructure observations conducted after two years of sewer exposure using

BAC microstructural analysis techniques, i.e., SEM-BSE images, QEMSCAN analysis, and XRD analysis, for concrete exposed at NAS M19.

### 5.2.1. Laboratory control test results

#### 5.2.1.1. Compressive strength and saturated density at 28 days

Table 5.1 shows the compressive strength and saturated density of four concrete mixes at 28 days. The compressive strengths of SRPC + FA and SRPC + FA + HC were approximately 44 MPa, while SRPC + LS concrete with limestone was approximately 38 MPa and 40 MPa for CSA concrete. These values were less than the 50 MPa for conventional concrete with plain cement, and 0.4 w/b indicated in the previous UCT concretes, see Table D.1 in Appendix D. The coefficient of variation (CoV) was also substantially higher than the 4% compressive strength of the previous conventional laboratory mix, indicating that the reproducibility of these concrete specimens varied significantly due to the compaction voids observed in the cored specimens, see Figure 5.1.

Saturated densities of the LH concretes were below 2400 kg/m$^3$ (except for the mix containing HC), which was the average density for conventional concrete. Further, the saturated densities were generally significantly lower than the theoretical densities, reflecting the lack of full compaction of these mixes again.

*Table 5.1: Compressive strength and saturated density of LH concrete mix*

| Concrete mix | | SRPC + FA | SRPC + FA + HC | SRPC + LS | CSA |
|---|---|---|---|---|---|
| Av. Compressive strength | MPa | 44.8 | 43.8 | 37.8 | 40.3 |
| STDev. Compressive strength | MPa | 11.0 | 8.1 | 3.9 | 3.9 |
| CoV. Compressive strength | % | 24.6 | 18.5 | 10.3 | 9.7 |
| Theoretical density | kg/m$^3$ | 2383 | 2422 | 2383 | 2383 |
| Av. Saturated density (28 days) | kg/m$^3$ | 2379 | 2339 | 2326 | 2320 |
| STDev. Saturated density (28 days) | kg/m$^3$ | 57.1 | 35.8 | 24.0 | 4.4 |

#### 5.2.1.2. Durability Index (DI) results

The DI results are discussed based on the criteria to judge the quality of concrete, given in Table 5.2. Two index tests were conducted: The Oxygen permeability Index (OPI) test and the Water Sorptivity Index (WSI) test (with associated porosity), with their results indicated in

Table 5.3.

In terms of OPI, all values were above 10 (log value), indicating good quality concrete. However, it is postulated that better compaction would have provided even better quality concrete, see Figure 5.1. The OPI results further indicate that the compaction voids were mainly not interconnected, which would have led to very low OPI values. The water sorptivity index indicated excellent to good quality concrete, and their index values were between 4 and 8 mm/√hr. However, the coefficients of variation (CoV) of these indexes were high compared to typical laboratory concretes, i.e., < 2.0% for OPI (Alexander, Ballim & Mackechnie, 2018) and < 7% for WSI (Alexander, 2004), indicating that the degree of compaction was variable. The values of water-penetrable porosity were also less than 10%, indicating that the concrete matrixes were dense despite the concrete having a significant amount of compaction voids.

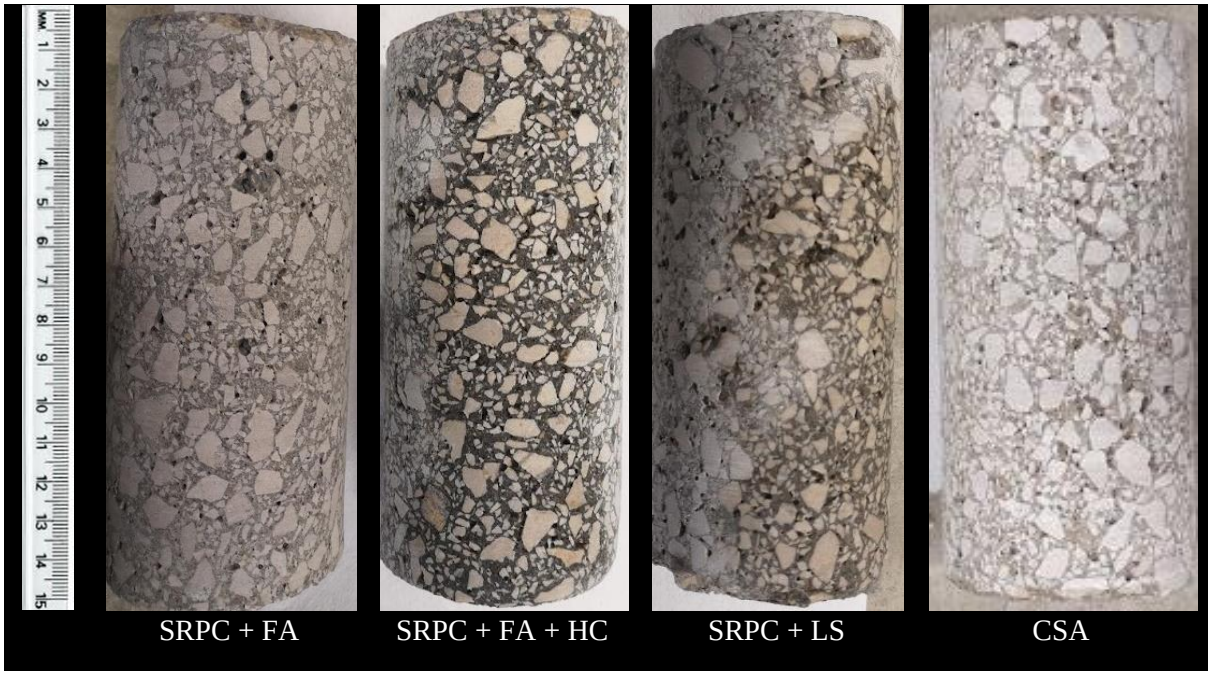


*Figure 5.1: Visual appearance of the LH concrete core samples (150 mm height and 70 mm diameter) at 28 days, indicating visible compaction voids. The SRPC+FA+HC concrete appears dark due to the dark colour of the HC(iron-based admixture*

*Table 5.2: Criteria to judge the quality of concrete from the results of the durability index (DI) test (Alexander, Mackechnie & Ballim, 1999)*

| Quality of concrete | Oxygen permeability Index (OPI) log scale | Water sorptivity index (WSI) $mm/h^{0.5}$ |
|---|---|---|
| Excellent | >10 | < 6 |
| Good | 9.5 – 10 | 6 - 10 |
| Poor | 9.0 - 9.5 | 10 - 15 |
| Very Poor | < 9 | > 15 |

*Table 5.3: Durability results of the concrete specimens cast at LH laboratory in Lyon and delivered for sewer site study*

| Concrete Mix | | SRPC + FA | SRPC + FA + HC | SRPC + LS | CSA |
|---|---|---|---|---|---|
| Oxygen permeability, k $x10^{-11}$ [m/s] | Av. | 1.98 | 3.36 | 2.75 | 3.70 |
| Oxygen Permeability Index (OPI), | Av. | 10.68 | 10.56 | 10.56 | 10.65 |
| | STDev. | 0.13 | 0.33 | 0.31 | 0.67 |
| | CoV,% | 1.22 | 3.13 | 2.93 | 6.29 |
| Water Sorptivity Index (WSI) $[mm/h^{0.5}]$ | Av. | 5.41 | 6.01 | 4.57 | 7.07 |
| | STDev. | 0.89 | 0.59 | 0.43 | 2.13 |
| | CoV, % | 16.47 | 9.85 | 9.36 | 30.06 |
| Porosity [%] | Av. | 8.10 | 8.44 | 9.36 | 6.87 |
| | STDev. | 0.18 | 0.35 | 0.61 | 0.65 |
| | CoV,% | 2.21 | 4.11 | 6.49 | 31.28 |

It was concluded that the LH concrete did not fully comply with the quality of concrete recommended for sewer concrete construction, which led to the preparation of the 'UCT concrete mixes. Despite these shortcomings, it was decided to continue with field exposure and testing of the LH concrete to understand the performance of poorly compacted concrete in a sewer environment. Therefore, the following section indicates the sewer performance of the LH concretes.

### 5.2.2. Visual observation of LH concrete

The following are visual observations of the LH concrete specimens exposed to biogenic attack in three sewer sites at different exposure durations. Physical deterioration, i.e., material loss, spalling, discolouration, and cracking of concrete specimens, was observed visually and recorded by taking photographs and comparing them with the initial state of the concrete specimens. Unfortunately, the specimens' photographs before exposure were not well taken. However, since the specimens after two months of exposure displayed only minor signs of corrosion, they were suitable for comparison.

#### 5.2.2.1. Visual observation of LH concrete at LPS

Due to the aggressivity of the LPS, LH concrete specimens at this site experienced early signs of deterioration after about four months of exposure, see Figure 5.2. However, due to the rise and fall of wastewater at this site, the deterioration products built up on the surface of the concrete specimens were usually washed away before or during specimen retrieval for regular monitoring. This was not the case at four months of exposure since corrosion products with yellow-whitish colour were still observed. It was evident that, at this time of retrieval, the level of wastewater in the manhole had been too low to wash away the built-up layer. After six months, however, the corrosion products were eroded or washed away; thus, the main feature of interest on the concrete surface was the black stains, regarded as microorganism biofilm (see Figure 5.3).

After 9.6 months of exposure, there were signs of corrosion layer removal, as a small depth of epoxy coating without concrete contact was observed on the surface of concrete specimens. Also, minor whitish corrosion deposits demarcated with yellowish staining were observed at the CSA specimen edges.

After 18 months of exposure, all specimens experienced substantial corrosion. Approximately 2-3 mm depth of the concrete surface layer was removed entirely. Wastewater penetrated the concrete-epoxy coating interface and eroded built-up corrosion products. Subsequently, the epoxy coating lost adhesion to the concrete, and extensive cracking was observed on the coating surface. On the newly exposed concrete surface, it was observed that once the cement matrix reacted with acid, it was quickly eroded, leaving smooth calcite aggregate particles standing proud. This indicates that incorporating reactive aggregates in sewer concrete to improve the resistance of concrete under acid attack will be affected by the relative resistance between cement matrix and aggregates. Further, hydraulic actions must be considered since these erode the matrix at a more rapid rate than in the absence of such actions.

After 25 months, similar visual observations as at 18 months of exposure were noted, although the thickness loss increased substantially. Based on the physical observations, all binder systems deteriorated significantly at this site. However, actual deterioration rates can only be determined by mass or dimension measurements.

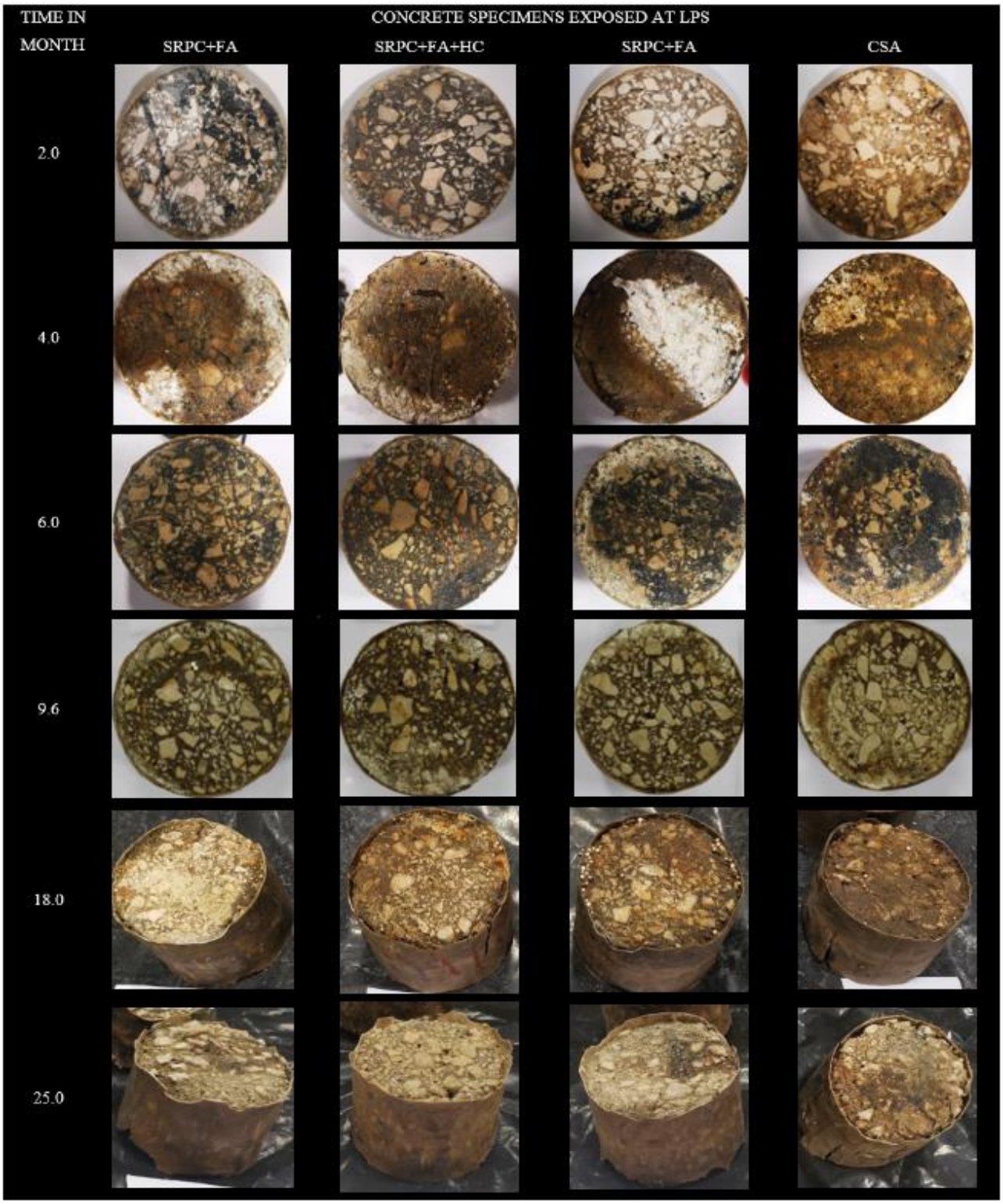


*Figure 5.2: Visual observation of concrete specimens exposed at LPS manhole for two years*

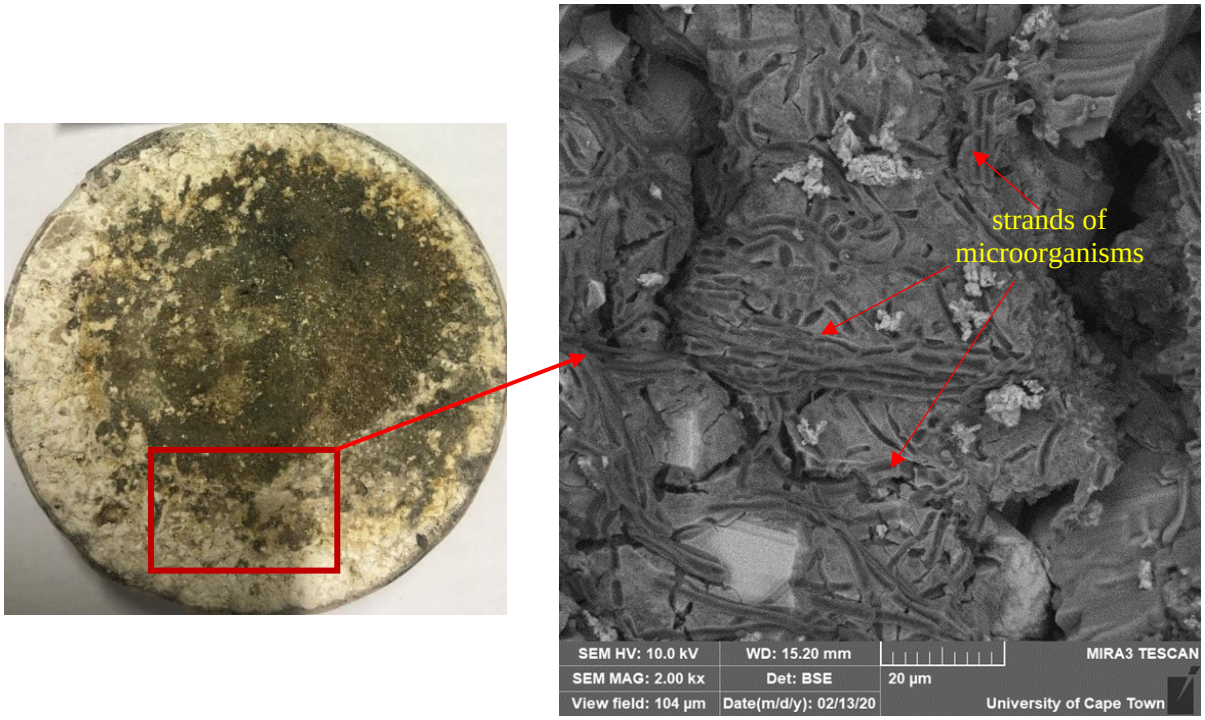


*Figure 5.3: Microorganism biofilm formed on the exposed surface of CSA concrete specimen at the age of six months in the LPS Manhole*

#### 5.2.2.2. Visual observation of LH concrete at NAS M19

Concrete at NAS M19 experienced signs of corrosion from about six months of exposure, with increasing deterioration evident after 9.6 months, see Figure 5.4. After two months of exposure, the exposed surfaces were discoloured due to wastewater contamination and microorganism biofilm formation. At four months of exposure, crystalline-type products with the appearance of sand particles were observed on the surface of the concrete. These are the initial corrosion products. After 6 months, corrosion signs were revealed, with minor white paste-like deposits and reddish/brownish staining on the concrete edges. After 9.6 months, intensive corrosion began to occur, starting from the edge toward the centre of the specimens. The reddish/brownish stains demarcated the corroded and non-corroded surfaces. Such staining was also observed by Grengg, Martin and Bertron (2017).

After 18 months, massive corrosion product build-up was observed on the concrete surface. The deposits appeared whitish mixed with black and reddish staining. These were removed without effort from the concrete surface, and when crushed with fingertips, their texture was smooth and soft, wet paste-like products with fine sand (quartz) particles. The products were mainly observed from the edge towards the centre of the specimen. Due to these massive deposits, uneven thickness loss was observed. The greater the corrosion deposits, the more the concrete was damaged and lost thickness. Unlike the LPS manhole, the corrosion products were not washed away or eroded in situ since there were no sewer hydraulic actions on the specimens but only gently removed in the laboratory for mass and dimension measurement. It was observed that both cement matrix and calcite aggregates were corroding and producing these end products. Similar visual observations were made after 25 months, although more corrosion products and cracking of epoxy coating for CSA concrete were observed.

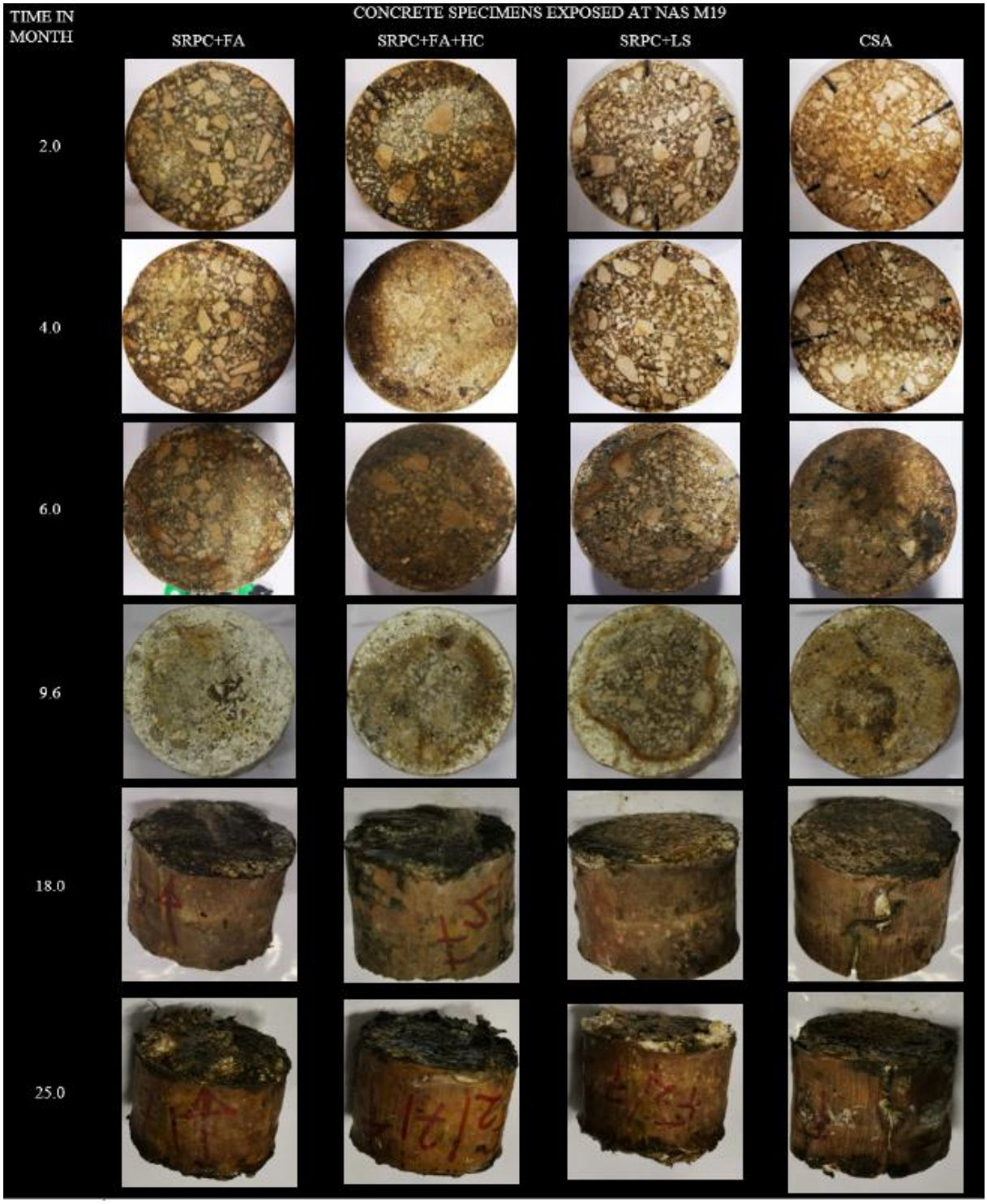


*Figure 5.4: Visual observation of concrete specimens exposed at NAS manhole 19 for two years*

The more intensive corrosion products at the concrete edges, i.e., at the concrete-epoxy coating interface, for all concretes, were due to specimen orientation when fixed in the basket for site exposure. The exposed surface was oriented vertically, allowing acid produced to flow towards the edges and accumulate at the epoxy coating. As a result, the corrosion front over the exposed surface was non-uniform, as reported in other literature (Okabe et al., 2007; Jiang et al., 2014). More material loss was observed at the edges and less at the centre.

For the SRPC-based concretes, i.e., SRPC+FA, SRPC+FA+HC and SRPC+LS, their edges were entirely covered with corrosion deposits, with the reddish/brownish stains demarcating the corrosion boundaries. For the CSA concrete, the most significant observation was the blisters observed on the epoxy-coated surface. These blisters indicated concrete expansion due to either ongoing ettringite production from hydration or the penetration of acid through the concrete-epoxy interface to form degradation products. Generally, the SRPC+FA and SRPC+LS concrete showed 'massive' corrosion products, followed by SRPC+FA+HC concrete, with CSA concrete showing fewer corrosion products on the exposed surface after 25 months of exposure. The visual observations offered an initial qualitative assessment of concrete corrosion performance.

### 5.2.2.3. Visual observation of LH concrete at NAS M 54

Figure 5.5 shows only minor changes on the exposed surface of concrete specimens subjected to the NAS manhole 54 for approximately two years. At about 18 months, sand-like products were observed on the entire exposed surface, and dark concrete surface discolouration occurred, with whitish products on the concrete surface, especially for SRPC concrete.

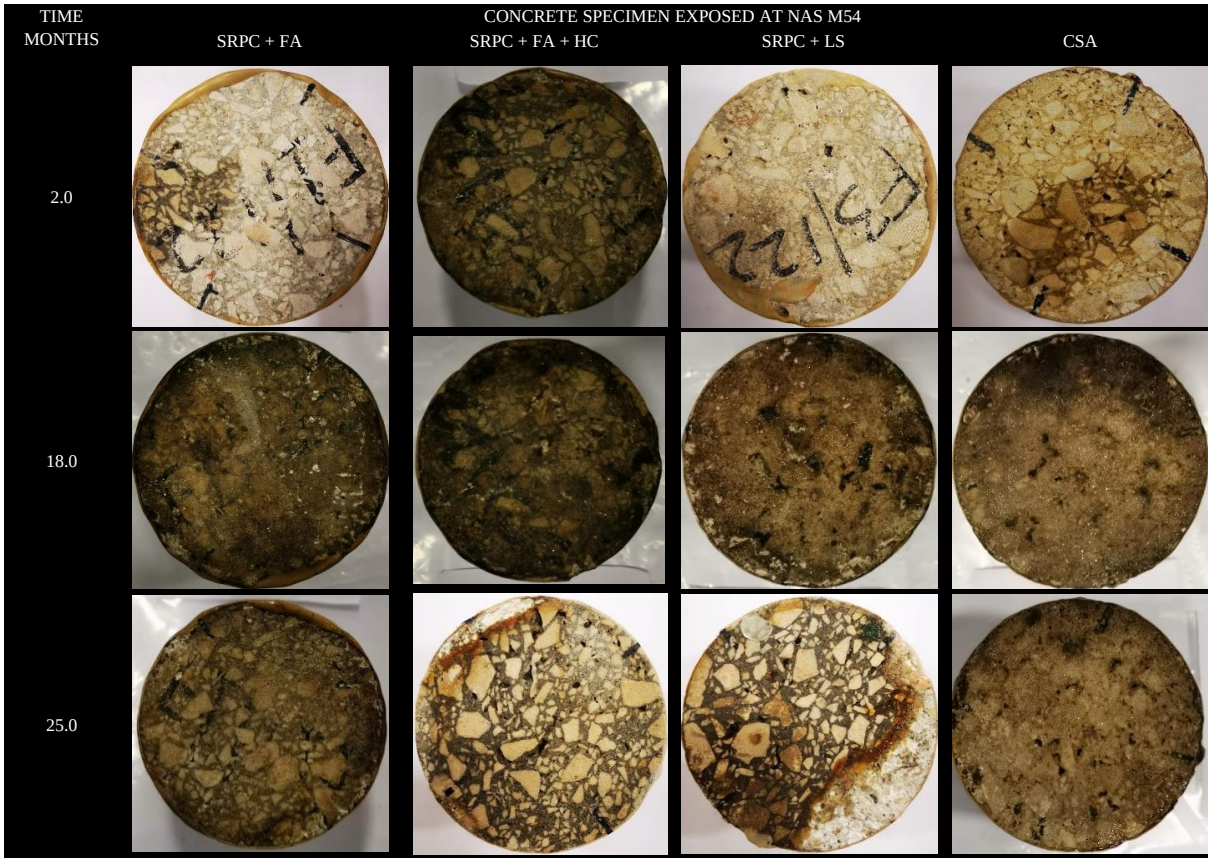


*Figure 5.5: Visual observation of LH concrete specimens exposed at NAS manhole 54 for two years*

At about 25 months of exposure, the development of whitish corrosion products demarcated with yellowish stains from the edges and the sand-like products on the entire exposed surface was observed as significant signs of deterioration at this site. The concrete specimens at this site took longer than at the other sites to exhibit deterioration due to low $H_2S$ gas concentrations below 10 ppm, as indicated in

Chapter 4. With this, it can be concluded that the aggressivity of this site is mild, with the absence of severe physical change on the exposed surface.

The visual observations indicated that the LPS site was the most aggressive, taking about four months to exhibit significant signs of corrosion, followed by NAS M19, showing corrosion signs at about six months, then NAS M54 as the least aggressive site, showing minor signs at about 18 months. In terms of binder performance, it was challenging to conclude based purely on visual observation since all concrete showed significant deterioration at both LPS and NAS M19 sites and minor deterioration at NAS M54.

### 5.2.3. LH concrete surface pH

Concrete surface pH measurements with time are presented in Figure 5.6 for LH concrete exposed at LPS, NAS M19 and NAS M54. The error bars indicate the standard variation of the pH readings. At the start of exposure, the initial concrete surface pH indicates 10 – 9, which is relatively low for 'fresh' concretes. Carbonation is likely attributed to lowering the pH since the specimens were exposed to air during concrete preparation for exposure. The initial surface pHs of SRPC + FA and SRPC+LS concretes were the highest at 9.9, followed by SRPC+FA+HC and CSA concrete with a pH of 9.4, see Appendix 0. Therefore, the differences in surface pHs between different concretes were relatively small. Thus, in this scheme, it was possible to confirm from other work that the pH of the CSA interstitial solution is lower than that of PC (Kleib et al., 2018).

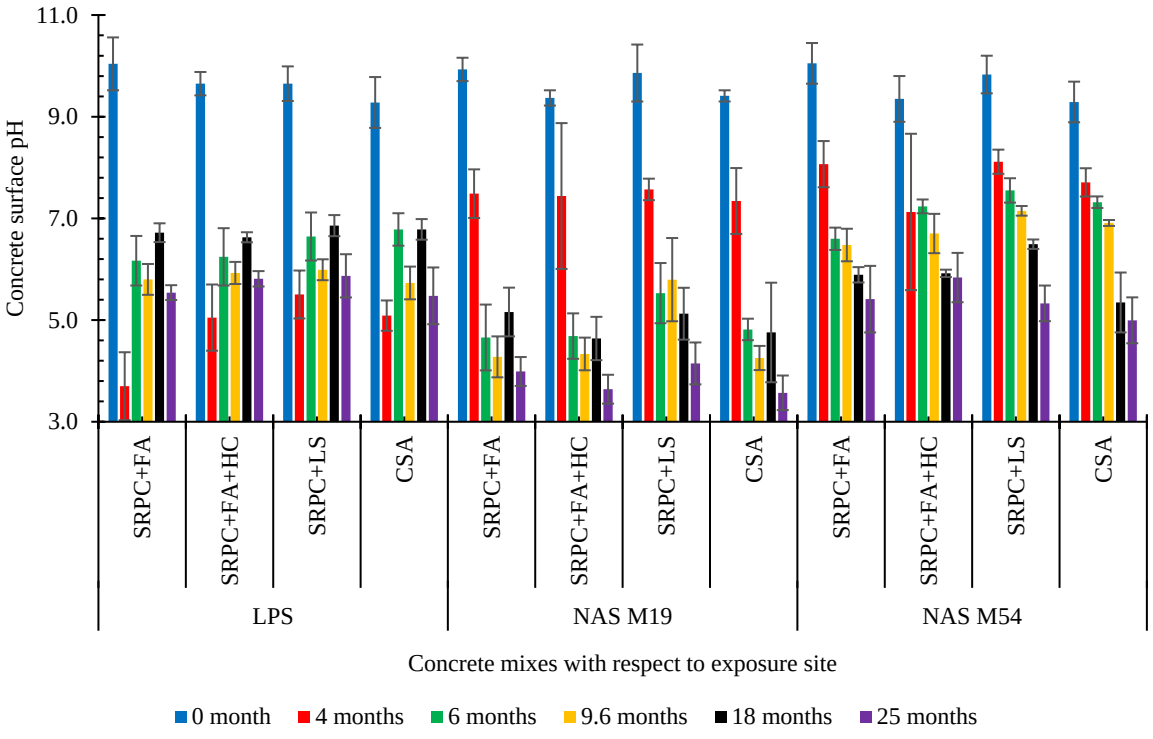


*Figure 5.6: Concrete surface pH of LH concrete at three sites, i.e., LPS, NAS M19 and NAS M54, for two years. The error bars indicate the standard deviation of the pH readings (see the readings in Appendix 0)*

According to various studies (Islander et al., 1991; Okabe et al., 2007; Hudon, Mirza & Frigon, 2011), a pH of 9 is suitable for the growth and colonisation of neutrophilic SOB on the concrete surface, thus producing acid which reduces the pH to 4. A pH of 4 is conducive to acidophilic SOB colonisation (Islander et al., 1991). Thus, this study indicates that the concrete surfaces were suitable for neutrophilic SOB colonisation from the beginning of the exposure.

#### 5.2.3.1. LH concrete surface pH results at LPS

At the LPS site, due to a continuous renewal of the exposed surface by hydraulic erosion, the concrete surface pH was generally maintained at around 6.0 during the exposure periods, which correlates to the wastewater pH. However, after four months of exposure, the specimens showed a low pH of 4 because, at the time of specimen retrieval, the corrosion product on the surface had not been washed away, thus, indicating the presence of acidophilic SOB activity, which also resembled the pH of corrosion products. At 25 months of exposure, the concrete surface pHs were as follow; 5.5 ± 0.1 for SRPC+FA concrete, 5.8 ± 0.2 for SRPC+FA+HC concrete, 5.9 ± 0.4 for SRPC+LS concrete, and 5.5 ± 0.6 for CSA concrete. The pH values indicate minor differences among concretes at this site.

#### 5.2.3.2. LH concrete surface pH results at NAS M19

After four months of exposure to NAS M19, the pH dropped to approximately 6, with SRPC+LS showing the highest pH values. This pH range concurs with the literature since the concrete surface started depicting some signs of corrosion. The neutrophilic SOB colonisation lasted up to about six months of exposure, after which minor corrosion, such as discolouration and whitish deposits, was noticed on the concrete edges.

At 9.6 months of exposure, the pH of all concretes, except SRPC+LS concrete, had decreased to approximately 4, which shows the presence of acidophilic SOB on the concrete surface, leading to the formation of aggressive acid with low pH. The acid then reacts with concrete, neutralises concrete alkalinity, and forms corrosion products. This concurs with visual observations at 9.6 months (Section 5.2.2.1), where massive corrosion deposits and discolouration on the concrete edges and surfaces were observed.

At 18 months, a slight pH increase was observed, which, however, decreased further at 25 months of exposure. At 25 months of exposure, the concrete surface pH values were as follows; 4.0 ± 0.7 for SRPC+FA concrete, 3.6 ± 0.3 for SRPC+FA+HC concrete, 4.1 ± 0.4 for SRPC+LS concrete, and 3.6 ± 0.3 for CSA concrete.

#### 5.2.3.3. LH concrete surface pH results at NAS M54

At NAS M54, a gradual surface pH decrease was observed throughout the monitoring period, with SRPC+LS concrete showing the highest pH values, except at 25 months. At about 25 months of exposure, the surface pHs of all concretes were above 5, indicating that the concrete was still under neutrophilic SOB colonisation. The concrete surface pH at 25 months of exposure was as follows; 5.4 ± 0.3 for SRPC+FA concrete, 5.8 ± 0.5 for SRPC+FA+HC concrete, 5.3 ± 0.4 for SRPC+LS concrete, and 5.0 ± 0.5 for CSA concrete.

#### 5.2.3.4. Discussion: LH concrete surface pH

The pH values on the exposed surface of any given specimen differed slightly, depending on where the pH point probe was placed. The coarse aggregate matrix was slightly protruding above the cement matrix. Since the aggregate was calcite, the high neutralisation capacity resisted pH reduction due to acid attack. The pH at the concrete specimen edges was lower, associated with the corrosion deposits, i.e., mainly gypsum. Overall, concrete surface pH decreased with exposure time for all concretes, see Figure E.1.

Interestingly, all concretes indicated pH values with minor discrepancies at each site. This implies that the different concretes responded similarly to the exposure environment and that the relative neutralisation effects are very similar up to two years of exposure. Generally, concrete at NAS M19 showed the lowest pH readings, indicating the evolution of SOB from neutrophilic to acidophilic. Concrete at the NAS M54 showed a gradual pH decrease, indicating gradual proliferation and colonisation of neutrophilic SOB. At LPS, concrete showed approximately constant pH values resembling the wastewater pH, indicating a continuous renewal of the exposed surface due to sewer hydraulics actions, except for surface pHs at four months, where the deterioration deposits were observed.

### 5.2.4. LH concrete mass changes

Figure 5.7 (extended scales in Figure 5.8) shows the mass change profiles of the concretes exposed at three sewer sites for two years[4]. The profiles were obtained after regular monitoring of the mass change of the concrete specimens, expressed as a percentage change of the original measurement before exposure. It was examined that the mass change of concrete specimens ranked and clustered according to the exposure site, with the LPS showing the highest mass loss, followed by NAS M19, then NAS M54 showing insignificant mass changes. This ranking indicates that a given concrete could have different performance levels depending on sewer aggressivity. Thus, other than the chemical composition of concrete, site aggressivity plays a significant role in defining the performance of concrete.

At the LPS, mass gain was observed in the first four months despite showing signs of corrosion, followed by mass loss throughout the monitoring period for all concretes. The mass loss ranking of the concretes, from the highest mass loss to the lowest, were as follows; SRPC+FA> SRPC+LS> SRPC+FA+HC> CSA after two years of exposure, with -13.08 ± 1.10%, -12.54 ± 0.53%, -12.04 ± 2.02%, and -10.00 ± 1.26% of the original mass of the concrete specimens, respectively.

At the NAS M19, the profiles show mass gain at the beginning of exposure to about six months for all concrete mixes, followed by mass loss for SRPC-based concrete and a continuous mass gain for the

[4] The photos in Figure 5.1 and Figure 5.5 show some corrosion between the specimens and the epoxy coating at the edges. It was not possible to account for this effect in the mass measurement, but clearly it would have had some effect. However, it would not have changed the overall ranking or conclusion.

CSA concrete despite showing a continuous built-up of corrosion products on its surface, see Section 5.2.2.2. However, after 18 months of exposure, the CSA concrete started experiencing mass loss. After two years of exposure, the mass change of concrete at this site ranked as follows, from the highest mass loss to the lowest; SRPC+FA> SRPC+LS> SRPC+FA+HC> CSA. with -3.22 ± 0.90%, -3.10 ± 0.57%, -2.27 ± 1.50%, and 1.22 ± 1.23% of the original mass of the concrete specimen, respectively.

At the NAS M54, all concretes experienced mass gain without any mass loss on the concrete surface. At this site, the mass gain of concrete ranking from the highest mass gain to the lowest were as follow; CSA> SRPC+FA> SRPC+FA+HC> SRPC+LS after two years of exposure, with 1.89 ± 0.02%, 1.63 ± 0.90%, 1.43 ± 0.01%, and 1.40 ± 0.09%, respectively.

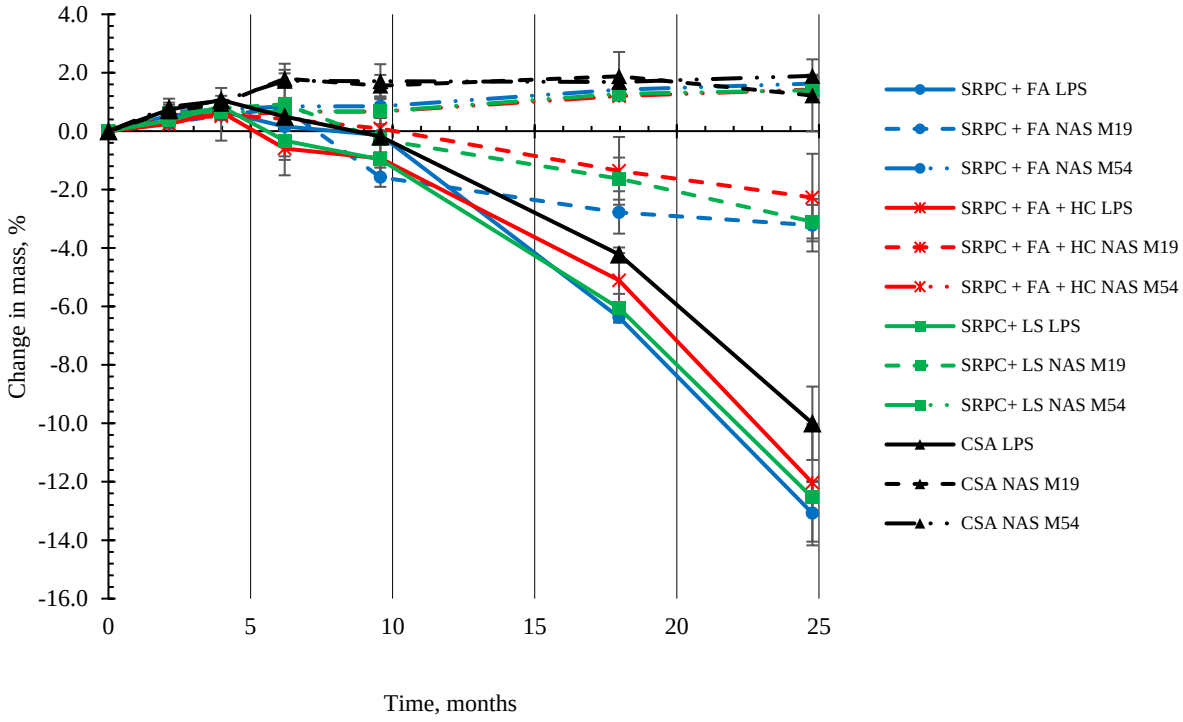


*Figure 5.7: Mass change of the LH concrete specimens exposed at three sites, i.e., LPS, NAS M19 and NAS M54, for two years. Positive (+ve) values indicate mass gain, and negative (-ve) values indicate mass loss. The error bars represent the standard deviations of the mass change. The solid lines represent the concrete specimens exposed at the LPS, the dash lines for the NAS M19 and the chain lines for the NAS M54. The colour code is as follows: blue: SRPC+FA concrete, green: SRPC+LS concrete, red: SRPC+FA+HC, and black: CSA concrete.*

The mass gain was associated with moisture absorption for SRPC-based concrete, while both moisture absorption and initial corrosion products accumulated within the concrete voids and at the concrete-epoxy coating interface for CSA concrete.

According to (Zhang & Glasser, 2002; Winnefeld, 2011; Li, Wang & Xu, 2022), CSA cement requires higher w/b (> 0.4) than SRPC cement to achieve full hydration. The CSA concrete had a low w/b of 0.4 and the mix was very dry, which resulted in a significant amount of compaction voids, and so the moisture absorbed could have promoted the formation of further hydration products, which contributed to a higher mass gain (Cao et al., 2022). The acid penetration through the surface and at the concrete-

epoxy coating interface would also influence the formation of initial corrosion products that appeared as blisters on the epoxy coating surface.

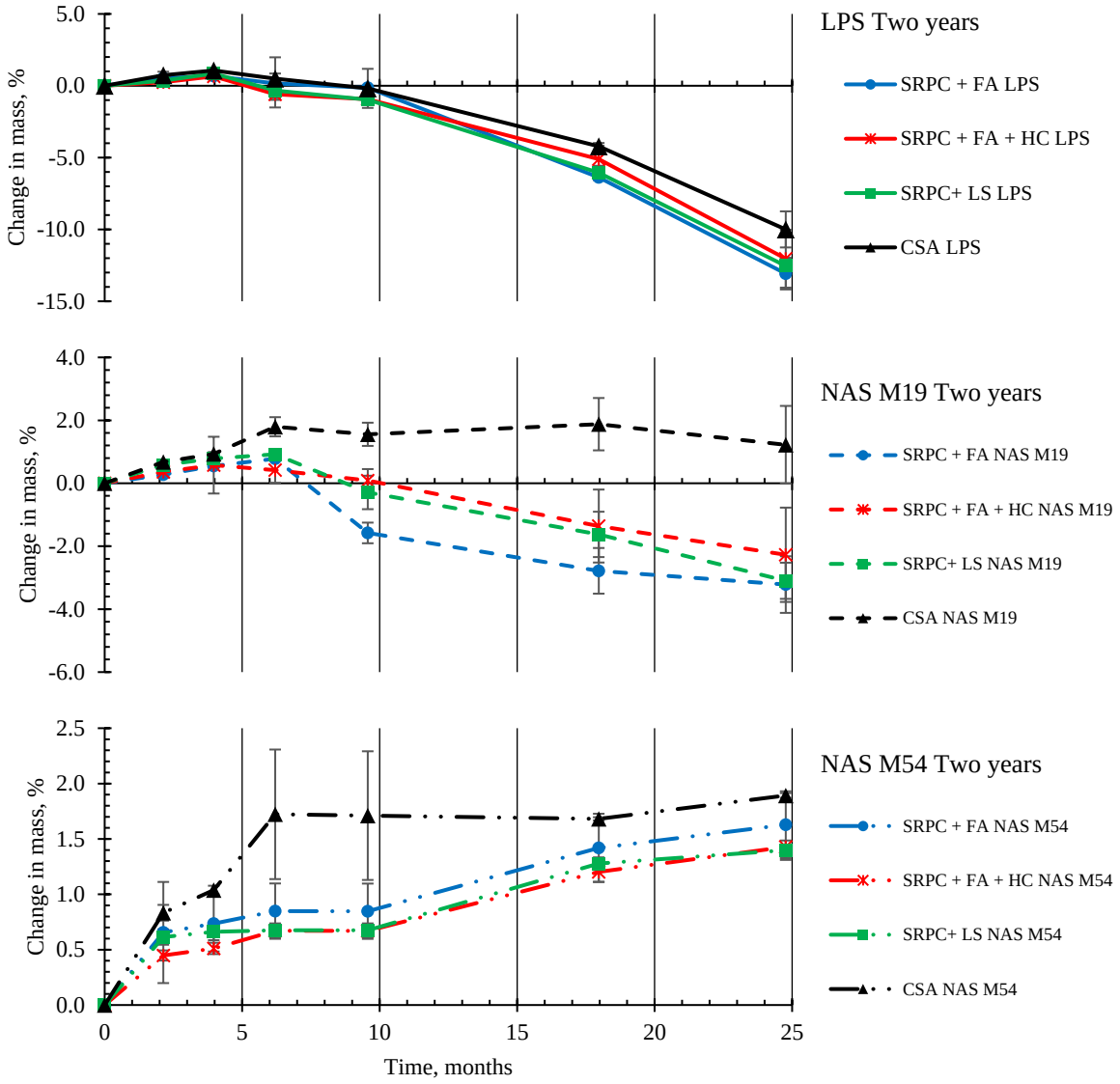


*Figure 5.8: Extension of Figure 5.7 indicating better precision for +ve values (below the X-axis)and -ve values (above the X-axis) of mass change of the concrete specimens exposed at three sites, i.e., LPS, NAS M19 and NAS M54, for two years.*

At the LPS, a substantial mass loss of concrete specimens was due to sewer hydraulic actions that eroded the corroded layer while renewing the exposure surface for new microbial colonisation at both concrete and epoxy coating-concrete interface. At the same time, significant aggregate fallout at this site was observed, contributing to a significant mass loss. At the NAS M19 site, the mass loss was associated with removing the corroded layer during regular monitoring (i.e., gentle removal) or if the layer dislodged in situ due to gravity. At the NAS M54 site, being a considerably less aggressive site, no mass loss was experienced.

At both LPS and NAS M19, SRPC + FA + HC concrete experienced less mass loss than SRPC + FA concrete. This behaviour might be associated with the effect of HC, the iron-based additive, which would have provided additional resistance against abrasion, see Section 3.2.2.3. The SRPC+LS concrete

also performed better than the SRPC+FA concrete due to the limestone (LS) filler, which provides more alkali material ($CaCO_3$) to neutralise the acid (Siad et al., 2010), also the reason behind a high surface pH observed in Section 5.2.3.2. On the other hand, CSA concrete experienced a counteracting effect between mass loss and mass gain. The CSA specimens experienced mass loss and mass gain from initial corrosion and water absorption, respectively. Also, it is interesting that CSA did not perform well under hydraulic erosion conditions, i.e., the LPS. This might be associated with the gibbsite being washed away or eroded by the hydraulic action, see appendix H.3.

### 5.2.5. LH concrete thickness changes

Thickness changes are presented in Figure 5.9 for concrete exposed at LPS, NAS M19, and NAS M54 for two years. Due to the uneven and non-uniform corrosion fronts over the exposed surface, thickness changes varied around the specimen perimeter; the error bars indicate variability.

At the LPS and the NAS M19 sites, the thickness change profiles had a similar trend to the mass change profiles, showing minor thickness gain in the first four and six months of exposure, respectively, then thickness loss throughout the monitoring period, while the NAS M54 site indicated no thickness change over the entire duration of exposure. Unlike mass change profiles, thickness profiles exhibited greater scatter without distinguishing the performance of the different sites.

LPS and NAS M19 sites indicated varying degrees of thickness loss, with LPS concretes experiencing slightly higher loss than at NAS M19. At the LPS, the ranking of thickness loss from the highest to the lowest was as follows; SRPC+FA> SRPC+LS> SRPC+FA+HC> CSA after two years of exposure, with -6.42 ± 0.76 mm, -5.37 ± 0.27 mm, -4.37 ± 0.54 mm, and -2.86 ± 0.25 mm, respectively. A similar ranking was observed at the NAS M19 site, with thickness loss of -5.56 ± 1.05 mm, -4.48 ± 0.27 mm, -3.69 ± 1.23 mm, and -1.97 ± 0.59 mm, respectively. At the NAS M54 site, the concrete specimens essentially experienced negligible loss in thickness, which is also related to the mass gain observed in the previous section. Table 5.4 summarises the thickness loss and equivalent corrosion rate of the LH concrete subjected to the NAS M19 and the LPS site for 2 years.

*Table 5.4: Summary of thickness loss and equivalent average corrosion rate of the LH concrete subjected to the NAS M19 and the LPS site for 2 years.*

| Concrete | SRPC+FA | SRPC+FA+HC | SRPC+LS | CSA |
|---|---|---|---|---|
| NAS M 19, mm | 5.56 ± 1.05 | 3.69 ± 1.23 | 4.48 ± 0.27 | 1.97 ± 0.59 |
| Corrosion rate, mm/yr | 2.78 ± 0.78 | 1.85 ± 0.87 | 2.24 ± 0.19 | 0.99 ± 0.42 |
| LPS, mm | 6.42 ± 0.76 | 4.37 ± 0.54 | 5.37 ± 0.27 | 2.86 ± 0.25 |
| Corrosion rate, mm/yr | 3.21 ± 0.54 | 2.19 ± 0.38 | 2.69 ± 0.19 | 1.43 ± 0.18 |

According to the mass change profiles, concrete specimens at the NAS M19 site were expected to indicate substantially lower thickness loss than at the LPS. The opposite was observed because the corrosion products at the concrete-epoxy coating interface and at the concrete exposed surface added to the mass change at NAS M19, unlike at the LPS, where the wastewater thoroughly washed these products and caused a significant aggregate fallout contributing to substantial mass loss. Also, the thickness loss of the NAS M19 specimens was noticeably uneven; at some points where massive corrosion deposits were observed, a more significant thickness loss was observed.

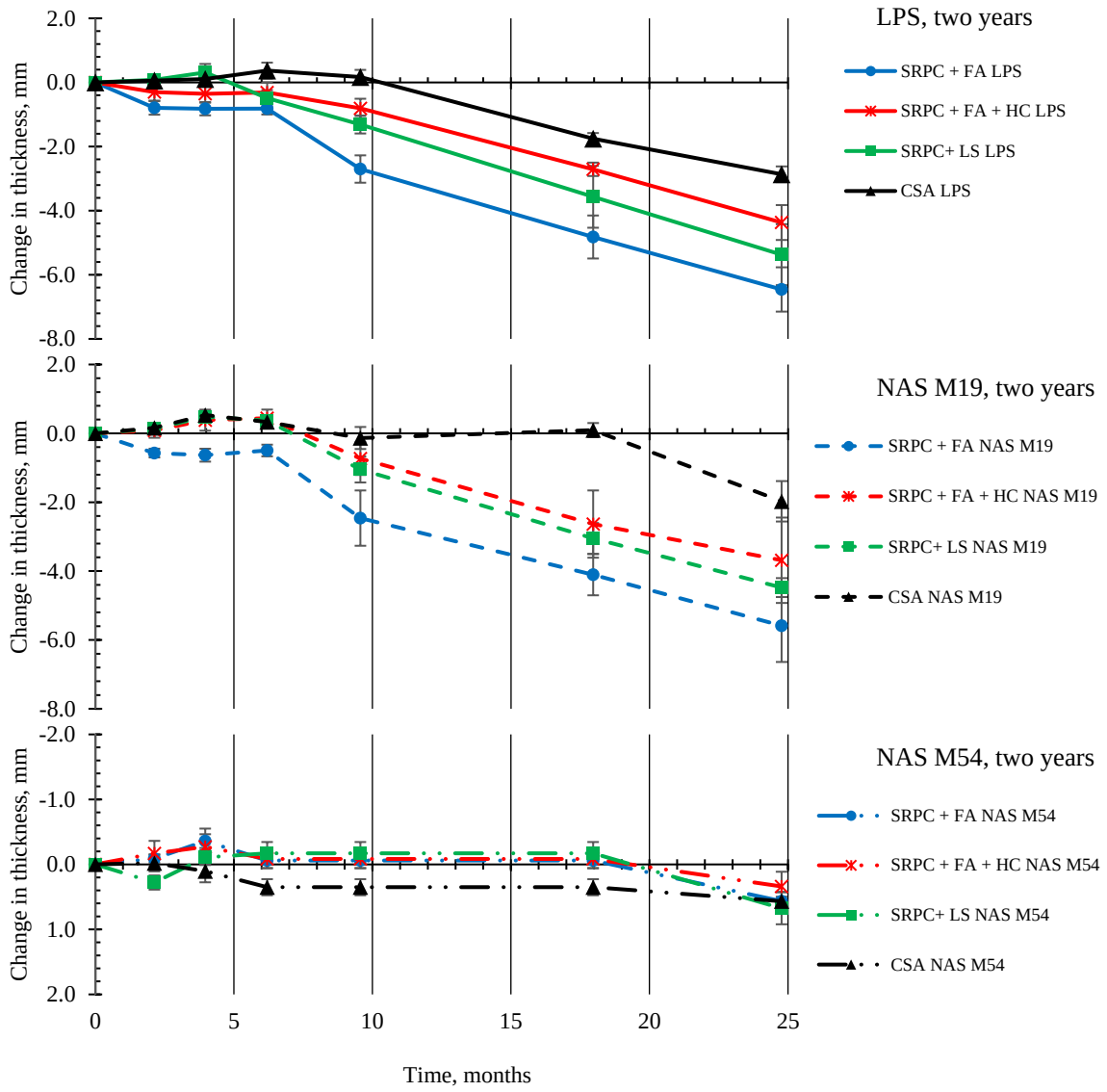


*Figure 5.9: Thickness of the LH concrete specimens exposed at three sites, i.e., LPS, NAS M19 and NAS M54, for two years. Positive (+ve) values indicate thickness gain, and negative (-ve) values indicate thickness loss. The error bars represent the standard deviations of the thickness change. The colour code is as follows: blue: SRPC+FA concrete, green: SRPC+LS concrete, red: SRPC+FA+HC, and black: CSA concrete.*

For SRPC-based mixes, SRPC+FA+HC concrete has superior performance than SRPC+FA and SRPC+LS at both LPS and the NAS M19, indicating that HC improved the abrasion resistance of concrete. On the other hand, CSA concrete exposed at LPS only started to experience thickness loss at about ten months of exposure and about 18 months at NAS M19. When comparing the change in mass and thickness of CSA concrete, where a substantial mass gain was observed, no change in thickness was observed. This could be related to the relatively high percentage of compaction voids in this concrete. The continuous ettringite formation due to further hydration and acid penetration in the CSA concrete compaction voids and at the concrete-epoxy coating interface led to a substantial mass gain with no thickness change. More corrosion material was formed where thickness loss was experienced, leading to a higher expansion and loss of corrosion products. It was also noted that higher mass loss did not necessarily imply higher thickness loss. As aggregate incorporation in concrete plays a significant

role, thickness loss might be measured, but with less mass loss due to protruding aggregates and vice versa. Similar thickness and mass change profiles were observed in Attiogbe and Rizkalla (1988)

### 5.2.6. LH concrete BAC microstructural analysis

Three microstructural analyses and results, i.e., SEM-BSE images, QEMSCAN analysis, and XRD analysis, are discussed herein for the concrete at NAS M19 after two years. This was done to minimise data presentation and because these specimens contained a significantly visible layer of corrosion products, unlike those at the LPS and NAS M54.

The SEM BSE image analysis aims to study concrete morphology evolution after corrosion; identify and distinguish the altered zone (transition and deteriorated), corrosion front, and intact zone; and evaluate altered depth that could not be measured under bulk thickness change.

The QEMSCAN analysis observed the mineralogical distribution and evolution of concrete phases from the altered zone to the intact zone using SEM samples. The analysis essentially assists in understanding the role of each mineral phase when concrete is subjected to BAC. The phases of interest were calcite and quartz from the aggregates. In the cement matrix, they were calcium silicate (Ca-silicate), amorphous silica (donated as fine quartz particles), calcium aluminate (Ca-aluminate), portlandite, gypsum, ettringite, gibbsite and on some occasions, magnesium silicate (Mg-silicate), Fe-phases, and aluminium silicate (Al-silicate) depending on the type of binder system.

The XRD analysis was conducted on the deteriorated zone, i.e., 0 mm ( the exposed surface), 100 µm, and 200 µm from the exposed surface. In the intact zone, only one layer at about 5 mm from the exposure surface was analysed. The analysis aimed to confirm the cementitious phases observed under QEMSCAN analysis. Since only 16% (by mass) of the concrete microstructure was the cement matrix and about 80% from the aggregate matrix, the main phases observed were calcite and quartz from the aggregates rather than from the cement matrix. The following discussions indicate the findings in each binder system.

#### 5.2.6.1. SRPC+FA concrete

##### *5.2.6.1.1. SEM-BSE images*

Figure 5.10 shows the SEM-BSE image for SRPC+FA concrete after two years of exposure at NAS M19. In Figure 5.10 (A), the altered zone is about 1.0 mm in width and consists of loose fine aggregate particles and a fragmented cement matrix with high porosity. Its colour is slightly different from the intact concrete. However, the altered depth differs between the cement matrix and coarse aggregate particles. The depth of the altered zone at the coarse aggregate particle is approximately 0.2 mm, less than in the cement matrix. This indicates that the deterioration rate of the cement matrix is higher than that of aggregates.

With the aggregate particle, i.e., calcite, the acid reacts uniformly with the exposed aggregate surface without leaving any residue, as indicated by Girardi and Maggio (2011). However, the attack progresses differently with the aggregate surface near the altered cement matrix, in this case, on the top side of the particle. The aggregate particle dissolves, as on the front face, and loses cohesion based on the altered matrix while dislodging from the cement matrix. On the other hand, quartz fine aggregate particles do

not react with the acid and detach from the cement matrix in the altered zone. Also, in the altered zone, the transition and deteriorated zones were not easy to distinguish.

Figure 5.10 (B) shows cracks in the altered zone through calcite aggregate particles and the cement matrix. The cracks indicate further acid penetration into the concrete, leading to loss of cement matrix cohesion and aggregate detachment. Figure 5.10 (C) shows two fly ash particles in the altered zone: bright and dark particles. The dark particle contains microcracking as a sign of disintegration, and the bright one seems intact. Since the fly ash particles used in this study consist of silica (54%) and alumina (33%), the dark particle may be alumina-rich, and the bright, silica-rich due to low solubility of silicon (Kashiwakura et al., 2013), which explains the dark particle's microcracking.

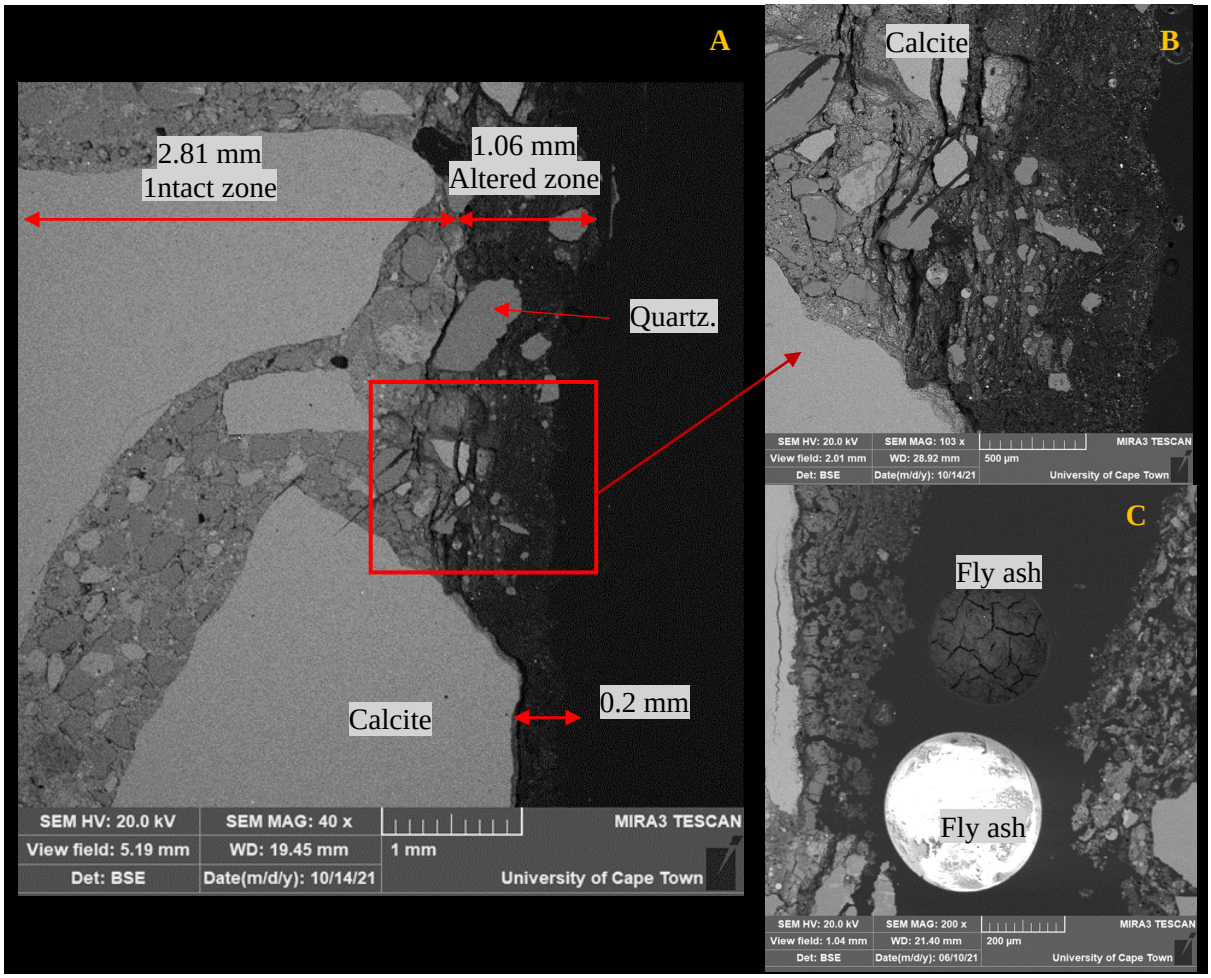


*Figure 5.10: SEM-BSE image for SRPC+FA concrete after two years of exposure at NAS M19*

*5.2.6.1.2. QEMSCAN analysis*

The intact and altered zones under QEMSCAN analysis were easily distinguished based on the mineralogical distribution, see Figure 5.11. It was evident that the intact zone was dense, mainly containing calcium silicate in the cement matrix. In contrast to the SEM analysis, in this analysis, the transition zone was observed between the intact zone and the deteriorated zone, mainly consisting of a continuous and consistent layer of Mg-silicate and some gypsum deposits. This indicated a possibility of magnesium ion migration which reacts with silicate from calcium silicate phases after decalcification.

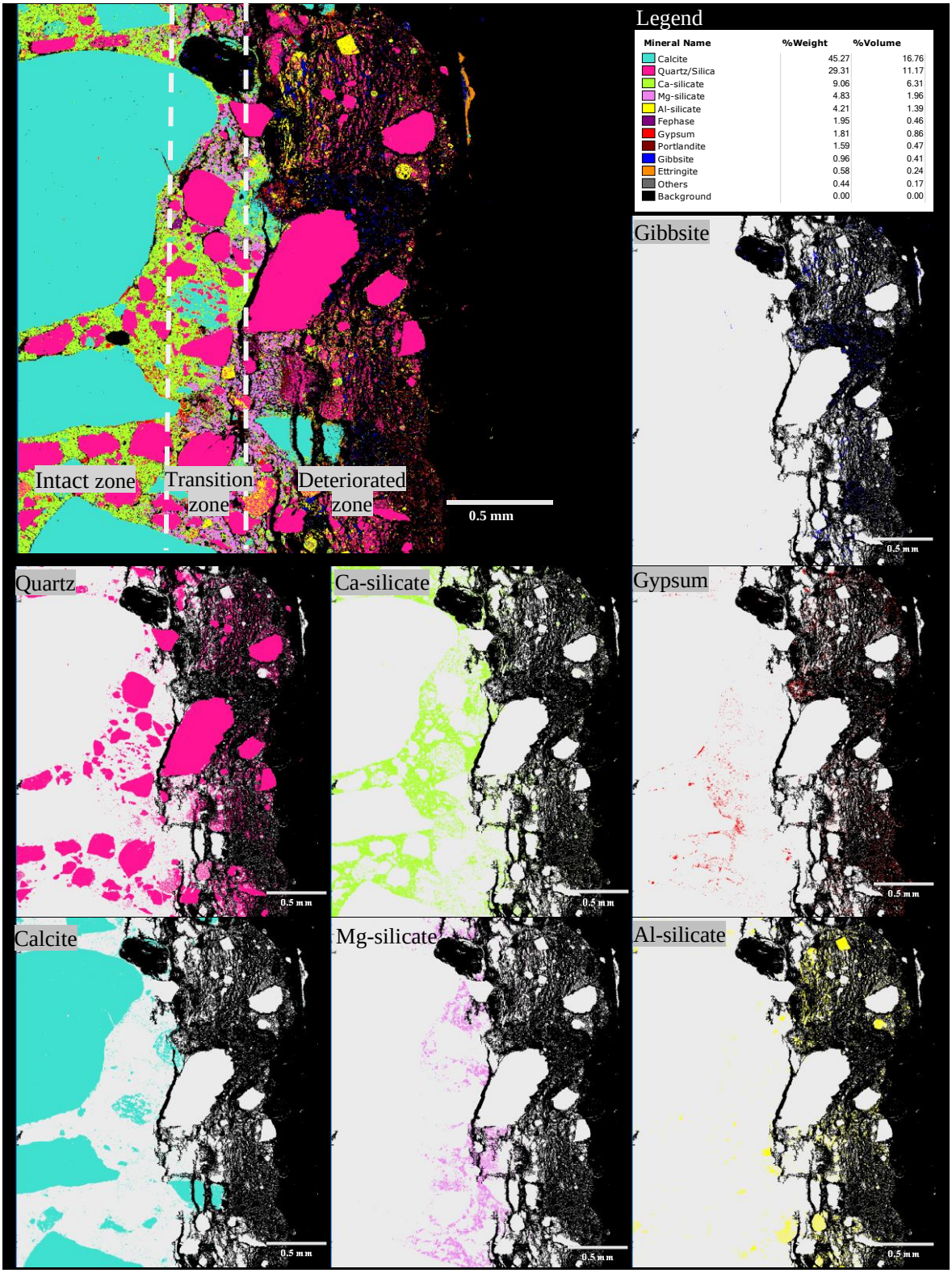


*Figure 5.11: QEMSCAN analysis of SRPC+FA concrete from the LH concrete specimens subjected to the NAS M19. The first image in the first row indicates a general distribution of concrete mineralogical phases on the concrete cross-section based on the SEM-BSE image, with the legend indicating the colour code, percentage weight and percentage volume of each mineral over the cross-section. Other images depict the distribution of selected minerals on the cross-section.*

On the other hand, the deteriorated zone was very porous, consisting of disintegrated cementitious phase particles of Al-silicate, gibbsite, gypsum, and amorphous silica (observed as fine quartz particles).

Regarding composition, 45.3% calcite and 29.3% quartz were the main observed phases from 80% of the concrete composite being the aggregate component. In the cement matrix, the percentage weights of mineralogical phases from the highest to the lowest were 9.1%% ca-silicate, 4.8% Mg-silicate, 4.2% Al-silicate, 2.0% Fe-phases, 1.8% gypsum, 1.6% portlandite, 1.0% gibbsite, and 0.6% ettringite. However, these compositions were somewhat subjective since they depended on the selected area for analysis.

Calcite particles disintegrate immediately after the concrete composite loses its integrity, i.e., at the interface of the transition zone and deteriorated zone. It is possible that at the interface, the pH of the concrete is lower than 8.0 as calcite dissolves at a pH lower than that (Dyer, 2017). Quartz aggregates detach from the transition zone, while at the extremity of the deteriorated zone, finer disintegrated quartz particles were observed. These finer quartz particles were associated with a silica-rich zone after Al- and Mg- silicate disintegration since it was challenging to map them separately. Furthermore, Fe-phases may be from fly ash.

Therefore, in this binder system, it can be concluded that the main cementitious phase before the attack is calcium silicate, containing some aluminium, iron, and magnesium oxides. Once sulphuric acid from the sewer contacts the concrete surface, it penetrates the concrete leading to the decalcification of calcium silicate. As a result, magnesium ions migrate into the transition layer to react with silicate to form Mg-silicate, aluminium ions in the deteriorated zone to form Al-silicate and gibbsite, and calcium ions react with sulphate ions to form gypsum.

*5.2.6.1.3. XRD analysis*

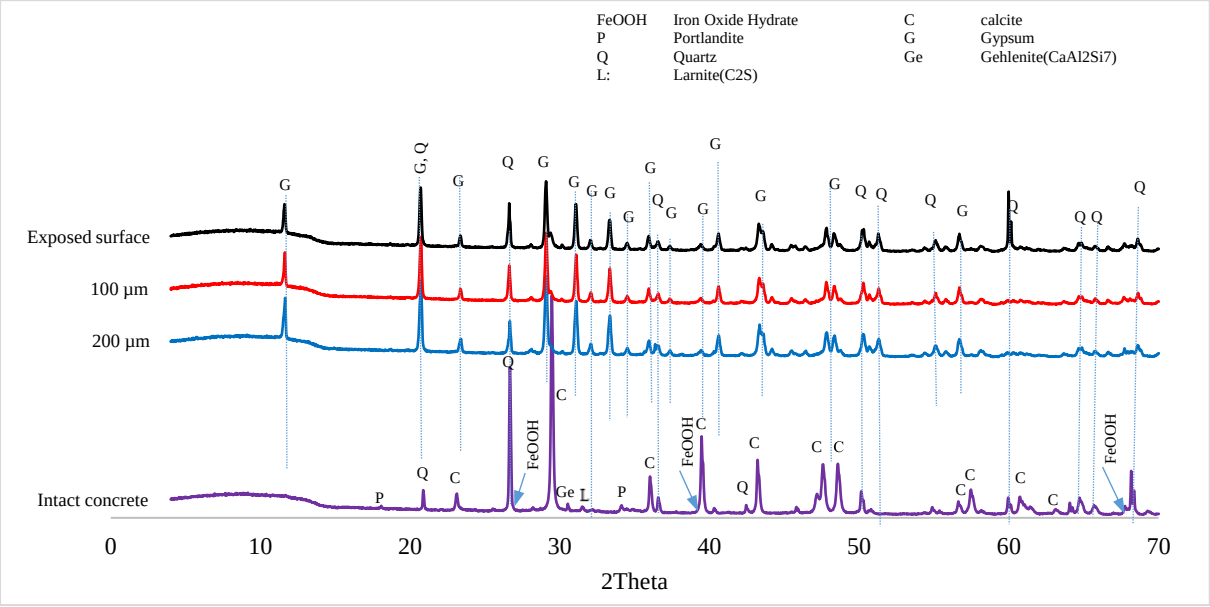


*Figure 5.12: XRD analysis on the SRPC + FA concrete after 2 years of exposure*

Figure 5.12 confirm the presence of portlandite, calcite, and quartz phases in the intact concrete, as well as a significant amount of gypsum peaks at the exposed surface and 100 µm depth from the exposed

surface, were observed. Gypsum peaks, however, decrease at 200 µm. On the contrary, calcium silicate and magnesium silicate are not detected.

#### 5.2.6.2. SRPC+FA + HC concrete

**i.** *SEM-BSE images*

Similar observations as in the SRPC + FA + HC concrete are observed in the altered zone of the SRPC + FA + HC concrete, see Figure 5.13. The altered zone consists of a massive deposit of fragmented cement and aggregate particles, with a thickness of about 1.64 mm, wider than SRPC + FA concrete. It should be noted that the measured thicknesses are only spotted values likely to vary, depending on where the measurements were taken. Figure 5.13(B) shows fine aggregates, i.e., quartz, detach from the cement matrix in the altered zone but remain unaltered. The altered zone shows deterioration of cementitious products, leading to increased porosity and matrix cohesion loss.

The iron-based additive in this concrete manifests as bright particles (with an irregular shape) distributed throughout the concrete microstructure. Iron particles are bright due to their high atomic weight; see Figure 5.13(C). These particles appear to be not hydrating in the intact concrete or dissolving in the deterioration layer, thus indicating their non-participation in chemical reactions in concrete.

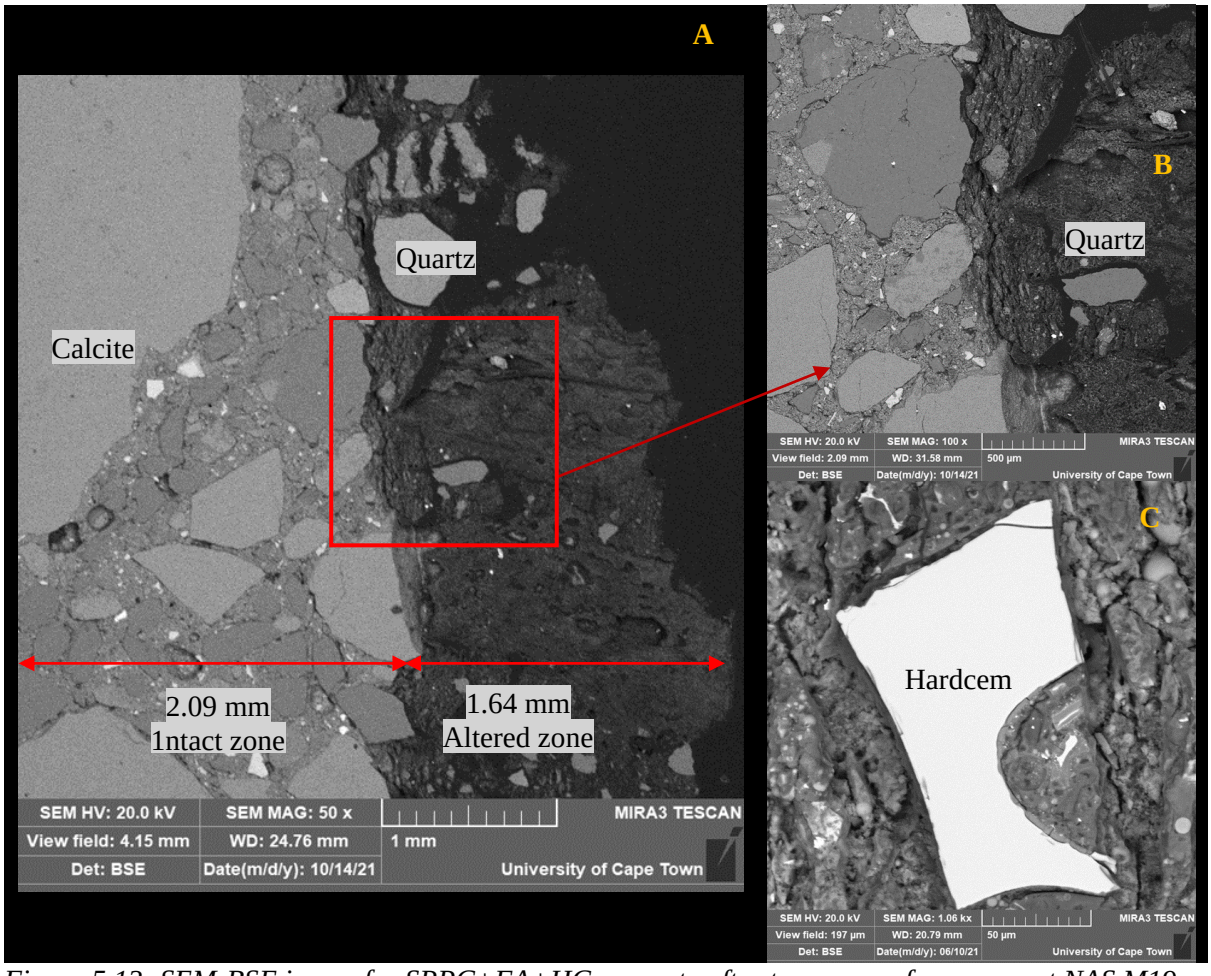


*Figure 5.13: SEM-BSE image for SRPC+FA+HC concrete after two years of exposure at NAS M19*

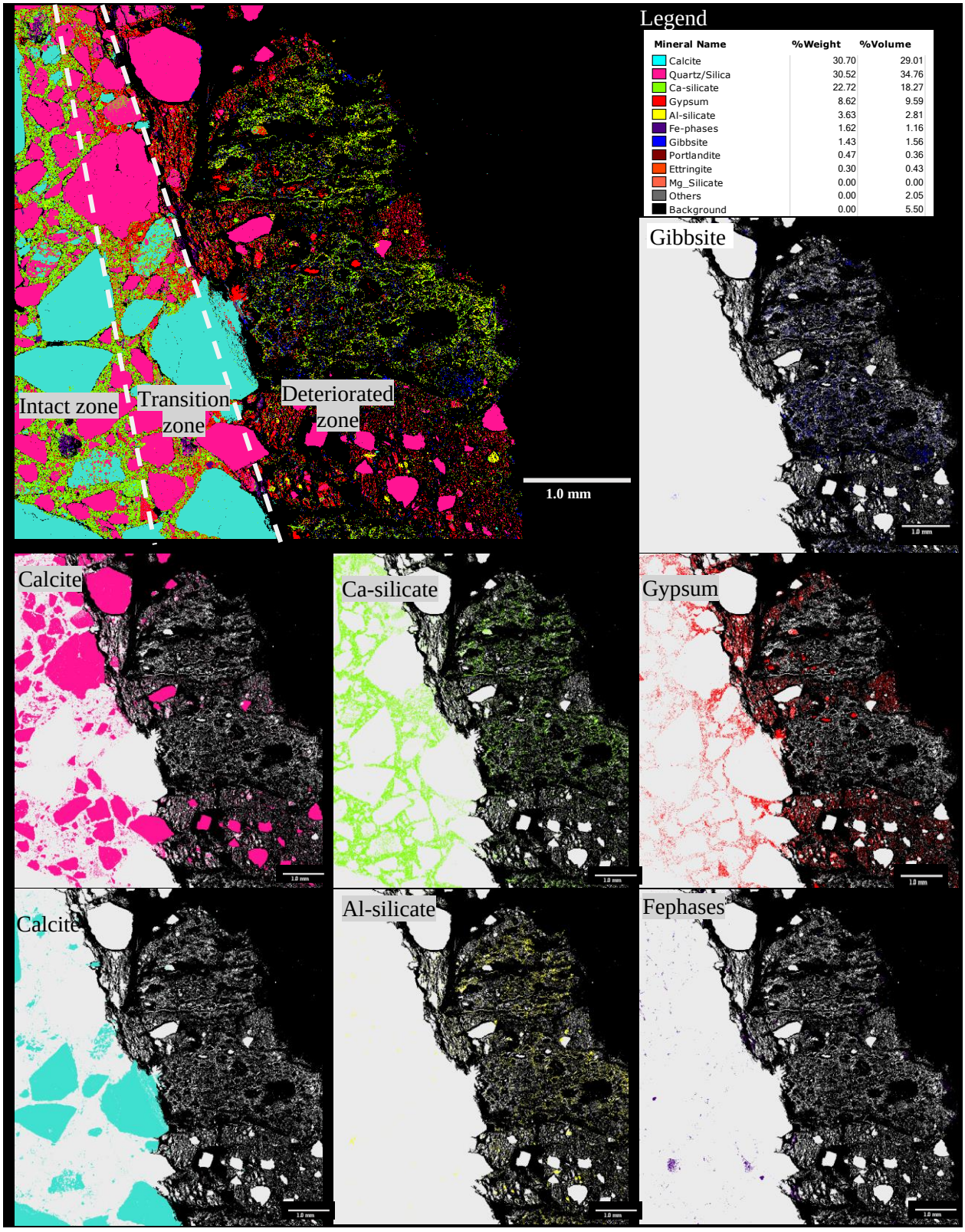


*Figure 5.14: QEMSCAN analysis of SRPC+FA+HC concrete from the LH concrete specimens subjected to the NAS M19. The first image in the first row indicates a general distribution of concrete mineralogical phases on the concrete cross-section based on the SEM-BSE image, with the legend indicating the colour code, percentage weight and percentage volume of each mineral over the cross-section. Other images depict the distribution of selected minerals on the cross-section*

*5.2.6.2.1. QEMSCAN analysis*

As for the SRPC +FA concrete, the intact, transition, and deteriorated zones under QEMSCAN analysis were easily distinguished using the mineralogical distribution, see Figure 5.13. The intact zone was dense, mainly containing calcium silicate in the cement matrix. The transition zone consists of a continuous and consistent layer of gypsum deposits, and the deteriorated zone consists of Al-silicate and gypsum and gibbsite. The iron-based additives are denoted as the Fe-phases, distributed through the microstructure but showed little influence chemically. Mg-silicate, on the other hand, was not observed in this concrete, possibly due to a selected area for the analysis since iron-based additives could not have affected its formation.

In terms of composition, 30.7% calcite and 30.5% quartz were the main observed phases from the aggregate, and in the cement matrix, the composite highest to the lowest were 22.7% ca-silicate, 9.6% gypsum, 3.6% Al-silicate, 1.6% Fe-phases, 1.4 gibbsite, 0.5% portlandite, and 0.3% ettringite.

*5.2.6.2.2. XRD analysis*

XRD analysis of SRPC + FA + HC concrete is shown in Figure 5.15 and is similar to that of SRPC + FA concrete. It demonstrates the presence of portlandite, calcite, and quartz phases in the intact concrete and a wide range of gypsum peaks at the exposed surface and at 100 µm depth from the exposed surface. However, gypsum peaks diminish at 200 µm, while calcium silicate and magnesium silicate are not identified.

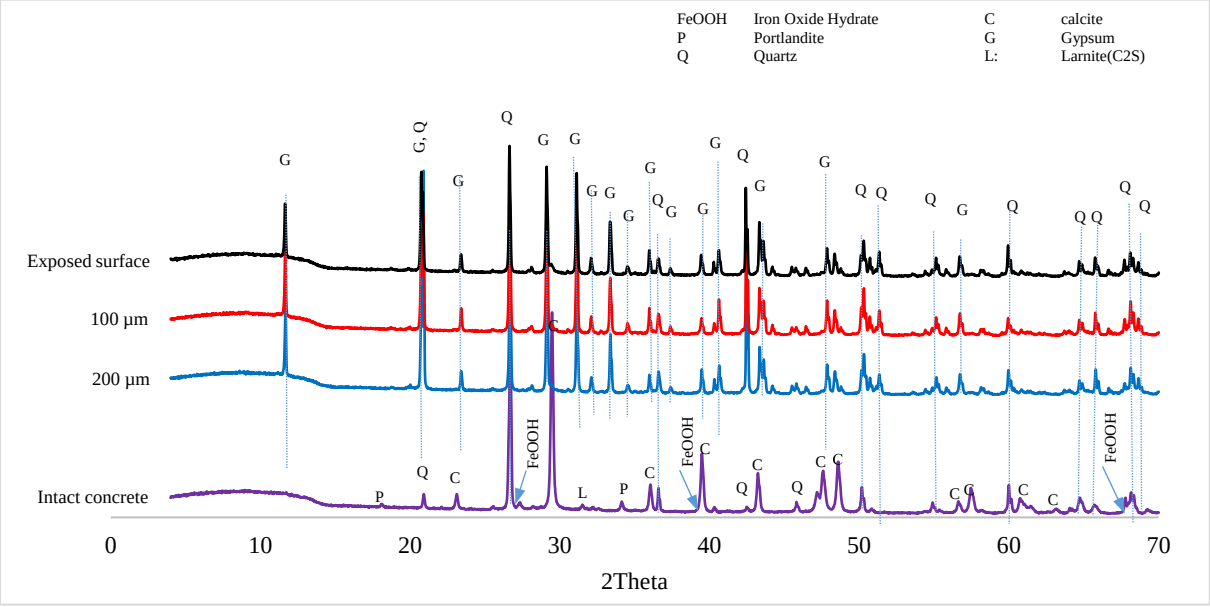


*Figure 5.15: XRD analysis of SRPC + FA + HC concrete after 2 years of exposure*

### 5.2.6.3. SRPC+ LS concrete

**i.** *SEM-BSE images*

Figure 5.16 shows SEM-BSE images for SRPC+LS concrete after two years of exposure at NAS M19. In Figure 5.16 (A), about 1.41 mm of the concrete depth had deteriorated, demarcated by a crack, which with time, might cause the deteriorated zone to detach. This kind of deterioration appears in this

concrete because it contains ingredients of similar chemical composition, i.e., CaO-based materials: 20% ground limestone ($CaCO_3$) mixed with 80% SRPC (approximately 63% CaO) and calcareous ($CaCO_3$) aggregates.

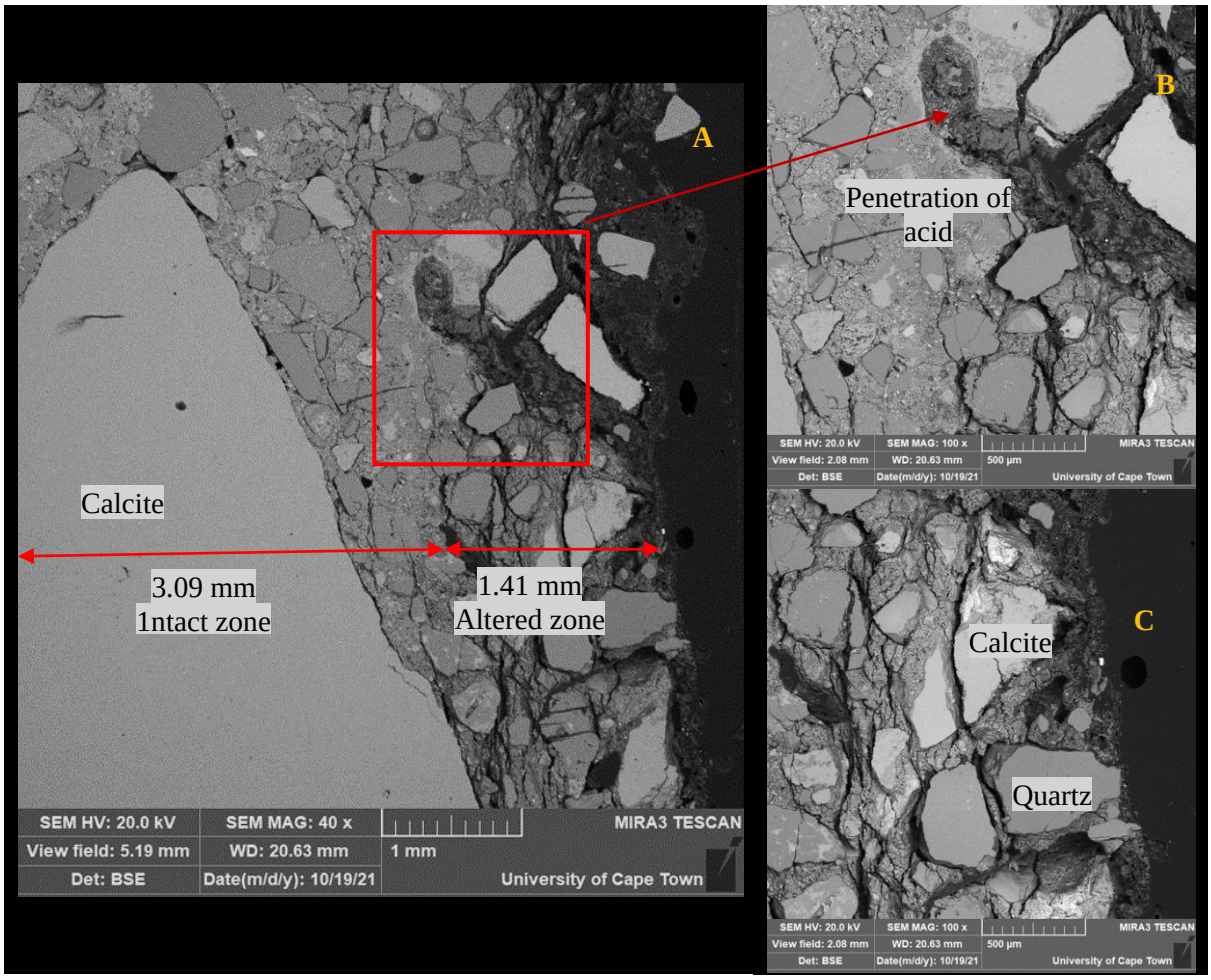


*Figure 5.16: SEM-BSE image for SRPC+LS concrete after two years of exposure at NAS M19*

It is shown in the literature that, due to the ground limestone filler effect, when it is added to concrete, it improves the concrete pore structure by reducing porosity and permeability. However, under acid attack, this effect is not beneficial since its CaO-based nature makes it susceptible to readily react with acid from the exposed surface despite a possibly denser concrete microstructure. Dissolving CaO-based components provide ready access for further acid penetration and crack formation, as shown in Figure 5.16(B). A partially attacked piece of concrete separated by the crack can easily detach if the crack is parallel to the exposed surface. In this scenario, the concrete might frequently renew its exposed surface.

However, compared with SRPC+FA concrete, this concrete performed slightly better in terms of mass and thickness change. This can be explained by more corrosion product build-up within the microstructure, which increases its mass, counteracting the mass loss. On the other hand, the lower thickness loss might be explained by less aggregate fall-out due to the similar deterioration rate between the cement matrix and aggregate matrix. Thus, a given quantity of acid takes more time to dissolve at a certain concrete depth with a high CaO content.

In Figure 5.16 (C), the light grey aggregate particles represent dissolved calcareous aggregate (calcite, see Figure 5.17 ). Dark grey aggregates represent siliceous sand particles (quartz, see Figure 5.17) that do not experience acid deterioration but with a crack extending from calcite. Dark spots in the concrete matrix represent compaction voids.

*5.2.6.3.1. QEMSCAN analysis*

Regarding QEMSCAN analysis, SRPC +LS concrete zonation was more easily distinguished by the mineralogical composition. The intact zone in Figure 5.17 consisted of calcium silicate phases. With acid penetration, decalcification resulted in the formation of Mg-silicates in the transition zone and gibbsite, gypsum, and Al-silicate in the deterioration zone. The location indicated in Figure 5.16(B) as acid penetration consists of gibbsite and gypsum.

Like SRPC+FA concrete, calcite aggregate disintegrated to gypsum at the transition-deteriorated zone interface. Quartz particles detached from the cement matrix, leading to cement-aggregate bond loss with increasing porosity and loss of matrix cohesion.

Regarding weight composition, calcite and quartz (43.2% and 31.6%, respectively) were the main observed phases from the aggregate matrix. In the cement matrix, the percentage weights of mineralogical phases from the highest to the lowest were 11.2%ca-silicate, 3.8% Al-silicate, 3.5% Mg-silicate, 2.7% gypsum, 2.0% portlandite, 0.9% Fe-phases, 0.7% gibbsite, and 0.5% ettringite

Contrary to the literature where ettringite formation is indicated in the transition zone at a pH higher than 10.7, in this analysis, ettringite was detected randomly all over the cross-section. Thus, the ettringite observed was not due to acid penetration. Similarly, minor iron phases were spotted in this concrete mix.

Generally, replacing SRPC with limestone had minor alterations to the cementitious phase's formation, apart from a larger quantity of gypsum and portlandite than in the SRPC+FA concrete. However, the formation of Mg-silicate in the transition zone raises further debate about its role in decelerating the deterioration rate of concrete. There is a possibility of magnesium ion migration to the transition zone, which reacts with silicate after calcium silicate decalcification. With that, Mg-silicate possibly offers some inhibiting action to the acid-producing bacteria due to its ability to maintain a higher surface pH (Merachtsaki et al., 2020).

*5.2.6.3.2. XRD analysis*

Figure 5.18 confirms the presence of portlandite, calcite and quartz in the intact concrete, while in the altered zone, gypsum and some ettringite peaks were observed.

.

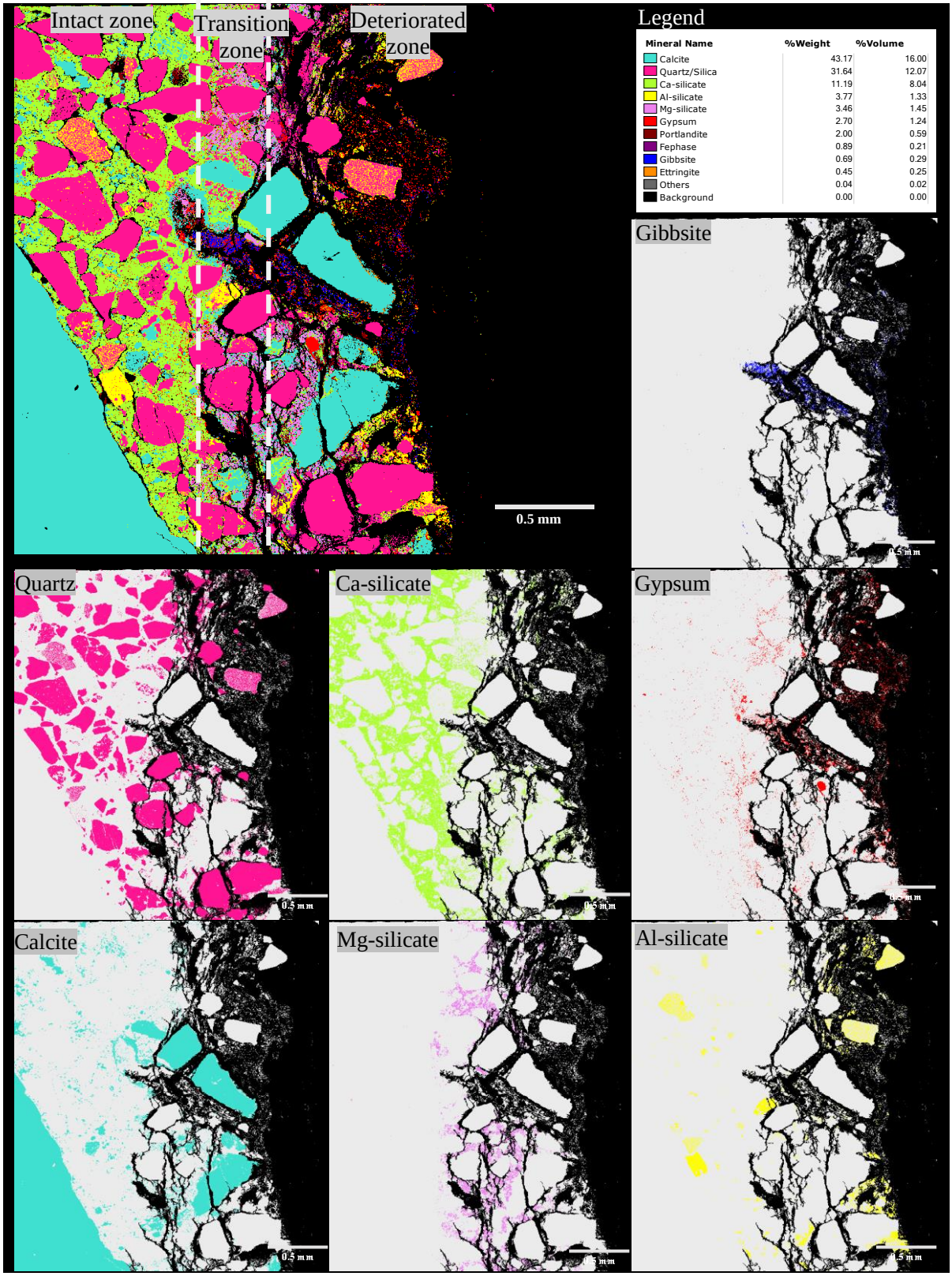


*Figure 5.17: QEMSCAN analysis of SRPC+LS concrete from the LH concrete specimens subjected to the NAS M19. The first image in the first row indicates a general distribution of concrete mineralogical phases on the concrete cross-section based on the SEM-BSE image, with the legend indicating the colour code, percentage weight and percentage volume of each mineral over the cross-section. Other images depict the distribution of selected minerals on the cross-section.*

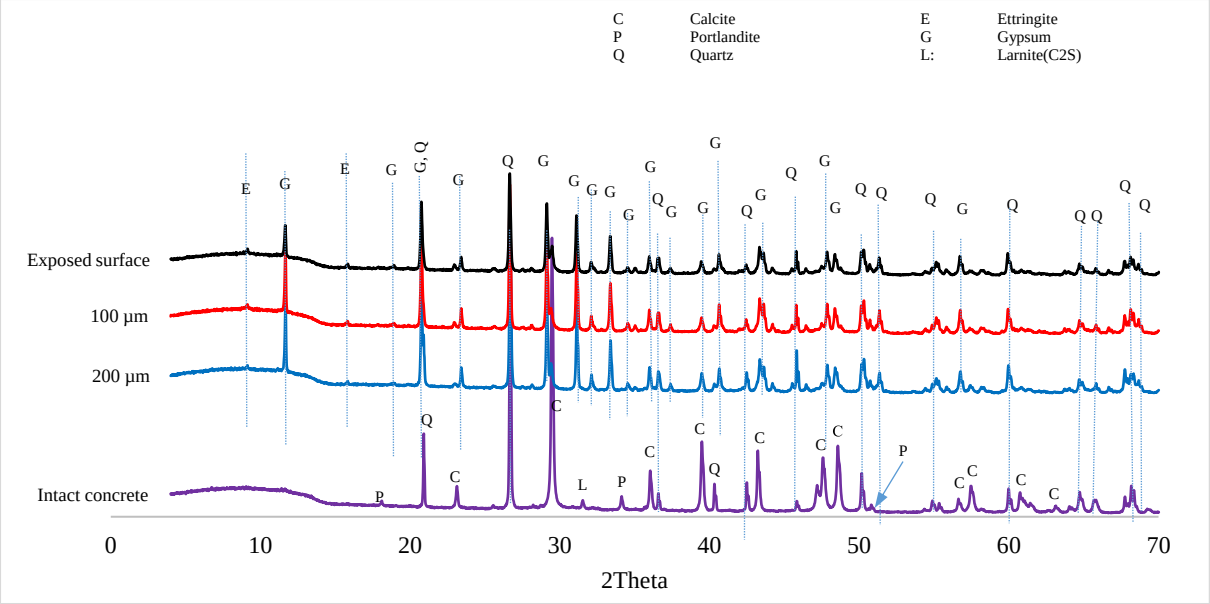


*Figure 5.18: XRD analysis of SRPC + LS concrete after two years of exposure*

### 5.2.6.4. CSA concrete

CSA concrete, by contrast, has a different concrete microstructure because it contains a higher amount of ettringite than other cementitious hydrates, see the XRD results on the intact concrete Figure 5.21.

**i.** *SEM-BSE images*

Figure 5.19 (A) shows an altered zone about 1.26 mm in width with increased porosity and loss of cohesion. In the altered zone, the cementitious particles are disaggregated, while in the intact concrete, they remain compact. The brightness of both zones is similar, which makes it difficult to demarcate between the altered and intact zones, especially in the cement matrix. However, the two zones can easily be distinguished in the aggregate matrix. As in the previous concretes, calcite aggregates dissolve and crack at the surface, while quartz remains unaltered.

It was mentioned in Section 5.2.5 that CSA concrete experienced insignificant thickness change but significant mass gain. The reason was related to the increasing formation of ettringite phases in the pore and void spaces due to acid penetration and the continued CSA hydration due to absorbed moisture. In this concrete, anhydrous CSA cement remained in the system after initial hydration, see Ye-elimite in Figure 5.21, which could be activated for further hydration under a sufficient supply of moisture from the sewer. The presence of excess voids compensated for the increased volume by providing more space for the formation of ettringite without causing substantial expansion of the concrete matrix. Figure 5.19(B) shows ettringite deposits in the CSA concrete voids.

Figure 5.19 (C) analysed the black organic material, which appears as strands in the microstructure in Figure 5.19 (A). These strand-like materials are rich in carbon and oxygen, see Table 5.5, indicating that they are likely organic matters that penetrated the concrete microstructure. It should be noted that these organic materials are only observed in the CSA concrete, which also could have added to a substantial mass gain.

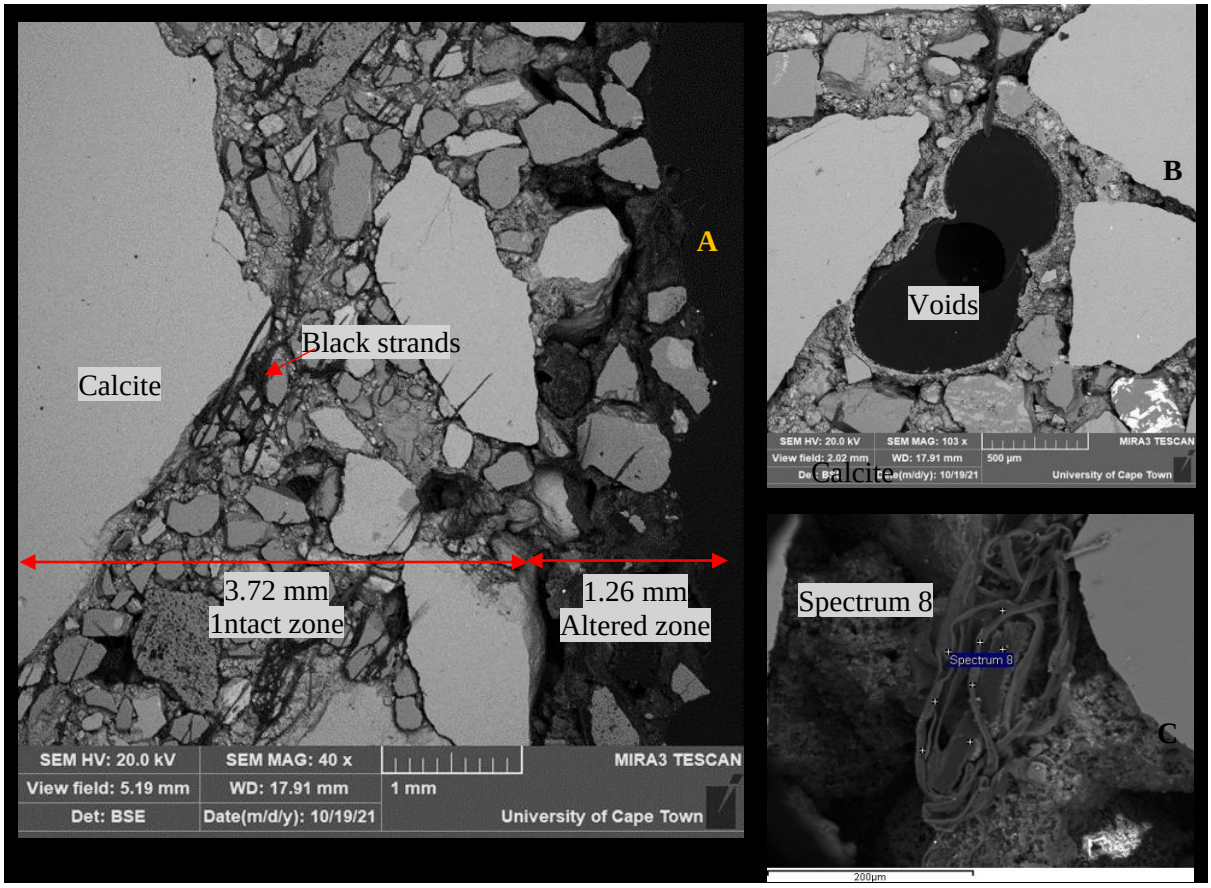


*Figure 5.19: SEM-BSE image for CSA concrete after two years of exposure at NAS M19*

*Table 5.5: Spectrum 8 in Figure 5.19(C shows the elemental composition of 'black-like materials' in the form of strands*

| Spectrum 8 | C | O | Al | Si | S | Cl | Ca | Fe |
|---|---|---|---|---|---|---|---|---|
| Mean | 57.46 | 35.8 | 0.53 | 0.77 | 0.52 | 0.19 | 2.97 | 1.74 |
| Std. deviation | 18.03 | 13.12 | 0.58 | 0.77 | 0.44 | 0.32 | 3.45 | 4.26 |
| Max. | 85.43 | 46.23 | 1.6 | 2.26 | 1.31 | 0.83 | 9.71 | 12.19 |
| Min. | 38 | 13.73 | 0 | 0 | 0 | 0 | 0 | 0 |

*5.2.6.4.1. QEMSCAN analysis*

As discussed earlier, the compaction of the CSA concrete was somewhat challenging, resulting in significant voids. As well, significant organic materials appearing as strands were observed throughout the cross-section. Since these are rich in carbon and oxygen, they simply do not appear in the QEMSCAN analysis, see Figure 5.20.

However, concrete zonation was identified by depicting the distribution of selected minerals. The transition zone was not clearly distinguished from the deteriorated zone; as explained under SEM analysis, this might be related to forming secondary ettringite phases in the transition zone due to acid penetration, leading to difficulties in distinguishing it from the original ettringite after hydration.

Besides, calcite and quartz (44.3% and 32.9%, respectively) were abundantly observed. The cement matrix consisted of a higher percentage weight of ettringite phases of about 6.2%, followed by 6.0% portlandite, 4.2% Al-silicate, 3.9% CaAl-Silicate, 1.2% Fe-phases, 0.7 % gypsum, and 0.6% gibbsite.

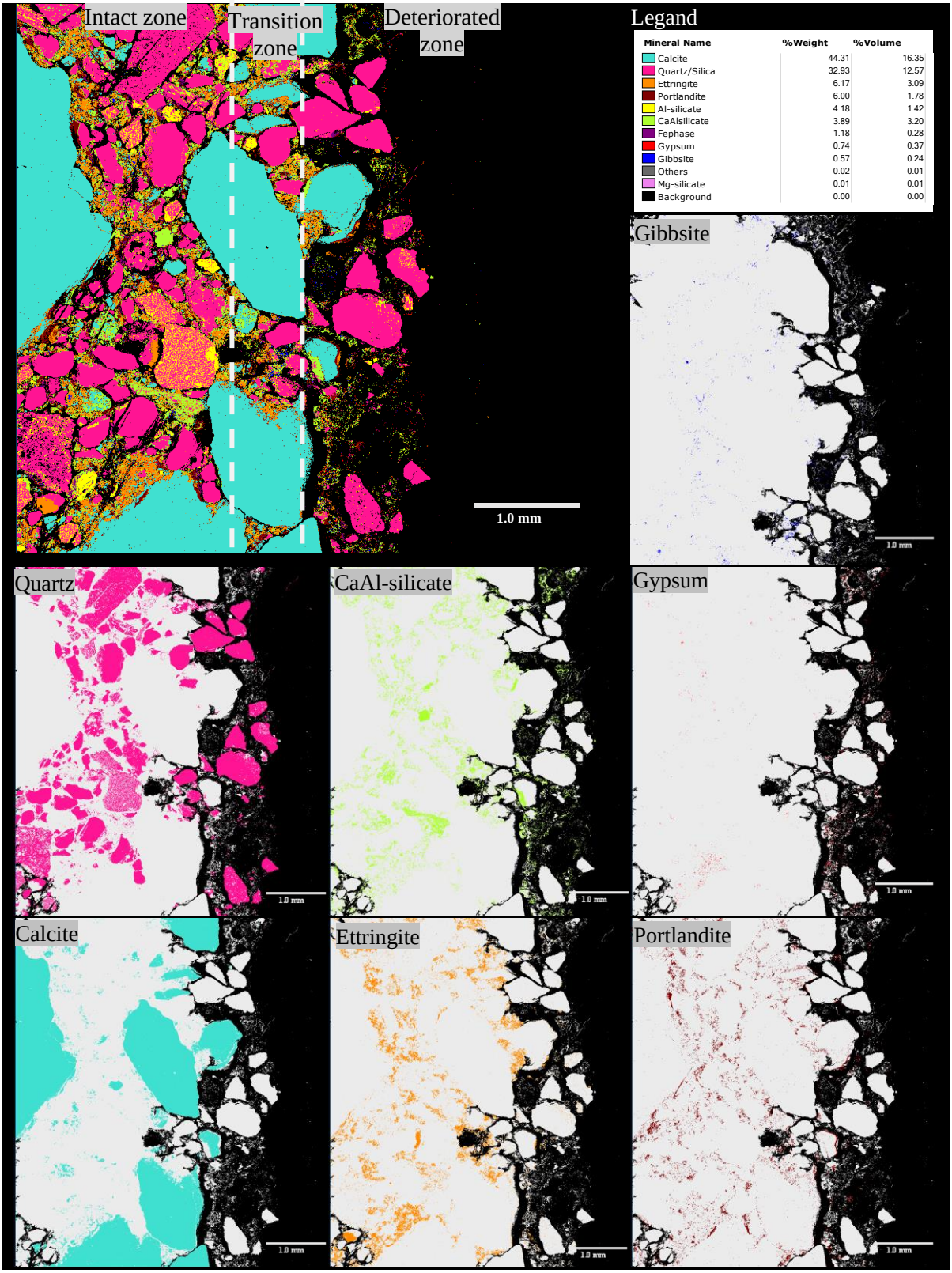


*Figure 5.20: QEMSCAN analysis of CSA concrete from the LH concrete specimens subjected to the NAS M19. The first image in the first row indicates a general distribution of concrete mineralogical phases on the concrete cross-section based on the SEM-BSE image, with the legend indicating the colour code, percentage weight and percentage volume of each mineral over the cross-section. Other images depict the distribution of selected minerals on the cross-section.*

Thus, the main hydration phase of this concrete was ettringite, portlandite, and some aluminate phases, while the Mg-silicate layer was not observed in this concrete

Ettringite and portlandite were only observed in the intact zone, and calcium aluminium silicate and gibbsite were observed in both intact and altered zone. On the contrary, gypsum was mainly observed in the altered zone. Calcite and quartz behaved similarly regardless of the binder system used.

As hypothesised under SEM-EDS analysis, the voids near the exposed surface were filled with ettringite, then gibbsite and gypsum, while those in the intact zone were filled with only ettringite. This indicates that once the acid penetrates, ettringite decomposes into gypsum and gibbsite. In this concrete mix, the minimal amounts of gibbsite and gypsum make them tricky to observe, but precise observation is seen later in the UCT concrete mixes.

*5.2.6.4.2. XRD analysis*

In terms of XRD analysis, Figure 5.21 shows the presence of ettringite, Portlandite, gypsum, and Yeelimite in the intact concrete, as well as calcite and quartz phases from aggregates. The ettringite peak disappears after BAC. At the exposed surface, a significant amount of gypsum is observed, thus supporting the transformation of ettringite to gypsum in the deterioration zone.

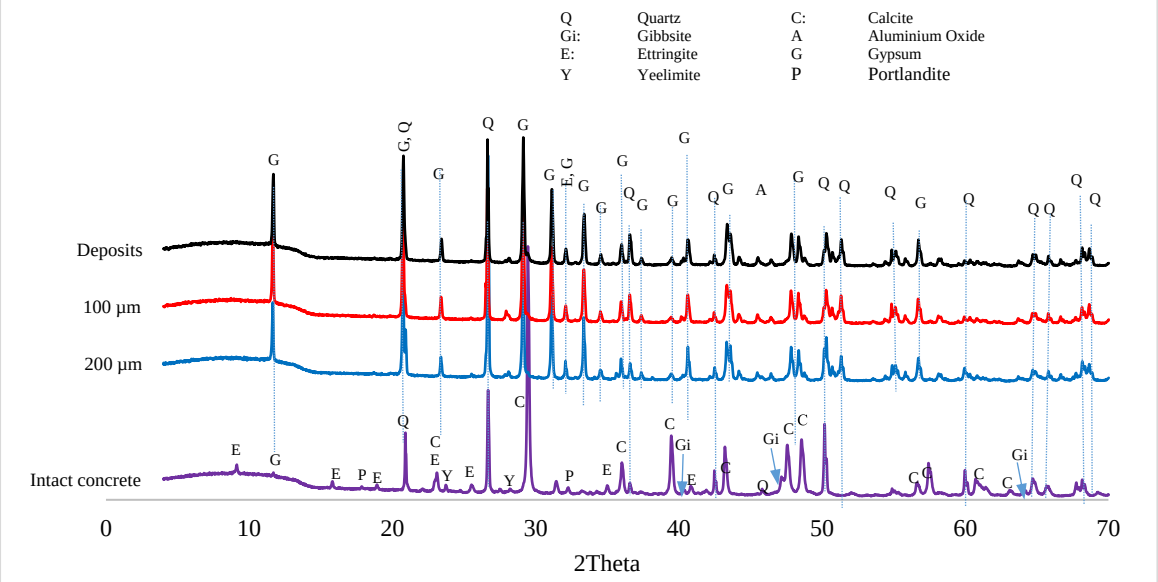


*Figure 5.21: XRD analysis of CSA concrete after 2 years of exposure*

### 5.2.6.5. Section closure

Using SEM-BSE images, two distinct zones were observed for the SRPC – based concretes exposed at the NAS M19, i.e., an intact zone and an altered zone. The altered zone was further subdivided into the transition and deteriorated zones. These zones were readily distinguished under QEMSCAN analysis with phase distribution. Contrarywise, the CSA transition zone was not clearly demarcated from the deteriorated zone. Similar SEM-BSE observations were noted for the concrete exposed at the LPS, see appendix H. However, the altered zone consisted merely of the transition zone without detecting the deteriorated zone because of the wetting and drying cycles at this site, which removed all loose and easy-to-dissolve corrosion products.

All concretes contained calcite and quartz aggregates in high proportion, as confirmed in the XRD analysis since about 80% of the concrete composite was aggregates. In the intact concrete, the cementitious phases were calcium silicate and portlandite for the SRPC-based concrete, and ettringite, portlandite, and calcium aluminium-silicate for the CSA concrete. In the transition zone, Mg-silicate was observed in the SRPC-based concrete, except for the concrete with iron-based additives, indicating a possibility of magnesium ion migration to react with silicate from calcium silicate phases after decalcification.

In the CSA concrete, the transition zone was challenging to distinguish due to the superimposition of secondary ettringite and original ettringite phases. In the deteriorated zone, the main phases were gypsum for all concrete mixes. Also, due to a significant amount of compaction voids in the CSA concrete, organic matter was observed in the concrete microstructure. Ettringite formation was observed in the voids. The presence of these voids made it more difficult to draw firm conclusions on the performance of CSA concrete since in the absence of these voids, further ettringite formation might have caused cracking of the concrete matrix. Further discussion in this regard is provided under UCT concrete

Calcite aggregates started to disintegrate immediately at the interface of the transition zone and deteriorated zone for all concretes. On the contrary, quartz aggregates detached from the transition zone.

### 5.2.7. General conclusions: LH concretes

Although the LH concrete mixes were less than fully compacted, their performance in three live sewer environments for two years was investigated, and the following insights were extracted;

- The performance of concrete varies significantly, depending on the sewer exposure environment; sewer hydraulic actions tend to accelerate the deterioration rate.
- Improving sewer concrete performance by incorporating reactive aggregates depends on the relative potential of both cement and aggregate matrix in resisting BAC and hydraulic sewer erosion. In cases when sewer hydraulic erosion is limited, cement matrix and reactive aggregates participate in neutralising the attacking acid.
- Concrete surface pH varies with time, indicating progressive microbial colonisation and biological activities. However, it is postulated that the surface pH measurement resembles the neutralised pH of the concrete after the attack, i.e., that of corrosion products, and not the pH of SOBs generated and attacking acid.
- Despite a sewer being considered less aggressive due to low $H_2S$ gas concentrations below 10 ppm, It can still cause corrosion on the concrete surface in the long term because microbial activities, i.e., SOBs evolution and colonisation, progress with time leading to concrete surface pH reduction.
- During the initial stage of BAC, concrete tends to exhibit mass gain associated with moisture absorption and initial corrosion build-up in the porosity and compaction voids. In the case of LH concrete, a significant mass gain was observed due to a substantial amount of compaction voids since their degree of compaction was not fully achieved.

- A higher mass loss does not necessarily imply a higher thickness loss. This is because aggregate incorporation in concrete plays a significant role. A high thickness loss might be measured, but with less mass loss due to protruding aggregates and vice versa.
- In terms of binder system performance, CSA concrete has superior performance than SRPC-based concrete, iron-based improves the abrasion resistance of SRPC concrete, while limestone, in conjunction with calcite aggregates, provides more alkali material to neutralising acid
- Concrete microstructural analysis indicates that SRPC- based concrete deteriorates to exhibit three distinct zones, i.e., the intact zone, the transition zone, and the deteriorated zone, while CSA concrete does not show the transition zone due to the superimposition of ettringite from the penetrated acid and hydration.
- SRPC-based concrete is rich in calcium silicate hydrates in the intact zone and Mg-silicate in the transition zone, except with iron-based additives, and Al-silicate, gypsum, and quartz fines in the deteriorated zone. CSA concrete contains ettringite and portlandite in the intact zone, and gibbsite, gypsum and other aluminate phases are in the deteriorated zone.
- SRPC concrete's poorer performance is associated with the decalcification of Ca-silicate because of its susceptibility to biogenic acid attack; however, the formation of Mg-silicate in the transition zone possibly decelerates its attack. CSA's better performance is associated with gibbsite and additional gibbsite from ettringite transformation, which contributes to the biogenic acid resistance.
- Despite the CSA concrete's superior performance in mass and thickness bulk measurements, microstructure analysis showed that it still experiences significant deterioration, although at a slower rate than SRPC-based concrete.
- Finally, despite the poor concrete quality due to inadequate compaction, LH concrete mixes exhibited relatively good performance but posed some difficulties in providing conclusive insights, especially for the CSA binder. Thus, the following section provides a better understanding of the performances of these binders and other binder systems added to the UCT concrete.

## 5.3. UCT concrete mixes: results and discussion

This part of the experimental investigation and discussion chapter discusses the results obtained after exposing the UCT concretes to two sewer sites, NAS M19 and LPS. The chapter aims to better understand and consolidate the aforementioned insights on the performance of CSA and SRPC-based binders with fly ash and iron additives. The aim was also to compare their performance to the superior sewer-performing binder (CAC) and the poorly performing binder (CEM II AL). Moreover, the study intended to explore the impact of blending CAC and SRPC in sewer concrete. Dolomite aggregates were used to prepare these concrete mixes to compare their performance with LH concrete with calcite aggregate.

This part of the chapter contains six subsections; the first subsection discusses the laboratory control test results, which entail compressive strength, saturated density, and durability index results after 28 days of curing. The second section examines the visual observation of the UCT concretes at NAS M19 and LPS. The third section discusses the change in the mass of concrete specimens with exposure time. The fourth section discusses the evolution of concrete surface pH of the UCT concrete with exposure time. The fifth section discusses the change in thickness of the concrete specimens with time. Finally, the sixth section discusses the microstructural analysis of the UCT concrete after being subjected to sewer environments for two years. The microstructural analysis was conducted only on the concrete specimens subjected to NAS M19, and the analysis entailed SEM BSE images, QEMSCAN analysis and XRD analysis. The microstructural analysis was not conducted for the specimens subjected to the LPS analysis because the specimens were inadvertently lost on site before the end of exposure duration.

### 5.3.1. Laboratory control test results

The laboratory control test results of UCT concretes aim to quantify the quality of concrete specimens in terms of complying with the quality of concrete recommended for sewer concrete construction indicated in Fourie (2007); see Appendix D. Also, the tests aim to characterise the mixes - for comparison between these mixes, LH concrete mixes, and previous UCT work.

#### 5.3.1.1. Saturated density after 28 days of curing

Figure 5.22 shows the average saturated densities of UCT concrete after 28 days of curing. The results indicate that all concrete had densities above 2500 kg/m$^3$, similar to that obtained in previous UCT studies (Fourie, 2007; Kiliswa, 2016) for concrete sewer specimens with similar aggregate types. The densities were also within the typical sewer pipe density range, between 2400 and 2600 kg/m$^3$ (Fourie, 2007).

Since all concretes had similar aggregate constituents, but different binder systems, the differences in saturated densities can be ascribed to the different binder systems. It was noted that Portland-based binder systems (i.e., SRPC+FA+HC, CEM II AL, and SRPC+FA) had lower densities than the alumina-based binder systems (i.e., CAC+SRPC, CSA, and CAC). The densities from the lowest to the highest were as follows; SRPC+FA+HC< CEM II AL<SRPC+FA< CAC+SRPC<CSA and CAC. CAC and CSA concrete had densities of approximately 2575 kg/m$^3$. The highest density of CAC was associated with its aluminate hydrates, i.e., $C_3AH_6$ and $AH_3$, which have relative densities of 2.52 and 2.40,

respectively (Hewlett, 2019). A blend of CAC and SRPC had a density approximately equal to that of SRPC+FA, while SRPC+FA+HC had the lowest density.

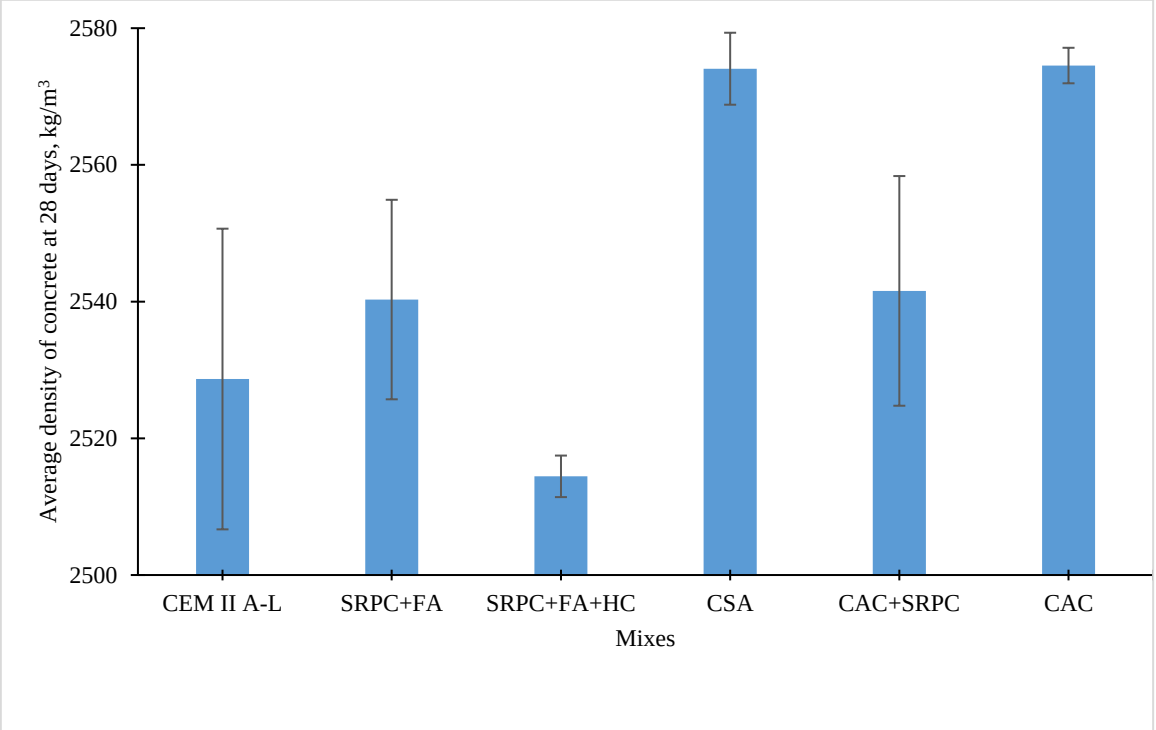


*Figure 5.22: Average saturated density of UCT concretes after 28 days of curing*

### 5.3.1.2. Compressive strength after 28 days of curing

Figure 5.23 shows the average compressive strength of UCT concretes at 28 days of curing. The results indicate that, after 28 days of age, all concretes had compressive strengths within the concrete sewer pipe strength range, i.e., between 50 MPa and 80 MPa, see Appendix D.1, except CAC with the highest compressive strength of 89.0 ± 2.6 MPa. The compressive strengths from the lowest to the highest were as follows; CEM II AL< CAC+SRPC< CSA<SRPC+HC< SRPC+FA+HC<CAC.

The high CAC compressive strength was associated with forming the stable hydrates, $C_3AH_6$ and $AH_3$ (Hewlett, 2019). Since all concrete mixes were cured at 40$^{o}$C for three days, for CAC concrete, the metastable hydrates ($C_2AH_8$ and $C_4AH_{13}$) were assumed to have converted to stable hydrates ($C_3AH_6$ and $AH_3$). With this conversion, concrete porosity increases with a decrease in compressive strength. However, for concrete with a w/b ratio below 0.4, a significant amount of anhydrous cement remains in the system, which after the initial formation of metastable hydrates, reacts with the water released by the conversion reaction, leading to an increase in strength (Hewlett, 2019)

CEM II AL concrete had the lowest strength but is comparable with the 28-day strength of CEM II A-L 52.5N. Blending CAC with SRPC reduces the strength to approximately equal to CEM II AL. The SRPC+ FA with and without HC had approximately equal strength (ranging between 74.7 and 78.7 MPa) but higher than CEM II AL due to pozzolanic reactions and faster hydration of fly ash at a higher temperature (40$^{o}$C) (Deschner et al., 2013). The CSA binder system used here has a high-quality Ye'elimite CSA (Caltra Nederland BV, 2010); therefore, higher strength than CEM II AL was expected,

which can be attributed to bonding and interlocking between ettringite crystals (Hargis et al., 2013; García-Maté et al., 2015; Zhang et al., 2021).

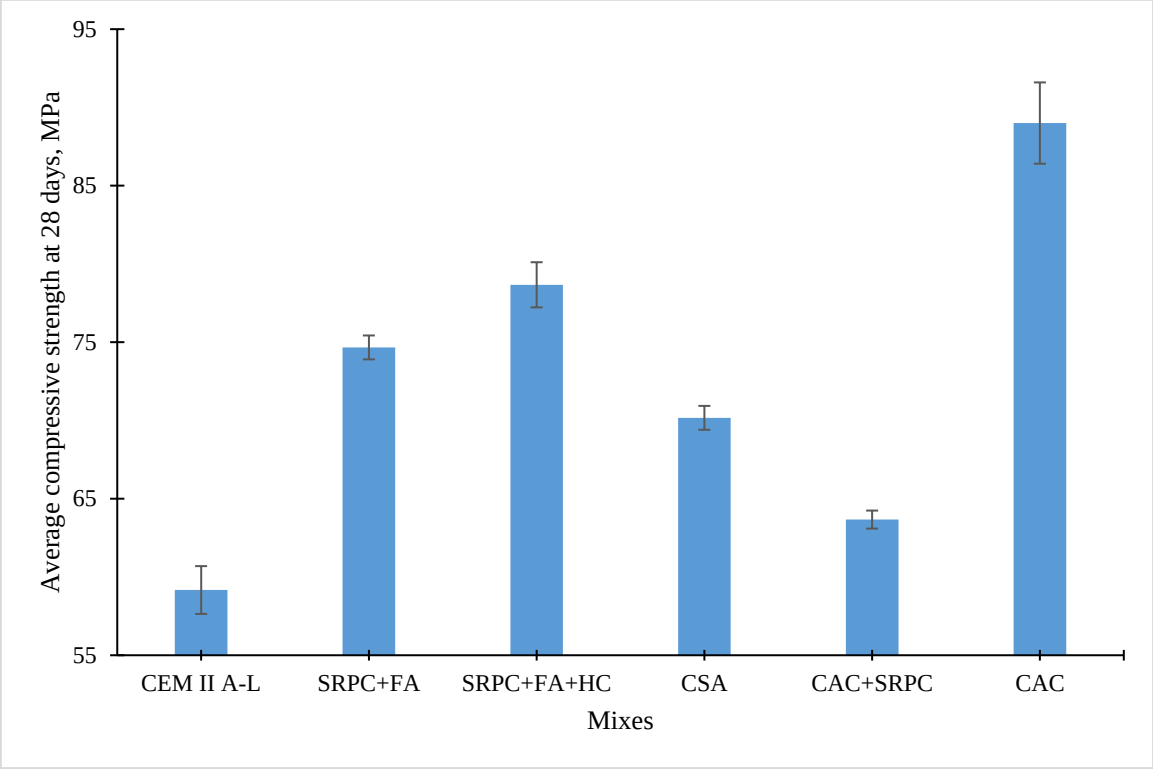


*Figure 5.23: Average compressive strength of UCT concrete at 28 days*

### 5.3.1.3. Durability Index (DI) results

The DI results in this study were used to evaluate the quality of concrete on site for its long-term performance in sewers to eliminate the impact of poor quality concrete in understanding the influence of binder systems, as observed in the LH concrete. Therefore, excellent quality, in terms of OPI, WSI and water-penetrable porosity, was aimed. A summary of the UCT concrete DI results is shown in Appendix I and discussed based on the criteria presented in Table 5.2.

#### *5.3.1.3.1. Oxygen permeability Index (OPI) test results*

The OPI results of the UCT concrete mixes at 28 days of curing are presented in Figure 5.24. All OPI values were above 10 (log value), indicating excellent quality concrete, see Table 5.2. CAC concrete had the lowest OPI value at 10.2, while other concrete OPI values were significantly higher, ranging between 10.8 to 11.3. These high OPI values indicate that all concretes had low oxygen gas permeability, i.e., low Darcy permeability coefficient. Practically, this would tend to limit the ingress of gases, including $H_2S$ and $CO_2$, into the dense concretes. Thus, carbonation was only experienced on the exposed surface, insinuating a low surface pH, as indicated in Section 5.3.4 below. However, in the case of CAC, the OPI value indicates a relatively higher oxygen gas permeability, which relates to the highest porosity, as indicated in Figure 5.26.

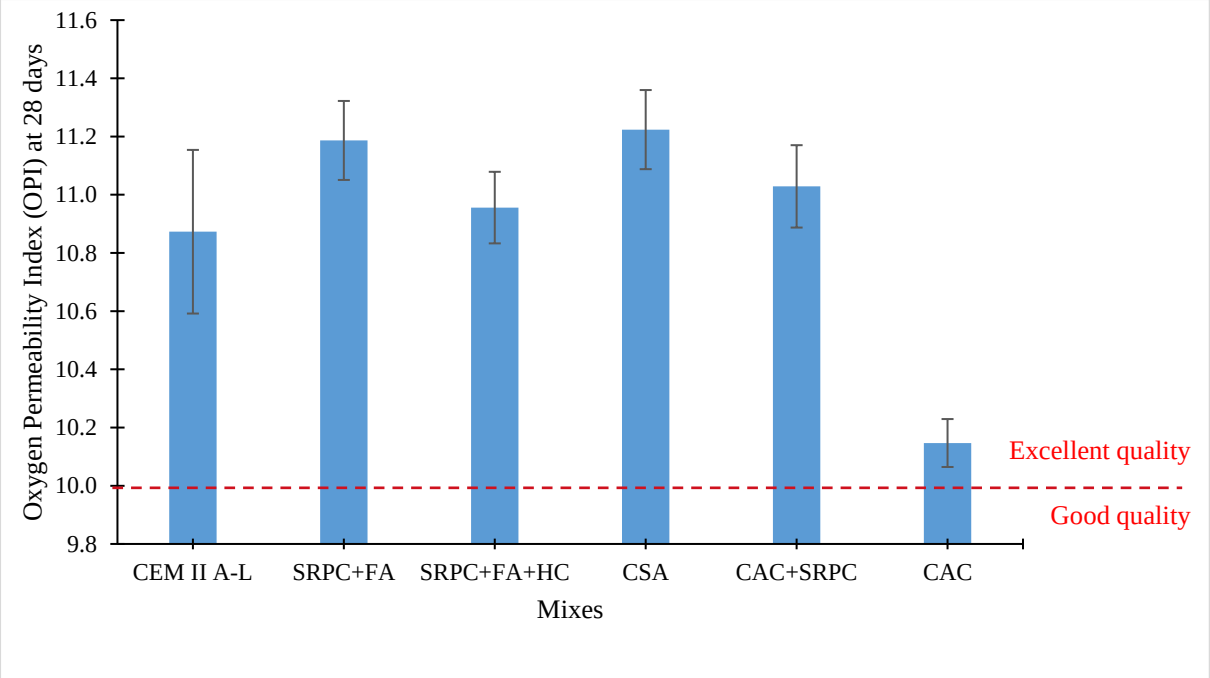


*Figure 5.24: Oxygen permeability Index (OPI) results of UCT concrete at 28 days*

*5.3.1.3.2. Water Sorptivity Index (WSI) and porosity test results*

The WSI results of UCT concrete mixes after 28 days of curing are presented in Figure 5.25. These results are discussed alongside the water-penetrable porosity results in Figure 5.26. According to Alexander, Mackechnie and Ballim (1999) and Moore, Bakera and Alexander (2021), concrete with WSI values below 6 mm/hr$^{0.5}$ and porosity less than 10% is considered excellent quality concrete. Those with WSI values between 6 and 10 mm/hr$^{0.5}$ and porosity below 10% are considered excellent to good quality concrete. With this information, CEM II AL, SRPC+FA, and SRPC+FA+HC are regarded as excellent quality concretes, while CSA, CAC+SRPC, and CAC are excellent to good quality concretes.

However, it was observed that CSA had the lowest porosity and highest WSI value, which was expected because the two parameters are inversely related (Moore, Bakera & Alexander, 2020, 2021). The low porosity was associated with ettringite formation, with a high expansion volume leading to pore filling within the concrete microstructure (Zhang & Glasser, 2002; Winnefeld & Lothenbach, 2010; Hargis et al., 2013). On the other hand, CAC concrete showed the highest porosity but without the lowest WSI value. The high porosity indicated the conversion of metastable hydrates to stable hydrates, which tends to increase porosity and decrease strength (Hewlett, 2019). Contrarywise, this was not the case when CAC was blended with SRPC since CAC+SRPC had lower porosity than CAC but approximately equal WSI values.

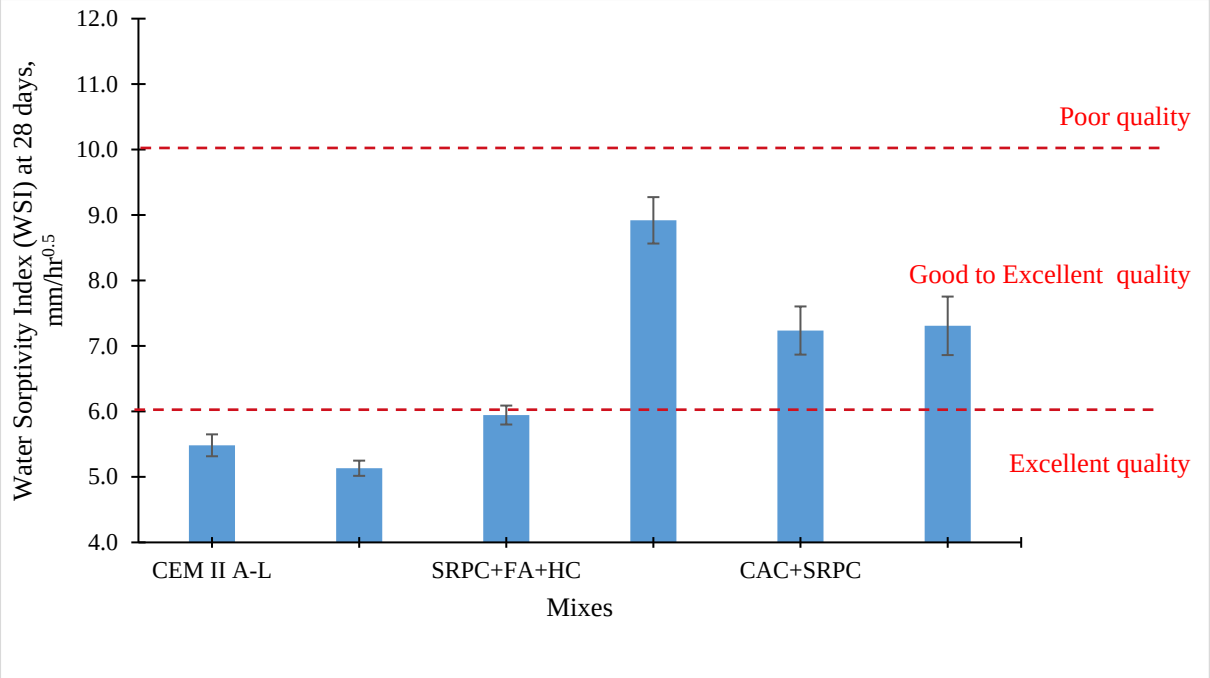


*Figure 5.25: Water sorptivity index (WSI) of UCT concrete mixes after 28 days*

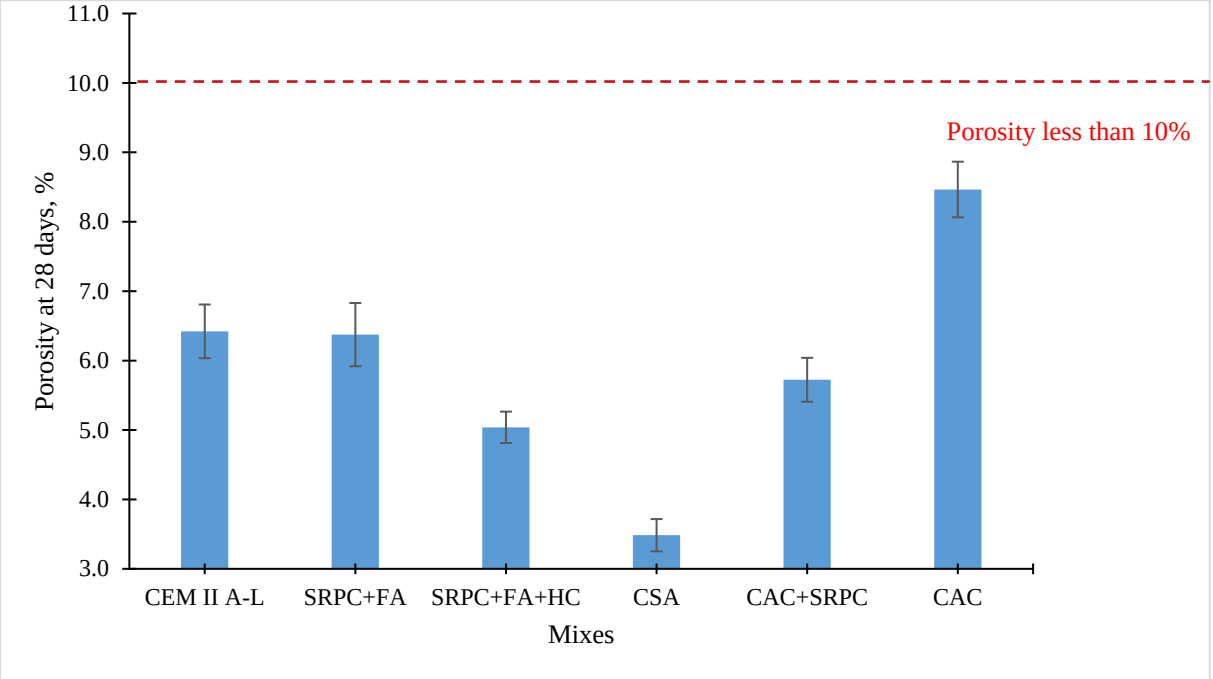


*Figure 5.26: Water absorption porosity of UCT concrete mixes at 28 days*

### 5.3.2. Section closure

It is crucial to ensure that the structural performance and limited penetrability of sewer concrete are achieved during concrete preparation to eliminate the deterioration of concrete associated with structural failure and transport properties. Therefore, the control test results indicate that the UCT concrete specimens used in this study had compressive strengths, saturated densities, and durability indexes within the concrete sewer pipe range, see Appendix D. On the other hand, all concrete mixes

designed and cast at UCT have excellent quality, compared to the LH concrete, which exhibited poor quality in terms of durability index results. Thus, the deterioration mechanisms observed herein are mainly related to BAC and not accelerated concrete transport behaviour due to poor quality, as exhibited in the LH concrete. In this light, the observations noted in the subsequent sections qualified to simulate the behaviour of sewer concrete when subjected to a sewer environment. Thus, they can be used to recommend binder systems for sewer concrete study and to advance the LFM model.

In that case, a traditional compaction method during concrete mixing and casting, i.e., the use of superplasticiser to increase concrete workability and compaction by vibration in the present case, can be used to prepare concrete specimens for concrete sewer study only. However, this method does not allow mechanical properties testing at a green state as in the sewer pipe construction industries where mechanical compaction is employed. Moreover, it should be noted that the mechanical compaction method used by Fourie (2007) and Kiliswa (2016) in the laboratory, when adopted in this study, coarse aggregates were crushed, thus inducing microcracking, which might influence the penetration of aggressive gases into concrete.

### 5.3.3. UCT concrete visual observations

As discussed in the introduction, Section 5.1, UCT concrete specimens were only exposed to two sewer sites, i.e., NAS M19 and LPS. Therefore, visual observation results are discussed accordingly. Unfortunately, due to various challenges associated with working in the public environment, the UCT concrete specimens subjected to the LPS site were lost before completing two years of exposure. Therefore, the results herein show only 15 months of exposure at LPS and 26 months at NAS M19. The discussion was also conducted based on two UCT concrete mix categories; Portland-based binder systems, i.e., CEM II AL, SRPC +FA and SRPC+FA+HC, and Alumina-based binder systems, i.e., CSA, CAC, and CAC+SRPC.

#### 5.3.3.1. Visual observations of UCT concrete at NAS M19

Figure 5.27 shows the visual observation of UCT concrete specimens exposed at the NAS M19 for approximately two years. At this site, observations were conducted after 8, 15, and 26 months. Before exposure, the exposed surfaces of Portland-based binders were predominantly grey, and those of Alumina-based binders were light yellow, distinguishing between cement matrix and aggregate particles. These specimens were exposed in February 2020, the summer season in South Africa.

After eight months of exposure (i.e., in September, spring season), Portland-based binder concretes experienced corrosion on the cement matrix, while aggregate particles, i.e., dolomite, showed minor corrosion signs. The cement matrix changed to a whitish colour as a sign of minor corrosion deposits, mainly observed on the edges of the specimens. By contrast, Alumina-based concretes showed black stains on the exposed surface, indicating microbial colonisation. At this time, no sign of corrosion deposits on these concretes was noticed on their surfaces. Since the concrete specimens were exposed throughout winter, it can be postulated that the aggressivity of the site was mild because, during the winter season, low concentrations of $H_2S$ gas are emitted, see Chapter 4.

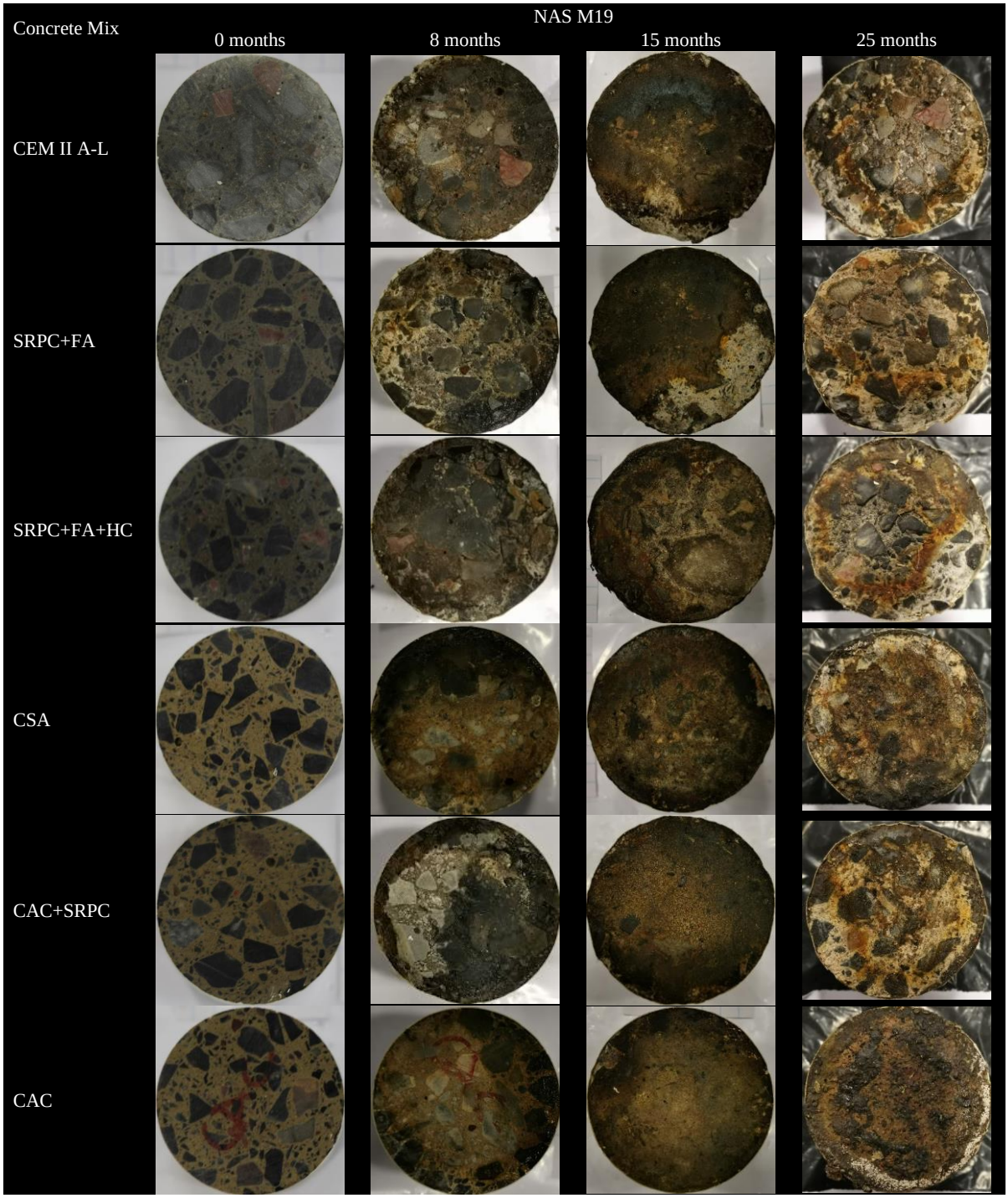


*Figure 5.27: Visual observation of UCT concrete specimens exposed at NAS M19 for 0, 8, 15, and 26 months*

At 15 months of exposure, all concretes, except CAC, had blisters on the epoxy-coated curved surfaces. On the Portland-based concretes, aggregates exhibited signs of corrosion as surface depressions and disintegrated particles on the aggregate surface. CEM II AL and SRPC+FA concrete edges showed significant whitish paste-like deposits. SRPC+FA+HC concrete had brownish staining demarcating severely corroded surface edges, possibly iron-rich deposits, as observed by Taheri et al. (2021). Regarding alumina-based concretes, there was no sign of corrosion material loss apart from their

surfaces being covered with dark stains, probably biofilm. CSA and CAC+SRPC surfaces were covered with distinct crystal-like growths on the entire surface and minor corrosion deposits on some edges. The CAC surface had some whitish spots on the edges. Generally, the Portland-based concretes appeared more severely corroded after this duration than alumina-based concretes.

After 26 months of exposure (see Figure 5.28), all concrete cement matrixes and aggregates were severely corroded. Yellowish stains demarcating severely corroded surfaces and whitish deposits covering the exposed surfaces were observed on the Portland-based concretes, as observed by Okabe et al. (2007). Their edges were deteriorating and losing more cement-based materials and corrosion deposits. Dolomite aggregates slightly protruded on the exposed surfaces, also detected by Hudon, Mirza & Frigon (2011), showing signs of dissolution, i.e., small depressions and disintegrated particles on the aggregate surface. The aggregate protrusion indicates that the aggregate deterioration rate was lower than the cement matrixes, unlike calcite aggregates on the LH concrete. This implies that the dolomite deterioration rate is slower than calcite, which might be related to its integrity or the extra magnesium carbonate.

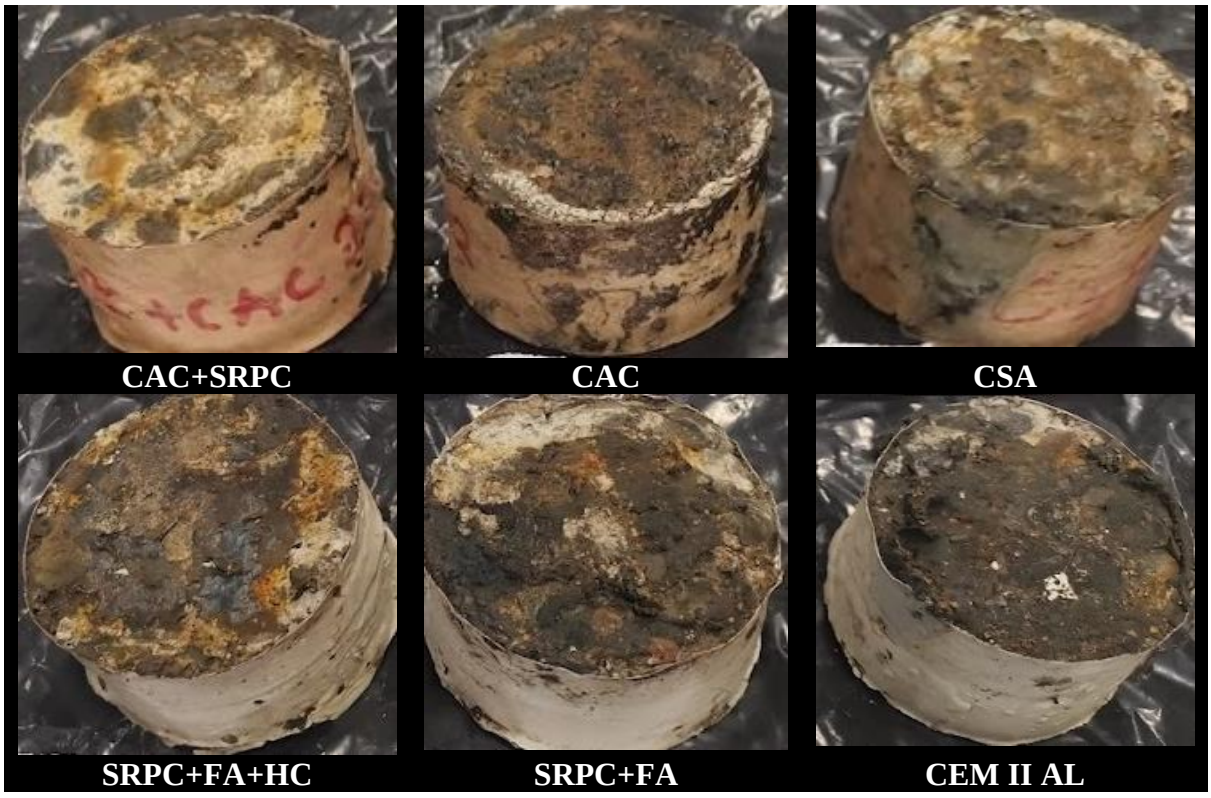


*Figure 5.28: Visual observation of UCT concrete specimens exposed at NAS M19 at 26 months, indicating corroded surfaces and epoxy coating is peeling off, especially for the Portland-based concrete.*

In the case of alumina-based concretes, material losses started from the specimen edges to the centre of the concrete specimens. For CSA concrete, severe deterioration was observed, while its cement matrix changed to brownish and then whitish as a sign of corrosion deposits. Yellowish stains and significant material loss were observed on the CAC + SRPC concretes. On the contrary, CAC concrete indicated

mud-like deposits on the entire exposed surface, which changed into whitish corrosion deposits towards the edges. Its epoxy coating was still intact, and no significant material loss was observed.

Based on visual observations at this site, it was concluded that alumina-based concretes had superior performance than Portland-based concretes. Portland-based concretes also experienced signs of corrosion earlier than alumina-based concretes. After eight months of exposure, despite being subjected to a winter season, Portland-based concretes, especially their cement matrixes, started experiencing severe corrosion. At about 15 months of exposure, corrosion was evident on the aggregate particles, indicating that aggregate particles had a lower rate of deterioration than the cement matrix. In the case of alumina-based concretes, cement matrixes and aggregate particles experience less sign of corrosion up to 15 months of exposure. However, at 26 months of exposure, all concretes showed significant severe corrosion. In comparison, CAC concrete had superior performance than CSA, while a blend of CAC and SRPC did not improve the performance of concrete visually.

#### 5.3.3.2. Visual observation of UCT concretes at LPS

UCT concrete visual observations at LPS are presented in Figure 5.29 for up to 15 months of exposure. The specimens were exposed in February 2020, the summer season, and then retrieved after eight months, i.e., September 2020. From April to September 2020, South Africa was under Lockdown due to the COVID-19 pandemic, which led to erratic monitoring and sewer pump station control. Consequently, the site suffered a breakdown due to flooding and lack of maintenance, which took four months to repair. The specimens were stored in the laboratory fridge at 4$^{o}$C for four months during the repair period. In January 2021, the specimens were returned to the site for further exposure. In August 2021, i.e., after 15 months of exposure, the specimens were retrieved for regular monitoring and then returned to the site to complete the exposure duration of two years. However, due to various challenges associated with working in the public environment, the specimens were inexplicably lost from the manhole before completing two years of planned exposure duration. Therefore, the physical observations are presented herein for 8 and 15 months of exposure.

Before exposure, the exposed surfaces of Portland-based concrete were grey, and those of alumina-based concretes were light yellow. However, after eight months of exposure, Portland-based concrete surfaces changed to yellowish, black stains were observed on the edges, and aggregate particles protruded. On the other hand, alumina-based concrete showed minor deterioration and black deposits covering the surface. CAC concrete, however, contains brownish stains. Due to the effect of sewer hydraulic actions at this site, no corrosion products were observed on the surface of all concrete.

At 15 months, all concretes, including CAC, experienced signs of material loss, while dolomite aggregates tended to resist the attack as there was no sign of aggregate dissolution on the exposed surface, and the particles protruded the surface. However, the rates of cement matrix dissolution contrasted from one binder system to another. For all concrete, blisters were still observed on the epoxy surface. The epoxy coatings of Portland-based concrete were significantly damaged, see Figure 5.30. SRPC+FA+HC aggregates detached, and minor corrosion products were observed at the edges and epoxy layer interface. Physically, SRPC+FA+HC concrete seemed severely damaged, followed by SRPC+FA, then CEM II AL concrete.

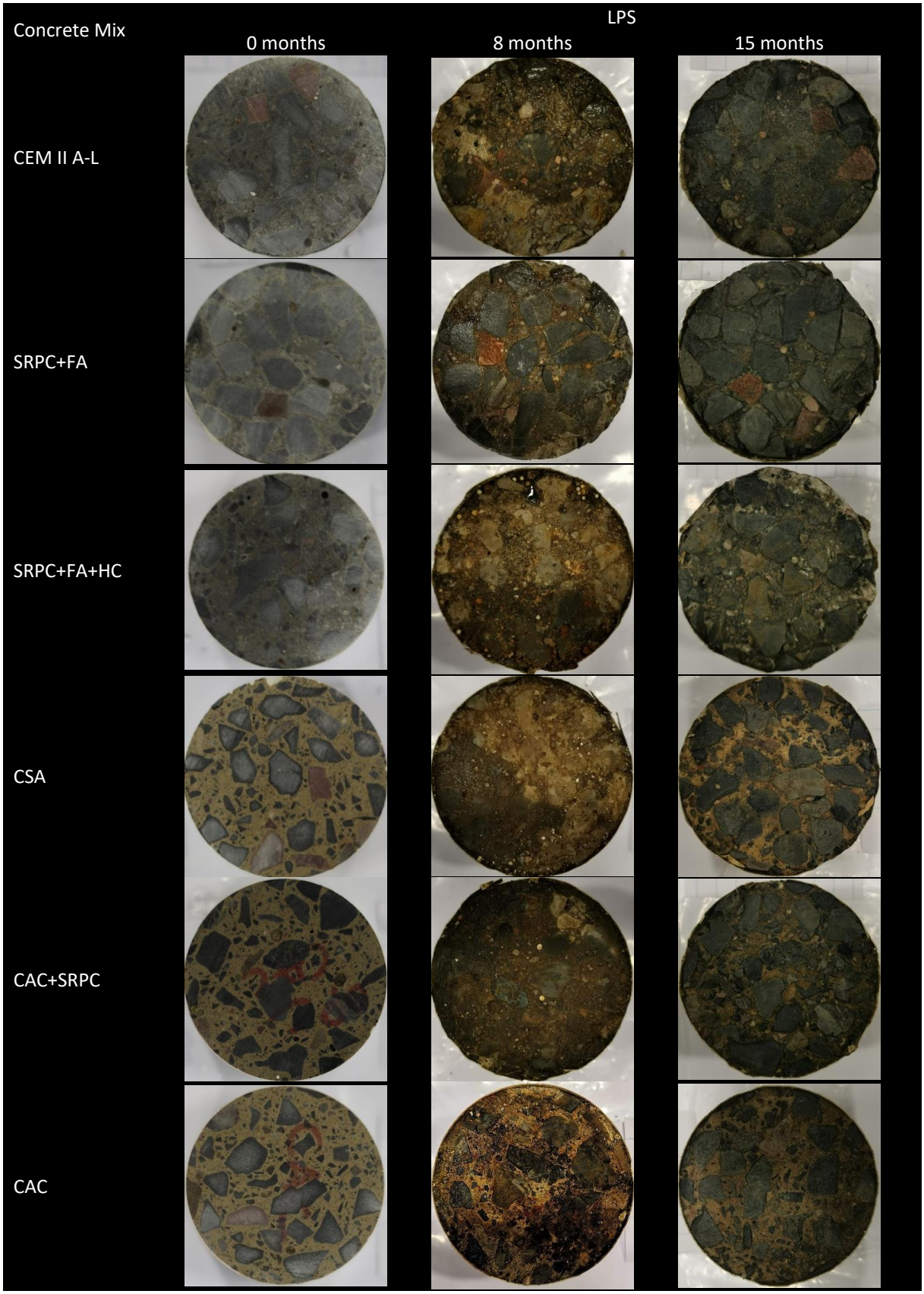


*Figure 5.29: Visual observations of UCT concrete specimens exposed at the LPS manhole for 15 months*

Regarding alumina-based concrete, CAC concrete showed superior performance than all other concretes. However, its cement matrix deteriorated on the exposed surface, illustrated by the remaining epoxy coating after corrosion product removal. This implies that CAC concrete does not entirely resist corrosion but has the slowest rate of deterioration. Similar visual observations were reported by Khan et al. (2019). On the other hand, the CSA cement matrix corroded on the surface, leaving aggregate particles protruding. This indicates that the CSA deterioration rate is somewhat higher than CAC concrete. Furthermore, a blend of CAC+SRPC showed physical damage similar to CSA, yet less than Portland-based concrete. Generally, this indicates that under sewer hydraulic actions, alumina-based concretes have superior performance than Portland-based concretes.

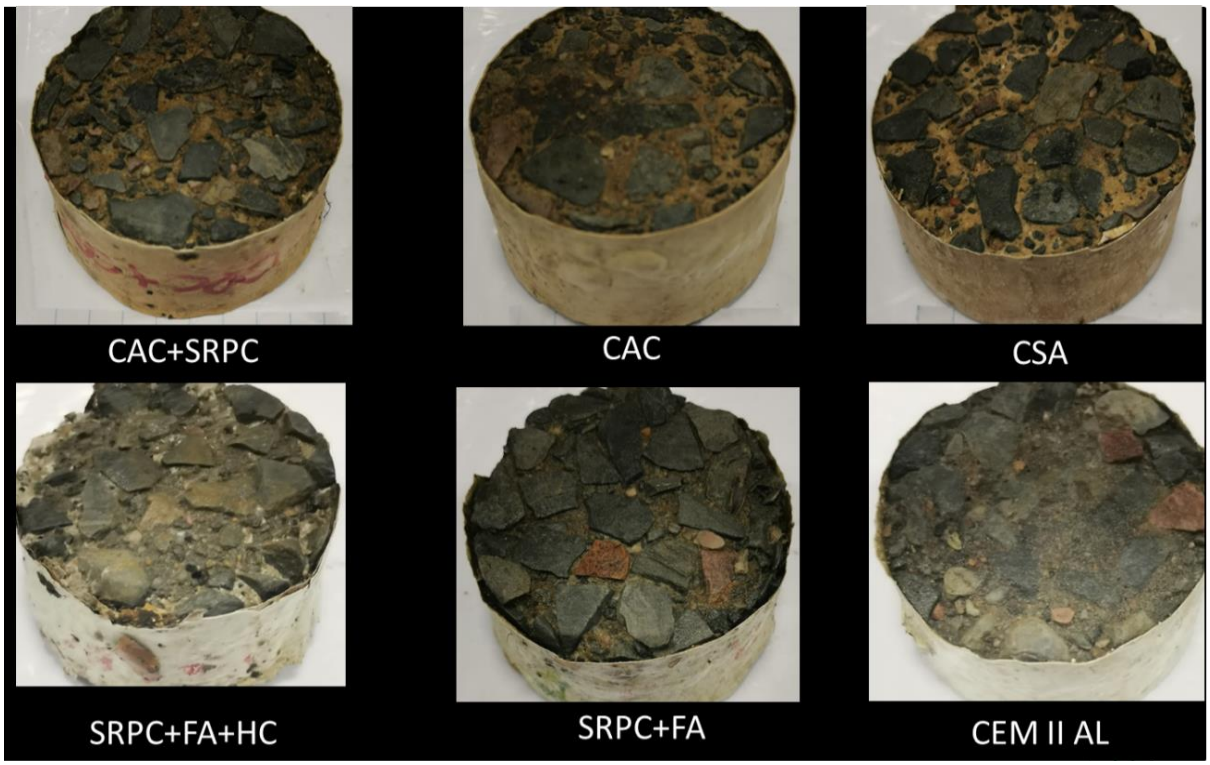


*Figure 5.30: Visual observation of UCT concrete specimens subjected to the LPS manhole for 15 months, showing protruded aggregate particles on the surface and damaged exposed surface, especially for the Portland-based concrete.*

#### 5.3.3.3. Section closure

Generally, it can be concluded that Portland-based concretes exhibit severe deterioration, both on the concrete exposed surface and the epoxy coating layer, than alumina-based concrete at both sites. However, LPS was more aggressive than the NAS M19 due to its sewer hydraulic actions. Consequently, significant corrosion product removal and renewal of exposed surfaces with aggregate protrusion was observed on both Portland and alumina-based concrete surfaces. CAC concrete exhibited the highest resistance potential against BAC and sewer hydraulic action since it exhibited less aggregate protrusion and damaged cement matrix for the LPS exposure. CSA deterioration rate is somewhat higher than CAC concrete, and a blend of CAC+SRPC showed physical damage similar to CSA.

### 5.3.4. UCT concrete surface pH

As discussed in the literature review Chapter 2, concrete surface pH is one of the key factors that define the extent and stage of concrete deterioration due to microbial growth in sewer environments (Islander et al., 1991; Khan et al., 2019). Therefore, in this study, the evolution of concrete surface pH was evaluated to understand BAC stages with time caused by sewer aggressivity and microbial activity (Haile, Nakhla & Allouche, 2008).

#### 5.3.4.1. UCT concrete surface pH at NAS M19

Figure 5.31 shows the surface pH measurements of UCT concrete specimens exposed at the NAS M19 up to 26 months. The error bars represent the standard deviations of the surface pH measurements. At the start of exposure, all concretes had a surface pH between 10.0 and 8.8 lower than fresh concrete surface pH, possibly due to carbonation during sample preparation and before exposure in the sewer. CEM II A-L had the highest surface pH, followed by SRPC+FA+HC and CAC+SRPC, and then SRPC+FA, and CSA showed the lowest values.

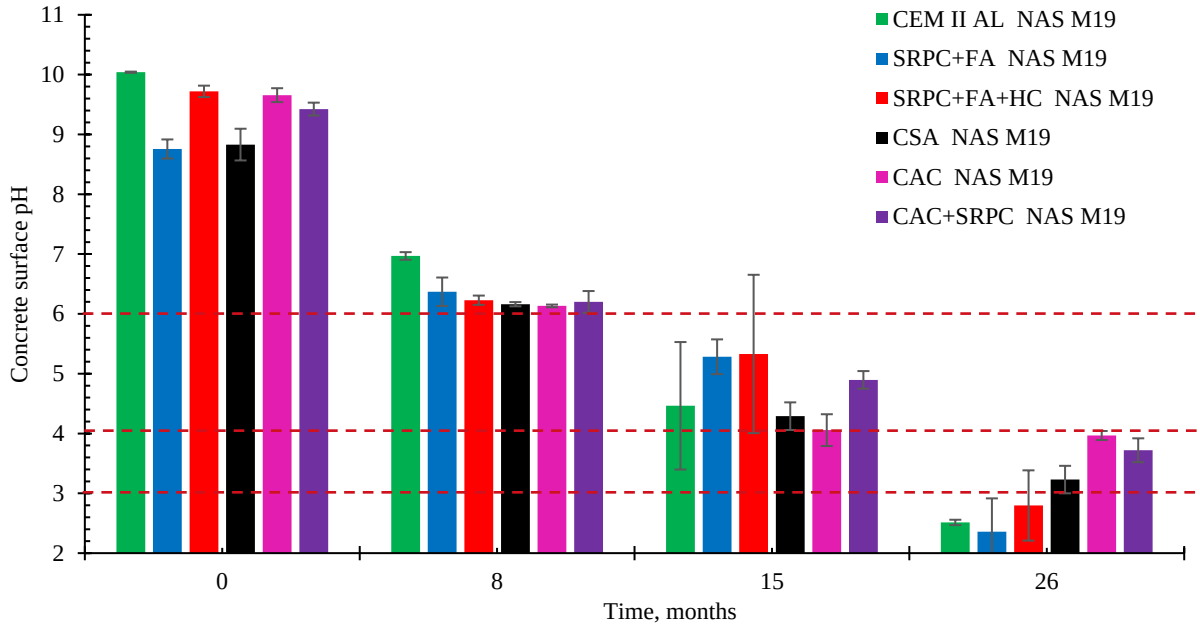


*Figure 5.31: Concrete surface pH readings of UCT concrete specimens exposed at the NAS M19 for up to 26 months. The error bars represent the standard deviations of the pH change (more details in Appendix J).*

After eight months of exposure, all concretes had similar surface pH of around 6. Neutrophilic SOBs were assumed to have colonised the concrete surface at this stage, preparing a conducive environment for further acidophilic SOB colonisation (Islander et al., 1991). CEM II AL exhibited higher pH than the other concretes, presumably due to a higher CaO content, i.e., high Portlandite, which provides additional neutralisation capacity, producing higher pH.

At 15 months of exposure, all concretes had pHs between 6 and 4, which indicates an increase in acid aggressivity and an increase in corrosion product build-up on the exposed surface concrete, which shields the 'fresh' substrate from the measurement. SRPC+FA and SRPC+FA+HC had pHs slightly

above 5, followed by CAC+SRPC and CEM II AL between 5 to 4.5, and CSA and CAC at pHs of about 4. It is clear that at this stage, CAC had the lowest pH of about 4, which might be associated with less calcium ion leaching as indicated (Aboulela et al., 2021) and gibbsite formation, which is stable at a pH of around 3 - 4.

However, at 26 months of exposure, the pH values decreased considerably, approaching stable values, especially for Portland-based concretes (CEM II AL, SRPC+FA, and SRPC+FA+HC), which had pHs below 3, while alumina-based concrete had pHs ranging between 4 and 3. At these pHs, the acidophilic SOBs were assumed to have entirely colonised the concrete surfaces. The surface pH of SRPC+FA concrete is similar to that observed by Kaempfer & Berndt (1999) on thin wet film on the pipe wall surface of the concrete with PC and fly ash. In the case of alumina-based concrete, the pH values concur with the literature that alumina-based concrete surface pHs, especially CAC and CSA concrete, tend to plateau at pH between 3 and 4, ascribed to gibbsite formation on the exposed surface, see Section 5.3.8.6 and 5.3.8.5, respectively (Hewlett & Liska, 2019: 575).

Thus, it can be concluded that, at the NAS M19, the gradual evolution of concrete surface pH was observed with time due to successive microbial colonisation on the concrete surface, leading to aggressive acid generation and continuous corrosion product deposition on the exposed surface in the absence of severe sewer hydraulic actions, as indicated in Section 5.3.3.1.

#### 5.3.4.2. UCT concrete surface pH at LPS

At the LPS manhole, the results are presented for up to 15 months in Figure 5.32. It was observed that the concrete surface pHs at LPS after 8 months of exposure were between 7 and 6, similar to those measured at the NAS M19. However, after 15 months of exposure, the surface pH was generally between 5.5 and 5.0, with CAC+SRPC showing the lowest value of about 4.5. These pH readings were somewhat higher than those observed at NAS M19 because, at the LPS site, the concrete specimens showed fewer corrosion deposits than at NAS M19 due to sewer hydraulic actions, which significantly accelerated the deterioration by continuously removing the corrosion products (Fytianos et al., 2021).

Despite the LPS being more 'aggressive' in terms of $H_2S$ gas concentration and sewer hydraulic actions, see Chapter 4, the surface pHs of concrete at 15 months of exposure were still higher than those observed at NAS M19 at the same duration. This suggests that concrete surface pH does not necessarily infer the sewer aggressivity but merely the interaction between the concrete alkaline reactive components and acid generation, i.e., the corrosion deposition, mainly gypsum. Therefore, for sewer zones such as the tidal zone, significant damage may be detected, but with little or no corrosion products due to continuous removal by the wastewater flow. Consequently, a higher concrete surface pH is detected, presenting the pH of the remaining substrate.

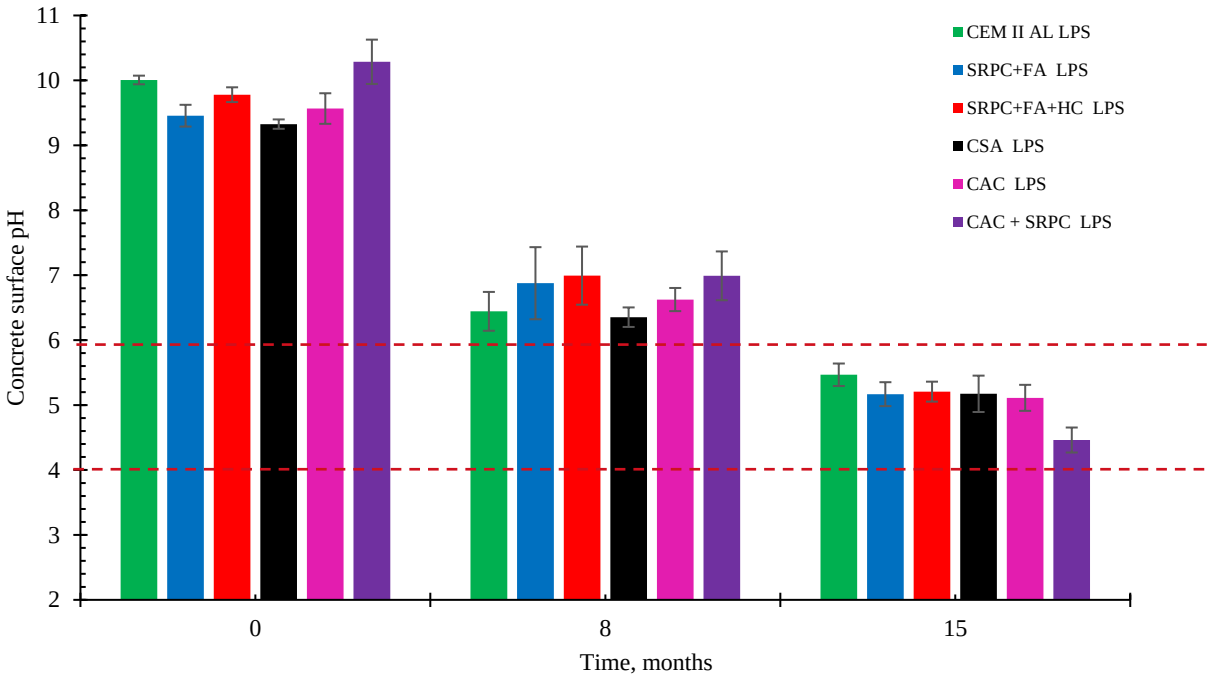


*Figure 5.32: Concrete surface pH readings of UCT concrete specimens exposed at the LPS manhole for 15 months. The error bars represent the standard deviations of the pH changes (more details in Appendix J)*

### 5.3.5. UCT concrete mass changes

The following sections discuss the change in mass of UCT concrete specimens subjected to the NAS M19 and the LPS site conditions. More data on this section are presented in Appendix 0.

#### 5.3.5.1. UCT concrete mass changes at NAS M19

Figure 5.33 demonstrates the mass change of the UCT concrete specimens exposed at the NAS M19 for 26 months. The positive values indicate mass gain, and the negative values indicate mass loss. The error bars represent the standard deviations of the mass change measurements. The results imply that Portland-based concretes experienced greater mass loss than alumina-based concretes. Up to 15 months of exposure, alumina-based concrete showed no mass loss. CAC and CSA concrete showed a slight increase in mass gain, while CAC+SRPC had no change in mass. This behaviour of mass gain was also observed by Khan et al. (2019) on the CAC mortar after 12 months of exposure to the sewer environment. By contrast, Portland-based concretes showed significant mass loss within 8 months of exposure. The mass gain is ascribed to moisture absorption and organic matter penetration into the concrete microstructure (Khan et al., 2019).

As observed in Section 5.2.4, CSA concrete (LH concrete) showed a continuous mass gain of about 1.8% and simultaneous thickness loss until the end of exposure duration. Its mass gain was associated with ongoing hydration due to moisture absorption and initial corrosion product build-up in the voids and at the epoxy-concrete interface, which counteracted the mass loss due to corrosion product removal on the exposed surface, i.e., thickness loss. This might not be the case in the UCT concrete since the CSA concrete microstructure was dense with the lowest water-penetrable porosity. Hence the moisture absorption was possibly experienced on the thin outer surface layer (i.e., transition zone) of the exposed

surface, stimulating further hydration of anhydrous phases (see Figure 5.54) in the CSA concrete, and secondary ettringite was produced. Since ettringite is an expansive material, in the absence of space (voids or pores) to accommodate its expansive pressure, microcracks (see Figure 5.52) were induced in this layer, providing access for organic matter penetration, thus mass gain. However, in the presence of microbially-generated acid, ettringite decomposed to form gypsum and gibbsite; since gypsum has low structural strength, material loss occurs.

For the case of CAC concrete, the initial mass gain might be related to the formation of initial corrosion products (i.e., ettringite in the transition layer, see Figure 5.56) with organic matter and acid penetration on the thin outer layer of the exposed surface. However, with ettringite formation, microcracks were expected to induce expansive pressure in the microstructure to accelerate the deterioration. This behaviour was not the case since CAC had the highest porosity to accommodate the pressure. Nevertheless, after several years of exposure, the slight mass gains at the beginning will have no appreciable influence and can therefore be ignored for practical purposes.

After 26 months of exposure, all concretes indicated mass losses. The order of mass loss at this site from the lowest to the highest were as follows; CAC < CSA < CAC+SRPC < CEM II AL < SRPC+FA+HC < SRPC+FA. The mass loss was associated with the loss of concrete materials (cement matrix and aggregates) due to corrosion on the exposed surfaces. In that case, CAC concrete portrayed the best performance in terms of mass loss, and SRPC+FA+HC showed the worst performance. However, the performance of Portland-based concrete is inconclusive as the thickness change results indicate the opposite.

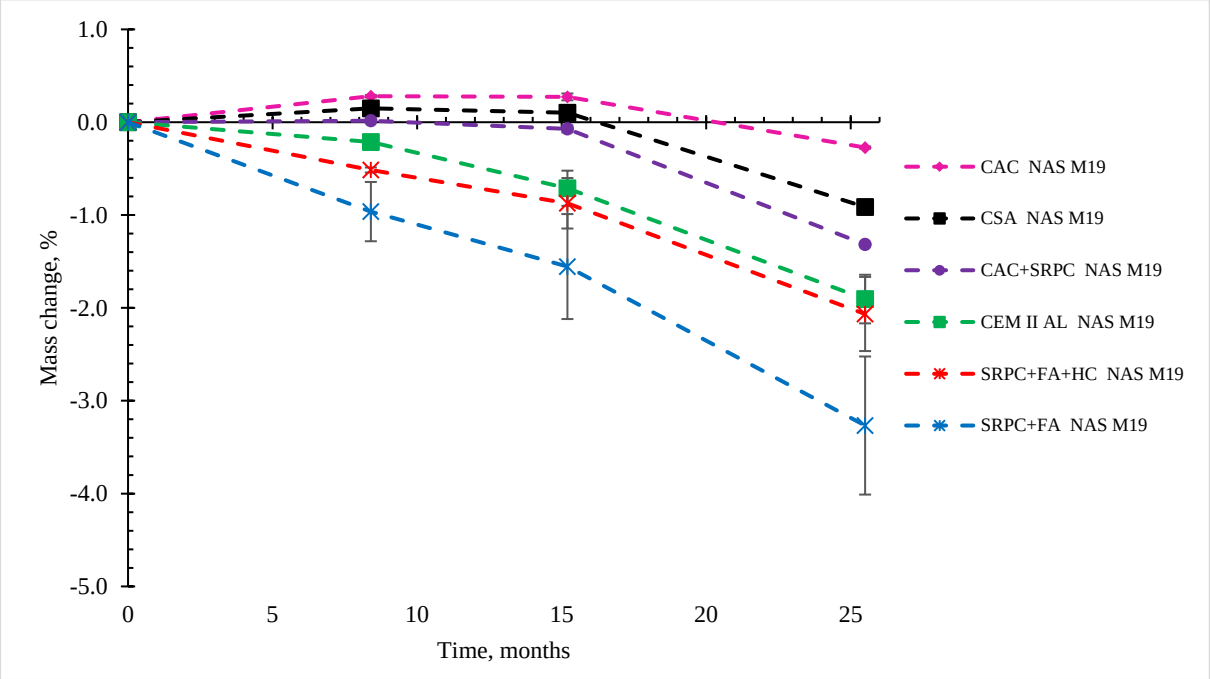


*Figure 5.33: Mass change of the UCT concrete specimens exposed at the NAS M19 for two years. Positive (+ve) values indicate mass gain, and negative (-ve) values indicate mass loss. The error bars represent the standard deviations of the mass change.*

### 5.3.5.2. UCT concrete mass changes at LPS

The UCT concrete mass changes with time at LPS are displayed in Figure 5.34. At this site, all concretes experienced significant mass loss already by eight months of exposure, which contrasts with the companion CAC and CSA concerts in the NAS M19 site, which experienced mass gain up to 15 months of exposure. Such significant mass losses were chiefly associated with aggressive BAC due to a high $H_2S$ gas concentration and the sewer hydraulic action of this site (see Chapter 4). As corrosion took place, corrosion products and protruding-lose aggregate particles were continuously removed by sewer hydraulic actions and hence renewed the exposed surface (Mori et al., 1992; Fernandes et al., 2012).

However, the aggregate fallout/loss depended on the cement and aggregate matrix deterioration rate. In the cases where cement deterioration was faster than aggregate deterioration, significant aggregate particles protruded and fell out, see Section 5.3.3.2. Consequently, a higher mass loss was experienced. In cases where both cement and aggregate matrix had an approximately equal deterioration rate, corroded surfaces showed a more uniform corrosion front, with less aggregate protrusion and fallout, hence less mass loss. This scenario is very evident in the alumina-based concrete, where less aggregate protrusion was observed, see Section 5.3.3.2.

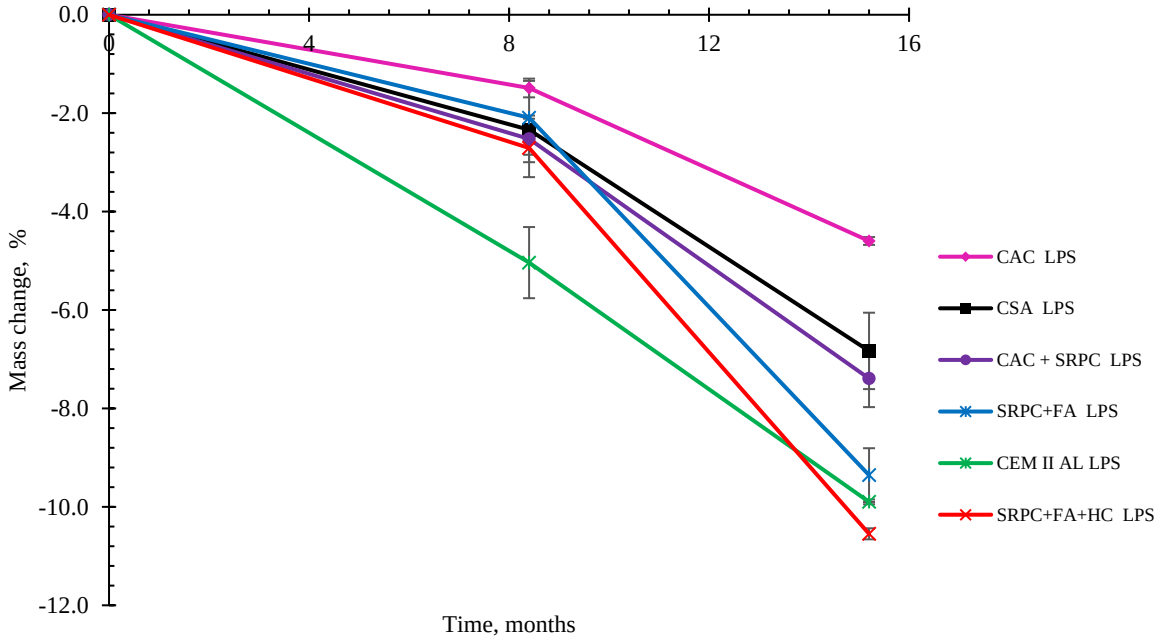


*Figure 5.34: Mass change of the UCT concrete specimens exposed at the LPS manhole for 15 months. Positive (+ve) values indicate mass gain, and negative (-ve) values indicate mass loss. The error bars represent the standard deviations of the mass change.*

At 8 months, CEM II AL showed the highest mass loss, while other concretes were clustered in a similar range, showing 2-3% mass loss. This indicates that, at this duration, CEM II AL had less resistance against sewer abrasion, which was not the case after 15 months of exposure. At 15 months of exposure, the mass loss from the lowest to the highest was as follows; CAC < CSA < CAC+SRPC < SRPC+FA < CEM II AL < SRPC+FA+HC. The ranking was not entirely similar to that of Portland-based concretes at NAS M19, where CEM II AL concrete performed better than SRPC+FA+HC and

SRPC+FA but with minor discrepancies. Further explanations regarding this contradictory performance are provided in Section 5.3.5.3.

### 5.3.5.3. Section discussion and closure

It is clear from the results presented and discussed above that a steady state condition has not been achieved even after two years of exposure. Comparing concrete performance at the NAS M19 and the LPS sites, it is evident that the combined corrosion and sewer hydraulic actions leading to significant aggregate fallout at the LPS site accelerated the rate of deterioration, see Figure 5.35.

In terms of binder systems, as observed in the visual observations, alumina-based binder systems exhibited better performance than Portland-based binder systems. For alumina-based concrete, CAC concrete showed superior performance, followed by the CSA, then a blend of CAC and SRPC at both sites. CSA's better performance in comparison with PC-based concretes in terms of mass loss corresponds with the results obtained by Yang et al. (2018) and Cao et al. (2022) under sulphuric acid attack

For Portland-based concrete, their performance depended significantly on the exposure site. At the NAS M19, CEM II AL performed better, followed by the SRPC+FA+HC, then SRPC+FA (supposedly, iron-based additive exhibited its abrasion resistance as indicated in the LH concrete Section 5.2). At the LPS site, concrete with an iron-based additive (HC) was expected to enhance the abrasion resistance of SRPC+FA concrete. However, the opposite was observed, as SRPC+FA+HC concrete showed the lowest performance in terms of mass change, followed by CEM II AL and SRPC+FA concrete. However, these results are insufficient to conclude more generally on concrete performance; thus, thickness change results must also be presented and discussed.

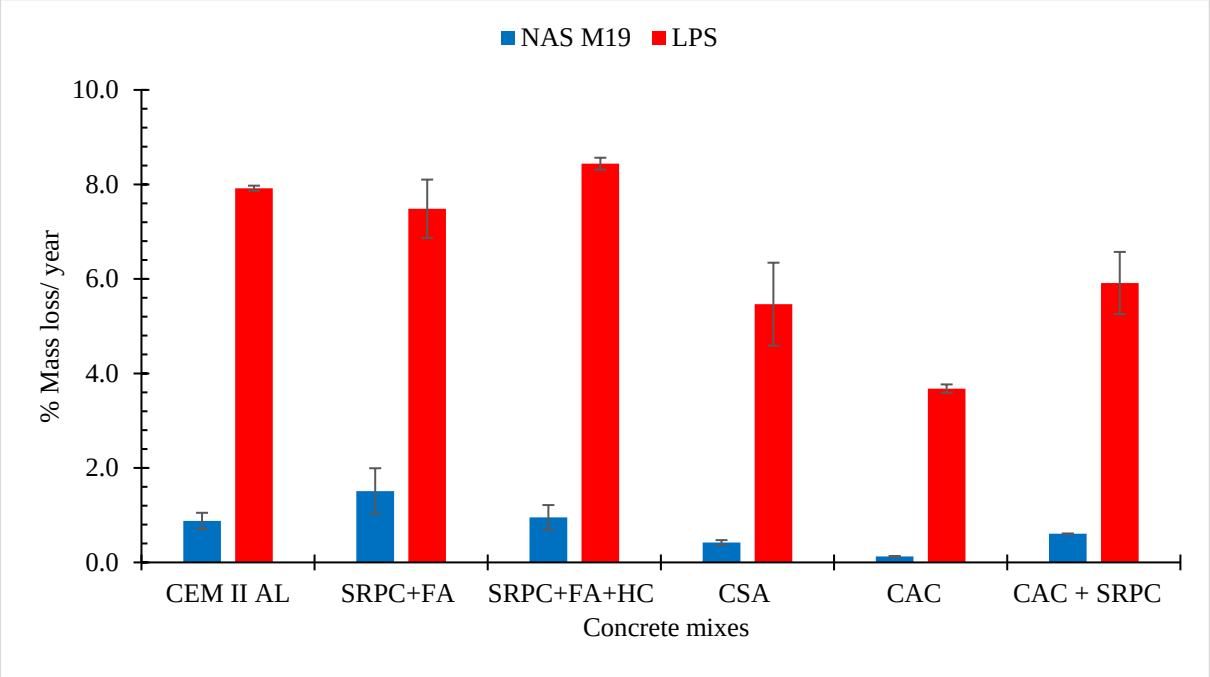


*Figure 5.35: Mass loss comparisons of the UCT concrete specimens subjected to the NAS M19 and the LPS site for 26 months and 15 months, respectively.*

### 5.3.6. UCT concrete thickness changes

The following section discusses the UCT concrete thickness changes at both NAS M19and LPS. More data on this section are presented in Appendix 0.

#### 5.3.6.1. UCT concrete thickness changes at NAS M19

Figure 5.36 illustrates thickness changes of the UCT concrete specimens exposed at the NAS M19 for 26 months. The figure indicates that all concretes had experienced thickness loss, accelerating after about 8 months of exposure, except CAC concrete which showed minor loss throughout the exposure duration. The thickness losses from the lowest to the highest were as follows; CAC<CAC+SRPC <CSA < SRPC+FA+HC < SRPC+FA <CEM II AL, see their magnitudes summarised in Table 5.6. Likewise, these results indicate that alumina-based concretes performed better than Portland-based concrete.

In terms of Portland-based concrete, 2.78 ± 0.47 mm of CEM II AL, 2.21 ± 0.69 mm of SRPC+FA, and 1.99 ± 0.30 mm of SRPC+FA+HC were lost within 26 months, which is equivalent to average corrosion rates of 1.78 ± 0.31 mm/yr, 1.02 ± 0.45 mm/yr, and 0.92 ± 0.20 mm/yr, respectively. The rate indicates that SRPC+FA with and without iron-based additives had a minor difference compared to the LH concrete observations, with SRPC+FA having a slightly higher rate than SRPC+FA+HC. Since the compaction and quality of UCT concrete were superior to LH concretes, it can be confirmed that iron-based additive (HC) contributes little to improving concrete resistance against BAC without sewer hydraulic actions. On the contrary, CEM II AL showed significant thickness loss, while it had lower mass loss compared to other Portland-based concretes in Section 5.3.5.1. This implies that it had significant corrosion products, i.e., gypsum or ettringite, attached or deposited on the exposed layer, that contributed to lower mass loss.

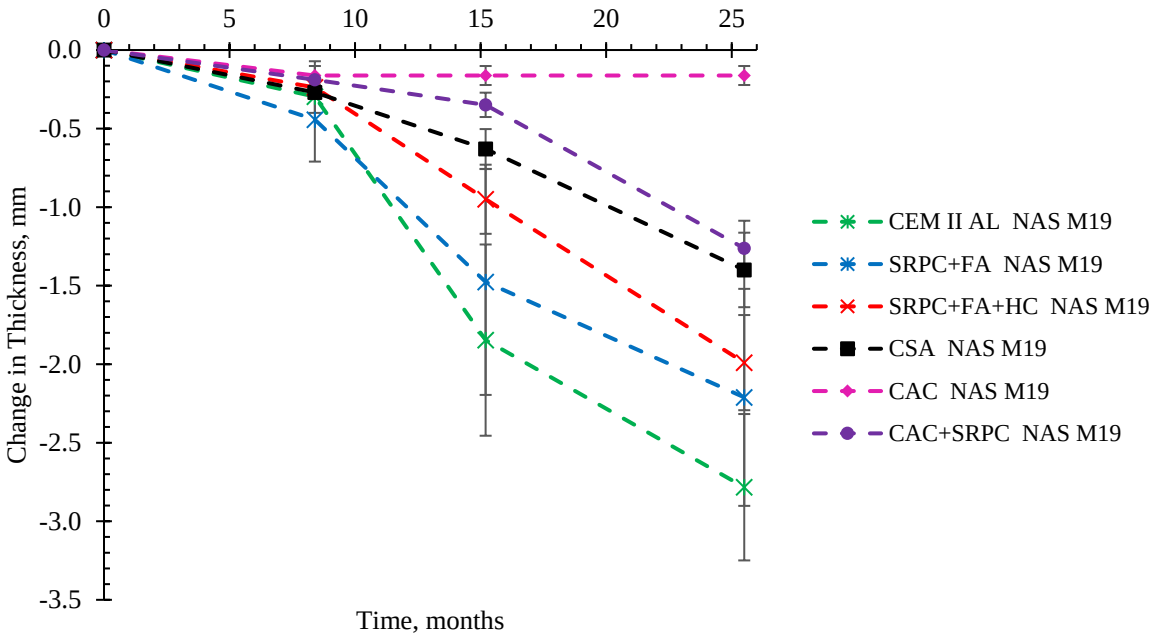


*Figure 5.36: Thickness of the sample specimens exposed at the NAS M19 for 26 months. Positive (+ve) values indicate thickness gain, and negative (-ve) values indicate thickness loss. The error bars represent the standard deviations of the thickness change.*

For alumina-based concrete, 1.40 ± 0.24 mm of CSA, 1.26 ± 0.18 mm of CAC+SRPC, and 0.16 ± 0.06 mm of CAC were lost on site, which is equivalent to average corrosion rates of 0.65 ± 0.13 mm/yr, 0.07 ± 0.04 mm/yr, and 0.58 ± 0.12 mm/yr, respectively. Despite CAC+SRPC and CSA concrete exhibiting no mass loss up to 15 months of exposure, they experienced thickness loss. This implies that the mass gain due to the formation of secondary cement or corrosion products as the result of moisture and sulphuric acid absorption and organic matter penetration compensated for the mass loss due to sewer corrosion.

#### 5.3.6.2. UCT concrete thickness changes at LPS

At LPS, all concretes exhibited continuous thickness loss after 8 months of exposure as shown in Figure 5.37. The thickness losses from the lowest to the highest were as follows; CAC< CAC+SRPC < CSA < SRPC+FA < SRPC+FA+HC < CEM II AL, see the magnitude in Table 5.6. These results prove that alumina-based concretes demonstrated superior performance than Portland-based concrete regardless of the exposure site.

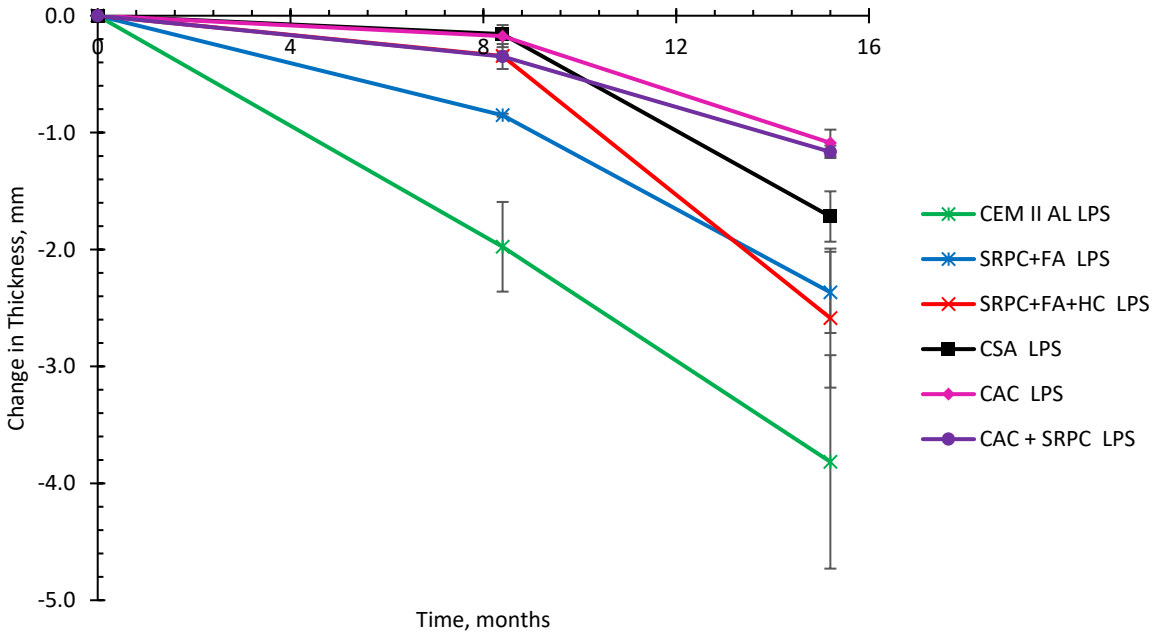


*Figure 5.37: Thickness of the sample specimens exposed at the LPS manhole for 15 months. Positive (+ve) values indicate thickness gain, and negative (-ve) values indicate thickness loss. The error bars represent the standard deviations of the thickness change.*

For Portland-based concrete, 3.82 ± 0.91 mm of CEM II AL, 2.37 ± 0.35 mm of SRPC+FA, and 2.59 ± 0.59 mm of SRPC+FA+HC were lost within 15 months, which is equivalent to average corrosion rates of 3.05 ± 1.03 mm/yr, 1.89 ± 0.40 mm/yr, and 2.07 ± 0.67 mm/yr, respectively. As in the NAS M19, CEM II AL depicted the highest thickness loss, followed by SRPC+FA with and without iron-based additive (HC). This implies that fly ash enhances PC concrete performance, while the significance of iron-based additives is contradicting. At 8 months of exposure, SRPC+FA+HC concrete seemed to perform better than SRPC+FA concrete, while at 15 months, the opposite was observed. This

observation might imply that the abrasion resistance of iron-based additives does not contribute greatly to long-term performance under both sewer hydraulic erosion and BAC.

However, for alumina-based concrete, 1.72 ± 0.22 mm of CSA, 1.16 ± 0.05 mm of CAC+SRPC, and 1.09 ± 0.11 mm of CAC were lost on site after 15 months of exposure, which is equivalent to average corrosion rates of 1.38 ± 0.25 mm/yr, 0.93 ± 0.06 mm/yr, and 0.87 ± 0.13 mm/yr, respectively. CAC and CSA concrete at 8 months had approximately similar thickness loss values, while CAC+SRPC concrete had a slightly higher value. At 26 months of exposure, CAC and CAC+SRPC concrete had similar thickness losses, while CSA indicated a significantly higher value. Nonetheless, CAC concrete illustrated the best performance at both sites.

### 5.3.7. Corrosion rate discussion

Biogenic acid corrosion in a live sewer environment is generally a slow process (Wells & Melchers, 2014b; Grengg et al., 2017; Grengg, Mittermayr, Ukrainczyk, Koenders, et al., 2018; Khan et al., 2019), which requires long-term study of several years to determine a steady and roughly constant average corrosion rate (Wu, Hu & Liu, 2018). Therefore, a summary of average corrosion rates of the UCT concrete presented in Table 5.6 only indicates the estimated average corrosion rates of sewer concrete at the initial corrosion stage (i.e., 15 and 26 months of exposure at LPS and NAS M19, respectively), which may change before approaching a constant value in long-term exposure.

*Table 5.6: Thickness losses and equivalent average corrosion rates of the UCT concrete specimens subjected to the NAS M19 and the LPS site for 26 months and 15 months, respectively.*

| Concrete | Thickness loss, mm | | | | | |
|---|---|---|---|---|---|---|
| | **CEM II AL** | **SRPC+FA** | **SRPC+F+HC** | **CSA** | **CAC** | **CAC+SRPC** |
| NAS M 19 at 26 months, mm | 2.78 ± 0.47 | 2.21 ± 0.69 | 1.99 ±0.30 | 1.40 ± 0.24 | 0.16 ± 0.06 | 1.26 ± 0.18 |
| Corrosion rate, mm/yr | 1.28 ± 0.30 | 1.02 ± 0.45 | 0.92 ± 0.20 | 0.65 ± 0.13 | 0.07 ± 0.04 | 0.58 ± 0.12 |
| LPS at 15 months, mm | 3.82 ± 0.91 | 2.37 ± 0.35 | 2.59 ± 0.59 | 1.72 ± 0.22 | 1.09 ± 0.11 | 1.16 ± 0.05 |
| Corrosion rate, mm/yr | 3.05 ± 1.03 | 1.89 ± 0.40 | 2.07 ± 0.67 | 1.38 ± 0.25 | 0.87 ± 0.13 | 0.93 ± 0.06 |

Based on these rates, concretes at the LPS manhole exhibited higher average corrosion rates than those at the NAS M19, which was associated with a high $H_2S$ gas concentration and sewer hydraulic actions, which also concur with their mass change results, as well as with the LH concrete results in Section 5.2. Sewer drying and wetting cycles at the LPS manhole influenced a continuous removal of the corroded layer and protruding aggregate particles, hence the renewal of the exposed surface, which consequently accelerated the deterioration, see Figure 5.38. However, aggregate fallout (in this case, good-quality dolomite) depends largely on the deterioration rate of the binder system. For binders with higher deterioration rates, significant dolomite aggregate fallout is experienced, and vice versa. In contrast, concretes exposed to NAS M19 did not experience the same impact. Here, concrete experienced corrosion due to BAC, without losses due to erosion, which resulted in substantial microbial activities for acid production and subsequent corrosion product build-up, see Figure 5.38. The corrosion products

were occasionally removed on site due to gravity and occasional sewer flooding and, in the laboratory, during the cleaning of specimens for bulk measurements.

In addition, comparing the average corrosion rate of UCT concrete (Table 5.6) and LH concrete (Table 5.4), it is clear that LH concretes had higher average corrosion rates at both sites, implying that poor quality concrete accelerates the deterioration mechanisms. However, it should be noted that different aggregate types were used, which somehow contributed to the corrosion rate, i.e., the solubility of calcite aggregate is higher than dolomite aggregate. Because of these two contributory factors (concrete quality and solubility of calcite), it was challenging to articulate the contribution of binder systems in LH concrete.

Furthermore, Portland-based concrete generally had a higher corrosion rate than alumina-based concrete, with CEM II A-L concrete having the highest rate and CAC concrete the lowest. With these findings, the performance of sewer concrete can be scaled between two concretes: CEM II AL and CAC of this study. Figure 5.39 indicates the performance of the UCT concrete subjected to two sewer sites relative to CEM II AL concrete performance. Their performances were obtained after normalising the corrosion rate of each concrete with that of the CEM II A-L concrete at each exposure site, where 100% indicates the resistance potential of CEM II AL at each site, and higher values indicate increased resistance.

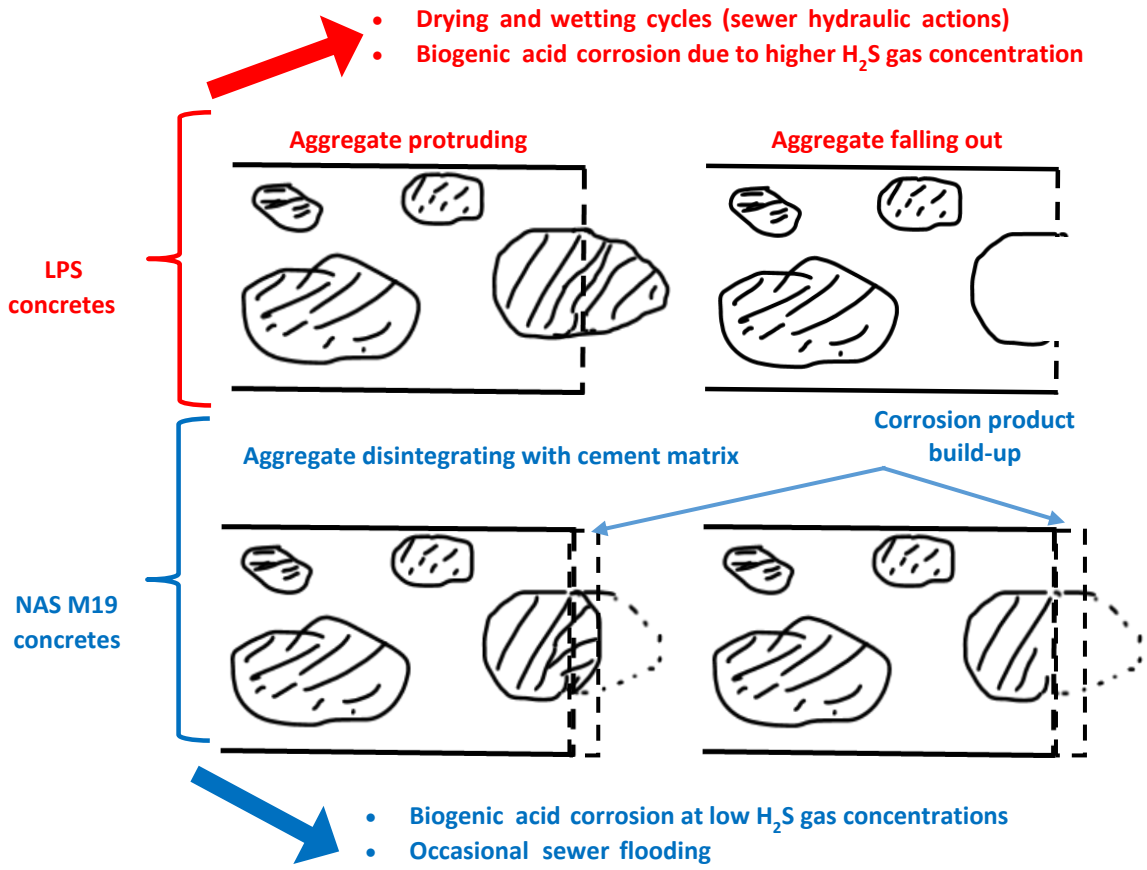


*Figure 5.38: Diagram illustrating the corrosion mechanisms of concrete specimens exposed to LPS and NAS M19. Chapter Chapter 4 describes the sewer environmental conditions of LPS and NAS M19.*

Since all concrete had similar constituent compositions, it is assumed that the increased percentage points out the influence of binder systems in resisting sewer aggressivity. At NAS M19, the performance of SRPC+FA concrete, relative to CEM II AL, is 23 ± 17%; SRPC+FA+HC is 28 ± 2%; CSA is 50%; CAC+SRPC is 54 ± 2%; while CAC is 94 ± 2% higher than CEM II AL concrete. At LPS, the performance of SRPC+FA concrete is 37 ± 9%; SRPC+FA+HC is 32 ± 1%; CSA is 54 ± 8%; CAC+SRPC is 68 ± 9%; while CAC is 71 ± 6% higher. Based on this, it can be concluded that

i) CAC binder system has the highest performance, and CEM II AL has the lowest,
ii) a blend of CAC and SRPC improves the performance of concrete when compared to CSA and SRPC-based concrete,
iii) the performance of the CSA binder ranks between that of CAC and SRPC-based concrete,
iv) incorporating fly ash in the Portland-based concrete increases the resistance against biogenic acid attack, and
v) iron-based additives have little contribution to improving the resistance of SRPC-based concrete
vi) according to the literature, SRPC cement performs well in sulphate environments. However, this attack contrasts with sulphuric acid environments since the nature of the attack differs.

The following section presents the microstructure analysis results of the UCT concrete to understand the influencing factors behind these performances.

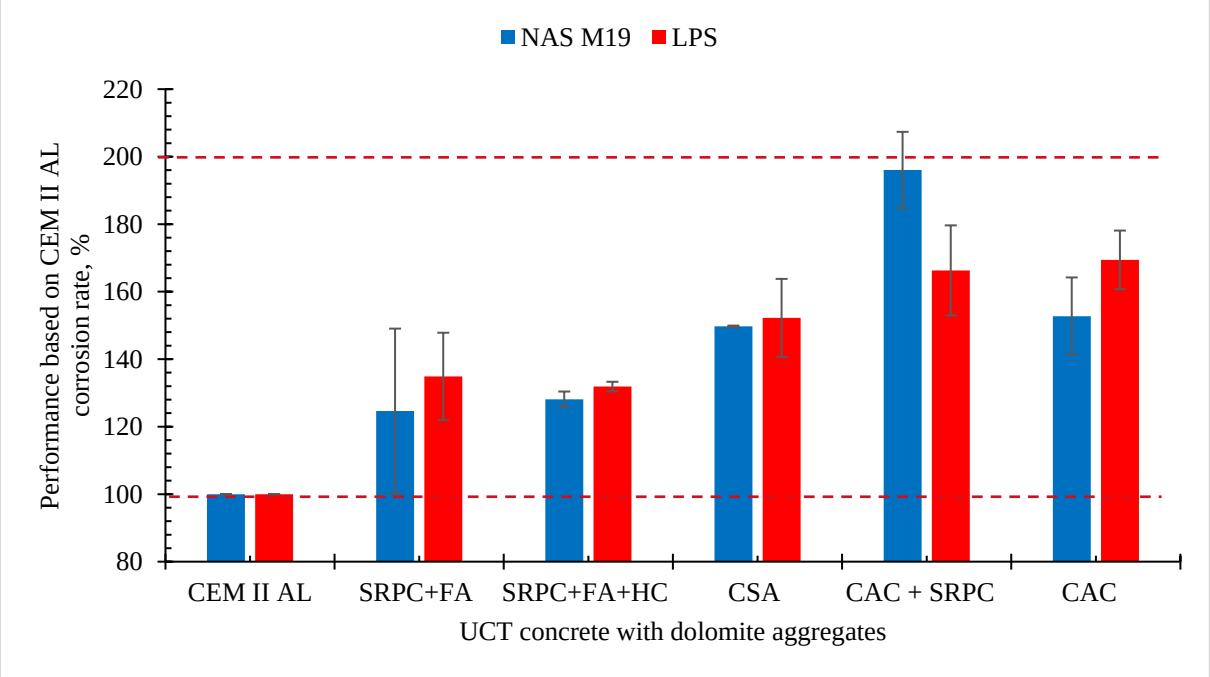


*Figure 5.39: Performance indicator of the UCT concretes subjected to two sewer sites, based on CEM II AL concrete*

### 5.3.8. UCT concrete BAC microstructural analysis at NAS M19

The microstructural analysis discusses the UCT concrete specimens subjected to NAS M19 for 26 months (i.e., about two years). These concretes were given better compaction than the LH concretes.

Thus, the zones (i.e., intact zone, transition zone and deteriorated zone) were distinctly differentiated, mainly by observing porosity increase due to deterioration across the section and the evolution of mineralogical phases. Also, it should be noted that the UCT concretes used crushed coarse and fine dolomite aggregates and siliceous pit sand, which were different from those used for the LH concretes (calcite aggregates). This section, therefore, discusses three microstructural analyses and results, i.e., SEM-BSE images, QEMSCAN analysis, and XRD analysis for each concrete mix, with similar principles as in Section 5.2.6.

#### 5.3.8.1. CEM II AL concrete

*5.3.8.1.1. SEM-BSE images*

The SEM-BSE image for CEM II AL concrete after 26 months of exposure to NAS M19 is shown in Figure 5.40. Figure 5.40 (A) shows the intact and altered zone. The intact zone is very dense, with a minimum porosity mainly due to hydration. The altered zone is very porous with fragmented fine particles, see Figure 5.40 (B), detaching from the intact cement matrix. The coarse aggregate particle contains a distinct crack, which may cause the fractured part to detach, thus exposing a newly aggregate surface for attack. The altered zone depth is about 2.1 mm in the cement matrix and about 1.1 mm in the aggregate matrix, measured from where the crack is observed.

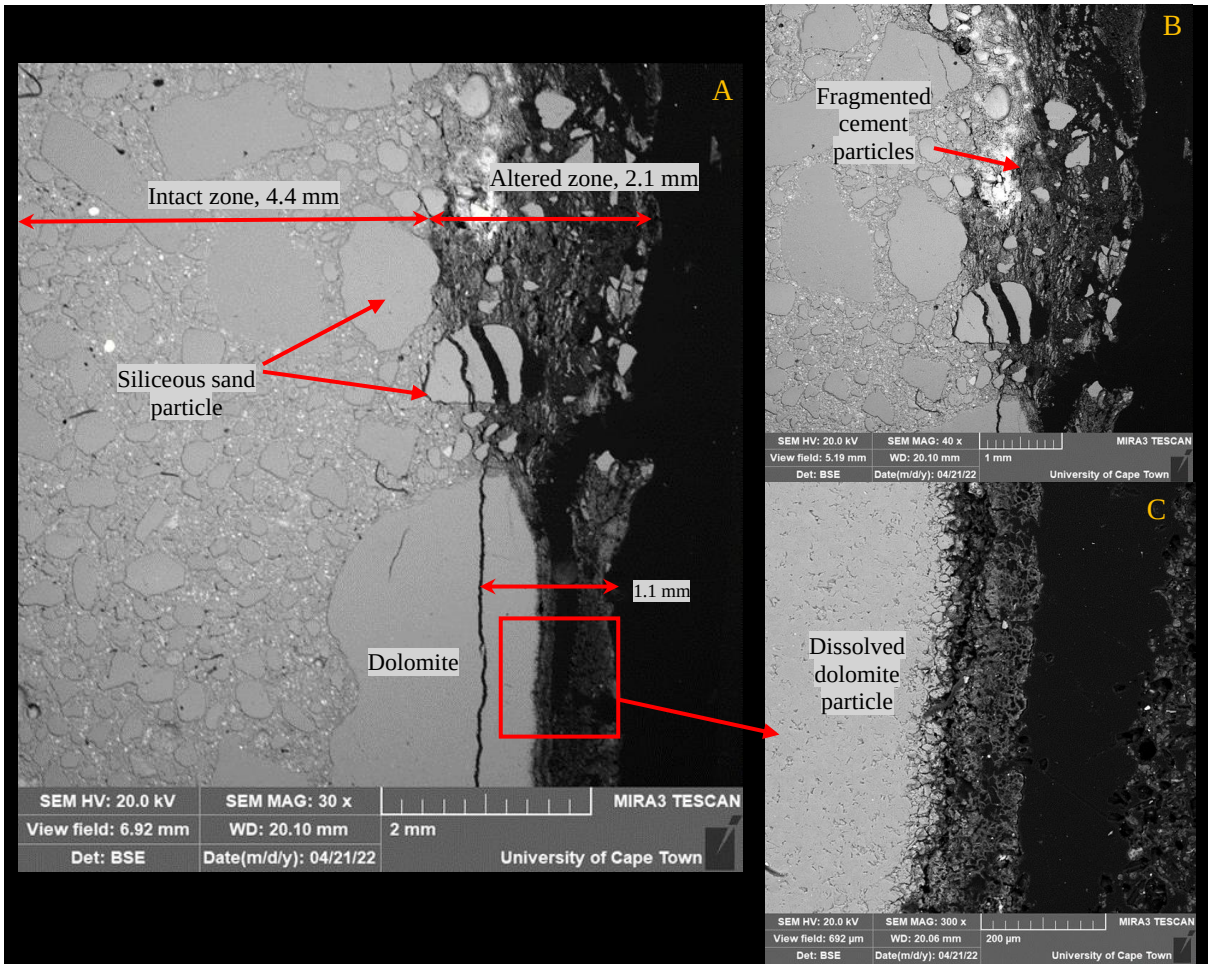


*Figure 5.40: SEM-BSE image for CEM II AL concrete after two years of exposure at NAS M19*

Coarse aggregate particles, i.e., dolomite, disintegrate in three layers (see Figure 5.40 (C). The first layer near the exposed surface is weak and very porous, followed by a disintegrated layer, but it exhibits better integrity and cohesiveness. The final layer is separated by a crack from the intact aggregate particle, with its surface slightly dissolved, fractured, and disintegrated. The disintegration of coarse particles, i.e., dolomite, differs from the calcite aggregate particles observed in the LH concrete, see Appendix L. Calcite reacts with the acid to form gypsum only. Dolomite, on the other hand, consists of magnesium and calcium carbonate, which react with acid to form gypsum and magnesium sulphate (MgSO4) but does not precipitate due to its high solubility (Cao et al., 2020). However, both are calcareous aggregates. They decelerate the corrosion rate of Portland-based (and other) concretes by dissolving and disintegrating along with the cement matrix deterioration, resulting in a slower rate and an even and uniform corroded surface (Pather, Ekolu & Quainoo, 2021).

*5.3.8.1.2. QEMSCAN analysis*

Figure 5.41 shows the QEMSCAN analysis of CEM II AL concrete from the UCT concrete specimens subjected to the NAS M19 for 26 months. As the legend shows, the concrete microstructure mainly consists of dolomite and quartz (48.8% and 20.7%, respectively), which is associated with about 80% of the concrete composite being the aggregate component. In the cement matrix, the percentage weights of mineralogical phases from the highest to the lowest were 11.6% Ca-silicate, 10.3% gypsum, 5.0% Portlandite, 1.8% Fe/Al silicate, 1.1% Ca-aluminate, 0.4% Mg-silicate, 0.2% gibbsite, and 0.1% ettringite.

Under QEMSCAN analysis, the intact and altered zones (transition and deteriorated zone) were distinguished based on the mineralogical distribution. It was evident that the intact zone was dense, mainly containing calcium silicate and portlandite in the cement matrix. Unlike the SEM analysis, in this analysis, the transition zone was observed between the intact zone and the deteriorated zone, mainly consisting of a coherent layer of gypsum and Mg-silicate deposits similar to LH concrete observation. This consolidates the possibility of magnesium ion migration with acid penetration in the transition zone, as calcium silicate and portlandite decalcify with acid penetration to form gypsum and Mg-silicate.

In the deteriorated zone, quartz was significantly observed; some particles were detaching from the transition zone, some were cracked, and some finer particles were widely distributed in the deteriorated zone. The finer quartz particles were associated with a silica-rich layer (Hudon, Mirza & Frigon, 2011) following Ca-, Al- and Mg- silicate disintegration, as it was challenging to map them separately. Additionally, more Fe/Al-silicates were observed in the deteriorated zone, while gibbsite and ettringite were insignificant.

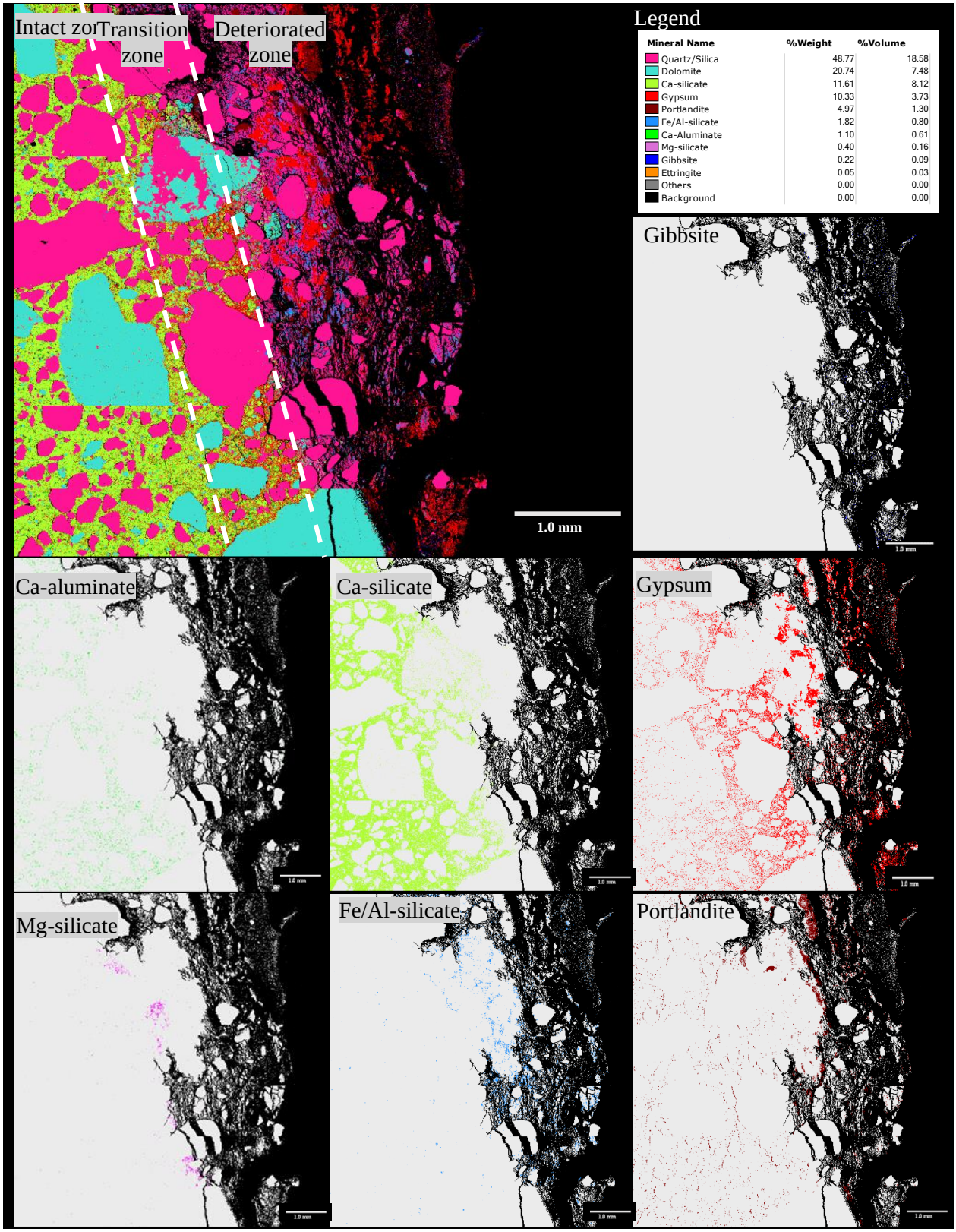


*Figure 5.41: QEMSCAN analysis of CEM II AL concrete from the UCT concrete specimens subjected to the NAS M19 for 2 years. The first-row image indicates a general distribution of concrete mineralogical phases on the concrete cross-section based on the SEM-BSE image, with the legend indicating the colour code, percentage weight and percentage volume of each mineral over the cross-section. Other images depict the distribution of selected phases on the cross-section.*

Therefore, as expected, the main cement phases before the acid attack are calcium silicate and portlandite, which contain some aluminium, iron, and magnesium oxides. Once sulphuric acid is generated on the exposed concrete surface, it decalcifies calcium silicate and portlandite (Okabe et al., 2007; Grengg, Mittermayr, Ukrainczyk, Koenders, et al., 2018). As a result, calcium ions react with sulphate to form gypsum, magnesium ions migrate into the transition zone to react with silicate, then iron and aluminium ions in the deteriorated zone form Fe/Al-silicate, while some ions form gibbsite. Thus, gypsum is observed in the transition zone along with Mg-silicate, with the deteriorated zone exhibiting gibbsite and Fe/Al-silicate. Thus, the poor performance of CEM II A-L concrete is associated with decalcifying calcium-containing phases.

*5.3.8.1.3. XRD analysis*

The XRD analyses shown in Figure 5.42 confirm that the intact zone consists of portlandite and calcium silicate in the cement matrix, as well as dolomite and quartz phases from the aggregates. After acid penetration, the exposed surface and 100 µm depth from the exposed surface indicate significant gypsum peaks, which decrease at 200 µm depth. Some Mg silicate peaks are also observed in the altered layer, as in the QEMSCAN analysis.

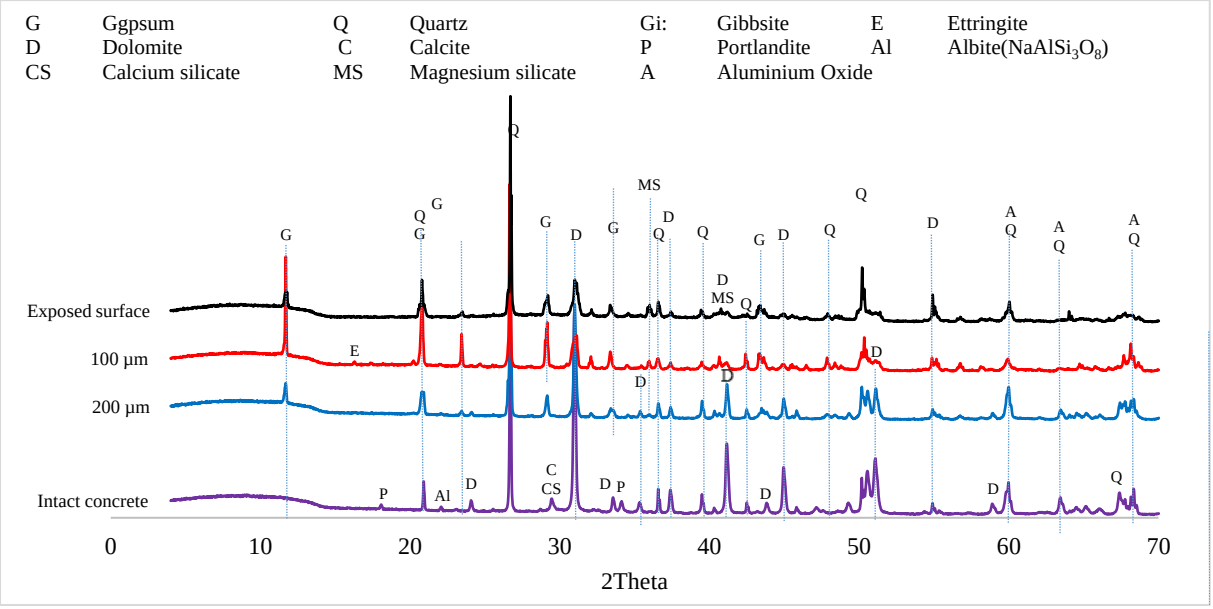


*Figure 5.42: XRD analysis results of the CEM II AL concrete from the UCT concrete specimens subjected to the NAS M19 for 2 years. The results are presented in four layers, i.e., the exposed surface, 100 µm and 200 µm from the exposed surface, and the intact concrete.*

### 5.3.8.2. SRPC+FA concrete

**i.** *SEM-BSE images*

Figure 5.43 shows the SEM-BSE image for SRPC+FA concrete after 26 months of exposure at NAS M19. Figure 5.43 (A) indicates a very dense concrete microstructure, with fly ash particles and some voids observed in the intact zone. In the altered zone, the microstructure is very porous with fragment cement particles and some loose aggregate particles. Generally, the maximum depth of the altered zone is about 1.7 mm, slightly lower than that observed in the CEM II A-L concrete. The corrosion front

seems even in the cement matrix with siliceous (quartz) aggregates. In contrast, a large piece of dolomite aggregate protrudes while dissolving on its exposed surface (observed in the QEMSCAN image Figure 5.44). Also, under this analysis, two sub-zones (deteriorated and transition zone) are not easily distinguished.

Figure 5.43 (B) indicates a fly ash particle obtained from the intact zone, while Figure 5.43 (C) indicates a fly ash particle obtained from the altered zone. It is clear that in the altered zone, after acid exposure, fly ash particle shapes are less distinct due to the leaching of metal ions, as observed in (Steenari, Schelander & Lindqvist, 1999; Blanco, Garcia & Ayala, 2005; Losey et al., 2018). Fly ash behaviours in the UCT concrete after the attack is not similar to that in the LH concrete, see Figure 5.10, possibly due to the concrete surface pH. That is, SRPC+FA from LH concrete had average surface pH of about 4.0 and that from UCT concrete was about 2.36 after about 2 years of exposure. This indicates that at low pH below 3, fly ash particle also disintegrates, resulting in the leaching of metals such as Al, Fe, and Mg (Losey et al., 2018).

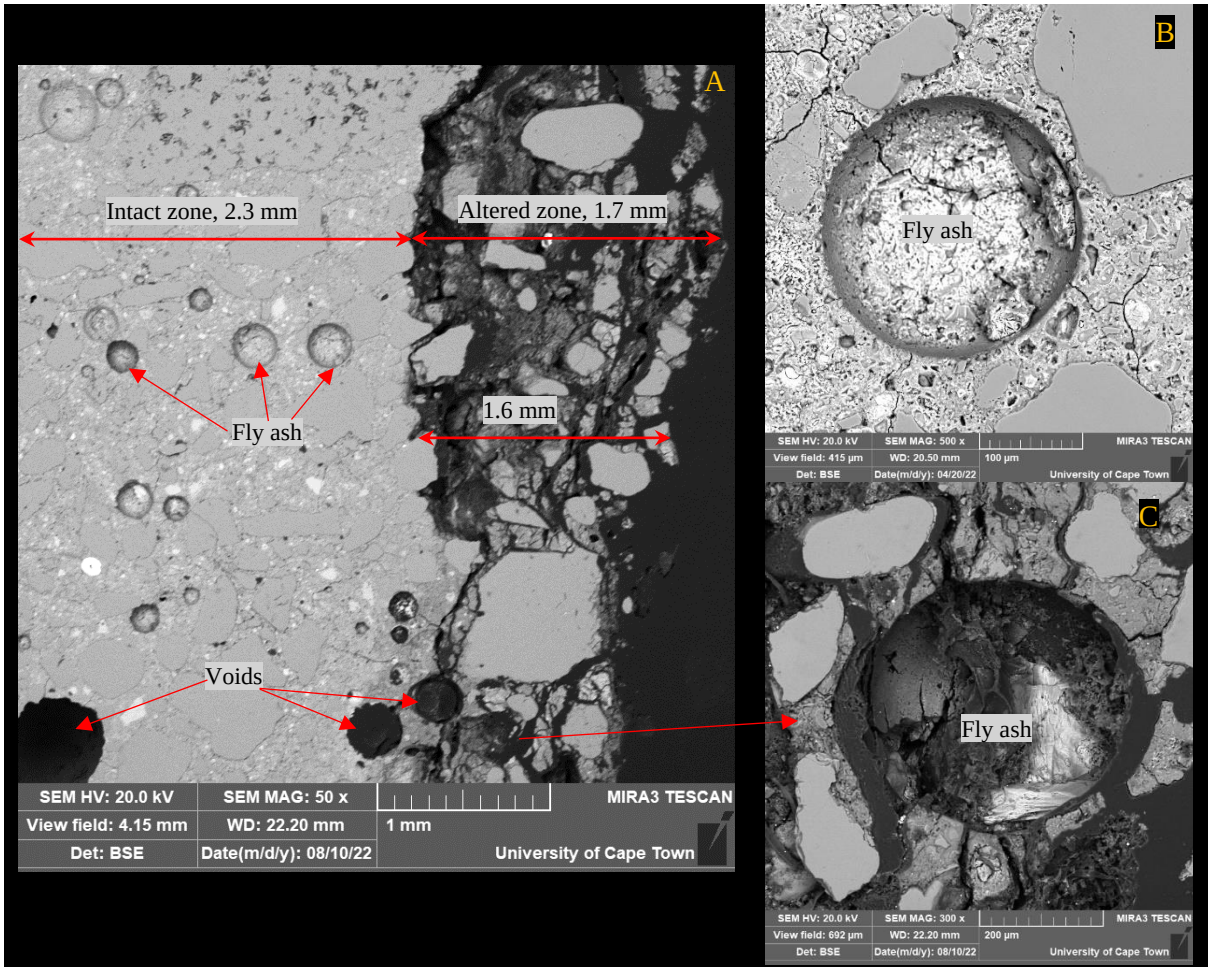


*Figure 5.43: SEM-BSE image for SRPC+FA concrete after two years of exposure at NAS M19*

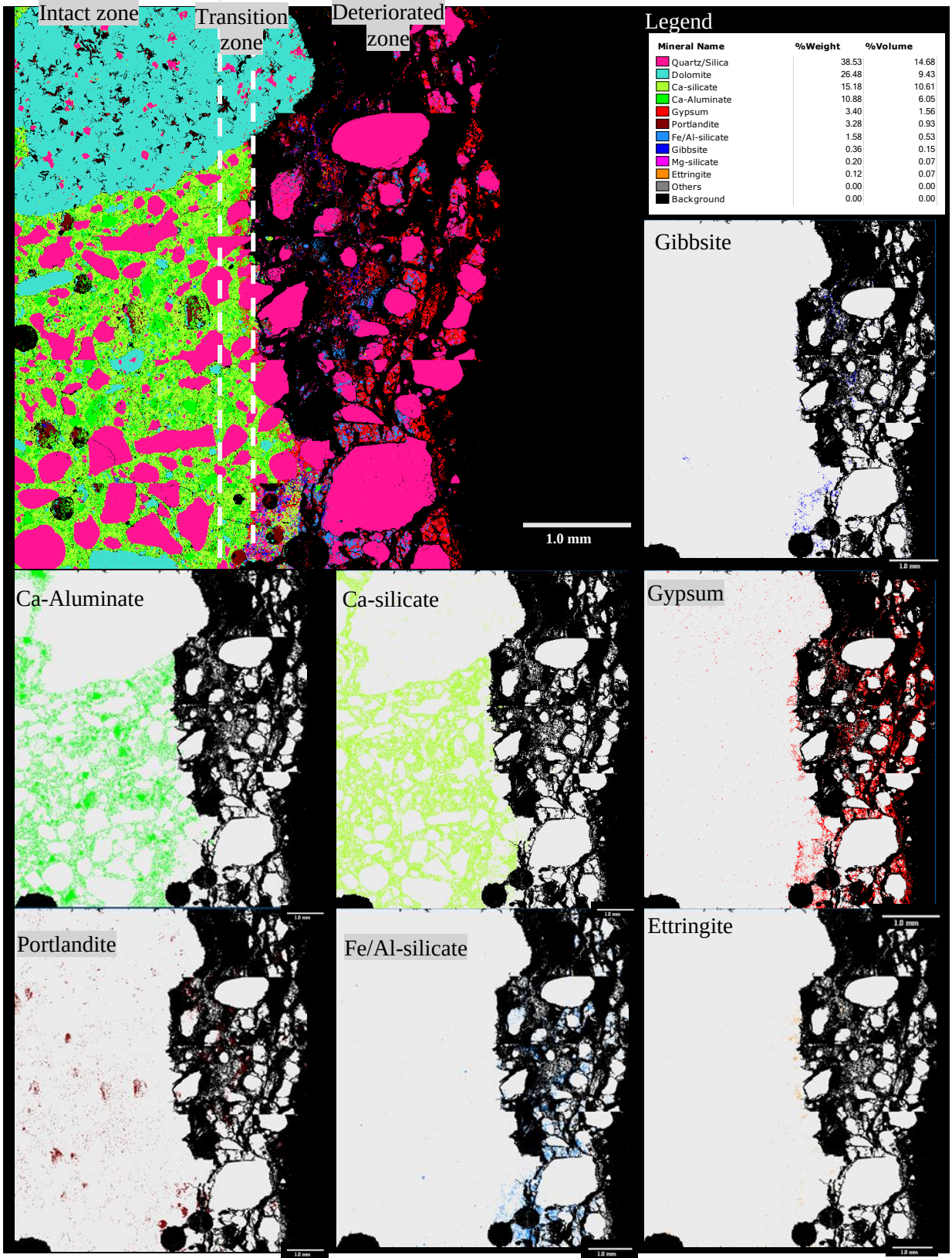


*Figure 5.44: QEMSCAN analysis of SRPC+FA concrete from the UCT concrete specimens subjected to the NAS M19 for 26 months. The first image in the first row indicates a general distribution of concrete mineralogical phases on the concrete cross-section based on the SEM-BSE image, with the legend indicating the colour code, percentage weight and percentage volume of each mineral over the cross-section. Other images depict the distribution of selected minerals on the cross-section*

*5.3.8.2.1. QEMSCAN analysis*

The QEMSCAN analysis of SRPC+FA concrete is presented in Figure 5.44. Its concrete microstructure also contained a high composition of dolomite and quartz from the aggregate (26.5% and 38.5%, respectively). The cement matrix consisted of a higher percentage of Ca-silicate of about 15.2%, followed by 10.9% Ca-aluminate, 3.4% gypsum, 3.3% portlandite, 1.6% Fe/Al-silicate, 0.5% gibbsite, 0.2% Mg-silicate, and 0.1% ettringite.

With mineralogical distribution as indicated the transition zone was identified although thinner than the deteriorated zone. The intact zone consists mainly of Ca-silicate, Ca-aluminate, and portlandite. Ca-aluminate in this concrete was significantly higher than in the CEM II A-L concrete due to the 20% fly ash content, with about 34% $Al_2O_3$. The transition zone consists of some Mg-silicate (not shown), minor ettringite, gibbsite and partly gypsum, although at the lowest concentration. The deteriorated zone consists of gypsum as the primary corrosion product, Fe/Al silicate phases and partly gibbsite. Fe/Al silicate phase probably originated from fly ash particle disintegration (Losey et al., 2018).

The deterioration mechanism of this concrete differs from that of CEM II AL (UCT concrete) and LH concrete with SRPC+FA. Its concrete matrix dissolves completely immediately after it contacts the acid, resulting in a uniform corrosion front and a thin transition zone, unlike the CEM II AL and LH concrete with SRPC+FA, where the transition zone was visually broader with a defined layer of gypsum and Mg silicate. It is possible that a significant amount of CaO in the CEM II AL concrete and the LH concrete with SRPC+FA, mainly from calcite, might be the reason behind a broad transition zone. In conclusion, the performance of SRPC+FA concrete (UCT concrete) might be associated with the presence of alumina, which has a high neutralisation capacity than CaO.

*5.3.8.2.2. XRD analysis*

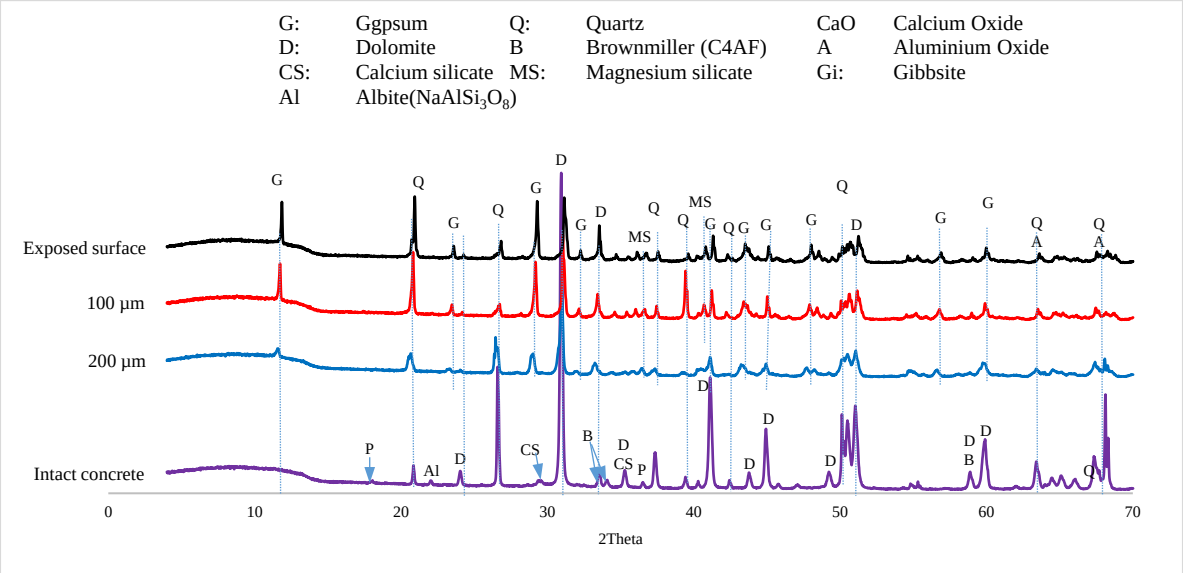


*Figure 5.45: XRD analysis results of the SRPC+FA concrete from the UCT concrete specimens subjected to the NAS M19 for 2 years. The results are presented in four layers, i.e., the exposed surface, 100 µm and 200 µm from the exposed surface, and the intact concrete.*

The XRD analysis confirms the presence of portlandite, calcium silicate and ca- aluminate ($C_4AF$) in the intact zone. However, their peaks are less intense, see Figure 5.45. In the altered zone, i.e., the exposed surface, 100 µm and 200 µm, indicates the presence of gypsum as the deterioration deposits, and its peaks decrease with depth from the exposed surface. Dolomite and quarts are also observed throughout the depth, with MS (Mg-silicate) being observed mainly in the exposed surface and 100 µm layer.

### 5.3.8.3. SRPC+FA+HC concrete

*5.3.8.3.1. SEM-BSE images*

The SEM-BSE image for SRPC+FA+HC concrete after 26 months of exposure at NAS M19 is shown in Figure 5.46. As observed in the previous concrete, the altered zone was differentiated from the intact zone with porosity increase and loss of cement matrix cohesion. The altered depth herein is about 2.8 mm, significantly broader than CEM II AL and SRPC+FA concrete (Figure 5.46 (A).

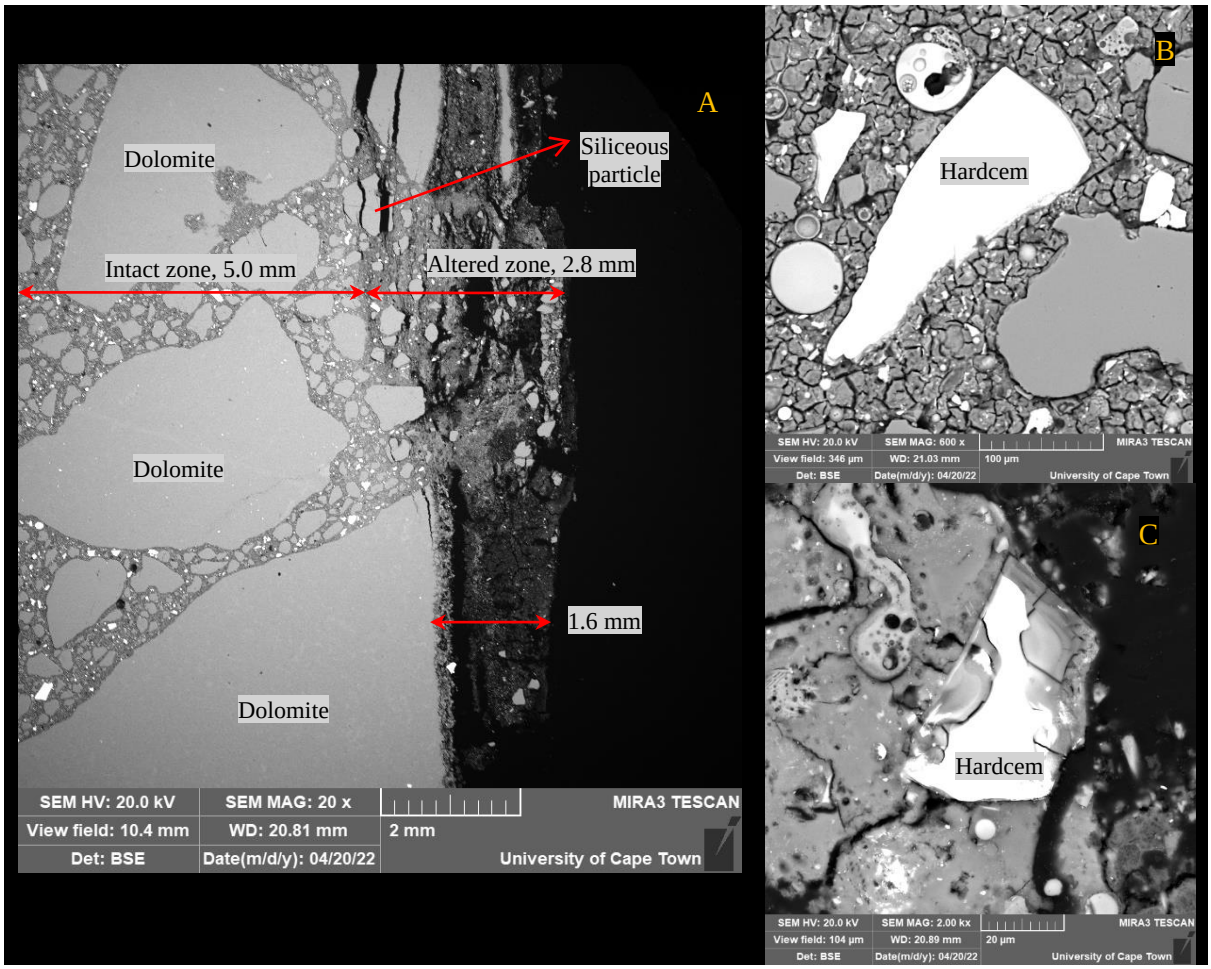


*Figure 5.46: SEM-BSE image for SRPC+FA+HC concrete after two years of exposure at NAS M19; B showing iron-based additive particle (Hardcem) in the intact zone, and C in the deteriorated zone*

As in the previous concrete, the behaviour of aggregate particles is similar, where dolomite aggregate disintegrates uniformly on the exposed surface to form gypsum (see QEMSCAN results in Figure 5.47). Siliceous sand particles appeared cracked, loose and detached from the cement matrix in the altered zone. The crack through siliceous particles originated from dolomite aggregate as it disintegrated due

to acid penetration. The corrosion front herein was non-uniform since the deterioration rate of the cement matrix was higher than that of the aggregate (dolomite).

SRPC+FA+HC concrete had similar features as the SRPC+FA concrete but with about 11% addition of iron-based additive particles. These particles were brighter and distributed in the entire concrete microstructure. In the intact zone, the intact particles showed no signs of dissolution or participation in the hydration process (see Figure 5.46 (B). However, in the altered zone, see Figure 5.46 (C), the particle seems to dissolve, which was not observed in the LH concrete (see Figure 5.13 (C)). Iron-based additives possibly dissolve at a very low pH below 3 since the surface pH of the SRPC+FA+HC from LH concrete was 3.6 and from UCT concrete was 2.80.

*5.3.8.3.2. QEMSCAN analysis*

QEMSCAN analysis of SRPC+FA+HC concrete is presented in Figure 5.47, with 54.8% dolomite and 17.7% quartz. Since its concrete microstructure had a significant amount of aggregate, examining the influence of its cement matrix was challenging. The cement matrix consisted of a higher percentage of gypsum of 11.6%, then Ca-silicate of 6.3%, followed by 2.9% Al-silicate, 2.7% ca-aluminate, 2.3% portlandite, 1.0% Mg-silicate, 0.4% Fe-phases, 0.2% ettringite, and 0.1% gibbsite.

Like LH concrete with SRPC+FA+HC, iron-based additives herein were denoted as Fe-phases. The dissolution of these Fe-phases in the concrete microstructure was minimal; hence their influence chemically was not observed. In the intact zone, the main cementitious phases were Ca-silicate and ca-aluminate and portlandite. In the transition zone, gypsum and Mg-silicate were highly observed with some minor ettringite and gibbsite. Mg-silicate in the transition was also observed in the CEM II AL concrete, yet its role is not well understood. In the deteriorated zone, the concrete consisted of Al-silicate along with gypsum.

*5.3.8.3.3. XRD analysis*

The XRD analysis confirms the presence of portlandite, calcium silicate, ca-aluminate (C4AF), and some goethite (FeOOH) in the intact zone. However, their peaks are less intense; see Figure 5.48. In the altered zone, i.e., the exposed surface, 100 µm and 200 µm, indicates the presence of gypsum as the deterioration deposits, and its peaks decrease with depth from the exposed surface. Dolomite and quarts are also observed throughout the depth, with MS (Mg-silicate) being observed mainly in the exposed surface and 100 µm layer.

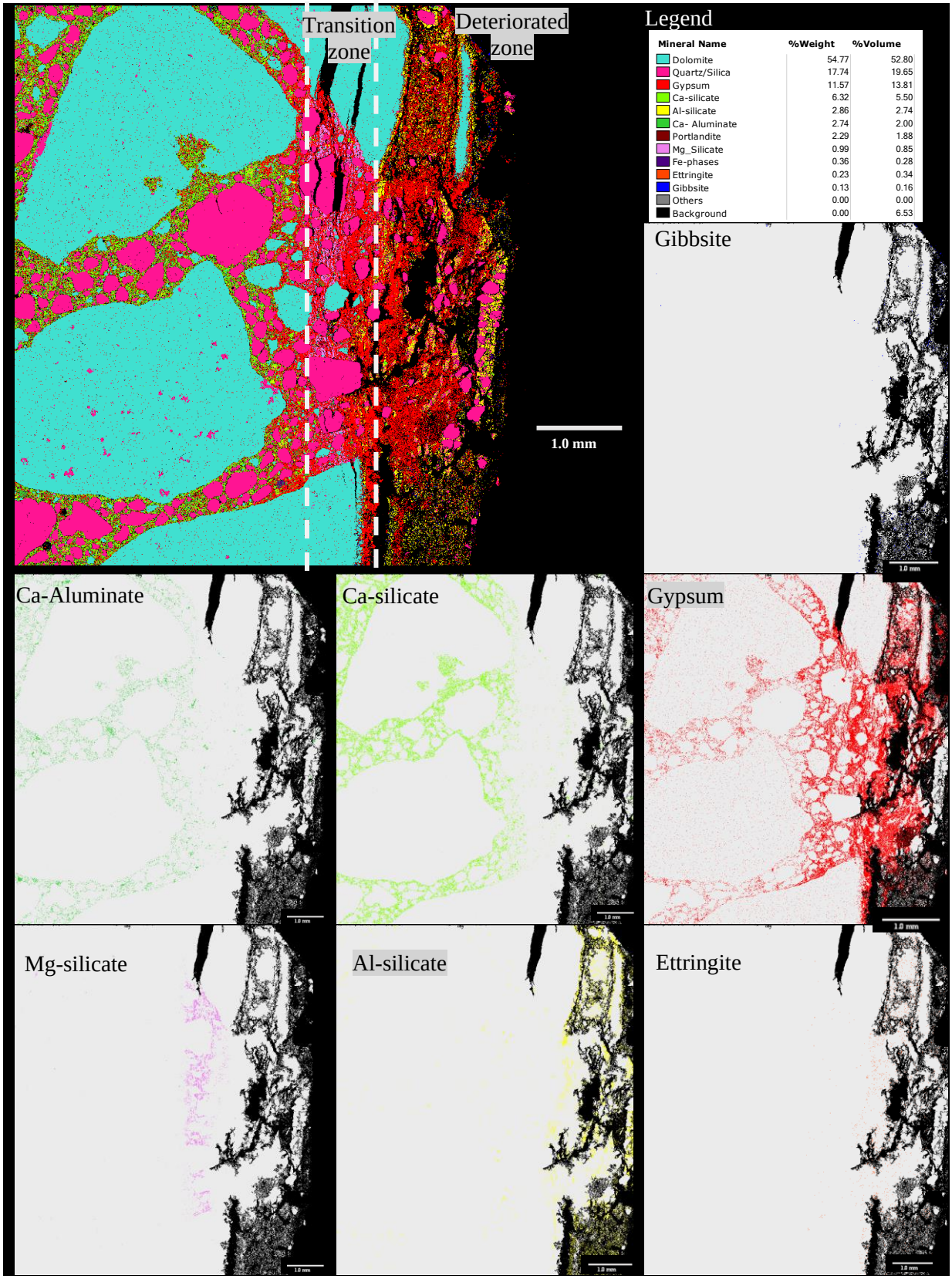


*Figure 5.47: QEMSCAN analysis of SRPC+FA+HC concrete from the UCT concrete specimens subjected to the NAS M19 for 26 months. The first image in the first row indicates a general distribution of concrete mineralogical phases on the concrete cross-section based on the SEM-BSE image, with the legend indicating the colour code, percentage weight and percentage volume of each mineral over the cross-section. Other images depict the distribution of selected minerals on the cross-section*

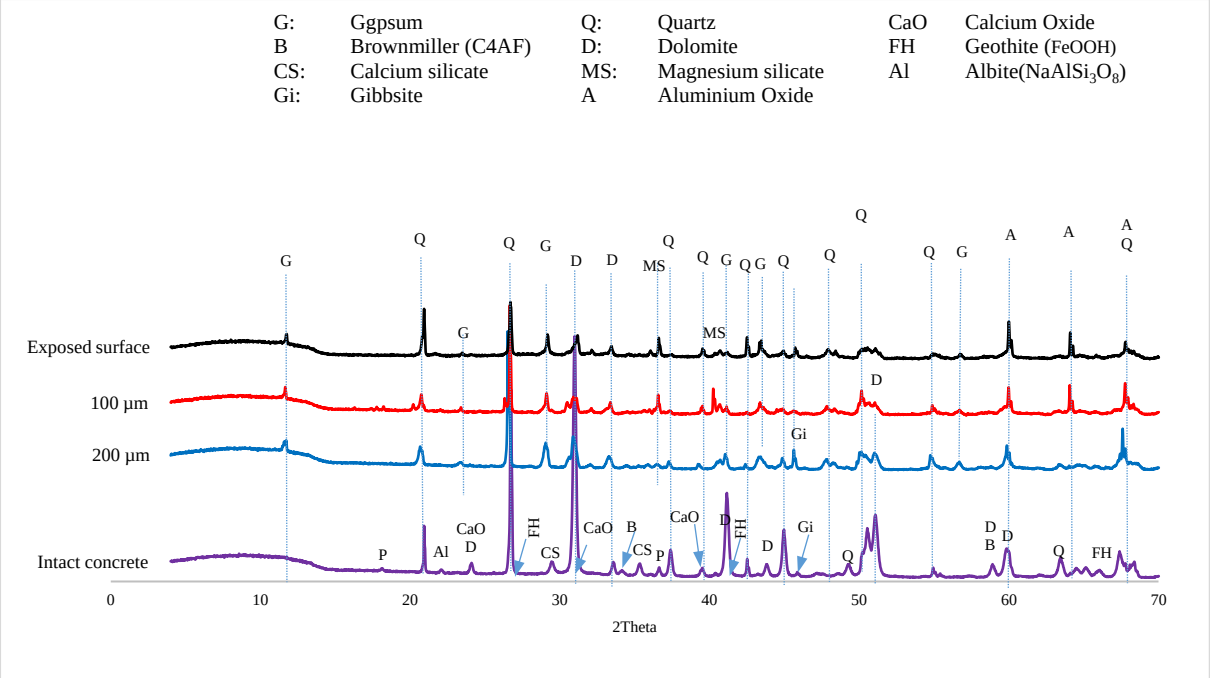


*Figure 5.48: XRD analysis results of the SRPC+FA+HC concrete from the UCT concrete specimens subjected to the NAS M19 for 2 years. The results are presented in four layers, i.e., the exposed surface, 100 µm and 200 µm from the exposed surface, and the intact concrete*

### 5.3.8.4. CAC+SRPC concrete

*5.3.8.4.1. SEM-BSE images*

CAC+SRPC concrete consists of 50% CAC and 50% SRPC cement. Therefore, its morphology combines CAC and SRPC, as shown in Figure 5.49. Figure 5.49 (A) shows the CAC+SRPC concrete microstructure, which contained a significant content of siliceous sand particles. Two concrete zones are also observed, the intact zone and the altered zone, further subdivided into the transition and deteriorated zones. The transition zone consisted of a thin whitish deposit layer, identified as the Mg-silicate phase under QEMSCAN analysis.

The maximum depth of the altered zone was about 1.43 mm, slightly lower than Portland-based concrete (Section 5.3.8.1 to 5.3.8.3). Since the selected section for this analysis consists of less coarse aggregate particles, it can be seen that the corrosion front is uniform and even. Moreover, Figure 5.49 (B) and Figure 5.49 (C) indicate the disintegration of dolomite particles in layers as observed in CEM II A-L and SRPC+FA-based concrete. However, the rate of dolomite deterioration was approximately equal to that of the cement matrix.

*5.3.8.4.2. QEMSCAN analysis*

In terms of mineralogical distribution, Figure 5.50 presents a general distribution of concrete mineralogical phases on the CAC+SRPC concrete cross-section. As observed in the previous concrete mixes, CAC+SRPC concrete microstructure mainly consists of quartz and dolomite (48.9% and 22.8%, respectively) from the aggregates. In the cement matrix, the percentage weights of mineralogical phases from the highest to the lowest were 16.3% Ca-silicate, 6.3% Portlandite, 2.1% Mg-silicate, 1.9% gypsum, 1.5% Fe/Al silicate, and 0.3% Ca-aluminate.

In the intact zone, the main phases were Ca-silicate, portlandite (as confirmed in Figure 5.50) and some Fe/Al silicate. After acid penetration, gypsum was precipitated in the transition and deteriorated zones. Minor calcium aluminate, gibbsite and ettringite were detected in this concrete, which indicated that blending CAC and SRPC concrete does not necessarily increase the formation of gibbsite and calcium aluminate phases. On the contrary, a noticeable layer of Mg silicate was observed in the transition zone and deteriorated zone. Its role in this concrete is not well understood. It may imply magnesium ions migration, a similar mechanism observed in CEM II AL and other SRPC-based concrete, or from dolomite disintegration. These ions react with silicate after calcium silicate decalcification. Herewith, Mg-silicate may offer some inhibiting action to the acid-producing bacteria due to its ability to maintain a higher surface pH (Merachtsaki et al., 2020). On the other hand, this observation may indicate the interaction between the aggregate and cement matrix on the concrete under BAC. Therefore, it is recommended to explore further the influence and interaction between cement matrix and soluble acid aggregates, particularly dolomite, and the contribution of magnesium ions in affecting concrete deterioration.

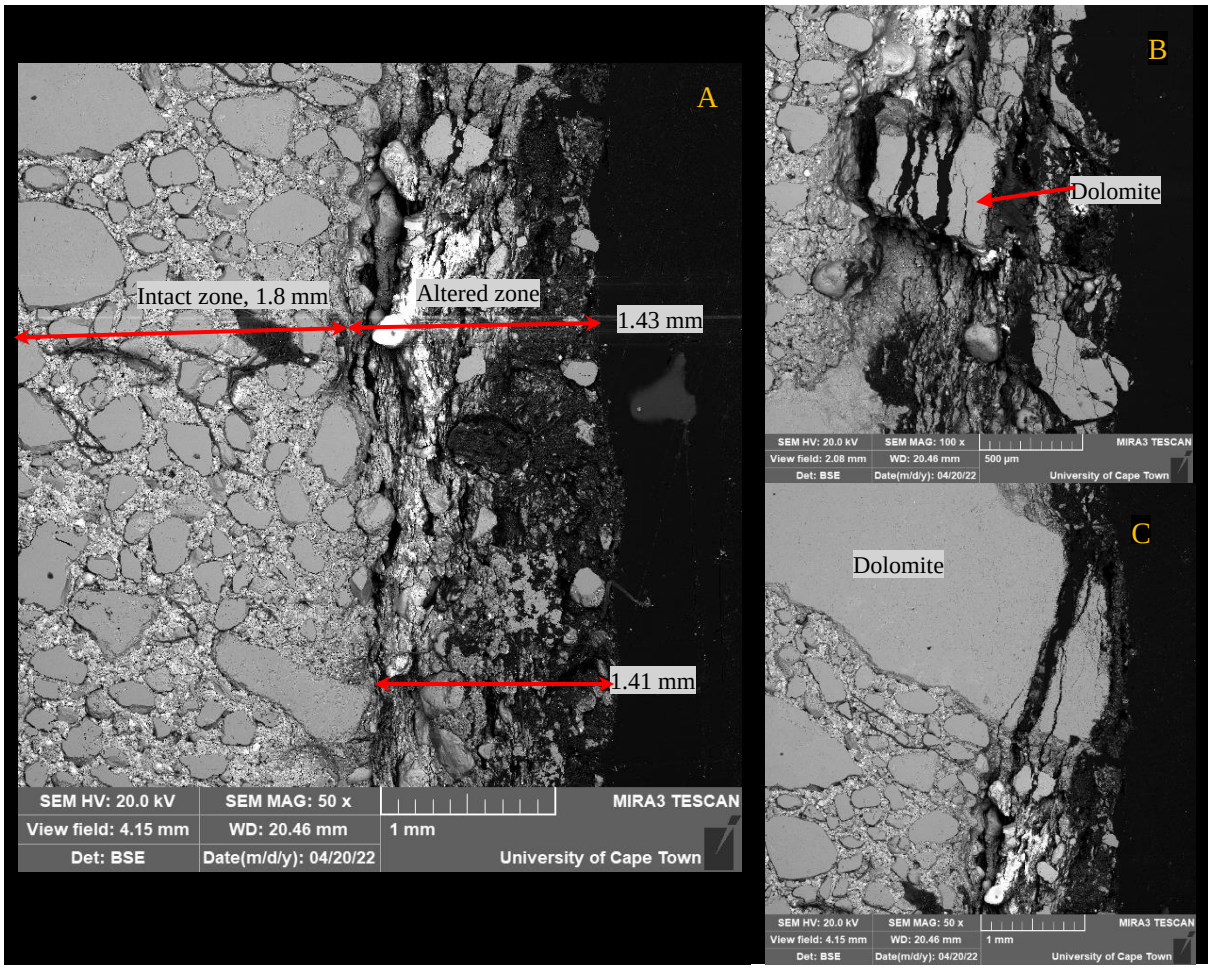


*Figure 5.49: SEM-BSE image for CAC+SRPC concrete after two years of exposure at NAS M19*

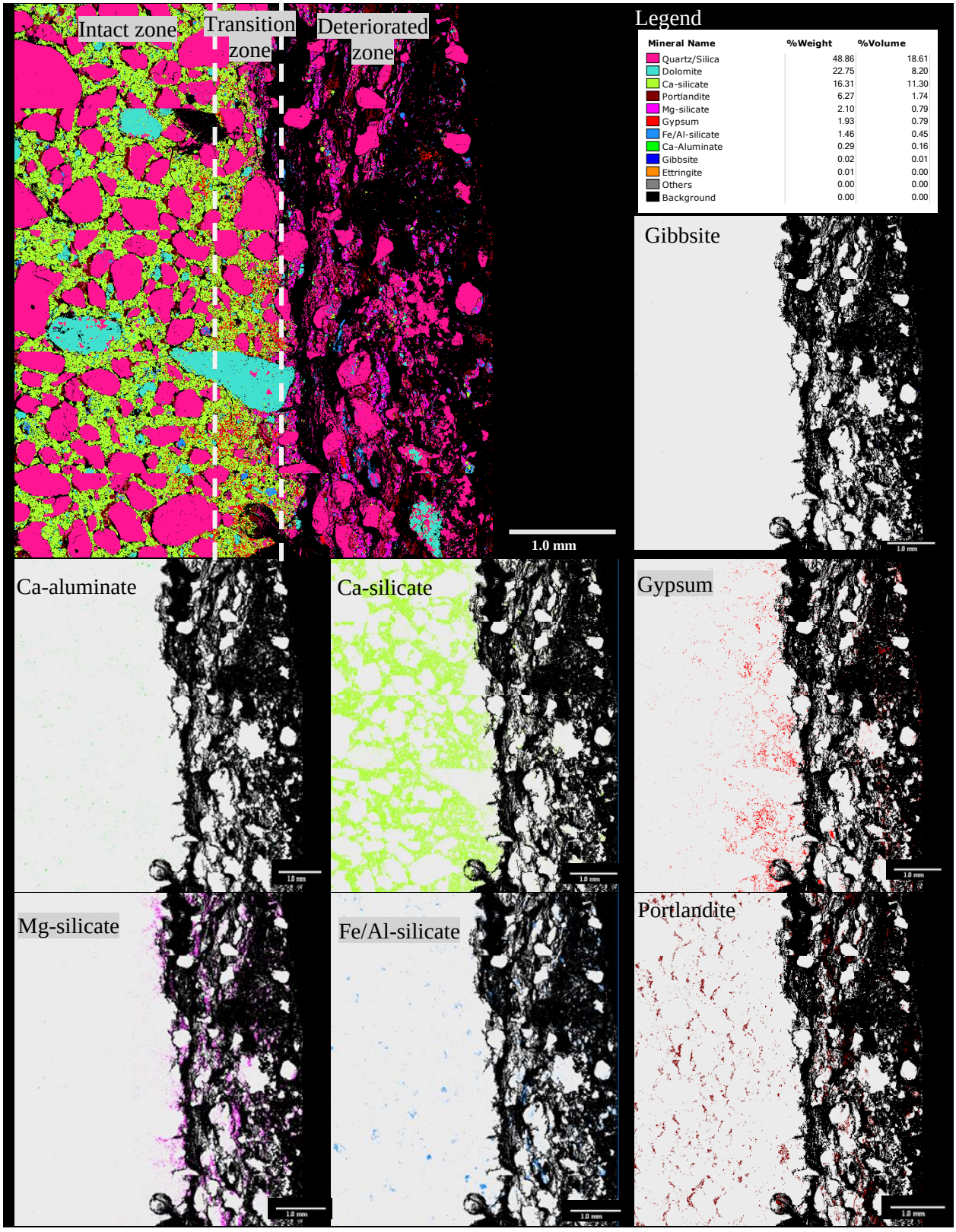


*Figure 5.50: QEMSCAN analysis of CAC+SRPC concrete from the UCT concrete specimens subjected to the NAS M19 for 26 months. The first image in the first row indicates a general distribution of concrete mineralogical phases on the concrete cross-section based on the SEM-BSE image, with the legend indicating the colour code, percentage weight and percentage volume of each mineral over the cross-section. Other images depict the distribution of selected minerals on the cross-section*

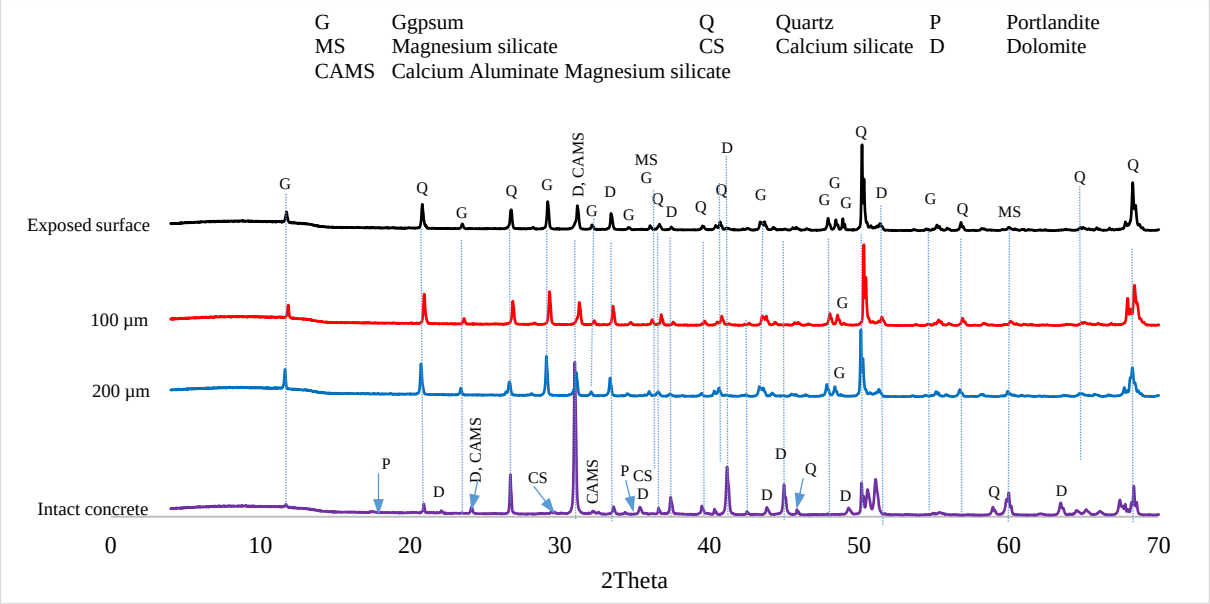


*Figure 5.51: XRD analysis results of the CAC+SRPC concrete from the UCT concrete specimens subjected to the NAS M19 for 2 years. The results are presented in four layers, i.e., the exposed surface, 100 µm and 200 µm from the exposed surface, and the intact concrete*

*5.3.8.4.3. XRD analysis*

The XRD analysis results in Figure 5.51 also prove that the CAC+SRPC intact concrete mainly consists of calcium silicate, portlandite and calcium aluminate. On the other hand, the altered zone was gypsum and Magnesium silicate. As well, dolomite and quartz peaks are significantly observed. This observation suggests that the performance of CAC+SRPC concrete may be related to good compatibility between its cement matrix and dolomite aggregate, with which a magnesium silicate layer possibly offers acid-inhibiting behaviour. It, therefore, suggested carrying out further study to prove this hypothesis

### 5.3.8.5. CSA concrete

*5.3.8.5.1. SEM-BSE images*

Figure 5.52 shows the SEM-BSE image for CSA concrete after 26 months of exposure at NAS M19. The intact zone consists of a very dense microstructure with some voids and a significant amount of coarse aggregate. There was no clear demarcation between the intact and altered zone, although the estimated altered zone depth is 0.9 mm in the cement matrix and 0.7 mm in the aggregate matrix. This observation indicates that the aggregate and cement deterioration rate is approximately similar. Figure 5.52 (B) indicates the deterioration behaviour of dolomite aggregate similar to that observed in the CEM II AL, where the aggregate dissolved in three layers. The first layer near the exposed surface is weak and very porous, followed by a dissolved layer, which has higher integrity and is more cohesive. A crack separates the last layer from the intact aggregate particle, with its surface slightly dissolved, fractured, and disintegrated. The fractured part may fall out and expose a new exposure site. Siliceous sand particles in this concrete detached from the cement matrix. Figure 5.52 (C) shows a continuous microcracking parallel to the exposed surface, yet no clear demarcation between the deteriorated and transition zones is observed.

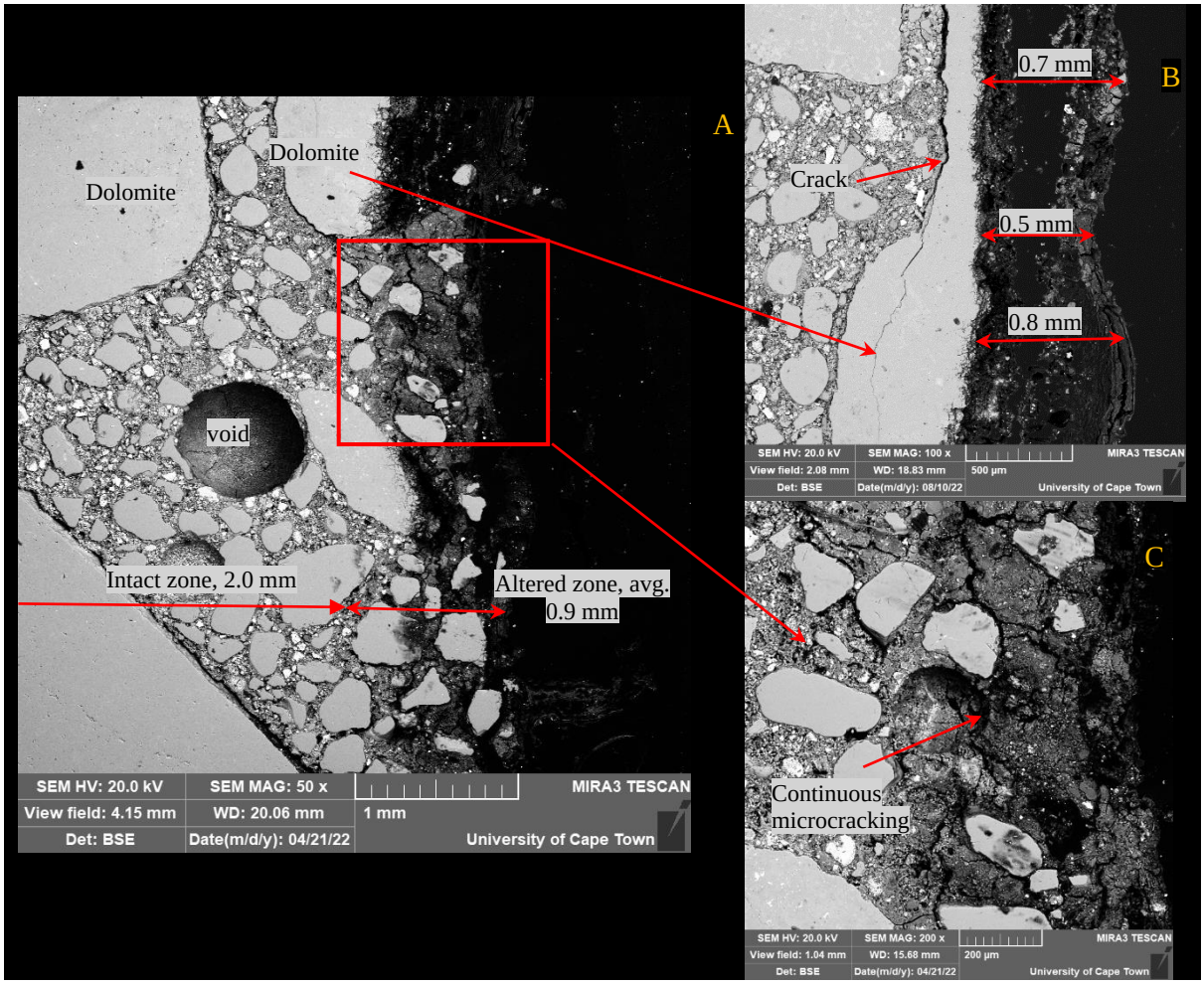


*Figure 5.52: SEM-BSE image for CSA concrete after two years of exposure at NAS M19*

*5.3.8.5.2. QEMSCAN analysis*

As observed under SEM analysis, QEMSCAN analysis of CSA concrete (Figure 5.53) also indicates no clear demarcation between the deteriorated and transition zones. This observation is similar to the LH concrete with a CSA binder system. This was associated with the superimposition of ettringite in the transition zone, i.e., ettringite formation due to CSA hydration and acid penetration. A similar observation was pointed out by Aboulela (2022).

The concrete microstructure consists of 49.5% dolomite and 24.8% quartz. This higher composition of aggregate phases compared to those evaluated from other UCT concrete was associated with the location selected for analysis. In the cement matrix, the phase composition ranked from the highest to the lowest were as follows; 9.9% ettringite, 7.7% Ca-aluminate, 4.1% gibbsite, 2.2% Portlandite, and 1.9% gypsum.

In the intact zone, the main phases were ettringite and calcium aluminate, along with some gibbsite, gypsum and portlandite. Gibbsite is part of hydration products when ye'elimite hydrates in the presence of gypsum only. In the presence of portlandite and gypsum, ye'elimite hydrates to form more ettringite. This reaction is preferred to hydration in the absence of portlandite (see hydration reaction in section 2.4.3 of the literature review) (Hargis et al., 2013; Damion, Cepuritis & Chaunsali, 2022).

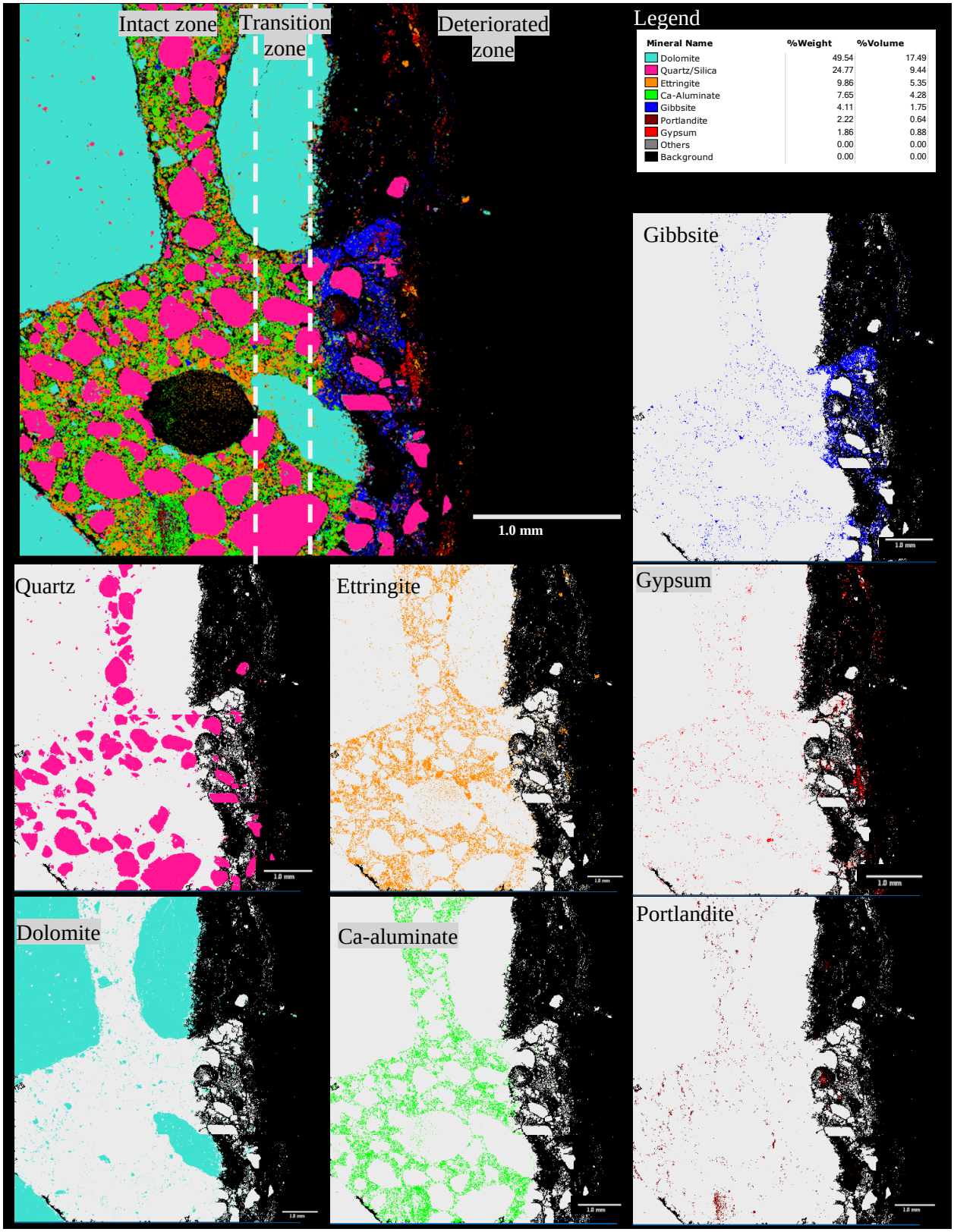


*Figure 5.53: QEMSCAN analysis of CSA concrete from the UCT concrete specimens subjected to the NAS M19 for 26 months. The first image in the first row indicates a general distribution of concrete mineralogical phases on the concrete cross-section based on the SEM-BSE image, with the legend indicating the colour code, percentage weight and percentage volume of each mineral over the cross-section. Other images depict the distribution of selected minerals on the cross-section*

After acid penetration, ettringite decomposed to produce additional gibbsite and gypsum in the deteriorated zone since ettringite becomes unstable in a low pH environment.(Hargis et al., 2017; Damion, Cepuritis & Chaunsali, 2022). Interestingly, a clearly defined layer of secondary gibbsite is observed in the deteriorated zone

*5.3.8.5.3. XRD analysis*

The XRD analysis results in Figure 5.54 also prove that the CSA intact concrete mainly consists of ettringite, gibbsite, calcium aluminate, and other phases such as anhydrite, ye'elimite, and calcium iron oxide, similar to those observed in the literature (Zhang & Glasser, 2002; Winnefeld & Lothenbach, 2010; Berger et al., 2011; Cao et al., 2022). The presence of ettringite and gibbsite indicates the hydration of ye'elimite under a sufficient supply of gypsum (Odler, 2003; Habert, 2014).

The altered zone consists of gypsum, aluminium oxide, magnesium-bearing phases, dolomite, and quartz peaks. Gypsum formation indicates the dissolution of the calcium-rich phases, while magnesium phases, such as Magnesium Iron silicate, Magnesium Aluminium silicate, and Hercynite-Magnesia, imply the interaction between the CSA cement phases and dolomite phases. It, therefore, suggested carrying out further study to prove this hypothesis.

Under XRD analysis, gibbsite was not observed in the deteriorated zone as significantly mapped under QEMSCAN analysis. According to Aboulela (2022), only amorphous gibbsite is formed in the deteriorated zone of CSA concrete, which could not be detected under the XRD analysis. This is because amorphous phases produce wide X-ray scattering profiles, which can be difficult to detect in XRD patterns with high peaks of crystalline phases (Achilles et al., 2018).

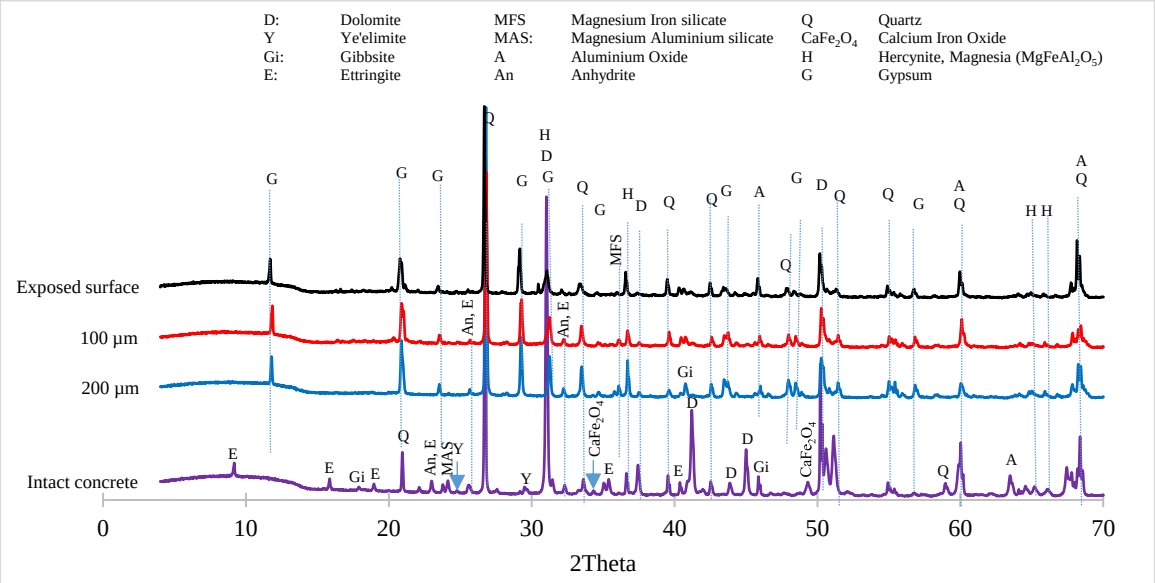


*Figure 5.54: XRD analysis results of the CSA concrete from the UCT concrete specimens subjected to the NAS M19 for 2 years. The results are presented in four layers, i.e., the exposed surface, 100 µm and 200 µm from the exposed surface, and the intact concrete*

### 5.3.8.6. CAC concrete

*5.3.8.6.1. SEM-BSE images*

The morphology of CAC concrete after 26 months of exposure to NAS M19 is shown in Figure 5.55. A very dense CAC concrete microstructure with some pores in the intact zone is examined (Figure 5.55 (A)). The altered zone consists of very few fragmented cement particles and a maximum depth of 1 mm less than that observed in previous concretes. A uniform and even corrosion front is observed, implying that the cement matrix deterioration rate is equal to that of the aggregate matrix. Organic matters are observed at the interface between the altered and intact zone; see Figure 5.55 (B).

Figure 5.55 (C) shows the morphology of these fragmented cement particles, which significantly differs from that observed in the previous concrete. Also, it was challenging to identify the transition zone under this analysis. Generally, it can also be noted that the microstructure of CAC concrete exposed to biogenic acid attack has fewer micro-cracks within the cement and aggregate matrices than SRPC-based concrete. The varying depths of attack and development of micro-cracks within various CAC-based matrices can also be explained by specific properties of the corrosion products, certain chemical reactions, and the theory of crystallisation pressure (Bizzozero, Gosselin & Scrivener, 2014; Kiliswa, 2016)

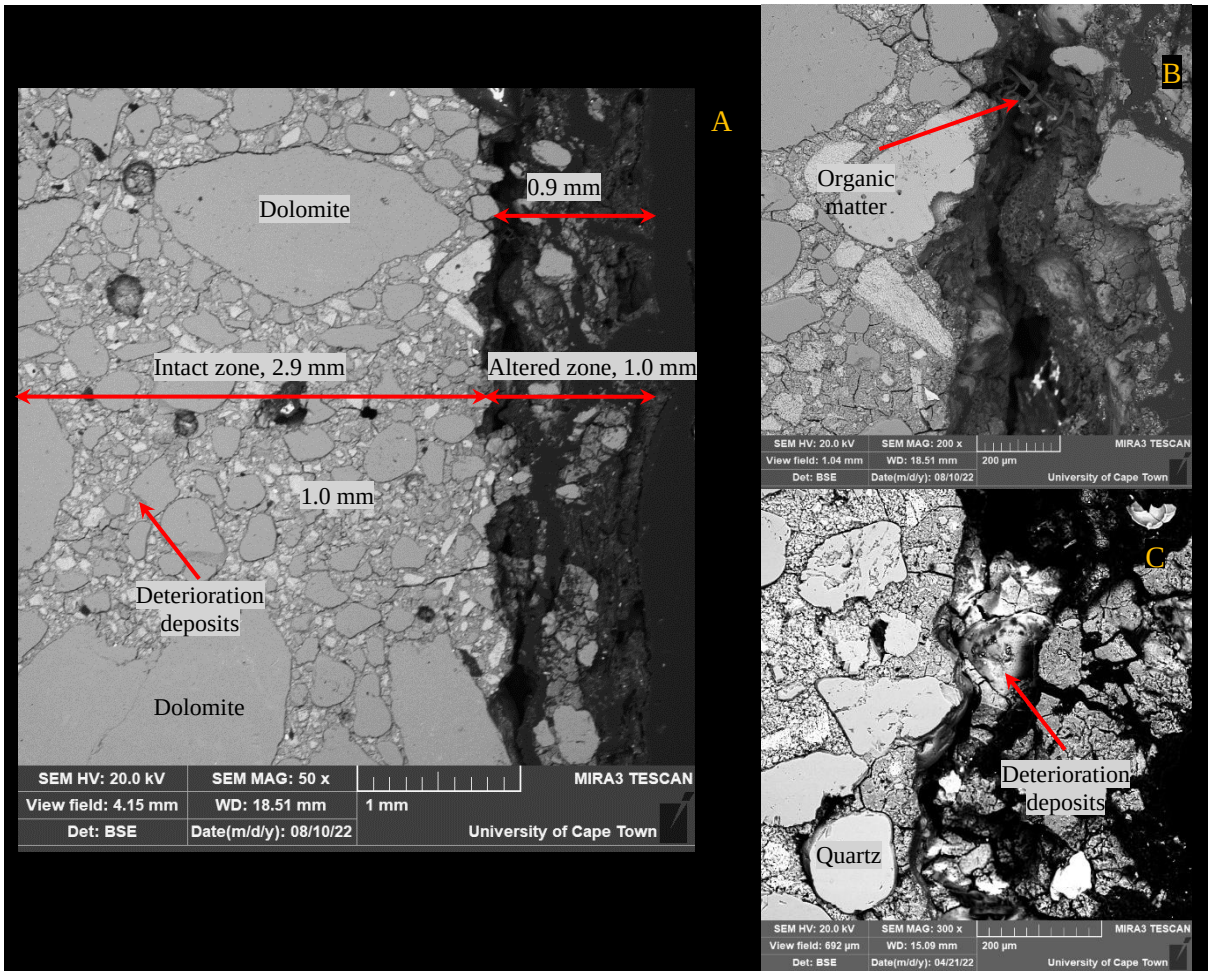


*Figure 5.55: SEM-BSE image for CAC concrete after two years of exposure at NAS M19*

*5.3.8.6.2. QEMSCAN analysis*

QEMSCAN analysis of CAC concrete shown in Figure 5.56 indicates that the concrete microstructure consists of 34.5% quartz and 33.5% dolomite aggregates. The cement phases, ranked from the highest to the lowest, are 13.2% Ca-aluminate, 6.3% ettringite, 3.1% gypsum, 3.0% gibbsite, 2.4% portlandite, 2.0% Ca-silicate, and 1.3% Fe/Al silicate.

The main phases in the intact zone are ca-aluminate, portlandite, gibbsite and ca-silicate, supported by XRD results in Figure 5.56. In the deteriorated zone, a significant amount of gibbsite and gypsum is observed, as well as some minor phases, such as Fe/Al silicate and Mg-silicate.

As pointed out earlier, it was challenging to distinguish between the deteriorated and transition zone under the SEM-BSE image. However, under QEMSCAN analysis, a distinct layer of secondary ettringite was observed in the transition zone, which was associated with acid penetration into the concrete matrix due to the gypsum reaction with calcium aluminate hydrate (O'Connell, McNally & Richardson, 2010). Nevertheless, no ettringite was observed within the deteriorated zone due to the rapid thermodynamics of gypsum formation (Davis et al., 1998). Ettringite is found only in the deeper sections of the concrete microstructure, with a pH higher than 10.7 (Davis et al., 1998; Beddoe & Dorner, 2005; Hudon, Mirza & Frigon, 2011). Also, Kiliswa (2016) indicated that CAC-based concrete tends to have a broader and more cohesive altered zone than PC-based concrete. It is, therefore, possible that the broader zone is attributed to ettringite formation, which later disintegrated to gibbsite and gypsum in the deteriorated zone. However, this observation contradicts the literature that no ettringite is formed in the CAC-based concrete (Hewlett, P., & Liska, 2019: 575). Additionally, it is possible that this wide zone lasts longer due to its high pH and hence contributes to the better performance of CAC concrete, but it is not clear how long it last before it corrodes. With this, further analysis and study are recommended.

*5.3.8.6.3. XRD analysis*

Under XRD analysis, the intact concrete consisted of gibbsite, Katoite, and calcium aluminium oxide, which all fall under the Ca-aluminate mapped in the QEMSCAN analysis. On the exposed surface, the main phases observed were gypsum, quartz, and dolomite, while ettringite and gibbsite peaks were not observed. At 200 µm and 500 µm depth from the exposed surface, minor peaks of ettringite were observed, though it was inconclusive since its prominent peaks were not observed. As it was difficult to analyse the microstructure below 0.5 mm, proving the presence of ettringite in the transition zone was impossible. However, the XRD analysis results by Khan et al. (2019) indicated ettringite presence within 3 mm depth of CAC mortar specimens after being subjected to a sewer environment. Therefore, further study is recommended to confirm its presence and role in the transition as it is believed to accelerate PC-based concrete deterioration due to its expansive nature.

Additionally, the influence of dolomite aggregate was also observed; with dolomite disintegration, magnesium ions were released, then reacted with aluminium silicate to form magnesium aluminate silicate, see exposed surface XRD pattern.

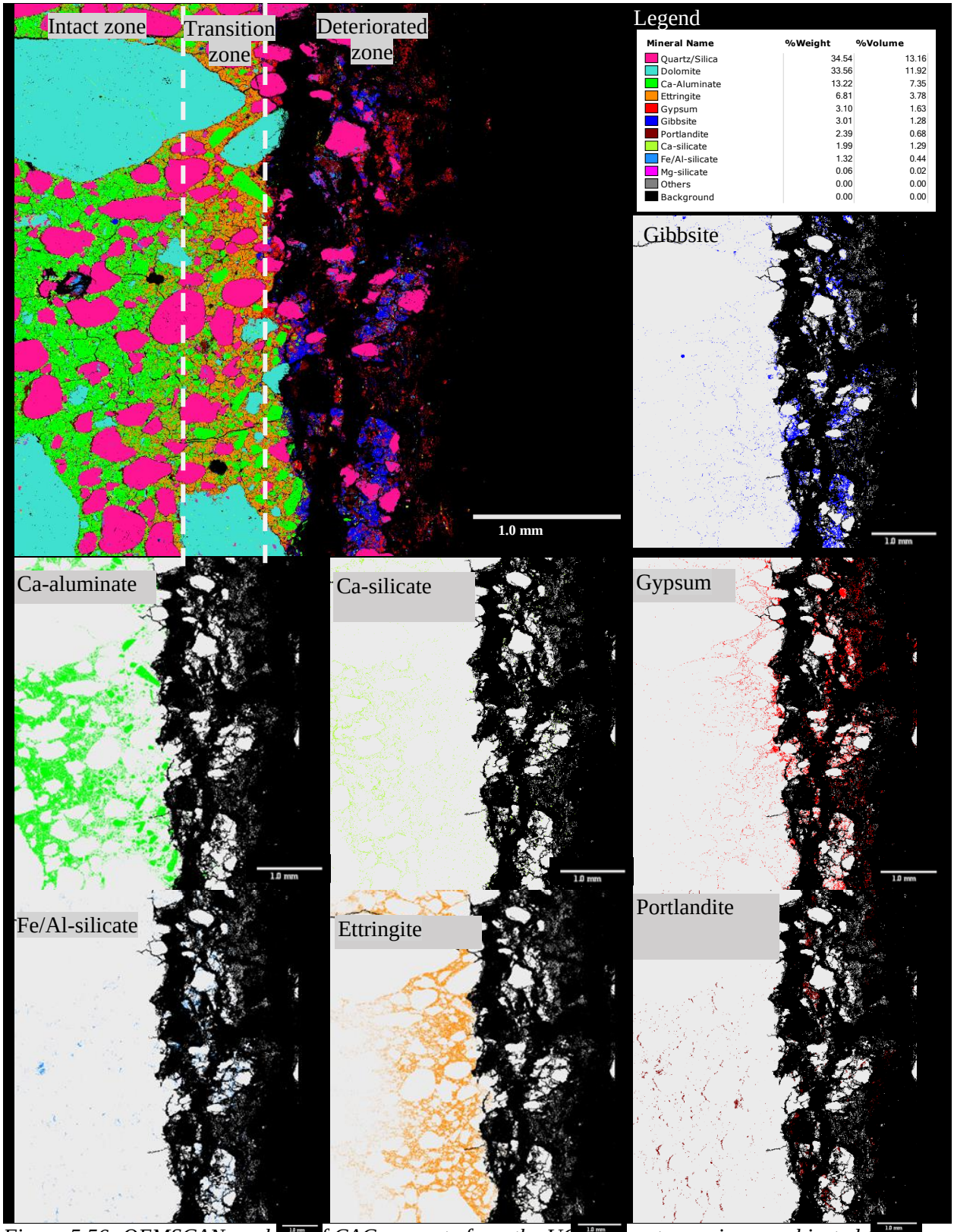


*Figure 5.56: QEMSCAN analysis of CAC concrete from the UCT concrete specimens subjected to the NAS M19 for 26 months. The first image in the first row indicates a general distribution of concrete mineralogical phases on the concrete cross-section based on the SEM-BSE image, with the legend indicating the colour code, percentage weight and percentage volume of each mineral over the cross-section. Other images depict the distribution of selected minerals on the cross-section*

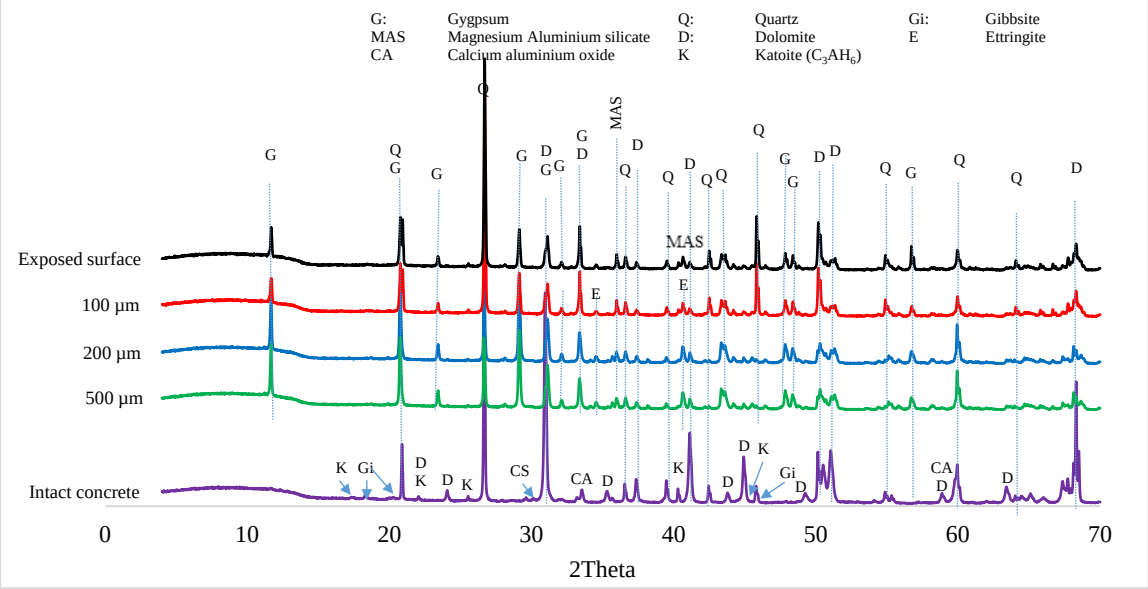


*Figure 5.57: XRD analysis results of the CAC concrete from the UCT concrete specimens subjected to the NAS M19 for 2 years. The results are presented in four layers, i.e., the exposed surface, 100 µm and 200 µm from the exposed surface, and the intact concrete*

### 5.3.9. Discussion of deterioration mechanisms

Based on the UCT concrete microstructure investigations above, BAC affects different concretes differently, depending on the binder chemical composition, hydration phases, and cement-aggregate interaction in terms of their phase compatibility and deterioration rates. The SEM-BSE and QEMSCAN analyses indicate that, in addition to the depth of the concrete 'lost' on-site due to corrosion over the exposure period, the remaining concrete samples that were retrieved consist of two sub-zones in the alteration zone, i.e., the transition and the deteriorated zone, which define the extent to which acid has penetrated the concrete microstructure.

The deteriorated zone is usually less cohesive with significant porosity, loose aggregate particles and disintegrated cement particles (mainly gypsum and silica). The transition zone is a thin layer between the intact and deteriorated zones. It retains a measure of integrity and cohesiveness but less than the intact zone. The transition zone is demarcated from the deteriorated zone between the corrosion front and a location where secondary phases (corrosion products) stop to mark the end of acid penetration. With SEM analysis, this zone is difficult to observe because of its integrity, cohesiveness and lower porosity. With QEMSCAN analysis, it can be identified with sulphur-bearing phases such as gypsum and ettringite, and in some binders such as CAC+SRPC, with Mg-silicate, gibbsite or Al/Fe silicate layer, indicating calcium-deficient layers (Kiliswa, Scrivener & Alexander, 2019).

#### 5.3.9.1. PC based binders

The main hydration products of Portland-based concrete are portlandite and hydrated calcium silicate, both of which are susceptible to acid corrosion. They react with sulphuric acid to produce gypsum and ettringite, which are expansive and have lower mechanical properties. As a result, the concrete becomes more porous, degrades quickly and reduces its intended function (Grengg et al., 2016; Grandclerc et al.,

2018; Cao et al., 2020). For this reason, CEM II AL concrete performed poorly in this study. Figure 5.58 indicate the deterioration mechanism of PC-based hydrates under BAC.

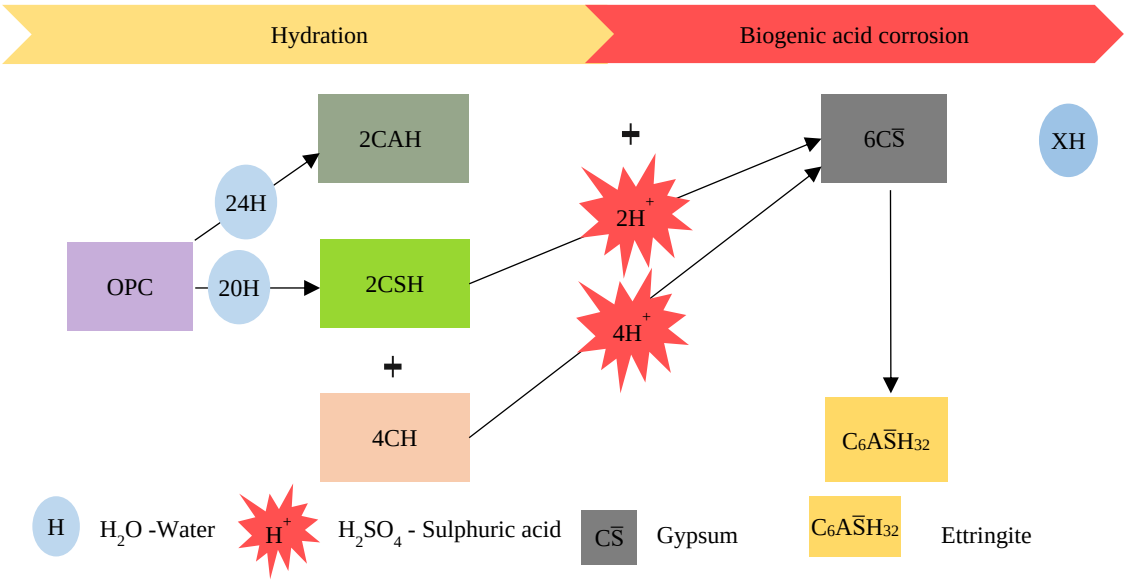


*Figure 5.58:Hydration, dissolution and deterioration mechanism of PC under BAC*

### 5.3.9.2. CAC binder system

CAC is well known as a better acid-resistant binder due to its long chain of dissolution of its hydrates, leading to more gibbsite formation and high neutralisation capacity, as well as gibbsite stability at pH between 3.5 and 4. The literature also indicates that the corrosion end products, mainly gibbsite and stratlingite, offer some mechanical or physical integrity to the altered zone, which provides a barrier to further corrosion (Khan et al., 2019; Kiliswa, Scrivener & Alexander, 2019). In this study, QEMSCAN analysis indicated that the main hydration products of CAC concrete were calcium aluminate hydrate (CA and $C_3AH_6$) and gibbsite, which, with acid penetration, form a broad layer of secondary ettringite in the transition zone (Eq. 5.1), followed by gibbsite and gypsum in the deteriorated zone, see Figure 5.59. The ettringite layer in the transition zone was presumed to be the layer observed by Kiliswa (2016) and Khan et al. (2019). However, its presence was inconclusive since this zone could not be analysed under XRD due to the smothering of aggregate content. This raises concerns about the layer's stability since secondary ettringite, which is expansive, can induce microcracking in the concrete microstructure, thus accelerating deterioration. It is thus hypothesised that a significant amount of gibbsite in this layer (that provides physical integrity) may retain some layer integrity, hence offering microstructure endurance and resistance.

$$C_3AH_6 + 3C\bar{S} + 26H \rightarrow C_6A\bar{S}_3H_{32}$$ (Chapter 5.1)

$$C_6A\bar{S}_3H_{32} + 3H_2SO_4 \rightarrow 6C\bar{S} + 2AH_3 + 32H$$ (Chapter 5.2)

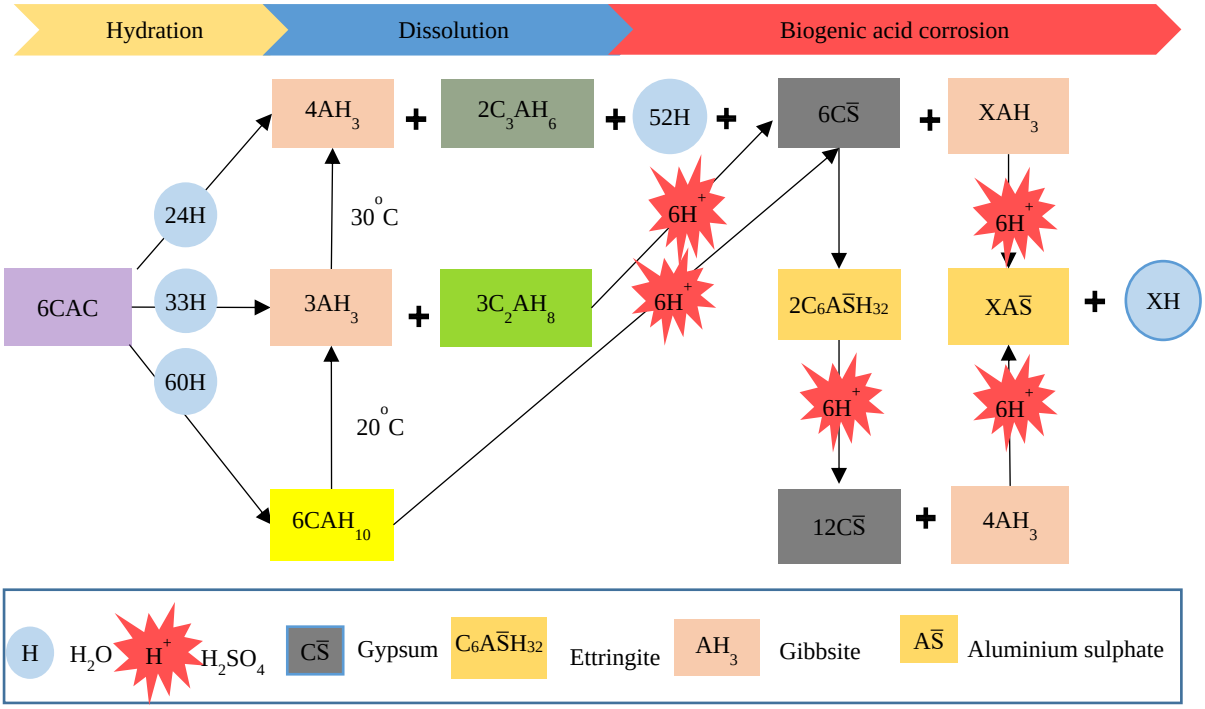


*Figure 5.59: Modified hydration, dissolution, and deterioration mechanism of CAC under BAC (Refer to Figure 2.9). Note; ettringite is formed only in the transition zone.*

### 5.3.9.3. CSA Binder system

The main hydration products of CSA concrete are ettringite, gibbsite and calcium aluminate hydrates, and some residual portlandite, gypsum and Ye'elimite. Under BAC, ettringite decomposes to form gibbsite and gypsum in the deteriorated layer (Eq. 5.2) since it is unstable at a pH lower than 10.7. However, with acid penetration, secondary ettringite is formed in the transition zone from the gypsum and calcium aluminate hydrate reaction (O'Connell, McNally & Richardson, 2010). As a result, the transition zone in the concrete microstructure is complex to define due to ettringite superimposition. Nonetheless, the CSA microstructure has low porosity, as an outcome of the original ettringite volumetric expansion. Therefore, secondary ettringite formation promotes microcracking within the microstructure, which amplifies the attack (as seen in Figure 5.52 (C)). Therefore, ettringite superimposition explains why CSA has poorer performance than CAC-based concrete, despite having gibbsite. Figure 5.60 indicate the deterioration mechanism of CSA hydrates under BAC.

### 5.3.9.4. Other binder systems

Blending SRPC with fly ash in the SRPC-based concrete increases the calcium aluminate hydrate phases in the concrete microstructure. It is, therefore, believed that these aluminate phases should improve the performance of SRPC+FA and SRPC+FA+HC concrete compared to CEM II AL. However, the susceptibility of calcium silicate and portlandite to readily react with acid impairs the influence of the aluminate phases, unlike in the performance of alumina-based concrete. In contrast, a blend of CAC and SRPC outperformed the PC-, SRPC-, and CSA-based concrete. The reason behind its performance is not well known. However, it can be associated with magnesium-bearing phases. It is also hypothesised that Mg-silicate offers some inhibiting action to the acid-producing bacteria due to Mg+ ions' ability to maintain a higher surface pH (Merachtsaki et al., 2020).

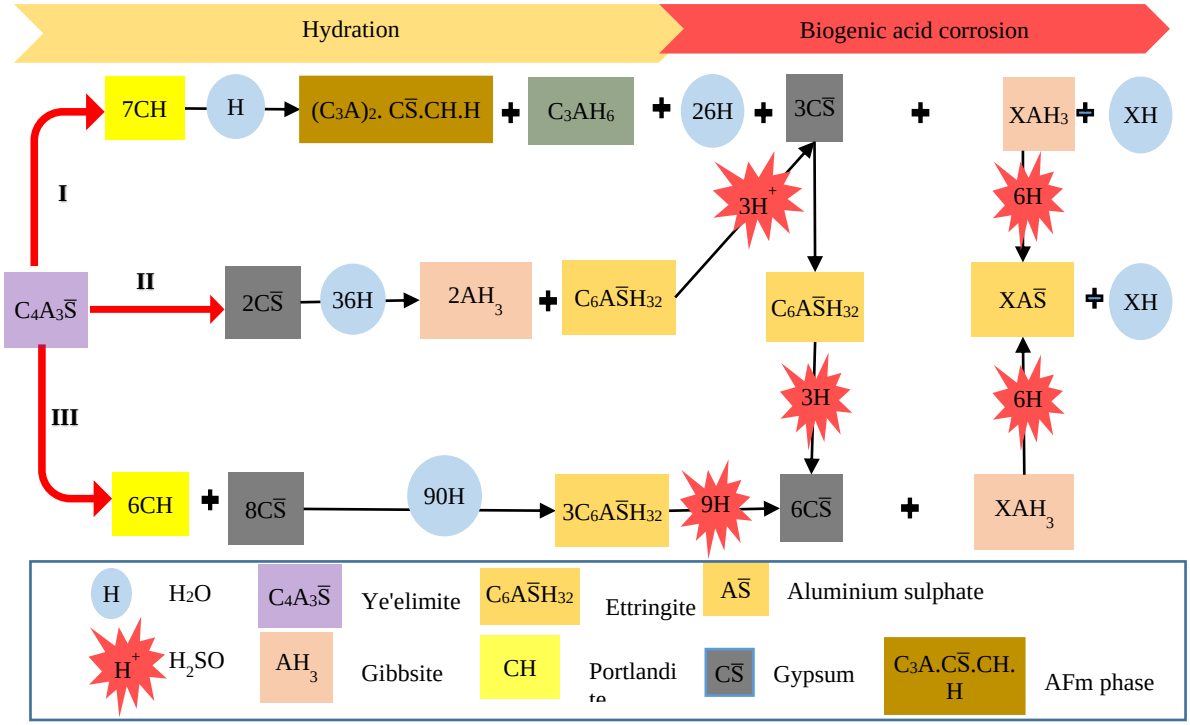


*Figure 5.60: Hydration, dissolution, and deterioration mechanism of CSA under BAC. Note CSA hydration takes place in three ways depending on the amount of CH and CS̄*

### 5.3.10. Influence of aggregates on BAC

When acid-reactive aggregates are incorporated into concrete, they effectively retard the progress of concrete deterioration because they corrode along with the cement matrices, leading to a slower corrosion rate and occasionally a more uniform corrosion front (Pather, Ekolu & Quainoo, 2021). A uniform corrosion front occurs when the deterioration rates of the cement and aggregate matrix are approximately equal or match. When not matched, an uneven corrosion front is observed, leading to aggregate protrusion or fallout, and hence an accelerated concrete corrosion rate. Therefore, aggregate and cement matrix deterioration rates that are comparable or similar should be considered when selecting aggregates for the best sewer concrete performance.

In this study, alumina-based concretes (CAC, CA+SRPC, and CSA) had reasonably uniform corrosion fronts, suggesting that their cement and dolomite matrices had roughly equal deterioration rates. On the other hand, Portland-based concretes exhibit uneven corrosion fronts. For the SRP+FA concrete, dolomite aggregate protruded from the exposed surface, while for the CEM II AL and SRPC+FA+HC concrete, the altered zones had higher depths in the cement matrixes than the dolomite aggregate particles. Siliceous sand particles generally detached from the cement matrix. This observation suggests that the rate of Portland-based cement deterioration is higher than that of dolomite aggregate, which is indeed usually observed in practice. Therefore, apart from improved microstructural characteristics and a reduced diffusion rate, the superior performance of alumina-based concrete is most likely to result from good compatibility with dolomite aggregate.

Additionally, although dolomite and calcite are calcareous aggregates, their deterioration mechanism in sewers differ. Calcite reacts with the acid to form gypsum only, while dolomite reacts with the acid

to form gypsum and magnesium carbonate, which dissociates into magnesian ions because magnesium sulphate (MgSO4) does not precipitate due to its high solubility.

## 5.4. Chapter closure and remarks

In conclusion, the discussion on the experimental investigation results of sewer concrete aimed to highlight; i) the importance of studying the performance of concrete in live sewer environments, ii) the influence of different sewer environments on concrete deterioration, iii) the behaviour of different concrete microstructures under BAC, and iv) the influence of aggregate types on the sewer concrete mixes. Based on the above objectives, and based on the specific materials studied, the following highlights are extracted from this chapter.

- The quality of sewer concrete is essential in comprehending the performance of a binder. Therefore, durability and strength control tests should be performed to ensure that the concrete is fit for purpose since poor quality concrete tends to accelerate the deterioration mechanisms.
- During the initial stage of BAC, sewer concrete may experience mass gain due to the initial corrosion product formation, organic matter and acid penetration. However, after several years of exposure, this initial mass gain would have no appreciable influence and can therefore be ignored for practical purposes.
- Regarding the BAC monitoring test results, aluminate-based concrete has superior performance than Portland-based concrete, regardless of sewer environmental exposure. However, under sewer hydraulic action combined with high gas concentration, a significantly higher corrosion rate can be observed on both concrete types.
- Concerning binder performance ranking, the CAC binder system ranks the highest and CEM II AL the lowest. Other binder systems rank in between as follows; CAC>CAC+SRPC>CSA >SRPC+FA with and without HC> CEM II A-L.
- Portland-based concrete's poorer performance is associated with the decalcification of calcium silicate hydrates and portlandite because of their susceptibility to BAC. However, incorporating fly ash into Portland-based concrete improves the performance, whereas Iron-based additives have little influence.
- CSA's better performance compared with Portland-based concrete is associated with the formation of ettringite, which provides more neutralisation capacity than calcium silicate and portlandite, and its transformation to gibbsite, which is stable at pH between 3 and 4. On the other hand, its poorer performance compared to CAC is associated with ettringite superimposition (ettringite present after hydration and newly formed due to acid penetration) in the transition zone due to its expansive nature. It induces microcracking in this the zone, hence accelerating the deterioration.
- CAC's superior performance is associated with the long chain of dissolution of its hydrates, leading to more gibbsite formation and high neutralisation capacity. However, CAC tends to have a broader transition zone filled with ettringite due to its stability at a high pH, which with acid penetration, transforms to form more gibbsite in the deteriorated zone.

- Besides the chemical influence of binders in improving the performance of concrete, good compatibility between cement and aggregate matrixes plays a significant role in influencing the deterioration of concrete. With this, the superior performance of alumina-based concrete, including (CAC+SRPC) results from good compatibility with dolomite aggregate. Therefore, during sewer concrete mix design, selecting aggregates and binder systems with roughly comparable or similar deterioration rates is advised.
- A distinct layer of magnesium silicate was observed in the transition zone of various concretes in this study. However, its source and role remain elusive. With acid penetration, Mg+ ions possibly migrate into the transition zone to react with silicate and offer acid-inhibiting potential to concrete, or it may originate from dolomite disintegration. With this, it is recommended to explore further the contribution of magnesium ions and the influence and interaction between cement matrix and aggregates in affecting concrete under BAC.

# CHAPTER 6. REACTIVE TRANSPORT MODELLING OF CONCRETE UNDER BAC

## 6.1. Introduction

As discussed in Section 2.11, reactive transport modelling was selected to understand concrete deterioration mechanisms under BAC and compare model outcomes with the field observations. Despite numerous available models, the HYTEC model (van der Lee et al., 2002) was of interest due to its versatile applications in modelling the deterioration mechanisms of cement-based materials in various aggressive environments. The model can elucidate the transport mechanism of cement-based materials, the chemical reactions between the acid and the material, and the phase evolutions and assemblages of the materials during BAC. As an outcome, it allows profile plotting showing corrosion zonation. With this, the most deterioration-influential or susceptible phases and elements, and the rates, can be evaluated to track the deterioration progress. More importantly, it can give a more fundamental understanding of the deterioration phenomena, and it was in this way that the model was most utilised. In achieving this, the following sub-objectives were studied:

i) To understand the influence of acid attack mode and its effect on the dissolution and precipitation of cementitious phases while varying the pH of attacking acid.
ii) To compare the modelling performance of Portland and alumina-based binder systems with the experimental field observations
iii) Finally, to extract essential information from the reactive transport modelling approach that can assist in refining the LFM model.

In this case, the acid attack modes can be described as follows; see Figure 6.1 for schematic demonstrations.

i) **Open system**, where the acid attacks the cementitious material by a continuous supply of sulphuric acid on the exposed surface, leaching cementitious ions from the composite and their removal from the system.
ii) **Closed system**, where acid attacks the cementitious material while restricting the removal of ions leached from the scenario by exposing the cementitious surface to an ‘infinite’ sulphuric acid reservoir.

These modes are related to aggressivity zones encountered in typical sewers under BAC. That is, i) reflects the erosion or tidal zone, where a corrosion layer is constantly removed, and ii) a partial erosion zone, mainly the area between the crown and tidal zones, and the crown zone itself, where there is a massive built-up of corrosion layers of gypsum growing with time. This massive build-up layer of gypsum in the closed system represents the infinite reservoir of acid, which limits ions leaching outside the system.

Based on the BAC microstructural analyses in Section 5.3.8, the open system proved reasonable to the modelling assumptions necessary for obtaining meaningful outcomes. In other words, it was possible to obtain reliable results for the open system mode, that corresponded reasonably with the

microstructural observations and analyses, including a first-level assessment of kinetic factors. This was not the case for the closed system, largely because of the difficulty in assigning a value for the 'acid reservoir' that could be justified from real-life studies. Consequently, this modelling aspect was not pursued to a useful outcome. This aspect needs further investigation to resolve the difficulties. However, this was not detrimental to the overall work of this study since the modelling was mainly used to elucidate the observations from the live sewer sections that were studied and was a secondary aspect of the main work. Thus, the present work only deals with the open system mode of attack.

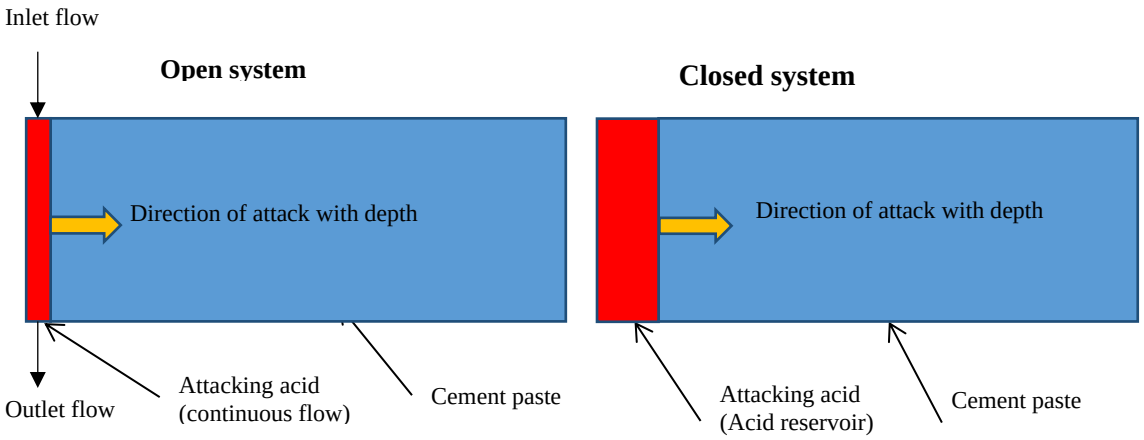


*Figure 6.1: A schematic set of the two attack modes of BAC on cement paste with 10 mm depth using HYTEC. The open system shows the inlet and outlet flow of acid, while the closed system shows an infinite acid reservoir without any outlet and inlet.*

## 6.2. Methodology

The HYTEC model (Lagneau, 2016) was used to model the deterioration of cement paste under BAC, combined with PHREEQC (PH Redox Equilibrium)(Parkhurst & Appelo, 2013). PHREEQC was used to obtain input data on the cementitious phases of cement paste after hydration and predict possible secondary steps after the attack.

### 6.2.1. Material

The concrete mix designs shown in Table 3.5, except the CAC+SRPC concrete mix, were used for modelling. (Information regarding the mix designs is shown in Section 3.2

### 6.2.2. PHREEQC modelling

Cementitious hydrates of each mix were thermodynamically modelled using PHREEQC, based on XRF results of the binders and the w/b ratio of the concrete mix. The degree of hydration of SRPC was assumed to be 80%, 20% for FA (Feng et al., 2004; Lam, Wong & Poon, 2000), and 50 % at 40$^{o}$C for CSA (Wang, Li & Xu, 2017) and CAC (Ukrainczyk, 2010) after 28 days of maturity.

In this analysis, the hydration temperature of all binder systems was set at 23$^{o}$C for Portland-based binders and 40$^{o}$C (Goergens & Goetz-Neunhoeffer, 2021) for alumina-based binders. Appendix M shows PHREEQC Input data obtained from XRF results of binders. With this data, the cementitious hydrates of each binder system were modelled and presented in Table 6.2. Details regarding modelling

in the PHREEQC are obtained in Appendix M. The Chess|THERMODDEM (2014) database was employed in this case.

### 6.2.3. Effective diffusion coefficient of concrete

HYTEC only considers a constant effective diffusion coefficient for cationic, neutral and anionic species (De Windt & Devillers, 2010); hence, a single effective diffusion coefficient of ionic species through concrete was used for each concrete mix (Trotignon et al., 2007). The effective diffusion coefficient of concrete was estimated based on the diffusibility relationship, also called the formation factor ($Q$), that relates the ratio of the diffusion coefficient of ionic species in the bulk material ($D_i$) and in the pore solution ($D_{io}$), to that of the electrical conductivity measured in the bulk material ($\sigma$) and in the pore solution ($\sigma_o$), see Eq. (6.1)(Snyder et al., 2003).

$$Q = \frac{D_i}{D_{io}} = \frac{\sigma}{\sigma_o} \tag{6.1}$$

The concrete's electrical conductivity (σ) was determined according to SANS 3001-CO3-3 (2015), with minor alteration in sample preparation. Instead of vacuum saturating the specimens in NaCl solution, the mature specimens (96 days of age) were vacuum-saturated in water for seven days to achieve 'full' saturation. Schmidt-Döhl & Rostásy (1999) recommend that the coefficients measured for specimens saturated with water be employed.

Since the concretes used for this study had a low w/b ratio of 0.34, extracting pore solution for their electrical conductivity measurement was challenging (Olsson et al., 2018). Therefore, $\sigma_O$ was estimated from the contribution of alkalis in the binders and the mix proportions, see Table 6.1 (Alexander, Streicher & Mackechnie, 1999). The online pore solution conductivity calculator developed at the National Institute for Standards and Technology (NIST - USA) was used to calculate the value of $\sigma_O$ for each concrete (Snyder et al., 2003).

The diffusion coefficient of ions in the concrete pore solution ($D_{oi}$) was obtained from Isgor and Weiss (2019). By calculating the effective diffusion coefficient ($D_i$) of each species in the respective concrete mix, it was observed that the coefficients ranked from highest to lowest as follow, $OH^- > SO_4^{2-} > CL^- > K^+ > N^{a+} > Ca^{2+}$, all in the order of $10^{-9}$ $m^2/s$. This observation indicates that the variations in the effective diffusion coefficients of ionic species are minor to negligible in bulk volume. Regarding BAC, the effective diffusion coefficient of sulphate ($SO_4^{2-}$) ions was used as a constant effective diffusion coefficient of species through concrete, which is equal to 2.11 x $10^{-9}$ $m^2/s$ (Isgor & Weiss, 2019).

Nevertheless, it was acknowledged that concretes with different binder systems have different diffusion coefficients. Alumina-based binders have lower permeability than Portland-based binders; thus, determining their diffusion coefficient might be challenging. However, it was observed that the diffusion coefficient of CSA concrete estimated in this study at 0.34 w/b ratio was very close to the diffusion coefficient of $SO_4^{2-}$ calculated by the formation factor method and the Nernst-Einstein method in Hou, He and Liu (2021).

A further limitation of the HYTEC model is that it is not set up to model aggregate influence in concrete but only paste. It incorporates the aggregate mineral as finely dispersed particles mixed with

cementitious phases, which rapidly saturates the system and causes model failure. Therefore, the properties of cement paste within concrete were used to model the deterioration of concrete by assuming that aggregates offer no accessible porosity or any diffusion process in concrete. Thus, the initial porosities and effective diffusion coefficients of cement pastes were evaluated from concrete porosity and diffusion coefficient (Trotignon et al., 2007). Table 6.1 shows the effective diffusion coefficient of concrete and its equivalent values in cement paste used in the HYTEC modelling.

*Table 6.1: Effective diffusion coefficient of concrete used for HYTEC modelling*

| **Binder system** | **SRPC+FA+HC** | **SRPC+FA** | **CEM II AL** | **CSA** | **CAC** |
|---|---|---|---|---|---|
| Estimated $K^+$ concentration, M | 0.19 | 0.19 | 0.50 | 0.05 | 0.17 |
| Estimated $Na^+$ concentration, M | 0.04 | 0.04 | - | - | - |
| Estimated $OH^-$ concentration, M | 0.23 | 0.23 | 0.50 | 0.05 | 0.17 |
| Estimated $\sigma_o$, mS/cm [#] | 51.20 | 51.20 | 105.60 | 12.80 | 39.40 |
| Measured $\sigma$, mS/cm* | 0.15 | 0.17 | 0.52 | 0.01 | 0.01 |
| Formation factor, $Q$ x $10^{-3}$ | 2.93 | 3.32 | 4.91 | 0.63 | 0.25 |
| $D_{SO_4^{2-}}$ in concrete, x $10^{-12}$ $m^2/s$ | 6.19 | 7.13 | 10.36 | 1.33 | 0.54 |
| Concrete porosity, %** | 10.9 | 10.0 | 10.5 | 5.7 | 10.3 |
| Equivalent cement paste porosity, % | 36 | 34 | 36 | 20 | 37 |
| $D_{SO_4^{2-}}$ in cement paste, x $10^{-11}$ $m^2/s$ | 2.42 | 2.04 | 3.55 | 0.47 | 0.19 |

[#] NIST (Olsson et al., 2018), *SANS 3001-CO3-3 (SANS 3001-CO3-3, 2015). The effective diffusion coefficient of sulpate ion in cement paste ($D_{SO_4^{2-}}$) were used herein as the D value for modelling purposes

**Porosity of concrete obtained from Figure 5.26

### 6.2.4. HYTEC modelling

HYTEC modelling was conducted on a two-dimensional domain of the concrete composites. HYTEC input file consisted of hydrate contents, concrete porosity, effective diffusion coefficient, and a database (Chess|THERMODDEM, 2014) with a list of cementitious hydration phases; see Table 6.2.

*Table 6.2: HYTEC Input data for different binder systems (Data from PHREEQC: Appendix M)*

| **Cement hydrates** | **SRPC+FA** | **SRPC + FA + HC** | **CEM II A-L** | **CSA** | **CAC** |
|---|---|---|---|---|---|
| | **Mol/L** | | | | |
| C1.6SH | 5.338 | 5.075 | 4.852 | - | - |
| $C_3AH_6$[#] | 1.133 | 1.063 | 0.919 | 3.651 | 3.755 |
| Ettringite ($3CaO.Al_2O_3.3CaSO_4.32H_2O$) | 0.202 | 0.183 | 0.222 | 2.584 | - |
| Gibbsite ($Al(OH)_3$) or $AH_3$ | - | - | - | 11.834 | 11.778 |
| Portlandite ($Ca(OH)_2$) | 9.812 | 8.265 | 15.163 | - | - |
| Goethite (FeOOH) | 0.809 | 1.099 | 1.065 | 0.715 | 0.477 |
| Brucite ($Mg(OH)_2$) | 0.647 | 0.623 | 0.685 | 0.643 | 0.199 |
| Porosity | 0.34 | 0.36 | 0.36 | 0.20 | 0.37 |
| $D_{SO_4^{2-}}$ in cement paste, x $10^{-11}$ $m^2/s$ | 2.42 | 2.04 | 3.55 | 0.47 | 0.19 |

[#] The effect of incorporating $C_3AH_6$ in the model is discussed in Section 6.3.1.

As stated earlier, the BAC of concrete in this study was only modelled using the open system mode of attack to understand its influence on the dissolution and precipitation of cementitious phases while varying the pH of the attacking acid. In this case, the cement paste is attacked by a continuous supply of sulphuric acid on the exposed surface, resulting in cementitious ions leaching from the composite and removal from the system, see Figure 6.1. Under this mode, the attacking acid contains a continuous acid supply of a specific pH ($H^+$ ions), balanced by its equivalent of sulphate ($SO_4^{2-}$) ions to form $H_2SO_4$ acid. The pH values are;

i) pH 1: $H^+$ = 220.200 mmol/L $SO_4^{2-}$ = 110.0 mmol/L

ii) pH 2: $H^+$ = 14.100 mmol/L $SO_4^{2-}$ = 7.055 mmol/L
iii) pH 3: $H^+$ = 1.084 mmol/L $SO_4^{2-}$ = 0.542 mmol/L
iv) pH 4: $H^+$ = 0.102 mmol/L $SO_4^{2-}$ = 0.051 mmol/L

Note that the concentration of ions decreases with an increase in pH. Species diffuse across the acid-paste interface, thus changing the composition of the attacking acid. This process is simulated by calculating the equilibrium composition of the attacking acid mixed with the pore solution at the cement paste surface.

### 6.2.5. Boundary conditions

Under the open system, the exposed surface condition was initially fully saturated at 23°C. The main controlling factors were the initial porosity and effective diffusion coefficient. The lower the coefficient, the lower the ion exchange rate between the attacking acid and cement paste, and the slower the deterioration rate. Archie's coefficient of 1.0, as was adopted by Aboulela et al. (2019) and a minimum porosity threshold of 0.01 was used for modelling (De Windt & Devillers, 2010). The node size of the calculation grid was set to 0.05 mm.

The charge neutrality of the cement paste was satisfied by adding appropriate balancing ions, e.g. Na+ for the positive charge and $OH^-$ for the negative charge as defined by the ionic product of water (Beddoe, 2016). Based on this electroneutrality, the appropriate pH of the cement paste was evaluated by the HYTEC model.

### 6.2.6. Chemical equilibrium

The chemical reactions were calculated assuming reactive transport equilibrium, i.e., chemical reactions were considered instantaneous compared to diffusion. A discrete approach to C–S–H dissolution was used by considering CSH (1.6), CSH(1.2) and CSH(0.8), depending on the type of binder system. Portlandite, $C_3AH_6$, ettringite, goethite, amorphous silica, gibbsite, gypsum, monosulfoaluminate, and brucite from the Chess reactive transport database (Chess|THERMODDEM, 2014) were included in the modelling. Amorphous silica, gibbsite, and gypsum were considered as ultimate degradation products. See chemical reactions in Appendix B.1.1.

## 6.3. Analysis and discussion of results

This section discusses the performance of UCT concrete binder systems in reactive transport modelling subjected to the open system attack mode. The dynamic evolution of cementitious phases, pH and porosity in the cement paste profile is studied, and the influence of each binder system is illustrated. The distributions of ion exchange between the cement paste and the attacking acid are shown in Appendix O. The analysis is grouped into Portland-based binder systems, including SRPC+FA, SRPC+FA+HC, CEM II A-L binders, and alumina-based binder systems, being the CSA and CAC binders. The Portland-based binder systems contain mainly Portlandite and calcium silicate hydrates (CSH(1.6)). The alumina-based binder systems mainly consist of $C_3AH_6$ and gibbsite and ettringite mainly for CSA cement (Hou, He & Liu, 2021).

### 6.3.1. Effect of $C_3AH_6$ in the cement paste under BAC at pH of 1

In Portland-based binders, the presence of calcium aluminate hydrates ($C_3AH_6$), in the HYTEC Model, causes 'pore-clogging', or complete pore-filling, at a pH of 1 due to continuous deposition of ettringite and other secondary phases such as gypsum, CSH(0.8) and CSH(1.2) in the transition zone close to the original surface, see Figure 6.2. The deposit is mainly associated with a high sulphate ion concentration at pH1, i.e., 110.0 mmol/L, see Section 6.2.4. As $H^+$ and $SO_4^{2-}$ ions from the attacking acid penetrate the cement paste, $H^+$ ions cause the decalcification of CSH (1.6) and Portlandite, while $SO_4^{2-}$ ions react with $C_3AH_6$ and $Ca^{2+}$ ions to form ettringite (Eq. 6.2). Ettringite ($C_3A(CaSO_4)_3H_{32}$) has a high molar volume; thus, its deposition causes a decrease in the cement paste porosity to zero.

$$C_3AH_6 + Ca^{2+} + {SO_4}^{2-} + 6H \rightarrow C_3A(CaSO_4)_3H_{32} \quad (6.2)$$

Therefore, to understand the evolution of cementitious phases for Portland-based binders, $C_3AH_6$ was omitted in the HYTEC input file since it is not the main hydrated phase experimentally observed in the Portland-based binders. The literature indicates that in the presence of gypsum in PC-based binders, calcium aluminate (C3A) exists as ettringite or monosulphoaluminate (Hewlett, 2019).

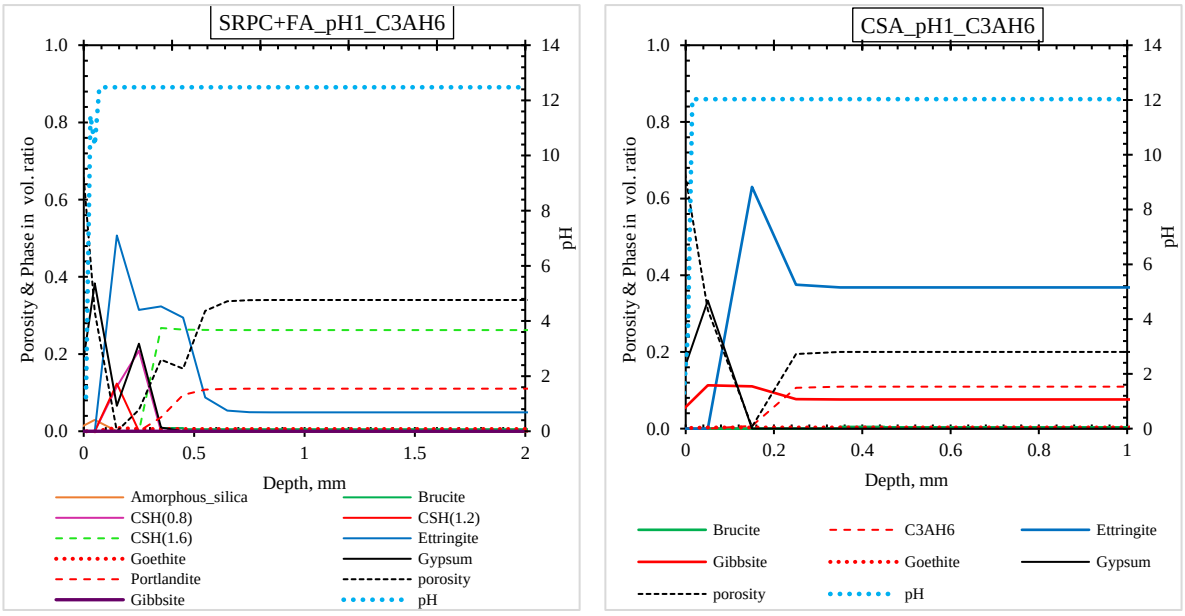


*Figure 6.2: Pore-clogging due to C3AH6 on the Portlandite (left column) and Aluminate (right column) based binder when subjected to the Sulphuric acid at pH1.In this figure, SRPC+FA represents the behaviour of Portlandite-based binder systems studied, and CSA represents the behaviour of alumina-based binder systems.*

In the alumina-based binder systems, a similar 'clogging' effect of $C_3AH_6$ was experienced, but in this case, pore-clogging is caused by ettringite formation only. HYTEC has limitations in accommodating the physical effects associated with ettringite formation, which can be misleading by indicating that the presence of $C_3AH_6$ enhances alumina-based binders to resist acid attack better. However, ettringite formation induces microcracking in the field by accelerating the deterioration due to its expansive nature. Therefore, since $C_3AH_6$ is the crucial phase for alumina-based binders, its concentration was

reduced until pore-clogging was no longer observed. The concentration of $C_3AH_6$ was then found to be 1.0 mol/L for both CSA and CAC cement paste compared with 3.6-3.7 mol/L in Table 6.2.

### 6.3.2. Effect of varying acid pH on SRPC+FA

Figure 6.3 shows profiles of SRPC+FA cement paste when subjected to the open system attack mode with varying pH after two years of exposure. In the first and second sets of figures (rows A and B), the evolution of cementitious phases, porosity, and pH in the profile is observed at pH1, pH2, pH3 and pH4. Row C shows cumulative calcium ions and $H_4SiO_4$ leaching for approximately two years. Their respective ionic profile after two years of exposure are shown in Appendix Figure O.1. It should be noted that the $C_3AH_6$ phase was omitted in the HYTEC input file due to the effects discussed in Section 6.3.1.

In this analysis, three zones of the cement paste composite after the attack are distinctly observed and defined using porosity and secondary cementitious fronts. The first zone is considered a 'deteriorated zone', the second zone is regarded as a 'transition zone,' and the third is the 'intact zone', as observed in Section 5.3.8. The ettringite front defines the deteriorated zone; the transition zone is between the ettringite front and the Portlandite front; and the intact zone is behind the Portlandite front, representing the non-deteriorated cementitious phase. Portlandite is the most unstable cementitious phase in contact with an acid solution (Georget, Prévost & Huet, 2018). Therefore, its dissolution forms the deepest reaction front, separating the intact zone from the altered zone, i.e., the transition and deteriorated zone.

#### 6.3.2.1. Deteriorated zone

The deteriorated zone is mainly observed at pH 1 and 2 and becomes less prominent at pH 3 and 4. At pH 1, the zone is characterised by a completely deteriorated/leached layer with high porosity of approximately 66%, followed by a broader layer containing amorphous silica, gypsum, and goethite, which reduces the porosity to less than 10%. The pH in this layer ranges from 1.0 to 3.9, with amorphous silica precipitating at a pH of 1.2 - 3.9, gypsum at 1.2 - 12.4, and goethite from 1.75. The goethite volume in this layer is higher than in the transition and intact zone, indicating its preferential accumulation at a pH below 2.0. The ionic profile (see Appendix Figure O.2) indicates that gypsum precipitates when the gradient of $Ca^{2+}$ ion leaching is zero while the sulphate ion penetration gradient is negative.

At pH 2, pH 3 and pH 4, the zone contains goethite only, while gypsum does not precipitate because the $SO_4^{2-}$ ion concentration from the attacking acid is insufficient for precipitation. The porosity is approximately 60%, while the pH varies from approximately 2.0 - 2.8 at pH 2 and 3.0 – 3.5 at pH 3 and 4.0 at pH 4. The thickness of this layer is approximately 3.85 mm at pH 1, 0.55 mm at pH 2, and 0.25 mm at pH 3 and pH 4 after two years of modelling.

.

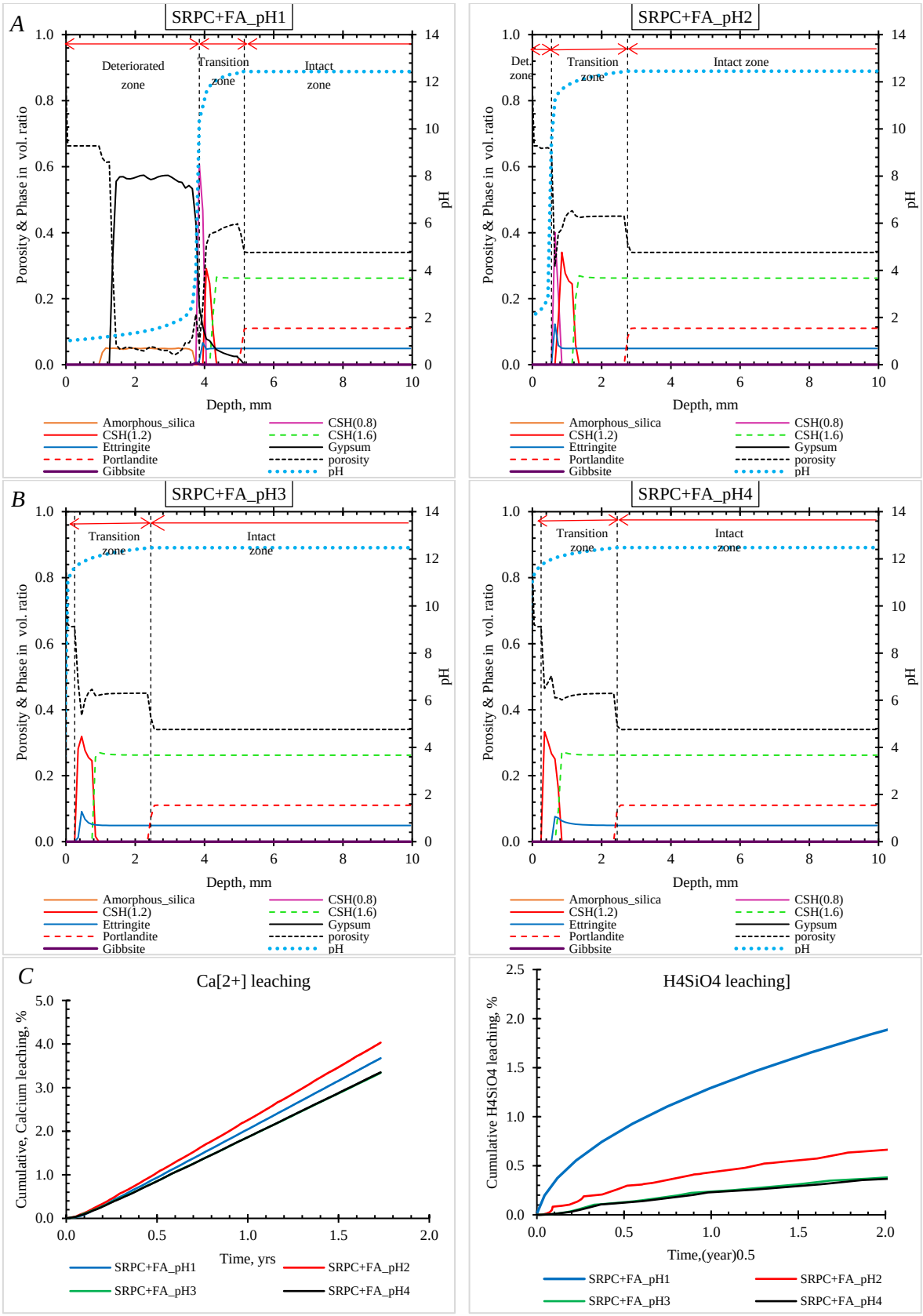


*Figure 6.3: After two years of exposure, profiles of SRPC+FA cement paste when subjected to the open system attack mode, with varying pH. The evolution of cementitious phases, porosity, and pH in the profile of SRPC+FA cement is observed at pH 1, pH 2, pH 3, and pH 4 in row A and row B. Row C shows the cumulative leaching of calcium and $H_4SiO_4$ ions for approximately two years.*

#### 6.3.2.2. Transition and intact zone

The transition zone contains the decalcified forms of calcium silicate hydrates, i.e., CSH (1.2) and CSH (0.8) and secondary ettringite, approximately 55% porosity with a rapid drop at a position where the ettringite front emerges, and the pH is above 10.8.

At pH1, the zone contains a peak of CSH (0.8), followed by CSH (1.2), then CSH (1.6), indicating the decalcification of calcium silicate hydrate. Gypsum formation gradually decreases to zero as the sulphate ion penetration decreases. A peak of brucite is observed at a pH of 10.4 to 11.5; see Appendix Figure O.1. A small secondary ettringite peak was observed, which indicated that not all penetrated sulphate ions reacted with calcium ions from the decalcification of CSH (1.6) and Portlandite to form gypsum

At pH 2, accumulation of CSH (0.8), followed by CSH (1.2), then CSH (1.6), brucite peak, and secondary ettringite are observed. At pH 3 and pH 4, CSH (0.8) and brucite peaks are not observed. Brucite and goethite profiles are not clearly seen because their volume is less than 1%. The thickness of the transition zone is approximately 1.3 mm at pH 1 and 2.2 mm at pH 2, pH 3 and pH 4. These values indicate that the transition zone is thinner at pH 1 than at pH 2, pH 3 and pH 4, meaning that the Archie Law-modified effective diffusion coefficient ($D(\omega)$) at pH 1 is higher than at pH 2, pH 3 and pH 4.

Irrespective of the pH of the attacking acid, the intact zone has the same cementitious volume and porosity as the initial state. The Portlandite front defines the zone, indicating the decalcification of Portlandite in the deteriorated and transition zones with sulphate ion penetration.

#### 6.3.2.3. Cumulative leaching of ions

Cumulative leaching of calcium ($Ca^{2+}$) ion and hydrous silica ($H_4SiO_4$) at the interface between the attacking acid and cement paste is extracted from the model analyses over two years, expressed as a percentage of its initial content in the undeteriorated form – Figure 6.3 row C. The rate of calcium ion leaching is higher at pH 2, followed by pH 1, while pH 3 and pH 4 show a similar rate. Total calcium leached at approximately two years is approximately 3.0%, 3.3%, 2.7% and 2.7% of the initial $Ca^{2+}$ content at pH 1, pH 2, pH 3 and pH 4, respectively. Calcium leaching at pH 1 is less than expected because the ions are held in the transition zone to form gypsum, which is not the case at pH 2, pH 3 and pH 4.

In the case of $H_4SiO_4$ leaching, the results indicate that pH 1 has the highest leaching rate, followed by pH 2, with pH 3 and pH 4 having the lowest rate. Total $H_4SiO_4$ leached after approximately two years is approximately 1.9%, 0.7%, 0.4% and 0.4% of the initial content at pH 1, pH 2, pH 3 and pH 4, respectively. The results indicated that the attacking acid with pH 1 is the most aggressive, followed by pH 2, while pH 3 and pH 4 give the lowest leaching.

#### 6.3.2.4. Performance of other Portland-based binders at pH1

Figure 6.4 presents the evolution of cementitious phases, porosity, and pH of SRPC+FA+HC and CEM II AL cement paste when subjected to the open system attack mode with pH 1 for two years. The

difference between the two binders and SRPC+FA (in Figure 6.3) is based on the concentration of cementitious phases, initial effective diffusion coefficient, and porosity.

CEM II A-L has the lowest CSH (1.6) and highest Portlandite content, followed by SRPC+FA, then SRPC+FA+HC cement paste. Regarding iron content, SRPC+FA+HC has slightly higher goethite content, but this does not relate to the 11.4% addition of iron-based additive (HC) since it was observed in the experiment investigation chapter ( Section 5.3.8.3) that it does not participate in any chemical reaction. SRPC+FA has the lowest porosity, and SRPC+FA+HC has the lowest effective diffusion coefficient.

All three Portland-based binder systems showed similar phases in the deteriorated and transition zones, as discussed in Section 6.3.2 at pH 1, but with different magnitudes. CEM II AL produced gypsum of approximately 60% paste volume, approximately 57% by the SRPC_FA, and approximately 50% by SRPC+FA+HC cement paste; this is associated with the highest Portlandite content in CEM II AL. Similarly, more amorphous silica is observed in the SRPC+FA and SRPC+FA+HC than in the CEM II A-L, which is also associated with low CSH (1.6) content. The pH and porosity profiles of SRPC+FA and SRPC+FA+HC are similar, while a minor difference is noted in the CEM II A-L in the deteriorated zone. In all Portland-based binder systems, goethite is observed in the deteriorated zone, while brucite is formed in the transition zone. Their deposition depended on the profile pH, where goethite is unstable below 2.0 and brucite below 10.9. However, brucite and goethite have an insignificant effect on the attack rate, possibly due to their low content.

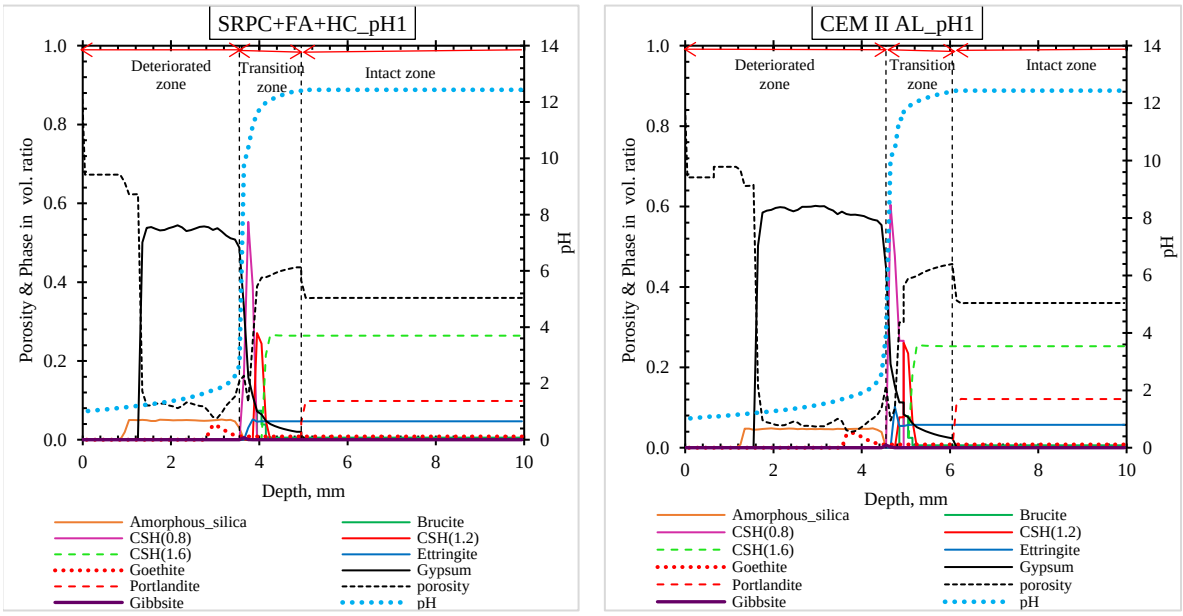


*Figure 6.4: Profiles of SRPC+FA+HC and CEM II AL cement pastes showing the evolution of cementitious phases, porosity, and pH in the profiles after being subjected to the open system attack mode of pH 1 for two years of exposure.*

### 6.3.3. Effect of varying acid pH on CSA

Figure 6.5 shows the CSA cement paste profile when subjected to the open system attack mode with varying pH for two years. The cementitious phases, porosity, and pH evolution in the cement paste profile are observed in the first and second sets of figures at pH 1, pH 2, pH 3 and pH 4 in row A and

row B. Row C shows the cumulative leaching of calcium and aluminium ions for approximately two years. Their respective ion distributions in the profile are shown in Appendix Figure O.3.

Three zones of cement paste after the attack are also distinctly observed in this binder, i.e., the deteriorated zone, the transition zone, and the intact zone. The deteriorated zone is marked by the ettringite front from the exposed surface; the transition zone is between the ettringite front and the $C_3AH_6$ front, while the intact zone is after the $C_3AH_6$ front; because it is the most unstable cementitious phase in the alumina-based binder systems when contact with an acid solution.

All three zones are distinctly observed at pH 1 and 2, while at pH 3 and 4, the deteriorated zone is not observed as in the SRPC+ FA binder. This behaviour is associated with (i) sulphate ions concentration and its gradient, which decreases with an increase in the attacking acid pH, and (ii) the respective Archie Law-modified effective diffusion coefficient, which increases with an increase in the porosity.

#### 6.3.3.1. Deteriorated zone

At pH 1, the deteriorated zone contains a thin layer with a porosity of approximately 68% and pH of approximately 1.0 – 1.3, followed by a layer with gypsum only, then with a peak of goethite (not shown in the figure because of its low volume ratio) and secondary gibbsite. Gypsum starts to precipitate at a pH of 1.4, goethite at 1.9, and secondary gibbsite at 3.6. With gypsum precipitation, the porosity decreases to 57%, then to 30% with gibbsite precipitation. Also, with gibbsite precipitation, the pH profile in this zone is maintained at about 3.6, which explains why the deteriorated zone is not examined at pH 3 and 4 since their attacking acid pHs are significantly higher to allow gibbsite dissociation. The thickness of this zone after two years is 2.35 mm at pH 1 and 0.55 mm at pH 2, with porosity of approximately 68% and secondary gibbsite.

#### 6.3.3.2. Transition and intact zone

The transition zone contains secondary ettringite and a slight increase in gibbsite volume. The precipitation of secondary ettringite significantly decreases the porosity to approximately 9% at pH 1 and 5% at pH 2. As discussed in Section 6.3.1, with a significant content of $C_3AH_6$, more ettringite precipitates, leading to pore-clogging. The pH in this zone gradually increases from 10.4 to 11.9 as secondary ettringite precipitation, resulting from a gradual penetration of sulphate ions (Appendix Figure O.3) and decalcification of $C_3AH_6$.

After two years, the thickness of this zone is approximately 1.3 mm, 1.6 mm, 1.2 mm, and 1.1 mm at pH 1, pH 2, pH 3, and pH 4, respectively. Similarly, the transition zone is thinner at pH 1 than at pH 2, pH 3 and pH 4, indicating that the Archie Law-modified effective diffusion coefficient at pH 1 is significantly higher to allow a rapid ionic exchange between the intact zone and altered zone, i.e., calcium and aluminium ion leaching and sulphate ion precipitation.

At all pHs of the attacking acid, the intact zone had similar cementitious phase volumes and porosities as the initial state before the attack. The zone is defined by the $C_3AH_6$ front, indicating the decalcification of $C_3AH_6$ in the deteriorated and transition zone with sulphate ion penetration. Unlike the Portland-based binder, CSA cement does not contain calcium silicate hydrates to form amorphous silica in the deteriorated zone or the decalcified calcium silicate in the transition zone.

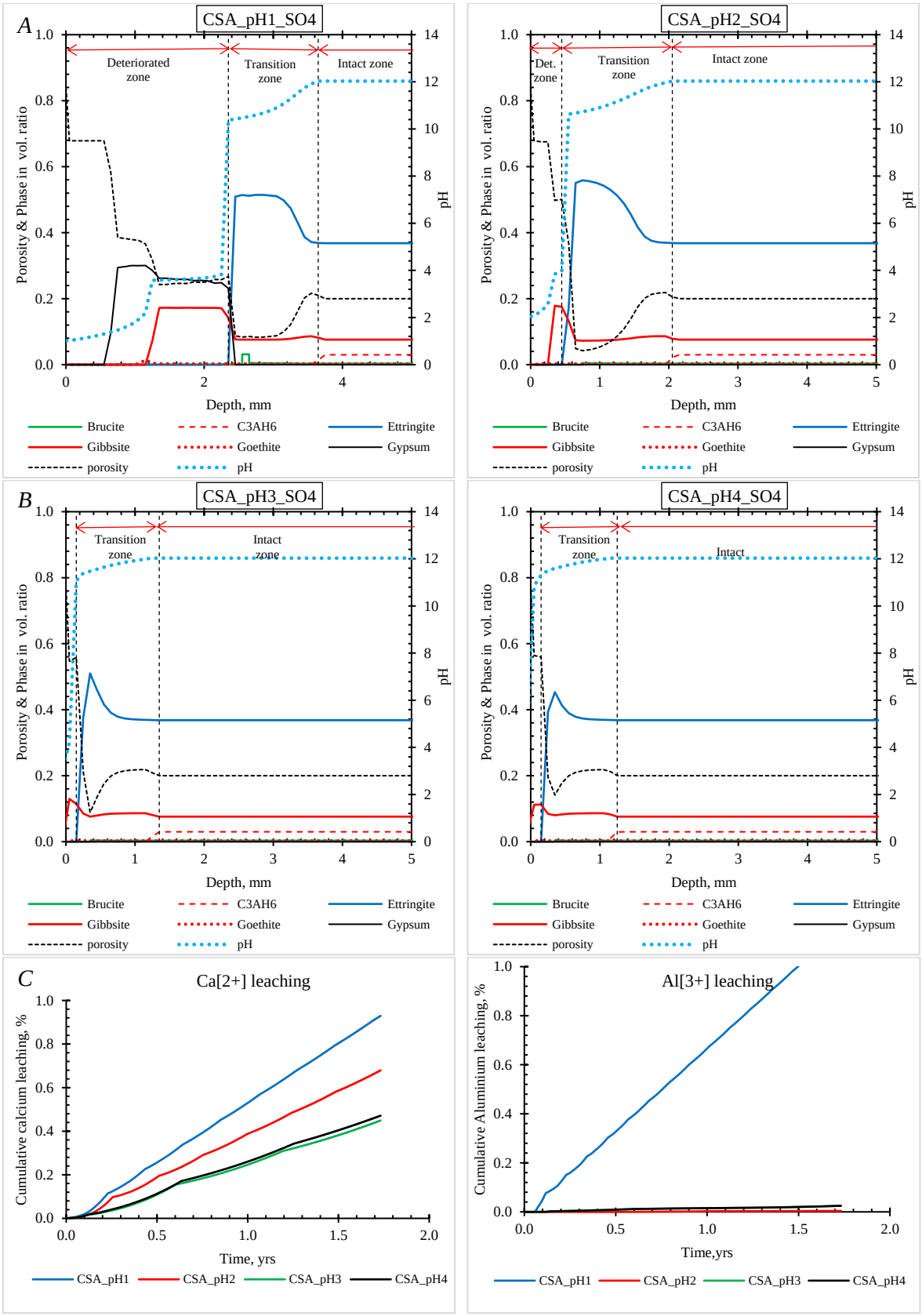


*Figure 6.5: Profiles of CSA cement paste when subjected to the open system attack mode of varying pHs after two years of exposure. The evolution of cementitious phases, porosity, and pH in the profile of CSA cement is observed at pH 1, pH 2, pH 3, and pH 4 in row A and row B. Row C shows the cumulative leaching of Calcium and Aluminium ions for approximately two years.*

#### 6.3.3.3. Cumulative leaching of ions

The calcium leaching figure indicates that pH 1 causes the highest cumulative ion leaching at the cement paste–attacking acid interface, followed by pH 2, while pH 4 and pH 3 show the least. This trend differs from that observed in SRPC+FA cement paste, where more calcium was held in the transition layer to form gypsum. The total cumulative calcium leaching after two years is 0.7%, 0.5%, 0.3% and 0.4% of the initial calcium content for pH 1, pH 2, pH 3, and pH 4, respectively. These values are also significantly lower than those observed for SRPC+FA cement paste.

In the case of aluminium ion leaching, substantial ion leaching is observed at pH 1 with approximately 0.9%, decreasing further to approximately zero at pH 2, pH 3, and pH 4, which explains the stability of aluminium phases when attacking acid pH is higher than 1.

### 6.3.4. Effect of varying acid pH on CAC

Figure 6.6 shows CAC cement paste profiles when subjected to the open system attack mode with varying pH after two years of exposure. The cementitious phases, porosity, and pH evolution in the cement paste profile are observed in row A and B at pH 1, pH 2, pH 3 and pH 4. The third set shows the cumulative leaching of calcium and aluminium ions for two years. Their respective ion distribution in the profile is shown in Appendix Figure O.4.

As observed in the previous cement pastes, CAC cement paste also distinctly shows three zones at pH 1 and 2, while at pH 3 and 4, the deteriorated zone is not visible. The zones in this binder system were defined differently from the previous binder systems. The deteriorated zone and the intact zone are separated by the transition zone defined by the thickness of secondary ettringite. It should be noted that CAC cement paste does not contain ettringite as its initial phase, like CSA.

#### 6.3.4.1. Deteriorated zone

At pH 1, the deteriorated zone is a thin layer with approximately 59% porosity, pH below 3.6, followed by a gibbsite and gypsum layer that reduces the porosity to approximately 39%. Gypsum precipitates at pH 2.2 and gibbsite at pH 3.6. Gibbsite in this zone is formed after the decalcification of $C_3AH_6$; see Eq. (6.3).

$$C_3AH_6 + 3SO_4^{2-} \rightarrow 3CaSO_4 + AH_3 + 3H_2O \quad (6.3)$$

At pH 2, only gibbsite is observed; gypsum formation is not favoured because of low sulphate ion concentration, and so do secondary ettringite since the profile pH is less than 10.4. As at pH 1, gibbsite precipitates at a pH of 3.6, which reduces the porosity from 57% to 46%. The precipitation of gibbsite at a pH above 3 is why CAC concrete surface pH in sewers tends to plateau at pH of approximately 3 to 4 (Kiliswa, 2016; Kiliswa, Scrivener & Alexander, 2019). It is also a similar reason why the deteriorated zone is not observed at pH 3 and 4, as indicated in the CSA cement paste.

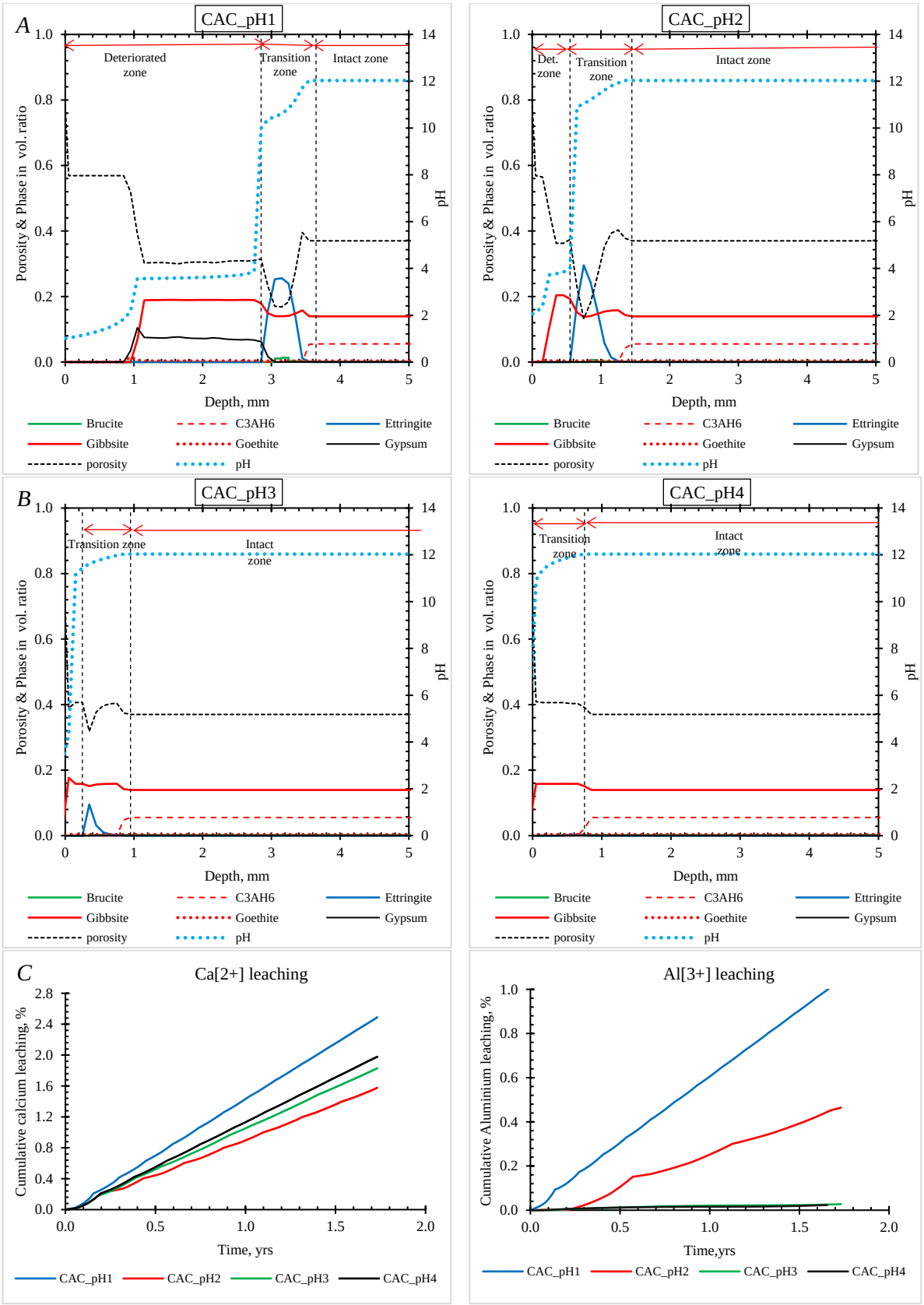


*Figure 6.6: Profiles of CAC cement paste when subjected to the open system attack mode of varying pH after two years of exposure. The evolution of cementitious phases, porosity, and pH in the profile of SPC+FA cement is observed at pH 1, pH 2, pH 3 and pH 4 in row A and B. Row C shows the cumulative leaching of Calcium and aluminium ions for approximately three years.*

#### 6.3.4.2. Transition zone

In the transition zone, secondary ettringite formation is preferred over gypsum because of a low concentration of sulphate ion penetration and a high-profile pH above 10.4. With ettringite formation at pH 1, the transition zone's pH increases gradually to 12.0. Its porosity decreases to approximately 17% due to a high expansion volume of ettringite. The same behaviour is observed at pH 2, whereas ettringite precipitates at a profile pH between 10.8 and 12.0, further decreasing porosity to approximately 13%. Ettringite in this zone coincides with the field experiment in Section 5.3.8.6.

At pH 3, secondary ettringite was also observed in the transition layer, with a lower volume ratio than at pH 1 and 2. On the contrary, at pH 4, only a slight increase in gibbsite concentration is observed due to the decalcification of $C_3AH_6$.

After two years, the thickness of the deteriorated zone is approximately 2.85 mm, 0.55 mm, 0.25 mm, and 0.05 mm, and the transition zone is approximately 0.8 mm, 0.9 mm, 0.7 mm, and 0.7 mm at pH 1, pH 2, pH 3 and pH 4, respectively. This analysis indicated the aggressivity of the attacking acid ranked as follows; pH 1 > pH 2 > pH 3 >pH 4.

#### 6.3.4.3. Cumulative leaching of ions

The cumulative leaching of calcium ion from highest to lowest ranked as follow; pH 1 > pH 4 > pH 3 >pH 2. The ion leaching at pH 1 is significantly higher than at other pHs because of its high aggressivity. pH 2 shows the lowest calcium leaching, followed by pH 3 because calcium ions are held in the transition zone to form secondary ettringite, unlike at pH 4, where ettringite does not precipitate. On the other hand, cumulative aluminium ion leaching ranked as follows; pH 1 > pH 2 > pH 3 and 4. This ranking indicates that aluminium phases can significantly dissociate when the attacking acid pH is lower than 2; above that, the phases are stable.

### 6.3.5. General discussions on the effect of varying acid pH

Generally, it was observed that cementitious phase evolution and corrosion zonation in the cement paste profile correspond well with the field observations when the attacking acid has a pH of 1, see Section 5.3.4. The same is not apparent for pH 2, pH 3 and pH 4, which was a somewhat surprising observation, thus raising a discussion regarding the pH of sulphuric acid produced by SOBs in sewers.

The phenomenon appears to be associated with the relatively high concentration of sulphate and hydrogen ions at pH 1. Other controlling factors, such as initial diffusion coefficient, phase concentrations and porosity, were constant and thus had little or no effect. At higher pHs of 2, 3 and 4, the results show insufficient sulphate ion concentrations to form the observed gypsum in actual sewer concrete deterioration.

In the literature, most pH measurements are of the concrete surface pH, which depends on the chemical composition of the concrete and the colonisation of acid-generating bacteria, which is not necessarily the pH of the acid produced by the bacteria. The minimum concrete surface pH measured ranges between 4.0 and 2.0; rarely, a pH of 1.0 is measured (Kiliswa, 2016). Despite the relatively high concrete surface pHs measured, gypsum, amorphous silica (for Portlandite-based binders) and gibbsite

(for alumina-based binder) are invariably observed on the deteriorated surface in field specimens – a situation that is not replicated in the modelling at pH > 1.

Consequently, this observation suggests that the pH of the attacking acid in sewers should be around 1.0 to produce a deteriorated zone with significant gypsum. Thus, the hypothesis is that the actual pH of the attacking acid in the sewer is mainly around 1.0. However, this pH is challenging to measure because, on the concrete substrate, it is neutralised by concrete alkaline species to maintain equilibrium.

### 6.3.6. Performance comparison of Portland and alumina-based binder systems

Comparing the Portland- and alumina-based binder systems, Portland-based binders consist of amorphous silica and gypsum in the deteriorated zone, while alumina-based binders consist of gibbsite and gypsum. Because of gibbsite precipitation in the alumina-based binder systems, pH levels at 3, which is also why the CAC concrete surface pH in sewers tends to plateau at approximately 3 to 4; see Section 2.4.2 and 5.3.4 (Kiliswa, 2016; Kiliswa, Scrivener & Alexander, 2019). In CSA concrete, gibbsite and gypsum were also observed in the deteriorated zone, see Section 5.3.8.5, and the surface pH was approximately 3, see Section 5.3.4. However, according to Aboulela (2022), only amorphous gibbsite is formed in the CSA deteriorated zone.

In the transition zone, Portland-based binders consist of a decalcified form of calcium silicate hydrates and ettringite, while alumina-based binder systems consist of secondary ettringite and gibbsite. The deterioration of Portland-based binders is governed by Portlandite decalcification, while that of alumina-based binders is governed by $C_3AH_6$ decalcification.

The difference between the alumina-based binders, i.e., CAC and CSA, derives from the ettringite composition and formation. CSA contains ettringite initially, while CAC initially contains no ettringite. However, in both binders, secondary ettringite is formed due to the penetration of sulphate ions from the attacking acid. In CSA binder, secondary ettringite formation promotes microcracking within the microstructure, as seen in Section 5.3.8.5, which amplifies the attack. This is because of ettringite superimposition, explaining why CSA has poorer performance than CAC-based concrete, despite having gibbsite. On the other hand, secondary ettringite in the CAC binder is hypothesised to contribute to the CAC concrete's best performance. This is due to its stability at a pH higher than 10.7, although not clear how since it is well known to induce microcracking in the concrete microstructure due to its expansive volume. With this, further analysis and study are recommended.

Regarding the behaviour of ettringite under sulphuric acid attack, ettringite is only stable at a pH above 10.7; below that, it disintegrates to form gypsum and gibbsite; when the pH is below 3, gibbsite dissociates to form aluminium ions. For this reason, the cumulative leaching of aluminium ions at attacking acid pH 3 and 4 in the CSA and CAC was approximately zero.

Figure 6.7 shows the cumulative leaching of calcium and aluminium ions of Portland and alumina-based binder systems per square root of time. In terms of cumulative calcium ion leaching at the interface, CEM II A-L had the highest leaching of approximately 3.8% of the initial content, followed by SRPC-based cement paste (i.e., SRPC+FA and SRPC+FA+HC) with comparable calcium ion leaching of approximately 3.0%, then, CAC with 2.0%, and CSA with 0.8%.

Regarding aluminium ion leaching, CEM II A-L had the highest leaching of approximately 5.2%, followed by SRPC+FA+HC of approximately 3.8%, 3.5% for the SRPC+FA cement paste, and 0.9 % for CAC and CSA. This result indicates that Portland-based binder systems experience a higher leaching rate than alumina-based systems. The rate corresponded well with the effective diffusion coefficient for Portland-based binder systems: the higher the diffusion coefficient, the higher the leaching rate. The opposite was observed for alumina-based binder; CAC had the lowest diffusion coefficient but showed a higher calcium leaching rate than CSA and a similar aluminium leaching rate, possibly due to the presence of ettringite which binds calcium ions.

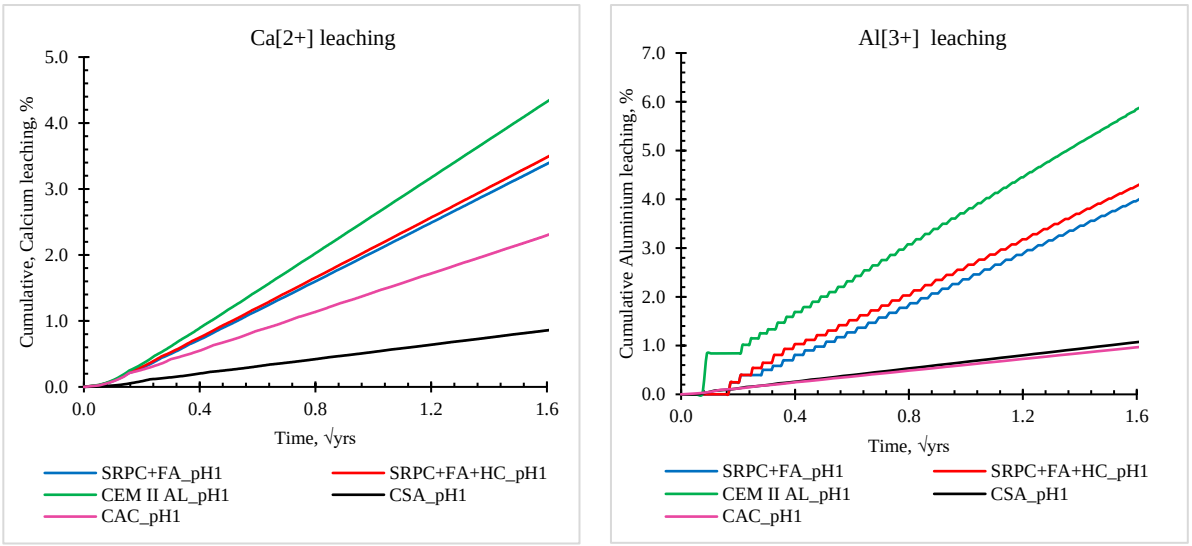


*Figure 6.7: The cumulative Calcium and aluminium ion leaching of Portland- and alumina-based binder systems per square root of time*

Figure 6.8 shows the deteriorated zone depth and the total altered depth against the square route of time for Portlandite and alumina-based binder systems. The total altered depth is expressed as the summation depth of the deteriorated and transition zone. It should be noted that the altered depth under HYTEC modelling is the summation of the thickness loss and altered depth measured under field investigation in chapter 5. The figure indicates that the rate obeys Fick's law of diffusion, i.e., that the attack rate is proportional to the square root of time. It is also observed that the rates of deteriorated zones are lower than those of altered zones. Altered zone rates indicate the acid penetration rate into the concrete, which causes the initial evolution of cement hydration phases to form the transition zone. Deteriorated zone rates indicate a complete evolution of the hydration phases in the transition zone into corrosion products, which can be lost in the field. Besides, the results indicate that the Portland-based binders have higher rates than alumina-based binder systems, with CEM II AL experiencing the most rapid attack, mainly due to its high effective diffusion coefficient and portlandite content. Alumina-based binder systems had the lowest attack rate, possibly due to their low diffusion coefficients and the presence of $C_3AH_6$, which produced a gibbsite layer after the attack.

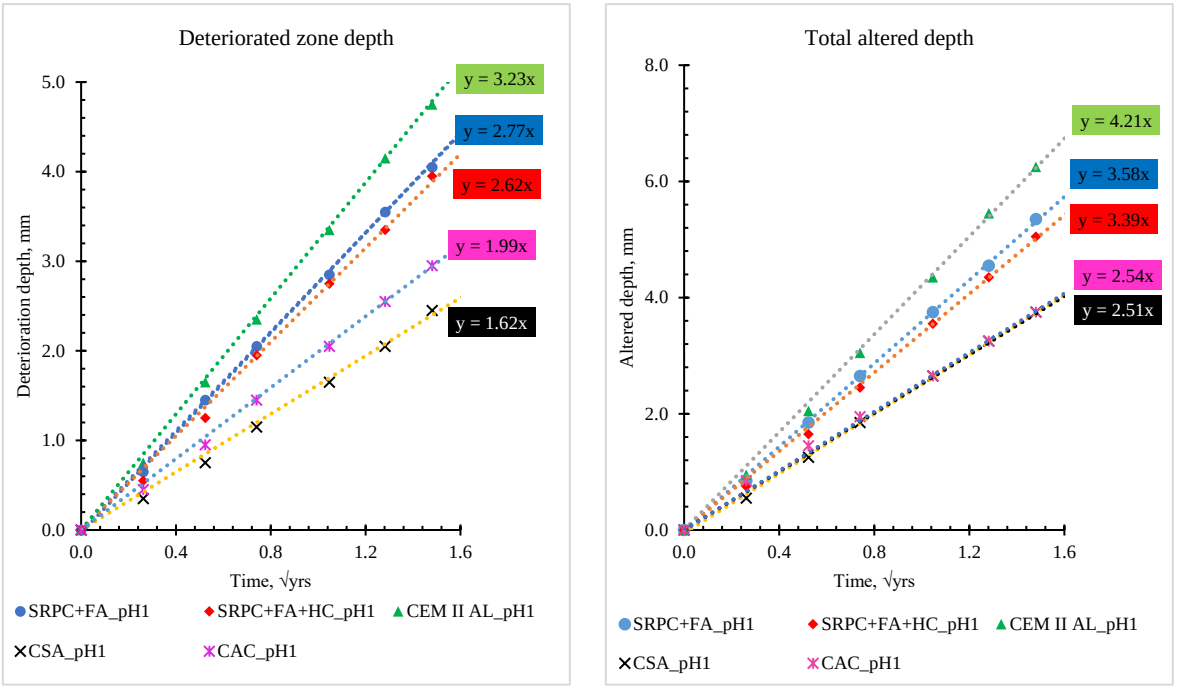


*Figure 6.8: Deteriorated zone depth and total altered depth of Portland and alumina-based concrete against the square root of time.*

## 6.4. HYTEC modelling results against field observations

In Chapter 5, it was observed that concrete subjected to the LPS lost more thickness than NAS M19 due to high $H_2S$ gas concentration and sewer hydraulic actions. LPS concrete specimens were subjected to frequent wetting and drying cycles, which allowed the corrosion layer formation during the dry cycle and wash out during the wet cycle. On the other hand, the NAS M19 concrete specimens were installed in the sewer headspace platform remote from the wastewater flowline, which means the corrosion layer build-up on the concrete exposed surface was rarely washed or worn away by the wastewater, only occasionally when the sewer was flooded. With such sewer conditions, the LPS represents the erosion zone or tidal zone, and NAS M19 represents a partial erosion zone (region between crown zone and tidal zone). This means that the attack mode experienced by the LPS concrete is closely related to the open system mode, while the NAS M19 is more related to the closed system mode. Since the closed system mode was not pursued in this study, the open system results are used for comparison.

### 6.4.1. Field-measured thickness loss against predicted altered zone

The field thickness losses can be correlated with the predicted deteriorated zone depth. Figure 6.9 compares the predicted deteriorated zone depths at pH1 with the field thickness losses at the LPS and NAS M19 after two years of exposure. Note that the thickness losses of concrete exposed at the LPS after two years were extrapolated from the corrosion rate, see Section 5.3.7 since the measurements after two years were not conducted as the specimens were lost on site before the end of the exposure period.

LPS thickness losses correlate reasonably well with the predicted deteriorated zone depths, while NAS M19 thickness losses lack meaningful correlation. The lack of correlation for the NAS M19 results is reasonable since the open system mode simulated the tidal zone and not the partial erosion zone. In the

case of LPS, the correlation indicated that the deteriorated depth of concrete is similar to that of cement paste, implying that the aggregate component has a lesser influence on corrosion rate in the presence of sewer hydraulic actions. With sewer hydraulic actions, the deteriorated zone and protruding aggregate are washed out simultaneously before aggregate dissolution.

In terms of ranking the performance of these binder systems both in the field and HYTEC modelling, the open system results correlated well with the field results in both sites, ranking from the highest thickness loss to the lowest as follows; CEM II AL > SRPC+FA> SRPC+FA+HC > CSA> CAC. However, after two years of field exposure, SRPC+FA and SRPC+FA+HC concrete show relatively similar thickness losses, implying that iron-based additive has insignificant influences in resisting the attack in long-term exposure.

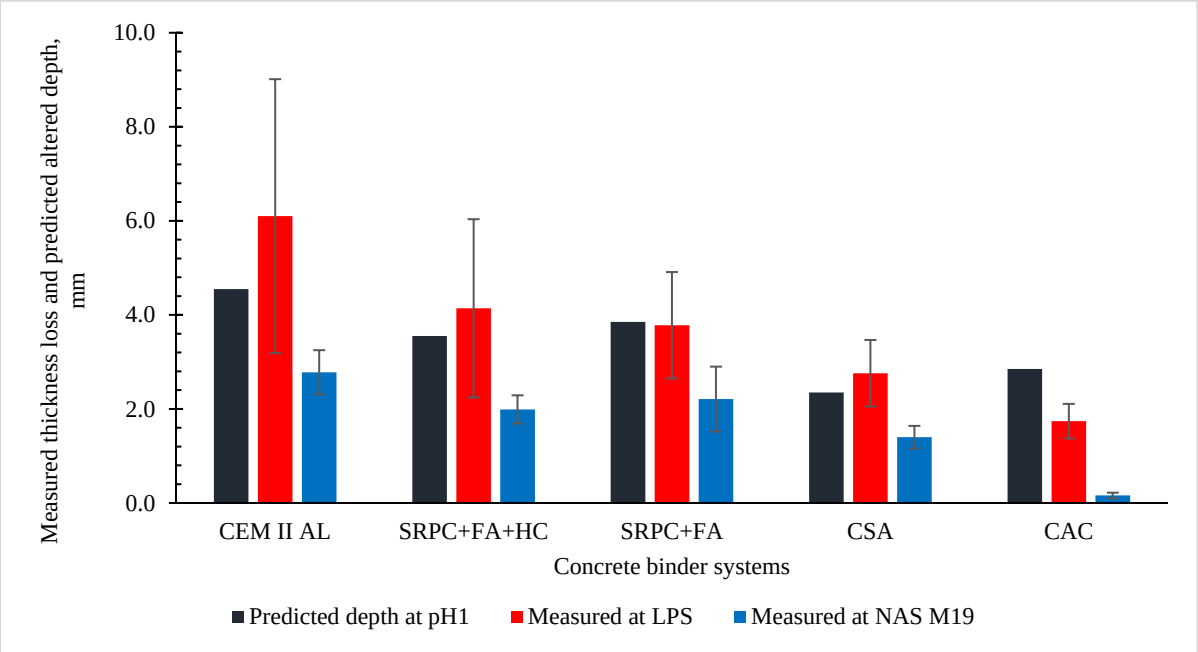


*Figure 6.9: Comparison between field-measured thickness loss of concrete and reactive transport predicted deteriorated zone depth of cement paste matrix of concrete after two years*

### 6.4.2. Concrete microstructure evolution

BAC microstructural analysis was conducted only on NAS M19 concrete specimens. Therefore, its observations are compared with the modelling microstructure results of the open system attack modes. Despite not incorporating dolomite aggregates in the modelling, it was observed that both exposure conditions (field exposure and modelling) agree on the concrete zonation and cementitious phases evolutions. Both exposures exhibited three distinct concrete zones, i.e., the deteriorated zone, the transition zone, and the intact zone. The HYTEC model deteriorated zone infers the total thickness loss on-site and the deteriorated zone measured on the SEM-BSE images. In both cases, the deteriorated zone is less cohesive with significantly high porosity, while the transition zone is a thin layer between the intact and deteriorated zones with integrity stronger than deteriorated zone but weaker than the intact zone.

The main hydration phases of Portland-based concrete are portlandite and hydrated calcium silicate (CSH), which react with sulphuric acid to form amorphous silica (quartz) and gypsum in the

deteriorated zone and gypsum and ettringite in the transition zone. In the case of alumina-based concrete, the main hydration products of CAC are calcium aluminate hydrate ($C_3AH_6$) and gibbsite, which with acid penetration, a broad layer of secondary ettringite is formed in the transition zone, followed by gibbsite and gypsum in the deteriorated zone. On the contrary, CSA hydration products are ettringite, gibbsite and calcium aluminate hydrates, which react with acid to form more gibbsite and ettringite in the transition zone and more gibbsite and gypsum in the deteriorated zone. The formation of more ettringite in the transition zone explains the QEMSCAN observation regarding the complexity of defining the transition zone in the CSA concrete microstructure.

Besides the main phases observed in each binder system, other minor phases, such as brucite and goethite, contributed to neutralising the attacking acid. Therefore, they are essential and should be considered when evaluating the neutralisation potential of a binder.

## 6.5. Chapter conclusion

From this chapter, the following main insights provide a better understanding of Portland and alumina-based binder system performance when subjected to acid attack at different pH.

- The presence of calcium aluminate hydrates causes pore-clogging at a pH1 due to continuous ettringite deposition. The effect is only observed in the alumina-based binder systems when a significant amount of $C_3AH_6$ (above 1.0 mol/L) is applied. This modelling effect can be misleading, indicating that the binder has a high potential to resist the attack; by contrast, in the field, the continuous ettringite deposition leads to severe concrete damage due to its expansive nature by inducing microcracking. Due to this, the model fails to address the physical effects associated with ettringite deposition.
- Under BAC, corrosion zonation, i.e., formation of a deteriorated zone, transition zone, and intact zone, is governed by ionic exchanges and the concentrations between the attacking acid and exposed cementitious surface. The three zones are distinctly observed when a binder system is subjected to the attacking acid of pH 1 due to the high sulphate and hydrogen ion concentrations. Thus, this raises the question of the pH of the attacking acid in concrete sewers; it is hypothesised that irrespective of their aggressivity classification, the bacteria produce acid at a low pH, and the difference in attack rates becomes a question of the acid production rates.
- All Portlandite-based binder systems behaved similarly under BAC, with gypsum and amorphous silica in the deteriorated zone and decalcified calcium silicate and ettringite forms in the transition zone.
- All alumina-based binder systems contain gypsum and gibbsite in the deteriorated zone and secondary ettringite in the transition zone. Due to gibbsite stability at a pH 3-4, their deteriorated zone pH tends to plateau at above 3 before gibbsite dissolution
- The deterioration of Portlandite-based binder systems is governed by the decalcification of Portlandite, while the decalcification of $C_3AH_6$ governs the deterioration of alumina-based binder systems. Therefore, Portlandite and $C_3AH_6$ dissolution forms the deepest reaction front, separating the intact zone from the altered zone.

- Other minor phases, such as brucite and goethite, neutralised the attacking acid. Therefore, they are essential and should be considered when evaluating the neutralization potential of a binder.

Finally, the HYTEC model, taken on its own, is not at this stage a viable tool for predicting the deterioration rate of concrete under sulphuric acid attack due to its limitation in incorporating aggregate components and accommodating the physical effects associated with the expansive nature of ettringite. However, it is a useful tool to help understand the deterioration mechanism of a cement paste matrix in concrete under acid attack. Significant insights into the behaviour of different binder systems and the characteristics of the attacking acid have been provided by this tool. Therefore, this tool is handy to engineers and researchers interested in understanding and developing binder systems that can resist acid attack and in designing robust concrete for sewer systems. With that said, sewer concrete designers and engineers still demand a simple and viable tool that can incorporate various sewer environment conditions, aggregate components, and binder systems, which is addressed in Chapter 7.

# CHAPTER 7. ADVANCEMENT OF LIFE FACTOR METHOD (LFM)

## 7.1. Introduction

Based on numerous deterministic models reviewed in Section 2.10, the LFM model is a preferred, commonly used, and practical model for sewer concrete design. Despite its preference, the model is restricted to modelling plain PC-based concrete with limited aggregate types. It fails to consider modern concrete mixes with a broader range of binder systems and aggregate types when subjected to different sewer-aggressive environments. Kiliswa (2016) refined the model to incorporate only two binders, i.e., PC and CAC, and introduced a factor which defines the influence of sewer environmental conditions, such as temperature and RH of a particular sewer. However, his improved model did not precisely quantify the environmental factors to cover various sewer environments, and the model was complicated to apply since most parameters were empirically evaluated.

With such limitations, the model requires further advancement to cover different sewer aggressivity, various ranges of modern binder systems, and aggregate influencing components. Therefore, this chapter intends to modify this model to reduce its limitations, increase its broader usage, and significantly contribute to sewer design and applications. In doing so, the knowledge extracted from the previous chapters, i.e., Chapter 4, Chapter 5, and Chapter 6, is employed herein.

## 7.2. Fundamental knowledge of the LFM model

LFM model background is provided in Section 2.10.1. In summary, the LFM model, shown in Eq. 7.1, comprises three essential terms, i.e., average $H_2S$ flux to the pipe wall ($\phi_{sw}$,), which predicts the rate of acid generated on the sewer wall based on hydraulic parameters and sulphide concentration in the wastewater, efficiency factor ($k$), which defines the amount of acid that remains on the pipe wall to react with the concrete, and alkalinity ($A$), which establishes the amount of calcium oxide contained in the concrete to neutralise the attacking acid. Based on this, the corrosion rate of sewer concrete can be determined by evaluating the sulfuric acid generation rate on the concrete wall and the concrete potential for neutralising the acid (Kaempfer & Berndt, 1999). Thus, the principal interpretation of Eq. 7.1 is given in Eq. 7.2.

$$C_{avg} = 11.4k\frac{\phi_{sw}}{A} \tag{7.1}$$

Where,

| | |
|---|---|
| $C_{avg}$ | Average (annual) corrosion rate (mm/yr) |
| $k$ | Efficiency factor |
| $\phi_{sw}$ | Average $H_2S$ flux to the pipe wall ($g/m^2/h$), |
| $A$ | Concrete alkalinity (g $CaCO_3$ per g concrete material) |

$$C_{avg} = \frac{Average\ acid\ generated\ on\ a\ m^2\ of\ a\ sewer\ pipe\ wall\ per\ year\ (\frac{g_{G.H_2SO_4}}{m^2 yr})}{Average\ acid\ neutralized\ by\ a\ m^3\ of\ a\ concrete\ pipe\ (\frac{g_{N.H_2SO_4}}{m^3})} \quad (7.2)$$

A small concrete section from a sewer concrete pipe, shown in Figure 7.1, is used to illustrate and define Eq. 7.2. The average acid generated on a $m^2$ of a sewer pipe wall per year ($\frac{g_{G.H_2SO_4}}{m^2 yr}$) accounts for the rate of acid generation on the sewer wall condensate film, which is evaluated according to Eq. 7.3.

$$\frac{g_{G.H_2SO_4}}{m^2 yr} = \frac{grams\ of\ generated\ H_2SO_4}{\Delta l \times L_{\propto} \times t}, \text{ where } G \text{ stands for generated} \quad (7.3)$$

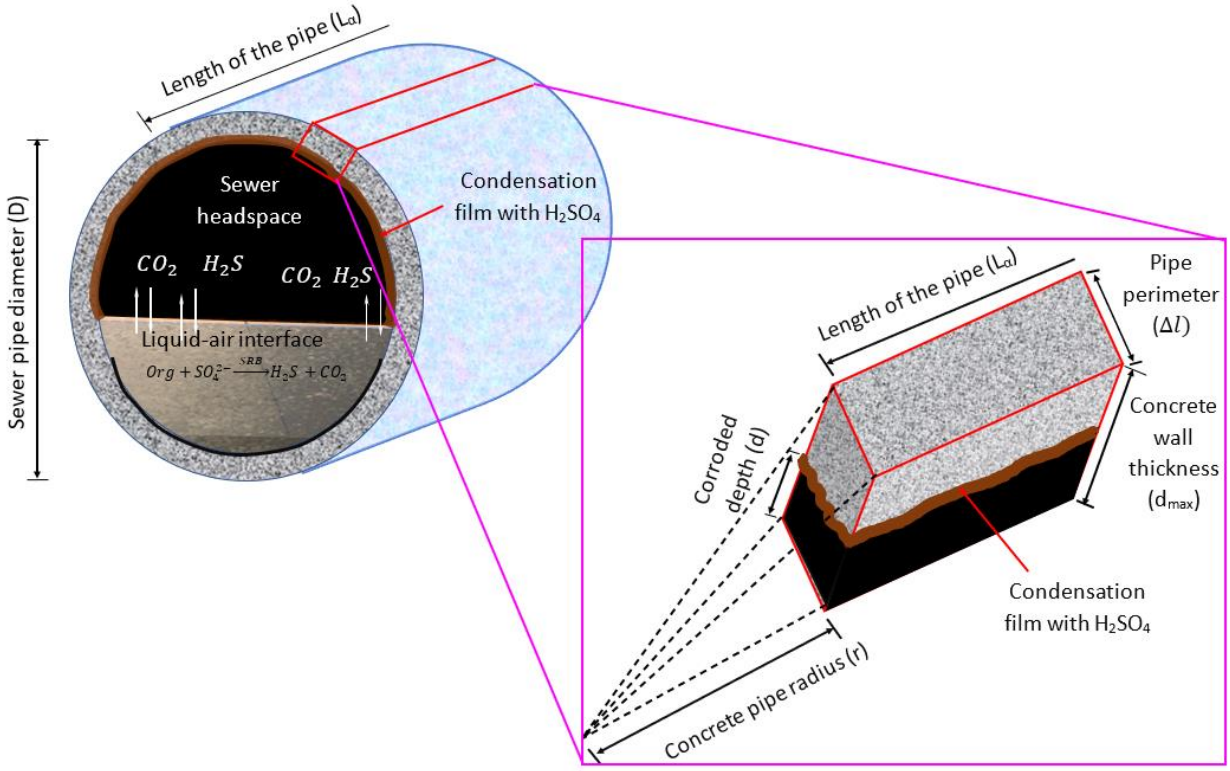


*Figure 7.1: Conceptual diagram illustrating the corrosion depth of sewer concrete pipe*

On the other hand, the average acid neutralised by one $m^3$ of a concrete pipe ($\frac{g_{N.H_2SO_4}}{m^3}$) indicates the amount of concrete dissolved or reacted with the generated acid on the sewer concrete wall. In other words, it accounts for the response or acid neutralisation capacity of various cementitious composites, i.e., a combined effect of aggregate and binder system in concrete in resisting the attacking acid. The acid neutralisation capacity of a $m^3$ of concrete is evaluated according to Eq. 7.4

$$\frac{g_{N.H_2SO_4}}{m^3} = \frac{grams\ of\ neutralized\ H_2SO_4}{d \times \Delta l \times L_{\propto}}, \text{ where N stands for neutralised} \quad (7.4)$$

When substituting Eq. 7.3 and Eq. 7.4 in Eq. 7.2, the corrosion rate of concrete can be defined as Eq. 7.5

$$C_{avg} = \frac{grams\ of generated\ H_2SO_4}{\Delta l \times L_{\propto} \times t} \times \frac{d \times \Delta l \times L_{\propto}}{grams\ of\ neutralized\ H_2SO_4} \quad (7.5)$$

Eq. 7.5 can be simply to Eq. 7.6

$$C_{avg} = \frac{grams\ of generated\ H_2SO_4/_t}{grams\ of\ neutralized\ H_2SO_4/_d} \equiv \frac{\phi_{se}}{MR \times \rho} \quad (7.6)$$

Where;

| | |
|---|---|
| $C_{avg}$ | Average corrosion rate (mm/yr) |
| $t$ | Exposure duration, yr |
| $d_{max}$ | Concrete wall thickness, m |
| $d$ | Corroded depth, m |
| $\Delta l$ | Concrete wall circumference of a small section, m |
| $L_{\propto}$ | Infinity Length of a sewer concrete pipe, m |
| $\phi_{se}$ | Sewer environmental factor, g of generated $H_2SO_4$/ $m^2$ yr |
| $MR$ | Material resistance factor, g of neutralised $H_2SO_4$ per g of concrete |
| $\rho$ | Density of concrete, kg/$m^3$ |

Based on Eq. 7.6, the rate of acid generation can be referred to sewer environmental factor ($\phi_{se}$) and the acid neutralisation capacity of the concrete is referred to as the 'Material Resistance' factor (MR). The following sections illustrate the principles used to evaluate these factors.

### 7.3. Sewer environmental factor ($\phi_{se}$)

The sewer environmental factor represents all the factors contributing to acid generation on the sewer pipe wall. This comprises $H_2S$ gas concentration in the sewer headspace, temperature, RH, and sewer hydraulic actions (wastewater velocity, turbulence flow, and sewer gradient), assuming SOBs are sufficient to oxidise the gas into acid (Nielsen, Hvitved-Jacobsen & Vollertsen, 2012).

These factors were considered in the average $H_2S$ flux to the pipe wall ($\phi_{sw}$) in Eq. 7.1 by EPA (1985) when developing the LFM model. However, the challenge associated with this parameter is that it was developed based on the prediction of $H_2S$ gas concentration from measured wastewater parameters such as dissolved sulphide in the wastewater, sewer gradient, wastewater velocity, and wastewater pH. Subsequently, numerous devices for accurately measuring $H_2S$ gas concentration in the sewer headspace have been developed and have become accessible. Besides, once the gas is readily available in the sewer headspace, the key factors attributed to the oxidation of gas to acid are related to $H_2S$ gas adsorption and oxidation rate on the sewer wall surfaces and not the properties of wastewater, see Section 2.9. This is because $H_2S$ adsorption and oxidation are quicker processes than $H_2S$ release from the bulk water of a gravity sewer (Vollertsen et al., 2008).

According to various studies evaluating $H_2S$ adsorption and oxidation rate (Nielsen, Hvitved-Jacobsen & Vollertsen, 2005, 2012; Vollertsen et al., 2008), the model developed by Vollertsen et al. (2008) and improved by Nielsen, Hvitved-Jacobsen and Vollertsen (2012) was found effective in predicting the

average $H_2S$ adsorption and oxidation rate to the pipe wall, $\phi_{se}$ (Eq. 7.7: Background provided in Section 2.9.1). However, instead of being expressed as mg sulphur per $m^2$ per second, it should be expressed in g of $H_2SO_4$ per $m^2$ of sewer pipe wall per hour to accommodate unit conversion; see Eq. 7.8.

$$\phi_{se} = \left(101325 \frac{34}{RT} \frac{V_g}{A_c} k_p\right) Re^m P_{H_2S}^n \tag{7.7}$$

The Vollertsen et al. model in Eq. 7.7 indicates that the $H_2S$ adsorption rate of the sewer concrete surface is related to the $H_2S$ oxidation rate, which implies that all adsorbed $H_2S$ gas by the concrete surface is oxidised into $H_2SO_4$. With this observation, the oxidation reaction expressed in Eq. 7.8, i.e., one mole of $H_2S$ is equivalent to one mole of $H_2SO_4$, is valid for the unit conversion.

$$H_2S + 2O_2 \rightarrow H_2SO_4 \tag{7.8}$$

| | | |
|---|---|---|
| I mole of $H_2S$ produces | ≡ | 1 mole of $H_2SO_4$ |
| 34 g/mol of $H_2S$ | ≡ | 98 g/mol of $H_2SO_4$ |
| $\phi_{se}\ g\ of\ sulphur/m^2h$ | ≡ | ? |

Thus, Eq. 7.7 can be expressed as Eq. 7.9

$$\phi_{se}\ g\ of H_2SO_4/m^2h = \frac{98}{34} * 3600 \left(101325 \frac{34}{RT} \frac{V_g}{A_c} k_p\right) Re^m P_{H_2S}^n \tag{7.9}$$

The average $H_2S$ flux to the pipe wall, which in this study refers to the sewer environmental factor, can be expressed in Eq. 7.10

$$\phi_{se} = 3600 \left(101325 \frac{98}{RT} \frac{V_g}{A_c} k_p\right) Re^m P_{H_2S}^n \tag{7.10}$$

Where,

| | |
|---|---|
| $\phi_{se}$ | Sewer environmental factor to the sewer wall pipe, expressed in g of $H_2SO_4$/ $m^2$ h. This is defined as $F_{H_2S}$ , the surface-specific rate of $H_2S$(g) adsorption and oxidation in Vollertsen et al. (2008). |
| 3600 | Converts seconds to hours |
| 101325 | Standard atmospheric pressure in Pa |
| 98 | Molar mass of $H_2SO_4$ gas, g/mol |
| $R$ | Universal gas constant (8.314 $m^3$ Pa/K mol) |
| $T$ | Temperature in K |
| $V_g$ | Total gas volume ($m^3$) in the sewer headspace |
| $A_c$ | Concrete surface area subjected to sewer gas ($m^2$) |
| $k_p$ | $H_2S$ adsorption rate constant ($ppm^{(1-n)}$/second) ranges from 0.019 to 0.177 depending on the type of concrete wall and oxidation rate of $H_2S$ to $H_2SO_4$ (Vollertsen et al., 2008) |
| $n$ | Reaction order, ranging from 0.45 to 0.75 (Vollertsen et al., 2008) |
| $Re$ | Reynold number of the sewer headspace airflow |
| $m$ | Empirical power equal to 0.65 |
| $P_{H_2S}$ | Sewer headspace $H_2S$ gas concentration, in ppm |

### 7.3.1. Reynolds Number definition

Reynolds Number describes flow conditions as follows; flow is laminar when Re < 2300, transient when 2300 < Re < 4000, and turbulent when Re > 4000 (Nielsen, Hvitved-Jacobsen & Vollertsen, 2012). The Reynolds number, see Eq. 7.11, indicates the effect of sewer headspace airflow on $H_2S$ adsorption and oxidation by the exposed concrete surface (Nielsen, Hvitved-Jacobsen & Vollertsen, 2012). In this study, these parameters were not measured/studied. However, to achieve the aim of this study, the scenario involving turbulent airflow, is considered. to be conservative. Clearly, further study on this aspect is recommended.

$$Re = \frac{\rho_a v d}{\mu} \tag{7.11}$$

Where,

| | |
|---|---|
| $Re$ | Reynold number of sewer headspace airflow |
| $\rho_a$ | Sewer headspace air density in kg/m$^3$ |
| $v$ | Air- velocity in m/s |
| $d$ | Sewer headspace, non-wetted hydraulic diameter in m |
| $\mu$ | Air dynamic viscosity in kg/m/s |

For example, consider Re = 4000 for a half-full flow sewer pipe with a diameter of 0.9 m. At standard conditions, properties of air are $\mu$ = 1.8515 x10$^{-5}$ m$^2$/s and $\rho_a$ = 1.185kg/m$^3$ (Mackenzie, 2020). The ideal air velocity, $v$, will be equal to 0.07 m/s. Lowe (2016) indicates that the air velocity in sewer is typically less than the water velocity, with average air velocities usually in the range of 5% to 30% of average water velocities. With this, the velocity of wastewater will range from 0.23 to 1.40 m/s. These velocities are at the lower end of the range for most large-diameter sewers. Therefore, the assumption of Re above 4000 for the sake of modelling is reasonable.

### 7.3.2. Application example of sewer environmental factor ($\phi_{se}$)

Referring to the Virginia Experimental Sewer (VES) study by Kiliswa (2016), the sewer environmental and hydraulic conditions were as follows;

- $H_2S$ concentration in sewer headspace, average annual — 35 ppm
- Sewer hydraulic velocity — 2.5 m/s
- Sewer headspace temperature — 23$^o$C
- Pipe diameter — 0.9 m
- Pipe flow conditions — half full

For calculation purposes, assume that the $H_2S$ adsorption rate of concrete with low permeability ($k_p$ ) is 0.05 ppm$^{(1-n)}$/s and n is 0.50. This assumption is tested against the field date to confirm its validity in Section 7.7.2.

The following is the sewer environmental factor ($\phi_{se}$) calculation:

- Reynolds number ($Re$): consider a turbulent sewer headspace airflow for the worst-case scenario; $Re > 4000$: Assume Re = 5000.

– Concrete exposed surface area and volume of $H_2S$ gas in the sewer headspace calculations:

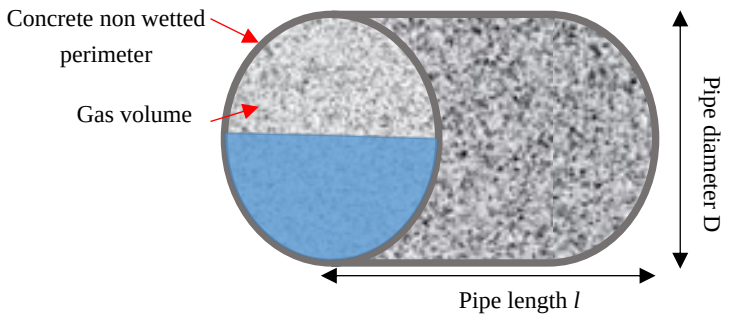


*Figure 7.2: Schematic diagram illustrating a half-full wastewater flow in a sewer concrete pipe*

For half-full flow, see Figure 6.2, the concrete surface area = non-wetted perimeter* length of the pipe

$$A_c = \frac{\pi D}{2} l = \frac{\pi \times 0.9}{2}\ l$$

The volume occupied by gas, $V_g = \frac{\pi d^2}{8} l = \frac{\pi \times 0.9^2}{8} l$

Therefore, $\frac{V_g}{A_c} = \frac{\pi \times 0.9^2}{8} \times \frac{2}{\pi \times 0.9} = \frac{0.9}{4}$

– Temperature = 273 + 23 = 296 K

The sewer environmental factor ($\phi_{se}$) expressed in g of generated $H_2SO_4$/ $m^2$ h, use Eq. 7.10

$$\phi_{se} = 3600 \left(101325 \times \frac{98}{8.31 \times 296} \times \frac{0.9}{4} \times \frac{0.05}{1000000}\right) \times 5000^{0.65} \times \left(\frac{35}{1000000}\right)^{0.5}$$

$\phi_{se}$= 0.245 g/$m^2$ h

(Note that 1 ppm means one part per million (1/1000000))

Figure 7.3 shows the relationship between $H_2S$ gas concentration in the sewer headspace and the sewer environmental factor ($\phi_{se}$ in g of $H_2SO_4$) of concrete with different $H_2S$ adsorption constant rates ($k_p$) and n = 0.5, based on VES. The figure is similar to that of Sun et al. (2014), where it was also observed that the flux is more sensitive at lower $H_2S$ gas concentrations than at higher concentrations. This observation concurs with the literature that higher $H_2S$ gas concentrations do not necessarily mean proportionally higher corrosion rates, but the corrosion rate is sensitive to the $H_2S$ adsorption rate of a particular concrete surface (Sun et al., 2014, 2015; Jiang et al., 2015; Grandclerc et al., 2017).

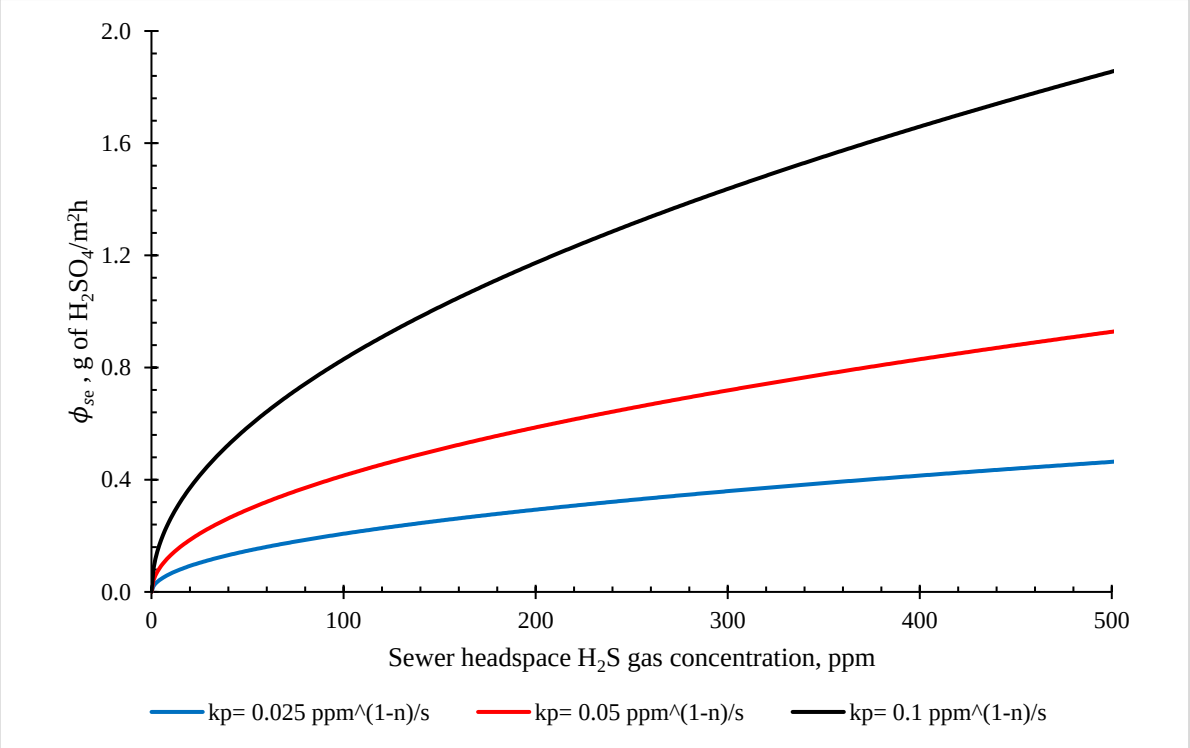


*Figure 7.3: Relationship between $H_2S$ gas concentration in sewer headspace with sulphide flux to the sewer pipe wall ($\phi_{sw}$ in g of $H_2SO_4$) at different concrete surface $H_2S$ adsorption rates ($k_p$) based on sewer conditions stated in 7.3.1, where n= 0.5.*

## 7.4. Material Resistance (MR) Factor

The 'Material Resistance' (MR) factor, representing the average acid neutralisation capacity of the concrete, accounts for the response of various cementitious materials (a combination of aggregate and binder systems in concrete) when subjected to a sewer environment. It comprises the acid neutralisation factor of binders, $\varphi$ (Section 7.5) and the aggregate reactivity factor, $\beta$ (Section 7.6), see Eq. 7.12.

$$MR = (\varphi + \beta) \tag{7.12}$$

Where,

| | |
|---|---|
| $MR$ | Material resistance, in g of $H_2SO_4$ to be neutralised by g of concrete |
| $\varphi$ | Acid neutralisation factor of binders in g of $H_2SO_4$ to be neutralised by g of concrete |
| $\beta$ | Aggregate reactivity factor in g of $H_2SO_4$ to be neutralised by g of concrete |

## 7.5. Acid neutralisation factor of binders ($\varphi$)

Four principal oxides of binder, i.e., CaO, $Al_2O_3$ $Fe_2O_3$, and MgO, contained in almost all cementitious phases observed in Chapter 5 and Chapter 6, are responsible for neutralising sulphuric acid under BAC in concrete (Pistor & Taylor, 1935). For instance, CaO exists in calcium silicate hydrate (CSH), ettringite, Portlandite, Calcium aluminate hydrates ($C_3AH_6$), and monosulphoaluminate, $Al_2O_3$ in

gibbsite, ettringite, $C_3AH_6$, and monosulphoaluminate, $Fe_2O_3$ in goethite, and MgO in Brucite. The acid neutralisation factor of binders can be evaluated based on the potential of these oxides in reacting with the acid.

The content of these oxides can be obtained from the XRF analysis of a binder before hydration. The amounts required to neutralise sulphuric acid can be quantified with simple chemical reaction principles. Therefore, the following subsections quantify the equivalent oxide content in the binders required to neutralise sulphuric acid when exposed to a sewer.

### 7.5.1. Calcium Oxide (CaO)

The chemical reactions between calcium oxide and sulphuric acid are presented in Eq. 7.13. From the equation, the amount of $H_2SO_4$ to be neutralised by CaO of a binder in concrete is evaluated in Eq. 7.14. However, CaO contributed by the gypsum in the binder should be deducted. This deduction applies mainly to binders such as CSA, which consists of about 15.71% of $SO_3$(g) in XRF analysis, equivalent to 10.99% of CaO.

Sulphuric acid reaction with CaO

$$CaO + H_2SO_4 \rightarrow CaSO_4 + H_2O \tag{7.13}$$

| | | |
|---|---|---|
| 56 g/mol of CaO | ≡ | 98 g/mol of $H_2SO_4$ |
| wt% CaO in cement | ≡ | ? |

Therefore, the amount of sulphuric acid to be neutralised by the equivalent CaO in the binder is given by Eq. 7.14

$$\varphi_{CaO} = \frac{98}{56} \times \frac{wt\%_{CaO}}{100} \frac{C}{\rho} \tag{7.14}$$

### 7.5.2. Aluminium oxide ($Al_2O_3$) in a binder

Similar principles are applied to aluminium oxide ($Al_2O_3$) obtained in a binder.

$$Al_2O_3 + 3H_2SO_4 \rightarrow 2Al^{3+} + 3{SO_4}^{2-} + 3H_2O \tag{7.15}$$

| | | |
|---|---|---|
| 1 mole of $Al_2O_3$ neutralise | ≡ | 3 moles of $H_2SO_4$ |
| 1 mol x 102 g/mol of $Al_2O_3$ | ≡ | 3 mol x 98 g/mol of $H_2SO_4$ |
| $wt\%_{Al_2O_3}$ in cement | ≡ | ? |

Therefore, the amount of sulphuric acid to be neutralised by the equivalent $Al_2O_3$ in the binder is given by Eq. 7.16

$$\varphi_{Al_2O_3} = \frac{294}{102} \times \frac{wt\%_{Al_2O_3}}{100} \frac{C}{\rho} \tag{7.16}$$

### 7.5.3. Iron oxide ($Fe_2O_3$) in a binder

Similar principles are applied to Iron oxide obtained in a binder.

$$Fe_2O_3 + 3H_2SO_4 \rightarrow 2Fe^{3+} + 3SO_4{}^{2-} + 3H_2O \quad (7.17)$$

| | | |
|---|---|---|
| 1 mole of $Fe_2O_3$ neutralise | ≡ | 3 moles of $H_2SO_4$ |
| 1 mol x 157 g/mol of $Fe_2O_3$ | ≡ | 3 mol x 98 g/mol of $H_2SO_4$ |
| $wt\%_{Fe_2O_3}$ in cement | ≡ | ? |

Therefore, the amount of sulphuric acid to be neutralised by the equivalent $Fe_2O_3$ in the binder is given by Eq. 7.18

$$\varphi_{Fe_2O_3} = \frac{3 \times 98}{157} \times \frac{wt\%_{Fe_2O_3}}{100} \frac{C}{\rho} \quad (7.18)$$

### 7.5.4. Magnesium Oxide (MgO) in a binder

Magnesium oxide is explicitly applied for the binder system containing slag since it has a high amount of magnesium oxide. Therefore, similar principles are applied.

$$MgO + H_2SO_4 \rightarrow Mg^{2+} + SO_4{}^{2-} + 2H_2O \quad (7.19)$$

| | | |
|---|---|---|
| 40 g/mol of $MgO$ | ≡ | 98 g/mol of $H_2SO_4$ |
| $wt\%_{MgO}$ in cement | ≡ | ? |

Therefore, the amount of sulphuric acid to be neutralised by the equivalent $MgO$ in the binder is given by Eq. 7.20.

$$\varphi_{MgO} = \frac{98}{40} x \frac{wt\%_{MgO}}{100} \frac{C}{\rho} \quad (7.20)$$

### 7.5.5. Total acid neutralisation factor of a binder ($\varphi$)

The total acid neutralisation factor of a binder under sulphuric acid attack is given as the summation of the acid neutralisation factor provided by calcium oxide (Eq. 7.14), aluminium oxide (Eq. 7.16), iron oxides (Eq. 7.18), and magnesium oxide (Eq. 7.20); see Eq. 7.21 and Eq. 7.22.

$$\varphi = \varphi_{CaO} + \varphi_{Al_2O_3} + \varphi_{Fe_2O_3} + \varphi_{MgO} \quad (7.21)$$

$$\varphi = \left(\frac{1}{56} \times \frac{wt\%_{CaO}}{100} + \frac{3}{102} \times \frac{wt\%_{Al_2O_3}}{100} + \frac{3}{157} \times \frac{wt\%_{Fe_2O_3}}{100} + \frac{1}{40} \times \frac{wt\%_{MgO}}{100}\right) \times \frac{98}{1} \times \frac{C}{\rho} \quad (7.22)$$

Where:

| | |
|---|---|
| $\varphi$ | Acid neutralisation factor of binders in g of $H_2SO_4$ to be neutralised by g of concrete |
| $wt\%$ | XRF oxide composition contained in the binder system, mainly CaO, $Al_2O_3$ $Fe_2O_3$, and $MgO$ |
| $C$ | Binder/cement content in concrete in kg/m$^3$ |
| $\rho$ | Density of concrete, kg/m$^3$ |

### 7.6. Aggregate reactivity factor (β)

The effect of aggregates in concrete under BAC is challenging to incorporate in the modelling due to their physical properties. Therefore, to consider these properties, the behaviour of different reactive aggregates and their response to sulphuric acid attacks must be understood.

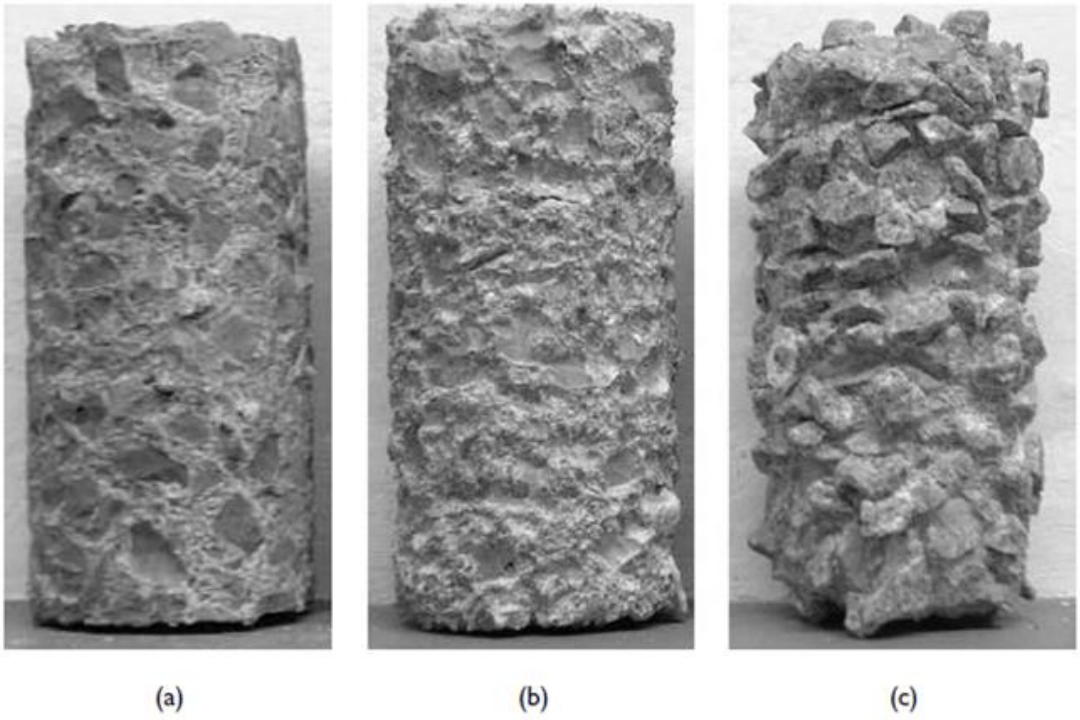


*Figure 7.4: Concrete cylinder under sulphuric acid: (a) Smooth surface – component dolomite; (b) 'Cratered' surface – fractured limestone; and (c) Very rough surface due to aggregate fallout. Cylinders with original dimensions of 80 mm diameter by 150 mm by Clyde Fourie, UCT) (Alexander & Mindess, 2005).*

Figure 7.4 shows the surfaces of concretes made with (a) strong and competent dolomite aggregates, (b) weak fractured limestone aggregate, and (c) strong and acid-insoluble granite aggregates after sulphuric acid attack (Alexander & Mindess, 2005). In the case of dolomite, the concrete surface is relatively smooth, suggesting that the attack is equally distributed over the whole surface. A cratered surface is noticed in the concrete with limestone aggregates, indicating weak and internally fractured aggregate particles. Only the binder has been attacked for the concrete with granite aggregate, resulting in rapid deterioration and early aggregate fallout. Hughes and Guest (1978) also indicate that competent limestone aggregate concrete is preferable since it erodes more smoothly and creates less debris than

comparable siliceous aggregate concrete. Thus, it is clear that the contributing effect of aggregate deterioration is vital for a complete picture of sewer concrete deterioration.

In simplifying the overall contribution of aggregates in the LFM model, this can be expressed as an 'aggregate reactivity factor'( β) to define various scenarios in which the aggregates can contribute to neutralising the attacking acid. For example, while some aggregates, such as calcareous aggregates, are reactive under acidic conditions, others, such as siliceous aggregates, are not. Also, some aggregates might contain reactive and non-reactive components, and some concrete mixes may contain reactive and non-reactive aggregates. Therefore, under sulphuric acid attack, different aggregates react and behave differently when combined with different cement/binder systems in concrete. The following illustrates four possible reactive behaviour of aggregates in concrete, as highlighted in Figure 7.5;

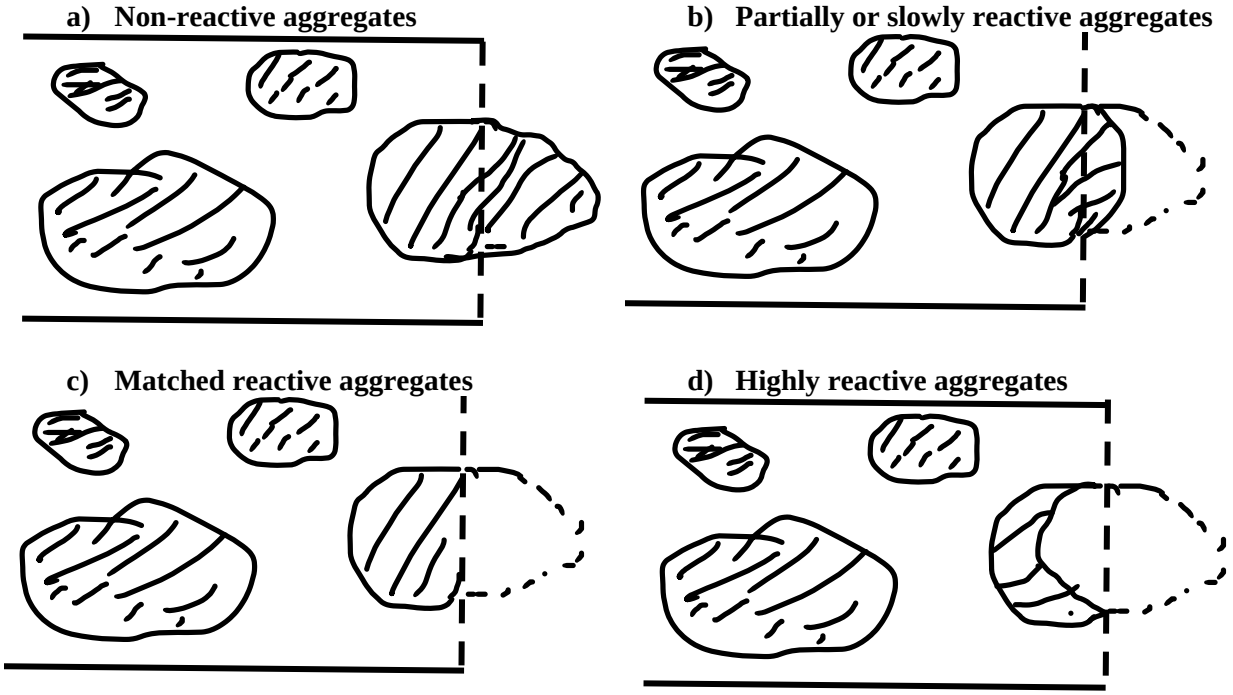


*Figure 7.5: Aggregate reactivity behaviour in concrete under sulphuric acid attack, based on their deterioration rate*

**a) Non-reactive aggregates**

In this case (Figure 7.5, a)), the rate of concrete deterioration is governed by the rate of cement paste deterioration, $C_{cp}$. However, the presence of these non-reactive aggregates tends to accelerate the concrete corrosion rate as the acid attack is concentrated on the cement phase only, resulting in the aggregate particles dislodging from the cement matrix. Consequently, it causes the loss of concrete mass and section thickness and exposes fresh concrete surfaces to attack. As Chang et al. (2005) indicated, only cement hydration products react with the acid in concrete with siliceous aggregates, and the neutralisation effect during the attack is minimal. Therefore, an 'aggregate dislodging effect' ($f^{(\text{Agg,})}$) needs to be introduced to quantify the mass loss of the concrete section. The rate of concrete deterioration ($C_{conc}$) can be described as in Eq. 7.23.

$C_{agg}$ = 0; thus, $C_{conc} = C_{cp}.f^{(\text{Agg,})}$ (7.23)

**b) Partially or slowly reactive aggregates**

In this case (Figure 7.5, b), aggregates are partially or slowly reactive; consequently, the cement paste deterioration rate ($C_{cp}$) exceeds that of aggregates ($C_{agg}$). The aggregate fallout during the acid attack is slower than in case (a) but still exposes fresh concrete for further attack. Therefore, the concrete deterioration rate ($C_{conc}$) is defined by the cement paste deterioration rate ($C_{cp}$) modified by the aggregate deterioration rate ($C_{agg}$), expressed as an aggregate reactivity factor ($\beta$) and the 'aggregate dislodging effect'. In this case, the concrete deterioration rate can be expressed as Eq. 7.24.

$$C_{cp} > C_{agg} \text{ and } C_{cp} \neq C_{agg} \text{ thus, } C_{conc} = \frac{C_{cp}}{\beta} f^{(\text{Agg,})} \quad (7.24)$$

**c) Matched reactive aggregate**

In this case (Figure 7.5, c)), the aggregate deterioration rate ($C_{agg}$) equals the cement paste deterioration rate ($R_{cp}$). Aggregate fallout is not experienced as the aggregates consume acid at the same rate as the cement matrix, thereby slowing the movement of the deterioration front. For instance, Pather, Ekolu and Quainoo (2021) indicate that calcareous aggregate types, especially dolomite, effectively reduce the progress of acid attack upon PC concretes, as these aggregates corrode along with cement paste, leading to slower uniform surface wear. Therefore, the concrete deterioration rate is defined by the cement paste deterioration rate and the complementary effect of aggregate deterioration, as shown in Eq. 7.25.

$$C_{cp} = C_{agg} = C_{conc} \text{ thus, } C_{conc} = \frac{C_{cp}}{\beta} \quad (7.25)$$

In this case, β has a value greater than in b) above and significantly slows the overall rate of concrete attack.

**d) Highly reactive aggregate, or aggregate with a high internal surface area**

In this scenario (Figure 7.5, d)), aggregates might have high interconnected porosity or internal surface area due to fracturing during production or processing. Thus, the aggregate deterioration rate is greater than the cement paste deterioration rate. The effect of aggregate dislodging also may not be experienced, except for finer aggregate fractions or 'intact' particles. Therefore, the concrete deterioration rate is defined by the cement paste deterioration rate and the contributing effect of the aggregate reactivity, as shown in Eq. 7.26.

$$C_{cp} < C_{agg} \text{ thus, } C_{conc} = \frac{C_{cp}}{\beta} \quad (7.26)$$

In this case, β has a value greater than in b) and c) above since the internal surface area of the aggregates has an 'acid sink' effect. This effect tends to retard the overall attack rate on the concrete by an appropriate value.

Where:

| | |
|---|---|
| β | Aggregate reactivity factor, in g of neutralised acid per g of concrete |
| $C_{cp}$ | Deterioration/corrosion rate of cement paste |
| $C_{agg}$ | Deterioration/corrosion rate of aggregates |

| | |
|---|---|
| $C_{conc}$ | Deterioration/corrosion rate of concrete |
| $f^{(\text{Agg,})}$ | Aggregate dislodging effect |

Based on overall knowledge of aggregate reactivity and physical effects, the aggregate reactivity factor ($\beta$) under sulphuric acid attack can be defined as a function of the following sub-factors:

- Acid neutralisation factor of acid-reactive components of aggregate ($\gamma$) see Section 7.6.2
- The fractional surface area of aggregate on a unit area of concrete being attacked by acid (including internal surface area, i.e., scaling factor based on aggregate porosity and/or aggregate internal fracture surface from processing) ($F_{SA}$), see Section 7.6.3
- The acid solubility of aggregate; the percentage of aggregate soluble in acid ($A_s$), see Section 7.6.4.

### 7.6.1. Aggregate dislodging effect

The aggregate dislodging effect ($f^{(\text{Agg,})}$) refers to the situation where non-reactive or slowly reactive aggregates are 'dislodged' from the matrix, i.e., the particle 'fallout', representing a mass loss for fine and coarse aggregate particles. It is insignificant in determining the corrosion rate of cement paste but affects the overall mass loss of the concrete.

The aggregate dislodging effect can be evaluated based on the aggregate grading (particle size distribution) curve, see Figure 7.6. The fundamental idea is that, as the deterioration front of concrete advances, it intercepts aggregate particles that might be consumed by the acid or left intact and slowly dislodge and fall out, thereby representing mass loss and section loss.

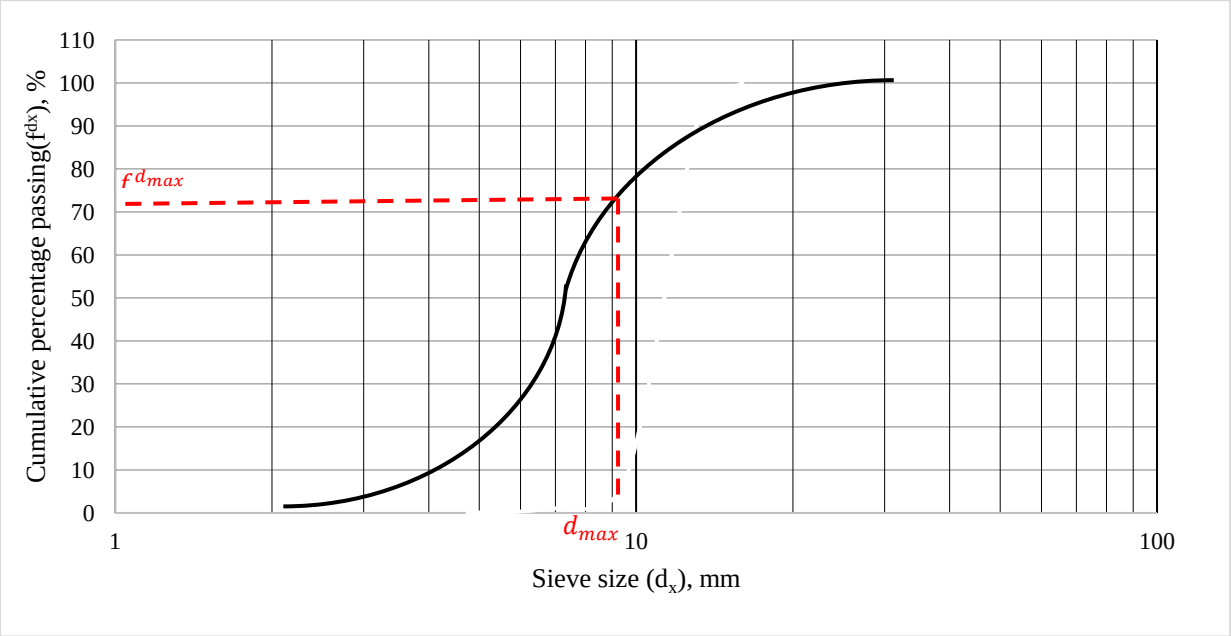


*Figure 7.6: Representation of aggregate particle distribution curve and how it can be applied to evaluate the mass loss of concrete under biogenic acid attack*

In the case of non-reactive or slowly reactive aggregates, the cement paste phase primarily governs the rate of the deterioration front. Using a simplified slice approach and considering the maximum size of the aggregate ($d_{max}$), mass loss from aggregate dislodgement and fallout can be determined when the

deterioration front reaches the same depth as $d_{max}$. At this depth, it can be assumed that a full range of aggregate particles, on average, have been dislodged and fallen out. For increments of depths less than $d_{max}$, a proportional mass loss based on the PSD curve can be assigned. Once $d_{max}$ has been achieved for the first slice, the next slice is done similarly. Thus, cumulative mass loss can be calculated per increment of degradation front advance, at a given time, as in Eq. (7.27)

$$M_{dx} = f^{dx} \rho_{agg} d_x \text{ where } d_x = C_{avg}.t_x \quad (7.27)$$

Assume that the mass loss of the concrete when the deterioration front equals the maximum aggregate size ($d_{max}$) is the mass ratio of the total aggregates in the mix (typically about 70-80%; in sewer pipes typically 80-85%); refer to Figure 7.6; thus, the mass loss is determined as Eq. (7.28). The equivalent mass loss of aggregate, say at 1 mm depth of deterioration front, is determined as Eq. (7.29).

$$M_{dmax} = f^{dmax} \rho_{agg} d_{max} \; where \; d_{max} = C_{avg}.t_{dmax} \quad (7.28)$$

$$M_{1\,mm} = f^{1\,mm} \rho_{agg} x\ 1\ mm\ x \frac{1\ m}{1000\ mm}, \text{ in kg/m}^2 \quad (7.29)$$

Where,

| | |
|---|---|
| $d_{max}$ | Maximum aggregate size, mm |
| $M_{dmax}$ | Cumulative mass loss of the concrete when corrosion depth is equal to $d_{max}$ |
| $f^{dmax}$ | Total cumulative percentage aggregate passing a maximum aggregate size, % |
| $t_{dmax}$ | Time at which the deterioration front is equal to the maximum aggregate size, years |
| $\rho_{agg.}$ | Density of aggregates, kg/m$^3$ |
| $C_{avg}$ | Average corrosion rate of concrete, mm/year |
| $d_x$ | Sieve size *x*, mm |
| $M_{dx}$ | Cumulative mass loss of the concrete at a depth of corrosion front equal to $d_x$ |
| $f^{dx}$ | Total cumulative percentage passing x mm sieve size, % |
| $t_{dx}$ | Time at which the deterioration front is equal to any d aggregate size, years |

### 7.6.2. Acid neutralisation factor of aggregates (γ)

The acid neutralisation factor of aggregates can be defined based on the concept applied in evaluating the acid neutralisation capacity or alkalinity of a material/mineral. Alkalinity is the capacity of solutes in an aqueous system to neutralise acid, consisting of the sum of titratable carbonate and non-carbonate chemical species in a filtered water sample. On the other hand, acid neutralisation capacity is the equivalent sum of all bases or base-producing materials in an aqueous system that can be titrated with an acid to an equivalence point (Radtke et al., 1998). Thus, the alkalinity of a material is its acid-neutralisation capacity only if the material does not contain acid components. Hence, the acid neutralisation factor of reactive acid components of aggregate ($\gamma$) is taken as the total amount of alkaline components in aggregates required to neutralise an equivalent strong acid, in this case, sulphuric acid.

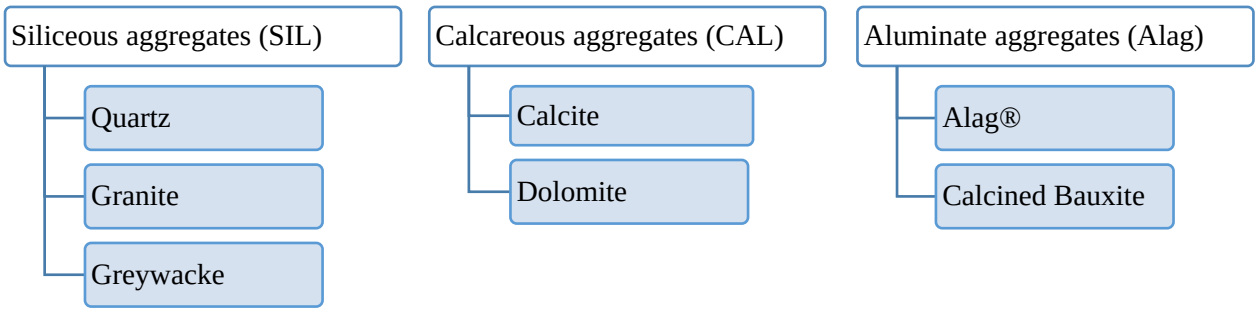


*Figure 7.7: Types of aggregates used in sewer concrete mix design.*

Commonly used aggregates in sewer concrete are siliceous (non-reactive) aggregates, calcareous aggregates (including calcite or limestone and dolomitic aggregates), and alumina-based aggregates, see Figure 7.7. For calcareous aggregates, their carbonates are the main constituent that can participate in neutralising acid, e.g. one mole of dolomite is required to neutralise two moles of sulphuric acid. In comparison, one mole of calcite or limestone is needed to neutralise one mole of sulphuric acid. For alumina-based aggregates, aluminium and calcium oxides participate in neutralising acid, i.e., one mole of aluminium oxide is required to neutralise three moles of sulphuric acid and one mole of calcium oxide to neutralise one mole of acid.

Based on the fundamental chemical reaction principles in Section 7.5, the acid neutralisation factor of aggregates, $\gamma$, can be evaluated as follows:

**a) Dolomite aggregates**

$$Ca.Mg(CO_3)_2 + 2H_2SO_4 \rightarrow CaSO_4 + MgSO_4 + 2CO_2 + 2H_2O \qquad (7.30)$$

1 mol of $Ca.Mg(CO_3)_2$ ≡ 2 moles of $H_2SO_4$

1 mol x 184 g/mol of $Ca.Mg(CO_3)_2$ ≡ 2 mol x 98 g/mol of $H_2SO_4$

$(\frac{100}{56} x \frac{wt\%_{CaO}}{100g\_agg} + \frac{83}{40} x \frac{wt\%_{MgO}}{100g\_agg})$ of $Ca.Mg(CO_3)_2$ ≡ $\gamma$ of $H_2SO_4$

$$\gamma_{DOL} = (\frac{100}{56} x \frac{wt\%_{CaO}}{100} + \frac{83}{40} x \frac{wt\%_{MgO}}{100}) \frac{2 \text{ x } 98}{1 \text{ x } 184} \qquad (7.31)$$

Assume a pure dolomite aggregate contains 50% CaO and 50% MgO, the $\gamma_{dolomite}$ is 2.06 g of $H_2SO_4$ neutralised by 1 g of dolomite aggregates.

**b) Calcite aggregate**

$$CaCO_3 + H_2SO_4 \rightarrow CaSO_4 + CO_2 + H_2O \qquad (7.32)$$

1 mol x 100 g/mol of $CaCO_3$ ≡ 1 mol x 98 g/mol of $H_2SO_4$

$\frac{100}{56} x \frac{wt\%_{CaO}}{100g\_agg}$ of $CaCO_3$ ≡ $\gamma$ of $H_2SO_4$

$$\gamma_{CAL} = \frac{98}{56} x \frac{wt\%_{CaO}}{100} \quad (7.33)$$

Assume a pure calcite aggregate contains 100% CaO, the $\gamma_{calcite}$ is 1.75 g of $H_2SO_4$ neutralised by 1 g of calcite aggregates.

**c) Calcium aluminate aggregate**

Calcium aluminate aggregate (Alag®) is a refractory aggregate composition comprising a calcium aluminate clinker having the chemical formula $(CaO)_n(Al_2O_3)_x$, where n is an integer from 1 to 12 and x from 1 to 24. Depending on the fusion temperature and alumina content, various crystalline phases such as calcium aluminate (CA), calcium di-aluminate ($CA_2$), tricalcium aluminate ($C_3A$), monocalcium hexa-aluminate ($CA_6$). and mayenite ($C_{12}A_7$) can be formed.

Under sulphuric acid attack, aluminium and calcium oxide are responsible for neutralising acid as follows:

$$CaO + H_2SO_4 \rightarrow CaSO_4 + H_2O \quad (7.34)$$

1 mol x 56 g/mol of $CaO$ ≡ 1 mol x 98 g/mol of $H_2SO_4$

wt% of $CaO$ in aggregate ≡ $\gamma$ of $H_2SO_4$

$$Al_2O_3 + 3H_2SO_4 \rightarrow Al_2(SO_4)_3 + 3H_2O \quad (7.35)$$

1 mol x 102 g/mol of $Al_2O_3$ ≡ 3 mol x 98 g/mol of $H_2SO_4$

wt% of $Al_2O_3$ in aggregate ≡ $\gamma$ of $H_2SO_4$

The acid neutralisation factor of calcium aluminate aggregate is therefore given as:

$$\gamma_{Alag} = \left(\frac{wt\%_{CaO}}{100} x \frac{1}{56} + \frac{wt\%_{Al_2O_3}}{100} x \frac{3}{102}\right) x\ 98 \quad (7.36)$$

Assuming a pure calcium aluminate aggregate contains 60% $Al_2O_3$ and 40 % CaO, the $\gamma_{CAagg}$ is 2.43 g of $H_2SO_4$ neutralised by 1 g of calcium aluminate aggregates

Where,

| | |
|---|---|
| $\frac{100}{56}$ | Molar mass ratio of $CaCO_3$ and CaO |
| $\frac{83}{40}$ | Molar mass ratio of $MgCO_3$ and MgO |
| $wt\%_{CaO}$ | Percentage weight of CaO in aggregates, from XRF result of aggregates |
| $wt\%_{Al_2O_3}$ | Percentage weight of $Al_2O_3$ in aggregates, from XRF result of aggregates |
| $wt\%_{MgO}$ | Percentage weight of MgO in aggregates, from XRF result of aggregates |
| $\frac{100}{56} x \frac{wt\%_{CaO}}{100}$ | grams of $CaCO_3$ in one gram of aggregates |
| $\frac{83}{40} x \frac{wt\%_{MgO}}{100}$ | grams of $MgCO_3$ in one gram of aggregate |
| $\gamma_{DOL}$ | Acid neutralisation factor of dolomite aggregate in g of $H_2SO_4$ per g of dolomite aggregate |
| $\gamma_{CAL}$ | Acid neutralisation factor of calcite aggregate in g of $H_2SO_4$ per g of calcite aggregates |
| $\gamma_{Alag}$ | Acid neutralisation factor of calcium aluminate aggregate in g of $H_2SO_4$ per g of calcium aluminate aggregate |
| 98 | Molar mass of $H_2SO_4$ in g/mol |

### 7.6.3. The fractional surface area of aggregates ($F_{SA}$)

The fractional surface area ($F_{SA}$) of aggregate is equivalent to the aggregate volumetric ratio in the concrete if taken over a sufficient surface area. It also accounts for aggregate porosity and internal fracture surface area from aggregate processing. Therefore, a scaling factor *(*$\varepsilon$) presents aggregate porosity and internal fracture surface area, while the aggregate content accounts for the aggregate volumetric ratio in the concrete.

The scaling factor ($\varepsilon$), see Eq. 7.37, is obtained using, for example, water absorption test techniques, where the lower limit, $\varepsilon$ = 1, i.e., only the external surface area, is accounted for. The upper limit depends on the amount of internal surface area.

$$F_{SA} = \frac{A}{\rho}\varepsilon \tag{7.37}$$

Where:

| | |
|---|---|
| $F_{SA}$ | Fractional surface area of aggregate in concrete |
| $A$ | Aggregate content in concrete, kg/m$^3$ |
| $\rho$ | Density of concrete, kg/m$^3$ |
| $\varepsilon$ | Scaling factor |

### 7.6.4. Acid solubility ($A_s$) of aggregate

Not all reactive aggregate components on a unit surface area of concrete completely participate in the neutralisation process. It is only a certain fraction of aggregates, defined as 'acid solubility' ($A_s$), that can participate. Examples of acid solubility of various aggregates are indicated in Table 7.1. The acid solubility can be obtained from the acid insolubility ($A_{ins}$) test for aggregates described in SANS 6242 (2008), see Eq. 7.38.

$$A_s = 1 - A_{ins} \tag{7.38}$$

Where:

$A_s$ Aggregate acid solubility

$A_{ins}$ Aggregate acid insolubility

*Table 7.1: Acid solubility and insolubility of various aggregates*

| Aggregate types | Acid insolubility, % | Acid solubility, % | References |
|---|---|---|---|
| Siliceous crushed river gravel aggregates, 20/10 mm | 99.9 | 0.1 | (Chang et al., 2005) |
| Silica sand | 97.0 | 3.0 | (Chang et al., 2005) |
| Limestone aggregates, 25 mm | 0.5 | 99.5 | (Chang et al., 2005) |
| Olifantsfontein dolomite stone, 13 mm | 4.2 | 95.8 | (Kiliswa, 2016) |
| Roodepoort quartzite stone, 13 mm | 90.0 | 10.0 | (Kiliswa, 2016) |
| Olifantsfontein dolomite crusher sand | 6.3 | 93.7 | (Kiliswa, 2016) |
| Roodepoort siliceous pit (filler) sand | 93.9 | 6.1 | (Kiliswa, 2016) |

*Table 7.2: Aggregate reactivity factor ($\beta$) calculation example based on the mix proportions of a typical SRPC+FA concrete used in this study*

| Aggregate type | SI unit | Fine aggregates | | Coarse Aggregate |
|---|---|---|---|---|
| | | Siliceous pit sand | Dolomite crusher fines | Dolomite coarse aggregate |
| Acid insolubility ($A_{s_i}$) obtained from (Fourie, 2007; Kiliswa, 2016) | - | 0.939 | 0.063 | 0.042 |
| Acid solubility ($A_s$) | - | 0.061 | 0.937 | 0.958 |
| Fractional surface area of aggregate on a unit area of concrete, $F_{SA}$ | - | 0.2 | 0.2 | 0.4 |
| Acid neutralisation factor of aggregate ($\gamma$) | $\frac{g\_acid}{g\_aggregate}$ | 0 | 1.129 | 1.129 |
| The aggregate reactivity factor per unit surface area of concrete, $\beta_i$ | $\frac{g\_acid}{g\_concrete}$ | 0 | 0.211 | 0.433 |
| Total $\beta$ | $\frac{g\_acid}{g\_concrete}$ | | 0.644 | |

### 7.6.5. The overall aggregate reactivity factor ($\beta$)

When considering all the above factors, the overall aggregate reactivity factor of aggregates in concrete can be evaluated as in Eq. (7.39). This factor considers the contribution of different aggregate types and content incorporated into a mix.

$$\beta = \sum_{i=1}^{n} \frac{A_i}{\rho} \varepsilon_i \, \gamma_i \mathrm{A}_{s_i} \tag{7.39}$$

Where:

$\beta$ Total Aggregate reactivity factor in $g$ to neutralise $H_2SO_4$ per $g$ of concrete

| | |
|---|---|
| $A_i$ | Aggregate *i* content in concrete, kg/m$^3$ |
| $\rho$ | Density of concrete, kg/m$^3$ |
| $\varepsilon_i$ | Scaling factor of aggregates *i* |
| $A_{s_i}$ | Acid solubility of aggregates *i* |
| $i$ | Aggregate types, i.e., aggregate type 1 to type n |

Table 7.2 shows aggregate reactivity factor (β) calculation example based on the mix proportions of a typical SRPC+FA concrete used in this study, with the specific set of aggregates used and tested; assume a scaling factor of all aggregates is one, i.e., $\varepsilon = 1$.

## 7.7. Advanced LFM

Based on the above, the advanced LFM is given in Eq. (7.40):

$$C_{avg} = 365 \times 24 \times \frac{\phi_{sw}}{(\varphi + \beta)\rho} \; or \; 365 \times 24 \times \frac{\phi_{sw}}{\text{MR}\,\rho} \tag{7.40}$$

Where:

| | |
|---|---|
| $C_{avg}$ | Average concrete corrosion rate, mm/yr |
| $365 \times 24$ | Converts days to hours in a year |
| $\phi_{sw}$ | Sewer environmental factor in g of $H_2SO_4$ per m$^2$ produced per h, see Section 7.3: Eq. (7.10) |
| $\varphi$ | Acid neutralisation factor of binders in g of neutralised $H_2SO_4$ per g of concrete, Section 7.5; Eq. (7.22) |
| $\beta$ | Aggregate reactivity factor in g to neutralise $H_2SO_4$ per g of concrete, see Section 7.6; Eq. (7.39) |
| $\rho$ | Density of concrete, kg/m$^3$ |
| MR | Material Resistance Factor, $(\varphi + \beta)$, in of neutralised $H_2SO_4$ per g of concrete |

### 7.7.1. Advanced LFM model applications

Assuming

- The average density ($\rho$) of all concrete mixes is about 2500 kg/m$^3$,
- VES sewer environmental condition given in Section 7.3.2 results in a sewer environmental factor ($\phi_{sw}$) of 0.245 g/m$^2$/h for 35 ppm $H_2S$ gas concentration and
- Oxide compositions of various binder systems and aggregates are given in Table 7.3, as obtained from this study and Kiliswa's work.

Taking typical concrete mixes (with constituents in percentages) and applying the advanced LFM (Eq. (7.41)), the corrosion rates in mm/yr of the concrete mixes can be estimated. Table 7.4, shows corrosion rate computations of various concrete mixes provided by Kiliswa (2019) and other mixes, to cover a broad range of binder systems and aggregate types. The other mixes were designed hypothetically based on those in Kiliswa (2019) in percentages but with different binder and aggregate types, with their chemical compositions shown in Table 7.3. The corrosion rates of these mixes, see Table 7.4, were evaluated under sewer environmental conditions of 35 ppm annual average $H_2S$ gas concentrations, an annual average sewer headspace temperature of 23$^o$C, and sufficient RH (70%-100%) to assume that concrete surfaces of all mixes had 0.05 ppm(1-n)/s $H_2S$ adsorption constant rate.

*Table 7.3: XRF oxide composition of the various binders and aggregates*

| Binder/aggregate | Oxide chemical formula and composition. % | | | | | | | | | | |
|---|---|---|---|---|---|---|---|---|---|---|---|
| | **CaO** | **$SiO_2$** | **$Al_2O_3$** | **$Fe_2O_3$** | **MgO** | **$SO_3$** | **$K_2O$** | **NaO** | **Others** | **LOI** | **Total** |
| PC/CEM II AL | 63.20 | 20.00 | 4.03 | 3.19 | 0.91 | 2.94 | 0.18 | 0.18 | 0.48 | 4.39 | 99.50 |
| SRPC | 67.95 | 21.45 | 3.14 | 2.17 | 0.95 | 1.85 | 0.10 | 0.16 | 0.06 | 1.63 | 99.46 |
| CAC | 37.60 | 4.40 | 38.50 | 15.10 | 0.70 | 0.20 | 0.10 | 0.10 | 1.71 | 1.09 | 99.50 |
| CSA | 41.75 | 4.7 | 30.37 | 1.53 | 0.62 | 15.71 | 2.11 | 0.68 | 1.09 | 0.81 | 99.9 |
| FA | 2.40 | 48.70 | 27.90 | 9.50 | 1.60 | 1.20 | 4.20 | 1.50 | 1.47 | 1.03 | 99.50 |
| SF | 0.20 | 96.00 | 0.30 | 0.10 | 0.60 | 0.20 | 0.50 | 0.30 | 0.26 | 0.99 | 99.45 |
| GGBS | 42.20 | 33.50 | 13.30 | 1.20 | 6.00 | 0.04 | 0.70 | 0.40 | 0.87 | 1.31 | 99.52 |
| DOL | 33.26 | 4.90 | 0.34 | 0.90 | 22.26 | 0.02 | 0.02 | 0.02 | 7.48 | 30.80 | 100.00 |
| SIL | 0.11 | 95.60 | 1.61 | 0.80 | 0.00 | 0.00 | 0.00 | 0.00 | 0.71 | 0.69 | 99.52 |
| Alag | 37.60 | 4.40 | 38.50 | 15.10 | 0.70 | 0.20 | 0.10 | 0.10 | 1.71 | 1.29 | 99.70 |
| CAL | 55.48 | 0.29 | 0.02 | 0.00 | 0.08 | 0.00 | 0.00 | 0.00 | 0.41 | 43.63 | 99.91 |

*Table 7.4: Computation of Advanced LFM model for concrete mix designs proposed by (Kiliswa, 2016) and extra mixes to cover a wide range of binder and aggregate types. Corrosion rate prediction of concrete with different binder systems and aggregate types, at $k_p$ = 0.05; n = 0.5, $H_2S$ = 35 ppm, $\phi_{sw}$ = 0.245 g/m$^2$/h and Density of concrete = 2500 kg/m$^3$*

| Concrete mix design | SCM | Cement | Coarse Agg. | Crusher sand | Filler sand | $\varphi$ | $\beta$ | MR | Predicted corrosion rate |
|---|---|---|---|---|---|---|---|---|---|
| | % | % | % | % | % | $\frac{g\_acid}{g\_concrete}$ | $\frac{g\_acid}{g\_concrete}$ | $\frac{g\_acid}{g\_concrete}$ | mm/yr |
| CAC/AlagTM_20 | | 20 | 40 | 20 | 20 | 0.41 | 1.06 | 1.47 | 0.58 |
| CAC/AlagTM_16 | | 16 | 44 | 10 | 30 | 0.33 | 0.95 | 1.28 | 0.67 |
| CAC/DOL_23 | | 23 | 44 | 17 | 16 | 0.47 | 0.65 | 1.12 | 0.77 |
| CAC/DOL_18 | | 18 | 47 | 18 | 17 | 0.37 | 0.69 | 1.06 | 0.81 |
| CAC/CAL_23 | | 23 | 44 | 17 | 16 | 0.47 | 0.56 | 1.03 | 0.83 |
| CAC/DOL_16 | | 16 | 48 | 18 | 18 | 0.33 | 0.70 | 1.03 | 0.84 |
| CSA/DOL_23 | | 23 | 44 | 17 | 16 | 0.38 | 0.65 | 1.02 | 0.84 |
| CSA/DOL_18 | | 18 | 47 | 18 | 17 | 0.29 | 0.69 | 0.98 | 0.87 |
| CAC/CAL_18 | | 18 | 48 | 18 | 18 | 0.37 | 0.60 | 0.97 | 0.88 |
| CSA/DOL_16 | | 16 | 48 | 18 | 18 | 0.26 | 0.70 | 0.96 | 0.89 |
| CSA/CAL_23 | | 23 | 44 | 17 | 16 | 0.38 | 0.56 | 0.93 | 0.92 |
| PC/DOL_23 | | 23 | 44 | 17 | 16 | 0.29 | 0.65 | 0.94 | 0.91 |
| CAC/CAL_16 | | 16 | 48 | 18 | 18 | 0.33 | 0.60 | 0.93 | 0.92 |
| PC/DOL_18 | | 18 | 47 | 18 | 17 | 0.22 | 0.69 | 0.91 | 0.94 |
| PC/GGBS/DOL_18 | 6 | 12 | 47 | 18 | 17 | 0.15 | 0.69 | 0.84 | 1.02 |
| PC/FA/DOL_18 | 4.5 | 13.5 | 47 | 18 | 17 | 0.16 | 0.69 | 0.85 | 1.01 |
| PC/DOL_16 | | 16 | 48 | 18 | 18 | 0.21 | 0.70 | 0.90 | 0.95 |
| PC/SF/DOL_18 | 1.5 | 16.5 | 47 | 18 | 17 | 0.19 | 0.69 | 0.88 | 0.97 |
| PC/CAL_23 | | 23 | 44 | 17 | 16 | 0.29 | 0.59 | 0.88 | 0.98 |
| CSA/CAL_18 | | 18 | 47 | 18 | 17 | 0.29 | 0.59 | 0.89 | 0.97 |
| CSA/CAL_16 | | 16 | 48 | 18 | 18 | 0.26 | 0.60 | 0.87 | 0.99 |
| PC/CAL_18 | | 18 | 47 | 18 | 17 | 0.22 | 0.59 | 0.82 | 1.05 |
| PC/CAL_16 | | 16 | 48 | 18 | 18 | 0.20 | 0.60 | 0.80 | 1.07 |
| CAC/SIL_23 | | 23 | 44 | 17 | 16 | 0.47 | 0.00 | 0.47 | 1.82 |
| CSA/SIL_23 | | 23 | 44 | 17 | 16 | 0.38 | 0.00 | 0.38 | 2.29 |
| CAC/SIL_18 | | 18 | 47 | 18 | 17 | 0.37 | 0.00 | 0.37 | 2.33 |
| CAC/SIL_16 | | 16 | 48 | 18 | 18 | 0.33 | 0.00 | 0.33 | 2.62 |
| CSA/SIL_18 | | 18 | 47 | 18 | 17 | 0.29 | 0.00 | 0.29 | 2.92 |
| PC/SIL_23 | | 23 | 44 | 17 | 16 | 0.29 | 0.00 | 0.29 | 3.00 |
| CSA/SIL_16 | | 16 | 48 | 18 | 18 | 0.26 | 0.00 | 0.26 | 3.29 |
| PC/SIL_18 | | 18 | 47 | 18 | 17 | 0.22 | 0.00 | 0.22 | 3.83 |
| PC/SIL_16 | | 16 | 48 | 18 | 18 | 0.20 | 0.00 | 0.20 | 4.31 |

#### 7.7.1.1. Effect of aggregates and binder systems on predicting corrosion rate of concrete

Drawing on the data in Table 7.4, Figure 7.8 presents the predicted corrosion rate of various concrete mixes with different binder systems and aggregate types exposed to a sewer with annual average $H_2S$ gas of 35 ppm and an annual average temperature of 23$^{o}$C. The $H_2S$ adsorption rate constant of all concrete surfaces is assumed to be 0.05 $ppm^{(1-n)}/s$.

From the figure, the following is observed.

i) The model distinctly demonstrates the performance of different binder systems when combined with different aggregate types.

ii) The ratio of the highest to lowest corrosion rates of all concrete mixes is approximately 7.4. When excluding ALAG concrete, the ratio is 5.6, 4.7 for PC concrete mixes, 3.9 for CSA concrete, and 3.4 for CAC concrete.

iii) The model and the ratios indicate that PC concrete has the highest corrosion rate, CAC concrete has the lowest corrosion rate, while CSA concrete lies between PC and CAC concrete. Concrete with 23% PC has a rate similar to the 18% CSA, and the 23% CSA has a similar rate to 18% CAC. However, aggregates also have a profound influence – see below.

iv) The model also indicates that the higher the cement content, the lower the corrosion rate. This is because the corrosion rate in the model is inversely related to the material resistance factor; the higher the binder content, the higher the material resistance, hence the lower the corrosion rate and vice versa.

However, this contrasts to some extent with Kiliswa's and the VES observations, which indicate that PC concrete with higher cement content has a higher corrosion rate. The elaboration behind this is that higher PC content provides access to a more susceptible cement matrix and hence a higher corrosion rate. Thus further study may be required to clarify this discrepancy.

v) For any given binder type, concrete with siliceous aggregates (SIL) shows the highest corrosion rate, followed by concrete with calcite (CAL), then dolomite (DOL) aggregates, while aluminate (ALAG) aggregate concretes show the lowest corrosion rate.

vi) For calcite (CAL) and dolomite (DOL) aggregate concrete, PC concretes with and without SCMs show approximately equal corrosion rates with minor differences as their material factor increases. This observation indicates that combining calcareous aggregates in PC concrete improves the performance of PC-based sewer concrete, as observed by (Alexander & Fourie, 2011; Goyns & Alexander, 2018). However, dolomite aggregates have a higher neutralisation capacity than calcite aggregates, suggesting that dolomite aggregate should be preferred in sewer concrete.

vii) Similarly, CAC concrete with calcium aluminate aggregates significantly increased the concrete's material factor, resulting in a lower corrosion rate than the PC-based concrete with siliceous or calcareous aggregates.

It can be concluded that CAC has a larger neutralisation capacity than PC concrete, as also indicated in the literature (Hewlett, P., & Liska, 2019: 575 ). That is to say, one gram of CAC can neutralise around 40% more acid than a gram of PC, meaning that for the same production of biogenic acid by bacteria, CAC-based concretes will exhibit greater longevity.

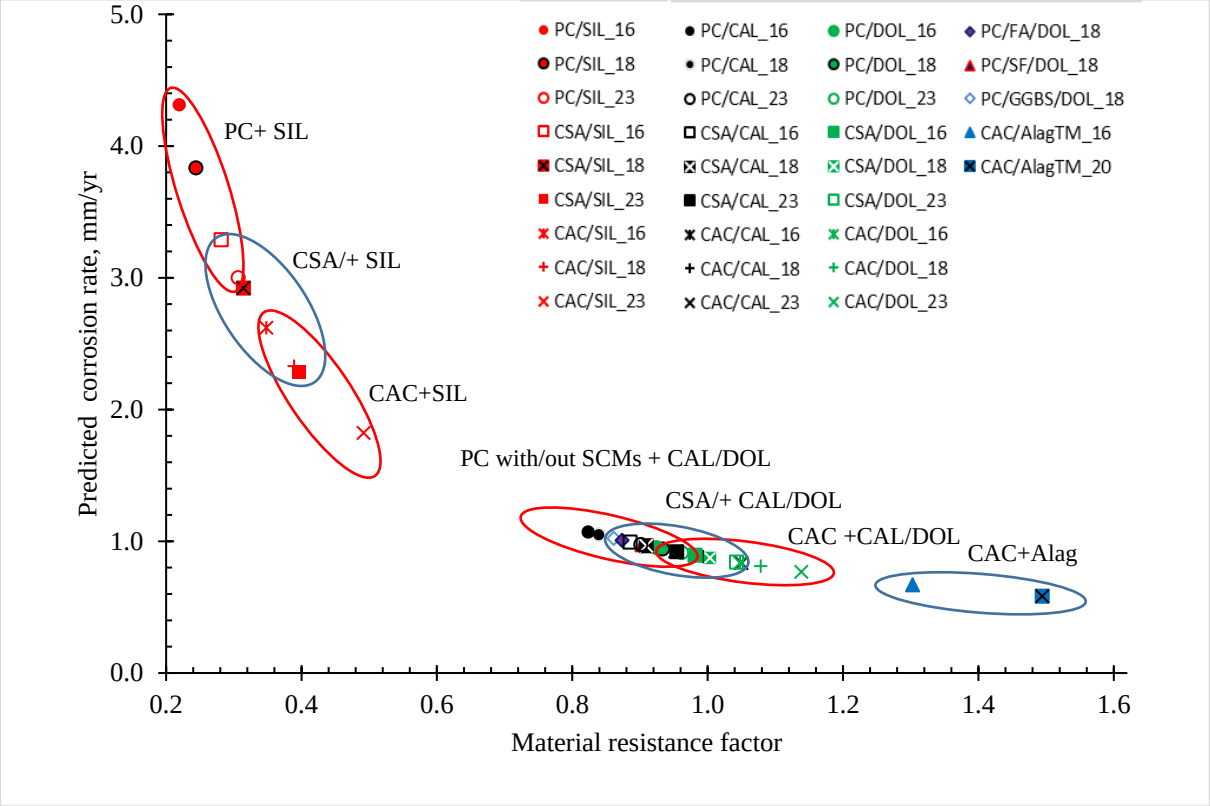


*Figure 7.8: Corrosion rate prediction of various concrete mixes with different binder systems and aggregate types exposed to a sewer with an average $H_2S$ gas of 35 ppm and 23°C, where the $H_2S$ adsorption rate of all concrete surfaces is assumed to be 0.05 ppm$^{(1-n)}$/s. Data is provided in Table 7.4.*

### 7.7.1.2. Effect of varying $H_2S$ gas concentrations in corrosion rate prediction

Figure 7.9 illustrates the effect of varying $H_2S$ gas concentrations in the sewer headspace. Similar sewer environmental conditions, as in Figure 7.8, were applied in predicting the corrosion rate but with varying gas concentrations, see Appendix P.

The model indicates that concrete corrosion rates increase with increased gas concentration. Significant variation of corrosion rate with $H_2S$ gas concentration was observed mainly on the SIL based concretes. Corrosion rates decreased further as the material resistance factor increased, with minor variation for concrete with calcareous aggregates (CAL and DOL), followed by concrete with aluminate (ALAG) aggregates. That is to say, the corrosion rates of ALAG-based concrete at 20 ppm, 50 ppm, and 100 ppm are close, with values approximately equal to 1 mm/yr.

However, due to the behaviour of sewers which tend to have large fluctuations of $H_2S$ concentrations due to the diurnal sewage flow and retention times, intermittent pumping of sewage from pressure pipes into gravity pipes, and seasonal changes, the application of a constant annual $H_2S$ concentration in the Advanced LFM might not be sufficient. As observed in the previous chapters, the highest $H_2S$

concentrations in sewers were observed during peak hours and in summer, and during this period, significant mass and thickness losses of concrete were observed. Therefore, according to Sun et al. (2015), who studied the effect of short- and long-term increases in $H_2S$ levels on the $H_2S$ uptake rate of concrete surfaces with an active corrosion layer; there is a need to incorporate a correction factor for the $H_2S$ fluctuations when average $H_2S$ levels are used in the prediction. This, therefore, suggests a further study to determine a suitable correction factor depending on the sewer behaviour.

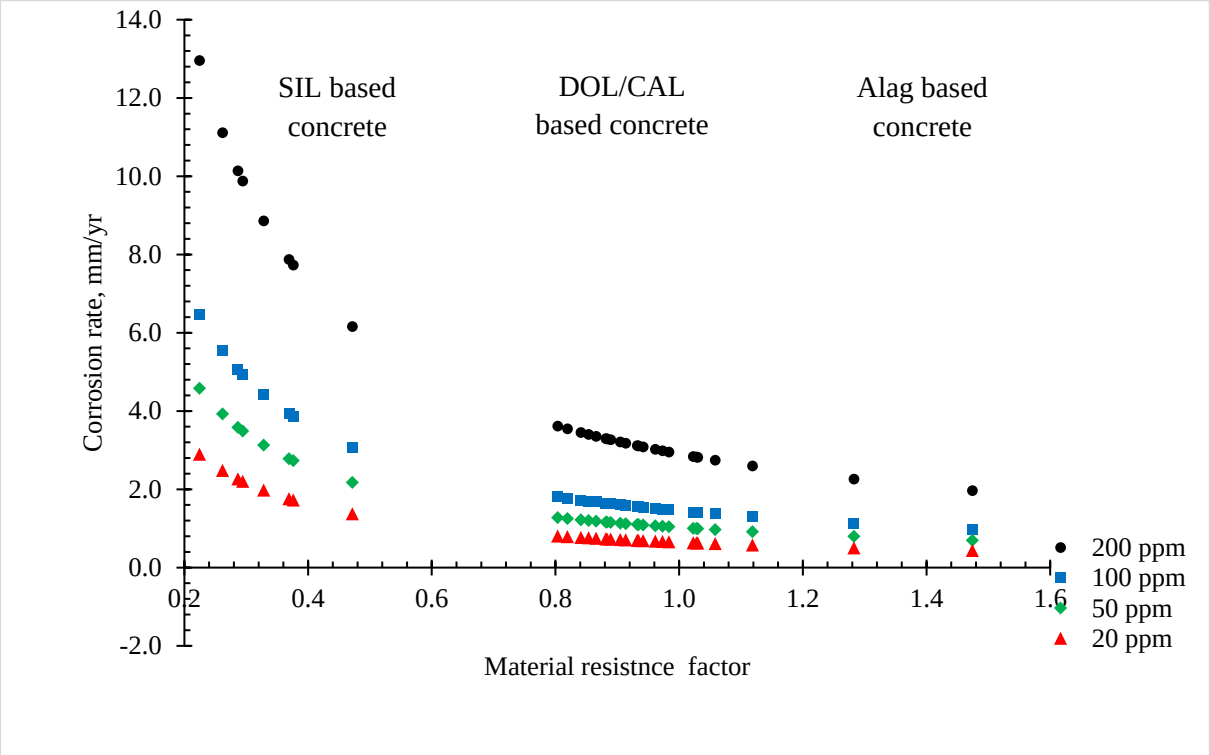


*Figure 7.9: Corrosion rate prediction of various mixes exposed to a sewer with varying annual average $H_2S$ gas concentration and 23°C temperature, where the $H_2S$ adsorption rate of all concrete is assumed to be 0.05 $ppm^{(1-n)}/s$.*

### 7.7.2. Advanced LFM predictions versus field-measured corrosion rates

This section compares the field-measured and predicted corrosion rates of sewer concrete mixes subjected to the sewer environments of VES and NAS M19, and LPS. The section aims to find the correlation between the predicted and measured corrosion rate of sewer concrete and to highlight the influence of the $H_2S$ adsorption rate constant in the LFM as an essential parameter in correlating factors associated with acid generation on the concrete and those associated with acid neutralisation, see Section 2.9 and Figure 2.13.

#### 7.7.2.1. Comparison at Virginia Experimental Sewer (VES)

Figure 7.10 compares field-measured corrosion rates of various sewer concrete extracted from previous work at Virginia Experimental Sewer (VES) and predicted corrosion rates of similar concrete at different $H_2S$ adsorption rate constants of concrete surfaces. The sewer environmental conditions of VES indicated in Section 7.3.2 were used for prediction, and the measured corrosion rates from previous work are indicated in Appendix Q (Goyns, 2009; Alexander & Fourie, 2011; Kiliswa, 2016; Goyns & Alexander, 2018)

The measured corrosion rates of PC-based concrete with dolomite aggregates correlate with the prediction values at $k_p$ equal to or above 0.05 ppm$^{(1-n)}$)/s and when n is 0.5. These results signify that the corrosion rate of concrete depends significantly on the $H_2S$ adsorption rate constant. Thus, it suggests that a single constant cannot be applied to predict the corrosion rate of concrete with different binder types. It is, therefore, essential to identify $H_2S$ adsorption rate constants of different concretes with respect to the binder system and aggregate type.

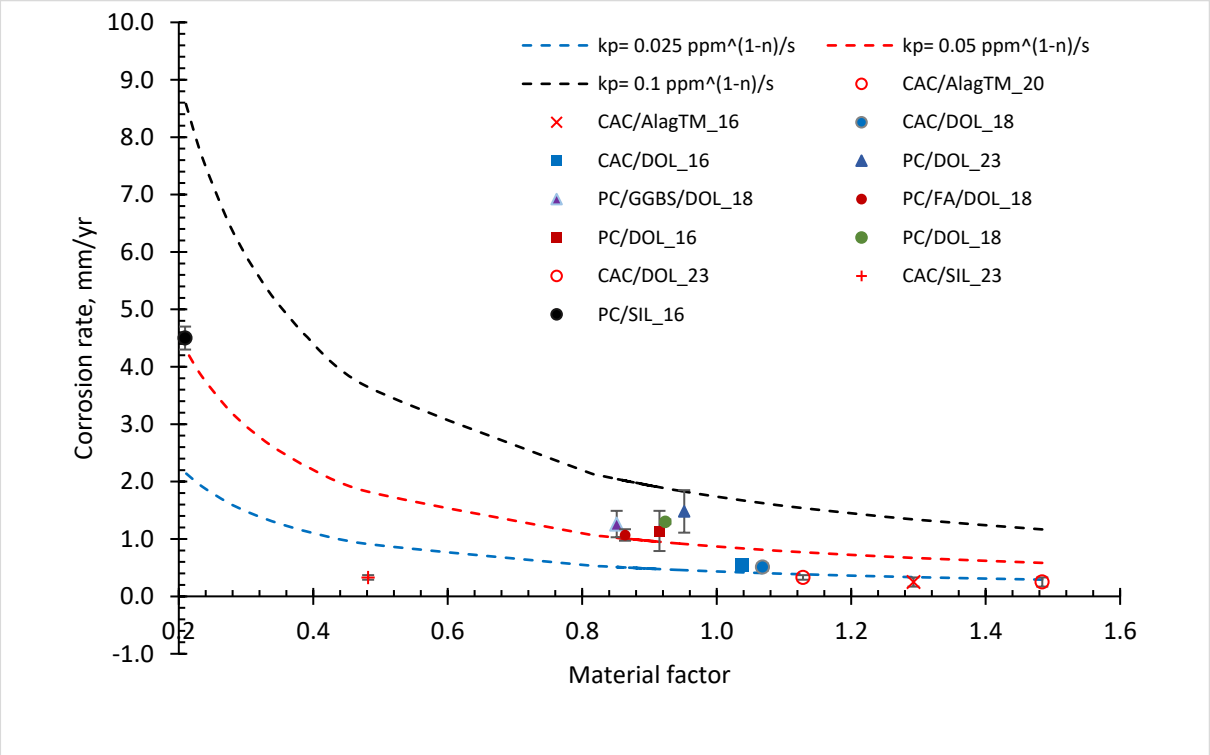


*Figure 7.10: Comparison of field measured versus predicted corrosion rates of different binder systems at different $H_2S$ adsorption rates, w, where the $H_2S$ adsorption rate constant ($k_p$) of concrete surfaces were 0.025 ppm$^{(1-n)}$/s, 0.05 ppm$^{(1-n)}$/s and 0.1 ppm$^{(1-n)}$/s and n = 0.5*

### 7.7.2.2. Comparison at NAS M19 and LPS

Based on the findings at VES regarding the influence of $H_2S$ adsorption rate constants of concrete surfaces, similar principles were employed in predicting corrosion rates of UCT concrete studied herein, see Section 5.3. LH concrete findings were not included herein due to their concrete quality, which compromised their corrosion rate.

In Section 4.3.1, it was indicated that applying a constant annual $H_2S$ concentration in the corrosion rate prediction modelling might not be sufficient due to a significant fluctuation of $H_2S$ gas concentrations. However, this section observed that the 90th percentile of the maximum monthly sewer environmental conditions, i.e., $H_2S$ gas concentration, RH, and temperature, per year could be used to predict the corrosion rates of UCT concrete at each site. Appendix S shows the maximum monthly sewer environmental conditions of LPS and NAS M19.

It should be noted that concrete subjected to LPS experienced both sewer hydraulic erosion and biogenic sewer corrosion, and those subjected to NAS M19 experienced mainly biogenic acid corrosion and only

occasional sewer erosion during flooding, refer to Chapter 4 and Chapter 5. Due to this, different Reynolds numbers for turbulent flow conditions were used to highlight the difference in sewer hydraulic behaviour, see Table 7.5. Appendix R shows the evaluation of UCT concrete MR factors based on their ingredient mix proportions (Table 3.5), chemical composition (Table 3.2), and 28-day saturated densities (Figure 5.22)

Therefore, Table 7.5 compares the field-measured (Table 5.6) and LFM-predicted corrosion rate of UCT concrete at NAS M19 and LPS. It was observed that, by varying the '$k_p$' values of concrete, the advanced LFM model could predict the corrosion rate of UCT Concrete at LPS and NAS M19. CEM II A-L concrete had the highest $k_p$ value of about 0.05 ppm$^{(1-n)}$)/s as indicated in Section 7.7.2.1, followed by SRPC +FA with and without HC of about 0.04 ppm$^{(1-n)}$)/s, then CSA and CAC+SRPC concrete with about 0.025 ppm$^{(1-n)}$)/s, and CAC with the lowest $k_p$ value of about 0.02 ppm$^{(1-n)}$)/s. These values fall between the $k_p$ range provided by Nielsen, Hvitved-Jacobsen and Vollertsen (2012), i.e., 0.019 to 0.177 ppm$^{(1-n)}$)/s. The results also show that the $k_p$ value is determined by the type of concrete and not by sewer aggressivity. This is because the corrosion rates of a given concrete at two different sewers were predicted using a single $k_p$ value.

*Table 7.5: UCT concrete mixes: field measured against LFM predicted corrosion rate at LPS and NAS M19*

| UCT Concrete Mix | Measured corrosion rate, mm/yr | | | | $k_p$# | LFM Predicted corrosion rate, mm/yr | | | |
|---|---|---|---|---|---|---|---|---|---|
| | LPS | | NAS M19 | | | LPS | | NAS M19 | |
| | Avg | STDEV | Avg | STDEV | Ppm (1-n))/s | Avg | STDEV * | Avg | STDEV* |
| CEM II AL | 3.05 | 1.03 | 1.28 | 0.03 | **0.050** | 2.78 | 0.42 | 1.29 | 0.19 |
| SRPC+FA | 1.89 | 0.40 | 1.02 | 0.45 | **0.040** | 2.24 | 0.34 | 1.04 | 0.16 |
| SRPC+FA+HC | 2.07 | 0.67 | 0.92 | 0.20 | **0.040** | 2.24 | 0.34 | 1.04 | 0.16 |
| CSA | 1.38 | 0.25 | 0.65 | 0.13 | **0.025** | 1.37 | 0.20 | 0.63 | 0.09 |
| CAC + SRPC | 0.93 | 0.06 | 0.58 | 0.12 | **0.025** | 1.29 | 0.19 | 0.60 | 0.09 |
| CAC | 0.87 | 0.13 | 0.07 | 0.03 | **0.020** | 0.97 | 0.15 | 0.45 | 0.07 |

| Sewer environmental conditions: | Site | $H_2S$, ppm | Temp ,$^oC$ | RH, % | Re | n |
|---|---|---|---|---|---|---|
| # $k_p$ varied with concrete type from 0.019 to 0.177 (Nielsen, Hvitved-Jacobsen & Vollertsen, 2012) | LPS | 352 | 26 | 90 | 5000 | 0.5 |
| *15% of the predicted corrosion rate was considered as STDEV | NAS M19 | 102 | 28 | 96 | 4000 | 0.5 |

Figure 7.11 shows the correlation between predicted and measured corrosion rates of UCT concrete at LPS and NAS M19. The linear regression analysis of this data indicates the correlation coefficient, R-value, of 0.99, close to 1.0, which implies a very positive correlation between predicted and measured corrosion rates. The coefficient of determination ($R^2$), on the other hand, is 0.98, indicating a variance of about 98% between measured and predicted corrosion rates. The slope of the linear regression line is approximately equal to 1, indicating that the predicted rate was equal to the measured rate. However, the LFM model slightly overpredicted the corrosion rate of the CAC concrete at NAS M19 and underpredicted that of CEM II A-L at LPS. Generally, the LFM model was 98% successful in predicting the corrosion rate of the UCT concrete.

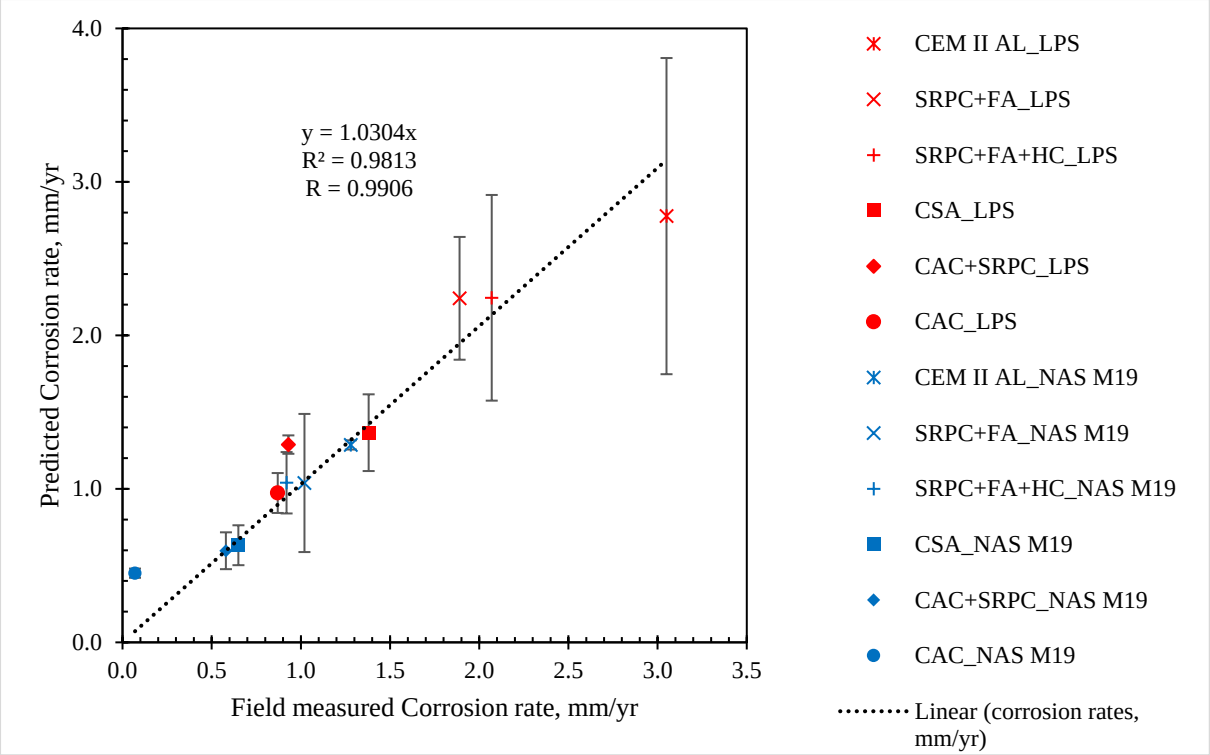


*Figure 7.11: UCT concrete mixes: Correlation between LFM predicted and field measured corrosion rate of UCT concrete at LPS and NAS M19*

#### 7.7.2.3. Influence of $H_2S$ adsorption rate constant ($k_p$) of sewer concrete

The comparison between field-measured and predicted corrosion rates indicates that the $H_2S$ adsorption rate constant, $k_p$, of a concrete surface is significant in evaluating or predicting the corrosion rate of concrete.

The rate constant can be identified based on the methodology used by Grandclerc et al. (2017) in the effect of cement composition on $H_2S$ adsorption and its subsequent oxidation on cementitious material surfaces. Ggrandclerc's observations concur with the current prediction observations. In their study, they ranked the $H_2S$ adsorption rate of mortars from the highest to the lowest as follows; ordinary Portland cement CEM I > blended Portland cement (i.e., CEM III > CEM IV > CEM V) > Calcium Aluminate Cement (CAC) > super-sulphated cement (SSC). It was clear that CAC-based mortar had a lower $H_2S$ adsorption rate constant than PC-based mortars, showing that different binder systems significantly influence the $H_2S$ adsorption rate. They added that hydroxyl ions and ferrous compounds in the binder favoured $H_2S$ adsorption more than sulphate ions. Even though the study was conducted on mortar-based materials, it nevertheless provides a guide to establishing the $H_2S$ adsorption rate constant of various concrete mix designs. Also, they pointed out that the $H_2S$ adsorption rate constant increases with RH, emphasising the importance of the sewer concrete condensate film that allows SOBs to procreate and facilitate the ionic exchange from the surface into the concrete.

Further, in the reactive transport modelling in Chapter 6, it was observed that concrete with the lowest diffusion coefficient, i.e., CAC and CSA, also had the lowest corrosion rate. This also suggests that concretes with low diffusion coefficients, such as CAC, have the lowest $H_2S$ adsorption rate, which

significantly reduces the corrosion rate of concrete. Therefore, the $H_2S$ adsorption rate constant seems to closely correlate with the diffusion coefficient of concrete. However, this is a hypothesis worth exploring philosophically and experimentally in future.

## 7.8. Chapter closure and conclusion

This chapter presented the approaches to advance the LFM model to overcome limitations, increase its broader usage, and significantly contribute to sewer design and applications. The model was successfully modified after revising the original fundamental principles employed during its development. The parameters were redefined to consider the influence of various binder systems, aggregate types, and sewer aggressivity separately. The advanced LFM model consists of three parameters, i.e., sewer environmental factor ($\phi_{se}$) and Material Resistance (MR) factor, including the acid neutralisation factor of a binder ($\varphi$) and the aggregate reactivity factor ($\beta$).

The sewer environmental factor defined the rate of acid generation and oxidation on the sewer concrete wall. It was derived from the $H_2S$ adsorption and oxidation rate model by Nielsen, Hvitved-Jacobsen and Vollertsen (2012). It considers factors such as sewer environmental conditions, i.e., temperature, RH and $H_2S$ gas concentration, sewer hydraulic action affects on airflow dynamics through Reynolds number, and $H_2S$ adsorption rate constant (kp). With this factor, the corrosion rate of concrete subjected to any sewer environmental conditions could be evaluated.

The acid neutralisation factor of binder defined the chemical potential of binder systems in concrete in neutralising the attacking acid. The factor was derived from simple acid-base reactions, where the amount of sulphuric acid to be neutralised by the alkali oxides in the binder, namely, $Al_2O_3$, CaO, $Fe_2O_3$, and MgO, was evaluated. With this parameter, the contribution of any binder system in sewer concrete can be evaluated and used in determining the corrosion rate of concrete.

The aggregate reactivity factor defines the chemical and physical contribution of aggregates in concrete to neutralise and accelerate the corrosion rate of concrete, respectively. Different aggregates perform differently in concrete when coupled with different binders. Some aggregates tend to dislodge or fall out from the concrete's exposed surface, hence accelerating the corrosion rate of concrete. The aggregate reactivity factor was defined as a function of three factors; the acid neutralisation factor of acid-reactive components of aggregates, the fractional surface area of aggregates on a unit area of concrete, and the acid solubility of aggregate. The aggregate dislodging effect ($f^{(\mathrm{Agg,})}$) was only necessary in determining the overall mass loss of concrete due to corrosion, whereas the corrosion rate of concrete is mainly governed by the deterioration rate of the cement matrix. With this factor, the contribution of the aggregate component in sewer concrete with more than one aggregate type was considered.

In the application of the advanced LFM model to determine the corrosion rate of various concrete mixes with a wide range of binder systems and aggregate types under different sewer environmental conditions, the following insights were extracted.

i) Various binder systems, from the PC, CSA and CAC-based mixes with and without SCMs, could be incorporated into the model, provided their chemical composition is known. The model could also successfully rank their performance similar to their field performance.

ii) Three aggregate types, i.e., siliceous (SIL), calcareous (CAL and DOL), and aluminate (ALAG), which are commonly used in sewer concrete, could be incorporated in the model, provided their chemical composition, acid solubility and aggregate content are known. Also, the model successfully ranks their performance similar to how they behave in the field.

iii) Sewer environmental conditions, i.e., $H_2S$ gas concentration, RH and temperature, and sewer hydraulic actions affecting airflow dynamics, are integrated into the model. However, the model is applied when RH in the sewer condensate film is sufficient to produce sulphuric acid, i.e., RH ranging between 70% and 100%.

iv) Due to a significant fluctuation of $H_2S$ gas concentration in sewers, applying constant average annual values in the Advanced LFM might not be adequate. Therefore, further study is required to determine a suitable correction factor depending on the sewer characteristics. However, in this study, the 90th percentile of maximum monthly $H_2S$ gas concentrations per year was found appropriate to predict concrete corrosion rates at different sewer sites.

v) The influence of sewer hydraulic action on affecting airflow dynamic is represented in the model using the Reynolds number. However, further study is suggested to improve the implications of using the Reynold number since, in this model, only an extreme scenario, i.e., turbulent airflow, was considered.

vi) The rate constant of $H_2S$ adsorption and oxidation in the concrete sewer is an essential parameter in determining the corrosion rate of concrete. It provides a link or connection between the acid generated due to sewer aggressivity and the potential of concrete to neutralise the acid. However, the rate depends solely on the concrete type. It was inferred that concrete with low permeability has the lowest adsorption rate constant and vice versa. Therefore, further study is suggested to evaluate the $H_2S$ adsorption and oxidation constant rate of different concrete types

The advanced LFM model is user-friendly and relatively simple to apply once the concrete mix design and the chemical composition of all concrete ingredients are presented. This model applies to sewer biogenic acid corrosion in the presence of sulphur species, i.e., sulphuric acid. The equations derived herein cannot be used to predict the corrosion rate of concrete by other forms of acid attack.

# CHAPTER 8. CONCLUSIONS AND RECOMMENDATIONS

## 8.1. Introduction

This chapter highlights insights, information, and knowledge extracted from this study in eight sections. After the first section, Introduction, the second section outlines the knowledge gaps filled by the study. The third section restates the aim and four main objectives, while the fourth section provides the methodology overview. The fifth section discusses the general findings and conclusions from this study, based on chapters Chapter 4Chapter 5Chapter 6 and critical discussions based on the first three objectives of this study. The sixth section discusses developments and applications of the LFM as a means of achieving the last objective of this study. The seventh section outlines the recommendations for sewer construction and further study, and the final section lists the challenges encountered while conducting this research.

## 8.2. Knowledge gaps from the literature

Studying concrete performance in live sewers is critical in enhancing the in-depth knowledge of Biogenic Acid Corrosion (BAC), developing mitigation measures, and developing service life prediction models. However, much of the research has concentrated on understanding the performance of various binder systems in simulated laboratory conditions, at the cement paste and mortar levels, with much less live sewer environment testing at the concrete level. Moreover, most existing BAC prediction models were developed based on cement paste or mortar performance, which does not immediately connect with the performance of concrete in sewers. Consequently, an essential aspect, that of the coarse aggregates, is overlooked. Accordingly, such models cannot be directly applied in sewer concrete design for field applications. Therefore, it is strongly suggested that concrete, as a fundamental component, should be considered in studying the performance of binder systems and developing efficient and effective BAC prediction models.

While the construction industry is shifting its practices towards adopting modern binders such as CSA, data and information on their performances in sewers are limited. Besides, this fairly rapid move to alternative binder systems presents difficulties in developing reliable and broadly applicable models. Thus, there is imperative to investigate the performance of these binders in live sewer environments and establish effective means of incorporating them in sewer design and construction. Along with field investigations, reactive transport modelling can be applied to provide a more fundamental comprehension of their chemistry and response in acid environments. This approach can be beneficial in understanding the materials and contributing to developing reliable prediction models that engineers can easily apply during sewer concrete design when various modern binders are preferred.

Additionally, during sewer concrete design, binders are selected depending on the degree of sewer aggressivity to most efficiently utilise the materials and minimise construction costs. Sewer aggressivity is defined based on sewer environmental conditions, such as sewer headspace temperature, relative humidity, $H_2S$ gas concentration, and sewer hydraulic parameters because these are easily measured. Therefore, in developing BAC prediction models, it is crucial to find means of applying or utilising these sewer environmental conditions in the modelling. Despite numerous BAC prediction

models for sewer concrete design, the Life Factor Method (LFM) prediction remains the most commonly applied deterministic model for predicting corrosion rates of sewer concrete and can quickly be advanced to cover these shortcomings.

### 8.3. Aim of this study

The study aimed to improve the BAC prediction model of sewer concrete corrosion based on the Life Factor Method (LFM), specifically to cover a broader range of binder systems and aggregate types in different sewer environments. This aim was achieved by establishing the following four objectives.

i) To study the influence of different binder systems, namely, CAC, CSA, PC, and SRPC with fly ash (FA) and iron-based additives (HC), in their influence on BAC of sewer concrete,
ii) To better understand the mechanism of biogenic acid corrosion in concrete sewers when different binder systems and aggregates are used,
iii) To study BAC of such concretes at different sewer aggressivity levels encountered in live sewer environments, and
iv) To use the insight and information from the above to advance and extend the Life Factor Method (LFM) for predicting concrete corrosion rate.

The first three objectives were achieved through the composite of a literature review, a field experimental investigation, and reactive transport modelling using the HYTEC model. The findings from these studies gave information about the influence of different sewer conditions, such as temperature, relative humidity, $H_2S$ gas concentration and sewer hydraulic actions, on BAC and the behaviour of aforementioned binder systems in different sewer environments, which were crucial in successfully refining the LFM model. Consequently, the advanced LFM model was designed to include input parameters encompassing a broader selection of binder systems, aggregate types, and sewer environmental factors, rendering a user-friendly and straightforward model for industrial application that, in initial validation, shows promise of being reliable.

### 8.4. Methodology overview

In this study, two types of concrete mix designs were used, i.e., ‘LH’ concretes and ‘UCT’ concretes. The LH concretes did not fully comply with the quality of concrete recommended for sewer concrete construction due to inadequate compaction, which led to the preparation of the UCT concrete mixes. Nevertheless, it was decided to continue the field exposure of the LH concretes to understand the performance of poorly compacted concrete in a sewer environment since this would not alter the basic deterioration mechanisms.

The primary purpose of the LH concrete mixes was to understand the influence of fly ash (FA), limestone (LS), and iron-based additives (HC) in improving the performance of Sulphate Resisting Portland Cement (SRPC) in sewers; to study the performance of Calcium Sulpho-Aluminate (CSA) cement as a novel binder system; and to study the combined influence of calcite aggregate and binder systems. The UCT concretes aimed to understand better and consolidate insights on the performance of CSA and SRPC-based binders with fly ash and iron additives when high-quality concrete with dense, competent dolomite aggregates was considered; to compare their performance to the superior sewer-

performing binder (CAC) and the poorly performing binder (CEM II AL); and to explore the impact of blending CAC and SRPC in sewer concrete.

LH concretes consisted of four binder systems, i.e., SRPC + FA, SRPC + FA + HC, SRPC + LS, and CSA. The UCT concrete consisted of six binder systems, i.e., CEM II AL, SRPC+FA, SRPC+FA+HC, CAC+SRPC, CSA, and CAC, which were further grouped into two groups; Portland-based binder systems, i.e., CEM II AL, SRPC+FA and SRPC+FA+HC, and alumina-based binder systems, i.e., CSA, CAC, and CAC+SRPC. The LH concretes were prepared with calcite aggregates and siliceous river sand, and UCT concretes with high-quality dolomite aggregates and siliceous pit sand.

In achieving these objectives, the concrete specimens from each concrete mix were prepared, tested for their quality using laboratory control tests, exposed to the sewer environment, and monitored for their deterioration mechanisms using BAC monitoring and BAC microstructural analyses. The LH concretes were exposed to three sewer sites in the City of Cape Town sewer system for two years, i.e., LPS, NAS M19 and NAS M54, while UCT concretes were only exposed to the LPS and NAS M19 after observing that NAS M54 was minimally aggressive. The UCT concrete at NAS M19 was monitored for two years, while at LPS for 15 months only due to the loss of specimens, as a consequence of working in the public environment where environmental control is less assured.

Laboratory control tests were conducted after 28 days of water curing at 20.0±3.0$^{o}$C before exposure, BAC monitoring and analysis were conducted regularly during the entire exposure duration, and BAC microstructure analysis was conducted at the end of the exposure period. Laboratory control tests confirmed the quality of concrete and entailed compressive strength, saturated density, and durability index tests. BAC monitoring and analysis encompassed a scheme for monitoring the deterioration of concrete in sewers and included visual observations, concrete surface pH monitoring, and mass and thickness change measurements. BAC microstructural analysis described techniques employed for understanding the deterioration mechanisms of concrete at the microstructural level. It entailed SEM-BSE image analysis, QEMSCAN, and XRD analysis. Laboratory control tests and BAC monitoring analyses were conducted on all concrete types, while BAC microstructural analysis was mainly conducted on the concretes subjected to the NAS M19 to limit the total amount of fieldwork and because some LPS concretes were lost on site.

Besides field investigations, the study focused on understanding the influence of the binders used in the UCT mixes in resisting BAC, using reactive transport modelling. All UCT concrete mixes were studied, except the CAC+SRPC, because it was complex to elucidate its cement phases after hydration. Due to the limitations and complications associated with incorporating aggregate components in the HYTEC model, the modelling focused on the cement matrix only.

### 8.5. Overall findings and conclusions

Despite the LH concretes not complying with the quality of concrete recommended for sewer concrete construction (due to poor compaction), their performance in three live sewer environments provided useful findings, insight and conclusions on general BAC mechanisms. UCT concrete, on the other hand, showed explicit deterioration behaviour of good-quality concrete in conjunction with high-quality aggregates. With UCT concrete performances, recommendations for selecting the most durable sewer

concrete mix designs could be provided. However, it was accentuated that concrete quality (in terms of mechanical and physical properties) is essential in comprehending the performance of a binder since poor-quality concrete tends to accelerate deterioration. Therefore, laboratory control tests should be performed to ensure that the concrete is fit for research and practice.

The following subsections draw the main findings and conclusions extracted from the studies on the sewer environmental conditions (Chapter 4), the experimental investigations (Chapter 5), and the reactive transport modelling (Chapter 6).

### 8.5.1. Sewer environmental conditions

This study intended to cover various sewer aggressivity levels encountered in live sewer environments. Therefore, three sewer sites, i.e., NAS M19, NAS M54 and LPS, were studied to characterise their aggressivity, understand their influence on the performance of concrete, and obtain sewer environmental parameters that can be applied in an advanced LFM.

The NAS M54 is the most upstream manhole on the Northern Area Sewer line, receiving mainly domestic wastewater, while the NAS M19 is a downstream manhole receiving both domestic and industrial wastewater. The LPS is a manhole between minor and major pumps of the Langa Pump Station. It receives mainly domestic wastewater pumped periodically from the minor pump station, as well as a continuous domestic wastewater flow.

Three sewer headspace conditions were monitored and studied: gas concentrations ($H_2S$, CO, and $CO_2$), ambient temperature, and relative humidity (RH). The gas concentrations in the sewer headspace varied during the day, seasonally, and sometimes due to periodic sewer occurrences such as flooding. The variation of the gas at the LPS was caused by the frequent pumping of wastewater from the pump station, which periodically increased the gas concentration peak. Further, the hydraulic situation at LPS, with regular flooding of the manhole due to the pumping cycles, meant that this condition mimicked the so-called 'tidal zone' in a typical sewer, in that erosion of the corrosion products occurred, exposing fresh surfaces for BAC. The gas concentrations at NAS M19 were affected by the peak hours of wastewater flow caused by the population served by the sewer line, with the highest peaks in the morning and evening hours. The gas concentrations in the NAS M54 were minor, with peaks depending on the peak wastewater flow. The overall temperature measurements ranged between 15$^{o}$C and 30$^{o}$C, with the RH measurements ranging between 70% and 100%. This agrees with the literature to be a suitable condition for microbial activity.

$H_2S$ gas concentrations were relatively low during the cold seasons and high in the hot seasons. This was mainly associated with the influence of temperature in catalysing metabolic reactions of SRBs in generating more sulphide species in the wastewater and with low wastewater flow volume during the hot, dry seasons, which creates sufficient sewer headspace volume for gases to accumulate. In terms of $CO_2$, all sites showed the lowest average $CO_2$ concentration in winter and the highest in summer. Despite seasonal fluctuations, the $CO_2$ gas in the sewer headspace remained high; thus, concrete surface carbonation was hypothesised to lower the initial surface pH. However, this aspect was recommended for further study since it was not directly covered in this study. Besides $H_2S$ and $CO_2$ gas, CO gas was observed in the sewer headspace, with its diurnal curves mimicking the $H_2S$ diurnal curves. With this,

a concern was raised about whether CO gas plays any functional purpose in influencing the concentration of $H_2S$ gas in sewers. Due to this, further study on this aspect is suggested.

In conclusion,

i) the LPS was related to a mostly erosion zone, i.e., a tidal zone in the sewer, due to its highest $H_2S$ gas concentrations and vigorous sewer hydraulic actions and wetting and drying cycles.
ii) The NAS M19 was associated with a partial erosion zone, mainly in the regions between the crown and tidal zones. This is because its corrosion was mainly associated with $H_2S$ gas concentrations, RH, temperature, and occasional sewer hydraulic actions such as flooding and splashing.
iii) The NAS M54 represented purely a crown zone, where the corrosion is attributed to $H_2S$ gas concentrations and not with the effect of sewer hydraulic actions.

It was recommended that careful attention be taken when selecting sewer environmental condition parameters, especially $H_2S$ gas concentration, for sewer corrosion rate prediction. This is because $H_2S$ concentrations in sewers fluctuate significantly and predicting corrosion rate based on the average $H_2S$ concentration may be inaccurate. In this research, the maximum $H_2S$ gas concentration of a sewer was recommended for predicting concrete corrosion rate using the advanced LFM model.

### 8.5.2. Field experimental investigation

#### 8.1.1.1. Visual observations

BAC visual observations offered an initial qualitative assessment of concrete corrosion performance. In the case of LH concrete, it was challenging to conclude their performance based purely on visual observation since all concrete showed significant deterioration at both LPS and NAS M19 and minor deterioration at NAS M54. At NAS M19, LH concrete experienced signs of corrosion from about six months of exposure, with increasing deterioration evident after about 10 months. Corrosion began from the edge toward the centre of the disc specimens, with reddish/brownish stains demarcating corroded and non-corroded surfaces. After 18 months, significant corrosion deposits and material loss were observed on the exposed surface of the concrete discs, with both cement and aggregate (calcite) matrix showing signs of corrosion. At LPS, LH concrete experienced early deterioration after about four months, with both cement and aggregate matrixes showing signs of corrosion. Due to the sewer hydraulic actions, corrosion products were removed, leaving the exposed surface with protruded corroded aggregates (calcite).

In the case of UCT concretes, Portland-based concretes exhibited more severe corrosion than alumina-based concrete at both LPS and NAS M19. At NAS M19, Portland-based binder concretes experienced more corrosion on the cement matrix than on the aggregate matrix. Aggregates (dolomite) protruded on the exposed surface with minor surface depressions and disintegrated particles. The cement matrix changed to whitish deposits, with more deposits on the specimen edges. By contrast, alumina-based concretes, at early exposure time, showed black stains on the exposed surface, indicating microbial colonisation. With time, corrosion deposits, especially for CSA and CAC+SRPC concrete, were observed on the exposed surface. At LPS, all UCT concretes showed signs of corrosion product removal

and aggregate protrusion. As mentioned above, even at early exposure durations, Portland-based concrete was severely corroded with signs of aggregate fallout, which created uneven or roughly exposed surfaces. CAC concrete, on the other hand, exhibited the highest resistance potential against BAC and sewer hydraulic action since it exhibited less aggregate protrusion and deteriorated cement matrix at both sites. Moreover, more severe visual damage was observed at both sites during the hot seasons than in the cold seasons. This coincided with the $H_2S$ gas measurements in the sewer, where higher gas concentration was observed during hot than cold seasons.

#### 8.1.1.2. Concrete surface pH

Concrete surface pH decreased with time, indicating progressive microbial colonisation and biological activity. pH readings on the exposed surface of any given specimen differed slightly, depending on where the pH point probe was placed. With protruded corroded aggregates, high pH readings were observed due to high aggregate alkalinity, i.e., carbonates of both calcite and dolomite. At the concrete specimen edges, the pH was lower due to the accumulation of acid from the centre of the specimen due to the vertically oriented exposed surface and massive corrosion deposits.

In the case of LH concretes, all concretes indicated similar pH values with minor discrepancies at each site, implying that different concretes responded similarly to the exposure environment and that the relative neutralisation effects were very similar up to two years of exposure. However, this was likely associated with calcite aggregate dissolution since it significantly neutralised the attacking acid. pH readings also varied with exposure site:

i) At NAS M19, LH concrete showed the lowest pH readings, indicating the evolution of SOB from neutrophilic to acidophilic.
ii) Despite NAS M54 having the lowest $H_2S$ gas concentrations, a gradual surface pH decrease was observed, indicating gradual proliferation and colonisation of neutrophilic SOB.
iii) At LPS, LH concrete showed approximately constant pH values of about 6, indicating a continuous renewal of the exposed surface due to sewer hydraulics actions.

In the case of UCT concrete, due to the absence of severe sewer hydraulic actions at NAS M19, a gradual evolution of concrete surface pH was observed with time due to successive microbial colonisation on the concrete surface, leading to the aggressive acid generation and continuous corrosion product deposition on the exposed surface. Portland-based concretes had pHs below 3 after two years of exposure, while alumina-based concrete pH values plateaued between 3 and 4, which concurred with the literature. This was mainly for CAC and CSA concrete, ascribed to gibbsite formation on the exposed surface. At LPS, the surface pH values of concrete at 15 months of exposure were higher than those observed at NAS M19, which accentuates that:

i) concrete surface pH does not necessarily infer the sewer aggressivity but rather the interaction between the concrete and acid generation on its surface, and
ii) for sewer zones such as the tidal zone, significant damage may be detected, but with little or no corrosion products due to continuous removal by the wastewater flow. Consequently, a higher concrete surface pH is detected, presenting the pH of the remaining substrate.

#### 8.1.1.3. Mass and thickness changes

At the initial stages of BAC, the concrete specimens exhibited mass gain, but this was of relatively short duration (up to 15 months, depending on the binder type), which after several years of exposure, would have no appreciable influence on the overall losses. The mass gain was associated with,

i) for LH concrete, moisture absorption and initial corrosion build-up in the compaction voids and excess porosity since compaction was not fully achieved, and
ii) for UCT concrete, initial corrosion product formation and acid and organic matter penetration at the thin layer of the exposed surface before thickness loss.

Mass loss was associated with removing the deteriorated concrete zone by either

i) sloughing off under gravity and occasional flooding in the sewer for concretes at NAS M19 or
ii) sewer hydraulic erosion and aggregate fallout for concrete at LPS, which in turn caused thickness losses.

Moreover, it was noted that higher mass loss did not necessarily imply higher thickness loss since aggregate fallout and protrusion played a significant role.

In the case of LH concretes, all showed a similar ranking in terms of mass and thickness changes, with CSA having superior performance than SRPC+FA+HC, followed by SRPC+LS, and then SRPC+FA at both LPS and NAS M19. This indicated that HC somewhat improved the abrasion resistance of LH concrete. SRPC+LS's superior performance over SRPC+FA was due to the limestone filler, which provided more alkali material ($CaCO_3$) to neutralise the acid. At NAS M19, continuous formation of ettringite in the CSA concrete compaction voids and at the concrete-epoxy coating interface due to further hydration and acid penetration led to a substantial mass gain with no thickness change, which was not the case at LPS, because of sewer hydraulic actions, which continuously removed the deteriorated zone.

In the case of UCT concretes, alumina-based binder systems exhibited superior performance compared with Portland-based binder systems. For alumina-based concrete, CAC concrete showed superior performance with approximately no mass or thickness losses at NAS M19, and the lowest losses at LPS, followed by CAC + SRPC, then CSA. Despite CAC+SRPC and CSA concrete exhibiting no mass loss up to 15 months of exposure at NAS M19, they experienced thickness loss, implying the mass gain due to the corrosion products on the exposed surface compensated for the mass loss, which was not the case at LPS. For Portland-based concretes, their performance depended significantly on the exposure site. In terms of mass loss, the rank at NAS M19 was CEM II AL <SRPC+FA+HC< SRPC+FA, and SRPC+FA+HC < CEM II AL < SRPC+FA at LPS. In terms of thickness loss, the rank at NAS M19 was SRPC+FA+HC < SRPC+FA <CEM II AL and SRPC+FA < SRPC+FA+HC < CEM II AL at LPS. CEM II AL presented significantly higher thickness loss at both sites, and lower mass loss at NAS M19 than other concretes, implying that it had significant corrosion products deposited on the exposed layer, contributing to lower mass loss. Note that this layer was removed at LPS.

Since the quality of UCT concretes was superior to LH concretes, it can be confirmed that the iron-based additive (HC) contributed little or negligibly to improving concrete resistance against BAC. Since SRPC+FA had lower thickness losses than CEM II AL, it can be concluded that fly ash enhances PC concrete performance.

Generally, findings from BAC monitoring and analysis led to the following conclusions:

i) Portland-based concretes have higher corrosion rates than alumina-based concretes, with CEM II A-L concrete having the highest rate and CAC concrete the lowest, regardless of sewer environmental exposure. This confirms the literature knowledge.

ii) CSA concrete performance ranks between that of CAC and SRPC-based concrete, while a blend of CAC and SRPC improves the performance of concrete compared to CSA and SRPC-based concrete. This adds knowledge regarding the performance of CSA in sewers in comparison to other binders.

iii) In terms of SCMs and additives, incorporating fly ash in the Portland-based concrete slightly increases the resistance against BAC, as known in the literature; iron-based additives have little or no contribution to improving the resistance of SRPC-based concrete; and ground limestone filler, in conjunction with calcite aggregates, provides more alkali material to neutralising acid but does not necessarily reduce the resistance against BAC.

iv) According to the literature, SRPC cement performs well in sulphate environments, but this study does not indicate similar performance in sewer environments. This is because the nature of the attack differs

v) Under the combined effect of BAC and sewer hydraulic erosion, significantly higher corrosion rates are observed on all concretes due to significant aggregate fallout and continuous renewal of concrete exposed surfaces. This highlights the significance of course aggregates in sewer concrete.

#### 8.1.1.4. BAC microstructural analysis of concrete

BAC microstructural analysis indicated that all concretes deteriorate to exhibit three distinct zones, i.e., the intact zone, the transition zone, and the deteriorated zone, except CSA concrete, which does not show the transition zone due to the superimposition of ettringite from acid penetration and hydration. The analyses also depicted the difference in cement and aggregate matrix deterioration rates. For UCT concretes, PC-based binders had higher deterioration rates than the embedded dolomite aggregate, leading to an uneven corrosion front; alumina-based concretes had comparable corrosion rates to dolomite aggregate, leading to a more uniform corrosion front. For LH concretes, calcite aggregates and SRPC-based cement neutralised the attacking acid; however, due to the vertical specimen orientation, acid tended to accumulate at the specimen edges, leading to an uneven corrosion front.

A high proportion of concrete mineralogical phases were from the aggregate matrix, with LH concretes containing calcite and quartz and UCT concretes having dolomite and quartz. In the cement matrix, the phases varied depending on the binder system.

Regarding LH concretes,

i) In the intact zone, SRPC-based concretes had calcium silicate hydrates and portlandite, and CSA concrete had mainly ettringite and some portlandite and calcium aluminium-silicate.
ii) In the transition zone, Mg-silicate was detected in SRPC-based concrete, except for concrete with iron-based additives (probably due to the area selected for analysis), implying magnesium ion migration to react with silicate from calcium silicate phases decalcification.
iii) In the deteriorated zone, SRPC-based concrete was rich in Al-silicate, gypsum, and amorphous silica, and CSA concrete contained gibbsite, gypsum, and other aluminate phases.

The amorphous silica was associated with a silica-rich zone after Al- and Mg- silicate disintegration. Due to compaction voids in CSA concrete, organic matter and ettringite were found in the voids, thus, leading to complexity in concluding CSA performance since, in the absence of these voids, ettringite development could have caused concrete microcracking, as observed in the UCT concretes. Despite the superior performance of the CSA concrete in terms of mass and thickness measurements, microstructure analysis showed that it still experiences significant deterioration, although at a slower rate than SRPC-based concrete.

Regarding Portland-based 'UCT' concretes.

i) CEM II AL contained calcium silicate hydrate and portlandite in the intact zone; gypsum and Mg-silicate deposits in the transition zone, confirming the possibility of magnesium ion migration with acid penetration; and amorphous silica and more Fe/Al-silicates in the deteriorated zone.
ii) SRPC+FA contained calcium silicate hydrates, calcium aluminate hydrates, and portlandite in the intact zone; minor Mg-silicate, ettringite and gibbsite and some gypsum in the transition zone; and mainly gypsum in the deteriorated zone.
iii) SRPC+FA+HC concrete had a similar composition as SRPC+FA in the intact zone but with iron-based additive particles distributed through the cross-section and without any chemical influence; gypsum and Mg-silicate were abundantly observed in the transition zone, with some minor ettringite and gibbsite; and gypsum together with Al-silicate in the deteriorated zone.

Regarding alumina-based UCT concretes;

i) CAC+SRPC consisted of calcium silicate hydrates, portlandite and some Fe/Al silicate in the intact zone; a noticeable layer of Mg silicate in the transition zone; followed by gypsum in the deteriorated zone. Minor calcium aluminate hydrates, gibbsite and ettringite, were detected in the intact zone, indicating that blending CAC and SRPC does not necessarily increase their formation.
ii) CSA consisted mainly of ettringite and calcium aluminate, along with some gibbsite, gypsum and portlandite in the intact zone. With acid penetration, more gibbsite and gypsum were observed in the deteriorated zone. As explained earlier, the transition zone was hardly distinguished from the deteriorated zone. However, a continuous microcrack was observed

parallel to the exposed surface in one specimen under observation, indicating concrete expansion due to secondary ettringite formation with acid penetration.

iii) CAC consisted of calcium aluminate hydrates and gibbsite in the intact zone and ettringite in the transition zone, formed due to acid penetration, which, further acid penetration and pH decrease to below 10.7, disintegrated to gibbsite and gypsum in the deteriorated zone.

This investigation found that the transition zone of various concretes had a distinct 'layer' of magnesium silicate, but it was difficult to determine its origin and its significance to deterioration. This layer is possibly due to magnesium ion migration into the transition zone due to acid penetration or dissociation/dissolution of dolomite, which reacts with silicate to provide concrete with some acid-inhibiting potential. In light of this, it is advised to conduct further investigations on the presence of magnesium ions and how they affect concrete under BAC, as well as how the cement matrix and aggregates interact. Moreover, fly ash and iron-based additives possibly also disintegrate at low pH below 3, resulting in the leaching of metals such as Al and Fe. This is because their particles disintegrated or dissolved in the deteriorated zone.

### 8.5.3. Reactive transport modelling

Reactive transport modelling was used in this study to attempt a more fundamental understanding of BAC on UCT binder systems, through coupling chemical reactions and transport processes. This modelling intended to provide an understanding of the influence and effect of varying sulphuric acid pH on the dissolution and precipitation of cementitious phases; compare the modelling performance of Portland and alumina-based binder systems with the experimental field observations; and finally, extract information that could assist in refining the LFM model.

The modelling had intended to model two acid attack modes; an 'Open System' to simulate the 'tidal' zone, and a 'Closed System' to simulate the partial erosion zone. Subsequently, due to difficulties in assigning a value for the 'acid reservoir' that could justify real-sewer corrosion in the predominant acid attack zone, the Closed System was not further pursued. Further study on this aspect is recommended.

Based on the open system modelling observations, it was identified that continuous ettringite deposition caused by the presence of calcium aluminate hydrates ($C_3AH_6$) at pH 1 results in pore clogging. This effect was mostly seen in the alumina-based binder systems when a significant amount of $C_3AH_6$ was used, while in the Portland-based binder system, the phase was ignored since it is minor. This effect may be deceptive, suggesting that the binder has excellent potential for BAC resistance; yet, in practice, continuous ettringite deposition causes significant concrete damage because of its expansive nature by inducing microcracking. The physical implication of ettringite deposition is, therefore, not considered by the HYTEC model. The limitations of such models, therefore, need to be taken into consideration when interpreting HYTEC model outcomes.

Reactive transport modelling also indicated three corrosion zones, namely, the deteriorated zone, the transition zone, and the intact zone;

i) The deterioration in the model was governed by ionic exchanges and their concentrations in the attacking acid and the exposed cementitious surface, which was impossible to detect in the field investigation.

ii) The deterioration of Portland-based binder systems was governed by the decalcification of Portlandite, while the decalcification of $C_3AH_6$ governed the deterioration of alumina-based binder systems.

iii) Hence, Portlandite and $C_3AH_6$ dissolution formed the deepest reaction front, demarcating the intact and transition zones.

Interestingly, these zones were distinctly observed only when the binder systems were subjected to acid attack at pH 1, while such zones were not observed with higher pH values in the models. This led to a hypothesis that, regardless of sewer aggressivity, SOBs on the sewer concrete wall generate acid with a low pH near 1, to produce gypsum and establish these distinct corrosion zones. The difference in corrosion rates between sewers of different aggressivities is then a function of the rate at which the acid is formed, and hence of $H_2S$ gas concentration. This hypothesis is rather intriguing and requires further exploration to clarify concerns about the pH of SOB-generated acid in sewers and whether the concrete surface pH measured in live sewers resembles the pH of corroded concrete or the pH of the SOB-generated acid.

Regarding the fundamental understanding of BAC on binder systems, reactive transport modelling provided the following further insights;

i) All Portland-based binder systems, i.e., CEM II AL, SRPC+FA and SRPC+FA+HC, have similar performance under BAC, with gypsum and amorphous silica in the deteriorated zone and decalcified calcium silicate and ettringite in the transition zone. This is similar to the BAC microstructural analysis findings.

ii) Alumina-based binder systems contain gypsum and gibbsite in the deteriorated zone and secondary ettringite in the transition zone. Due to gibbsite stability at a pH of 3-4, the deteriorated zone pH plateaus at a pH above 3, below which gibbsite dissolves, agreeing with the field observations.

iii) Also, it confirms the formation of secondary ettringite in the CAC transition zone, and ettringite superimposition is the reason behind the difficulties in demarcating the CSA transition zone in the BAC microstructural analysis work.

iv) Additionally, when assessing the neutralisation potential of a binder, other minor phases such as brucite and goethite should also be considered since they contribute to neutralising the acid.

Moreover, thickness losses at LPS correlated reasonably well with the predicted deteriorated zone depths, indicating that the deteriorated depth of concrete is similar to that of the cement matrix, provided that aggregates have less influence on the concrete corrosion rates. In this case, LPS sewer hydraulic actions removed the deteriorated zone and protruding aggregate before aggregate dissolution. In the absence of sewer hydraulic actions, aggregates dissolve to provide more materials to neutralise the attacking acid, consequently decelerating the corrosion rate and low thickness losses would have been observed.

In terms of ranking of binder system performance, field and HYTEC modelling observations showed a similar trend, from the highest thickness loss to the lowest, as follows; CEM II A-L > SRPC+FA and

SRPC+FA+HC > CSA> CAC. After two years of field exposure, SRPC+FA and SRPC+FA+HC concrete show similar thickness losses, confirming that iron-based additive has insignificant influences in resisting BAC.

Finally, it was concluded that reactive transport modelling can provide an understanding of the binder system deterioration mechanisms. This tool may assist engineers and researchers interested in comprehending and developing binder systems that can resist acid attacks and designing robust concrete for sewer systems.

### 8.5.4. Critical discussions and conclusions

This section highlights how combining sewer environmental conditions, field experimental investigation, and reactive transport modelling findings aided in providing conclusions to the first three objectives of this study.

#### 8.1.1.5. Influence of binders (PC, SRPC, CSA, and CAC), fly ash, and iron-based additives on concrete under BAC

The poorer performance of Portland-based concretes is associated with calcium silicate hydrates and portlandite decalcification because of their susceptibility to BAC to form gypsum and amorphous silica. Blending SRPC with fly ash increases the calcium aluminate hydrate phases, which would improve the performance of SRPC-based concrete compared to CEM II AL. Iron-based additives, on the other hand, have little or no contribution to improving the resistance of SRPC-based concrete.

CSA's improved performance over Portland-based concrete is associated with the formation of ettringite, which provides more neutralisation capacity than calcium silicate hydrates and portlandite, and its transformation to gibbsite, which is stable at pH between 3 and 4. On the other hand, its poorer performance compared to CAC is associated with ettringite superposition in the transition zone; due to its expansive nature, microcracks are induced, accelerating the deterioration.

CAC's superior performance is associated with the long chain of dissolution of its hydrates, leading to more gibbsite formation and high neutralisation capacity. However, CAC tends to have a broader transition zone filled with ettringite due to its stability at a high pH, which with acid penetration, transforms to form more gibbsite in the deteriorated zone. The performance of a blend of CAC and SRPC is not well understood. However, it may be ascribed to the hypothesis on magnesium-inhibiting potential from Mg-silicate.

#### 8.1.1.6. Influence of aggregates on concrete under BAC

Aggregates substantially influence the corrosion rate of concrete since they comprise about 70-80% of the concrete composition. Incorporating non-reactive aggregates in sewer concrete causes an attack on the cement matrix only, resulting in aggregate protrusion and eventually fallout; with this, the overall concrete corrosion rate is accelerated. The opposite is observed when reactive aggregates are incorporated; they tend to provide more acid-neutralising material to the concrete, leading to both aggregate and cement matrix, which in turn, decelerates the overall concrete corrosion rate. However, when the corrosion rate of the cement matrix matches that of the aggregates, a uniform corrosion front is observed. When unmatched, an uneven corrosion front is observed, also causing aggregate protrusion

or fallout and, ultimately, accelerating the overall concrete corrosion rate, but less compared to non-reactive aggregates. Therefore, when selecting aggregates for optimum sewer concrete performance, rates of aggregate and cement matrix deterioration that are equivalent or similar should be regarded.

In the case of high-quality dolomite aggregates, alumina-based concretes had reasonably uniform corrosion fronts, suggesting that their cement and dolomite matrices had roughly equal deterioration rates, except under sewer hydraulic action, where aggregate protrusion was observed. Portland-based concretes exhibited uneven corrosion fronts due to dolomite aggregate protrusion and significant aggregate fallout in the presence or absence of sewer hydraulic actions. These findings revealed that Portland-based cement matrix corrodes faster than dolomite aggregates, commonly found in practice. Therefore, the enhanced performance of alumina-based concrete is due to excellent compatibility with dolomite aggregate in addition to improved microstructures and a lower diffusion rate.

In the case of calcite aggregates, both SRPC-based cement and aggregate participate in neutralising the acid, by providing a greater quantity of acid-reactive materials. The deterioration of a CSA cement matrix does not match that of calcite because calcite aggregates deteriorate more quickly than the CSA binder system, resulting in a higher corrosion rate.

Furthermore, although dolomite and calcite are both calcareous aggregates, their deterioration mechanisms and rates in sewers differ. In the present case, calcite dissolves rapidly, producing more $Ca^{2+}$ and $CO_3^{2-}$ ions on the concrete surface. These ions then swiftly react with sulphuric acid to form more gypsum and a higher concrete surface pH because H+ ions ionise water. Dolomite reacts with the acid to form gypsum and magnesium carbonate, dissociating into magnesium ions because magnesium sulphate ($MgSO_4$) does not precipitate due to its high solubility. Dolomite aggregates, therefore, deteriorated slowly by initially exhibiting surface depression and particle dissolution. Siliceous sand particles, on the other hand, do not react with acid.

#### 8.1.1.7. Influence of sewer environmental conditions

The field studies showed that a particular concrete exhibits various performance levels depending on sewer environmental conditions. Sewer hydraulic actions, for instance, accelerate the deterioration rate due to the continuous removal of corroded surfaces and renewal of exposure surfaces. $H_2S$ gas concentration determines the acid production rate on the exposure surface; hence the higher the $H_2S$ gas concentration, the higher the corrosion rate. Sewer headspace temperature catalyses the production, adsorption, and oxidation process of $H_2S$ gas in sewers, while relative humidity provides conducive environments for SOB colonisation on the sewer condensate film. Therefore, in addition to the concrete physical and chemical properties, sewer environmental conditions are critical factors in assessing concrete performance.

Additionally, it was found that $H_2S$ gas concentrations below 10 ppm can still cause corrosion on the concrete, albeit in the long term, because microbial activities progress with time, leading to continuous concrete surface pH reduction. In the case of higher $H_2S$ gas concentrations, the present work did not attempt to establish a threshold, but this is evidently an important issue. This also relates to when biotic oxidation rather than abiotic oxidation becomes a dominant cause of acid deterioration.

## 8.6. Advanced LFM model

The final objective of this research was to apply the knowledge extracted from the literature review, field investigations, and reactive transport modelling to advance the LFM model to cover a broader range of binder systems and aggregate types in different sewer environments, see Chapter 7.

### 8.6.1. Fundamental LFM development

Based on a fundamental interpretation of the original LFM model, the corrosion rate of concrete can be considered as the ratio of the average acid generation rate per $m^2$ of unsubmerged sewer wall and the average acid neutralised per $m^3$ of concrete exposed to the acid attack. In this study, the average acid generation rate per $m^2$ of sewer wall was referred to as the 'sewer environmental factor' ($\phi_{se}$) and the average acid neutralised by a $m^3$ of concrete as the 'Material Resistance Factor' (*MR*), which combines the 'acid neutralisation factor of the binder' ($\varphi$) and the 'aggregate reactivity factor' ( $\beta$). This way, the vital influence of both binder and aggregate types could be included rationally and intrinsically.

### 8.6.2. Sewer environmental factor development

The sewer environmental factor ($\phi_{se}$) was evaluated based on the factors attributed to the acid production on the sewer pipe wall, which are $H_2S$ gas concentration, temperature, RH in the sewer headspace, and sewer hydraulic actions. The $H_2S$ adsorption and oxidation prediction model by Vollertsen et al. (2008) was adopted since it could significantly and effectively incorporate these factors. It uses Reynolds numbers (*Re*) to define how the sewer airflow is influenced by sewer hydraulic parameters and $H_2S$ adsorption and oxidation rate constant ($k_p$) to define the potential of exposed surfaces in adsorbing and subsequently promoting oxidisation of the gas into acid.

### 8.6.3. Material resistance factor development

In evaluating the acid neutralisation factor of the binder ($\varphi$), four principal binder oxides, i.e., CaO, $Al_2O_3$ $Fe_2O_3$, and MgO, responsible for formulating most cementitious hydration phases that neutralise sulphuric acid under BAC, were considered. Using a simple acid-base reaction, the equivalent amount of sulphuric acid to be neutralised by these oxides was quantified and regarded as the acid neutralisation factor of a binder ($\varphi$). In determining the aggregate reactivity factor ($\beta$), the behaviour and reactivity of aggregates in concrete subjected to BAC were observed and described in four ways, i.e., non-reactive, partially reactive, matched reactive, and highly reactive aggregates. Based on this, the aggregate reactivity factor ($\beta$) was evaluated as a function of the acid neutralisation factor of acid-reactive components of aggregate ($\gamma$), the fractional surface area of aggregates ($F_{SA}$), and the acid solubility of aggregates ($A_s$).

The principles applied in determining the acid neutralisation factor of aggregates ($\gamma$) were similar to those of the binder ($\varphi$), considering the four principal oxides in various aggregate types. The fractional surface area of aggregates ($F_{SA}$) was taken as the aggregate volumetric ratio in concrete, with a scaling factor to account for aggregate porosity and aggregate internal fracture surface area. SANS 6242, the acid insolubility test of aggregates, was applied to evaluate the acid solubility ($A_s$). With these factors, the contribution of various aggregate types and contents in concrete mix designs could be integrated. Additionally, the aggregate dislodging effect ($f^{(\mathrm{Agg,})}$) was introduced when non-reactive or slowly

reactive aggregates are ‘dislodged’ from the matrix, i.e., aggregate fallout, to evaluate or predict mass losses for fine and coarse aggregate particles in concrete under BAC.

### 8.6.4. Application of the advanced LFM model

Finally, the advanced LFM model was developed and applied to theoretical concrete mix designs with different binder and aggregate types to predict their corrosion rates. Four types of binder systems, i.e., PC, PC with SCMs, CSA and CAC, and four aggregate types, i.e., SIL, CAL, DOL, and ALAG, were used in this study. Virginia Experimental Sewer (VES) was used as the primary study site to evaluate sewer environmental factors. Finally, the $H_2S$ gas concentration and $H_2S$ adsorption and oxidation rate constant ($k_p$) were varied to study their influence on corrosion rate.

### 8.6.5. Advanced LFM model findings

From the application, the model was capable of predicting the performance of different binder systems when combined with different aggregate types. The model indicated that PC concrete had the highest corrosion rate, and CAC concretes the lowest corrosion rate, while CSA concrete lies between PC and CAC concrete, as in the field observations. Concrete with siliceous aggregates (SIL) showed the highest corrosion rate, followed by concrete with calcite (CAL), then dolomite (DOL) aggregates, while aluminate (ALAG) aggregate concretes showed the lowest corrosion rate. This observation indicated that combining calcareous aggregates in the PC concrete improves the performance of PC-based sewer concrete. However, the dolomite aggregates had a higher neutralisation capacity than calcite aggregates, suggesting that dolomite aggregate should be preferred in sewer concrete.

The effects of varying $H_2S$ concentrations indicated that the corrosion rate increased with increased gas concentration, with significant corrosion rate variation on the SIL based concretes. The comparison between the VES field measured corrosion rate and predicted corrosion rate of PC and CAC binder systems indicated that the corrosion rate of concrete depends on the $H_2S$ adsorption and oxidation rate constant. Thus, a single rate constant cannot be applied to predict the corrosion rate of concrete with different binder systems. It should be noted that VES gave independent data for validation.

Using rate constant ($k_p$) values from the VES and the sewer environmental conditions of LPS and NAS M19, corrosion rates of UCT concretes were predicted and compared with the field-measured rates. It was observed that the $k_p$ value is determined by the type of concrete and not by sewer aggressivity since the corrosion rates of a given concrete in two different sewers were predicted using a single $k_p$ value. A direct correlation was observed between predicted and measured corrosion rates with about 98% variance. However, the advanced LFM model slightly overpredicted the corrosion rate of the CAC concrete at NAS M19 and underpredicted that of CEM II AL at LPS. Moreover, it was observed that concretes with low diffusion coefficients had the lowest $H_2S$ adsorption rate constant, which significantly reduced the corrosion rate of concrete. Therefore, the $H_2S$ adsorption rate constant closely correlates with the diffusion coefficient of concrete; however, this hypothesis requires further study.

### 8.6.6. Importance of $H_2S$ adsorption and oxidation rate constant ($k_p$)

In this light, the $H_2S$ adsorption and oxidation rate constant (kp) of concrete in this model is an essential parameter in predicting the corrosion rate of concrete. It provides a link or connection between the acid

generated due to sewer aggressivity and the potential of concrete to neutralise the acid. However, the rate depends solely on the concrete type. It was inferred that concrete with low permeability has the lowest rate constant and vice versa. Also, Grandclerc et al. (2017) pointed out that the rate constants increase with RH, which emphasises the importance of the sewer concrete condensate film that allows SOBs to procreate and facilitate the ionic exchange from the surface into the concrete. Therefore, for future studies, Grandclerc et al. study can provide a guide for evaluating the rate constants of different concretes with respect to the binder system and aggregate type.

### 8.6.7. Specific highlights and conclusions on the LFM study

Based on the discussion above, the following highlights can be emphasised regarding the advanced LFM model development.

i) The model can incorporate various binder systems, from the PC, CSA and CAC-based mixes with and without SCMs.
ii) It can incorporate different aggregate types, specifically siliceous (SIL), calcareous (CAL and DOL), and aluminate (ALAG); and by extension, it can incorporate any aggregate for which the chemical composition is known.
iii) It considers the concrete mix proportions by incorporating all concrete ingredients that resist sulphuric acid attack.
iv) It considers different sewer environmental conditions: $H_2S$ gas concentration, temperature, and sewer hydraulic actions affecting airflow dynamics. The model is also applied when the relative humidity in the sewer is sufficient to produce sulphuric acid in the sewer condensate film.
v) It considers the $H_2S$ adsorption and oxidation rate constant for different concrete mix designs. It was inferred that concrete with low diffusivity has the lowest adsorption rate constant and vice versa.
vi) It is a user-friendly model once the concrete mix design and the chemical composition of the concrete ingredients are known.

Therefore, the advanced LFM model is user-friendly and relatively straightforward for industrial applications. However, it should be noted that this model is based on deterministic analysis and not probabilistic analysis

## 8.7. Recommendations

### 8.7.1. Recommendations for sewer design and construction

Based on this study, the following binder system was recommended for the construction of sewer concrete structures for industrial applications:

i) CAC is recommended for very aggressive sewer environments, such as high $H_2S$ gas concentrations and hydraulic turbulence.
ii) CSA and CAC blends are suitable for moderately aggressive sewer environments, for example, sewer structures in the mid-section of a sewer line.

iii) Portland-based binders with and without fly ash can be used for mild aggressive sewer environments, such as upstream conditions with low $H_2S$ gas concentrations and less severe hydraulic actions.

iv) However, all binder systems must be combined with acid-soluble aggregates to distribute acid attack uniformly over the exposed surface area. For better performance of concrete in the sewer, the rate of aggregate deterioration and cement matrix should be uniform or similar.

Additionally, this research demands follow-up work to develop clear, practical recommendations and provide knowledge regarding;

i) The choice of binder type, aggregate type, and their combination

ii) Relevant sewer concrete mechanical, physical, and durability properties for performance-based approaches

iii) Sewer environmental parameters for simplifying their applications in assessing and modelling the sewer concrete

iv) Practical application of the service life design model and interpretation of model results.

### 8.7.2. Recommendations for further studies

#### 8.1.1.8. From this research

i) It is recommended to explore further the influence and interaction between cement and aggregate matrices in the concrete under BAC, especially dolomite aggregates. This will assist in understanding the origin and significance of magnesium ions in the concrete under BAC.

ii) $CO_2$ gas concentration is well known to condition the concrete surface for microbial colonisation, through carbonation. However, its impact after SOB colonisation is not well known. It is possible that, in cases where continuous renewal of exposure surface is experienced, carbonation continues to take place. Therefore, further study is required in this regard, which will also assist in developing approaches for incorporating $CO_2$ gas concentration in the BAC prediction models.

iii) The concentration of CO gas was substantially detected in the sewer at even higher concentrations than the $H_2S$ gas, and its diurnal variation mimicked that of $H_2S$. In the literature, its contribution to BAC is rarely reported, despite being widely known as a toxic gas. Therefore, this raises a discussion of whether CO gas plays any significant role in influencing $H_2S$ gas concentration or interfering with SOB development in sewers.

iv) In the advanced LFM model, further study on Reynold's number is recommended to describe how the sewer airflow is influenced by sewer hydraulic parameters, such as turbulence flow, wastewater velocity and sewer gradient. Since this parameter was not studied in this work, the worst-case scenario was considered, i.e., turbulent airflow.

v) The model also indicates that the higher the cement content, the lower the corrosion rate. This is because the corrosion rate in the model is inversely related to the material resistance factor. However, this somewhat contrasts with Kiliswa's VES observations, which indicate

that PC concrete with higher cement content had a higher corrosion rate. The elaboration behind this is that higher PC content provides access to a more susceptible cement matrix and hence a higher corrosion rate. Thus, further study may be required to clarify this apparent contradiction.

vi) Due to the behaviour of sewers which tend to have large diurnal and seasonal fluctuations of $H_2S$ concentration, applying a constant annual $H_2S$ concentration in the advanced LFM might not be sufficient. In this study, a 90th percentile of the maximum monthly $H_2S$ gas concentrations was applied and deemed to provide a good correlation between measured and predicted corrosion rate. Therefore, further study is suggested to confirm the appropriate percentile of the sewer environmental condition for advanced LFM applications.

vii) Furthermore, it was found that the lowest corrosion rate was observed in the concrete with the lowest diffusion coefficient and lowest $H_2S$ adsorption rate constant, implying that the $H_2S$ adsorption rate constant closely correlates with the diffusion coefficient of concrete. However, this is a hypothesis worth exploring philosophically and experimentally in future.

#### 8.1.1.9. From the literature review:

i) There is insufficient information on detailed preconditioning factors and mechanisms that impact the proliferation of microorganisms on the submerged wall of concrete sewer pipes and how they are involved in biofilm formation in the aqueous phase.

ii) Information on the diversity, composition, and interaction of SRB and other microorganisms responsible for sulphide species formation is missing. The existence of fungi and heterotrophic bacteria other than SOB and their roles in biogenic acid formation also requires verification.

iii) Factors that favour iron accumulation in the transition zone and its influence on the corrosion rate and the growth of A. ferrooxidans require further exploration. Besides, the role and favourable conditions for A. ferrooxidans and their interaction with A. thiooxidans in creating conditions for altering concrete microstructure are not indicated.

iv) Another area to stress is the effect of BAC on concrete steel reinforcement. Most studies in BAC are mainly delegated to concrete matrix deterioration and less to the underlying steel inside the concrete. Various studies have indeed proposed to improve and increase the depth of the sacrificial layer of concrete or concrete cover that is anticipated to protect the reinforcement before the corrosion front reaches them. Yet there are few strategies to combat the attack if it reaches the reinforcement. Therefore, researchers should shift their interest in this area as more beneficial solutions might be recommended for the performance of sewers.

### 8.8. Challenges encountered during this study

The following were the challenges encountered while conducting this research.

i) Loss of concrete specimens: The investigation started with three sites: LPS, NAS M19, and NAS 54. After a year of LH concrete monitoring, NAS M54 was discovered to be

minimally aggressive, although not without value for the overall study. As a result, the third site for exposure of UCT concrete specimens was selected. Specimens at this site were washed away due to excessive sewer flooding after two months of exposure. Additionally, due to several difficulties operating in a public area, UCT concrete specimens at LPS were lost on-site after 15 months of exposure.

ii) South African COVID-19 pandemic Lockdown regulations: The LPS site experienced breakdowns during the lockdown due to erratic monitoring and sewer pump station control. This required additional time to repair, which slowed the progress of this work.

iii) Personal health issues: During the first year (2019) of this work, I had health problems that required a surgical procedure. It took more than two months to recover and resume my work activity.

iv) Safety issue: In the middle of the study, i.e., 2021, we encountered a mugging attempt at NAS M19 because the site is located in an isolated area with no social activities. This was detrimental to my progress for a period.

# References


Abdikheibari, S., Song, H.M., Cho, J. Il, Kim, S.J., Gwon, S.C., Park, K., Maluleque, B., Marleni, N., et al. 2016. In-situ evaluation of predictive models for H2S gas emission and the performance of optimal dosage of suppressing chemicals in a laboratory-scale sewer. *International Biodeterioration and Biodegradation*. 106:25–33.

Aboulela, A. 2022. Study of the resistance to biodeterioration of innovative and low-carbon cementitious materials for an application in sewerage networks. INSA, Toulouse.

Aboulela, A., Peyre-Lavigne, M., Huet, B., Patapy, C., Meulenyzer, S. & Bertron, A. 2019. Numerical modelling of sulfuric acid attack on OPC and CAC materials. *15th International Congress on the Chemistry of Cement*. (September).

Aboulela, A., Lavigne, M.P., Buvignier, A., Fourré, M., Schiettekatte, M., Pons, T., Patapy, C., Robin, O., et al. 2021. Laboratory test to evaluate the resistance of cementitious materials to biodeterioration in sewer network conditions. *Materials*. 14(3):1–24. DOI: 10.3390/ma14030686.

Achilles, C.N., Downs, G.W., Downs, R.T., Morris, R. V., Rampe, E.B., Ming, D.W., Chipera, S.J., Blake, D.F., et al. 2018. Amorphous phase characterization through x-ray diffraction profile modelling: implications for amorphous phases in gale crater rocks and soils. *49th Lunar and Planetary Science Conference 2018*. LPI Contri(2083):2661.

Aïtcin, P.-C. 2008. Chapter 9. Special Portland cements and other types of hydraulic binder. In *Binders for durable and sustainable concrete*. Taylor & Francis Group. 314–331.

Alani, A.M. & Faramarzi, A. 2014. An evolutionary approach to modelling concrete degradation due to sulphuric acid attack. *Applied Soft Computing*. 24:985–993.

Alexander, M.G. 2004. Durability indexes and their use in concrete engineering. In *Proceedings, International RILEM symposium: Concrete Science and Engineering*. 9–22. DOI: 10.1617/2912143586.002.

Alexander, M.G. & Beushausen, H. 2019. Durability, service life prediction, and modelling for reinforced concrete structures – review and critique. *Cement and Concrete Research*. 122(April):17–29.

Alexander, M.G. & Fourie, C. 2011. Performance of sewer pipe concrete mixtures with portland and calcium aluminate cements subject to mineral and biogenic acid attack. *Materials and Structures*. 44:313–330.

Alexander, M.G. & Mindess, S. 2005. *Aggregate in Concrete*.

Alexander, M.G., Mackechnie, J.R. & Ballim, Y. 1999.

Alexander, M.G., Streicher, P.E. & Mackechnie, J.R. 1999. Rapid chloride conductivity testing of concrete. *University of Cape Town, CoMSIRU*. Available: http://www.comsiru.uct.ac.za/sites/default/files/image_tool/images/333/Research/Downloads/Monograph_3.pdf [2017, April 03].

Alexander, M.G., Bertron, A. & Belie, N. De. 2013. *Performance of Cement-Based Materials in Aggressive Aqueous Environments, State-of-the-art Reports, Rilem TC 211-PAE*. V. 10. Springer.

Alexander, M.G., Bentur, A. & Mindess, S. 2017. *Durability of concrete: Design and construction*. CRC Press; Taylor & Francis Group.

Alexander, M.G., Ballim, Y. & Mackechnie, J. 2018. *Durability Index Testing Procedure Manual Ver. 4.5.1*. V. v. Available: http://www.comsiru.uct.ac.za.

Alonso, M.C., García Calvo, J.L., Hidalgo, A. & Fernández Luco, L. 2010. 10. Development and application of low-pH concretes for structural purposes in geological repository systems. In *Geological Repository Systems for Safe Disposal of Spent Nuclear Fuels and Radioactive Waste*. 286–322. DOI:

10.1533/9781845699789.3.286.

Angello, V.N. 2005. Dolomite and Limestone in South Africa : Supply and Demand. Report R49/20. *Department of Mineral and Energy, Republic of South Africa*. (October):1–67.

ASTM C1723. 2006. Standard Guide for Examination of Hardened Concrete Using Scanning Electron Microscopy1. *Annual Book of ASTM Standards*. 16(Reapproved 2004):1–95. DOI: 10.1520/C1723-16.can.

ASTM C188. 2017. Standard Test Method for Density of Hydraulic Cement. *America Society for Testing and Material*. 1–3. DOI: 10.1520/C0188-17.2.

Attiogbe, E.K. & Rizkalla, S.H. 1988. Response of concrete to sulfuric acid attack. *ACI Materials Journal*. 85(6):481–488.

Bakera, A.T., Alexander, M.G. & Beushausen, H. 2021. Corrosion prediction models for Biogenic acid. In *Young Concrete Researchers, Engineers and Technologist Symposium (YCRETS) Proceedings*. 175–185.

Barton, L.L., Fardeau, M.-L. & Fauque, G.D. 2014. Chapter 10. Hydrogen Sulfide: A Toxic Gas Produced by Dissimilatory Sulfate and Sulfur Reduction and Consumed by Microbial Oxidation. In *The Metal-Driven Biogeochemistry of Gaseous Compounds in the Environment*. P.M.H. Kroneck & M.E.S. Torres, Eds. Springer Netherlands. 237–277.

Bear, J. & Bachmat, Y. 1990. *Introduction to modelling of transport phenomena in porous media*. London: Kluwer Academic Publishers.

Beddoe, R.E. 2016. Modelling acid attack on concrete: Part II. A computer model. *Cement and Concrete Research*. 88:20–35.

Beddoe, R.E. & Dorner, H.W. 2005. Modelling acid attack on concrete: Part I. The essential mechanisms. *Cement and Concrete Research*. 35:2333 – 2339.

De Belie, N., Monteny, J., Beeldens, A., Vincke, E., Van Gemert, D. & Verstraete, W. 2004. Experimental research and prediction of the effect of chemical and biogenic sulfuric acid on different types of commercially produced concrete sewer pipes. *Cement and Concrete Research*. 34(12):2223–2236.

Bell, S.K., Joy, K.H., Pernet-Fisher, J.F. & Hartley, M.E. 2020. QEMSCAN as a method of semi-automated crystal size distribution analysis: Insights from Apollo 15 mare basalts. *Journal of Petrology*. 61(4). DOI: 10.1093/petrology/egaa047.

Berger, S., Coumes, C.C.D., Le Bescop, P. & Damidot, D. 2011. Influence of a thermal cycle at early age on the hydration of calcium sulphoaluminate cements with variable gypsum contents. *Cement and Concrete Research*. 41(2):149–160. DOI: 10.1016/j.cemconres.2010.10.001.

Berndt, M.L. 2011. Evaluation of coatings, mortars and mix design for protection of concrete against sulphur oxidising bacteria. *Construction and Building Materials*. 25(10):3893–3902.

Bertron, A. 2014. Understanding interactions between cementitious materials and microorganisms: a key to sustainable and safe concrete structures in various contexts. *Materials and Structures/Materiaux et Constructions*. 47(11):1787–1806.

Bertron, A., Peyre, M., Patapy, C. & Erable, B. 2017. Biodeterioration of concrete in agricultural , agro-food and biogas plants : state of the art and challenges. 83–89.

Bijelic, A. & Rompel, A. 2018. Polyoxometalates: more than a phasing tool in protein crystallography. *ChemTexts*. 4(3):1–27. DOI: 10.1007/s40828-018-0064-1.

Bizzozero, J., Gosselin, C. & Scrivener, K.L. 2014. Expansion mechanisms in calcium aluminate and sulfoaluminate systems with calcium sulfate. *Cement and Concrete Research*. 56:190–202. DOI: 10.1016/j.cemconres.2013.11.011.

Blanco, F., Garcia, M.P. & Ayala, J. 2005. Variation in fly ash properties with milling and acid leaching. *Fuel*. 84(1):89–96. DOI: 10.1016/j.fuel.2004.05.010.

Boehm, M., Devinny, J., Jahani, F. & Rosen, G. 1998. On a moving-boundary system modelling corrosion in sewer pipes. *Applied Mathematics and Computation (New York)*. 92(2–3):247–269. DOI: 10.1016/S0096-3003(97)10039-X.

Boon, A.G. 1995. Septicity in sewers: Causes, consequences and containment. *Water Science and Technology*. 31(7):237–253.

Buvignier, A. 2018. Caractérisation du rôle de l'aluminium dans les interactions entre les microorganismes et les matériaux cimentaires dans le cadre des réseaux d'assainissement École doctorale et discipline ou spécialité.

Caltra Nederland B.V. 2010. Calcium Sulfoaluminate Accelerator: Calumax Qiuick (CSA). *Caltra Nederland B.V, , Technical Datasheet*. (1):1. Available: https://caltra.com/product/calumex-quick/.

Cao, Q., Zou, H., Chen, X. & Yu, X. 2020. Interaction of sulfuric acid with dolomite (104) surface and its impact on the adsorption of oleate anion: A DFT study. *Physicochemical Problems of Mineral Processing*. 56(1):34–42. DOI: 10.5277/ppmp19070.

Cao, R., Yang, J., Li, G., Liu, F., Niu, M. & Wang, W. 2022. Resistance of the composite cementitious system of ordinary Portland/calcium sulfoaluminate cement to sulfuric acid attack. *Construction and Building Materials*. 329(January):127171. DOI: 10.1016/j.conbuildmat.2022.127171.

Carrera, L., Springer, F., Lipeme-Kouyi, G. & Buffiere, P. 2016. A review of sulfide emissions in sewer networks: Overall approach and systemic modelling. *Water Science and Technology*. 73(6):1231–1242.

Chalupecký, V., Fatima, T., Kruschwitz, J. & Muntean, A. 2012. Macroscopic corrosion front computations of sulfate attack in sewer pipes based on a micro-macro reaction-diffusion model. *arXiv preprint arXiv: …*. 1–10.

Chang, Z.-T., Song, X.-J., Munn, R. & Marosszeky, M. 2005. Using limestone aggregates and different cements for enhancing resistance of concrete to sulphuric acid attack. *Cement and Concrete Research*. 35:1486–1494.

Chappelle, C., Mccann, H., Jassby, D., Schwabe, K. & Szeptycki, L. 2019. Managing Wastewater in a Changing Climate. *Public Policy Institute of California (PPIC)*. (April):31.

Chess|THERMODDEM. 2014. Thermochemical and Mineralogical Tables for Geochemical Modeling. *Bureau de Recherches Géologiques et Minières*. 22. Available: http://thermoddem.brgm.fr.

Coppola, L., Bellezze, T., Belli, A., Bignozzi, M.C., Bolzoni, F., Brenna, A., Cabrini, M., Candamano, S., et al. 2018. Binders alternative to Portland cement and waste management for sustainable construction – Part 1. *Journal of Applied Biomaterials and Functional Materials*. 16(4):207–221.

Damion, T., Cepuritis, R. & Chaunsali, P. 2022. Sulfuric acid and citric acid attack of calcium sulfoaluminate-based binders. *Cement and Concrete Composites*. 130(December 2021):104524. DOI: 10.1016/j.cemconcomp.2022.104524.

Davis, J.L., Nica, D., Shields, K. & Roberts, D.J. 1998. Analysis of concrete from corroded sewer pipe. *International Biodeterioration and Biodegradation*.

Deschner, F., Lothenbach, B., Winnefeld, F. & Neubauer, J. 2013. Effect of temperature on the hydration of Portland cement blended with siliceous fly ash. *Cement and Concrete Research*. 52:169–181. DOI: 10.1016/J.CEMCONRES.2013.07.006.

Dyer, T. 2017. *Biodeterioration of concrete*. London, New York: CRC Press; Taylor & Francis Group.

Elmaleh, S., Delgado, S., Alvarez, M., Rodríguez-Gómez, L.E. & Aguiar, E. 1998. Forecasting of H2S build-up in a reclaimed wastewater pipe. *Water Science and Technology*. 38(10 pt 8):241–248.

Elmasry, M., Hawari, A. & Zayed, T. 2017. Cost benefit analysis for failure of sewer pipelines. *MATEC*

*Web of Conferences*. 120(January 2018).

EPA. 1974. Process design manual for sulphide control in sanitary sewerage systems. *United States Environmental Protection Agency*. 136.

EPA. 1985. Design Manual: Odor and Corrosion Control in Sanitary Sewerage Systems and Treatment Plants. *United States Environmental Protection Agency*.

EPA. 1992. Detection, Control, and Correction of hydrogen sulphide corrosion in existing wastewater system. *United States Environmental Protection Agency*. (9):1.

EPA. 1999. Collection Systems O&M Fact Sheet: Trenchless Sewer Rehabilitation, EPA 832-F-99-032. *United States Environmental Protection Agency*. (September):10.

EPA. 2000. Wastewater Technology Fact Sheet: Pipe construction and materials, EPA 832-F-00-068. *United States Environmental Protection Agency*. (September):5.

EPA. 2013. State of Technology for Rehabilitation, EPA/600/R-13/036. *United States Environmental Protection Agency*. (March):213.

Feng, X., Garboczi, E.J., Bentz, D.P., Stutzman, P.E. & Mason, T.O. 2004. Estimation of the degree of hydration of blended cement pastes by a scanning electron microscope point-counting procedure. *Cement and Concrete Research*. 34(10):1787–1793. DOI: 10.1016/j.cemconres.2004.01.014.

Fernandes, I., Pericão, M., Hagelia, P., Noronha, F., Ribeiro, M.A. & Maia, J. 2012. Identification of acid attack on concrete of a sewage system. *Materials and Structures/Materiaux et Constructions*. 45(3):337–350. DOI: 10.1617/s11527-011-9769-y.

Fourie, C.W. 2007. Acid resistance of sewer pipe concrete. University of Cape Town.

Fytianos, G., Tsikrikis, A., Anagnostopoulos, C.A., Papastergiadis, E. & Samaras, P. 2021. The inclusion of acidic and stormwater flows in concrete sewer corrosion mitigation studies. *Water (Switzerland)*. 13(3). DOI: 10.3390/w13030261.

García-Maté, M., De La Torre, A.G., León-Reina, L., Losilla, E.R., Aranda, M.A.G. & Santacruz, I. 2015. Effect of calcium sulfate source on the hydration of calcium sulfoaluminate eco-cement. *Cement and Concrete Composites*. 55:53–61. DOI: 10.1016/j.cemconcomp.2014.08.003.

Georget, F., Prévost, J.H. & Huet, B. 2018. Reactive transport modelling of cement paste leaching in brines. *Cement and Concrete Research*. 111(May 2017):183–196. DOI: 10.1016/j.cemconres.2018.05.015.

Germishuizen, C., Franzsen, S., Grobler, H., Simate, G.S. & Sheridan, C.M. 2018. Case study modelling for an ettringite treatment process. *Water SA*. 44(1):86–92.

Girardi, F. & Maggio, R. Di. 2011. Resistance of concrete mixtures to cyclic sulfuric acid exposure and mixed sulfates: Effect of the type of aggregate. *Cement and Concrete Composites*. 33(2):276–285. DOI: 10.1016/j.cemconcomp.2010.10.015.

Goergens, J. & Goetz-Neunhoeffer, F. 2021. Temperature-dependent late hydration of calcium aluminate cement in a mix with calcite – Potential of G-factor quantification combined with GEMS-predicted phase content. *Cement*. 5(June):100011. DOI: 10.1016/j.cement.2021.100011.

Goyns, A.M. 2009. Design Manual for Concrete Pipe outfall sewers. *Pipes, Infrastructural Products and Engineering Solution Division*. (April). Available: http://www.concrete-pipe.org/pdf/cp-manual.pdf.

Goyns, A.M. & Alexander, M.G. 2018. Combining corrosion and structural performance of concrete sewers: implications for pipe design and remaining life. In *Proceedings of the Final Conference of RILEM 253-MCI Microorganisms-Cementitious Materials Interactions Volume I*. 97–108.

Grandclerc, A., Guéguen-Minerbe, M., Nour, I., Dangla, P. & Chaussadent, T. 2017. Impact of cement composition on the adsorption of hydrogen sulphide and its subsequent oxidation onto cementitious

material surfaces. *Construction and Building Materials*. 152:576–586.

Grandclerc, A., Dangla, P., Gueguen-Minerbe, M. & Chaussadent, T. 2018. Modelling of the sulfuric acid attack on different types of cementitious materials. *Cement and Concrete Research*. 105(January):126–133.

Grengg, C., Baldermann, A., Dietzel, M., Mittermayr, F. & Leis, A. 2016. Concrete corrosion in an Austrian sewer system. In *Concrete Repair, Rehabilitation and Retrofitting IV*. F. Dehn, H.-D. Beushausen, M.G. Alexander, & P. Moyo, Eds. London: Taylor & Francis Group. 11–15.

Grengg, C., Mittermayr, F., Koraimann, G., Konrad, F., Szabó, M., Demeny, A. & Dietzel, M. 2017. The decisive role of acidophilic bacteria in concrete sewer networks: A new model for fast progressing microbial concrete corrosion. *Cement and Concrete Research*. 101:93–101.

Grengg, C., Martin, D. & Bertron, A. 2017. Microbial induced acid corrosion in sewer environments Statutory declaration. Graz University of Technology.

Grengg, C., Mittermayr, F., Ukrainczyk, N., Koraimann, G., Kienesberger, S. & Dietzel, M. 2018. Advances in concrete materials for sewer systems affected by microbial induced concrete corrosion: A review. *Water Research*. 134:341–352.

Grengg, C., Mittermayr, F., Ukrainczyk, N., Koenders, E., Koraimann, G., Kienesberger, S. & Dietzel, M. 2018. Microbial induced acid corrosion from a field perspective - Advances in process understanding and construction material development. In *RILEM TC 253-Microorganisms-Cementitious Materials Interactions, 25-26 June 2018, Toulouse*. 3–10.

Gu, J.D., Ford, T.E., Berke, N.S. & Mitchell, R. 1998. Biodeterioration of concrete by the fungus Fusarium. *International Biodeterioration and Biodegradation*. 41(2):101–109.

Gu, L., Bennett, T. & Visintin, P. 2019. Sulphuric acid exposure of conventional concrete and alkali-activated concrete: Assessment of test methodologies. *Construction and Building Materials*. 197:681–692.

De Gusseme, B., De Schryver, P., De Cooman, M., Verbeken, K., Boeckx, P., Verstraete, W. & Boon, N. 2009. Nitrate-reducing, sulfide-oxidizing bacteria as microbial oxidants for rapid biological sulfide removal. *FEMS Microbiology Ecology*. 67(1):151–161.

Gutiérrez-Padilla, M.G.D., Bielefeldt, A., Ovtchinnikov, S., Hernandez, M. & Silverstein, J. 2010. Biogenic sulfuric acid attack on different types of commercially produced concrete sewer pipes. *Cement and Concrete Research*. 40(2):293–301.

Gutierrez, O., Sharma, K.R. & Poch, M. 2009. Advanced assessment of Sulfide and Methane emissions from sewers of Mediterranean cities. 2006–2009.

Haberlah, D., Owen, M., Botha, P.W.S.K. & Gottlieb, P. 2012. SEM-EDS-Based protocol for subsurface drilling mineral identification and petrological classification. *Proceedings of the 10th International Congress for Applied Mineralogy (ICAM)*. 265–273. DOI: 10.1007/978-3-642-27682-8.

Habert, G. 2014. Assessing the environmental impact of conventional and 'green' cement production. In *Eco-efficient construction and building materials: Life cycle assessment (LCA), eco-labelling and case studies*. Woodhead Publishing Series. 199–238.

Haile, T., Nakhla, G. & Allouche, E. 2008. Evaluation of the resistance of mortars coated with silver-bearing zeolite to bacterial-induced corrosion. *Corrosion Science*. 50(3):713–720. DOI: 10.1016/j.corsci.2007.08.012.

Haile, T., Nakhla, G., Allouche, E. & Vaidya, S. 2010. Evaluation of the bactericidal characteristics of nano-copper oxide or functionalized zeolite coating for bio-corrosion control in concrete sewer pipes. *Corrosion Science*. 52(1):45–53.

Hargis, C.W., Kirchheim, A.P., Monteiro, P.J.M. & Gartner, E.M. 2013. Early age hydration of calcium sulfoaluminate (synthetic ye'elimite, C 4A3$\bar{S}$) in the presence of gypsum and varying amounts of

calcium hydroxide. *Cement and Concrete Research*. 48:105–115. DOI: 10.1016/j.cemconres.2013.03.001.

Hargis, C.W., Lothenbach, B., Müller, C.J. & Winnefeld, F. 2017. Carbonation of calcium sulfoaluminate mortars. *Cement and Concrete Composites*. 80:123–134. DOI: 10.1016/j.cemconcomp.2017.03.003.

Herisson, J., Guinot, D. & Saucier, F. 2018. Accelerated biodeterioration of various cementitious materials through an accelerated laboratory chamber. In *Final Conference of RILEM TC 253-MCI: Microorganisms-Cementitious Materials Interactions Volume 1*. 33–43.

Hewlett, P., & Liska, M. 2019. *Lea ' s Chemistry of Cement and Concrete Edited by*.

Hewlett, P. 2019. *Lea's Chemistry of Cement and Concrete*. 5th ed. Oxford, UK: Butterworth-Heinemann.

Hou, W., He, F. & Liu, Z. 2021. Characterization methods for sulfate ions diffusion coefficient in calcium sulphoaluminate mortar based on AC impedance spectroscopy. *Construction and Building Materials*. 289:123169. DOI: 10.1016/j.conbuildmat.2021.123169.

House, M. & Weiss, W.J. 2014. Review of Microbially Induced Corrosion and Comments on Needs Related to Testing Procedures. *Proceedings of the 4th International Conference on the Durability of Concrete Structures*. (July):94–103.

Hudon, E., Mirza, S. & Frigon, D. 2011. Biodeterioration of Concrete Sewer Pipes: State of the Art and Research Needs. *Journal of Pipeline Systems Engineering and Practice*. 2(2):42–52. DOI: 10.1061/(asce)ps.1949-1204.0000072.

Hughes, B.P. & Guest, J.E. 1978. Limestone and siliceous aggregate concretes subjected to sulphuric acid attack. *Magazine of Concrete Research*. 30(102):11–18. DOI: 10.1680/macr.1978.30.102.11.

Hvitved-Jacobsen, T., Jütte, B., Nielsen, P.H. & Jensen, N.A. 1988. Hydrogen Sulphide Control in Municipal Sewers. *Pretreatment in Chemical Water and Wastewater Treatment*. 239–247.

Hvitved-Jacobsen, T., Vollertsen, J. & Nielsen, A.H. 2013. *Sewer Processes: Microbial and Chemical Process Engineering of Sewer Networks, Second Edition*. Second ed. London, New York: CRC Press; Taylor & Francis Group.

Ikumi, T. & Segura, I. 2019. Numerical assessment of external sulfate attack in concrete structures. A review. *Cement and Concrete Research*. 121(April):91–105. DOI: 10.1016/j.cemconres.2019.04.010.

Isgor, O.B. & Weiss, W.J. 2019. A nearly self-sufficient framework for modelling reactive-transport processes in concrete. *Materials and Structures/Materiaux et Constructions*. 52(1):1–17. DOI: 10.1617/s11527-018-1305-x.

Islander, R.L., Devinny, J.S., Mansfeld, F., Postyn, A. & Shih, H. 1991. Microbial Ecology of crown corrosion in sewers. *Journal of Environmental Engineering*. 117(9):751–770.

Jahani, F., Devinny, J., Mansfeld, F., I. G. Rosen, Sun, Z. & Wang, C. 2001. Investigation of sulfuric acid corrosion of concrete: part I. Modelling and chemical observations. *Journal of Environmental Engineering*. 127(7):572–579.

Jensen, H.S. 2009. Hydrogen sulfide-induced concrete corrosion of sewer networks. PhD. Thesis. Aalborg University, Denmark.

Jensen, H., Biggs, C.A. & Karunakaran, E. 2016. The importance of sewer biofilms. *Wiley Interdisciplinary Reviews: Water*. 3(July/August):487–494.

Jensen, H.S., Nielsen, A.H., Hvitved-Jacobsen, T. & Vollertsen, J. 2009. Modelling of Hydrogen Sulfide Oxidation in Concrete Corrosion Products from Sewer Pipes. *Water Environment Research*. 81(4):365–373.

Jiang, G., Wightman, E., Donose, B.C., Yuan, Z., Bond, P.L. & Keller, J. 2014. The role of iron in

sulfide-induced corrosion of sewer concrete. *Water Research*. 49:166–174.

Jiang, G., Keller, J. & Bond, P.L. 2014. Determining the long-term effects of H2S concentration, relative humidity and air temperature on concrete sewer corrosion. *Water Research*. 65:157–169.

Jiang, G., Sun, X., Keller, J. & Bond, P.L. 2015. Identification of controlling factors for the initiation of corrosion of fresh concrete sewers. *Water Research*. 80:30–40.

Jiang, G., Keller, J., Bond, P.L. & Yuan, Z. 2016. Predicting concrete corrosion of sewers using artificial neural network. *Water Research*.

Joseph, A.P., Keller, J., Bustamante, H. & Bond, P.L. 2012. Surface neutralization and H2S oxidation at early stages of sewer corrosion: Influence of temperature, relative humidity and H2S concentration. *Water Research*. 46(13):4235–4245.

Jung, D., Gouello, J., Ponthieux, A., Parez, V. & Renner, C. 2015. Effects of sewer structure and hydrodynamics on H 2 S gas at a waterfall : modelling of H 2 S emission and best design practices. (April 2016):16–18.

Jung, D., Hatrait, L., Gouello, J., Ponthieux, A., Parez, V. & Renner, C. 2017. Emission of hydrogen sulfide (H2S) at a waterfall in a sewer: Study of main factors affecting H2S emission and modelling approaches. *Water Science and Technology*. 76(10):2753–2763.

Kaempfer, W. & Berndt, M. 1999. Estimation of Service Life of Concrete Pipes in Sewer Networks. *8th Conference on Durability of Building Materials and Components*. 1:36–45.

Kalogridis, D., Kostogloudis, G.C., Ftikos, C. & Malami, C. 2000. A quantitative study of the influence of non-expansive sulfoaluminate cement on the corrosion of steel reinforcement. 30:1731–1740.

Kashiwakura, S., Kumagai, Y., Kubo, H. & Wagatsuma, K. 2013. Dissolution of Rare Earth Elements from Coal Fly Ash Particles in a Dilute H2SO4 Solvent. *Open Journal of Physical Chemistry*. 03(02):69–75. DOI: 10.4236/ojpc.2013.32009.

Khan, H.A., Castel, A., Khan, M.S.H. & Mahmood, A.H. 2019. *Durability of calcium aluminate and sulphate-resistant Portland cement-based mortars in aggressive sewer environment and sulphuric acid*. V. 124.

Kiliswa, M.W. 2016. Composition and microstructure of concrete mixtures subjected to biogenic acid corrosion and their role in corrosion prediction of concrete outfall sewers. University of Cape Town, South Africa.

Kiliswa, M.W. & Alexander, M.G. 2014. Biogenic Corrosion of Concrete Sewer Pipes : a Review of the Performance of Cementitious Materials Sao Paulo, Brazil 2-5 September 2014. In *XIII Conference on Durability of Building Materials and Components, RILEM Proceedings Pro 96. Sao Paulo, Brazil, 2-5 September*. Sao Paulo, Brazil 2-5 September 2014. 1023–1030.

Kiliswa, M.W., Scrivener, K.L. & Alexander, M.G. 2019. The corrosion rate and microstructure of Portland cement and calcium aluminate cement-based concrete mixtures in outfall sewers: A comparative study. *Cement and Concrete Research*. 124(July):105818. DOI: 10.1016/j.cemconres.2019.105818.

Kleib, J., Aouad, G., Louis, G., Zakhour, M., Boulos, M., Rousselet, A. & Bulteel, D. 2018. The use of calcium sulfoaluminate cement to mitigate the alkali silica reaction in mortars. *Construction and Building Materials*.

Kung'u, F.T. 1999. *Sanitary sewer system rehabilitation techniques vary*. Available: https://www.wateronline.com/doc/sanitary-sewer-system-rehabilitation-techniqu-0002 [2018, February 14].

Kurdowski, W. 2017. *Cement and Concrete Chemistry*. New York London: Springer Dordrecht Heidelberg.

Lagneau, V. 2016. Mod ´ elisation coupl ´ ee chimie-transport avec HYTEC Application ` a la migration de polluants et aux g ´ Laurent De Windt , J ´ R-241116-LDEWI Centre de G ´ MINES ParisTech.

Lagneau, V. & van der Lee, J. 2010. Operator-splitting-based reactive transport models in strong feedback of porosity change: The contribution of analytical solutions for accuracy validation and estimator improvement. *Journal of Contaminant Hydrology*. 112(1–4):118–129. DOI: 10.1016/j.jconhyd.2009.11.005.

Lahav, O., Lu, Y., Shavit, U. & Loewenthal, R.E. 2004. Modeling Hydrogen Sulfide Emission Rates in Gravity Sewage Collection Systems. *Journal of Environmental Engineering*. 130(11):1382–1389.

Lahav, O., Sagiv, A. & Friedler, E. 2006. A different approach for predicting H2S(g) emission rates in gravity sewers. *Water Research*. 40(2):259–266.

Lam, L., Wong, Y.L. & Poon, C.S. 2000. Degree of hydration and gel/space ratio of high-volume fly ash/cement systems. *Cement and Concrete Research*. 30(5):747–756. DOI: 10.1016/S0008-8846(00)00213-1.

Larreur-Cayol, S., De Windt, L., Bertron, A. & Escadeillas, G. 2011. Deterioration of Cementitious Materials By Organic Acids. In *7th International Symposium on Cement Based Materials for a Sustainable Agriculture (CIGR International Symposium)*. 38–45.

Le-Bescop, P., Lothenbach, B., Samson, E. & Snyder, K.A. 2013. Chapter 7. Modeling Degradation of Cementitious Materials in Aggressive Aqueous Environments. In *Performance of Cement-Based Materials in Aggressive Aqueous Environments. State-of-the-Art Report, RILEM TC 211-PAE*. 178–196.

Leal, A.M.M., Kulik, D.A., Smith, W.R. & Saar, M.O. 2017. An overview of computational methods for chemical equilibrium and kinetic calculations for geochemical and reactive transport modeling. *Pure and Applied Chemistry*. 89(5):597–643. DOI: 10.1515/pac-2016-1107.

Lee, J. Van Der, Windt, L. De & Lagneau, V. 2008. Application of Reactive Transport Models in Cement- Based Porous Media. *International RILEM Symposium on Concrete Modelling – CONMOD'08*. (May):463–470.

der Lee, J. 1998. *Thermodynamical and mathematical concepts of CHESS. Technical Report ? Nr. LHM/RD/98/39*. Ecole des Mines de Paris,.

van der Lee, J., De Windt, L., Lagneau, V. & Goblet, P. 2002. Presentation and application of the reactive transport code HYTEC. *Developments in Water Science*. 47(C):599–606. DOI: 10.1016/S0167-5648(02)80114-9.

van der Lee, J., De Windt, L., Lagneau, V. & Goblet, P. 2003. Module-oriented modeling of reactive transport with HYTEC. *Computers and Geosciences*. 29(3):265–275.

Li, J., Wang, R. & Xu, Y. 2022. Influence of cellulose ethers chemistry and substitution degree on the setting and early-stage hydration of calcium sulphoaluminate cement. *Construction and Building Materials*. 344:128266. DOI: 10.1016/J.CONBUILDMAT.2022.128266.

Li, X., Kappler, U., Jiang, G. & Bond, P.L. 2017. The ecology of acidophilic microorganisms in the corroding concrete sewer environment. *Frontiers in Microbiology*. 8(April):1–16.

Losey, D.J., Sihvonen, S.K., Veghte, D.P., Chong, E. & Freedman, M.A. 2018. Acidic processing of fly ash: chemical characterization, morphology, and immersion freezing. *Environmental Science: Processes and Impacts*. 20(11):1581–1592. DOI: 10.1039/c8em00319j.

Lothenbach, B., Kulik, D.A., Matschei, T., Balonis, M., Baquerizo, L., Dilnesa, B., Miron, G.D. & Myers, R.J. 2019. Cemdata18: A chemical thermodynamic database for hydrated Portland cements and alkali-activated materials. *Cement and Concrete Research*. 115(October 2017):472–506. DOI: 10.1016/j.cemconres.2018.04.018.

Lowe, S. 2016. Sewer Ventilation: Factors Affecting Airflow and Modeling Approaches. *Journal of*

*Water Management Modeling*. 1–5. DOI: 10.14796/jwmm.c395.

Mackenzie, L.D. 2020. a. Appendix a: Properties of Air, Water, and Selected Chemicals. *Water and Wastewater Engineering: Design Principles and Practice, Second Edition*.

Matias, N., Matos, R.V., Ferreira, F., Vollertsen, J. & Matos, J.S. 2017. Release of hydrogen sulfide in a sewer system under intermittent flow conditions: The Ericeira case study, in Portugal. *Water Science and Technology*. 75(7):1702–1711.

Matias, N.M., Matos, J.S. & Ferreira, F. 2014. Hydrogen sulfide gas emission under turbulent conditions - An experimental approach for free-fall drops. *Water Science and Technology*. 69(2):262–268.

Merachtsaki, D., Fytianos, G., Papastergiadis, E., Samaras, P., Yiannoulakis, H. & Zouboulis, A. 2020. Properties and Performance of Novel Mg ( OH ) 2 -Based Coatings for Corrosion Mitigation in Concrete. (Mic).

Monteny, J., Vincke, E., Beeldens, A., De Belie, N., Taerwe, L., Van Gemert, D. & Verstraete, W. 2000. Chemical, microbiological, and in situ test methods for biogenic sulfuric acid corrosion of concrete. *Cement and Concrete Research*. 30:623–634.

Moore, A.J., Bakera, A.T. & Alexander, M.G. 2020. Water sorptivity and porosity testing of concrete. *Concrete Beton, Technical Note*. 162(September):13–16.

Moore, A.J., Bakera, A.T. & Alexander, M.G. 2021. A critical review of the Water Sorptivity Index (WSI) parameter for potential durability assessment : can WSI be considered in isolation of porosity ? *SAICE*. 63(2):27–34.

Mori, T., Nonaka, T., Tazaki, K., Koga, M., Hikosaka, Y. & Noda, S. 1992. Interactions of nutrients, moisture and pH on microbial corrosion of concrete sewer pipes. *Water Research*. 26(1):29–37.

De Muynck, W., De Belie, N. & Verstraete, W. 2009. Effectiveness of admixtures, surface treatments and antimicrobial compounds against biogenic sulfuric acid corrosion of concrete. *Cement and Concrete Composites*. 31:163–170.

Nielsen, A.H., Vollertsen, J. & Hvitved-Jacobsen, T. 2003. Determination of kinetics and stoichiometry of chemical sulfide oxidation in wastewater of sewer networks. *Environmental Science and Technology*. 37(17):3853–3858.

Nielsen, A.H., Hvitved-Jacobsen, T. & Vollertsen, J. 2005. Kinetics and stoichiometry of sulfide oxidation by sewer biofilms. *Water Research*. DOI: 10.1016/j.watres.2005.07.031.

Nielsen, A.H., Vollertsen, J., Jensen, H.S., Wium-Andersen, T. & Hvitved-Jacobsen, T. 2008. Influence of pipe material and surfaces on sulfide related odor and corrosion in sewers. *Water Research*.

Nielsen, A.H., Hvitved-Jacobsen, T. & Vollertsen, J. 2012. Effect of Sewer Headspace Air-Flow on Hydrogen Sulfide Removal by Corroding Concrete Surfaces. *Water Environment Research*. 84(3):265–273.

Nielsen, A.H., Vollertsen, J., Jensen, H.S., Madsen, H.I. & Hvitved-Jacobsen, T. 2014. Aerobic and Anaerobic Transformations of Sulfide in a Sewer System – Field Study and Model Simulations. *Proceedings of the Water Environment Federation*. 2006(9):3654–3670.

Nielsen, P.H., Raunkjær, K. & Hvitved-Jacobsen, T. 1998. Sulfide production and wastewater quality in pressure mains. *Water Science and Technology*. 37(1):97–104.

Noeiaghaei, T., Mukherjee, A., Dhami, N. & Chae, S.-R. 2017. Biogenic deterioration of concrete and its mitigation technologies. *Construction and Building Materials*. 149:575–586.

O'Connell, M., McNally, C. & Richardson, M.G. 2010. Biochemical attack on concrete in wastewater applications: A state of the art review. *Cement and Concrete Composites*. 32(7):479–485. Available: http://dx.doi.org/10.1016/j.cemconcomp.2010.05.001.

Oberholster, B. 2009. Chapter 10: Alkali-silica reaction. In *Fulton's concrete technology*. 9th ed. G. Owens, Ed. Midland. South Africa. 193–195.

Odler, I. 2003. Chapter 4. Cements containing calcium sulfoaluminate. In *Special Inorganic Cements, Modern Concrete Technology series*. CRC Press. 63–81.

Okabe, S., Odagiri, M., Ito, T. & Satoh, H. 2007. Succession of sulfur-oxidizing bacteria in the microbial community on corroding concrete in sewer systems. *Applied and Environmental Microbiology*. 73(3):971–980.

Olsson, N., Lothenbach, B., Baroghel-Bouny, V. & Nilsson, L.O. 2018. Unsaturated ion diffusion in cementitious materials – The effect of slag and silica fume. *Cement and Concrete Research*. 108(March):31–37. DOI: 10.1016/j.cemconres.2018.03.007.

Oviedo, E.R., Johnson, D. & Shipley, H. 2012. Evaluation of hydrogen sulphide concentration and control in a sewer system. *Environmental Technology (United Kingdom)*. 33(10):1207–1215.

Parande, A.K., Ramsamy, P.L., Ethirajan, S., Rao, C.R.K. & Palanisamy, N. 2006. Deterioration of reinforced concrete in sewer environments. In *Proceedings of the institution of Civil engineers*. 11–20.

Park, K., Lee, H., Phelan, S., Liyanaarachchi, S., Marleni, N., Navaratna, D., Jegatheesan, V. & Shu, L. 2014. Mitigation strategies of hydrogen sulphide emission in sewer networks - A review. *International Biodeterioration and Biodegradation*. 95:251–261.

Parkhurst, D.J. & Appelo, C.A.J. 2013. Description of Input and Examples for PHREEQC Version 3 - A Computer Program for Speciation, Batch-reaction, One-dimensional Transport, and Inverse Geochemical Calculations. In *U.S. Geological Survey Techniques and Methods*. 497.

Pather, B., Ekolu, S.O. & Quainoo, H. 2021. Effects of aggregate types on acid corrosion attack upon fly – Ash geopolymer and Portland cement concretes – Comparative study. *Construction and Building Materials*. 313(October). DOI: 10.1016/j.conbuildmat.2021.125468.

Péra, J. & Ambroise, J. 2004. New applications of calcium sulfoaluminate cement. *Cement and Concrete Research*. 34:671–676.

Pereira, A.L., Reis, M.A., Ferreira, L.L.H.C., Passos, E.R., Ribeiro, L.C., Novo, M.M.M. & Nakachima, P.M. 2017. Characterization of a new sintered calcium aluminate cement. *Refractories World Forum*. 9(3):1–4.

Petit-Boix, A., Sanjuan-Delmás, D., Gasol, C.M., Villalba, G., Suárez-Ojeda, M.E., Gabarrell, X., Josa, A. & Rieradevall, J. 2014. Environmental Assessment of Sewer Construction in Small to Medium Sized Cities Using Life Cycle Assessment. *Water Resources Management*. 28(4):979–997.

Peyre Lavigne, M., Bertron, A., Auer, L., Hernandez-Raquet, G., Foussard, J.N., Escadeillas, G., Cockx, A. & Paul, E. 2015. An innovative approach to reproduce the biodeterioration of industrial cementitious products in a sewer environment. Part I: Test design. *Cement and Concrete Research*. 73:246–256.

Pikaar, I., Sharma, K.R., Hu, S., Gernjak, W., Keller, J. & Yuan, Z. 2014. Water engineering. Reducing sewer corrosion through integrated urban water management. *Science (New York, N.Y.)*. 345(6198):812–4.

Pistor, A.F. & Taylor, H.W. 1935. Effects of Sewage Gases on Concrete Author. *Sewage Works Journal*. 7(4):697–705.

Pomeroy, R.D. 1959. Generation and Control of sulphide in filled pipes. *Sewage and Industrial Wastes*. 31(9):1082–1095.

Pomeroy, R.D. 1976. The problem of hydrogen sulphide in sewers. *Clay Pipe Development Association*.

Pomeroy, R.D. & Parkhurst, J.. 1977. The forecasting of sulfide buildup rates in sewers. In *8th International conference on Water Pollution Research*. V. 9. Sydney. 621–628.

Radtke, B.D.B., Wilde, F.D., Davis, J. V & Popowski, T.J. 1998. Alkalinity and Acid Neutralizing Capacity. *USGS TWRI Book 9*. 1–33. Available: http://water.usgs.gov/owq/FieldManual/Chapter6/section6.6/.

Roberts, D.J., Nica, D., Zuo, G. & Davis, J.L. 2002. Quantifying microbially induced deterioration of concrete: initial studies. *International Biodeterioration & Biodegradation*. 49:227–234. DOI: 10.1016/S0964-8305(02)00049-5.

Rubin, J. 1983. Transport of reacting solutes in porous media: Relation between mathematical nature of problem formulation and chemical nature of reactions. *Water Resources Research*. 19(5):1231–1252. DOI: 10.1029/WR019i005p01231.

Samson, E. & Marchand, J. 2007. Modeling the transport of ions in unsaturated cement-based materials. *Computers and Structures*. 85:1740–1756. DOI: 10.1016/j.compstruc.2007.04.008.

SANS 201. 2008. Sieve analysis, fines content and dust content of aggregates. *South African National Standards*.

SANS 3001-CO3-1. 2015. Civil engineering test methods Part CO3-1: Concrete durability index testing — Preparation of test specimens. *South African National Standards*.

SANS 3001-CO3-2. 2015. Civil engineering test methods Part CO3-2: Concrete durability index testing — Oxygen permeability test. *South African National Standards*.

SANS 3001-CO3-3. 2015. Civil engineering test methods Part CO3-3 : Concrete durability index testing — Chloride conductivity test. *South African National Standards*.

SANS 50196-2. 2014. Method of testing cement Part 2: Chemical analysis of cement. *South African National Standards*.

SANS 50197-1. 2013. Composition , specifications and conformity criteria for common cements. *South African National Standards*.

SANS 5844. 2006. Particle and relative densities of aggregates. *South African National Standards*.

SANS 5845. 2006. Bulk densities and voids content of aggregates. *South African National Standards*.

SANS 5861-1. 2006. Concrete tests Part 1: Mixing fresh concrete in laboratory. *South African National Standards*.

SANS 5861-2. 2006. Concrete tests Part 2: sampling of freshly mixed concrete. *South African National Standards*.

SANS 5863. 2006. Concrete tests- Compressive strength of hardened concrete. *South African National Standards*.

SANS 6242. 2008. Acid insolubility of aggregates. *South African National Standards*.

Saucier, F. & Kaitano, T. 2018. H2S Biogenic Corrosion : Why Using Calcium Aluminate Concrete and Mortars to Rehabilitate Corroded Sewer Infrastructures. *IMESA conference Port Elizabelt*. 143–148.

Schmidt-Döhl, F. & Rostásy, F.S. 1999a. Model for the calculation of combined chemical reactions and transport processes and its application to the corrosion of mineral-building materials: Part I. Simulation model. *Cement and Concrete Research*. 29:1039–1045 A.

Schmidt-Döhl, F. & Rostásy, F.S. 1999b. Model for the calculation of combined chemical reactions and transport processes and its application to the corrosion of mineral-building materials: Part II. Experimental verification. *Cement and Concrete Research*.

Scrivener, K., Cabiron, J.L. & Letourneux, R. 1999. High-performance concretes from calcium aluminate cements. *Cement and Concrete Research*. DOI: 10.1016/S0008-8846(99)00103-9.

Scrivener, K., Snellings, R. & Lothenbach, B. 2016. *A Practical Guide to Microstructural Analysis of*

*Cementitious Materials*. Baco Raton: CRC Press; Taylor & Francis Group. Available: www.crcpress.com.

Siad, H., Mesbah, H.A., Khelafi, H., Kamali-Bernard, S. & Mouli, M. 2010. Effect of mineral admixture on resistance to sulphuric and hydrochloric acid attacks in selfcompacting concrete. *Canadian Journal of Civil Engineering*. 37(3):441–449. DOI: 10.1139/L09-157.

Snyder, K.A., Feng, X., Keen, B.D. & Mason, T.O. 2003. Estimating the electrical conductivity of cement paste pore solutions from OH À , K + and Na + concentrations. 33:793–798. DOI: 10.1016/S0008-8846(02)01068-2.

Steefel, C.I., Appelo, C.A.J., Arora, B., Jacques, D., Kalbacher, T., Kolditz, O., Lagneau, V., Lichtner, P.C., et al. 2015. Reactive transport codes for subsurface environmental simulation. *Computational Geosciences*. 19(3):445–478. DOI: 10.1007/s10596-014-9443-x.

Steenari, B.M., Schelander, S. & Lindqvist, O. 1999. Chemical and leaching characteristics of ash from combustion of coal, peat and wood in a 12 MW CFB - a comparative study. *Fuel*. 78(2):249–258. DOI: 10.1016/S0016-2361(98)00137-9.

Sun, X., Jiang, G., Bond, P.L., Wells, T. & Keller, J. 2014. A rapid, non-destructive methodology to monitor activity of sulfide-induced corrosion of concrete based on H2S uptake rate. *Water Research*. 59:229–238.

Sun, X., Jiang, G., Bond, P.L. & Keller, J. 2015. Impact of fluctuations in gaseous H2S concentrations on sulfide uptake by sewer concrete: The effect of high H2S loads. *Water Research*. 81:84–91.

Sun, X., Jiang, G., Bond, P.L. & Keller, J. 2019. Periodic deprivation of gaseous hydrogen sulfide affects the activity of the concrete corrosion layer in sewers. *Water Research*. 157:463–471. DOI: 10.1016/j.watres.2019.03.074.

Taheri, S., Giri, P., Ams, M., Bevitt, J.J., Bustamante, H., Madadi, M., Kuen, T., Gonzalez, J., et al. 2021. Migration and formation of an iron rich layer during acidic corrosion of concrete with no steel reinforcement. *Construction and Building Materials*. 309(May):125105. DOI: 10.1016/j.conbuildmat.2021.125105.

Trotignon, L., Devallois, V., Peycelon, H., Tiffreau, C. & Bourbon, X. 2007. Predicting the long term durability of concrete engineered barriers in a geological repository for radioactive waste. *Physics and Chemistry of the Earth*. 32(1–7):259–274. DOI: 10.1016/j.pce.2006.02.049.

Ukrainczyk, N. 2010. Kinetic modeling of calcium aluminate cement hydration. *Chemical Engineering Science*. 65(20):5605–5614. DOI: 10.1016/j.ces.2010.08.012.

Valix, M., Zamri, D., Mineyama, H., Cheung, W.H., Shi, J. & Bustamante, H. 2012. Microbiologically induced corrosion of concrete and protective coatings in gravity sewers. *Chinese Journal of Chemical Engineering*. 20(3):433–438.

Vollertsen, J., Nielsen, A.H., Jensen, H.S., Wium-Andersen, T. & Hvitved-Jacobsen, T. 2008. Corrosion of concrete sewers-The kinetics of hydrogen sulfide oxidation. *Science of the Total Environment*.

Vollertsen, J., Nielsen, A.H., Jensen, H.S. & Rudelle, E.A. 2011. Modeling the corrosion of concrete sewers. In *12th International Conference on Urban Drainage, Porto Alegre/Brazil, 11-16 September 2011*.

Walker, B.S. 2013. Fine aggregate resources in the greater Cape Town area. Masters thesis. University of Cape Town.

Wang, P., Li, N. & Xu, L. 2017. Hydration evolution and compressive strength of calcium sulphoaluminate cement constantly cured over the temperature range of 0 to 80 °C. *Cement and Concrete Research*. 100(April):203–213. DOI: 10.1016/j.cemconres.2017.05.025.

Wei, S., Jiang, Z., Liu, H., Zhou, D. & Sanchez-Silva, M. 2013. Microbiologically induced deterioration

of concrete - A review. *Brazilian Journal of Microbiology*. 44(4):1001–1007.

Wells, T. & Melchers, R.E. 2014a. Findings of a 4 years study of concrete sewer pipe corrosion. *Corrosion and Prevention*. 1–12.

Wells, T. & Melchers, R.E. 2015. Modelling concrete deterioration in sewers using theory and field observations. *Cement and Concrete Research*. 77:82–96.

Wells, T. & Melchers, R.E.E. 2014b. An observation-based model for corrosion of concrete sewers under aggressive conditions. *Cement and Concrete Research*. 61–62:1–10. DOI: 10.1016/j.cemconres.2014.03.013.

Wells, T., Melchers, R.E. & Bond, P. 2009. Factors involved in the long term corrosion of concrete sewers. *49th Annual Conference of the Australasian Corrosion Association.* 345–356.

De Windt, L. & Devillers, P. 2010. Modeling the degradation of Portland cement pastes by biogenic organic acids. *Cement and Concrete Research*. 40(8):1165–1174.

Winnefeld, F.K. 2011. Concrete produced with calcium sulfoaluminate cement – a potential system for energy and heat storage. *First middle east conference on smart monitoring*. (February 2011):1–9.

Winnefeld, F. & Lothenbach, B. 2010. Hydration of calcium sulfoaluminate cements - Experimental findings and thermodynamic modelling. *Cement and Concrete Research*. 40(8):1239–1247. DOI: 10.1016/j.cemconres.2009.08.014.

Wu, L., Hu, C. & Liu, W.V. 2018. The sustainability of concrete in sewer tunnel-A narrative review of acid corrosion in the city of Edmonton, Canada. *Sustainability (Switzerland)*. 10(2).

Yang, Y., Ji, T., Lin, X., Chen, C. & Yang, Z. 2018. Biogenic sulfuric acid corrosion resistance of new artificial reef concrete. *Construction and Building Materials*. 158:33–41.

Yell, G. & Tripathi, V.S. 1991. Amodel for simulating transport of reactive multispecies components: Model development and demonstration. *Water resources researches*. 27(12):3075–3094.

Yongsiri, C., Vollertsen, J. & Hvitved-Jacobsen, T. 2004. Effect of temperature on air-water transfer of hydrogen sulfide. *Journal of Environmental Engineering*. 130(1):104–109.

Yongsiri, C., Vollertsen, J., Rasmussen, M. & Hvitved-Jacobsen, T. 2004. Air-Water Transfer of Hydrogen Sulfide: An Approach for Application in Sewer Networks. *Water Environment Research*. 76(1):81–88.

Yuan, H. 2014. Degradation modeling of concrete submitted to biogenic acid attack. PhD thesis. Université Paris-Est.

Yuan, H., Dangla, P., Chatellier, P. & Chaussadent, T. 2013. Degradation modelling of concrete submitted to sulfuric acid attack. *Cement and Concrete Research*. DOI: 10.1016/j.cemconres.2013.08.002.

Yuan, H., Dangla, P., Chatellier, P. & Chaussadent, T. 2015. Degradation modeling of concrete submitted to biogenic acid attack. *Cement and Concrete Research*. 70:29–38.

Zhang, L. & Glasser, F.P. 2002. Hydration of calcium sulfoaluminate cement at less than 24 h. *Advances in Cement Research*. 14(4):141–155. DOI: 10.1680/adcr.2002.14.4.141.

Zhang, L., De Schryver, P., De Gusseme, B., De Muynck, W., Boon, N. & Verstraete, W. 2008. Chemical and biological technologies for hydrogen sulfide emission control in sewer systems: A review. *Water Research*. 42(1–2):1–12.

Zhang, S., Wang, R., Xu, L., Hecker, A., Ludwig, H.M. & Wang, P. 2021. Properties of calcium sulfoaluminate cement mortar modified by hydroxyethyl methyl celluloses with different degrees of substitution. *Molecules*. 26(8). DOI: 10.3390/molecules26082136.

# Appendixes

## A. BAC mitigation measures

Besides modification of the concrete microstructure by altering the binder chemical composition, there are other approaches to mitigating BAC in concrete; i) limiting, in the first place, $H_2S$ generation and emission in the sewer system, and ii) preventing the growth of SOB on the sewer wall. The first approach involves applying physical, chemical and biological techniques that prevent or decrease $H_2S$ generation and emission in the sewer system. A list below describes the techniques involved;

i) Physical techniques include optimising hydraulic sewer design, such as flow velocity, flow rate, pipe alignment, and pipe diameter. Sewers are usually designed to flow at a depth between 50% and 60% of the pipe diameter under peak dry and full under peak wet weather flow conditions. Both flow conditions have negative impacts on influencing concrete corrosion. The partially full flow provides headspace for $H_2S$ gas emission, while full flow creates anaerobic conditions (septic) for sulphide species generation. Therefore, an optimum velocity and sewer alignment must be well designed to reduce the retention time and control sedimentation. However, the industry still believes that within a well-designed sewer network, where the pipe diameter, velocity and slope are chosen to minimise the risk of $H_2S$ generation, about 5% of the total length still suffer from BAC (Saucier and Kaitano, 2018).

ii) Biological techniques involve the addition of biological substances which kill or reduce the formation of SRB in the biofilm. This is achieved by increasing redox conditions, which involve the addition of thermodynamically favourable electron acceptor compounds such as oxygen, nitrate or nitrite. The technique is, however, inadequate because other bacteria consume oxygen and nitrite within the outer layers of the biofilm before meeting the objective. The permeability of oxygen through the biofilm is also reduced as the transport mechanism is limited to diffusion (Zhang et al., 2008; Jensen, Biggs and Karunakaran, 2016). Secondly, SRB formation is reduced by adding pH elevators or inhibitors such as biocides and molybdate[5] in the wastewater (Zhang et al., 2008; Oviedo, Johnson and Shipley, 2012). Shock treatment also involves the addition of strong alkalis such as sodium hydroxide (NaOH) or calcium hydroxide ($CaOH_2$) to wastewater, thereby elevating wastewater pH; consequently, SRB microbial activities are deactivated. However, this technique is also temporary since it is overpowered by the acidic condition built-up and re-establishment.

iii) Chemical techniques entail the introduction of nitrate-reducing and sulphide-oxidizing bacterial consortiums and chemical oxidants in wastewater. The consortiums actively convert $H_2S$ produced in wastewater to elemental sulphur and polysulfide ions, while the chemical oxidants remove the dissolved sulphide in the wastewater by precipitation or oxidation. Precipitation includes using metal salts such as iron in the form of $Fe^{2+}$ and $Fe^{3+}$ that react with sulphide in

[5] Molybdate is a compound containing an oxoanion with molybdenum in its highest oxidation state of 6. Example of those compounds are $Na_2MoO_4$ and $CaMoO_4$

the wastewater to ferrous or ferric sulphide (Eq. A.1 and A.2). Oxidation involves the addition of oxidants such as hydrogen peroxide ($H_2O_2$), oxygen ($O_2$), chlorine ($Cl_2$) or potassium permanganate ($KMnO_4$). These oxidants oxidise the dissolved sulphide to sulphate or elemental sulphur. The decomposition of sulphide into these forms prohibits $H_2S$ gas emission (De Gusseme et al., 2009; Zhang et al., 2008; Oviedo, Johnson and Shipley, 2012). The additional iron salts, however, are controversial. First, its precipitation, FeS, is black and has a high potential to settle and foul sewer pipes at a low flow and cause clogging (Oviedo, Johnson and Shipley, 2012). Besides, most iron salts used are FeCl and $FeSO_4$, which consequently increase the formation of aggressive acids such as HCl and $H_2SO_4$, which have adverse effects on concrete.

$$Fe^{2+} + HS^- \rightarrow FeS + H^+ \quad \text{(A.1)}$$

$$2Fe^{3+} + HS^- \rightarrow Fe^{2+} + S^0 + H^+ \quad \text{(A.2)}$$

iv) Adding heavy metals, such as iron, zinc, lead, silver and copper, to the wastewater can fall under chemical and biological techniques. It leads to metal sulphide precipitation which reduces sulphide species in the wastewater and kills microorganisms since these metals denature protein molecules of microorganism cells. This application, therefore, contributes intensively to decreasing sulphide generation and emission. However, this technique presents other challenges during wastewater treatment. These metals end up being discharged into the water bodies, posing adverse effects on the ecosystem. Due to this, governments set regulations to restrict their usage.

All the strategies above are accompanied by a high installation and maintenance cost, and if implemented, they are still short-term mitigation measures. The second approach is the prevention of SOB growth on the sewer wall. It includes; i) modification of the sewer headspace environment and ii) modification of concrete microstructure (Noeiaghaei et al, 2017; Zhang et al., 2008).

Modifying sewer headspace conditions involves providing sewer ventilation and gas treatment, which reduces the concentration of $H_2S$ and relative humidity in the sewer atmosphere. Ventilation, however, has a negative effect if directed to living organisms since the gas is toxic. The best way of modifying sewer headspace conditions is to vent the gas to the special treatment facilities.

Modifying concrete microstructure includes incorporating resisting materials (see section 2.4) and applying protective materials or coating systems such as bituminous and coal tar products, vinyl and epoxy resins, plasticised PVC sheets, and polyethene linings on the concrete surface. Such protective coating systems have no alkaline buffering capacity; thus, they can be easily inhabited by acidophilic SOB due to the quick drop in surface pH (Jiang et al., 2015). Apart from that, polymer linings worldwide usage has been reported by many operators to have a high rate of failure (Saucier and Kaitano, 2018). Another alternative is incorporating antimicrobial agents such as biocides and heavy metals into concrete mix design. However, this alternative has not always been successful due to antimicrobial agents and toxic biocides dissolving from the coatings.

# B. Thermodynamic modelling supplementary information

## B.1. Chemical reactions

Chemical reactions are divided into two categories depending on the phases involved during the reaction; heterogeneous and homogeneous reactions (Rubin, 1983). Homogeneous reactions occur in a single phase, such as in a liquid or gas phase, for example, surface complexation reactions and formation or dissociation of acids. Heterogeneous reactions involve at least two phases, typically between aqueous and solid phases (Rubin, 1983). Further, there are two groups of heterogeneous reactions: surface and classical reactions. Examples of surface reactions are the adsorption of ions and ion exchange, while classical reactions include oxidation, reduction, complex formation, dissolution and precipitation of mineral phases.

Steefel et al. (2015) provide a set of algebraic equations to describe various chemical reactions involved in the reactive transport models. These include mineral dissolution and precipitation reactions, surface complexation, ion-exchange reactions, gas–aqueous phase exchange, and microbially mediated homogeneous and heterogeneous reactions. In the case of BAC, cementitious materials are porous media with acid-based equilibrium, dissolution and/or precipitation kinetics, ion exchange phenomena and biological reactions. Grandclerc et al. (2018) provides excellent examples of both homogenous (in only the aqueous phase) and heterogeneous chemical reactions, as shown in Table B.1 and Table B.2. These chemical reactions can be modelled based on the chemical equilibrium approach, chemical kinetic laws, or a combination of both.

### B.1.1. Chemical equilibrium

The chemical equilibrium approach uses thermodynamic data of all solid, aqueous, and gas species present in the system to predict their concentration at the chemical equilibrium state (Ikumi & Segura, 2019). The thermodynamic data include the solubility products, complex formation constants, Gibbs free energy, enthalpy, entropy, heat capacity approximation coefficients, and molecular volume. These data are compiled in different databases; for instance, the cement-specific database (CEMDATA), which provides thermodynamic data for cement-based phases (Lothenbach et al., 2019), and CHESS which provides thermodynamic data for geochemical processes (der Lee, 1998).

Eq. B.1 gives an example of the chemical equilibrium Eq., which simulates the mineral dissolution and precipitation process at the equilibrium state. If the activity product (right-hand side of the equation) of the ions in the solution involved in the reaction is above the solubility product ($K_m$), precipitation occur due to a decrease in the ionic activity of the reactants; conversely, dissolution occurs (Ikumi & Segura, 2019).

$$K_m = \prod_{j=1}^{N} \left(\gamma_j c_j\right)^{v_{mj}} \quad (m = 1, \dots \dots M) \tag{B.1}$$

Where $\prod$ is the symbol representing a product over a set of terms, $N$ is the number of ionic species with concentrations designated $c_j$ and chemical activity coefficients $\gamma_j$. $v_{mj}$ stands for the stoichiometric

coefficient for ion species j, and $m$ is the number of solid phases formed. The assumption is that the activities of the species are the product of the species' concentrations and their activity coefficients.

A chemical reaction is classified as an equilibrium reaction if its time scale is shorter than the time scales of the transport processes (Le-Bescop et al., 2013). In this case, the Local Equilibrium Assumption (LEA) is assumed to be well-maintained throughout the porous system. The LEA assumes that a system can be considered as made up of subsystems where the rules of equilibrium thermodynamics apply. When the LEA is not valid, transport processes are faster than chemical reactions; thus, the chemical reactions are modelled based on the chemical kinetic laws.

*Table B.1: Heterogeneous chemical reactions taking place in cementitious materials under BAC (Grandclerc et al., 2018)*

| Heterogenous reaction taking place in the $CaO$-$Al_2O_3$-$SiO_2$-$SO_3$-$H_2O$ system | | Thermodynamic constant (K) |
|---|---|---|
| Solid phases | Dissolution reactions | |
| | Reaction involving calcium compounds | |
| Portlandite (CH) | $Ca(OH)_2 \leftrightharpoons Ca^{2+} + 2OH^-$ | 8.90 x $10^{-6}$ |
| | Reaction involving aluminium compounds | |
| Gibbsite ($AH_3$) | $Al(OH)_3{}^- \leftrightharpoons Al^{3+} + 6OH^-$ | 1.0 x $10^{-68}$ |
| | Reaction involving calcium-sulphur compounds | |
| Gypsum () | $CaSO_4.2H_2O \leftrightharpoons Ca^{2+} + SO_4{}^{2-} + 2H_2O$ | 3.72 x $10^{-5}$ |
| | Reactions involving calcium-aluminium-sulphur compounds | |
| AFm | $3CaO.Al_2O_3.CaSO_4.12H_2O$ $\leftrightharpoons 4Ca^{2+} + 2Al(OH)_4{}^- + 4OH^- + SO_4{}^{2-} + 6H_2O$ | 3.71 x $10^{-30}$ |
| Ettringite | $3CaO.Al_2O_3.3CaSO_4.32H_2O$ $\leftrightharpoons 6Ca^{2+} + 2Al(OH)_4{}^- + 4OH^- + 3SO_4{}^{2-} + 26H_2O$ | 2.80 x $10^{-45}$ |
| Hydrogarnet ($C_3AH_6$) | Reactions involving calcium-aluminium compounds $3CaO.Al_2O_3.6H_2O \leftrightharpoons 3Ca^{2+} + 2Al(OH)_4{}^- + 4OH^-$ | 3.2 x $10^{-22}$ |
| $C_2AH_8$ | $2CaO.Al_2O_3.8H_2O \leftrightharpoons 2Ca^{2+} + 2Al(OH)_4{}^- + 2OH^- + 3H_2O$ | 2.8 x $10^{-14}$ |
| $CAH_{10}$ | $CaO.Al_2O_3.8H_2O \leftrightharpoons Ca^{2+} + 2Al(OH)_4{}^- + 6H_2O$ | 2.5 x $10^{-8}$ |
| | Reaction involving calcium-silicon compounds | |
| C-S-H | $C_xS_yH_z \leftrightharpoons xCa^{2+} + 2xOH^- + ySiO_2{}^o + (z-x)H_2O$ | - |
| | Reaction involving silicon compounds | |
| Silica gel (SH) | $SH_u \leftrightharpoons SiO_2{}^o + uH_2O$ | 1.74 x $10^{-3}$ |

There are two approaches for solving the chemical equilibrium equations; the Law of Mass Action (LMA) and the Gibbs Energy Minimization (GEM) (Ikumi & Segura, 2019). The LMA states that the rate of a chemical reaction at a constant temperature is directly proportional to the product of the concentrations or activities of the species that influence the rate. The law is based on solving the system mass balance and mass action equations using Newton Raphson iteration (Le-Bescop et al., 2013). The GEM is based on mass and charge balance of the whole system, and equilibrium composition is calculated from the stoichiometric coefficients of the possible phases. Mostly, the GEM approach is not applied due to its complexity of integrating equilibrium solvers into the reactive transport calculators (Ikumi & Segura, 2019). However, both principles should yield the same equilibrium constants.

*Table B.2 Homogeneous chemical reactions taking place in cementitious materials under BAC (Grandclerc et al., 2018)*

| Homogeneous aqueous reactions taking place in the $CaO$-$Al_2O_3$-$SiO_2$-$SO_3$-$Na_2O$-$K_2O$-$H_2O$ system | Thermodynamic constant (K) |
|---|---|
| Dissociation reactions (in aqueous phase) | |
| Reactions involving calcium compounds | |
| $Ca(OH)_2{}^o \leftrightharpoons Ca^{2+} + 2OH^-$ | 1 |
| $Ca(OH)^+ \leftrightharpoons Ca^{2+} + OH^-$ | $1.66 \times 10^1$ |
| Reactions involving silicon compounds | |
| $SiO_2{}^o + 2H_2O \leftrightharpoons H_4SiO_2{}^o$ | $1.94 \times 10^{-3}$ |
| $H_4SiO_2{}^o \leftrightharpoons H_3SiO_2{}^- + H^+$ | $1.55 \times 10^{-10}$ |
| $H_3SiO_2{}^- \leftrightharpoons H_2SiO_2{}^{2-} + H^+$ | $4.68 \times 10^{-14}$ |
| $H_2SiO_2{}^{2-} \leftrightharpoons HSiO_2{}^{3-} + H^+$ | $1.0 \times 10^{-15}$ |
| Reaction involving sodium compounds | |
| $NaOH^O \leftrightharpoons Na^{2+} + OH^-$ | 1.5 |
| Reaction involving potassium compounds | |
| $KOH^O \leftrightharpoons K^+ + OH^-$ | 2.9 |
| Reactions involving sulphur compounds | |
| $H_2SO_4{}^o \leftrightharpoons HSO_4{}^- + H^+$ | $1.0 \times 10^6$ |
| $HSO_4{}^- \leftrightharpoons SO_4{}^{2-} + H^+$ | $1.0 \times 10^{-2}$ |
| Reaction involving aluminium compounds | |
| $Al(OH)_4{}^- \leftrightharpoons Al^{3+} + 4OH^-$ | $6.2 \times 10^{-1}$ |
| Reactions involving calcium-silicon compounds | |
| $CaH_2SiO_2{}^0 \leftrightharpoons Ca^{2+} + H_2SiO_2{}^{2-}$ | $3.89 \times 10^4$ |
| $CaH_3SiO_2{}^+ \leftrightharpoons Ca^{2+} + H_3SiO_2{}^-$ | $1.56 \times 10^1$ |
| Reaction involving calcium-sulphur compounds | |
| $Ca^{2+} + SO_4{}^{2-} \leftrightharpoons CaSO_4{}^0$ | $1.4 \times 10^{-3}$ |
| $Ca^{2+} + HSO_4{}^{2-} \leftrightharpoons CaHSO_4{}^+$ | $1.2 \times 10^1$ |

### B.1.2. Chemical kinetic laws

Chemical kinetics is the study of the rate of chemical reaction, which uses partial differential equations with empirical reaction rate constants to estimate the rate of formation of reaction products and the consumption of reactants. The kinetic laws are used to describe the disequilibrium or irreversible reactions when the use of chemical equilibrium calculations alone is not enough. The rate of the chemical reaction is determined using Eq. (B.2), and the equation is usually written in terms of primary species (reactants). For instance, the chemical reaction for the formation of gypsum can be described in terms of either the consumption of sulphate or the combination of both sulphate and portlandite, as follows.

Formation of gypsum; $[CH] + [SO_4^{2+}] \rightarrow [C\bar{S}H_2]$; $R = \frac{\partial[SO_4^{2+}]}{\partial t} = k_1[SO_4^{2+}] = k_2[SO_4^{2+}][CH]$

$$R_s = k_s \prod {a_i}^n \tag{B.2}$$

Where, $k_s$ is the reaction rate constant, $a_i$ is the activity of the primary species $i$ and $n$ is the partial order of reaction for the primary species $i$. The partial order for a reactant can only be determined experimentally and is often not indicated by its stoichiometric coefficient. A sum of all partial order for all reactants involved in the reaction defines the order of the kinetic law. Therefore, models based on the first-order kinetic laws describe a rate proportional to the concentration of a single reactant, whereas,

for those based on the second-order kinetic laws, the rate is proportional to the concentration of two reactants (Ikumi & Segura, 2019).

Mostly, differential equations used for modelling chemical kinetics translates into a more challenging mathematical and numerical problem than the algebraic equations used for modelling chemical equilibrium. Modelling chemical kinetics also requires more input data than chemical equilibrium, which requires only the equilibrium constant. Such input data include the rate constant at a reference temperature, activation energy, the reactive surface area for reactions involving species across different phases, and possibly some parameters to incorporate rate dependency on pH and the fugacity of a gas. Besides, the reaction rate constants are only known for pure phases in a controlled system, while unknown for most of the chemical reactions. As a result, a complete and accurate model description of kinetic processes can be challenging to determine (Leal et al., 2017).

### B.1.3. Combined chemical equilibrium and kinetic laws

There are cases when both kinetic laws and thermodynamic equilibrium are combined. This happens when the chemical equilibrium equations of certain phases are replaced by kinetic laws to account for phase formation in non-equilibrium conditions (Ikumi & Segura, 2019). For instance, this approach can be adopted to model ettringite dissolution and precipitation. Ettringite does not necessarily reach equilibrium at the end of each time step of the simulation, which is a necessary condition to reproduce crystallization pressures associated with ettringite growth in supersaturated solutions (Ikumi & Segura, 2019). Eq. B.3 provides an algebraic Eq. for chemical reactions controlled kinetically and at equilibrium.

$$R_s = k_s \left(1 - \frac{Q_s}{K_{eq}}\right) \prod {a_i}^n \tag{B.3}$$

Where, $k_s$ is the rate constant for the reaction, $Q_s$ is the ion activity product, and $K_{eq}$ is the chemical equilibrium constant.

The above chemical reaction equations are used in the reactive transport models to determine the concentrations of chemical species produced during a certain chemical process. However, these species' concentrations vary with time and space as the chemical reactions proceed and the species migrate within the system. Therefore, determining their concentration at a given time and space requires the application of partial differential equations to describe the transport process, as discussed below.

## B.2. Transport processes

Transport processes refer to the mechanisms of liquid, ion or molecular transfer in the pore solution and external environment (Le-Bescop et al., 2013). In reactive transport models, transport processes are combined and described by a set of partial differential equations as the sum of the unidirectional flux of each species involved in the chemical reactions. The extended Nernst–Planck equation describes the flux with an advection term, which yields the general ionic transport equation (Eq. B.4)(Le-Bescop et al., 2013).

$$J_i = -{D_i}^o \frac{\partial c_i}{\partial x} - \frac{{D_i}^o z_i F}{RT} c_i \frac{\partial \psi}{\partial x} - {D_i}^o c_i \frac{\partial \ln \gamma_i}{\partial x} - \frac{{D_i}^o c_i \ln \gamma_i c_i}{T} \frac{\partial T}{\partial x} + c_i v \quad \text{(B.4)}$$

Where $J_i$ is the unidirectional flux of species $i$, $c_i$ is the concentration of species $i$; ${D_i}^o$ is the diffusion coefficient of species $i$ in free water; R is the ideal gas constant; T is the temperature, and $v$ is the velocity of the liquid phase. The term $\gamma_i$, and $z_i$ correspond to the chemical activity coefficient and the valence number of the ionic species $i$, respectively. F is the Faraday constant, and ψ is the electrical potential. Thus, a general ionic transport Eq. (Eq. B.4) consists of five terms, which are:

- First term: Chemical potential gradient, an indication of diffusion of species from a high concentration to a low concentration;
- Second term: Electrical potential gradient, responsible for maintaining the macroscopic electroneutrality in the pore solution;
- Third term: Chemical activity gradient corresponds to a correction to the flux when the ionic strength of the pure solution is high;
- Fourth term: Temperature gradient or thermal diffusion, indicating the influence of temperature on the movement of ionic species. When the system is isothermal, the term is neglected;
- Fifth term: Advection associated with ionic transport caused by changes in moisture conditions in the pores due to the aqueous solution flow. The term accounts for non-saturated conditions.

The time-dependent response of the system is obtained by substituting Eq. B.4 into the mass conservation relationship (Eq. B.5), which provides a complete ionic transport Eq. (Eq. B.6). Eq. B.6 is only applied in the aqueous phase at the microscopic (pore) scale; the term $r_i$ is the chemical reaction rate accounting for chemical reaction and complexation in the solution.

$$\frac{\partial c_i}{\partial t} + \frac{\partial J_i}{\partial x} + r_i = 0 \quad \text{(B.5)}$$

$$\frac{\partial c_i}{\partial t} - \frac{\partial}{\partial x}\left({D_i}^o \frac{\partial c_i}{\partial x} + \frac{{D_i}^o z_i F}{RT} c_i \frac{\partial \psi}{\partial x} + {D_i}^o c_i \frac{\partial \ln \gamma_i}{\partial x} + \frac{{D_i}^o c_i \ln \gamma_i c_i}{T} \frac{\partial T}{\partial x} - c_i v\right) + r_i = 0 \quad \text{(B.6)}$$

Eq. B.6 only applies at the microscopic scale, but most transport processes occur at the macroscopic scale (structural level). Therefore, through a homogenization or averaging technique described in (Bear & Bachmat, 1990), the equation can be transformed to Eq. B.7, which is applicable at the macroscopic scale. The homogenization technique introduces the volumetric water content, $w$; the solid phase fraction, $\theta_s$ ; and the content of ionic species bound to the solid matrix, $c_i^s$. The diffusion coefficient, $D_i$ at the macroscopic scale is correlated to the diffusion coefficient in free water, ${D_i}^o$, by the geometric factor, $\tau$, (tortuosity) which accounts for the complexity of the porous network at the macroscopic scale; $D_i = \tau {D_i}^o$.

$$\frac{\partial(\theta_s c_i^s)}{\partial t} + \frac{\partial w c_i}{\partial t} - \frac{\partial}{\partial x}\left(D_i w \frac{\partial c_i}{\partial x} + \frac{D_i z_i F}{RT} w c_i \frac{\partial \psi}{\partial x} + D_i w c_i \frac{\partial \ln \gamma_i}{\partial x} + \frac{D_i c_i \ln \gamma_i c_i}{T} w \frac{\partial T}{\partial x} - c_i v\right) + w r_i = 0 \quad \text{(B.7)}$$

Generally, the term $\frac{\partial(\theta_s c_i^s)}{\partial t}$ accounts for the heterogeneous reactions, and the term $wr_i$ stands for homogeneous reactions (Samson & Marchand, 2007). However, this term is more applied in groundwater transport where homogeneous reactions are a significant part of the pollutant movement process. Bear in mind that most ionic transport models neglect the term associated with electrochemical potential and the electrical coupling between ions. This results from the computational complexity associated with the simulation of these phenomena, which requires a full description of the ionic species in the solution (Ikumi & Segura, 2019). Besides, for notation simplifications, the transport operator $\mathcal{L}(c_i)$ is introduced in Eq. B.7, see Eq. B.8.

$$-\frac{\partial}{\partial x}\left(D_i w \frac{\partial c_i}{\partial x} + \frac{D_i z_i F}{RT} w c_i \frac{\partial \psi}{\partial x} + D_i w c_i \frac{\partial \ln \gamma_i}{\partial x} + \frac{D_i c_i \ln \gamma_i c_i}{T} w \frac{\partial T}{\partial x} - c_i v\right) = \mathcal{L}(c_i) \quad \text{(B.8)}$$

### B.3. Supplementary information – Coupling chemical reaction with transport processes

The approaches for coupling the chemical and transport process include (Yell & Tripathi, 1991)

- Direct Substitution Approach (DSA)
- Operator Splitting Approach (OSA).

The DSA involves directly substituting the chemical reaction equations into the transport equations to form a highly nonlinear system of partial differential equations. Transport terms associated with electrical coupling and chemical activity effects are usually neglected, and the diffusion coefficient $D^*$ is considered uniform for all species to simplify the transport operator to a linear transport operator, $\mathcal{L}(.)$ (Eq. B.8). This approach was primarily applied in the groundwater transport model (Le-Bescop et al., 2013). The porosity, $\omega$, replaced the volumetric water content in Eq. B.9 because the system is assumed to be saturated.

$$\mathcal{L}(c_i) = \frac{\partial}{\partial x}\left[(c_i)v - \omega D^* \frac{\partial}{\partial x}(c_i)\right] \quad \text{(B.9)}$$

Due to the high consumption of computer time and the algebraic complexity associated with some chemical reactions such as dissolution and precipitation, the DSA is less used, and the OSA is more adopted. The OSA calculates the transport and chemical reaction equations separately. The linear transport operator (Eq. B.9) is solved first to estimate the species' initial concentration, which is then used in the chemical reaction equations. The loop proceeds to the next time step until the chemical equilibrium between the ions in the pore solution in the solid phases is maintained (Lagneau & van der Lee, 2010).

The operator splitting approach is divided into two classes: The Sequential Iterative Approaches (SIA) and the Sequential Non-Iterative Approaches (SNIA). The SAI solves the set of chemical reaction and transport equations simultaneously until convergence is reached, while in the SNIA, transport and chemistry are solved sequentially without iterations. SNIA is preferred over SIA because it completely decouples transport and chemistry and is easier to implement different transport and chemistry schemes in a single simulation platform (Le-Bescop et al., 2013).

## C. Sewer environmental conditions

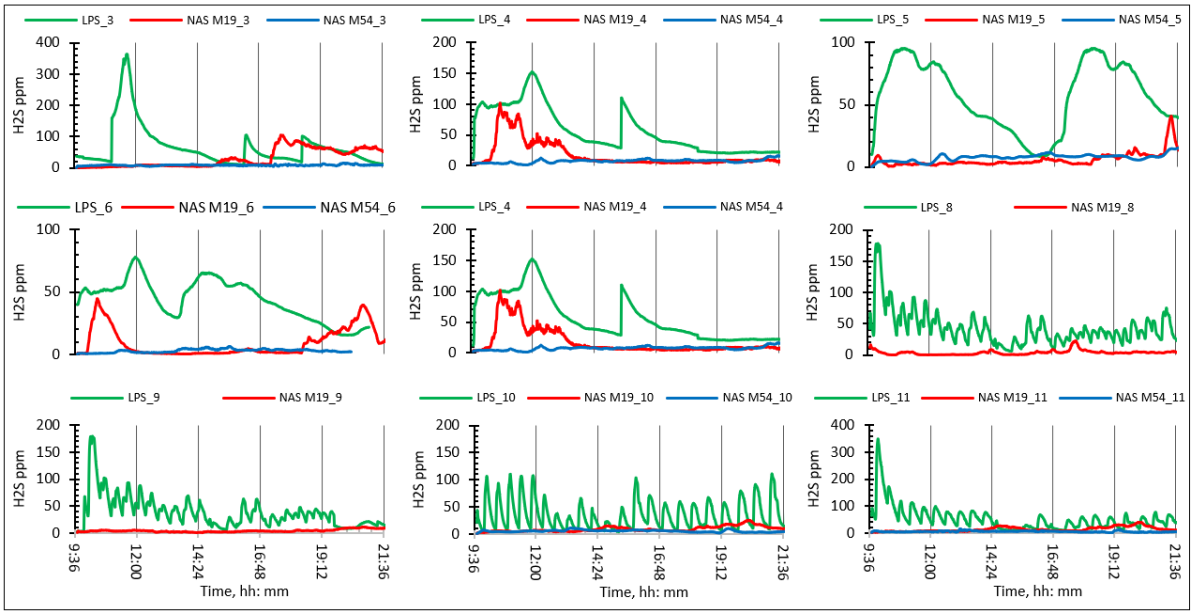


*Figure C.1: Diurnal and seasonal variation of $H_2S$ gas concentration in ppm of three sewer sites from March to November 2021*

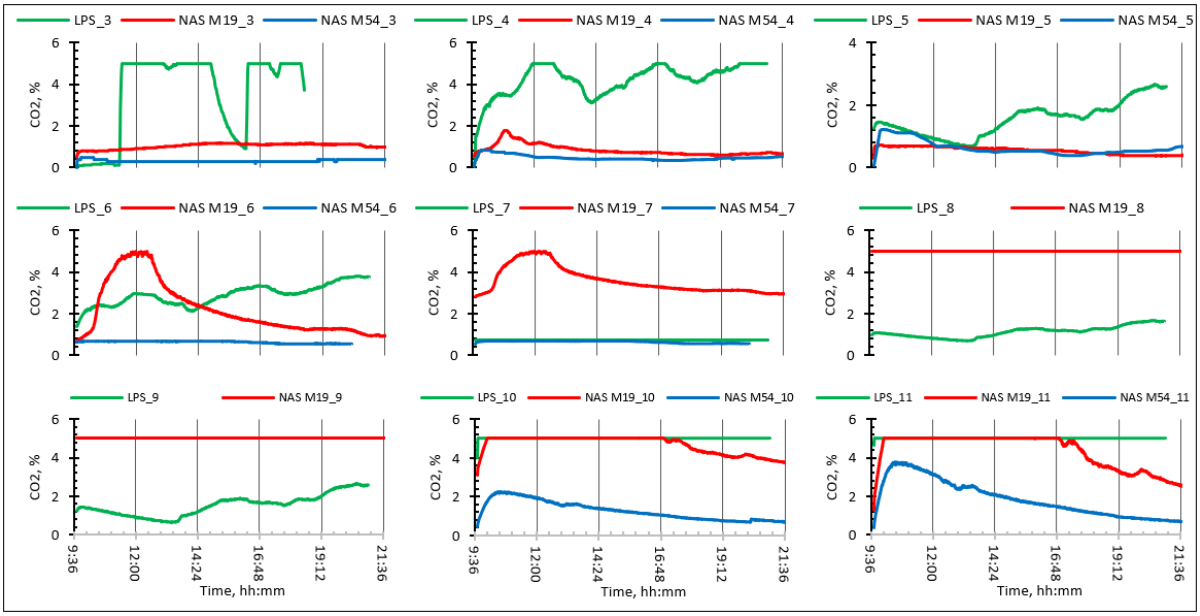


*Figure C.2: Diurnal and seasonal variation Carbon dioxide (CO2) gas, % of three sewer site measured from March to November 2021*

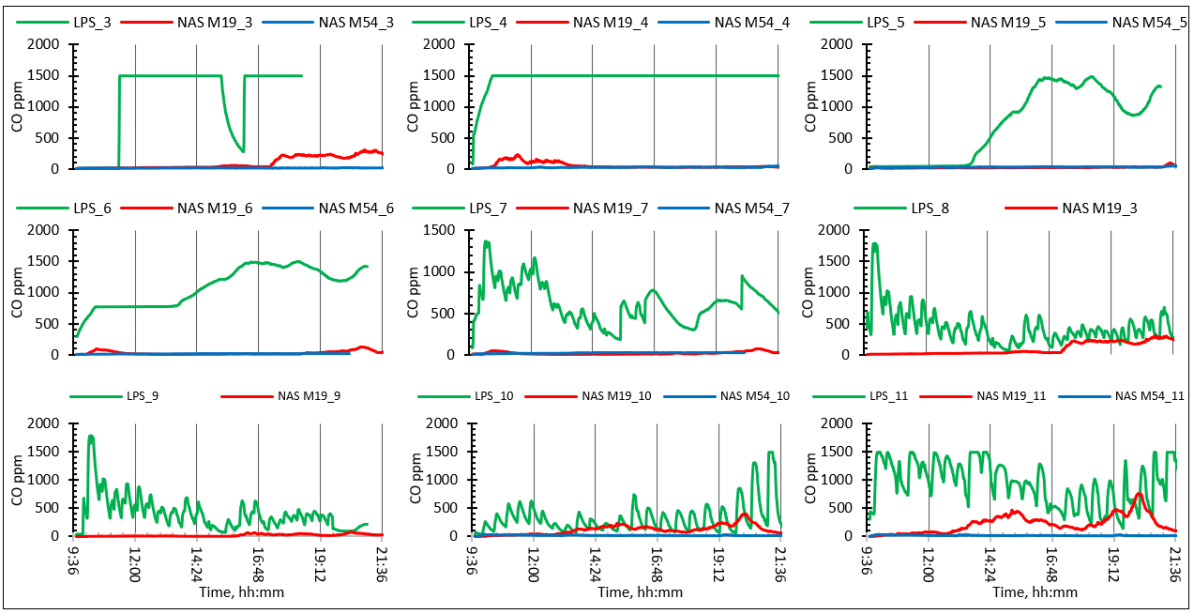


*Figure C.3: Diurnal and seasonal variation Carbon monoxide (CO) gas in ppm of three sewer site measured from March to November 2021*

# D. Quality of concrete recommended for sewer concrete construction

## D.1. Compressive strengths and relative density

*Table D.1: Compressive strengths and relative density (coefficient of variation less than 5 %) of concrete specimens and respective sewer pipe sections at 28 days (Fourie, 2007)*

| Factory | Pipe section (MPa) | Air-cure spec. (MPa) | Water-cure spec. (MPa) | Relative density (g/cm$^3$) | |
|---|---|---|---|---|---|
| | | | | *Pipe* | *Specimen* |
| **Olifantsfontein** | 67,2 | 76,4 | 78,3 | 2,57 | 2,51 |
| **Wadeville** | 56,4 | 65,1 | 69,8 | 2,38 | 2,47 |
| **Roodepoort** | 66,4 | 65,9 | 73,7 | 2,59 | 2,51 |
| **Kuilsriver** | 43,6 | 42,0 | 51,2 | 2,53 | 2,51 |
| **Blackheath** | 50,7 | 47,6 | 52,1 | 2,40 | 2,44 |

## D.2. Durability Index of five different concrete specimens and pipe sections

*Table D.2: Oxygen permeability index (OPI) (coefficient of variation less than 5 %), water sorptivity index (WSI)(coefficient of variation less than 10 %) and porosity (coefficient of variation less than 10 %) measurements of five different concrete specimens and pipe sections (Fourie, 2007)*

| Factory | OPI | | Water sorp. (mm/√hr) | | Porosity (%) | |
|---|---|---|---|---|---|---|
| | *Pipe* | *Specimen* | *Pipe* | *Specimen* | *Pipe* | *Specimen* |
| **Olifantsfontein** | 10,01 | 10,63 | 4,92 | 7,48 | 6,1 | 6,5 |
| **Wadeville** | 9,84 | 10,65 | 5,20 | 7,99 | 12,3 | 8,0 |
| **Roodepoort** | 10,37 | 10,79 | 4,89 | 4,75 | 8,2 | 8,2 |
| **Kuilsriver** | 10,06 | 10,58 | 4,75 | 4,17 | 8,6 | 8,9 |
| **Blackheath** | 10,20 | 10,42 | 6,69 | 5,29 | 10,6 | 10,4 |

## E. LH concrete surface pH results

*Table E.1: LH Concrete surface pH readings*

| Mix | Date | 16/04/2019 | 13/08/2019 | 19/10/2019 | 28/01/2020 | 06/10/2020 | 28/04/2021 |
|---|---|---|---|---|---|---|---|
| | months | 0.0 | 4.0 | 6.2 | 9.6 | 18.0 | 25.0 |
| SRPC + FA | LPS | 10.0 | 3.70 | 6.17 | 5.80 | 6.72 | 5.54 |
| | NAS M19 | 9.9 | 7.49 | 4.66 | 4.28 | 5.28 | 3.99 |
| | NAS M54 | 10.1 | 8.07 | 6.60 | 6.48 | 5.89 | 5.41 |
| SRPC + FA + HC | LPS | 9.7 | 5.05 | 6.24 | 5.93 | 6.63 | 5.81 |
| | NAS M19 | 9.4 | 7.44 | 4.69 | 4.33 | 5.51 | 3.64 |
| | NAS M54 | 9.4 | 7.13 | 7.24 | 6.70 | 5.92 | 5.84 |
| SRPC+ LS | LPS | 9.7 | 5.50 | 6.64 | 5.99 | 6.86 | 5.87 |
| | NAS M19 | 9.9 | 7.57 | 5.53 | 5.80 | 5.38 | 4.15 |
| | NAS M54 | 9.8 | 8.12 | 7.55 | 7.15 | 6.49 | 5.33 |
| CSA | LPS | 9.3 | 5.09 | 6.78 | 5.73 | 6.78 | 5.48 |
| | NAS M19 | 9.4 | 7.34 | 4.82 | 4.25 | 4.76 | 3.57 |
| | NAS M54 | 9.3 | 7.71 | 7.32 | 6.91 | 5.35 | 4.995 |
| **STDev pH readings** | | | | | | | |
| SRPC + FA | LPS | 0.5 | 0.67 | 0.49 | 0.30 | 0.18 | 0.15 |
| | NAS M19 | 0.2 | 0.48 | 0.65 | 0.40 | 0.73 | 0.28 |
| | NAS M54 | 0.4 | 0.45 | 0.22 | 0.32 | 0.15 | 0.65 |
| SRPC + FA + HC | LPS | 0.2 | 0.65 | 0.56 | 0.22 | 0.10 | 0.15 |
| | NAS M19 | 0.2 | 1.43 | 0.45 | 0.32 | 0.68 | 0.28 |
| | NAS M54 | 0.5 | 1.54 | 0.14 | 0.39 | 0.07 | 0.49 |
| SRPC+ LS | LPS | 0.3 | 0.47 | 0.47 | 0.21 | 0.21 | 0.43 |
| | NAS M19 | 0.6 | 0.21 | 0.59 | 0.82 | 0.59 | 0.41 |
| | NAS M54 | 0.4 | 0.24 | 0.24 | 0.10 | 0.09 | 0.35 |
| CSA | LPS | 0.5 | 0.30 | 0.32 | 0.32 | 0.20 | 0.56 |
| | NAS M19 | 0.1 | 0.65 | 0.21 | 0.24 | 0.98 | 0.34 |
| | NAS M54 | 0.4 | 0.28 | 0.11 | 0.06 | 0.59 | 0.45 |

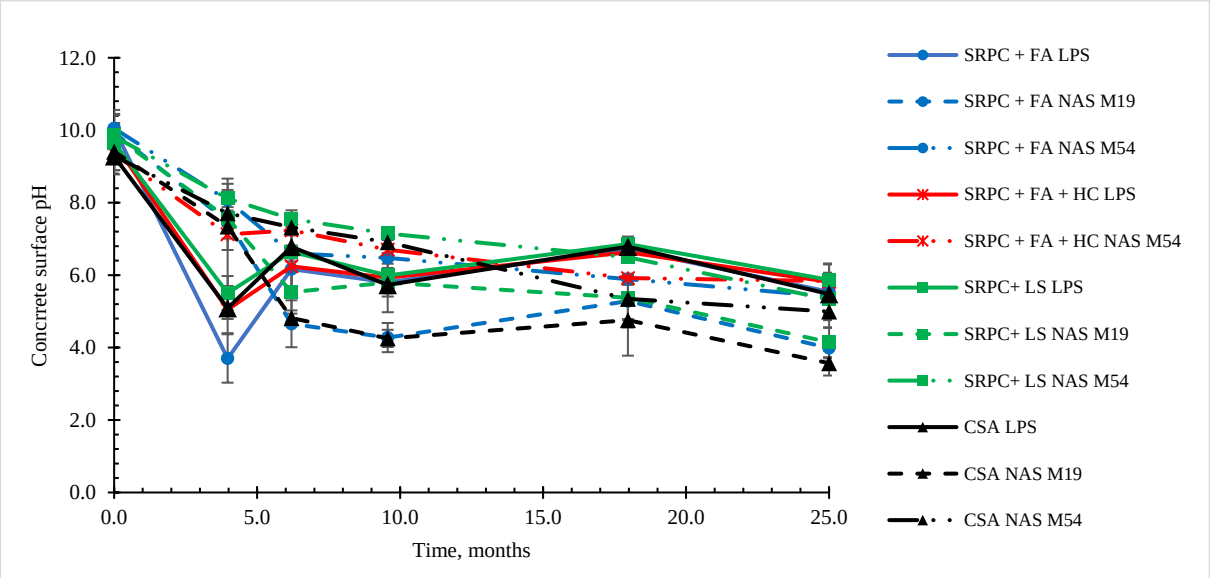


*Figure E.1: Overall LH concrete surface pH at NAS M19, NAS M54 and LPS*

## F. LH concrete mass change results

*Table F.1: LH concrete mass change at three sewer sites for two years*

| **Change in Mass, %** | | | | | | | | |
|---|---|---|---|---|---|---|---|---|
| | Dates | 16/04/2019 | 19/06/2019 | 13/08/2019 | 19/10/2019 | 28/01/2020 | 06/10/2020 | 28/04/2021 |
| Mix | Months | 0.0 | 2.1 | 4.0 | 6.2 | 9.6 | 18.0 | 24.8 |
| | LPS | 0.0 | 0.53 | 0.68 | 0.16 | -0.13 | -6.37 | -13.1 |
| SRPC + FA | NAS M19 | 0.0 | 0.28 | 0.55 | 0.78 | -1.58 | -2.78 | -3.2 |
| | NAS M54 | 0.0 | 0.65 | 0.74 | 0.85 | 0.85 | 1.42 | 1.6 |
| | LPS | 0.0 | 0.25 | 0.65 | -0.59 | -0.93 | -5.11 | -12.0 |
| SRPC + FA + HC | NAS M19 | 0.0 | 0.36 | 0.58 | 0.42 | 0.09 | -1.36 | -2.3 |
| | NAS M54 | 0.0 | 0.45 | 0.51 | 0.67 | 0.67 | 1.20 | 1.4 |
| | LPS | 0.0 | 0.36 | 0.85 | -0.33 | -0.97 | -6.06 | -12.5 |
| SRPC+ LS | NAS M19 | 0.0 | 0.58 | 0.78 | 0.92 | -0.29 | -1.62 | -3.1 |
| | NAS M54 | 0.0 | 0.61 | 0.66 | 0.67 | 0.67 | 1.28 | 1.4 |
| | LPS | 0.0 | 0.74 | 1.06 | 0.50 | -0.18 | -4.22 | -10.0 |
| CSA | NAS M19 | 0.0 | 0.67 | 0.93 | 1.80 | 1.56 | 1.88 | 1.2 |
| | NAS M54 | 0.0 | 0.83 | 1.04 | 1.72 | 1.71 | 1.68 | 1.9 |
| **STD in mass** | | | | | | | | |
| | | 16/04/2019 | 19/06/2019 | 13/08/2019 | 19/10/2019 | 28/01/2020 | 06/10/2020 | 28/04/2021 |
| Mix | Sites | 0.0 | 2.1 | 4.0 | 6.2 | 9.6 | 18.0 | 24.8 |
| | LPS | 0.00 | 0.10 | 0.10 | 0.13 | 0.06 | 0.18 | 1.10 |
| SRPC + FA | NAS M19 | 0.00 | 0.10 | 0.05 | 0.07 | 0.33 | 0.73 | 0.90 |
| | NAS M54 | 0.00 | 0.46 | 0.25 | 0.25 | 0.25 | 0.31 | 0.30 |
| | LPS | 0.00 | 0.15 | 0.22 | 0.27 | 0.21 | 0.94 | 2.02 |
| SRPC + FA + HC | NAS M19 | 0.00 | 0.09 | 0.90 | 0.40 | 0.36 | 1.16 | 1.50 |
| | NAS M54 | 0.00 | 0.05 | 0.05 | 0.04 | 0.04 | 0.09 | 0.01 |
| | LPS | 0.00 | 0.28 | 0.14 | 1.18 | 0.20 | 0.49 | 0.53 |
| SRPC+ LS | NAS M19 | 0.00 | 0.03 | 0.07 | 0.06 | 0.53 | 0.72 | 0.57 |
| | NAS M54 | 0.00 | 0.07 | 0.07 | 0.06 | 0.06 | 0.06 | 0.09 |
| | LPS | 0.00 | 0.24 | 0.14 | 1.48 | 1.36 | 0.23 | 1.26 |
| CSA | NAS M19 | 0.00 | 0.08 | 0.06 | 0.30 | 0.37 | 0.83 | 1.23 |
| | NAS M54 | 0.00 | 0.07 | 0.04 | 0.59 | 0.58 | 0.01 | 0.02 |

## G. LH concrete thickness change results

*Table G.1: LH concrete thickness change at three sewer sites for two years*

| Thickness change mm | | | | | | | | |
|---|---|---|---|---|---|---|---|---|
| | | 16/04/2019 | 19/06/2019 | 13/08/2019 | 19/10/2019 | 28/01/2020 | 06/10/2020 | 28/04/2021 |
| Mix | Months | 0.0 | 2.1 | 4.0 | 6.2 | 9.6 | 18.0 | 24.8 |
| | LPS | 0.00 | -0.79 | -0.82 | -0.82 | -1.37 | -3.93 | -6.12 |
| SRPC + FA | NAS M19 | 0.00 | -0.57 | -0.63 | -0.50 | -3.13 | -5.22 | -6.70 |
| | NAS M54 | 0.00 | -0.09 | -0.36 | -0.06 | -0.06 | -0.06 | 0.57 |
| | LPS | 0.00 | -0.30 | -0.35 | -0.31 | -0.81 | -2.71 | -4.37 |
| SRPC + FA + HC | NAS M19 | 0.00 | 0.08 | 0.38 | 0.44 | -0.73 | -2.63 | -3.69 |
| | NAS M54 | 0.00 | -0.17 | -0.27 | -0.08 | -0.08 | -0.08 | 0.34 |
| | LPS | 0.00 | 0.08 | 0.31 | -0.49 | -0.87 | -3.32 | -4.75 |
| SRPC+ LS | NAS M19 | 0.00 | 0.13 | 0.48 | 0.37 | -1.38 | -3.63 | -5.10 |
| | NAS M54 | 0.00 | 0.28 | -0.11 | -0.17 | -0.17 | -0.17 | 0.68 |
| | LPS | 0.00 | 0.06 | 0.11 | 0.37 | 0.17 | -1.75 | -2.86 |
| CSA | NAS M19 | 0.00 | 0.16 | 0.53 | 0.33 | -0.13 | 0.09 | -1.97 |
| | NAS M54 | 0.00 | -0.02 | 0.10 | 0.35 | 0.35 | 0.35 | 0.57 |
| STD thickness, mm | | | | | | | | |
| | LPS | 0.00 | 0.21 | 0.21 | 0.18 | 0.14 | 0.78 | 0.79 |
| SRPC + FA | NAS M19 | 0.00 | 0.13 | 0.19 | 0.17 | 1.00 | 0.73 | 1.26 |
| | NAS M54 | 0.00 | 0.07 | 0.11 | 0.12 | 0.12 | 0.12 | 0.14 |
| | LPS | 0.00 | 0.27 | 0.28 | 0.31 | 0.30 | 0.21 | 0.54 |
| SRPC + FA + HC | NAS M19 | 0.00 | 0.21 | 0.31 | 0.25 | 0.48 | 0.98 | 1.24 |
| | NAS M54 | 0.00 | 0.19 | 0.28 | 0.14 | 0.14 | 0.14 | 0.23 |
| | LPS | 0.00 | 0.14 | 0.26 | 0.25 | 0.27 | 0.55 | 0.27 |
| SRPC+ LS | NAS M19 | 0.00 | 0.17 | 0.15 | 0.11 | 0.62 | 1.03 | 0.88 |
| | NAS M54 | 0.00 | 0.11 | 0.11 | 0.17 | 0.17 | 0.17 | 0.25 |
| | LPS | 0.00 | 0.19 | 0.20 | 0.25 | 0.22 | 0.18 | 0.24 |
| CSA | NAS M19 | 0.00 | 0.11 | 0.12 | 0.18 | 0.32 | 0.21 | 0.59 |
| | NAS M54 | 0.00 | 0.13 | 0.17 | 0.12 | 0.12 | 0.12 | 0.07 |

## H. SEM-BSE images of LH concrete specimens at the LPS

### H.1. SRPC+FA concrete

Figure H.1 shows the SEM-BSE image for SRPC+FA concrete after two years of exposure at LPS. Figure H.1 (A) shows a continuous crack separating the intact from the altered zone. Two fly ash particles, dark and bright, seem detached from the altered zone. As indicated earlier, the dark particle contains microcracking as a sign of disintegration because it is alumina-rich, and the bright particle seems intact because it is silica-rich.

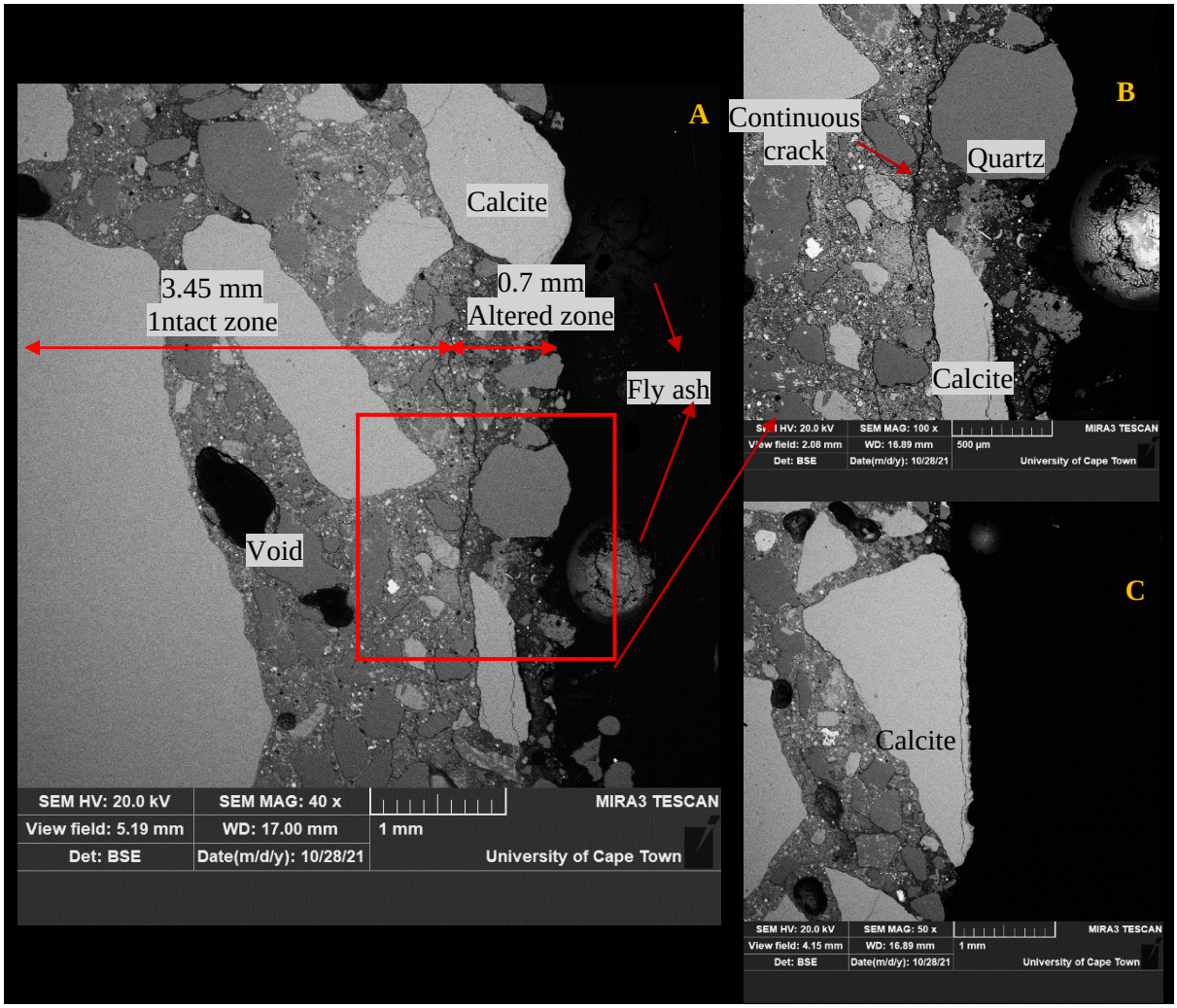


*Figure H.1: SEM-BSE image for SRPC+FA concrete after two years of exposure at LPS*

The presence of voids indicates that the degree of compaction was not fully achieved, as indicated in section 5.3.1. Figure H.1(B) shows a fragmented cement matrix with high porosity between quartz and calcite particles in the altered zone. In Figure H.1 (C), the calcite aggregate contains a vertical microcrack separating the intact aggregate matrix from a thin layer of dissolved aggregate matrix. Unlike in the NAS M19, the exposed surface of calcite aggregate seems smooth, indicating that the wastewater easily washed the dissolved surface.

## H.2. SRPC+FA+HC concrete

Figure H.2 shows the SEM-BSE image for SRPC+FA+HC concrete after two years of exposure at the LPS. Figure H.2 (A) indicates about 0.2 mm to 0.8 mm altered zone thickness separated by a vertical crack which passes through calcite aggregates and diverges the quartz particle. This crack is visibly distinct compared to that observed in the SRPC +FA concrete. The altered zone contains mainly a transition zone whose integrity is slightly more robust than the deteriorated zone to be washed by the wastewater. However, the zone can easily detach from the main concrete due to the sewer hydraulic actions associated with this site, exposing a new surface.

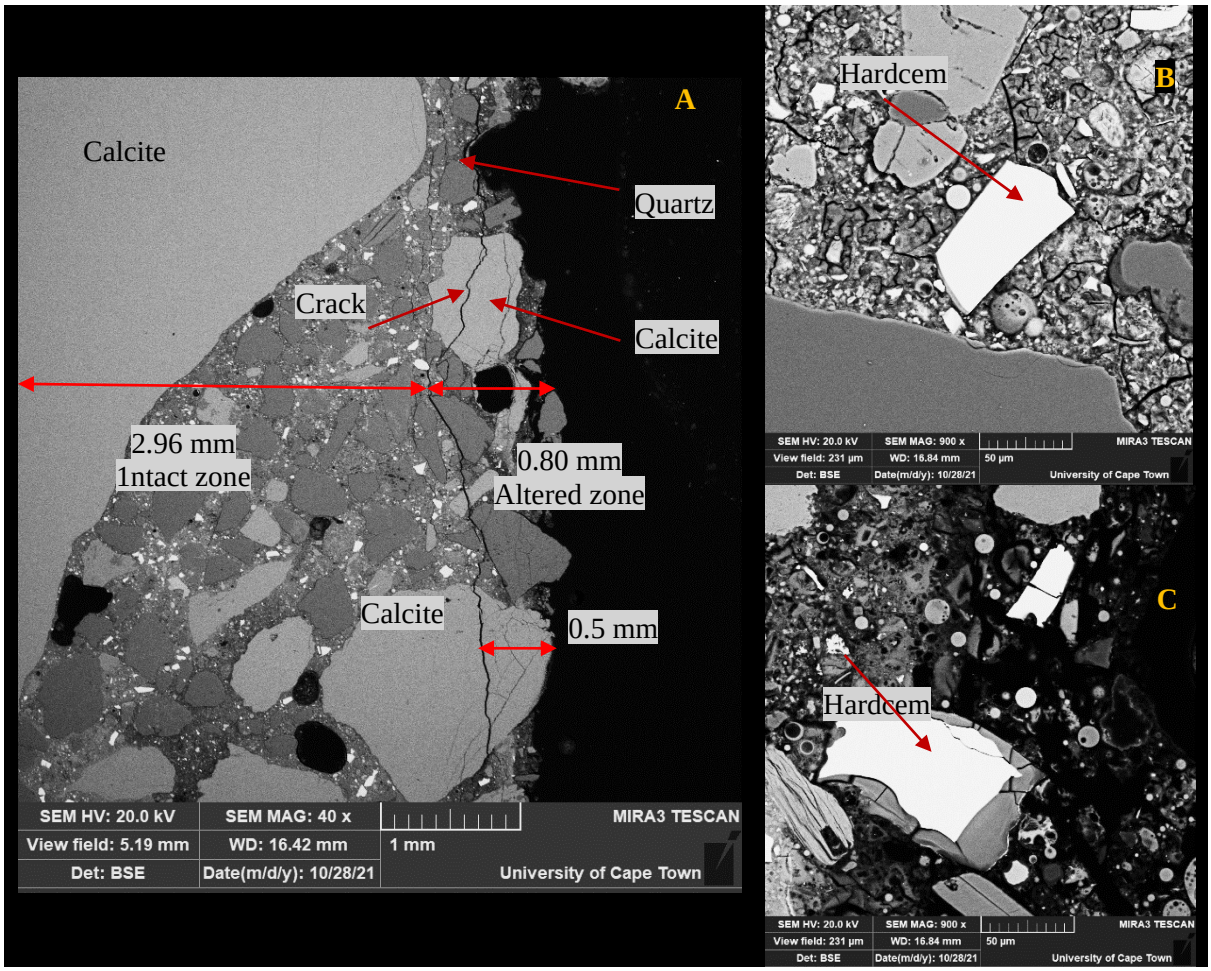


*Figure H.2: SEM-BSE image for SRPC+FA+HC concrete after two years of exposure at LPS*

As observed at NAS M19, the whitish particles in the concrete microstructure are the iron-based additive particles, which seem not to participate in the hydration reaction, see Figure H.2 (B) taken from the intact zone. However, in Figure H.2 (C), taken from the altered zone, the iron-based additive particle seems to be dissolving from its edge towards the centre, which indicates that these particles can only dissolve when the pH of the zone is like to be very low.

## H.3. CSA concrete

Figure H.3 shows the SEM-BSE image for CSA concrete after two years of exposure at the LPS. Figure H.3 (A) indicates the intact and altered zone whose brightness is similar, making it difficult to demarcate

between the altered and intact zones, especially in the cement matrix, as observed in Figure 5.19. However, the intact zone contains compaction voids filled with cementitious hydration, i.e., ettringite. See Figure H.3 (B), showing ettringite in the void. On the other hand, the altered zone is about 1.15 mm in width (at the maximum depth) with increased porosity and loss of cohesion in the cement matrix. About 0.4 mm of the altered zone was measured at the aggregate matrix, demarcated by a vertical crack passing through the aggregate but not extending to the cement matrix as observed in previous concrete.

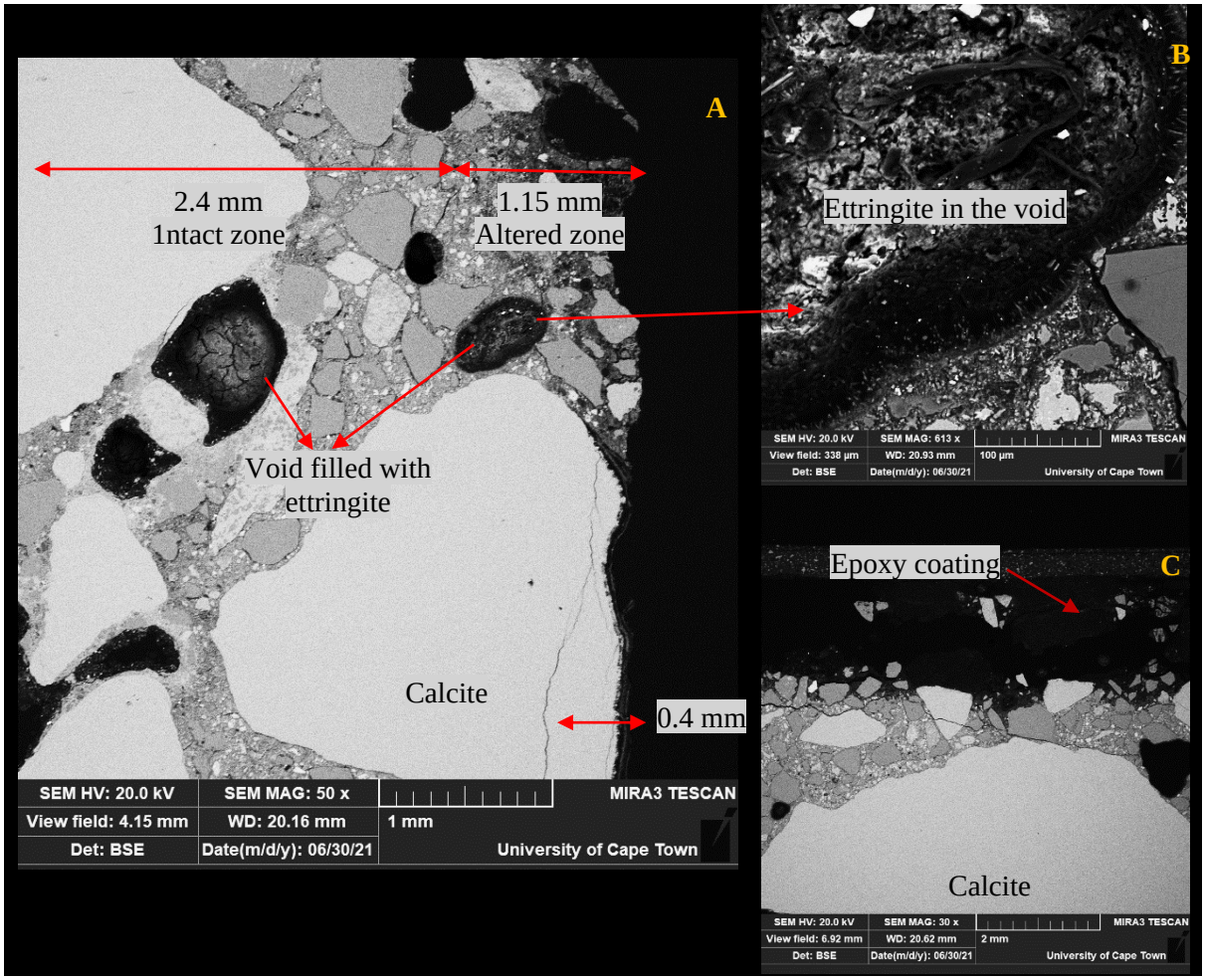


*Figure H.3: SEM-BSE image for CSA concrete after two years of exposure at LPS.*

Figure H.3 (C) shows signs of deterioration at the concrete epoxy coating interface, which in section 5.2.2.1 were referred to as blisters observed on the epoxy coated surface. Both corrosion products at the interface and ettringite formation in the voids were postulated to compensate for the increased volume by providing more space for ettringite formation without causing substantial expansion of the concrete matrix.

# I. Durability index results for UCT concrete

*Table I.1: Durability index results of UCT concrete*

| **Mix** | **1** | **2** | **3** | **4** | **5** | **6** |
|---|---|---|---|---|---|---|
| **Type** | **CEM II A-L** | **CEM I+FA** | **CEM I-FA+HC** | **CSA** | **CAC+OPC** | **CAC** |
| Avg. Oxygen gas permeability, k (m/s) | 1.6E-11 | 6.7E-12 | 1.1E-11 | 6.2E-12 | 9.8E-12 | 7.2E-11 |
| STDev. Of k x10 | 1.3E-11 | 2.1E-12 | 2.9E-12 | 1.9E-12 | 3.5E-12 | 1.5E-11 |
| Cov, % | 20 | 30 | 26 | 31 | 36 | 21 |
| Avg. Oxygen Permeability Index (OPI) | 10.87 | 11.19 | 10.96 | 11.22 | 11.03 | 10.15 |
| STDev. Of OPI | 0.28 | 0.14 | 0.12 | 0.14 | 0.14 | 0.08 |
| Cov % | 2.59 | 1.21 | 1.12 | 1.21 | 1.28 | 0.81 |
| Avg Water Sorptivity Index (WSI), $mm/hr^{0.5}$ | 5.48 | 5.13 | 5.95 | 8.92 | 7.24 | 7.31 |
| STDev of WSI | 0.17 | 0.12 | 0.14 | 0.35 | 0.37 | 0.45 |
| Cov % | 3.05 | 2.26 | 2.43 | 3.98 | 5.08 | 6.11 |
| Avg porosity, % | 6.42 | 6.37 | 5.04 | 3.48 | 5.72 | 8.46 |
| STDev of porosity, % | 0.39 | 0.46 | 0.23 | 0.23 | 0.32 | 0.40 |
| Cov % | 6.02 | 7.15 | 4.50 | 6.67 | 5.52 | 4.73 |

## J. UCT concrete surface pH results

*Table J.1: UCT Concrete surface pH readings*

| **Concrete surface pH** | | | | |
|---|---|---|---|---|
| Date | 28/01/2020 | 06/10/2020 | 28/04/2021 | 03/03/2022 |
| Months | 0 | 8 | 15 | 26 |
| CEM II AL LPS | 10.0 | 6.44 | 5.47 | #DIV/0! |
| SRPC+FA LPS | 9.5 | 6.88 | 5.17 | #DIV/0! |
| SRPC+FA+HC LPS | 9.8 | 6.99 | 5.21 | #DIV/0! |
| CSA LPS | 9.3 | 6.35 | 5.17 | #DIV/0! |
| CAC LPS | 9.6 | 6.63 | 5.11 | #DIV/0! |
| CAC + SRPC LPS | 10.3 | 6.99 | 4.46 | #DIV/0! |
| CEM II AL NAS M19 | 10.0 | 6.97 | 4.46 | 2.51 |
| SRPC+FA NAS M19 | 8.8 | 6.37 | 5.28 | 2.36 |
| SRPC+FA+HC NAS M19 | 9.7 | 6.23 | 5.33 | 2.80 |
| CSA NAS M19 | 8.8 | 6.16 | 4.29 | 3.23 |
| CAC NAS M19 | 9.7 | 6.13 | 4.06 | 3.97 |
| CAC+SRPC NAS M19 | 9.4 | 6.20 | 4.90 | 3.72 |
| **STDev of pH** | | | | |
| CEM II AL LPS | 0.07 | 0.30 | 0.17 | #DIV/0! |
| SRPC+FA LPS | 0.17 | 0.56 | 0.18 | #DIV/0! |
| SRPC+FA+HC LPS | 0.11 | 0.45 | 0.15 | #DIV/0! |
| CSA LPS | 0.07 | 0.15 | 0.28 | #DIV/0! |
| CAC LPS | 0.24 | 0.18 | 0.20 | #DIV/0! |
| CAC + SRPC LPS | 0.34 | 0.38 | 0.19 | #DIV/0! |
| CEM II AL NAS M19 | 0.01 | 0.06 | 1.07 | 0.05 |
| SRPC+FA NAS M19 | 0.16 | 0.24 | 0.29 | 0.56 |
| SRPC+FA+HC NAS M19 | 0.10 | 0.08 | 1.32 | 0.59 |
| CSA NAS M19 | 0.27 | 0.04 | 0.23 | 0.23 |
| CAC NAS M19 | 0.12 | 0.02 | 0.27 | 0.08 |
| CAC+SRPC NAS M19 | 0.11 | 0.18 | 0.15 | 0.20 |

## K. UCT concrete mass and thickness change results

*Table K.1: UCT concrete mass and thickness change at two sewer sites*

| **Change in Mass, %** | | | | |
|---|---|---|---|---|
| Date | 28/01/2020 | 06/10/2020 | 28/04/2021 | 03/03/2022 |
| Months | 0 | 8 | 15 | 26 |
| CEM II AL LPS | 0.0 | -5.04 | -9.90 | #DIV/0! |
| SRPC+FA LPS | 0.0 | -2.09 | -9.35 | #DIV/0! |
| SRPC+FA+HC LPS | 0.0 | -2.71 | -10.55 | #DIV/0! |
| CSA LPS | 0.0 | -2.34 | -6.83 | #DIV/0! |
| CAC LPS | 0.0 | -1.49 | -4.60 | #DIV/0! |
| CAC + SRPC LPS | 0.0 | -2.52 | -7.39 | #DIV/0! |
| CEM II AL NAS M19 | 0.0 | -0.21 | -0.71 | -1.90 |
| SRPC+FA NAS M19 | 0.0 | -0.96 | -1.55 | -3.27 |
| SRPC+FA+HC NAS M19 | 0.0 | -0.51 | -0.87 | -2.07 |
| CSA NAS M19 | 0.0 | 0.15 | 0.10 | -0.91 |
| CAC NAS M19 | 0.0 | 0.28 | 0.27 | -0.27 |
| CAC+SRPC NAS M19 | 0.0 | 0.02 | -0.07 | -1.32 |
| **STDev of mass, %** | | | | |
| CEM II AL LPS | 0.0 | 0.7 | 0.05 | #DIV/0! |
| SRPC+FA LPS | 0.0 | 0.8 | 0.55 | #DIV/0! |
| SRPC+FA+HC LPS | 0.0 | 0.6 | 0.11 | #DIV/0! |
| CSA LPS | 0.0 | 0.1 | 0.78 | #DIV/0! |
| CAC LPS | 0.0 | 0.2 | 0.08 | #DIV/0! |
| CAC + SRPC LPS | 0.0 | 0.5 | 0.58 | #DIV/0! |
| CEM II AL NAS M19 | 0.0 | 0.0 | 0.19 | 0.26 |
| SRPC+FA NAS M19 | 0.0 | 0.3 | 0.57 | 0.74 |
| SRPC+FA+HC NAS M19 | 0.0 | 0.0 | 0.27 | 0.40 |
| CSA NAS M19 | 0.0 | 0.1 | 0.04 | 0.08 |
| CAC NAS M19 | 0.0 | 0.0 | 0.04 | 0.01 |
| CAC+SRPC NAS M19 | 0.0 | 0.0 | 0.04 | 0.01 |
| **Change in thickness, mm** | | | | |
| Date | 28/01/2020 | 06/10/2020 | 28/04/2021 | 03/03/2022 |
| Months | 0 | 8 | 15 | 26 |
| CEM II AL LPS | 0.0 | -1.98 | -3.82 | #DIV/0! |
| SRPC+FA LPS | 0.0 | -0.85 | -2.37 | #DIV/0! |
| SRPC+FA+HC LPS | 0.0 | -0.34 | -2.59 | #DIV/0! |
| CSA LPS | 0.0 | -0.16 | -1.72 | #DIV/0! |
| CAC LPS | 0.0 | -0.17 | -1.09 | #DIV/0! |
| CAC + SRPC LPS | 0.0 | -0.35 | -1.16 | #DIV/0! |
| CEM II AL NAS M19 | 0.0 | -0.30 | -1.85 | -2.78 |
| SRPC+FA NAS M19 | 0.0 | -0.44 | -1.48 | -2.21 |
| SRPC+FA+HC NAS M19 | 0.0 | -0.24 | -0.95 | -1.99 |
| CSA NAS M19 | 0.0 | -0.27 | -0.63 | -1.40 |
| CAC NAS M19 | 0.0 | -0.16 | -0.16 | -0.16 |
| CAC+SRPC NAS M19 | 0.0 | -0.19 | -0.35 | -1.26 |
| **STDev of thickness change, mm** | | | | |
| CEM II AL LPS | 0.0 | 0.38 | 0.91 | #DIV/0! |
| SRPC+FA LPS | 0.0 | 0.01 | 0.35 | #DIV/0! |
| SRPC+FA+HC LPS | 0.0 | 0.04 | 0.59 | #DIV/0! |
| CSA LPS | 0.0 | 0.03 | 0.22 | #DIV/0! |
| CAC LPS | 0.0 | 0.09 | 0.11 | #DIV/0! |
| CAC + SRPC LPS | 0.0 | 0.11 | 0.05 | #DIV/0! |
| CEM II AL NAS M19 | 0.0 | 0.10 | 0.61 | 0.47 |
| SRPC+FA NAS M19 | 0.0 | 0.27 | 0.72 | 0.69 |
| SRPC+FA+HC NAS M19 | 0.0 | 0.01 | 0.22 | 0.30 |
| CSA NAS M19 | 0.0 | 0.02 | 0.13 | 0.24 |
| CAC NAS M19 | 0.0 | 0.06 | 0.06 | 0.06 |
| CAC+SRPC NAS M19 | 0.0 | 0.12 | 0.08 | 0.18 |

## L. Disintegration of calcite and dolomite aggregates in sewers

Dolomite reacts with sulphuric acid to form gypsum, and some magnesium ion which dissociate and react with other ions on the concrete surface to form Mg-bearing phases (Figure L.1). Calcite reacts with sulphuric acid to form Gypsum only (Figure L.2)

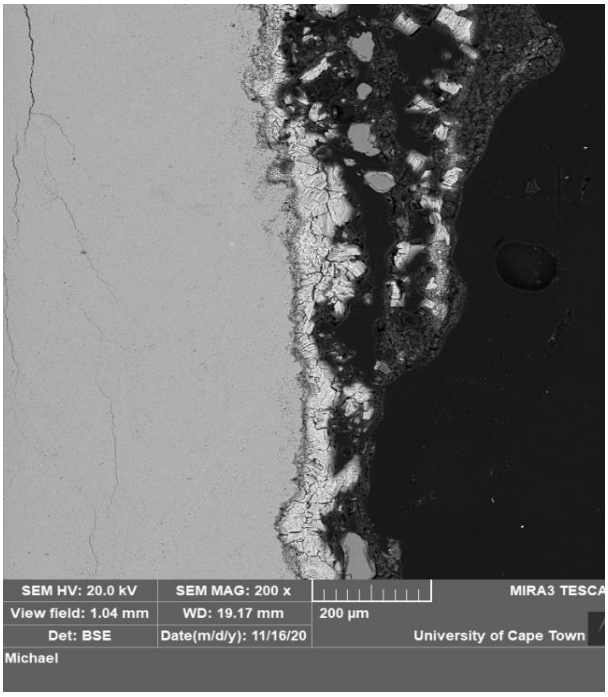


*Figure L.1: Calcite aggregate disintegration under BAC*

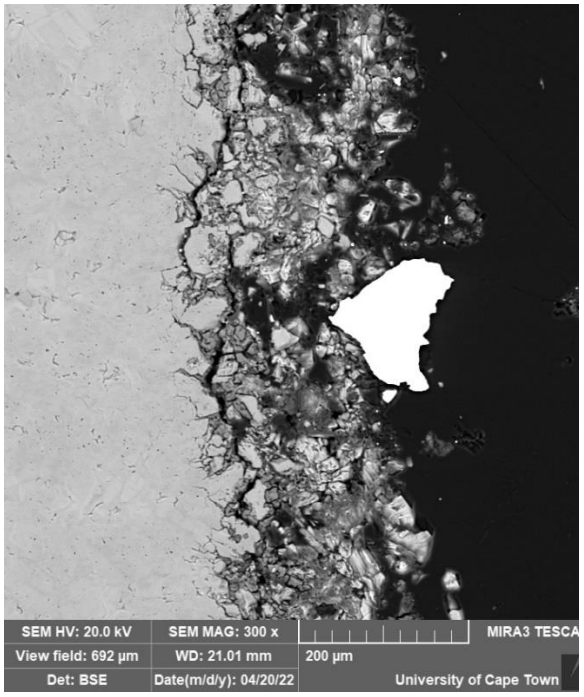


*Figure L.2: Dolomite aggregate disintegration under BAC*

## M. Predicting cementitious phases formed after hydration of concrete

### M.1. Estimation of concrete constituents' volume before and after hydration

The information required for this analysis is extracted from the concrete composition of each concrete mix design. The information includes the weight of individual constituents as per mix design, $M_i$ in kg/m$^3$, Density of each constituent, $\partial_i$ in g/cm$^3$ and the unit volume of an individual constituent, $V_i$ m$^3$/m$^3$

$$V_i = \frac{M_i}{1000\ x\ \partial_i} \quad \text{(M.1)}$$

Volume of total binders, $V_{tb}$

Volume of total water added, $V_{tw}$

Volume of total coarse aggregate, $V_{cagg.}$

Volume of total fine aggregates, $V_{fagg.}$

*Table M.1: Estimation of concrete constituents' volume before and after hydration of SRPC+FA concrete.*

| Mix | | | Before hydration | | After 28 days of maturity, after hydration | |
|---|---|---|---|---|---|---|
| Type | | Relative Density | SRPC+FA | | SRPC+FA | |
| Variables | | | 80% SRPC + 20% FA | | 80% SRPC + 20% FA | |
| w/b | 0.34 | $\partial_i$ | $M_i$ | $V_i$ | $M_i$ | $V_i$ |
| Constituents | Type | | kg/m3 | Unit volume | kg/m3 | Unit volume |
| Binder T1 | CEM I | 3.14 | 329.41 | 0.105 | 324.0 | 0.103 |
| Binder T2 | Fly Ash (FA) | 2.20 | 82.35 | 0.037 | 81.0 | 0.037 |
| Water | Potable | 1.00 | 140.00 | 0.140 | 137.7 | 0.138 |
| Coarse Aggregate | Olifantsfontein Dolomite, 13 mm | 2.87 | 1050.00 | 0.366 | 1032.6 | 0.360 |
| Fine Aggregate | Olifantsfontein Dolomite crusher | 2.87 | 484.72 | 0.169 | 476.7 | 0.166 |
| | Pit sand (filler) | 2.65 | 484.72 | 0.183 | 476.7 | 0.180 |
| Air to the system | Air content | | | | | 0.017 |
| | Total | | 2571.20 | 1.000 | 2528.7 | 1.00 |

### M.2. Estimating PHREEQC input data

The XRF data of each binder, $y_{iz}$ in g$_{_i}$/100 g$_{_binder(z)}$, the weight fraction of each binder, $x_{\_binder(z)}$, degree of hydration of each binder, $\alpha_{\_binder(z)}$ are required for this analysis

Reacted oxide of combined binders, $Ro_i$ in g$_{_i}$/100 g$_{_binder(z)}$

$$Ro_i = \sum (y_{iz} * x_{\_binder(z)} * \alpha_{\_binder(z)}) \quad \text{(M.1)}$$

Convert reacted oxides, in g$_{_i}$/100 g$_{_binder(z)}$ to g$_{_i}$/g$_{_binder}$ $= Ro_i * 100$

Convert reacted oxide in g$_{_i}$/g$_{_binder(z)}$ to Mol$_{_i}$/kg$_{_binder}$ $= \frac{Ro_i * 100}{Mm_i} * 1000$

$Mm_i$ stands for molar mass of individual oxide, in g_i/Mol_i

Table M.2 shows PHREEQC inputs of individual reacted Oxide in Mol_i/kg_binder

*Table M.2: Estimating PHREEQC input data for SRPC+FA concrete mix*

| Oxides | Molar mass | SRPC | FA | Reacted oxide | Reacted Oxides | Reacted oxides |
|---|---|---|---|---|---|---|
| | $Mm_i$ | $y_{iz}$ | $y_{iz}$ | $Ro_i$ | $Ro_i$ | PHREEQC inputs |
| | g/mol | (g/100g_binder) | (g/100g_binder) | g/100 g_binder | g/g_binder) | Mol/kg_binder |
| Lime | 56.08 | 67.95 | 4.32 | 43.66 | 0.44 | 7.79 |
| Amorphous_silica | 60.08 | 21.45 | 53.72 | 15.88 | 0.16 | 2.64 |
| Al2O3 | 101.96 | 3.14 | 32.94 | 3.33 | 0.03 | 0.33 |
| Hematite | 159.69 | 2.17 | 3.23 | 1.52 | 0.02 | 0.10 |
| MgO | 40.30 | 0.95 | 1.07 | 0.65 | 0.01 | 0.16 |
| SO3 | 80.06 | 1.85 | 0.00 | 1.18 | 0.01 | 0.15 |
| Rutile | 79.87 | 0.14 | 1.71 | 0.16 | 0.00 | 0.02 |
| Sum | | 97.65 | 96.99 | 66.38 | 0.66 | |
| | $(z)$ | SRPC | FA | | | |
| Weight fraction | $x_{\_binder(z)}$ | 0.80 | 0.20 | | | |
| Degree of hydration | $\alpha_{\_binder(z)}$ | 0.80 | 0.20 | | | |

*Table M.3: shows the PHREEQC input data estimated from the XRF analysis of each concrete mix design.*

| Binder systems | CEM II A-L | SRPC+FA | SRPC + FA + HC | CSA | CAC |
|---|---|---|---|---|---|
| Oxide constituents | Mol/kg of binder | | | | |
| CaO | 9.1 | 7.79 | 7.86 | 4.24 | 3.37 |
| $SiO_2$ | 2.55 | 2.64 | 2.77 | 0.45 | 0.45 |
| $Al_2O_3$ | 0.30 | 0.33 | 0.34 | 1.70 | 2.43 |
| $Fe_2O_3$ | 0.14 | 0.10 | 0.15 | 0.05 | 0.06 |
| MgO | 0.18 | 0.16 | 0.17 | 0.09 | 0.05 |
| $SO_3$ | 0.18 | 0.15 | 0.15 | 1.12 | 0.00 |
| $TiO_2$ | 0.02 | 0.02 | 0.02 | 0.09 | 0.04 |
| Degree of hydration | 0.8 | 0.8+0.2 | 0.8+0.2+0.2 | 0.5 | 0.5 |

## M.3. Prediction of cementitious phases in each concrete mix after hydration using PHREEQC

In this prediction, the most critical information is the water binder ratio (w/c). Therefore, all input oxides in the reaction block are divided by the w/Bratio. In the solution block, 1 kg of water is added as in input, which means the mass of the binder, i.e., $\frac{1\ kg\ of\ water}{w/c}$

The PHREEQC outputs after hydration are cement hydrates ($\mathrm{CH}\_y$) in Mol_y/1 kg_water, and residual water, ($R.w$) in kg/1 kg_binder.

Cement hydrates in Molarity, $CH_{PhQ\_y}$, in Mol/kg_water

$$CH_{PhQ\_y} = \frac{\mathrm{CH}\_y,\ \text{in Mol}\_\mathrm{y}/\ \text{in kg}\_\mathrm{water}}{R.w,\ \ in\ \mathrm{kg}/1\ \mathrm{kg}\_\mathrm{water}} \quad \text{(M.2)}$$

Calculation unit volume of concrete constituents after hydration, using PHREEQC outputs

Unit volume of residual water,

$$V_{r.w} = R.w * V_{tw} \quad \text{(M.3)}$$

Unit volume of individual cement hydrate,

$$V_{CH\_y} = \frac{M_{tw} * \mathrm{CH}\_y}{1000000} * Mv_y \quad \text{(M.4)}$$

$M_{tw}$ is the weight of water in the concrete mix design, $kg_{\_water}/m^3{}_{\_concrete}$

$Mv_y$ is Molar Volume of individual cement hydrate, $cm^3{}_{\_y}/Mol_{\_y}$

Unit Volume of total cement hydrates,

$$V_{CH} = \sum V_{CH\_y} \quad \text{(M.5)}$$

Unit volume of unhydrated binder,

$$V_{uCH} = \sum((1 - \alpha_{\_binder(z)})V_{\_binder(z)}) \quad \text{(M.6)}$$

Unit volume of pores

$$V_{pores} = 1 - (V_{cagg.} + V_{fagg.} + V_{uCH} + V_{CH} + V_{r.w}) \quad \text{(M.7)}$$

Calculate Molarity, in concrete, Mol/L

$$C_{CH\_y} = \frac{V_{CH\_y}}{Mv_y} * 1000 \quad \text{(M.8)}$$

The concentration of unreacted oxides

$$C_{uCH\_i} = \sum_{z=binder\ 1}^{binder\ n}\left(\frac{y_{iz}}{y_{iz}} * (1 - \alpha_{\_binder(z)})V_{\_binder(z)}\right) \quad \text{(M.9)}$$

The porosity of concrete ($V_{porosity}$) is the summation of chemical shrinkage, pores filled with water remained after hydration and Air content.

Air content was calculated based on the saturated density of the concrete after 28 days of curing. They were using the reverse calculation of the concrete design mix. The content of every constituent of concrete was calculated backwards into mass and, using their relative density, calculated their respective density. Chemical shrinkage was calculated as the difference between a unit volume of concrete and the sum of the volume of all concrete constituents. Pore containing water is equal to the volume of water that remained after hydration

$$V_{Total} = \frac{V_{solids} + V_{water}}{1 - Air_{content}} \quad \text{(M.10)}$$

$$Air_{content} = \frac{V_{Total} - (V_{solids} + V_{water})}{V_{Total}} \quad \text{(M.11)}$$

$V_{Total} = 1.000$ m$^3$, $V_{water} = 0.138$ m3, $V_{solids}$ = 0.846 m$^3$ and $Air_{content}$ = 0.017 m$^3$

*Table M.4: Cementitious phases in each concrete mix design predicted using PHREEQC*

| Binder system | CEM II A-L | SRPC+FA | SRPC + FA + HC | CSA | CAC |
|---|---|---|---|---|---|
| Water/binder | | | 0.34 | | |
| Cement hydrates | | | Mol/kg of water | | |
| C1.6SH | 3.75 | 3.88 | 4.07 | - | - |
| C3AH6 | 0.71 | 0.82 | 0.85 | 1.50 | 2.77 |
| Ettringite ($3CaO.Al_2O_3.3CaSO_4.32H_2O$) | 0.17 | 0.15 | 0.15 | 1.06 | - |
| Gibbsite ($Al(OH)_3$) | - | - | - | 4.87 | 8.70 |
| Portlandite ($Ca(OH)_2$) | 11.72 | 7.13 | 6.63 | - | - |
| Goethite (FeOOH) | 0.82 | 0.59 | 0.88 | 0.29 | 0.35 |
| Brucite ($Mg(OH)_2$) | 0.53 | 0.47 | 0.50 | 0.26 | 0.15 |
| Water ($M_w$), kg of water | 0.36 | 0.44 | 0.43 | 0.04 | 0.41 |

## M.4. HYTEC Input calculation

in the HYTEC model, the concentration of non-hydrated cement, aggregate and sand are not required

$$CH_{Hytec\_y} = \frac{CH_{-y} * M_w}{1000 * V_{porosity}} \quad \text{(M.12)}$$

$M_w$ is the mass of water after hydration, 137.7 kg/m$^3$

*Table M.5: General conversion of PHREEQC output (cementitious phases) to HYTEC input data*

| Phase assemblage | PHREEQC output | | Molar volume | Unit volume | In concrete | HYTEC input |
|---|---|---|---|---|---|---|
| | $CH_{-y}$ | $CH_{PhQ\_y}$ | | $V_{CH\_y}$ | | $CH_{Hytec\_y}$ |
| | Mol in 0.44 kg_water | Mol/kg_water | cm$^3$/mol | m$^3$_i/m$^3$_concrete | Mol/L_concrete | Mol/L |
| Reacted oxide/water ratio | 2.94 | | | | | |
| C1.6SH | 3.88 | 8.771 | 144.09 | 0.08 | 0.53 | 5.338 |
| C4AH13 | 0.82 | 1.861 | 149.52 | 0.02 | 0.11 | 1.133 |
| Ettringite | 0.15 | 0.331 | 710.32 | 0.01 | 0.02 | 0.202 |
| Portlandite | 7.13 | 16.123 | 33.06 | 0.03 | 0.98 | 9.812 |
| Goethite | 0.59 | 1.329 | 20.82 | 0.00 | 0.08 | 0.809 |
| Brucite | 0.47 | 1.063 | 24.63 | 0.00 | 0.06 | 0.647 |
| Hydrates binder | $V_{CH}$ | | | 0.144 | | |
| Water (kg), ($R.w$) | 0.44 | | 18.00 | 0.061 | 3.38 | |
| Unhydrated binder | $V_{uCH}$ | | | 0.050 | | |
| Air content | $Air_{content}$ | | | 0.017 | | |
| Quartz sand | $V_{quartz.}$ | | 22.69 | 0.180 | | |
| Dolomite aggregates | $V_{dolomite.}$ | | 64.37 | 0.526 | | |

| | | | |
|---|---|---|---|
| chemical shrinkage | $V_{shrinkage.}$ | | 0.023 |
| Total volume of concrete | | | 1.000 |
| Total water, air, chemical shrinkage | | $V_{porosity}$ | 0.100 |
| Total porosity in cement paste | | $V_{porosity\_paste}$ | 0.340 |

## M.5. Volume ratio of concrete constituents before and after hydration

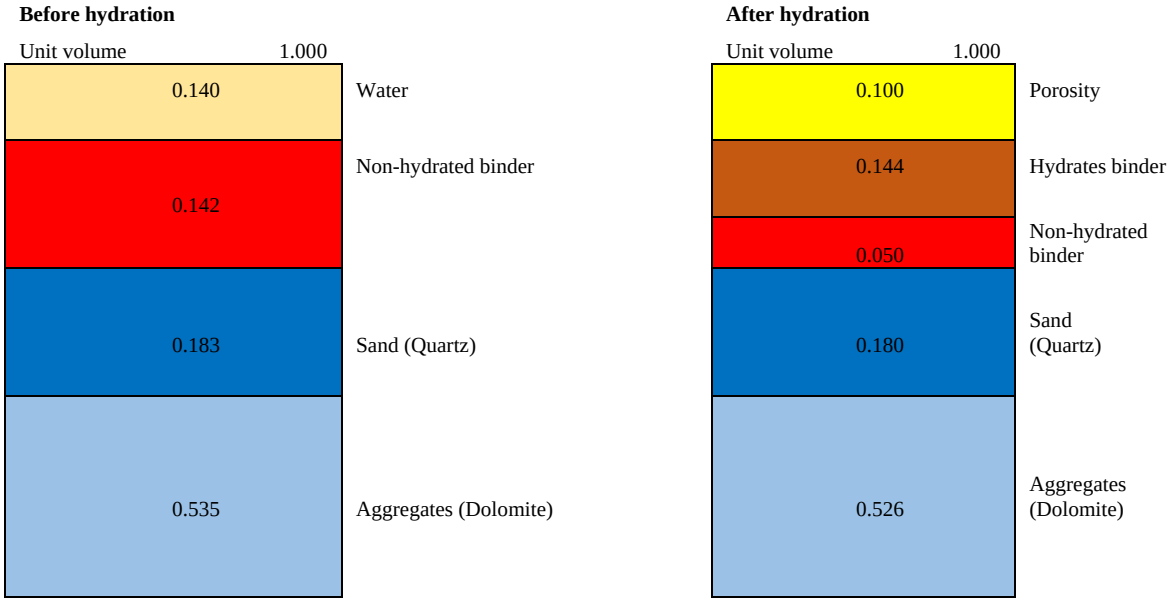

## N. Effect of considering $C_3AH_6$ in HYTEC modelling of acid attack at pH1

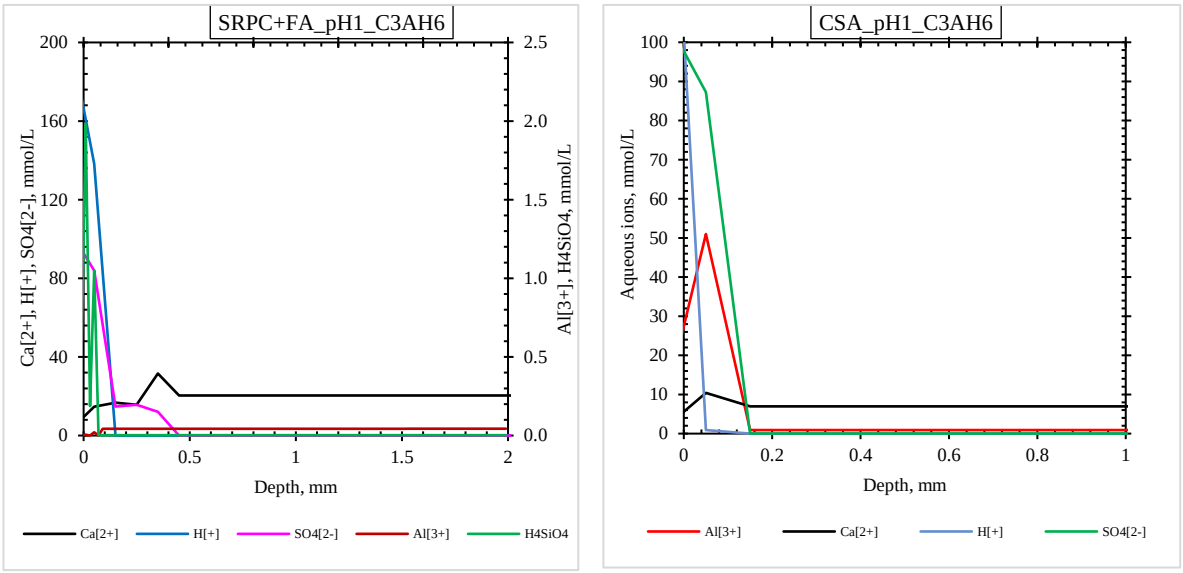


*Figure N.1: SRPC+FA and CSA cement paste with $C_3AH_6$*

## O. Distribution of aqueous ions in cement paste profile after two years of attack

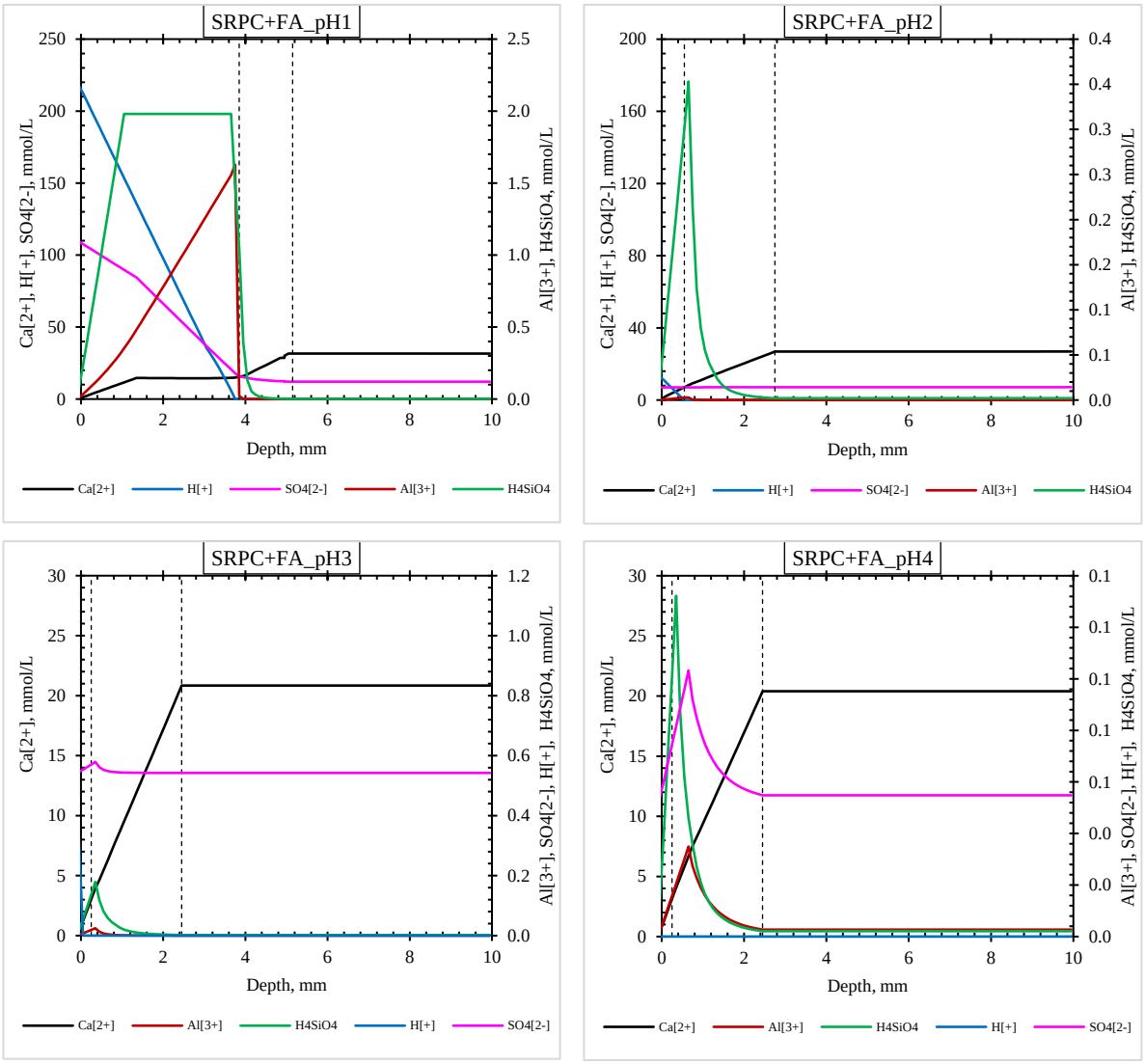


*Figure O.1: Profiles of SRC+FA cement paste show the aqueous ions' distribution when subjected to the open system attack mode of varying pH after two years of exposure*

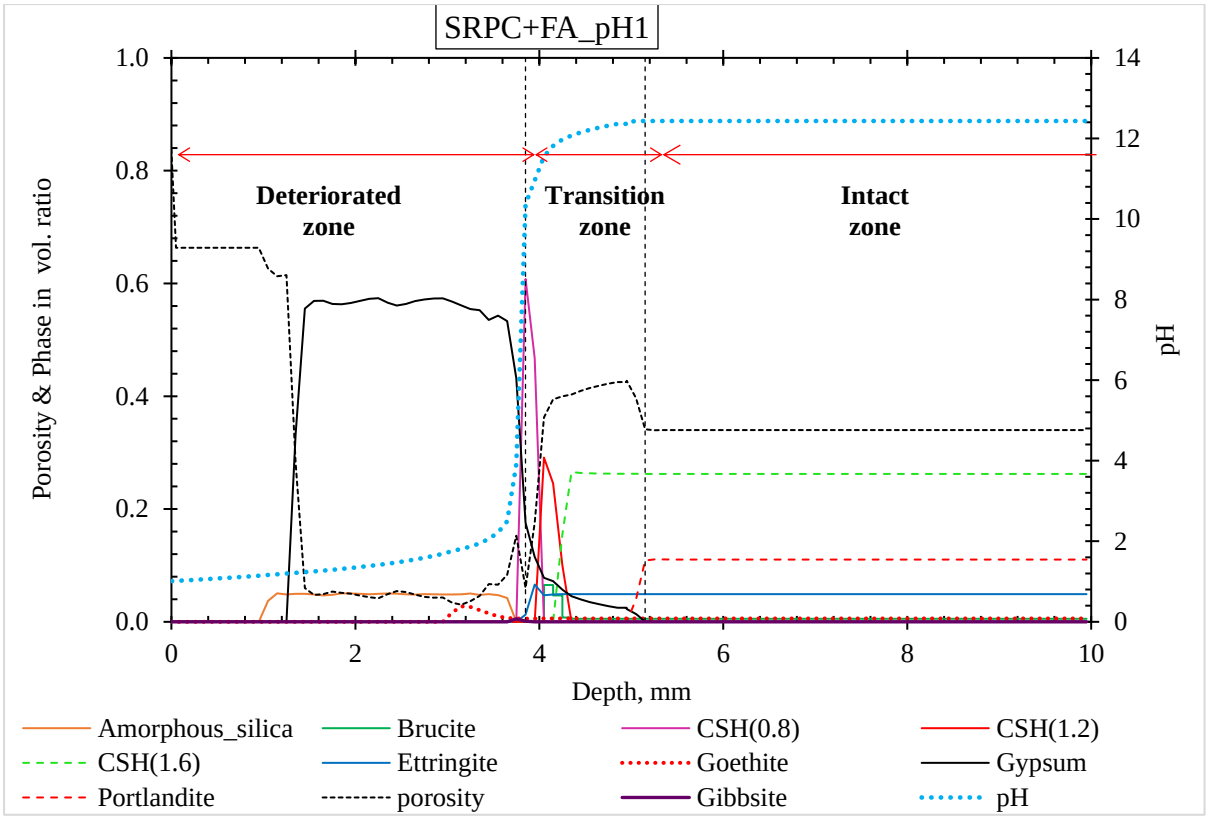


*Figure O.2: Evolution of all cementitious phases, porosity, and pH in the profile of SRPC+FA cement at pH1. This figure includes all phases that is brucite and goethite which were not shown in the main figure.*

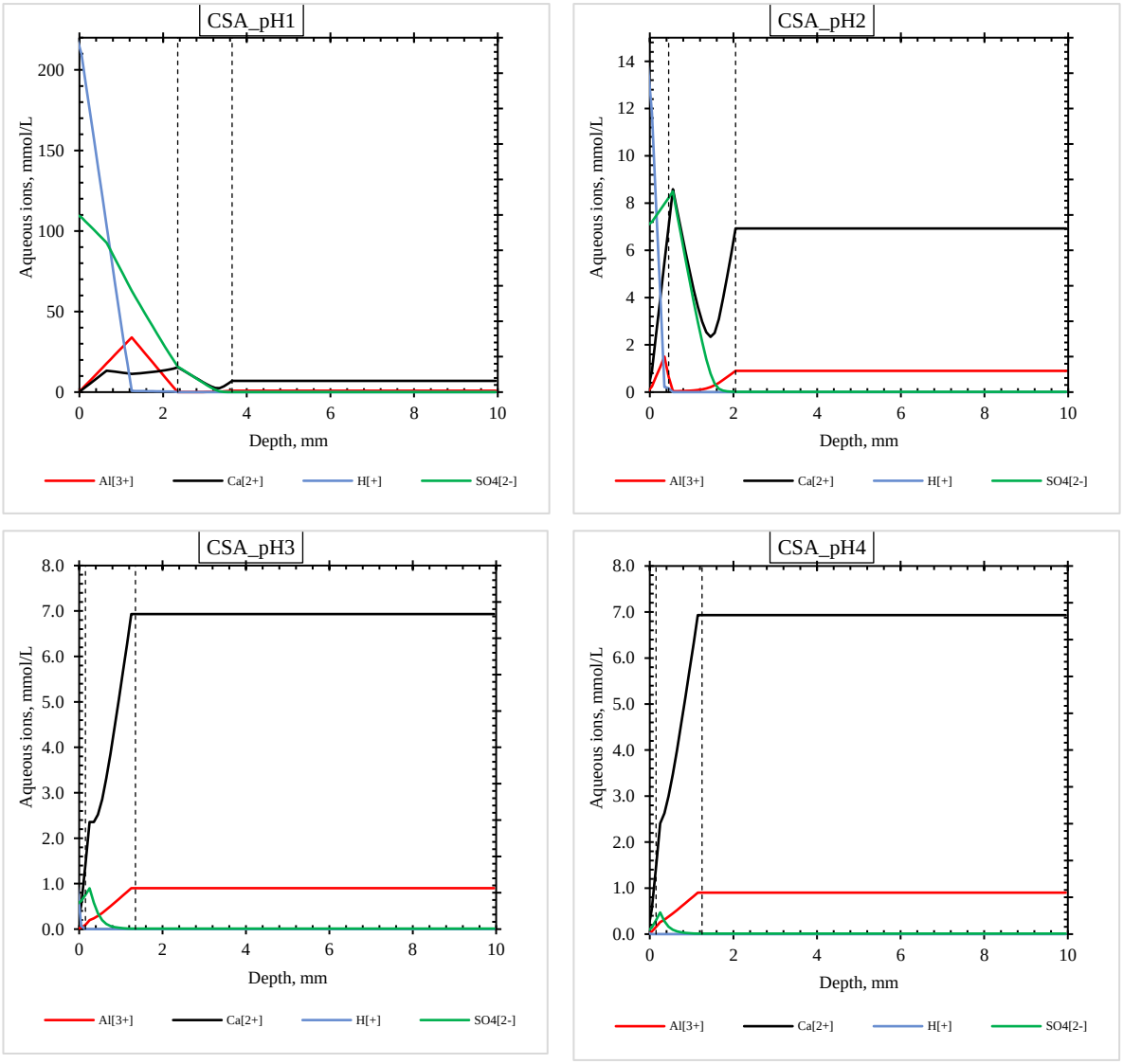


*Figure O.3: Profiles of CSA cement paste showing the distribution of aqueous ions when subjected to the open system attack mode of varying pH after two years of exposure*

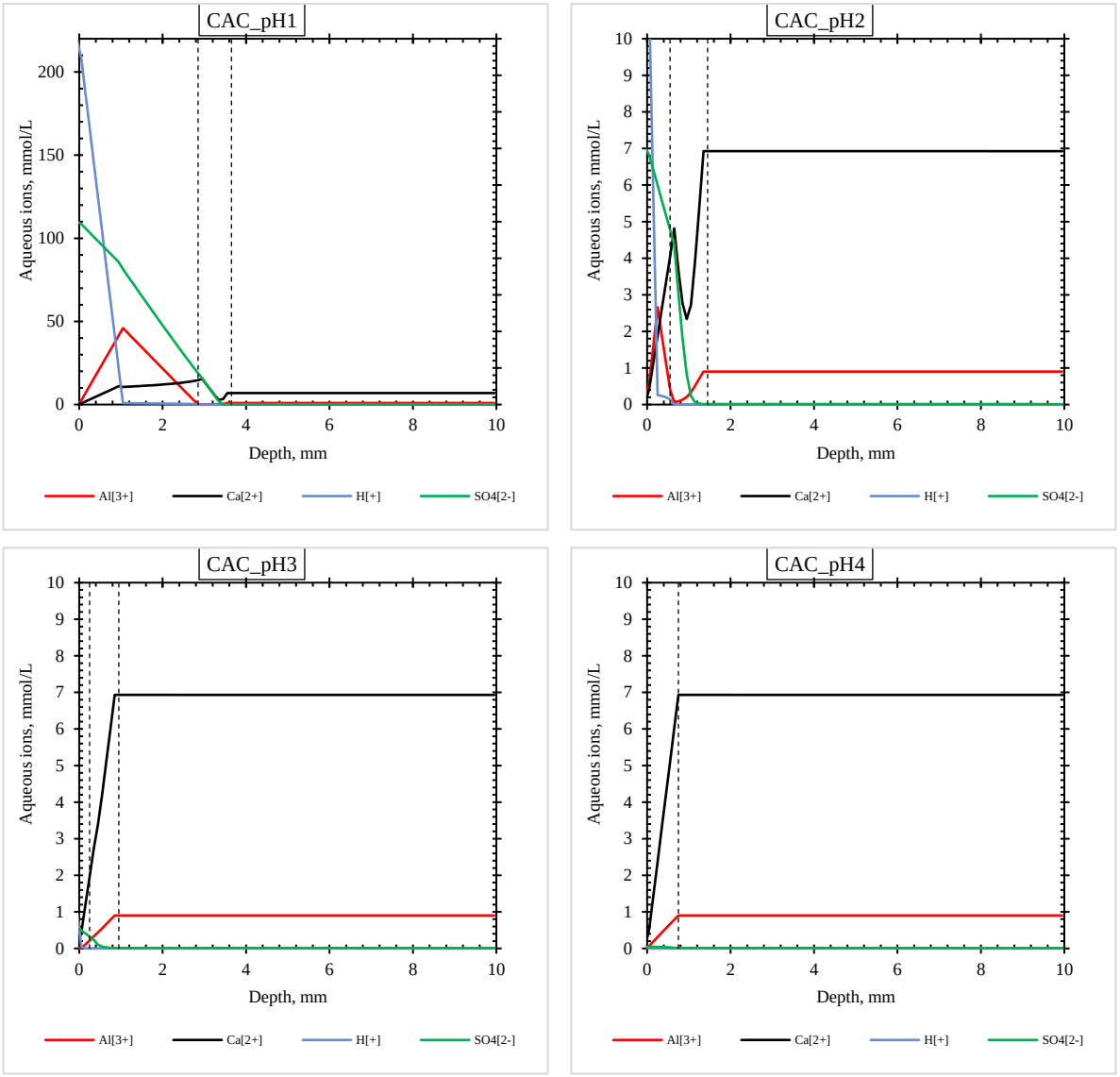


*Figure O.4: Profiles of CAC cement paste showing the distribution of aqueous ions when subjected to the open system attack mode of varying pH after two years of exposure.*

*Table O.1: Summary of deteriorated zone depth total altered depth and Corrosion rate at two years*

| Mode of Attack | Open system at pH1 | | |
|---|---|---|---|
| Binder systems | Deteriorated zone depth, mm | Total altered depth, mm | Predicted corrosion rate, mm/√yr |
| SRPC+FA | 3.85 | 5.15 | 3.59 |
| SRPC+FA+HC | 3.55 | 4.95 | 3.40 |
| CEM II A-L | 4.55 | 6.05 | 4.22 |
| CSA | 2.35 | 3.65 | 2.51 |
| CAC | 2.85 | 3.65 | 2.54 |

## P. Sewer environmental conditions at VES

Computation of Advanced LFM model for concrete mix designs proposed by (Kiliswa, 2016) and extra mixes to cover a wide range of binder and aggregate types at different $H_2S$ gas concentrations, Density of concrete = 2500 kg/m$^3$. Mix design details are shown in Table 7.4. The corrosion rates of mixes shown below were evaluated under different sewer environmental conditions, i.e., annual average $H_2S$ gas concentrations of 20 ppm, 35 ppm, and 50 ppm, an annual average sewer headspace temperature of 23$^o$C, and sufficient relative humidity (70%-100%) to assume that concrete surfaces of all mixes had 0.05 ppm(1-n)/s $H_2S$ adsorption rate

*Table P.1: Evaluation of predicted corrosion rate of a wide range of concrete mixes at different $H_2S$ gas concentrations*

| Concrete mix design | $\varphi$ | $\beta$ | MR | Predicted corrosion rate, at $k_p$ = 0.05; n = 0.5, mm/yr | | | |
|---|---|---|---|---|---|---|---|
| | $\frac{g\_acid}{g\_concrete}$ | $\frac{g\_acid}{g\_concrete}$ | $\frac{g\_acid}{g\_concrete}$ | 20 ppm | 50 ppm | 100 ppm | 200 ppm |
| CAC/AlagTM_20 | 0.41 | 1.06 | 1.47 | 0.44 | 0.70 | 0.99 | 1.97 |
| CAC/AlagTM_16 | 0.33 | 0.95 | 1.28 | 0.51 | 0.80 | 1.13 | 2.27 |
| CAC/DOL_23 | 0.47 | 0.65 | 1.12 | 0.58 | 0.92 | 1.30 | 2.60 |
| CAC/DOL_18 | 0.37 | 0.69 | 1.06 | 0.61 | 0.97 | 1.37 | 2.75 |
| CAC/CAL_23 | 0.47 | 0.56 | 1.03 | 0.63 | 1.00 | 1.41 | 2.82 |
| CAC/DOL_16 | 0.33 | 0.70 | 1.03 | 0.63 | 1.00 | 1.41 | 2.83 |
| CSA/DOL_23 | 0.38 | 0.65 | 1.02 | 0.64 | 1.00 | 1.42 | 2.84 |
| CSA/DOL_18 | 0.29 | 0.69 | 0.98 | 0.66 | 1.05 | 1.48 | 2.96 |
| CAC/CAL_18 | 0.37 | 0.60 | 0.97 | 0.67 | 1.06 | 1.49 | 2.99 |
| CSA/DOL_16 | 0.26 | 0.70 | 0.96 | 0.68 | 1.07 | 1.51 | 3.02 |
| CSA/CAL_23 | 0.38 | 0.56 | 0.93 | 0.70 | 1.10 | 1.56 | 3.11 |
| PC/DOL_23 | 0.29 | 0.65 | 0.94 | 0.69 | 1.09 | 1.54 | 3.09 |
| CAC/CAL_16 | 0.33 | 0.60 | 0.93 | 0.70 | 1.10 | 1.56 | 3.12 |
| PC/DOL_18 | 0.22 | 0.69 | 0.91 | 0.71 | 1.12 | 1.59 | 3.18 |
| PC/GGBS/DOL_18 | 0.15 | 0.69 | 0.84 | 0.77 | 1.22 | 1.73 | 3.46 |
| PC/FA/DOL_18 | 0.16 | 0.69 | 0.85 | 0.76 | 1.20 | 1.70 | 3.41 |
| PC/DOL_16 | 0.21 | 0.70 | 0.90 | 0.72 | 1.14 | 1.61 | 3.21 |
| PC/SF/DOL_18 | 0.19 | 0.69 | 0.88 | 0.74 | 1.16 | 1.65 | 3.29 |
| PC/CAL_23 | 0.29 | 0.59 | 0.88 | 0.74 | 1.17 | 1.65 | 3.30 |
| CSA/CAL_18 | 0.29 | 0.59 | 0.89 | 0.73 | 1.16 | 1.63 | 3.27 |
| CSA/CAL_16 | 0.26 | 0.60 | 0.87 | 0.75 | 1.19 | 1.68 | 3.36 |
| PC/CAL_18 | 0.22 | 0.59 | 0.82 | 0.79 | 1.25 | 1.77 | 3.55 |
| PC/CAL_16 | 0.20 | 0.60 | 0.80 | 0.81 | 1.28 | 1.81 | 3.62 |
| CAC/SIL_23 | 0.47 | 0.00 | 0.47 | 1.38 | 2.18 | 3.08 | 6.16 |
| CSA/SIL_23 | 0.38 | 0.00 | 0.38 | 1.73 | 2.73 | 3.87 | 7.73 |
| CAC/SIL_18 | 0.37 | 0.00 | 0.37 | 1.76 | 2.78 | 3.94 | 7.88 |
| CAC/SIL_16 | 0.33 | 0.00 | 0.33 | 1.98 | 3.13 | 4.43 | 8.86 |
| CSA/SIL_18 | 0.29 | 0.00 | 0.29 | 2.21 | 3.49 | 4.94 | 9.88 |
| PC/SIL_23 | 0.29 | 0.00 | 0.29 | 2.27 | 3.59 | 5.07 | 10.14 |
| CSA/SIL_16 | 0.26 | 0.00 | 0.26 | 2.49 | 3.93 | 5.56 | 11.11 |
| PC/SIL_18 | 0.22 | 0.00 | 0.22 | 2.90 | 4.58 | 6.48 | 12.96 |
| PC/SIL_16 | 0.20 | 0.00 | 0.20 | 3.26 | 5.16 | 7.29 | 14.58 |

Sewer environmental factor for Turbulence flow: Re > 4000, use Re = 5000

$$\phi_{sw} = 3600 \left(101325 * \frac{98}{8.31*(273+T)} * \frac{0.9}{4} * \frac{kp}{1000000}\right) * 5000^{0.65} * \left(\frac{H2S}{1000000}\right)^{n}$$

$\phi_{sw}$ is equal to 0.186 g/m$^2$/h , 0.293 g/m$^2$/h, 0.415 g/m$^2$/h, and 0.830 g/m$^2$/h at 20 ppm, 50 ppm, 100 ppm, and 200 ppm respectively. Temperature = 23$^o$C

## Q. Measured corrosion rate at VES against LFM predicted corrosion rate

*Table Q.1: Corrosion rates extracted from previous work at VES (Goyns, 2009; Alexander & Fourie, 2011; Kiliswa, 2016; Goyns & Alexander, 2018)*

| Concrete mix design | Measured corrosion rate, mm/yr at VES | | | | $\varphi$ | $\beta$ | MR | Predicted corrosion rate, at $H_2S$ = 35 ppm; n = 0.5, mm/yr | | |
|---|---|---|---|---|---|---|---|---|---|---|
| | Avg | Min | Max | STDev | $\frac{g\_acid}{g\_concrete}$ | $\frac{g\_acid}{g\_concrete}$ | $\frac{g\_acid}{g\_concrete}$ | kp= 0.025 | kp= 0.05 | kp= 0.1 |
| CAC/AlagTM_20 | 0.25 | 0.17 | 0.34 | 0.08 | 0.41 | 1.06 | 1.47 | 0.29 | 0.58 | 1.17 |
| CAC/AlagTM_16 | 0.25 | 0.17 | 0.34 | 0.08 | 0.33 | 0.95 | 1.28 | 0.34 | 0.67 | 1.34 |
| CAC/DOL_23 | 0.33 | 0.27 | 0.38 | 0.06 | 0.47 | 0.65 | 1.12 | 0.38 | 0.77 | 1.54 |
| CAC/DOL_18 | 0.51 | 0.45 | 0.57 | 0.06 | 0.37 | 0.69 | 1.06 | 0.41 | 0.81 | 1.62 |
| CAC/DOL_16 | 0.55 | 0.51 | 0.6 | 0.04 | 0.33 | 0.70 | 1.03 | 0.42 | 0.84 | 1.67 |
| PC/DOL_23 | 1.48 | 1.11 | 1.85 | 0.37 | 0.29 | 0.65 | 0.94 | 0.46 | 0.91 | 1.83 |
| PC/DOL_18 | 1.3 | 1.26 | 1.34 | 0.04 | 0.22 | 0.69 | 0.91 | 0.47 | 0.94 | 1.88 |
| PC/GGBS/DOL_18 | 1.26 | 1.03 | 1.5 | 0.23 | 0.15 | 0.69 | 0.84 | 0.51 | 1.02 | 2.04 |
| PC/FA/DOL_18 | 1.07 | 0.97 | 1.17 | 0.1 | 0.16 | 0.69 | 0.85 | 0.50 | 1.01 | 2.01 |
| PC/DOL_16 | 1.14 | 0.79 | 1.48 | 0.35 | 0.21 | 0.70 | 0.90 | 0.48 | 0.95 | 1.90 |
| PC/SF/DOL_18 | 1.14 | 0.98 | 1.3 | 0.16 | 0.19 | 0.69 | 0.88 | 0.49 | 0.97 | 1.95 |
| CAC/SIL_23 | 0.33 | 0.29 | 0.36 | 0.04 | 0.47 | 0.00 | 0.47 | 0.91 | 1.82 | 3.65 |
| PC/SIL_16 | 4.5 | 4.3 | 4.7 | 0.2 | 0.20 | 0.00 | 0.20 | 2.16 | 4.31 | 8.63 |

Sewer environmental factor for Turbulence flow: Re > 4000, use Re = 5000

$$\phi_{sw} = 3600\left(101325 * \frac{98}{8.31*(273+T)} * \frac{0.9}{4} * \frac{kp}{1000000}\right) * 5000^{0.65} * \left(\frac{H2S}{1000000}\right)^{n}$$

$\phi_{sw}$ is equal to 0.123 g/m$^2$/h, 0.245 g/m$^2$/h, and 0.491 g/m$^2$/h at kp equal to 0.025 ppm$^{(1-n)}$/s, 0.05 ppm$^{(1-n)}$/s and 0.1 ppm$^{(1-n)}$/s when H2S is equal to 35 ppm and temperature equal to 23$^o$C, respectively.

## R. Evaluation of UCT concrete Material resistance factor (MR)

UCT concrete MR factors were evaluated based on their ingredient mix proportions (Table 3.5), chemical composition (Table 3.2), and 28-day saturated densities (Figure 5.22). With an assumption that full hydration of concrete was achieved.

*Table R.1:: UCT concrete mix design with constituents in percentages, saturated density and predicted material resistance factor, according to the chemical composition (XRF in Table 7.3) of the binder and aggregates used*

| UCT Concrete Mix | Concrete ingredient, % | | | | | Saturated Density | $\varphi$ | $\beta$ | MR |
|---|---|---|---|---|---|---|---|---|---|
| | SCM | Cement | DOL Coarse Agg. | DOL Crusher sand | SIL Filler sand | kg/m$^3$ | $\frac{g}{g\_concrete}$ | $\frac{g\_acid}{g\_concrete}$ | $\frac{g\_acid}{g\_concrete}$ |
| CEM II AL | 0.0 | 16.3 | 41.5 | 19.8 | 19.8 | 2529 | 0.21 | 0.75 | 0.96 |
| SRPC+FA | 3.3 | 13.0 | 41.3 | 19.1 | 19.1 | 2540 | 0.21 | 0.74 | 0.95 |
| SRPC+FA+HC | 3.3 | 13.1 | 41.8 | 19.2 | 19.2 | 2514 | 0.21 | 0.75 | 0.96 |
| CSA | 0.0 | 16.0 | 40.8 | 18.5 | 18.5 | 2574 | 0.23 | 0.72 | 0.96 |
| CAC + SRPC | 8.1 | 8.1 | 41.3 | 19.7 | 19.7 | 2542 | 0.28 | 0.75 | 1.03 |
| CAC | 0.0 | 16.0 | 40.8 | 19.2 | 19.2 | 2575 | 0.34 | 0.73 | 1.08 |

# S. Sewer environmental conditions at LPS and NAS M19

*Table S.1:: Sewer environmental condition at LPS and NAS 19 used for calculating the 90th percentile of the maximum reading of monthly reading per year.*

| **Sewer environmental conditions LPS** | | | | | | | | | | |
|---|---|---|---|---|---|---|---|---|---|---|
| Months, 2021 | | March | April | May | June | July | August | September | October | November |
| H2S, ppm | Av. | 63 | 56 | 57 | 44 | 61 | 44 | 38 | 37 | 51 |
| | Max | 363 | 152 | 95 | 78 | 137 | 179 | 179 | 111 | 349 |
| | Min | 9 | 13 | 9 | 15 | 8 | 7 | 3 | 5 | 8 |
| Tempereture (ºC) | Av. | 26.5 | 23.9 | 23.6 | 23.5 | 17.7 | 17.7 | 18.2 | 22.2 | 22.1 |
| | Max | 28.3 | 24.3 | 24.3 | 24.3 | 19.5 | 19.5 | 20.1 | 22.8 | 22.8 |
| Relative humidity | Av. | 77.4 | 82.9 | 84.0 | 85.7 | 86.6 | 86.0 | 84.0 | 82.5 | 80.6 |
| | Max | 78.5 | 84.1 | 86.2 | 90.1 | 90.7 | 88.2 | 86.2 | 85.4 | 82.7 |
| $90^{th}$ percentile | | Max.$H_2S$ | **351** | **ppm** | Max.Temp | **25** | **oC** | Max.RH | **90.2** | **%** |

| **Sewer environmental condition NAS M19** | | | | | | | | | | |
|---|---|---|---|---|---|---|---|---|---|---|
| Months,2021 | | March | April | May | June | July | August | September | October | November |
| H2S, ppm | Av. | 30 | 17 | 6 | 9 | 7 | 4 | 5 | 9 | 14 |
| | Max | 105 | 101 | 41 | 45 | 23 | 23 | 12 | 25 | 40 |
| | Min | 0 | 3 | 1 | 0 | 0 | 1 | 1 | 1 | 1 |
| Tempereture (Oc) | Av. | 26.1 | 27.0 | 26 | 20.8 | 18.2 | 19.2 | 21.0 | 23.9 | 26.8 |
| | Max | 26.6 | 28.0 | 28 | 24.0 | 20.1 | 19.7 | 22.0 | 24.4 | 27.4 |
| Relative humidity | Av. | 85.1 | 85.8 | 90 | 94.4 | 97.8 | 90.8 | 85.3 | 79.9 | 74.4 |
| | Max | 88.0 | 88.2 | 92 | 95.5 | 98.2 | 92.2 | 87.2 | 81.2 | 75.4 |
| $90^{th}$ percentile | | Max.$H_2S$ | **102** | **ppm** | Max.Temp | **28** | **oC** | Max.RH | **96.04** | **%** |